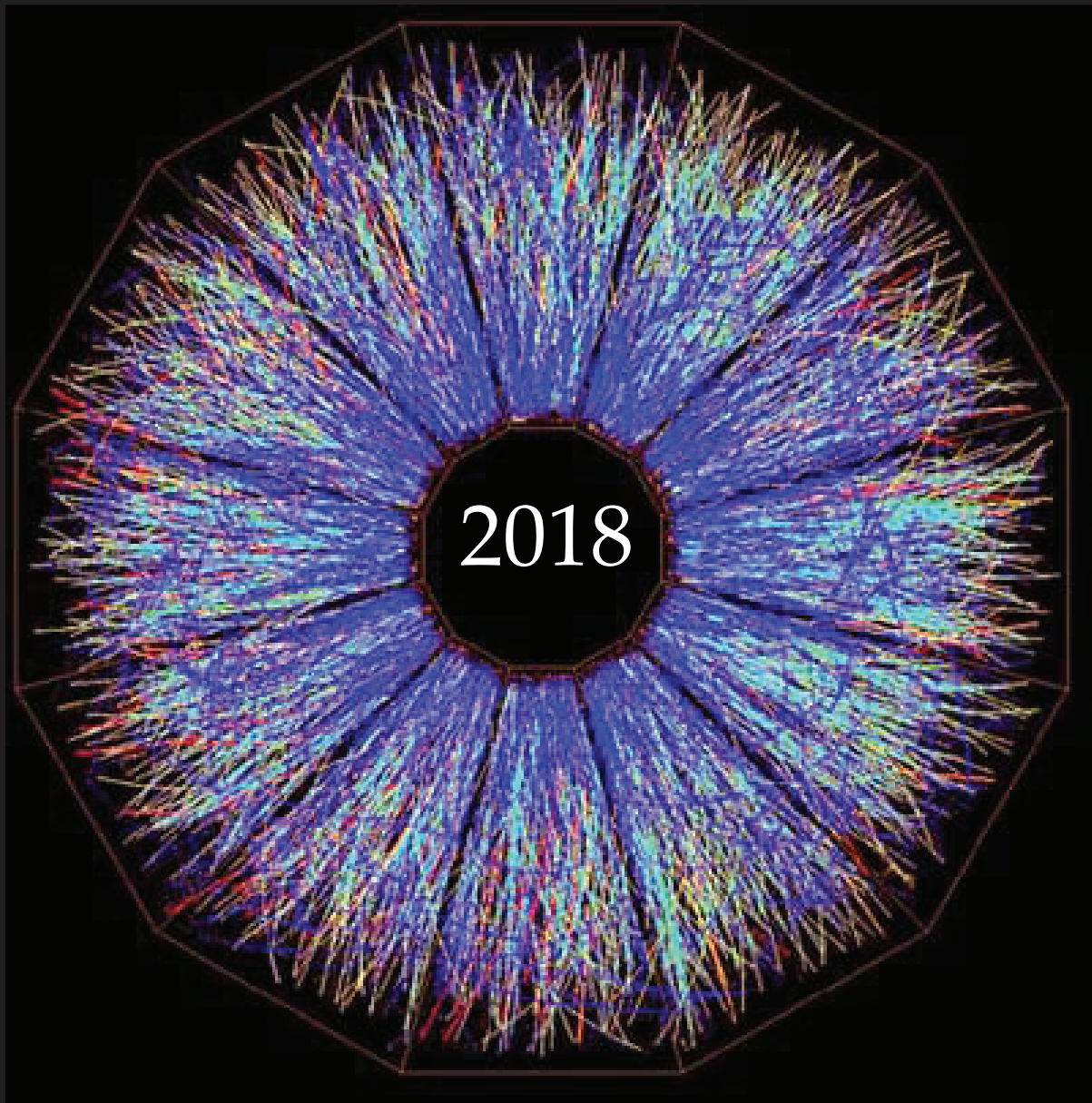


A Compilation of Internship Reports



Prepared for The Office of Educational Programs
Brookhaven National Laboratory
Office of Educational Programs

DISCLAIMER

This work was prepared as an account of work sponsored by an agency of the United States Government. Neither the United States Government nor any agency thereof, nor any of their employees, nor any of their contractors, subcontractors or their employees, makes any warranty, express or implied, or assumes any legal liability or responsibility for the accuracy, completeness, or any third party's use or the results of such use of any information, apparatus, product, or process disclosed, or represents that its use would not infringe privately owned rights. Reference herein to any specific commercial product, process, or service by trade name, trademark, manufacturer, or otherwise, does not necessarily constitute or imply its endorsement, recommendation, or favoring by the United States Government or any agency thereof or its contractors or subcontractors. The views and opinions of authors expressed herein do not necessarily state or reflect those of the United States Government or any agency thereof.



BROOKHAVEN
NATIONAL LABORATORY

Table of Contents

Dipole magnet reconfiguration	7
<i>Brandon Abad</i>	
Weak lensing with lyman- α forests	14
<i>Prakruth Adari</i>	
Locating the genes responsible for Arabidopsis mutants through map-based cloning	17
<i>Kathryn Bischoff</i>	
<i>Salimata Guene Fall</i>	
Assembly of magnet girders for the Cornell-Brookhaven National Laboratory Energy Recovery Linac Test Accelerator	23
<i>Brian Brenton</i>	
Finite element magnetic modelling of the LEReC 180° dipole magnet	27
<i>Tristan Britt</i>	
Testing and commissioning the cold electronics for the Short Baseline Near Detector	31
<i>Justin Bryant</i>	
Using a laser ion source to produce and study heavy ions from chemical compound targets	33
<i>Harry Chalfin</i>	
Enabling data collection for a cosmic ray shower detector	37
<i>Junjie Chen</i>	
Automating the development of a Global Nuclear Reaction Data Library	40
<i>Kayla Clements</i>	
XANES/EXAFS analysis of zirconium-based adhesive thin film	44
<i>Bryan Conry</i>	
Simulated analysis on the properties of ‘tree rings’ in the Large Synoptic Survey Telescope sensors	50
<i>Matthew S Decaro</i>	
Quench behavior estimate and its relation to turn-to-turn stress distribution for a 25 T HTS magnet	55
<i>John Delaney and Ryan Tomastik</i>	
Making sense of system logs: Implementing centralized system log storing, indexing, querying, and visualizing software on a heterogeneous network	61
<i>Jonathan Dolde</i>	
Extracting provenance metadata for the Exascale Computing Project Co-design Center for Online Data Analysis and Reduction.	65
<i>Mohammed Endris, Behiru Shifa, and Mulugeta Dugda</i>	

An intern’s experience as a construction safety engineer at a national laboratory	70
<i>Trevor Gallagher</i>	
A novel E3 ligase	72
<i>Vignesh Gunasekaran</i>	
The updating of radioactive material tags for activated materials	75
<i>Craig Hamilton</i>	
Single photon detection for Bell state coincidences using Timepix3 camera.	77
<i>Andrew Koehler Hardy</i>	
Radiation chemistry in molten salts and ionic liquids	80
<i>Chaudhary Harris</i>	
Developing sPHENIX subsystem outline interface drawings	86
<i>Michael Harris</i>	
Building and customizing a data repository with the Invenio/Zenodo platform	89
<i>John Harrison</i>	
Sample metadata acquisition at the National Synchrotron Light Source II.	92
<i>Sabrina Hernandez</i>	
Spectral and phenological drought assessment in common crops	96
<i>Gwen Hilles</i>	
Developing a monitoring tool for tracking changes in critical control values at NSLS-II . . .	99
<i>Jeremy Hirsch</i>	
Magnetic field measurements of the production Nb ₃ Sn quadrupole for the High Luminosity Large Hadron Collider Upgrade Program	102
<i>B.D Hunt and J. Rowe</i>	
Designing a two-channel data acquisition front-end board for a particle physics cosmic ray muon detector	106
<i>Ramez Kaupak</i>	
Value engineering on the infrastructure of the NSLS-II beamlines	108
<i>John Lavelle</i>	
Intercomparison of Particle-Soot Absorption Photometer (PSAP) Sample Filter Media. . .	112
<i>Pedro A. León Bergodere and Olga L. Mayol Bracero</i>	
Development of a flexible analysis portal based on Jupyter notebooks for the Brookhaven National Laboratory Scientific Data and Computing Center	116
<i>Kristy Li</i>	
Design and analysis for the ATF-II CO ₂ laser amplifier output window	120
<i>Paul Li</i>	

Developing a Matlab program to test preamplifiers for the sPHENIX detector	125
<i>Chris Marrs</i>	
The design and analysis of the liquid cooling system for the electromagnetic calorimeter of sPHENIX	129
<i>John Meier</i>	
Tests of astronomical image deblenders for gravitational lensing	133
<i>Lorena Mezini</i>	
Black carbon and carbon monoxide source assessment in the Amazon during the Green Ocean Amazon (GOAmazon) 2014/5 Campaign	138
<i>Maité Morales Medina and Olga L. Mayol-Bracero</i>	
Spectra of identified particles in gold on gold fixed target collision at 4.5 GeV with STAR detector	141
<i>Jesus D. Negrete and Jason Bryslawskyj</i>	
Development of the hardware for the puck visualization system for determining the presence of samples under liquid nitrogen	144
<i>Rachael Ng</i>	
Using Monte Carlo methods to estimate occupational dosage during ^{225}Ac production	149
<i>Drake Niedzielski</i>	
ENDF/B-VIII.0 library application to nuclear astrophysics.	158
<i>Lauren Osojnak</i>	
Investigating the structure of laccases for biofuels.	163
<i>Shahla Partowmah and Robert Collins</i>	
Electronic structure characterization of metal organic frameworks using ambient pressure photoelectron spectroscopy	166
<i>Brianna Perris</i>	
Lithographic calibration patterns for Low Energy Electron Microscopy.	171
<i>Brady Robertson</i>	
Purification and Crystallization of sucrose transporters (SUC2) from <i>Arabidopsis thaliana</i> . .	174
<i>Zahir Safie</i>	
Process controls using LabVIEW software	178
<i>Maxwell Santiago</i>	
Investigating the effects of drought on crop species using biochemical analysis	180
<i>Kelly Scanlon</i>	
CCD sensor calibration using ^{55}Fe spectra	183
<i>Jackson Schall</i>	

Comprehensive stray radiation measurements inside the first optical enclosure of the 07-ID-A beamline at NSLS-II	188
<i>Aaron R. Taylor, Erika I. Martinez. and Jessica E. Schweitzer</i>	
Wire-Cell tomographic imaging evaluation.	192
<i>Deepsana Shahi</i>	
Integrating X-ray simulation with data acquisition software	196
<i>Kaleb Swartz</i>	
Creation of the App Conversion Tool and App Discovery Tool for the centralized deployment mechanism of the NSLS-II control system using Bash and Ansible	199
<i>Ian Talla</i>	
Expression, purification, and characterization of sucrose transporter SUC1 from <i>Arabidopsis</i> <i>thaliana</i>	203
<i>Gianna Trillo</i>	
Evaluation of the ACQ1001-FMC Digitizer	206
<i>Abby Tse</i>	
Analysis of the Data Challenge 2 catalogs generated for the Large Synoptic Survey Telescope by the Dark Energy Science Collaboration using the Friends-of-Friends catalog matching algorithm.	211
<i>Bhairav Valera</i>	
Observational analysis of pollinators and their resources: Long Island Central Pine Barrens Forest	214
<i>Dulaine Vining</i>	
Implementation of a digital repository catalog prototype using the Invenio framework at the Scientific Data and Computing Center	216

Dipole magnet reconfiguration

Brandon Abad

Department of Mechanical Engineering, Worcester Polytechnic Institute, Worcester, MA 01609

Charles Pearson

Collider Accelerator Department, Brookhaven National Laboratory, Upton, NY 11973

Abstract

Throughout my ten weeks at Brookhaven National Laboratory (BNL), I worked on various mechanical engineering problems with the Collider Accelerator Department, the focus being to reconfigure a dipole magnet for a dark matter experiment. The goal of this project was to take two pre-existing dipole magnets and reconfigure them into one large dipole magnet. The final magnet had to meet the requirements of a magnetic field strength of 1 tesla and a gap of $2^{1/8}$ inches. While designing the magnet to meet the required field strength and gap size I also had to restrict the design to utilize the available operating resources in the building where the magnet would reside. These resources included available power, cooling water, space, and rigging capacity. In order to solve these problems I calculated the running temperature of the magnet, the flow rate of coolant needed, the number of turns in the coil, the total power needed, and designed parts to reduce the gap from $5^{1/8}$ inches to $2^{1/8}$ inches. The final weight of the magnet was 1400lbs requiring me to install a properly sized lifting eye to safely rig and transport the magnet. Before the magnet is assembled the coils needed to be tested for resistance, turn to turn insulation, ground insulation, and flow. These tests are necessary in ensuring the magnet is going to operate safely and as calculated. After the magnet passes the testing stage it is ready to be assembled and transported to the lab where it will be used. This 10-week internship program exposed me to real life mechanical engineering problems, allowed me to work on a project from start to finish, and experience problems along the way that I otherwise would not have experienced in a school setting.

I. Background

Dipole magnets are magnets that have two poles, a north and south. Dipole magnets can be in the form of a permanent magnet or an electromagnet. A permanent magnet is made of a magne-

tized material that can create its own magnetic field without the help of an electric current. These are common magnets that you may find on your refrigerator or used to decorate the back of your car. Electromagnets on the other hand are made of coiled wire around an iron core. When the wire has electric current flowing through it a magnetic field is created. This gives the operator the ability to turn the magnet on and off and control the strength of the magnetic field. This control comes from increasing the amperage, which in return increases the magnetic field strength.

Magnetic fields flow from the north pole of the magnet to the south pole and straighten where the poles are closest. The figure below is a simple bar dipole magnet with the depiction of the magnetic field lines:

The Dipole magnet I was working with was an electromagnet. This Dipole also had a gap of $2^{1/8}$ inches between the north and south pole. The Core of the magnet is made of low carbon steel. This material causes the magnetic fields to travel within it as it loops from the north pole to the south pole. An example of this is depicted below with a diagram of the magnet I designed:

A property of electromagnets is that they heat up due to the resistance in the coil and the amount of current flowing through the coil. To increase the magnetic field strength it is required to increase the current when operating the magnet. As current increases there are more electrons colliding with the conductor at a given point creating heat. This is known as

Joule Heating and can be represented by a derivation of Ohm's Law:

$$P = I^2 R$$

In this equation P is the power converted from electrical energy to thermal energy. Current being squared shows how much of an influence it has on the thermal energy of the coil.

When a non-magnetic conductor is placed in a magnetic field and moves within it, a current loop can be formed. This current loop is formed in the conductor and is known as an eddy current. The eddy current causes the conductor to create its own magnetic

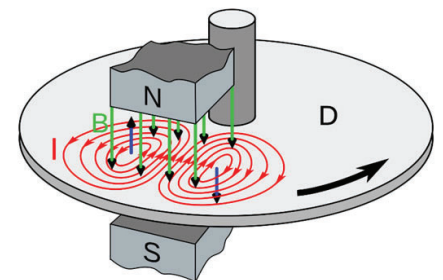
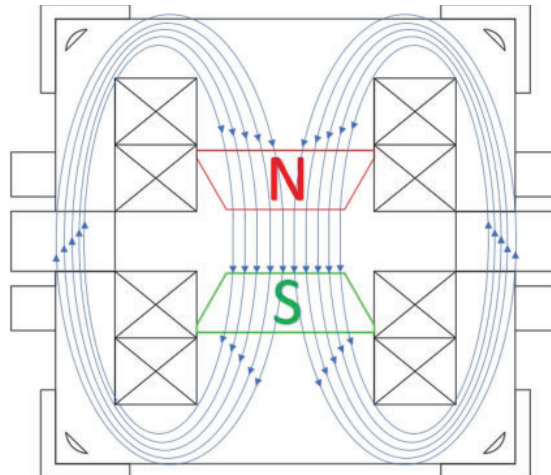
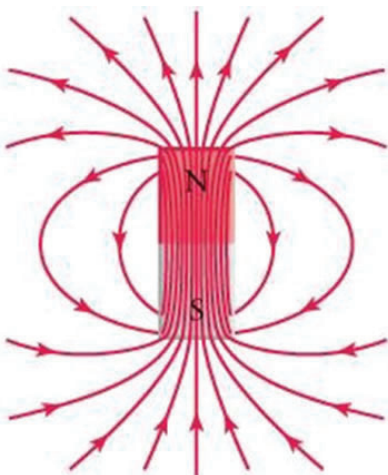


Figure 1 (left): Magnetic field line in a dipole bar magnet (texasgateway.org)

Figure 2 (center): Magnetic field lines in dipole magnet with $2^{1/8}$ gap

Figure 3: (right) Eddy Current Break

field opposing its motion. There are many applications for eddy currents, one being eddy current breaks.

In the figure above the red lines represent the eddy currents created from a spinning conductor inside of the magnetic field. These currents create magnetic fields, shown in blue, relative to the direction they are rotating. On the left edge of the magnet the magnetic flux is increasing, causing the current to flow counter-clockwise producing a magnetic field towards the north pole. On the right edge of the magnet the magnetic flux is decreasing causing the current to flow in the clockwise direction and producing a magnetic field towards the south pole. Both the magnetic fields that are created from the eddy current attract the moving plate to the fixed magnet opposing its motion.

The magnet I reconfigured will be used to test a cavity that will later be used for a dark matter experiment. This test will use eddy currents, as described above, to dampen the cavity lowering the amplitude in frequency caused from background vibrations. This method should work because the eddy current force on the cavity is proportional to the movement of the cavity. This means as the motion of the cavity increases the force dampening the cavity will also increase. Once the amplitude is lowered they will be able to tune the device to pick up very weak frequencies. The magnetic field will help in amplifying these frequencies. When the frequency is picked up, a voltage will be created sending a signal to the computer analyzing the test. This test will be conducted by securing the device between the pole tips of the magnet.

The device will then be exposed to a magnetic field of 1 tesla and the effects will be observed. If the test is successful in the 1 Tesla magnetic field that my magnet will produce it will then be experimented with at RHIC in a 10 Tesla magnetic field.

II. Design Methods

A. Constraints

My task was to create a magnet capable of producing a magnetic field of 10 kilogauss or 1 Tesla. I did not have the leisure of being able to design the magnet from scratch, but I was given two premade electro dipole magnets that I could reconfigure into one magnet with a stronger magnetic field. This forced me to work within the parameter of the magnets that I was given. These con-

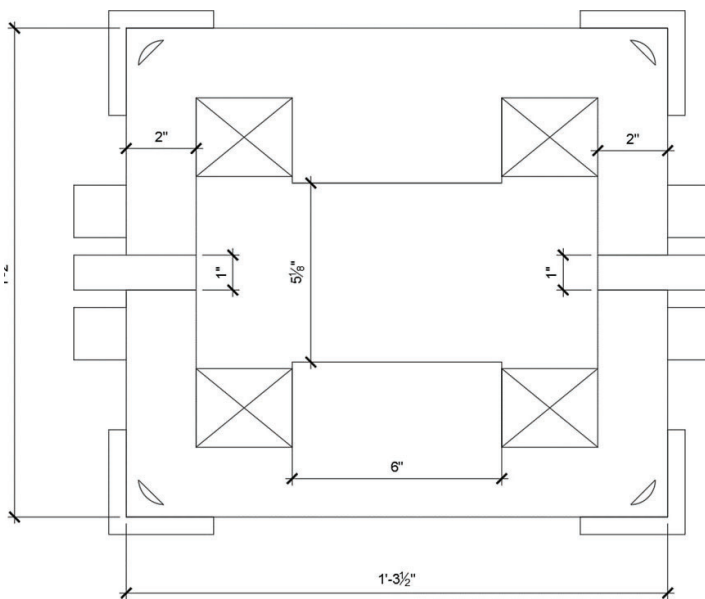


Figure 4: Original Dipole Magnet

straints were the number of coils that I had available for me to work with, the number of turns within the coils, the length of the coils and the size of the core. The size of the core could be slightly modified by designing spacers. I also had the ability to use from one to 4 coils, each with 24 turns and a length of about 1704 inches. Another constraint was the available current from the power source where the magnet was located and the available flow from the building to cool the magnet. I knew the building could produce 500 amps and produce a flow of 2 gallons per minute. This meant I had to keep the pressure drop within the magnet below 100 PSI. Once the magnet was complete a scientist was going to use the magnet by placing a device he developed between the poles. This meant the device had to fit forcing the minimum gap size to be $2^{1/8}$ inches. The smaller the gap size the stronger the magnetic field is.

B. Design

With all the constraints laid out I could now figure out if it would be possible to produce a magnetic field of 10 kilogauss with a gap of $2^{1/8}$ inches. The main concern was being able to produce the field with a pressure drop under 100 PSI. The best way to reduce the pressure drop is to add more turns in the coil. Due to my constraints I could only add turns in multiples of 24 until I reached 96 turns. The equation below explains how number of turns increases the current within the coil:

$$I = \frac{B_o * g}{.4\pi * N}$$

In this formula N represents the number of turns in the coil and I represents the total current in the coil. After running the calculations I found the best option would be to choose 96 turns which is 4 coils. With 4 coils the system required a pressure drop of 48.5 PSI to stay within a temperature rise of 50 degrees Fahrenheit. The magnet would also be drawing a current of

447.42 amps at 24.7 Volts and producing a magnetic field of 10 kilogauss. All the values fell well within the constraints I was given before starting the reconfiguration of the magnet. The full calculation can be found in the appendix.

Below (figure 4) is a drawing of one of the fully assembled original dipole magnets I was given to work with.

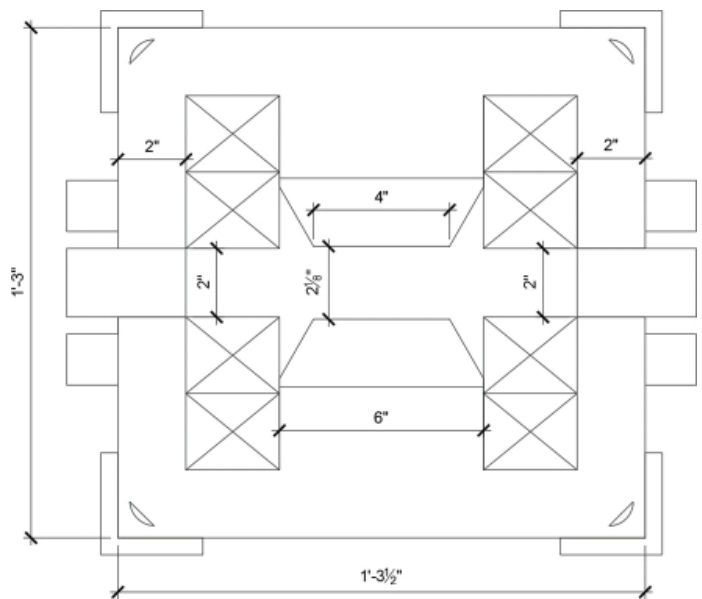


Figure 5: Reconfigured dipole magnet with 4 coils

From this drawing you can see the original design has two coils, the squares with x through them, and a gap of 5.125 inches. To reduce the gap to 2.125 inches I had to design a few new parts for the magnet. From the drawing above you can see there are two 1 inch spacers on either side of the magnet. When taking those out it reduces the magnet gap to 4.125 inches. I then decided to add new pole tips that would each be 2 inches tall reducing the gap to .125 inches. I added 2 inch spacers in place of the 1 inch spacers to make a gap of 2.125 inches between the pole tips.

Figure 5 (below) shows the drawing for the reconfigured magnet with 4 coils.

I designed the pole tips to reduce in width from 6 inches to 4 inches as seen in the figure above. This was to create a uniform magnetic field throughout the core of the magnet. After the magnetic field lines travel through the gap they arc to the right and left traveling down the 2 inch iron on either side of the magnet. Having the pole tips 4 inches wide condenses the field lines and allows them to divide evenly through the core as the loop from the north pole to the south pole. An example of this can be seen in figure 2. The photo below is the actual reconfigured magnet.

The unpainted iron on the right and left side of the magnet is the 2 inch spacers that I added. The coils run around the pole tips; the south pole is visible in this photo.

C. Coil configuration

On one end of each coil, copper leads are exposed for the electrical and coolant connections. The orientation of the coils is based on what the magnet is being used for and to avoid a short within the coil for the leads touching. The experiment that the magnet is going to be used for only called for access on one side of the magnet. This allowed me to place all the leads on the back side of the magnet so they could be easily covered. This is for safety measures and allows for the use of less buss work. Figure 7 is a diagram of the coil orientation.



Figure 6: Photo of reconfigured dipole magnet showing gap and spacers

Each copper lead is wired with bus work, represented by the dark black connections in the drawing. When wiring the coils I made sure the electric current is flowing the same direction for each coil. This ensures the magnetic field is traveling the same direction for each coil.

The copper that makes up the coil is hollow to allow for coolant to flow through it. The diameter of the hole is .1173 inches. Each coil is connected in parallel to give them maximum flow. Each coil requires a flow rate of .377 GPM and the building is capable of outputting 2 GPM. The entire magnet requires a combined flow of 1.5 GPM. The Magnet uses manifolds and hoses to connect the coils to the water source. The photos below show the copper leads with the holes for coolant, the manifold assembly, and the cover that was placed over the bus work for safety.

Before the magnet is assembled the coils need to be tested for turn to turn insulation, ground insulation, resistance, and flow. The technicians measure the flow by pumping water through each coil at 100psi. This value is then compared with the theoretical data from the calculations.

The next test is the turn to turn insulation test also known as ringing the magnet. This is done by pulsing a high voltage and reading the waveforms on an oscilloscope. If the coil is good it will form a wave pattern as shown in figure 11a. If the wave pattern resembles figure 11b it means there is an internal short within the coil and it should not be used.

The insulation to ground of the coil is tested next. This is done by immersing the entire coil besides its leads in water and applying 1150 VDC between the coil and ground for one minute. Evidence of an insulation breakdown, or a leakage current that exceeds 100 microamps at the required voltage deems a test failure and requires the coil to be repaired or discarded.

The resistance is then tested using a multimeter and compared to the theoretical resistance. The resistance of the coil should be within .1% of the theoretical resistance at 70 degrees Fahrenheit.

After the magnet was assembled it needed to be transported to another lab. Both buildings had overhead cranes capable of lifting the magnet. The magnet weighs a total of 1471lbs when fully

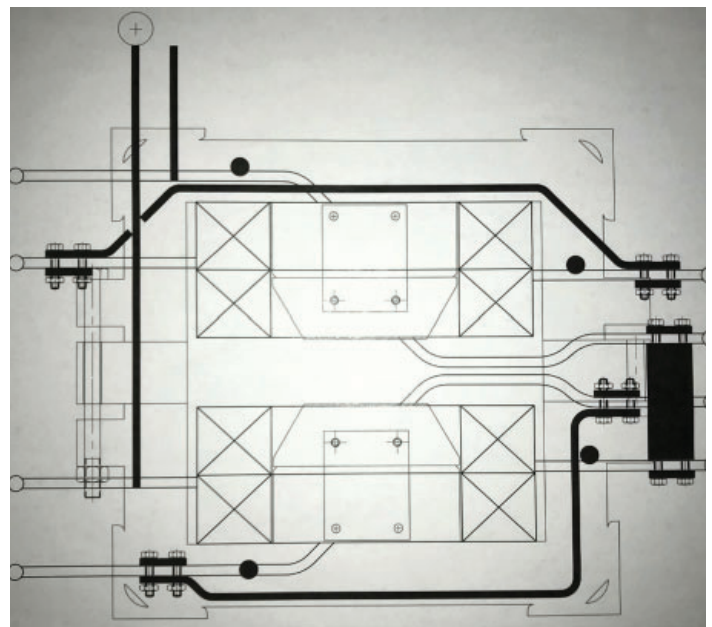


Figure 7: Coil Orientation

assembled. This allowed me to use the 3/4" diameter lifting eye that was already made with the original magnet. The 3/4" lifting eye is rated for 5200lbs. The crane then placed the magnet on a skid which was then easily moved with a pallet jack.

III. Acknowledgements

This project was supported in part by the Brookhaven National Laboratory (BNL), Collider Accelerator Department under the

BNL Supplemental Undergraduate Research Program (SURP).

This project was Funded by the NASA Space Radiation Laboratory (NSRL).

I would like to thank the Charlie Pearson, Adam Rusek, and Michael Sivertz for their guidance and professional leadership.

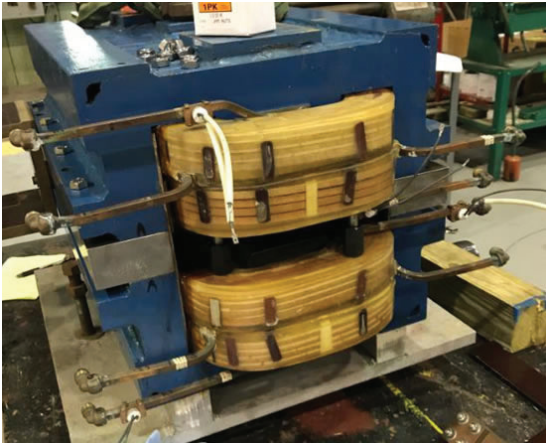


Figure 8: Coil configuration



Figure 9: Coolant pathway

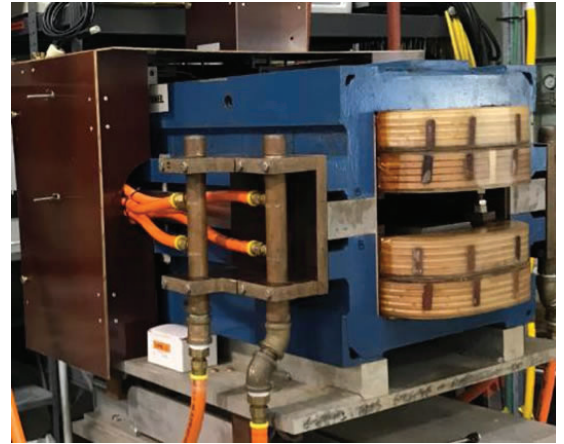


Figure 10: Coolant manifold and safety cover

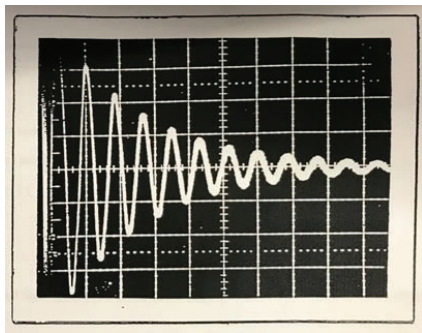


Figure 11a: Ringing pattern for a good coil

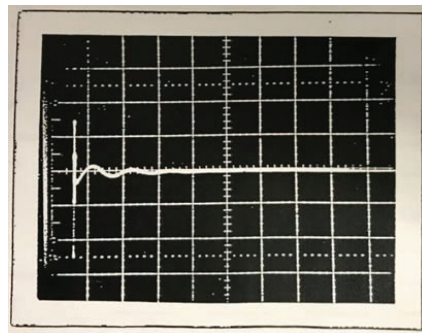


Figure 11b: Ringing pattern for a bad coil



Figure 12: 3/4" lifting eye

IV. Appendix

Magnet parameters:

**Assume hole area to be 20% of conductor cross-sectional area*

Coil	Cross-Sectional Area of Conductor	Cross-Sectional Area of Core
1 Coil = 24 Turns 1 Coil = 1704 in 4 Coil = 6816 in	Height = .322 in Width = .366 in Area = .8*1179 in ² Area = .09432 in ²	Area = 181.19 in ²
Hole Diameter	Cross-Sectional Area of Hole	Gap
$A = \pi r^2$.0236 = πr^2 $r = .0867$ in $D = .1733$ in	Area = .2*1179 in ² Area = .0236 in ²	2.125 in

Weight of Conductor (4 Coils)

Volume = 642.89 in³

Weight = 208.03lbs

Weight of Core

Volume = 4348.56 in³

Weight = 1263lbs

Total Weight of Magnet

Total = 1471lbs

Rigging

3/4 in diameter lifting eye

Rated for 5200lbs

Bus Work

-Allowed 1,000 amps/in²

-Running at 450 amps

-Bussing must be greater than .45 in²

Magnet under operating conditions

Number of H2O Circuits: 4

Flow (GPM): 1.508

Current (amps): 447.42

Voltage: 24.7

Resistance (OHMS): .0552

Pressure Drop (PSI): 48.5

Temperature Rise (F): 50

Power (KW): 11.04

Calculations:

2.125 in gap
96 turns

Resistance:

$$R_{roomtemp} = \frac{\eta L_c}{A}$$

$$R_{roomtemp} = \frac{(1.7 \times 10^{-9})(4328)}{.608}$$

$$R_{roomtemp} = .012\Omega$$

$$R_{operating} = \frac{(1.94 \times 10^{-6})(4328)}{.608}$$

$$R_{operating} = .0138\Omega$$

Current:

$$I = \frac{B_o g}{.4\pi N}$$

$$I = \frac{(10,000)(5.3975)}{.4\pi(96)}$$

$$I = 447.42 \text{ amps}$$

Power:

$$P = I^2 R$$

$$P = (447.42)^2 (.0138)$$

$$P = 2.76 \text{ KW per coil}$$

$$P = 11.04 \text{ KW total magnet}$$

Heat Load:

$$\dot{H} = P(3413)$$

$$\dot{H} = (2.76)(3413)$$

$$\dot{H} = 9428.4 \frac{\text{BTU}}{\text{hr}} \text{ per coil}$$

$$\dot{H} = 37713.6 \frac{\text{BTU}}{\text{hr}} \text{ total magnet}$$

Flow Rate:

$$\dot{M} = \frac{H}{C_p \Delta T}$$

$$\dot{M} = \frac{9428.4}{(1)(50)}$$

$$\dot{M} = 188.57 \frac{\text{lb}}{\text{hr}} \text{ per coil}$$

$$\dot{M} = 754.28 \frac{\text{lb}}{\text{hr}} \text{ total magnet}$$

Volumetric Flow:

$$Q = \frac{M}{\rho}$$

$$Q = \frac{188.57}{(62.4)(60)(231)}$$

$$Q = .377 \text{ GPM per coil}$$

$$Q = 1.508 \text{ GPM total magnet}$$

Velocity:

$$V = \frac{O}{A_{hole}}$$

$$V = \frac{(.377)(231)}{(12)(60)(.0236)}$$

$$V = 5.12 \text{ fps}$$

Reynolds Number

$$R_e = \frac{Vd}{\gamma}$$

$$R_e = \frac{(5.12)(.1733)}{(12)(4.7 \times 10^{-6})}$$

$$R_e = 1.6 \times 10^4$$

Relative Roughness:

$$RR = \frac{\epsilon}{d}$$

$$RR = \frac{4.5 \times 10^{-6}}{2.08}$$

$$RR = 2.16 \times 10^{-6}$$

Friction Factor (Moody Chart):

$$f = .028$$

Pressure Drop:

$$\Delta P = f \left(\frac{v}{d} \right)^2 \frac{1}{2G}$$

$$\Delta P = .028 * \frac{1704}{.1733} * \frac{5.12^2}{64.4} * .433$$

$$\Delta P = 48.5 \text{ PSI}$$

Nomenclature:

$R_{roomtemp}$ = Resistance @ Room Temperature

$R_{operating}$ = Resistance @ Operating Temperature

R = Resistance

η = Resistivity

L_c = Length of Coil

A = Area of Conductor

I = Current

B_o = Magnetic Field Through Gap

g = Gap

N = Number of Turns in Coil

P = Power

\dot{H} = Heat Load

C_p = Specific Heat of Water

ΔT = Temperature Rise

\dot{M} = Mass Flow Rate

Q = Volumetric Flow Rate

ρ = Density

V = Velocity

A_{hole} = Area of Hole

R_e = Reynold's Number

d = Hole Diameter

γ = Kinematic Viscosity

RR = Relative Roughness

ϵ = Pipe Roughness

f = Friction Factor

ΔP = Pressure Drop

G = Gravity

V. Bibliography

"Magnetic Field Lines." *Texasgateway.org*, www.texasgateway.org/resource/201-magnetic-fields-field-lines-and-force.

Weak lensing with Lyman- α forests

Prakruth Adari

Physics, Columbia University, New York, NY, 10027

Anže Slosar

Physics Department, Brookhaven National Laboratory, Upton, NY, 11973

Abstract

A method to create an accurate mass map of the universe that is independent of redshift would allow in depth study into the structure of the universe and the early evolution of the universe. Directly related to the mass map is the kappa map which can be generated by various methods and is also related to the lensing displacement. We explored the possibility of using Lyman- α (Lya) forests to generate a more accurate kappa map. Since Lya forests generally come from quasars whose positions are well measured and have an associated correlation function that can help measure distance between pairs, they are prime candidates for being able to recover a lensing displacement map and from there a kappa map. Using Python and common packages such as numpy, healpy, and some custom modules, we were able to compute the least squares fit to the positions of quasars and thus retrieve a displacement map between the lensed and unlensed positions of quasars. While it has been theorized that using Lya forests could create an accurate kappa map could be made, implementations so far have used an estimator function which was unable to reach the predicted values of signal to noise. The least squares fit was able to accurately retrieve the unlensed positions in a meaningful amount of time, but was not able to match the accuracy of the estimator method in creating the kappa map without greatly increasing the data size and computation time. Brookhaven National Laboratory will be able to better correct the effects of weak lensing in other projects, such as the Baryon Mapping Experiment. Through this summer I have improved on my python and physics skills by using tools such as numpy for numerical calculations and spherical harmonics for models on the full sky.

I. Background

A. Gravitational Weak Lensing

Lensing refers to the phenomena of the path of light bending or changing under the effect of gravity. While lensing has been predicted by general relativity and has been observed, weak lensing has only recently been measured. Instead of the drastic warping of images that are clear signs of lensing, weak lensing refers to a statistical measure that can be measured across the entire sky and is called the lensing potential. From the lensing potential we can take the derivative spatially to get the displacement map or transform into spherical harmonics to derivate twice and get the kappa map.

B. Spherical Harmonics

By holding a fixed radius, we are able to define our map as a function of RA and DEC, the standard astronomical angles. This not only reduces the complexity of our function, from at least 3 variables to 2, but also allows us decompose our function using

spherical harmonics.

Spherical harmonics on the surface of a sphere is analogous to Fourier series on the Cartesian plane; it allows us to decompose any function on a sphere into a sum of simpler functions on a sphere while also making differentiation and integration trivial. Since the decomposition gives us a constant for each frequency on the sphere, it becomes much easier to compare maps on a sphere.

C. Correlation Function of Lya Forests

The main benefit of using Lya forests, quasars (a deep sky object that used to be thought of as an extremely bright star but today are understood to usually be a galaxy or cluster of galaxies), is the correlation function (ξ) which measures the correlation between the spectrum received from any pair of quasars. The correlation function is dominated by the perpendicular distance, that is, the distance between two quasars if they both were on the surface a sphere.

Since lensing in spectrum can be measured and corrected for, we can measure the correlation in signal between two quasars and then the distance between them and compare against the correlation function to see if they are experiencing meaningful weak lensing.

$$\xi(r'_\perp, r'_\parallel) = \xi(r_\perp, r_\parallel) + \frac{d\xi}{dr} \Delta r_\perp$$

D. Kappa Map and Estimation

The kappa map is the line integral of mass along a line of sight which allows for a map of the distribution of mass density across the universe. The main limiting feature of the kappa map is its two dimensional nature since it has no radius component. There are a variety of methods to recover the kappa map but it has rather low accuracy. Two methods drafted by Anže Slosar would allow for a higher accuracy map using Lya forests and correlation functions. One method is the displacement method which I implemented, the other is the kappa estimator method. The kappa estimator takes the y_{ij} as the value for kappa at the midpoint of each pair and is currently being implemented and improved on by Samantha Youles. While the kappa estimator method works, it is expected to fail when the signal to noise ratio (SNR) becomes more realistic with noise far exceeding the signal. The displacement method should produce results comparable to the kappa estimator method and perform better when SNR becomes more realistic.

II. Method

A. Overview

The main project is split into two parts: 1. Using the correlation function, retrieve the unlensed points with an iterative least

squares fit, 2. Using the unlensed points, generate a displacement map to then turn into the kappa map.

B. Least Squares Fit

The problem of recovering the unlensed positions given the lensed positions along with a tensor $y_{ij} = r'_{ij} r_{ij} + eps$ which measures the difference between the lensed distance and the true distance with some added noise can be solved with an iterative least squares fit. Each pair of quasars gives us a y_{ij} measure which can be modified by wiggling around the position of one of the quasars which changes the r' value, till the sum of y_{ij}^2 is minimized for a single quasar across all pairs. Repeat over all quasars and we have a slightly more accurate set of points. Then we can update y_{ij} and iterate. Since the noise depends on true distance, for a fixed point, there are only so many nearby quasars which can give us meaningful results. Thus, we limit ourselves to the nearest 80 arcminutes with functionality to change the amount we use while also introducing error weighting (simple $1/eps$).

1. Single point solution

Wiggling around a single point to minimize the y_{ij} sum is non-trivial. While the set of possible points is limited by the lensing displacement which is often very small, it is computationally infeasible to brute force finding the least squares solution without fixing some resolution on a grid. Instead we can use the fact that the lensing displacement is very small and $r' \approx r$ and Taylor expand the distance formula to get a linear system that we can solve incredibly quickly.

2. Taylor Expansion

$$D_{ij} = \arccos(\cos(\theta_i)\cos(\theta_j) + \sin(\theta_i)\sin(\theta_j)\cos(\delta\phi))$$

The great circle distance between two points on a sphere

$$\bar{y}_j(\theta, \phi) = y_j(\theta_i, \phi_i) + (\nabla y_j(\theta_i, \phi_i)) \begin{bmatrix} \theta - \theta_i \\ \phi - \phi_i \end{bmatrix}$$

Taylor expansion of y_{ij} in spherical coordinates around the points (θ_i, Φ_i)

$$\frac{\partial y_j}{\partial \phi}(\theta_i, \phi_i) = \frac{\sin(\theta_i)\sin(\theta_j)\sin(\phi_j - \phi_i)}{\sqrt{1 - \cos(\theta_i)\cos(\theta_j) + \sin(\theta_i)\sin(\theta_j)\cos(\phi_i - \phi_j)}} = B \sin(\theta_i)$$

$$\frac{\partial y_j}{\partial \theta}(\theta_i, \phi_i) = \frac{\cos(\theta_i)\sin(\theta_j)\cos(\phi_i - \phi_j) - \sin(\theta_i)\cos(\theta_j)}{\sqrt{1 - \cos(\theta_i)\cos(\theta_j) + \sin(\theta_i)\sin(\theta_j)\cos(\phi_i - \phi_j)}} = A$$

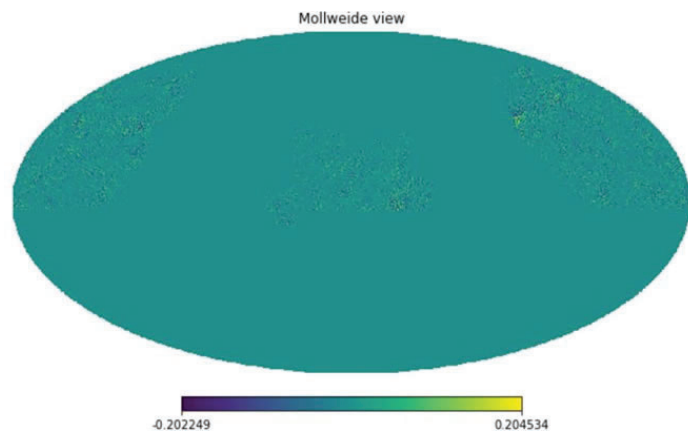


Fig 1: Generated kappa map with eBOSS coverage only

$$A\theta + B\phi = A\theta_i + B\phi_i - dy_j(\theta_i, \phi_i)$$

Using basic calculus and minimization techniques we can change each pair of quasars into a simple linear equation which can lead to an overdetermined system where we can calculate the least squares fit extremely quickly.

3. Iterations and Parallelization

While each pair has turned into a simple linear equation that can be solved easily using common linear technique, there would still be around 50 neighbors for each quasar with 160,000 quasars leading to 8 million calculations. Calculation of A and B is not at all efficient given the amount of sines, cosines, and square roots. Messier than the calculation of A and B is iterating. Since each iteration requires a recalculating r' for each pair of neighbors (8 million calculations) along with the actual linear equation (8 million calculations), each iteration would take around one hour to run. A single iteration is also rather ineffective and ideally we would be using 10 or 20 iterations to achieve much better results. In order to run the script several times a day (for testing purposes and ease), we used mpi4py to set up parallelization on our cluster.

C. Kappa Map

Now that we have an estimate to the original points we can generate the displacements in theta and phi to estimate the lensing displacement map. From the displacement map we have a spin-1 map we can use healpy (<http://healpix.sf.net>) to compute and then multiply by a factor proportional to the frequency ($\sqrt{l*(l+1)}$) to get the kappa map. While there is no limitation on where in the sky this can happen, we limited ourselves to sections of the sky that would be under observation from eBOSS which would give us the accurate quasar position measurements we need. Since we are only checking the validity of this method we can generate mock data and compare our results against the mocks to verify our method works. Comparing the results require the cross correlation

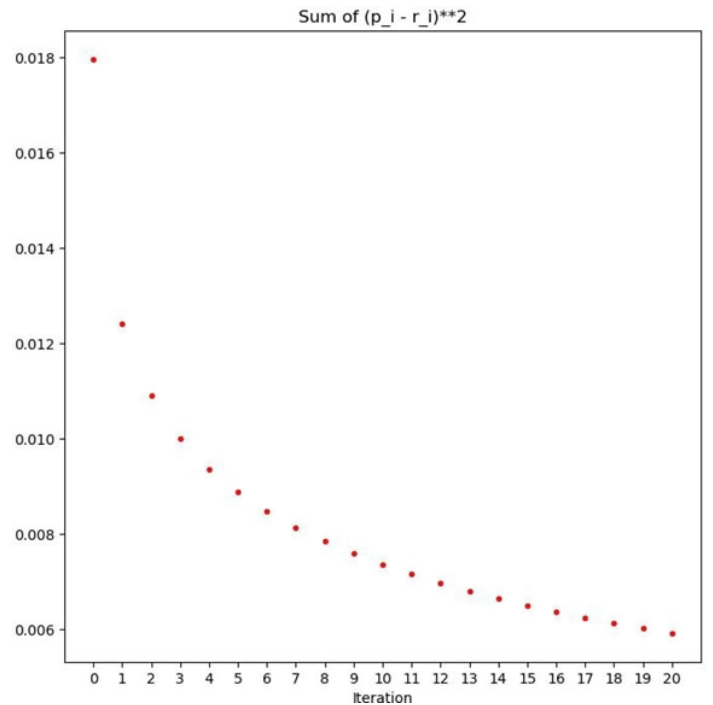


Fig 2: Sum of squared distances over iterations.

between the two spherical maps (the mock and the one we generate). The cross-correlation gives us the correlation between the two maps for each frequency but since it is noise dominated we end up dividing by the autocorrelation to account for noise.

III. Results and Discussion

While the least squares fit was able to accurately retrieve the points as seen by Figure 2, this method had some serious drawbacks. Running on 149,000 points, which is close to the expected 160,000, would take 48 hours for 20 iterations on a single core which is why the parallelization was added earlier. That being said, we were able to generate a pretty decent map. Working on mocks allow us to compare our generated map against the mock to see how effective the method and generated map is. We measure autocorrelation for our estimate (C_{ee}) and the autocorrelation for the “truth” generated by the mocks (C_{tt}), and the correlation between our estimate and the truth (C_{te}). To account for noise domination we only care about: C_{te}/C_{tt} and $C_{te} / \sqrt{C_{tt} * C_{ee}}$. The first gives us a correlation that should be 1 for perfect match (which is standard for correlation) and the second normalizes the correlations up to a scalar. As you can see in Figure 3, both measures worked well for healpix resolution of 64. While 20 iterations are unable to match the extremely clean results when using the true points, it is still much better than a single iteration. The bumplike nature is to be expected when only looking at neighbors with a certain distance. For this run we used neighbors within 80 arcminutes which translates to the mode of around 100 which is where the bump occurs. While this works for healpix resolution of 64, it starts to fail

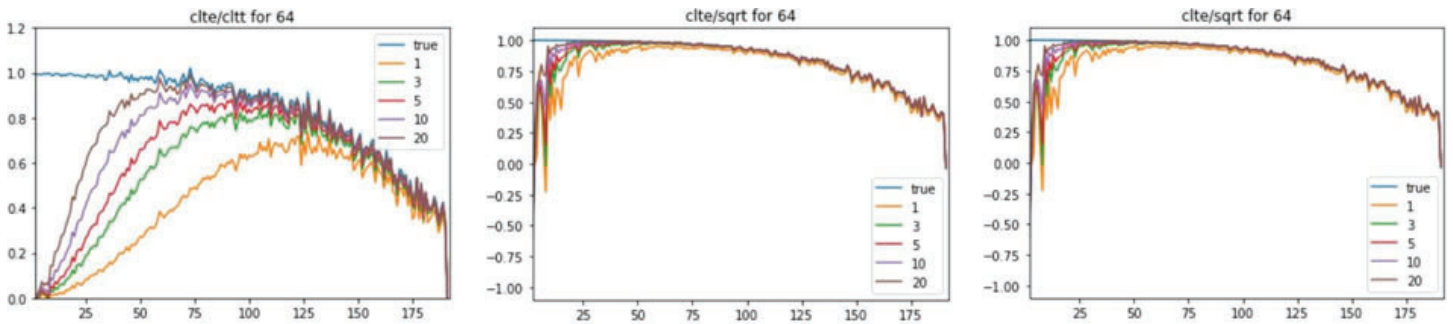


Fig 3: Correlations and comparison against results from kappa estimator (courtesy of Samantha Youles)

when the resolution goes above 256. Since we want a high resolution kappa map, limiting ourselves to 64 is rather silly. Shown in Figure 3 we can clearly see that the kappa estimator implemented by Samantha is far better than the displacement method. The fall in quality of the map has been attributed to the amount of “holes” in the displacement map that is used to generate the kappa map. We tried a few methods of dealing with the holes (generate a lower resolution and then use that to fill in the holes of the larger resolution) but were unable to surpass Samantha’s kappa estimator. We believe the use of a Wiener filter would greatly improve the displacement method but implementation would increase the computational complexity.

There is still a lot of investigating to be done. Most of our mocks were done with extremely high SNR which is not at all accurate. Going down to more realistic SNR such as 1/10 or 1/100 completely breaks both methods. The kappa estimator is almost completely noise and the least squares fit takes many more iterations to achieve the same level of accuracy. Investigation into the number of neighbors needed for both methods and ways to combine the two methods are still going on.

IV. References

1. Gorski, K.M., E. Hivon, A.J. Banday, B.D. Wandelt, F.K. Hansen, M. Reinecke, and M. Bartelmann, HEALPix: A Framework for High-resolution Discretization and Fast Analysis of Data Distributed on the Sphere, *Ap.J.*, 622, 759-771, 2005.

Locating the genes responsible for Arabidopsis mutants through map-based cloning

Kathryn Bischoff

Biology, Colby-Sawyer College, New-London, NH 03257

Salimata Guene Fall

STEM, Hudson County Community College, Jersey City, NJ 07306

Jillian Fan, Linhui Yu, Changcheng Xu

Biology Department, Brookhaven National Laboratory, Upton, NY 11973

Abstract

The negative impacts and limited availability of petrochemicals have led researchers to look at another energy source, lipids derived from plants. *Arabidopsis thaliana*, a widely used model organism, has been a major focus in the Biology Department at Brookhaven National Laboratory's (BNL) effort to enhance oil production. This project aims at locating and identifying the gene responsible for pgg1 synthesis using pgg1M6-1Ler F2 of pgg1m6-1 mutant and the M4-7Col2 mutant of Arabidopsis in the hopes of gaining knowledge of the mechanisms that control lipid biosynthesis. We utilized genotyping and gene mapping techniques to analyze Arabidopsis mutants. DNA extracted from the mutants which are then used in a Polymerase Chain Reaction (PCR) to make billions of copies of a target sequence using specific forward and reverse primers. For genotyping, homozygotes were identified via restriction digest using restriction enzymes followed by gel electrophoresis. Our results indicated that the M4-7 Col mutation was located on chromosome 5 between markers KLP and 3451, narrowing down to one possible gene. A linkage was identified on the marker AthBIO2b for the PGP1M6-1 Ler mutant, but the mutated gene is still under investigation. This project contributes to the DOE's research into alternative and renewable energy resources. This knowledge assists in furthering the understanding of lipid biosynthesis. As a result of this summer, we have accumulated new knowledge on genetic techniques, plants mechanisms, and gene mapping. We have gained new laboratory skills and valuable experiences in a highly regarded laboratory, which will be useful to further our education and future careers.

I. Background

A. Lipids as Biodiesel

Fossil fuels' poor consequences on the environment and lack of sustainability has been sparking interest to produce biofuel for decades. With fuel consumption projected to double in the next two decades, biofuel is the best solution to this overwhelming problem.⁹ The majority of biofuels consist of the monomeric sugar ethanol, however, monomeric sugars have been not as sustainable as once believed.^{8,9} An encouraging alternative is the utilization of lipids as biodiesel because of their shorter ignition delay periods and faster vaporization of fuel.¹⁰ Other benefits to biodiesel include: non-toxicity, biodegradability, and renewability.¹⁰ Research has shown that 100% biodiesel has characteristics that reduce some of the emissions compared to diesel, specifically carbon monoxide, hydrocarbons, and particulate matter (Figure 1.1).¹⁰ While there is strong data supporting biodiesel as an alternative, we do not know if biodiesel can compete with fossil fuels.

Research needs to continue to make plants as efficient as possible with their oil yield to reduce costs and environmental impacts of biodiesel, to hopefully one day replace traditional diesel fuels.^{8,9}

B. Map-based cloning

Map-based cloning, also called positional cloning, determines the unknown location of a gene by looking for linkage to previously known markers.^{1,5,6} This location can determine the uncertain function of the gene.^{1,5,6} The location is narrowed down from all chromosomes to a precise sequence along the gene which in turn, can give insight on what protein that sequence encodes.⁶ This forwards genetics technique is done through multiple steps including: genetic mapping (DNA extraction, genotyping, PCR, digestion, and gel electrophoresis), sequencing, and cloning. Genetic mapping works by determining the recombinant frequencies of specific markers. A low frequency of recombinants from testing a specific marker indicates on the map which direction to proceed in; the proportion of crossovers or recombination frequencies is directly related to the distance on a gene.⁷ This process of map-based cloning has been expedited recently thanks to the entire sequencing of the Arabidopsis Columbia genome and the availability of thousands of known primers.¹

C. Genetic Mapping Technique

PCR allows for a specific DNA sequence on the target DNA to be amplified.⁴ This works by initially separating the sample DNA strands utilizing heat, then forward and reverse primers annealing to the ends of the target sequence, and finally DNA polymerase (Taq enzyme) adding nucleotides to the one stranded DNA. This allows for the samples to contain billions of copies of the target sequence of the primer.⁴ There are three types of primers used in this process: Single Nucleotide Polymorphism (SNP), Cleaved Amplified Polymorphic Sequences (CAPS), and Simple Sequence Length Polymorphisms (SSLPs); each has their own procedure for analysis.^{2,3} PCR is crucial to map-based cloning be-

Emissions	Diesel	Biodiesel (100%)
Carbon Dioxide	100	-50%
Particulate Matter	100	-50%
Hydrocarbons	100	-67%
Nitrogen Oxide	100	+10%
Total Emissions	100	-74%

Figure 1.1: comparison of Diesel emissions to biodiesel emissions.¹²

cause it allows for many locations to be ruled out or confirmed for linkage; this test and check method of many different primers is called chromosome walking. These samples are then run through gel electrophoresis, where an electric current carries the negatively charged DNA toward the positive end of the chamber through a gel, separating the DNA bands by length. These bands are visualized under ultraviolet (UV) light. The position of the bands determine recombinant frequencies, which would conclude linkage; samples that only show one band indicate homozygotes, and samples that separate into two bands indicate heterozygotes/recombinants. Once the location is narrowed down to between two or three markers, the genes in between those markers can be compared using The Arabidopsis Information Resource (TAIR) database to identify the gene.¹¹ The desired gene is then sequenced to see where the mutation occurred, and cloning of that gene can be used for future testing of the function of the protein.

D. Arabidopsis Thaliana

Arabidopsis Thaliana has been commonly used as a model plant for geneticists for decades because of its low number of chromosomes, allowing the genome to be mutated easily. This has been crucial to many fields looking to understand plant mechanisms and genomics. There are two ecotypes of this species, Columbia (Col) and Landsberg (Ler). The mutants used in this experiment were PGPI M6-1 crossed with Ler and M4-7Col crossed with Ler. The M4-7 mutants have more total lipids compared to the wild type (Figure 1.2), darker green leaves, and a

Figure 1.2: Comparison of PC, PI/SL + DGDG + PE, PG, and MGDG lipid content of M4-7 mutant to wildtype lipid content. The figure shows an increase of overall lipid content of M4-7

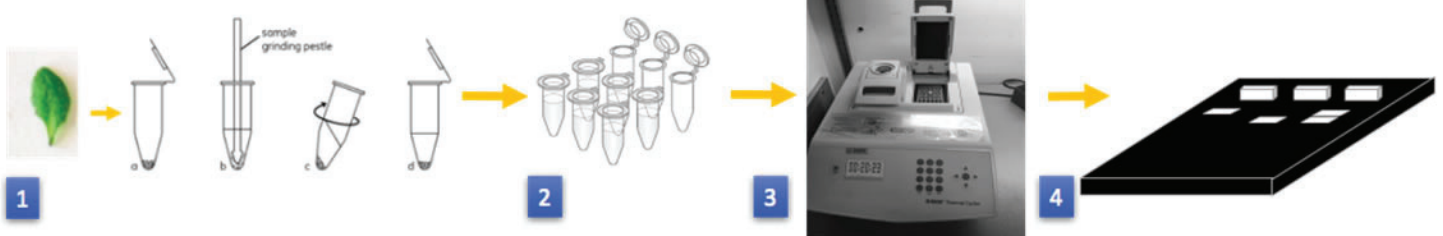
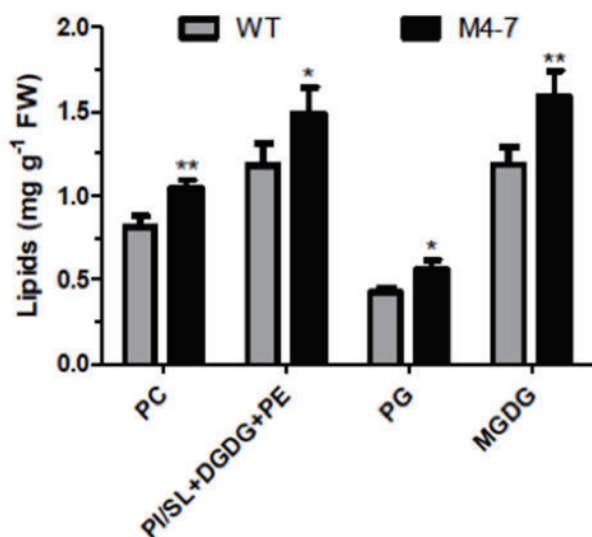


Figure 2.1: Displays simply the process of determining the recombination frequency

weaker stem. The *pgp1M6-1* mutants are more green than *pgp1* because *pgp1* is suppressed. These mutations could be affecting proteins involved in lipid biosynthesis, which is why these mutants are of interest.

II. Materials and methods

A. Mutants' growth condition

The process of seed planting was made on 1/2 Murashige and Skoog (MS) medium and 1% sucrose plates. We added 600µl sterilize solution on each tube containing the seeds which was made with 400 µl sterilized water, 100 µl bleach and 1drop of 0.2% Triton-100. The tubes were then placed on a shaker for 12 minutes. Afterwards, we washed the seeds four times with 800µl sterilized water. This process is followed by an addition of 100-200 µl of 0.1% agar. The seeds were then transferred to the agar plates, wrapped with foil and placed in 4°C for 2 to 3 days then transferred to the Percival to grow. A transfer to soil will then be made once the seeds have germinated and the plants mature. This F2 population is subsequently utilized to extract DNA.

B. DNA extraction

The genetic material of the mutants was obtained by mixing 200ml of DNA extraction buffer containing 200 µl Tris-Hydrochloride acid, 250 µl Sodium chloride (NaCl), 25 µl Ethylenediaminetetraacetic acid (EDTA) and 0.5% Sodium dodecyl sulfate (SDS) into a small tube followed by a small leaf cut from a plant. A blue pestle was used to grind the leaf inside the tube. To precipitate the DNA, 400 µl of a 100% Ethanol was added followed by shaking the tubes before placing them in the centrifuge to spin for five minutes at 13,000 rpm. We then discarded the supernatants being careful not to throw out DNA pellet. The final step involves the addition of 200 µl of TE buffer for dissolution which was made with 10 µl Tris-HCl and 1µl EDTA. The DNA is ultimately kept in 4°C for PCR use.

C. Polymerase chain reaction (PCR)

The first step in PCR is to make the reaction solution; this depends on the number of samples being tested. The stock includes for each sample: 15 µL of dH₂O, 5 µL of Taq buffer, 2 µL of Magnesium Chloride, 0.5 µL of deoxyribonucleotide triphosphate (dNTP), 0.15 µL of Taq enzyme, 1 µL of forward primer, and 1 µL of reverse primer. We vortexed the stock for ten seconds and then 23 µL of stock was added to each PCR tube. Then 2 µL of specific DNA was added to each sample. The samples are then capped and placed in a PCR device. The denaturation temperature is 95 °C for two minutes, the annealing step depends on the primers specific needs, but ranges from 48-58 °C for thirty seconds, and the final step is the extending step at 72 °C for anywhere between ten seconds to 5 minutes, depending on the size of the gene. The number of cycles range from 35-45, based on how clear of a gel

the previous PCR produced. All three types of primers were necessary to use.

D. Gel electrophoresis and Digestion

Once the PCR is complete, the samples are then run through gel electrophoresis. This was conducted in Tris/Borate/EDTA (TBE) buffer if the primers were SNP or SSLP. The samples were loaded into 3.5% concentration agarose gels; 10-15 μ L of each sample was loaded into each well. The gel was then run at 110v, 400ma, for twenty minutes and then scanned under the UV light.

An additional step of digestion was performed if the primers were CAPS. For M4-7Col2 population, 0.2 μ L EcoRI and 2 μ L EcpRI buffer for each sample was made and added to the 20 μ L samples after the PCR. Then we placed the samples in a 37 $^{\circ}$ C hot water bath for thirty minutes. After this, the samples were placed in a gel electrophoresis chamber, explained above, but in Tris/Acetic Acid/EDTA (TAE) buffer and a 1.5% concentration agarose gel. Pgp1 Homozygotes were identified using similar protocol. We used 7.6 μ l milli-Q water, 2 μ l of a 10X Buffer 3, 0.2 μ l BSA, 0.2 μ l BAMH1 restriction enzyme times the number of DNA samples we have. The digestion sample were then placed in a 37 $^{\circ}$ C incubator for 30-90 minutes. After the setting time, the samples are run in a agarose gel.

E. Identifying possible genes

Once a location is narrowed down to around 100-300 kb (kilobase), research on the possible genes can begin. This is done by utilizing the TAIR database and recording all of the genes between the two markers of interest.¹¹ The name, the function, and the coordinates of the gene were all recorded and placed into an excel file. Then the file is reviewed for genes that match the description of the gene being tested and match a location. The identification of a probable gene can then be used to design a primer for that gene to check for recombinant frequency (steps c and d above are repeated to do this) and used as the basis to sequence the gene and determine the location of the mutation.

III. Results and Discussion

A. Rough Mapping Results of pgp1m6-1Ler

After digestion, 13 pgp1 homozygotes of pgp1M6-1xLer F2 population were found which allowed us to proceed to rough mapping to localize the mutated gene. On chromosome 1, the markers nga63 and nga 111 showed 6 recombinants. The marker 6556 showed 4 recombinants and 3202 showed 7 recombinants. Chromosome 3 revealed more Landsberg on nga6, and 9 recombinants on marker nga126. The markers nga8 and 6371c indicated 5 recombinants, marker nga 1107 and nga 151 had 6 recombinants, all on chromosome 4. On the chromosome 5, 6 recombinants on marker MBK5-1 were obtained, 5 recombinants on nga139 and nga76. However, on chromosome 2, a linkage was identified on the marker AthBIO2b (Fig. 5.4). More Columbia was identified on this chromosome and only one recombinant which is #12

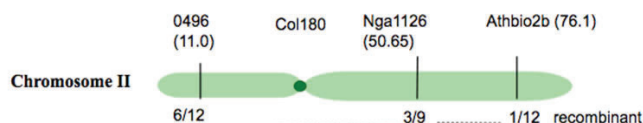


Figure 3.1: Pgp1M6-1 locus on Chromosome II of Arabidopsis Thaliana

in 13 plants. Nevertheless, Pgp1, the mutant deficit in phosphatidylglycerol biosynthesis is located at the same marker. (Appendix C).

B. Positional mapping results of M4-7Col2 homozygotes

Rough mapping indicated the M4-7 gene is located on chromosome 5, between markers nga76 and markers MBK-5. The key markers 1243 and 7733 were tested first in this region and yielded 0.18 and 0.33 recombination frequencies, however, these markers had different heterozygotes from each other, indication of flanking the marker of interest. Marker 3108 had a lower average frequency when tested with 4423, 0.00, then when tested with 2574, 0.35, indicating the gene was not between 2574 and 3108. 5425 and 4423 both had higher average recombination frequencies when tested with 7733, 0.53 and 0.17, indicating the gene was not past 4423. Further narrowing between 3108 and 4423 showed that 3451 had a higher average recombination frequency when tested with 2574 individuals, 0.13, than compared to the recombination frequency of 0.0 with 4423 individuals. CIW9 tested with 4423 heterozygotes and SNP 126 tested with CIW9 heterozygotes both had increased average frequencies, 0.67 and 0.43, indicating the gene was located between SNP 126 and 3451. When SNP 97 was tested with CIW9, it indicated an average frequency of 0.29, stating the gene was towards KLP. The lowest frequency from these markers was KLP with 4423 individuals at a frequency of 0. Since the region between KLP and 3451 could not be confirmed from our results, the gene is location is between 3451 and SNP 97. All of these results are consistent with the data in Figure 3.2 and Appendix A.

C. Identifying the M4-7 gene

After further analysis of the area between SNP 97 and 3451, 98 genes were located here. Based on all the information, the gene was identified. This was because the phenotypes of one of the mutants of this gene matches the phenotype of the M4-7Col2 mutants. The location of this gene is between KLP and 3451, which further confirms the identification because these markers had the lowest average frequencies. The description states it encodes for a cellulose synthase protein that synthesizes the secondary cell wall, which is also believed to be where our mutation resides.

IV. Conclusions and Recommendations

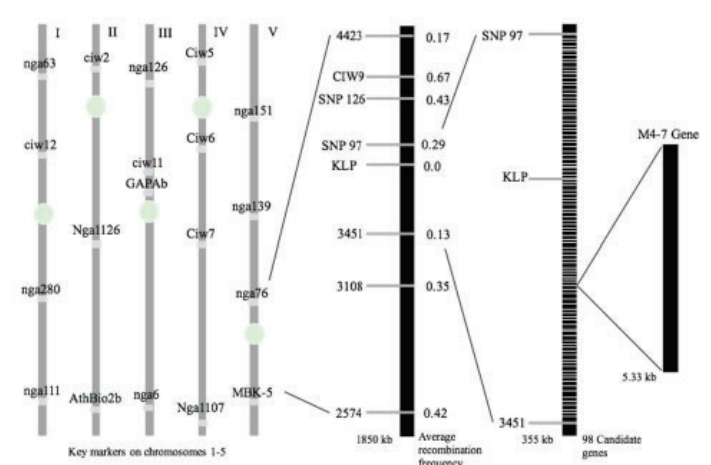


Figure 3.2: Positional mapping of M4-7Col2 using homozygous of M4-7col2 from F2 population of M4-7x Ler

This study investigated the loci and functions of Arabidopsis thaliana mutants PGP1M6-1 and M4-7Col2. Phosphatidylglycerol (PG) is a lipid that synthesizes in the chloroplast and holds a major component in the photosynthetic memory of the plant. The mutant *pgp1* is deficient in Phosphatidylglycerol which enables the plant to photosynthesize properly. The mutant has a reduction of 80% in plastidic phosphatidylglycerol phosphate synthase activity and the phenotype is yellow-green and flowering earlier than wild type (Appendix C). Our project aimed at evaluating possible genes responsible for PG synthesis. The results obtained reveals that PGP1M6-1 might be a *pgp1* suppressor. We believe that *pgp1* mutant has 50% less mutation since it is knocked out slightly and *pgp1M6-1* recovered 80 %-90% in phosphatidylglycerol. To further confirm, we can analyze the lipid phenotype and extract the total lipid from those plants to run a thin-layer chromatography (TLC) plate to see any changes on the PG content. The linkage found with our F2 population for *pgp1m6-1* is close to *pgp1* but there are chances our mutant could be located there also. Our recommendation to find the phenotypes and the mutated gene location would be to backcross *pgp1m6-1* with Columbia for a better visual of the phenotypes. Also, genotyping the F2 generation to find the sequence of the gene which will allow us to locate the gene.

The mutant M4-7 was determined to be located on chromosome 5 between markers SNP 97 and 3451 at the gene M4-7. M4-7 is a gene that is known to control cellulose production for second cell wall synthesis in Arabidopsis Thaliana. A future study

on the function of this gene is necessary; the location of the gene has been identified but the connection to cellulose synthesis is unknown. Even though the total lipid content of the M4-7 mutants increased, there is no evidence that this gene directly controls lipid biosynthesis. There are other studies stating this mutant has smaller cells than the wildtype, so the increase in total surface area could cause an increase in total lipid content.¹³ Our recommendation is to focus additionally on how a gene that affects cellulose, a carbohydrate, can also increase the production of lipids.¹³ This could be key to the further understanding how lipids are synthesized in plants and if so, can be vital to improving the biofuel industry.

V. Acknowledgements

We would like to express our sincere gratitude to our mentors Jillian Fan, Linhui Yu and Chancheng Xu for their professionalism and their great availability for the realization of this project. We also thank the Office of Educational programs at Brookhaven National Laboratory for welcoming and giving us the opportunity to expand our knowledge. This project was supported in part by the U.S. Department of Energy, Office of Science, Office of Workforce Development for Teachers and Scientists (WDTS) under the Science Undergraduate Laboratory Internships Program (SULI) and Community College Internships Program (CCI).

VI. Appendixes

Appendix A: Data from all of the PCR tests conducted to narrow location down to SNP 97 and 3451

Marker	Heterozygotes	Sample	Ratio	Freq.	Avg. Frequency
1243	(17-71)	1	10/55	0.1818	
7733	(17-71)	1	18/54	0.3333	
2574	(1-126)	2	6/126	0.0476	
4423	(1-126)	2	6/126	0.0476	
4423	(130-153)	3	1/23	0.0434	
2574	7733	1	0/18	0.0000	0.0000
2574	1243	1	3/7	0.4167	0.4167
3108	4423	1	0/3	0.0000	0.0000
3108	4423	2	0/6	0.0000	
3108	2574	1	1/5	0.2000	0.3500
3108	2574	2	3/6	0.5000	
3451	4423	1	0/2	0.0000	0.0000
3451	4423	2	0/6	0.0000	
3451	2574	1	1/4	0.2500	0.1250
3451	2574	2	0/6	0.0000	
KLP	4423	1 & 2	0/9	0.0000	0.0000
SNP 97	CIW9 & 63	1 & 2	2/7	0.2857	0.2857
SNP 126	CIW9 & 64	1 & 2	3/7	0.4286	0.4286
CIW9	4423	1 & 2	6/9	0.6667	0.6667
4423	7733	1	3/18	0.1667	0.1667
5425	7733	1	10/19	0.5263	0.5263

Appendix B: Key results from gel electrophoresis that indicate the recombination and homozygotes

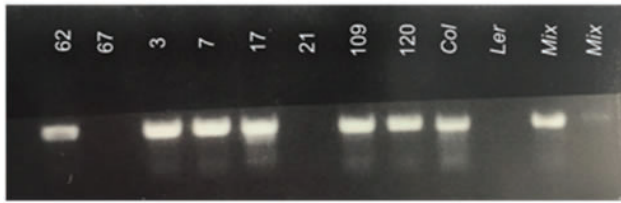


Figure 5.1 Results of Gel Electrophoresis of marker KLP with 4423 heterozygotes from samples 1 and 2. These individuals include 24, 62, 67, 3, 7, 17, 21, 109, and 120. This marker indicates all that were tested were Columbia, recombination of 0. The control Ler and Mix did not show up, but all are consistent with the Col control.

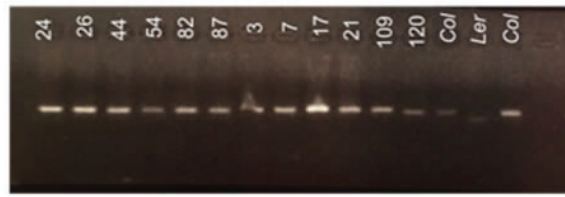


Figure 5.2 Results of Gel Electrophoresis of marker 3451 with both 2574 and 3451 from sample 2. This marker indicates that all tested were Columbia, with a recombination of 0. The control Ler and Mix did not show up, but all are consistent with the Col control.

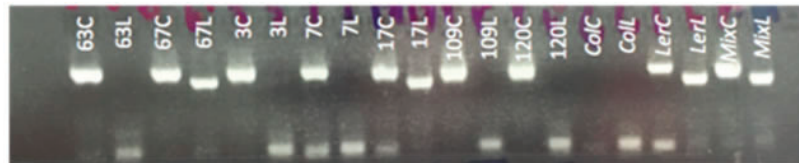


Figure 5.3 Results of Gel Electrophoresis of marker 3451 with both 2574 and 3451 from sample 2. This marker indicates that all tested were Columbia, with a recombination of 0. The control Ler and Mix did not show up, but all are consistent with the Col control.

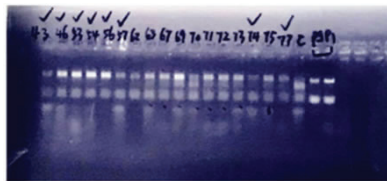


Figure 5.4: This image is one of the many digestions and gel electrophoresis performed to identify homozygotes in the F2 population with *pgp1* and Columbia controls. The checkmarks indicate the homozygotes found in this trial.

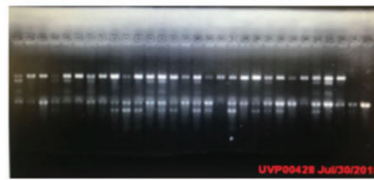
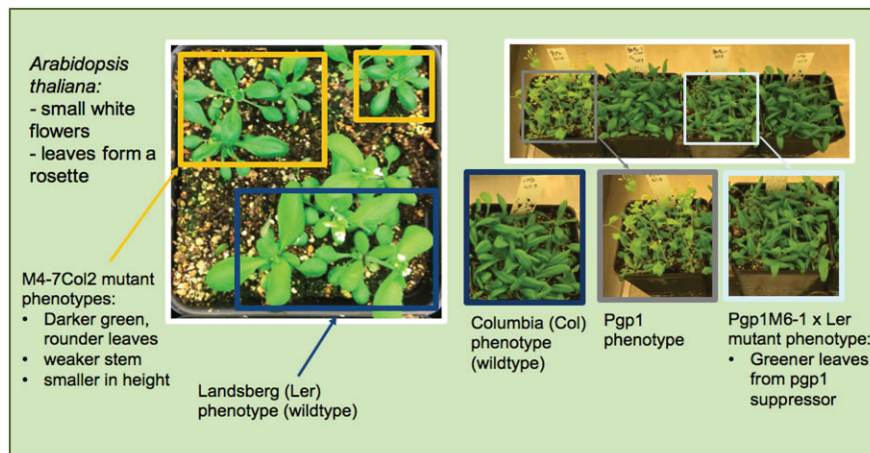


Figure 5.5: Two trials of the recent F2 population and *pgp1* control to identify homozygotes in order to distinguish the mutant's phenotype from *pgp1*. Homozygotes are shown with one band.



Figure 5.6: This image indicates the possible linkage of *pgp1M6-1* mutant on chromosome II. This marker shows the less recombinants (1) compared to the previously tested markers.

Appendix C: Phenotypes of the wildtype and mutant plants used in this experiment



VII. References

- ¹Jander, G., Norris, S. R., Rounsley, S. D., Bush, D. F., Levin I. M., Last, R. L. (2002). Arabidopsis Map-Based Cloning in the Post-Genome Era. *Plant Physiol*, 129(2): 440-50 <http://www.plantphysiol.org/content/plantphysiol/129/2/440.full.pdf>
- ²Shavrukov, Y. (2016). Comparison of SNP and CAPS markers application in genetic research in wheat and barley. *BMC Plant Biology*, 16(Suppl 1), 11. <http://doi.org/10.1186/s12870-015-0689-9>
- ³Martin, A. Collin, G. B., Asada, Y. Varnum, D. Martone, D. L., Nadeau, J. H. (1998). Simple sequence length polymorphisms (SSLPs) that distinguish MOLF/Ei and 129/Sv inbred strains of laboratory mice. *Mammalian Genome* 9: 668-670. <https://link.springer.com/content/pdf/10.1007/s003359900842.pdf>
- ⁴National Center for Biotechnology Information. (2017, Nov 09). *Polymerase Chain Reaction (PCR)*. Retrieved from <https://www.ncbi.nlm.nih.gov/probe/docs/techpcr/>
- ⁵Morton, N. E. (2003). Genetic epidemiology, genetic maps and positional cloning. *Phil. Trans. R. Soc. Lond. B*, 358, 1701–1708. DOI 10.1098/rstb.2003.1357 <https://www.ncbi.nlm.nih.gov/pmc/articles/PMC1693267/pdf/14561327.pdf>
- ⁶National Institutes of Health. National Human Genome Research Institute. “Talking Glossary of Genetic Terms.” Retrieved July 31, 2018, from <https://www.genome.gov/glossary/index.cfm?id=162>
- ⁷Lobo, I. & Shaw, K. (2008) Thomas Hunt Morgan, genetic recombination, and gene mapping. *Nature Education* 1(1):205 Retrieved from <https://www.nature.com/scitable/topicpage/thomas-hunt-morgan-genetic-recombination-and-gene-496>
- ⁸Demirel Y. Sugar versus lipid for sustainable biofuels. *Int J Energy Res*. 2018;42:881–884 <https://onlinelibrary.wiley.com/doi/pdf/10.1002/er.3914>
- ⁹Fortman, J. L. Biofuel alternatives to ethanol: pumping the microbial well. *Trends in Biotechnology*, 26, 7, 375-381, 2008 <https://cloudfront.escholarship.org/dist/prd/content/qt58v7s6c3/qt58v7s6c3.pdf>
- ¹⁰Mustafa, M. The potential of restaurant waste lipids as biodiesel feedstocks. *Bioresource Technology*, 98, 1, 183-190, 2007 <https://www.sciencedirect.com/science/article/pii/S0960852405005468>
- ¹¹The Arabidopsis Information Resource: Making and mining the “gold standard” annotated reference plant genome. *genesis* 2015 doi: 10.1002/dvg.22877
- ¹²Department of Energy. (26, Mar. 2018). Biodiesel Vehicle Emissions. Alternative Fuels Data Center. Retrieved from https://www.afdc.energy.gov/vehicles/diesels_emissions.html
- ¹³Rubio-Díaz S, Pérez-Pérez JM, González-Bayón R, Muñoz-Viana R, Borrega N, et al. (2012) Cell Expansion-Mediated Organ Growth Is Affected by Mutations in Three EXIGUA Genes. *PLOS ONE* 7(5): e36500. <https://doi.org/10.1371/journal.pone.0036500>

Assembly of magnet girders for the Cornell-Brookhaven National Laboratory Energy Recovery Linac Test Accelerator

Brian Brenton

Division of Engineering Programs, SUNY New Paltz, New Paltz, NY 12561

George Mahler

Collider Accelerator Department, Brookhaven National Laboratory, Upton, NY 11973

Abstract

Brookhaven National Laboratory (BNL) is in its final steps of production in a collaboration with Cornell University to assemble the magnet girders for the Cornell-BNL Energy Recovery Linac Test Accelerator (C-BETA). The production of such an accelerator is a significant step towards the development of the BNL's planned electron Relativistic Heavy Ion Collider (eRHIC) as technology used in CBETA is to be implemented in eRHIC. Here at BNL, the Collider Accelerator Department (CAD) is responsible for the assembly of the magnet girders; and so, we have designed a fixture for the assembly of the Halbach permanent magnets around the vacuum chamber and various other tools such as a pin remover, safety clamp and a hose fitting press to assist the assembly process. The accelerator's girders assembly process involves the construction of 27 support plates with its main constituents being the vacuum chamber, permanent magnets, and the corrector magnets. Three of the 27 having already been fully constructed. Once these components are assembled, the plate is moved using a crane, placed on a forklift, and put in a van to be transported to Cornell where it is then placed on the girders. The purpose of the addition of the magnet fixture, pin remover, forklift safety clamp, and hose fitting press to the assembly process is to enhance the efficiency and safety of the construction of the girders. These additions are currently being manufactured and once completed are to be tested by implementing them into the assembly process. Because of my time spent here at BNL, I have gained significant engineering experience ranging from design to assembly of particle accelerators and its constituents. Subsequently, I have also added to my repertoire the ability to use computer aided design software to assist in applying my engineering knowledge to various problems.

I. Background

A. C-BETA

The Cornell-Brookhaven National Lab Energy Recover Linac Test Accelerator (CBETA) is a particle accelerator that is being worked on by BNL in a collaboration with Cornell University. The accelerator serves as a prototype for BNL's planned e-RHIC using the Fixed Field Alternating Gradient (FFAG) permanent magnets and the Energy Recovery Linac (ERL) technology. BNL is now in its final steps of assembling the plates and transporting them to Cornell to be assembled on the girders (27 in total). The construction of C-BETA is expected to be completed by November of 2018 and scheduled to shoot beam as early as March of 2019.

II. Methods

A. Assembly of the MagnetGirders

The assembly process for constructing the girder plates involves great attention to detail and good engineering judgment. Each girder plate is unique and therefore drawings must be checked frequently to assemble the correct magnets and additional components. The first step in assembling the girders is to identify the plate you want to construct and lift it using an overhead bridge crane to the supporting work station. Next, the vacuum chamber is placed on the plate and held up by supports. These supports are of different designs specific to each plate and therefore should be double checked before being assembled. After the vacuum chamber is secured, the permanent magnets with appropriate corrector magnets are then assembled around the vacuum chamber. There are five variations of the permanent magnets that need to be taken into consideration during assembly. Corrector magnets are then assembled around the permanent magnets supporting and suspending them around the vacuum chamber. The final step in the construction of the plates is to assemble the hoses used for maintaining the temperature of the permanent magnets. Now, the girder plates are fully constructed and can be prepared to be shipped to Cornell. They are moved using a forklift and securely placed in the back of a van where they are transported to Cornell University to be placed on the girders.

B. Designing a MagnetFixture

The assembly of the Halbach magnets requires a secure method. In the past, the magnets have been brought together by hand which can be unstable. This is where the need for a fixture to help aid the assembly process arises. The five different variations of the Halbach magnets include the QF, QD, BD, BDT1, and BDT2. Figure 1 shows that all the halves of each variation of the magnets have forces of attraction except for BD. Additionally, the magnitudes of these forces vary from 55 lbf to 400 lbf. Figure 1 also highlights in red circles the use of a nuts and threaded rods on the BD and BDT2 magnets. This is because BD has a force of repulsion and therefore must be held together. Additionally, BDT2 simply does not have a great enough force of attraction to keep the magnets held together and requires the use of threaded rods and nuts. Furthermore, it is important to keep in mind that when designing the fixture that the magnets are approximately 7" x 7" x 5". However, they do have slight variations in their dimensions and size/shape that need to be taken into consideration when designing a fixture that fits all the magnets. We also want something that is safe and secure but does not interfere with the tight schedule and therefore should also be quick and efficient. Lastly, the fixture needs to undergo stress tests and calculations for each part including the buckling of rods under compression, tensile strength of screws and rods under tension, and any shear stress on screws.

Creo Simulation was used for static analysis, including stress and strain calculations of each part. It is also important to take note that the magnets come fully assembled from the manufacturer and therefore they need to be separated before being placed around the vacuum chamber.

C. Components of Fixture

The first problem addressed in designing the magnet fixture is how to secure each magnet, so they can be disassembled into halves and then assembled around the vacuum fixture. Each magnet comes with a pair of tapped holes on the top and bottom of each side.

Taking advantage of these tapped holes we designed plates with through holes, so screws can be used to secure the magnet

halves. The plates are made from aluminum as it meets the necessary strength requirements and is non-magnetic. Figure 2 shows the entire fixture as it would be used.

The fixture consists of two 1" – 8 threaded rods connected to two Zinc hand wheels. The threaded rods are supported by four ball-bearings to allow smooth rotation. The threaded rods are screwed into the driving plates which allow for the movement of the magnets along the track.

Additionally, the tracks for the plates have grooves cut where a screw may be used to prevent any unwanted wobbling. The screws used are stainless ¼ -20 socket head providing the necessary strength requirements and reliability. The one securing plate also has a removable side piece so that it may be adjusted to fit the BDT2 magnet as a hose fitting gets in the way. The use of shims has also been used to keep the magnet centered along the axis of the threaded rods.

D. Corrector Magnets and Pin Removal Tool

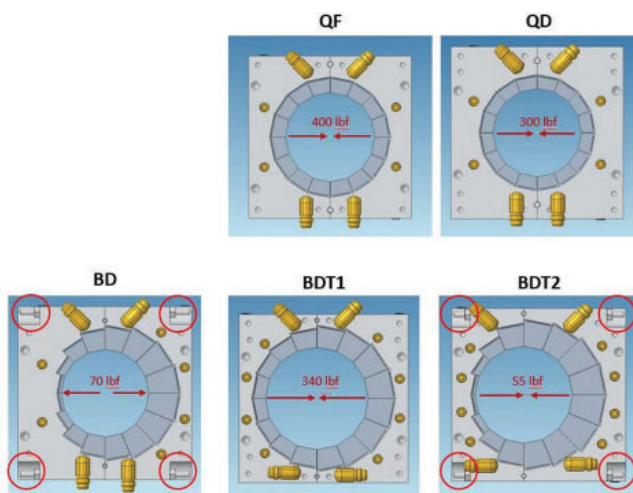


Figure 1: Five variations of the Halbach permanent magnets showing force vectors and important features.

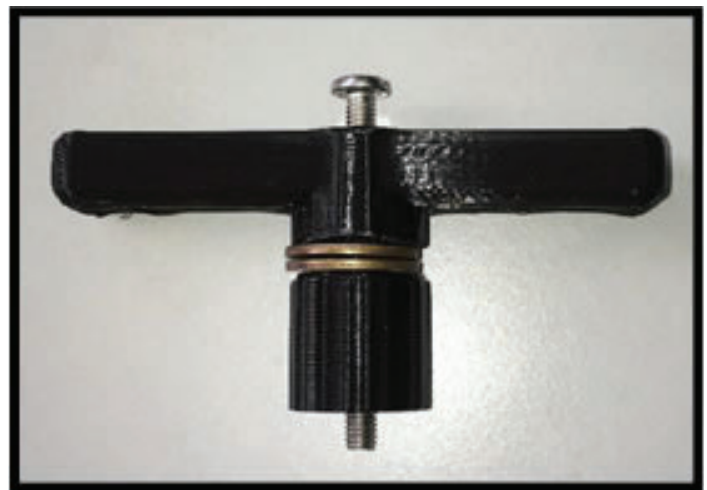


Figure 3: 3D printed prototype of the Pin Removal Tool.

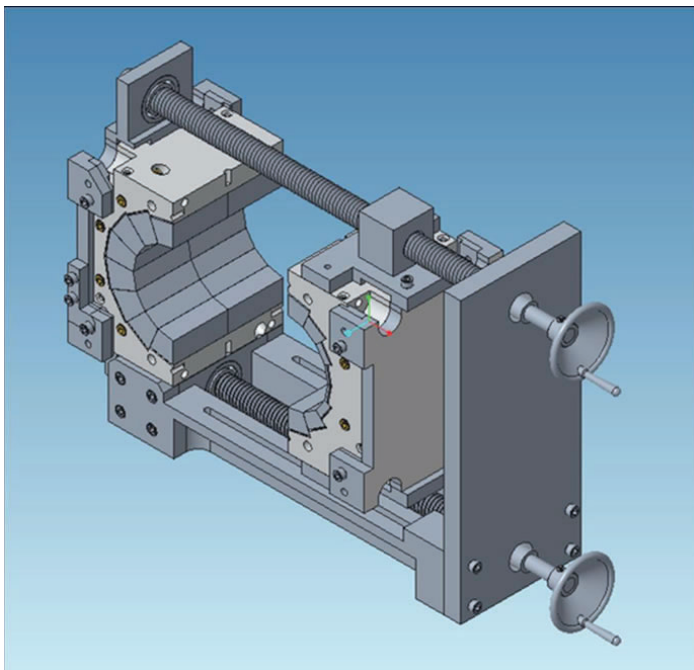


Figure 2: Magnet Fixture is used by turning the handwheels causing the driving plates to move the magnet.

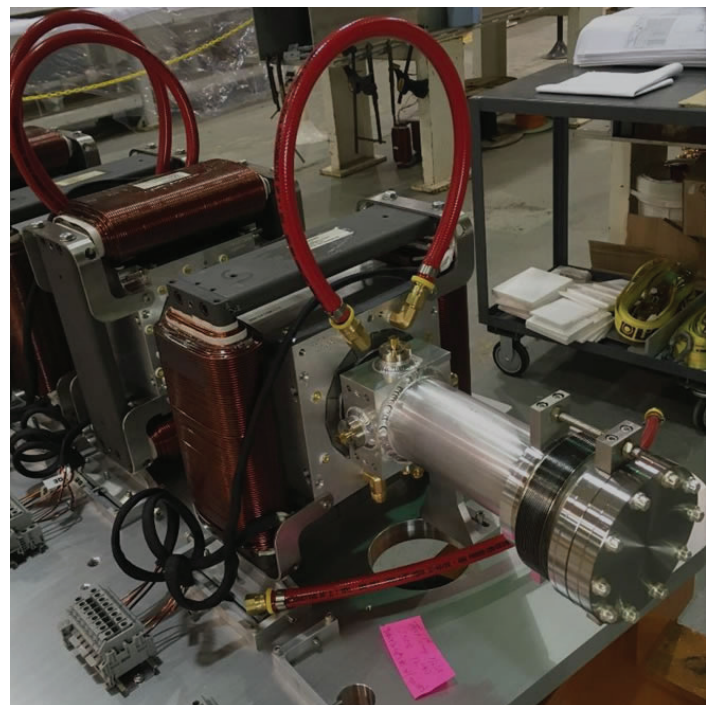


Figure 4: Corrector Magnet fully assembled around and supporting permanent magnet.

The corrector magnets which are these window shapes electro-magnets with coils also come fully assembled from the manufacturer. These magnets are placed around the permanent magnet and support the permanent magnet using brackets suspending them around the vacuum chamber. Getting these corrector magnets around the permanent magnet requires the disassembly of the correctors, but a locating pin on the corrector magnet is wedged into the assembly making it difficult to take apart. Therefore, we have designed a tool to remove the pins from the corrector magnet. The tool works by tightening the screw into the pins internal thread. Once fully threaded, turn the handle driving the nut down (driving the screw and pin up), removing the pin from the hole. The pin removal tool and corrector magnet can be seen in Figures 3 and 4 respectively.

E. Hose Fittingpress

The Halbach permanent magnets need to be kept at a constant temperature of 85° Fahrenheit and therefore require constant flow of water to maintain that temperature. The hoses used to provide the water are attached via a brass fitting. The fitting is usually inserted by means of clamping the hose down in a vise and slamming a hammer to force the fitting in. The design in Figure 5 shows a press which allows for easy insertion of the fitting without risk of pinching your finger. The press works by feeding the

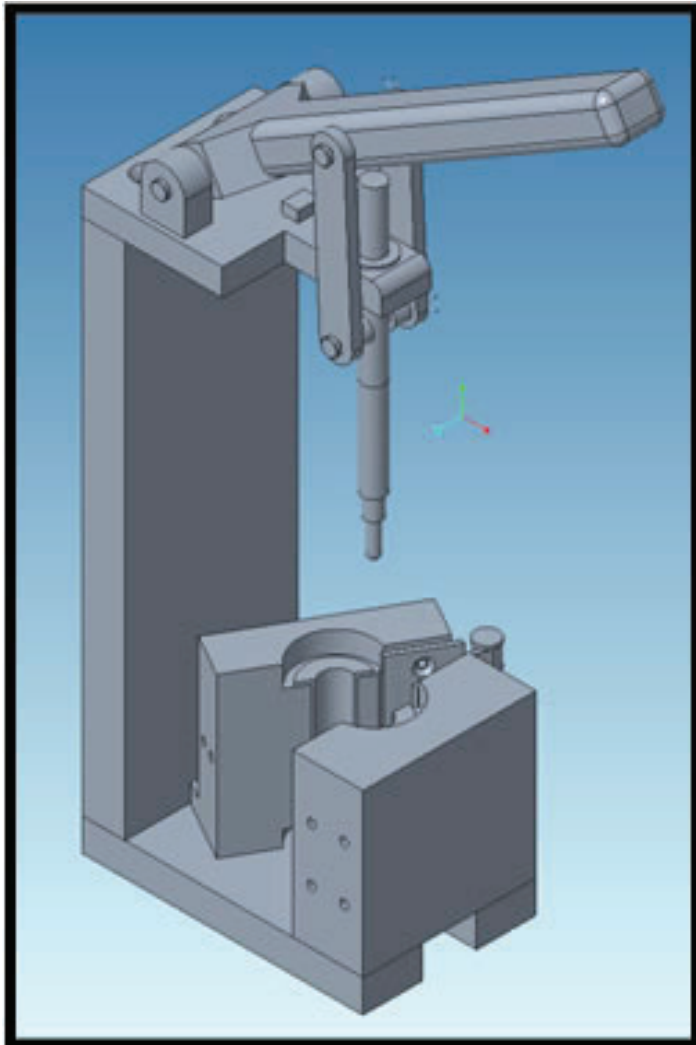


Figure 5: Lever system designed to press brass fittings into hoses.

hose through the opening in the bottom. Next, a toggle clamp is used on the side to quickly secure the hose and clamp it between two blocks. Finally, insert the fitting on the end of the plunge and use the lever to press it into the hose. The design also includes a hinge rated up to 50 lbs making the clamping method quick and secure. The locating rod connected to the lever arm by hinges is guided by a bushing providing smooth sliding motion. The top plate also has an extrusion where a stopper can be placed to rest the lever arm so that it doesn't get in the way when loading/unloading the hoses. Additionally, the parts in the hose fitting press were all rated up to 50 lbs of force. Creo Simulate was used to perform static analysis on each part and find stress concentrations that may be imposed during use.

III. Results

Looking at Figure 6 we can see what the girder plate looks like without the permanent magnets, corrector magnets, and hoses fully assembled. Figure 7 shows complete construction of the girder plates. Ideally, the magnet fixture, pin removal tool and hose fitting press will be implemented to help assist the assembly process upon construction. Figure 7 shows a picture of a fully constructed magnet girder plate that is about to be shipped to Cornell for assembly onto the girders.

IV. Conclusion

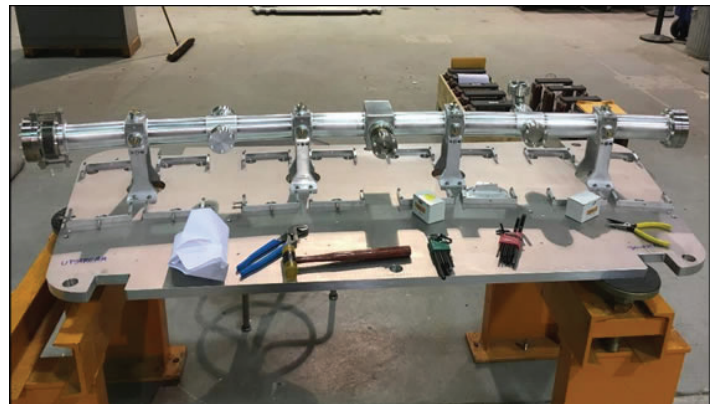


Figure 6: Girder plate with just vacuum chamber assembled.



Figure 7: Fully constructed girder plate being prepared to be shipped to Cornell.

The fixture, hose fitting press, and pin remover tool are all in the process of being manufactured. The forklift safety clamp design is no longer necessary as wooden crates are being used to secure and safely move the plates on the forklift. The fixture is closest to being done with the hose fitting press to be next on the list. We are also still waiting on some hardware including the handwheels, clevis pins, spacers, bushings and threaded rods. A prototype of the 3D printed tool has been tested and as expected the plastic is not strong enough and will have to be made from aluminum. Still, without the use of the tools, we have constructed three of the twenty-seven plates and transported them to Cornell for assembly onto the girders. As more parts come in and with the addition of tools we expect the assembly of each plate to become more efficient throughout this project. C-BETA is expected to be constructed by the end of 2018 and shooting beam by March 2019.

V. Acknowledgements

I would like thank George Mahler and Steve Trabocchi for their knowledge and guidance throughout these projects. This project was supported in part by the U.S. Department of Energy, Office of Science, Office of Workforce Development for Teachers and Scientists (WDTS) under the Science Undergraduate Laboratory Internships Program (SULI).

VI. References

Classe.cornell.edu. (2018). CLASSE: Energy Recovery Linac. [online] Available at: <https://www.classe.cornell.edu/Research/ERL/WebHome.html> [Accessed 8 Aug. 2018].

Finite element magnetic modelling of the LEReC 180° dipole magnet

Tristan Britt

Departments of Physics and Mathematics, Indiana University Bloomington, Bloomington, Indiana, 47421 USA

Honghai Song

Superconducting Magnet Division, Brookhaven National Laboratory, Upton, New York 11973 USA

Abstract

At the electron Relativistic Heavy Ion Collider (eRHIC), one of the experiments currently being conducted is the search for the quantum chromodynamic (QCD) critical point, as part of the Beam Energy Scan Phase-II physics programme. However, the electrons generated in the ring feature the property that the luminosity drops very quickly with energy and is too unstable or too low for producing sufficient data. Therefore, in order to improve the luminosity, the electrons are cooled in the Low Energy RHIC electron Cooling (LEReC) beamline, which counteracts intra-beam scattering (IBS) in the ring and therefore increases luminosity. One of the critical components of the beamline is the 180° dipole magnet, which transfers the cooled electrons from the yellow RHIC ring to the blue ring completely reversing the beam direction. In order to determine the exact behaviour of the beam in the magnets, finite element magnetic modelling (FEMM) was used via the OperaFEA® to determine the magnetic and auxiliary fields along various trajectories. These simulations were done for bend radii of $R = 330, 340, 350, 360, 370$ mm, elevations $Z = -20, -10, 00, +10, +20$ mm and for winding operational currents $I = 2.6586, 3.1911, 3.9833$ A.

I. INTRODUCTION

A. Design and motivation for the LEReC beamline

At the Relativistic Heavy Ion Collider (RHIC), an experiment was conducted, one that would launch electrons into heavy ions, as opposed to protons, to analyse the nature and properties of the particles resulting in/being produced by the collision. The quark-gluon plasma that results not only creates conditions similar to those of the universe at 10^{-40} s after the Big Bang, but these conditions are prime to examine the ground state of quantum chromodynamics (QCD) [2]. This is essential in order for science to understand the fundamentals of most other matter, namely baryons and mesons. The Low Energy RHIC electron Cooling

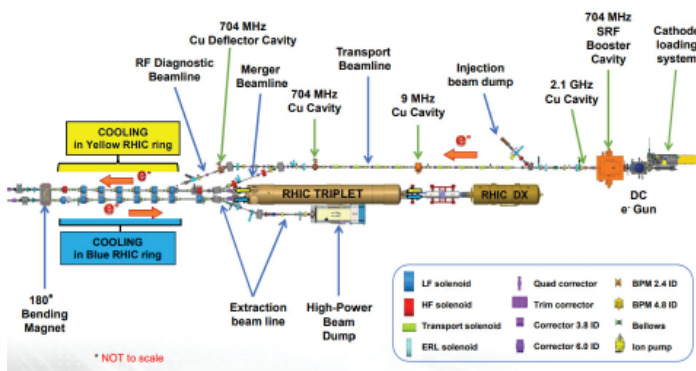


Fig. 1. LEReC beamline schematic in RHIC, as presented in [1].

(LEReC) beamline aims to generate higher luminosity bunches of electrons to make for more accurate targeting and increase in collision temperatures in further experiments. The beamline is generated by illuminating multi-alkali photocathode, *i.e.* CsK₂Sb or NaK₂Sb, inside the emission gun with a high power green-light laser. The electron beam is accelerated in an RF cavity and is boosted towards the 180° magnet. Then, once reversed in direction and focused, the beam is dumped for use in eRHIC.

II. Design of the 180° dipole LEReC magnet

In order to reverse the direction of the beamline, only a dipole magnet is needed, if designed correctly. In order to handle the load of the Lorenz forces caused by the bending electrons, and to create as nearly a perfect semi-circle bend of the electrons, a bedstead magnet was designed. The magnet is ultimately comprised of a Steel 1006 housing with a # 8 heavy-build copper wire wrapped bedstead magnet incased inside. Each coil features $N = 298$ turns of the copper wire, with the beamline entering one side of the inner chamber as is deflected out the near-opposite side of the same face.

The full set up features mounting for both Hall and NMR probes (to be explained later), as well as various other detector and current inputs¹.

III. COMPUTATIONAL SETUP

A. Hysteretic Considerations

The material that the magnet is a manufacture of is AISI 1006 Steel, a soft low-carbon alloy that exhibits, in theory, nonlinear behaviour when exposed to demagnetising and remagnetising fields. Unfortunately, hysteretic effects are difficult to manually take into account without the aid of supplemental software modules (such as OperaFEA's® Opera3D_DEMAG module or COMSOL Multiphysics's® AC/DC module V.5.3a). These models implement a Jiles-Atherton model, originally derived from first principles of energy distribution, and is described in detail

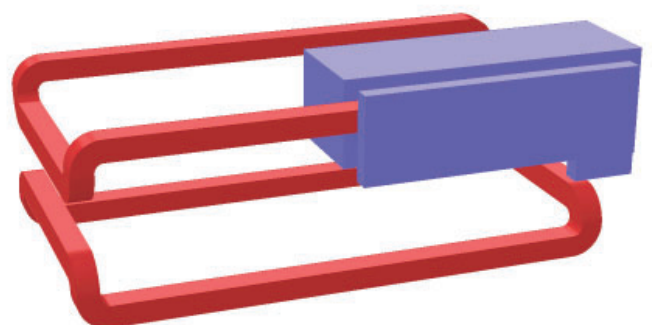


Fig. 2. 180° magnet, with only an eighth of the casing shown for the illustrative purposes only, as generated in Opera3D® Modeller.

elsewhere [3]. Although integration into simulation manually is possible, the model features 5 parameters which are currently unknown (or at least unpublished) for AISI 1006. These parameters can either be determined through numerical determination [5] or through particle swarm optimisation [4] (PSO). This would require physical experimentation and was precluded by the purposes of this research. Luckily, low-carbon steels feature major (and minor) hysteresis loops that only deviate to at most 5% from the average line through the entire hysteresis curve [6]. Meaning that if one already has first quadrant data in the B-H plane, simply reflecting that to the third quadrant would serve as a reasonable approximation of the whole hysteresis loop (cf Figure A.1 in Appendix: Figures).

B. Geometries of Regions of Interest

The beam features high luminosity and will be comparable to the single electron scenario. Therefore, we study the magnetic fields along the straight leg of entry, semi-circles² of radii $R = 330, 340, 350, 360, 370$ mm, and at verticle elevations $Z = 0, \pm 10, \pm 20$ mm, with operational winding currents of the magnet itself at $I = 2.6586, 3.1911, 3.9833$ A.

C. Current Ramping Cycle

Since current cannot be distributed within a given volume instantaneously, there must be a ramp cycle used to get the magnet to the desired operating current. Due to hysteresis effects in this situation, the following custom ramp cycle was used to induce proper demagnetisation and remagnetisation, minimising internal magnetisation, therefore allowing for more accurate measurements. With a ramp rate $dI/dt = 0.4$ A/s, an exponential rate c

$= 0.17$, the target current I A, the convergence factor $k = 0.017$, number of iterations $M = 24$, and hold time³ $T = 2$ s, the following discrete current distribution was followed:

$$i_n = \sum_{n=1}^M I \left(1 - (-1)^n [e^{-cn} - I] \right) \quad (1)$$

$$t_n = \sum_{n=1}^M \frac{|i_n - i_{n-1}|}{dI/dt} \quad (2)$$

For simulation, since the coils are wound tightly enough together to be approximated by uniform wrapping, this discrete current distribution must be transformed into a discrete current density distribution, which is done easily by a multiplicative factor or N/a where N is the number of turns of wire and a is the cross-sectional area of the bedstead conductor, in this case 30 cm^2 . The equivalence of target currents to target current densities is $I = 2.6586 \text{ A} \leftrightarrow J = 26.40876 \text{ A/cm}^2$, $I = 3.1911 \text{ A} \leftrightarrow J = 31.69826 \text{ A/cm}^2$, and $I = 3.9833 \text{ A} \leftrightarrow J = 39.56745 \text{ A/cm}^2$. This data is then tabulated into a `.tsv` file, imported into Opera3D[®] Pre-Processor as a `.tt` file, effectively creating a closed switch external circuit connected to the bedstead conductor.

D. Additional Considerations

When operational, the electron beam will enter one end of the magnet, be deflected across the magnet cavity in a semi-circle, and will eject very near its symmetric opposite from the cavity, as illustrated in Figure 3. The beam does not exit entirely symmet-

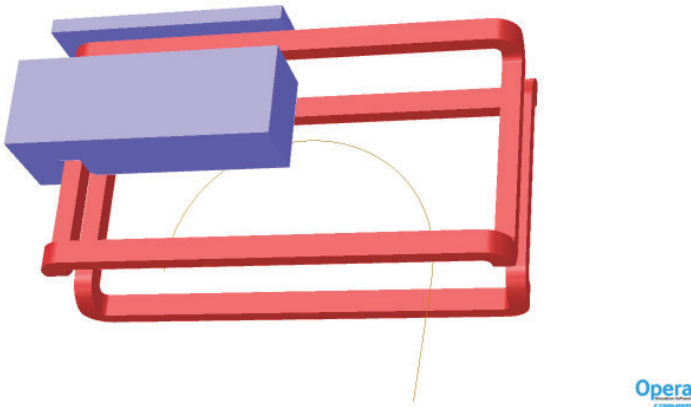


Fig. 3. Illustration of single electron with an acceleration potential of 1.6 MeV travelling through the magnet cavity, and ejecting nearly opposite from the point of entry.

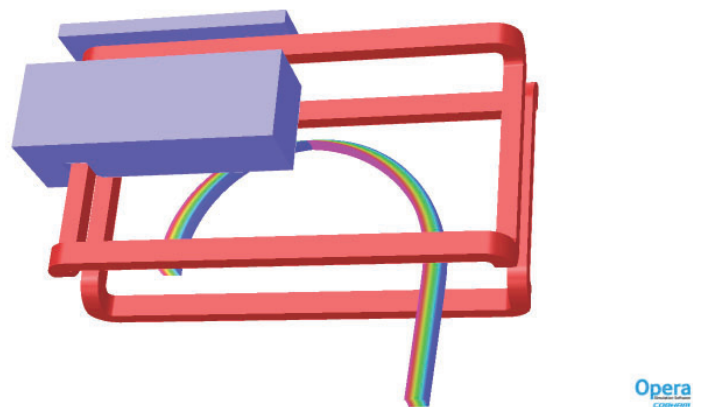


Fig. 4. A square electron beam with an acceleration potential of 1.6 MeV of width 5 cm is injected into the body cavity, and exits the cavity.

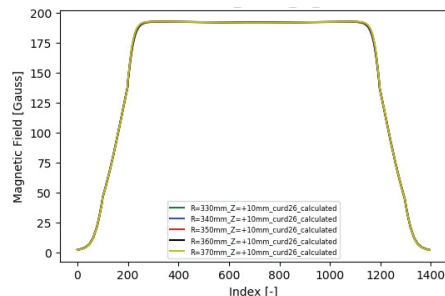


Fig. 5. $I = 2.6586$ A, $Z = +10$ mm for all radii calculated.

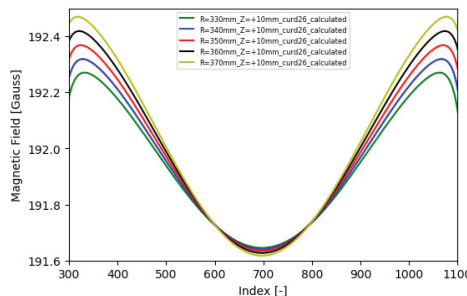


Fig. 6. Figure 5, magnified on the section inside the magnet.

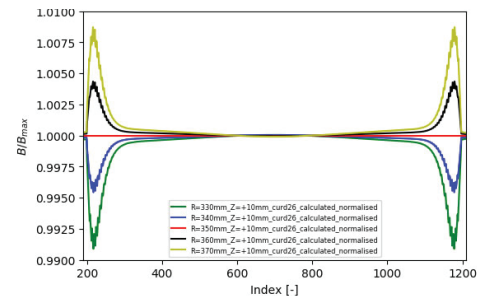


Fig. 7. $I = 2.6586$ A, $Z = +10$ mm for all radii calculated, magnified on the internal section of the magnet cavity, normalised to the maximum value of B_{350} .

rically, nor does it exist the cavity with a velocity perpendicular to the magnet casing. This is illustrated in Figure 4, where the electrons have been coloured based on their position along the axis perpendicular to the direction of entry. Note that the electrons initially on the outmost side of the beam exit the cavity as the innermost electrons and vice versa, implying each electron does not follow a uniform semi-circular path whilst in the body cavity, but one with very slight eccentricity.

IV. RESULTS

A. Exporting and Processing Data

OperaFEA[®] outputs the magnetic field data into 'buffers', being simple 2D geometries along which the data is recorded. The software cannot easily integrate more complex geometries, such as in this case which is 2 lines and a semi-circle. The data for each combination of parameters must therefore be exported and all 3 files need to be spliced together so the data for the entire trajectory is in a single file. The data can be exported as .csv files, which can be converted into .xlsx files, allowing for more easy usage in spreadsheet programs like Microsoft Excel[®] and also for data visualisation and analysis⁴.

B. Data Visualisation⁵

The following example is that of current density $J = 26.40876 \text{ A/cm}^2$ and $Z = +10\text{mm}$, which is reasonably indicative of the type of behaviour exhibited by the rest of the parameters.

C. Comparison to Measured Data and Discussion

For this, only the case of $R = 360 \text{ mm}$ is included here simply as a placeholder for the rest of the data, since the behaviour of all the radii is comparable. We note that the simulated is less than the measured data. This is a trend that is pervasive throughout the data. The critical item of note though is that the error is *uniform* across the combinations of parameters. This implies it is a systematic error either from simulation or from errors in the computer model of the magnet or in the material properties themselves. The overall error across all data points is 0.8-5.2% from the measured values, and this is generated by two items. Firstly, as was previously alluded to, hysteretic measurements are computationally difficult to include in simulations manually without the aid of additional software. Therefore, due to licensing issues, the results

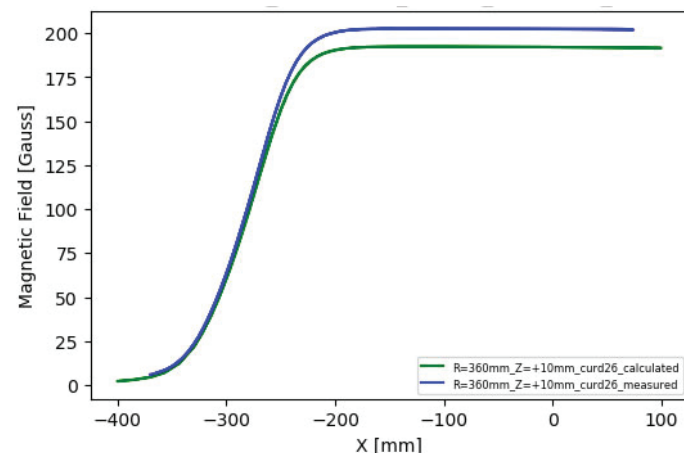


Fig. 8. $I = 2.6586 \text{ A}$, $Z = +10\text{mm}$, $R = 360\text{mm}$ illustrating the magnetic field as projected onto the X-axis along the path of measurement.

were unable to incorporate the full four quadrant BH curve, and the approximation as described in II.A was used. However, knowing that this approximation deviates from the true curve in theory by 5%, this approximated curve was adjusted by $\pm 5\%$. Across all combinations of parameters, this lead to a 1.1-3.0% error, a non-trivial portion of the overall error. Secondly, since full hysteretic effects were not included in the model, the nonlinear ramp cycle, described in II.C, was not used since the software could not properly model full memory demagnetising and remagnetising effects. Therefore, the second error arises from the fact that the target current was reached instantaneously in simulations, as opposed to 120-155 s (depending on J used). This error is hard to quantify since doing so requires the ability to model hysteretic effects, which is the central issue in these simulations in the first place.

V. CONCLUSION

The LEReC 180° bending magnet not only can effectively bend high near-relativistic electrons using only fields on the order of 200 Gauss, and previous measurements of the fields along various trajectories and other parameters of the magnet, including the nonlinearity of the magnetisation of the AISI 1006 steel housing, were proven to be accurate within the errors created by the simulation software and material properties inputted into said software. These errors could be reduced by manually implementing a full memory Jiles-Atherton hysteresis model into another simulation software, such as COMSOL Multiphysics[®] or another finite element magnetic modelling (FEMM) software.

VI. END NOTES

- ¹The schematic of the full set up is included in the appendices as the entire magnet composition does not pertain to this paper.
- ²The semi-circles have origin at the center of the inner side of the long section of the bedstead coil, and the straight sections are simply the linear continuations of these semi-circles at the given radii outside of the body cavity.
- ³After each discrete time step, the current is held steady for the hold time T as an attempt to minimise eddy effects within the magnet body.
- ⁴Various Python scripts were used to convert file types, order and organise data, and for data visualisation.
- ⁵Since there is an amount of data larger than is appropriate to include here, only the data for a single set of parameters will be included in the main text.

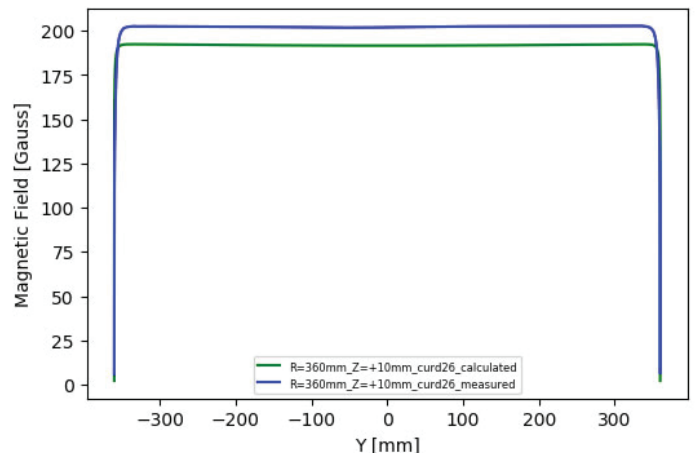


Fig. 9. $I = 2.6586 \text{ A}$, $Z = +10\text{mm}$, $R = 360\text{mm}$ illustrating the magnetic field as projected onto the Y-axis along the path of measurement.

VII. REFERENCES

- Alexei Fedotov. "Low Energy RHIC electron Cooling (LEReC)". RHIC and AGS Users Meeting, Brookhaven National Lab, New York, 2018. Powerpoint.
- Roberto Casalbuoni. "QCD critical point: a historical perspective". International Workshop The Critical Point and Onset of Deconfinement, Florence, Italy. 2006.
- A. J. Bergqvist, "A simple vector generalization of the Jiles-Atherton model of hysteresis," in IEEE Transactions on Magnetics, vol. 32, no. 5, pp. 4213-4215, Sept. 1996.
- Romain Marion, Riccardo Scorretti, Nicolas Siauve, Marie-Ange Raulet, Laurent Krhenbhl. Identification of JilesAtherton Model Parameters Using Particle Swarm Optimization. IEEE Transactions on Magnetics, Institute of Electrical and Electronics Engineers, 2008, 44 (6), pp.894-897.
- D. C. Jiles, J. B. Thoelke and M. K. Devine, "Numerical

determination of hysteresis parameters for the modeling of magnetic properties using the theory of ferromagnetic hysteresis," in IEEE Transactions on Magnetics, vol. 28, no. 1, pp. 27-35, Jan. 1992.

- J. Gyselinck, P.Dular, N. Sadowski, J. Leite, J.P.A. Bastos, (2004) "Incorporation of a JilesAtherton vector hysteresis model in 2D FE magnetic field computations: Application of the NewtonRaphson method", COMPEL The international journal for computation and mathematics in electrical and electronic engineering, Vol. 23 Issue: 3, pp.685-693

VIII. ACKNOWLEDGEMENTS

This project was supported in part by the U.S. Department of Energy, Office of Science, Office of Workforce Development for Teachers and Scientists (WDTS) under the Science Undergraduate Laboratory Internships Program (SULI). Also, many thanks to Honghai Song for his mentorship and expertise.

IX. APPENDIX

A. FIGURES

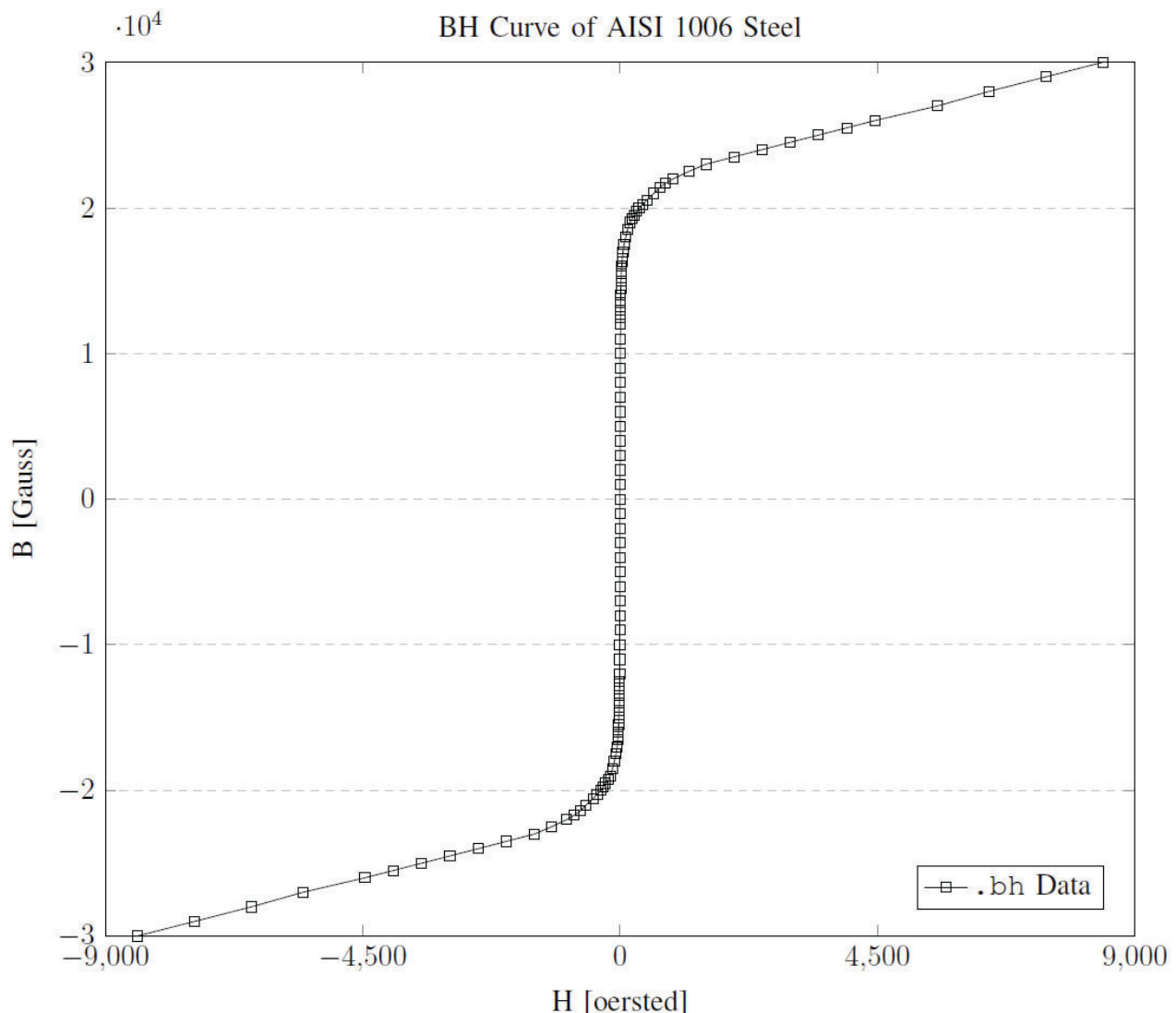


Fig. A.1. BH Curve for AISI 1006 Steel, using the thin hysteresis loop approximation of low-carbon steel alloys.

Testing and commissioning the cold electronics for the Short Baseline Near Detector

Justin Bryant

Department of Mathematics and Computer Science, Alabama State University, Montgomery, AL 36104

Mary Bishai

Department of Physics, Brookhaven National Laboratory, Upton, NY, 11973

Abstract

The Short Baseline Near Detector (SBND) at Fermilab is a 112-ton liquid argon time projection chamber (LArTPC) and will be one of three liquid argon neutrino detectors sitting in the path of the Booster Neutrino Beam (BNB) at Fermilab as part of the Short-Baseline Neutrino Program. SBND studies neutrino-Argon interactions and tests for the existence of sterile neutrinos, a new basic particle of matter that if found could have profound impact on particle physics and our understanding of the fundamental building blocks of matter [1]. The physics of the interactions between neutrinos and argon is an important element of future neutrino experiments that will utilize the LArTPC technology, such as the long-baseline Deep Underground Neutrino Experiment (DUNE). Brookhaven National Laboratory (BNL) is currently quality testing around 1200 front-end application specific integration circuits (FE ASICs) under cryogenic conditions. These front-end chips are an integral part of the TPC wire data collection system, in which they amplify the analog signal coming from the neutrino interactions with the argon, which carry a current to the wires in the anode plane assembly (APA). The current process involves performance testing on these ASICs in a specially designed cryogenic testing system. Prototypes of these electronics have been installed for testing at the SBND Vertical Slice Test (VST) site at Fermilab. The combined results of this research from these two laboratories will analyze the reliability and performance of SBND cold electronics.

I. Background

Neutrinos interact through two Standard Model forces: the weak force and gravity. It is this lack of interactions that gives them their ghostly nature. 50 percent of the neutrinos coming from the sun will pass through a light-year of lead without interacting. The challenge with searching for “sterile” neutrinos is that researchers are looking for a particle, already nearly massless, that does not interact through the weak force. The hints of sterile neutrinos come from a couple of experiments. The Liquid Scintillator Neutrino Detector (LSND) experiment at Los Alamos National Laboratory studied a decay-at-rest beam made of mainly muon neutrinos and found more electron neutrinos than they predicted. This was a similar signature of oscillation that had been seen for the known neutrino flavors, but at a distance and energy combination researchers weren’t expecting. A similar signal at a new location is a hint that an unknown kind of neutrino was hiding behind the scenes. There is a lot of ongoing work to confirm if this interpretation of the LSND results is correct. So far the results have been inconclusive from these experiments.

A. SBND

SBND is a liquid argon TPC. Charged particles passing

through the liquid argon create ionization, and an electric field maintained by appropriate voltages on the cathode and anode planes drifts the free electrons to the anode plane assemblies (APAs), where the charge is collected on wires. Each anode plane assembly consists of three wire planes with the wires running in different directions.

SBND will record over a million neutrino interactions per year. By providing such a high statistics measurement of the un-oscillated content of the booster neutrino beam, SBND is a critical element in performing searches for neutrino oscillations at the Fermilab Short-Baseline Program. The large data sample will also allow studies of neutrino-argon interactions in the GeV energy range with unprecedented precision. [1]

B. Cold Electronics

After studies of the transistor characteristics and lifetime at cryogenic temperature, BNL designed an FE ASIC suitable for 77K–300K operation and long lifetime with lower power consumption. Meanwhile, various commercial CMOS devices have been screened to find survivors at cryogenic temperature. Two CMOS devices, a low voltage regulator from TI and an Altera Cyclone IV FPGA are qualified for cold electronics development. Since high-resolution and low power consumption SAR architecture ADC becomes widely available, we started to characterize the performance of Commercial-Off-The-Shelf (COTS) ADC at cryogenic temperature since June 2017. Several COTS ADC chips have been identified as good candidates for operation at cryogenic temperature after initial screening test. One candidate, ADI AD7274 fabricated in TSMC 350nm CMOS technology, of which lifetime at cryogenic temperature has been studied since September 2017 [2].

The creation of a cold electronics system is motivated primarily in an effort to reduce the amount of noise in the readouts. A typical readout configuration with warm electronics consists of long cables connecting the sense wires to the front-end electronics, resulting in large electronics noise. Therefore, SBND chooses cold electronics as LAr TPC readout solution. CMOS cold FE ASICs are placed close to the wire electrodes to detect charge signals, followed by the ADC for signal digitization. Digitized signal will be further organized and transmitted to the downstream readout and Data Acquisition (DAQ) system [3]. Cold electronics decouple the electrode and cryostat design from the readout design. With electronics integral with detector electrodes the noise is independent of the signal cable lengths, and much lower than with warm electronics. To reduce the cable length, cold feed-throughs are implemented below the liquid level, which increases the cryostat complexity. The noise is significantly less than at room temperature when the front-end ASICs are operating under cryogenic conditions.

II. Objective

LArIAT is the repurposed ArgoNeuT detector, modified for use in a charged particle beam. It is a small volume Liquid Argon Time Projection Chamber (LArTPC) dedicated to the calibration and precise characterization of output response of these detectors. The charged particle test beam provides a controlled environment in which to tune simulations and to develop tools for particle identification, calorimetry, and event reconstruction without relying solely on simulation. The SBND's Vertical Slice Test (VST) is an integration of the cold and warm electronics with data acquisition (DAQ) and online monitoring using the LArIAT TPC. The goal of this project is to:

Develop code to create user settings input & LArIAT implementation for SBND VST Screen ADC ASICs for viable chips

III. Methods

A. Implementing LArIAT Map & user input settings

All the test code is written in Python and is stored in a GitHub repository under the "SBND_VST" & "configuration" directories. All test code is available on the DUNE GitHub repository at https://github.com/DUNE/femb_python.

B. ADC ASIC Testing

There are two ADC test stands: one horizontal, and one vertical; however, the test procedure remains the same for both. Each test board is connected to a programmable Rigol power supply and waveform generator. An ADC is then secured into the clamshell socket on the board, and the board is placed into a basket suspended above the dewar containing liquid nitrogen.

Using the ADC Test GUI, the board is initialized, and a window showing the read back from the 16 chips using an input sine wave will be shown. If the sine waves for all 16 channels is shown and stable, the cold tests can begin. The basket is then lowered into the dewar slowly, and the waveforms on the 16 channel GUI are monitored to make sure they are stable or revert to stability after each step of lowering it into the dewar. Tapping the chip and/or socket lightly may be necessary to restore stability. If the stability cannot be recovered, the test ends, and the chip gets labeled for retesting. After the chip is submerged completely, a series of tests are conducted through the GUI. Each test takes around 10 minutes to complete, and the chip will either pass or fail according to its

performance.

Test failures can be attributed to a number of errors, including: FEMB_UDP failure to read register, meaning that the ethernet connection between the FPGA mezzanine and the DAQ has been disconnected; and SPI readback errors, meaning that the software is unable to verify the chip is properly initialized by reading back the values from a register. Finally, the boards are removed from the liquid nitrogen, dried and warmed up to room temperature, and the chip is removed from the clamshell and placed in the appropriate box: "done testing" if the test completed, "retest" if it didn't complete, and "bad" if the chip is physically damaged or has failed tests twice on different boards.

IV. Results

A. Python code for the LArIAT APA mapping was successfully integrated into the front end electronics configuration file on the GitHub repository.

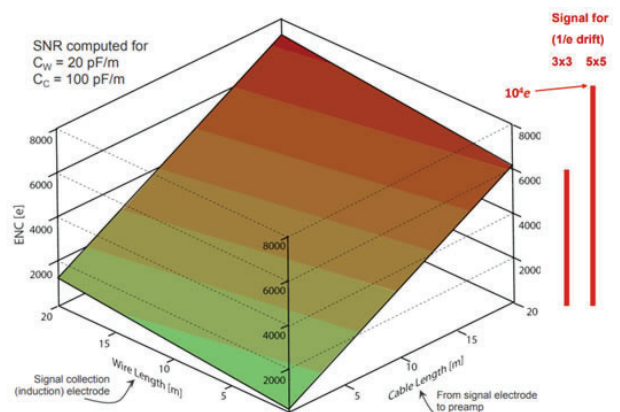
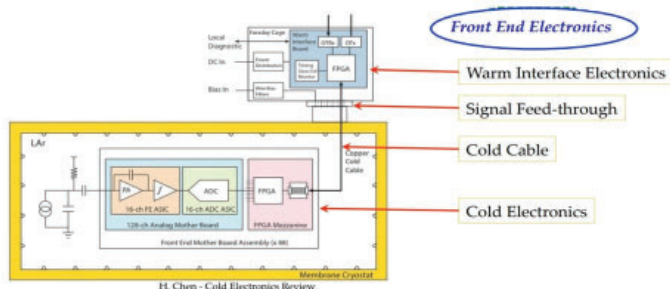
B. Over the course of one month, 263 total ASIC tests were conducted, and only 121 resulted in a successfully completed test, for a test completion rate of 46%. This is consistent with previous rates from testing these ADC ASICs.

V. Acknowledgements

I would like to thank Mary Bishai and Matt & Elizabeth Worcester for their patience and support throughout this project. This project was supported in part by the Brookhaven National Laboratory (BNL), Physics Department under the BNL Supplemental Undergraduate Research Program (SURP).

VI. References

- [1] "Short-Baseline Near Detector (SBND)." Fermilab | Short-Baseline Near Detector, 14 Aug. 2015, sbn-nd.fnal.gov/index.html
- [2] H. Chen, et al. "Lifetime Study of COTS ADC for SBND LArTPC Readout Electronics," 2018. PDF file.
- [3] Chen, H. "Cold Electronics Review". 12 Oct 2016. PDF file.
- [4] S. Gao, et al. "The Development of Front-End Readout Electronics for ProtoDUNE-SP LAr TPC," Proceedings of the 2017 Topical Workshop on Electronics for Particle Physics. 11-14 September 2017. PDF file.



Using a laser ion source to produce and study heavy ions from chemical compound targets

Harry Chalfin

Department of Physics, Brown University, Providence, Rhode Island 02912, USA

Masahiro Okamura

Collider-Accelerator Department, Brookhaven National Laboratory, Upton, New York 11973, USA

ABSTRACT

Our research team analyzed ions ejected from chemical compound targets when bombarded with lasers. In the main portion of the project, we fired a laser with energy 369 mJ at a target of zirconium dioxide. We found that the vast majority of the ions ejected were either Zr^{1+} or O^{1+} ions. Various species of polyatomic ions and contaminant ions were also detected. Very few ions of the ions detected were in charge states other than $1+$. We would like to perform a similar study with a lithium compound target in order to study lithium ions, which could be of great practical importance. We have been working to produce a lithium oxide target, but the task has proved to be challenging due to the chemical's reactive properties.

I. INTRODUCTION

The long-term goal of our research is to produce and harvest a beam of neutrons with high directivity. Neutron beams have various important applications, including boron neutron capture therapy of cancer. A typical method to produce neutrons is to bombard a stationary lithium material with protons, resulting in a nuclear reaction:



According to classical mechanics, the velocity of the center of mass remains constant in any collision. Here, if v denotes the original velocity of the protons (Hydrogen ions) as measured in

the lab's reference frame, then the velocity of the center of mass is $1/7v$. This means the resulting neutron shower will have a relatively small average velocity. In more technical terms, the resulting neutron beam has a low directivity. Our research team seeks to generate a neutron beam with a high directivity by conducting the same nuclear reaction as above, viewed from a different reference frame: instead of firing a beam of protons towards a lithium material, we intend to fire a beam of lithium ions towards a hydrogenous material. Let u be the relative velocity between the lithium ions and the hydrogenous material. In the lithium ions' reference frame, the center of mass of the system moves at $1/7u$, much like the above case; however, in the lab's reference frame, the center of mass of this system moves at $6/7u$. This means that we can produce a resulting neutron shower with a higher average velocity (in the lab's frame) than in we had used the other method, yielding a higher directivity. The neutrons in this beam will tend to travel towards a common region, where they can be captured more easily. [1]

In summary, to achieve our eventual goal of producing and harvesting neutrons, we must first collect a beam of lithium ions. That intermediate goal has been the central thrust of our recent and current work. Only a month ago did our team receive the necessary safety approval to handle lithium oxide (Li_2O), so the main portion of this project has been aimed at studying ions produced from a target of zirconium dioxide (ZrO_2), a less hazardous chemical. The "Further Research" section at the end of this report details our more recent attempts to produce laser targets from samples of Li_2O . Soon, we will conduct a nearly identical study

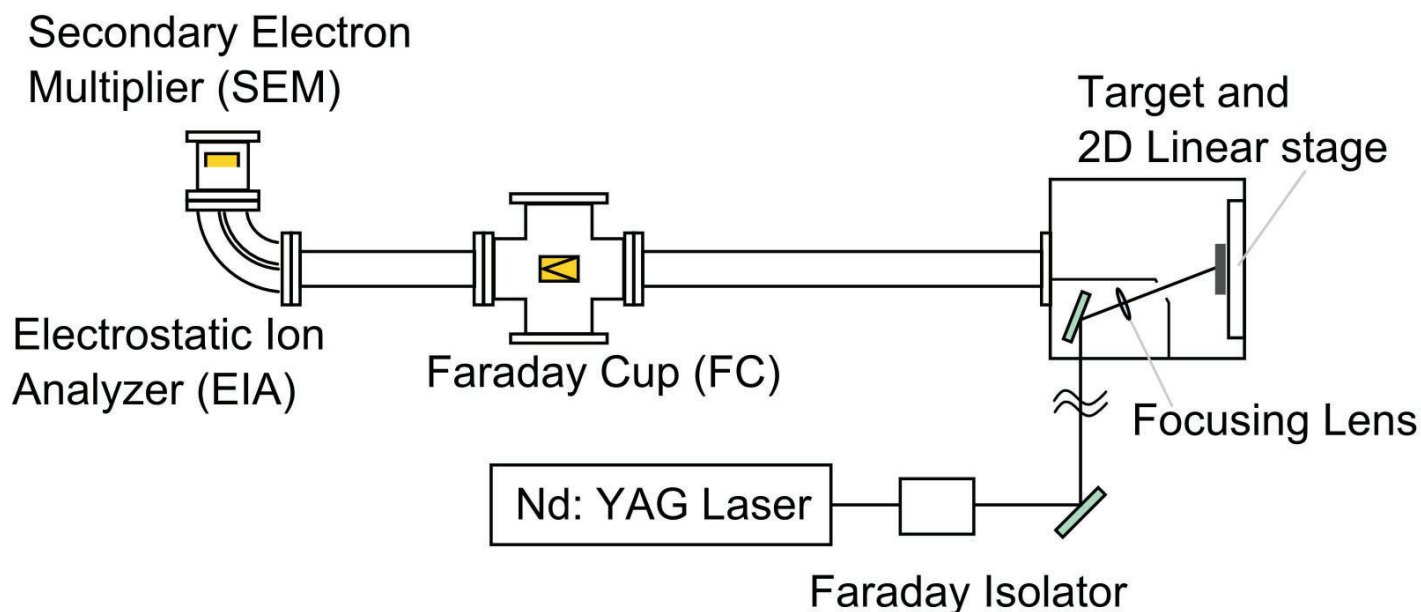


FIG. 1: A laser pulse is fired towards a chemical target, ejecting a plasma of free ions and electrons. The free particles travel down a vacuum tube towards various detectors which record data, enabling one to study the ions in detail.

as the one described in this report, but with Li_2O as our target substance instead of ZrO_2 .

II. MATERIALS AND METHODS

First, a powder sample of a certain chemical compound (in this case ZrO_2 , though in principle almost any solid compound could be used) is placed into a die and is subjected to high pressure (several tons over an area of a few hundred square mm or less). The sample is then gradually removed from the die and retains the shape of the die's cavity. At this point, the sample is somewhat cohesive but quite fragile. It is then placed in an oven and heated to a high temperature (several hundred degrees Celsius or higher) for a few hours. In the oven, the sample sinters; its molecules form strong bonds and the material becomes rigid and sturdy. The sample can now be used as a laser target.

In a vacuum chamber, a laser pulse is fired at the chemical target, which is now mounted on the chamber's inner wall. The laser pulse contains sufficient energy to cause the struck atoms to melt, vaporize, and become a plasma within a few nanoseconds. The plasma plume travels down a long tube which is perpendicular to the target. In the middle of the tube lies a Faraday cup, a device which detects particles and records their time of travel from their original location. This allows one to create a graph of the number of particles traveling by as a function of time.

The Faraday cup can also be lifted so as to allow the particles in the plasma to continue to travel down the tube. Eventually, the tube begins to curve sideways in a quarter circle arc of radius 100 mm. A pair of electrodes inside the curved tubing produce an electric field, and the potential difference between the electrodes can be controlled easily. The field will deflect the paths of the ions in the plasma. At the end of the curved tubing lies an SEM detector, a device which will measure the number of particles whose paths intersect a window of a few square centimeters in each small interval of time (that is, particles whose paths almost exactly follow the arc of the tubing).

III. THEORY

The laws of mechanics and electrostatics allow one to calculate the necessary conditions for a particle to follow a circular arc path and reach the SEM detector. If m is the mass of the particle, v is its speed, and R is the radius of curvature, then the centripetal force is given by:

$$F_{\text{centripetal}} = \frac{mv^2}{R} \quad (2)$$

It is important to note that v remains constant throughout the journey – the electric field is perpendicular to the path of the particle along the arc and hence performs no work on the particle. If q is the charge of the particle and E is the strength of the electric field, then the electrostatic force on the particle is given by:

$$F_{\text{electrostatic}} = qE = \frac{qV}{d} \quad (3)$$

Here, d is the distance from one wall of the tubing to the other and V is the potential difference between the walls. Combining equations (2) and (3), we have:

$$\frac{mv^2}{R} = \frac{qV}{d} \Rightarrow v = \sqrt{\frac{RVq}{dm}} \quad (4)$$

Notice how all quantities on the right side of equation (4) are completely determined: R and d are constants which depend only on the geometry of the setup, the potential difference V is controlled by the observer, and q/m is the ion's charge-to-mass ratio – because the chemical composition of the target is known, there are only a few possible charge-to-mass ratios for which one must account. This leads to an important point: at a given potential difference, all particles which arrive at the SEM detector must have traveled with one of only a few specific velocities, each velocity corresponding to a particular ion species in the plasma. As a result, if one were to graph the current detected at the SEM detector as a function of time, then at most moments in time one would see almost no current, but one would see sharp peaks at times when ions of a particular species arrive. One can analyze

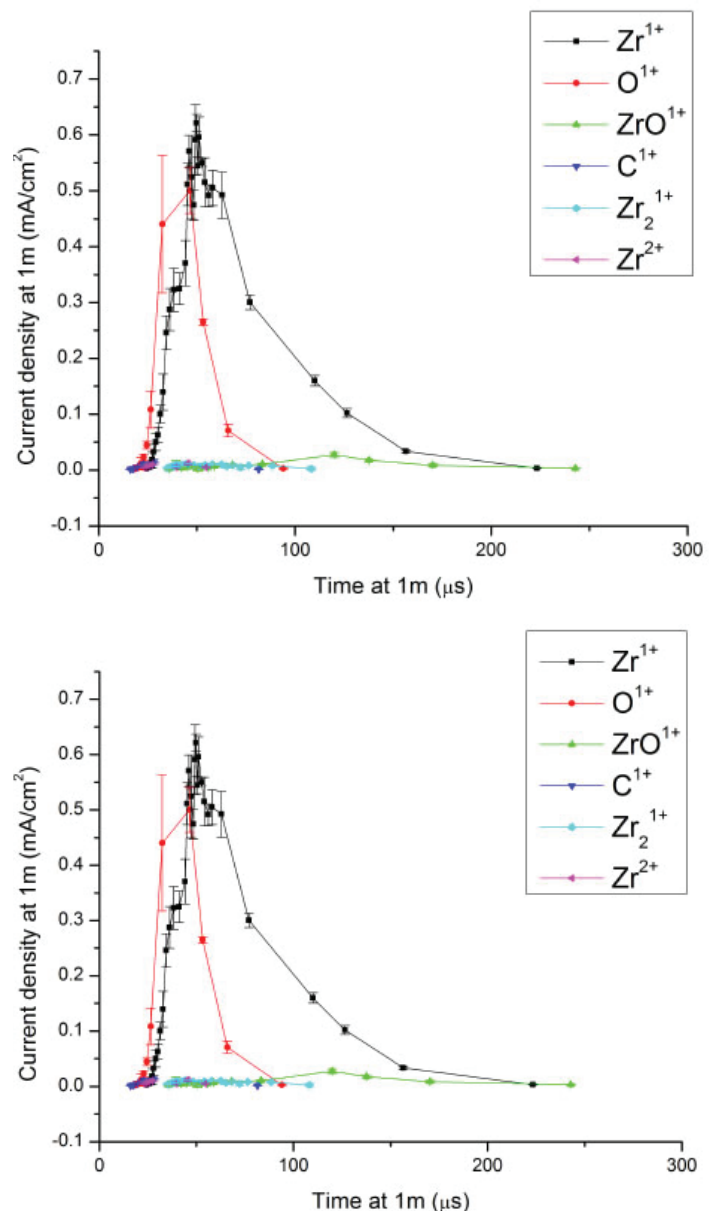


FIG. 2: Plot of current density at 1m as a function of travel time for each ion species (upper); the same data plotted on a logarithmic vertical scale (lower).

this data to study which ion species have been ejected by the target, in what quantities, and how quickly they have reached the SEM detector.

IV. RESULTS

We fired our laser at the ZrO_2 target with voltage values between the electrodes ranging from 0.5 V to 40 V. We measured the positions and heights of the current peaks and identified each peak with its corresponding ion species. We then used this data to create a plot of the current density resulting from each ion species as a function of time. See Figure 2.

Each data point represents an average of five independent measurements at a particular voltage. The error bars reflect the standard deviation in the five measurements.

V. DISCUSSION AND ANALYSIS

As is clear from Figure 2, the two most common ion species ejected were Zr^{1+} and O^{1+} – these are the two ions that can be produced by stripping a single electron from an atom in a ZrO_2 target. This highlights an important point: it is easier to create singly charged ions than ions in a highly-charged state; after the removal of one electron (which obviously carries a negative charge), an atom is left with a net positive charge, making it more difficult to remove any subsequent electrons. In more technical terms, an element's first ionization energy is always lower than its second ionization energy and any subsequent ionization energies. In our results, the only non-single charge species detected was Zr^{2+} , whose peak abundance was more than an order of magnitude weaker than that of the Zr^{1+} ion.

Also of considerable interest is that some ions produced (ZrO^{1+} and Zr_2^{1+}) were polyatomic (more than one nucleus). This came as a surprise to our group and might suggest that the laser energy we used was so low or the laser spot size was so large that the laser pulses did not have sufficient energy density to split the molecular bonds between these pairs of atoms; we hypothesize that if the laser energy were higher or the laser spot size were smaller, the abundances of these polyatomic ions would rapidly diminish. We used a laser energy of 369 mJ, with an uncertainty of 12 mJ. The laser spot was elliptically shaped, with a major axis of 3.2 mm and a minor axis of 2.4 mm, with an uncertainty of about 0.4 mm.

Trace amounts of C^{1+} ions were detected, suggesting that our target was contaminated by organic molecules. It is entirely possible that one of the researchers touched the target with bare hands or produced the target using equipment that had not been sterilized. We have taken this as a sign to try to avoid these sorts of contaminations with future targets.

Finally, more massive ions tended to have higher abundances at later times than less massive ions; this is expected as



FIG. 3: A powder sample of Li_2O before sintering (left); the sample after sintering (right). The sample has expanded and lost its geometric shape. Craters are now present on its surface, and stains on the plate below indicate some amount of melting.

it implies that the higher-mass ions have traveled more slowly through the vacuum tube. Soon, more careful studies may be able to determine if there is a specific mathematical relationship between an ion's mass m and its speed v as it travels away from the target. I hypothesize that all ion species are ejected from the target with the same average kinetic energy. That is, the product $\frac{1}{2}mv^2$ may be, on average, the same value regardless of ion species. An alternative possibility would be that all species are ejected carrying the same average momentum. In that case, the product mv would be, on average, the same for all. Without doing an in-depth analysis, both explanations appear to be consistent with our results, with the exception of the Zr_2^{1+} ion's data: its peak abundance occurred at an earlier time than that of the less massive ZrO^{1+} ion. However, it is difficult to trust that data due to the small abundances and the limited number of data points. The most reliable data here are undoubtedly those of the Zr^{1+} and O^{1+} ion species.

VI. CONCLUSIONS

The experiment performed here provides one with a useful method for generating Zr^{1+} ions (or O^{1+} ions), if one were interested in using them for, say, particle collider experiments. One can separate these ions from other ion species in the plasma using our setup or a similar mass spectroscopy setup. The disparity between the relative abundances of Zr^{1+} ions and Zr^{2+} ions in this experiment is substantial; to produce highly-charged ions, one should use a greater laser energy or direct the laser pulse in a smaller, more concentrated laser spot. Another possibility would be to harvest singly charged ions and subject them to a charge-multiplying mechanism.

VII. FURTHER RESEARCH

Our group has recently turned our attention towards lithium ions, with the goal of performing an analogous experiment using a lithium compound target. We have already purchased a pre-made target of lithium niobate (LiNbO_3), but at present, it has yet to arrive. We have also been hoping to press a powder sample of lithium oxide (Li_2O) and sinter it to create a sturdy target, much like how we created the ZrO_2 target. However, many of our attempted targets have swelled and deformed while baking in the oven. This is problematic because a deformed target is difficult to pin down to the laser chamber walls. After baking each sample, we made some other surprising findings:

Fresh liquid stains were present on the plate beneath each target, indicating that some of the sample had melted while in the oven. The sample we had heated to the highest temperature (1400°C) had melted entirely. This is surprising considering that the melting point of Li_2O is 1570°C. [2] (Different sources list different values, but all are greater than 1400°C.)

Each sample lost mass while baking.

Each sample expanded while baking (with the exception of the sample that melted completely), losing its orderly geometric shape – some were originally cylinders, while others were originally rectangular prisms.

Of the samples that didn't melt completely, little craters were present on the surface after baking.

The evidence collected suggests the following hypothesis: while each sample had been handled (before baking), it became contaminated with trace amounts of water vapor, possibly from

the air:



At room temperature, Li_2O reacts readily with water (H_2O) to form lithium hydroxide (LiOH), so LiOH was also present in the sintering Li_2O samples. The forward reaction decreases the entropy of the system, converting one mole of a solid and one mole of a gas into two moles of a new solid. According to thermochemistry, a chemical reaction which decreases the entropy of a system tends to proceed more slowly at higher ambient temperatures. At some critical temperature, the reaction will no longer proceed spontaneously, and at still higher ambient temperatures, the reverse reaction will become spontaneous.

I hypothesize that at the high temperatures inside the oven (a range of 700°C to 1400°C across the various trials), the chemical reaction (5) ran in reverse, causing the production of Li_2O and water vapor. The new gaseous H_2O put outward pressure on each sample as it sintered, causing it to swell and deform before the gas could escape at the surface. The craters would then be the locations on the surface where the water vapor had escaped. This hypothesis also explains the partial melting of the target: the melting point of LiOH is 462°C , much lower than that of Li_2O . [3] At the high temperatures inside the oven, some of the LiOH molecules took part in the reverse chemical reaction, while others simply melted, leaving stains on the plate beneath the target.

We have been searching for a method to produce new Li_2O targets that do not deform at the high temperatures necessary for sintering. Even though we have not yet achieved this goal, we have made an encouraging preliminary discovery. We heated a pressed Li_2O sample at a lower temperature (400°C) for a longer time period (16 hours), hoping that water vapor would escape before the sample sintered and hardened and that LiOH would remain solid at this temperature. We conducted this trial in a vacuum oven, hoping that less exposure to chemicals from the air would reduce the chance of a chemical reaction taking place inside the oven. After baking, the sample had retained its shape while only expanding slightly (no dimension grew by more than 3 percent), without leaving behind any craters. We intentionally tried to damage the sample by scratching it with a pair of tweezers, but it was rigid and sturdy, making it difficult to deform or erode. This suggests that our sample began to sinter before the

reverse chemical reaction began, meaning that this target could be used in our laser chamber, even if contaminated with some molecules of LiOH . See Figure 4.

We have installed this target into our laser chamber and, at present, have fired a few laser shots at it to determine its constituent atoms. These early results confirm that the target is composed primarily of lithium (isotopes ^7Li and ^6Li) and oxygen (^{16}O), with trace amounts of hydrogen (^1H). So indeed, the target is slightly contaminated with LiOH , but that is hardly an issue. More importantly, the target has retained its geometric shape, so it can be clamped to our laser chamber wall and used for study. The main issue with this target is that it is not quite as sturdy as we would like it to be – it did not sinter quite as much as we had hoped. This is a minor problem, as it means the laser pulses will erode the target somewhat rapidly, meaning the target will have a relatively short lifetime.

We are currently exploring various ideas to further improve our Li_2O targets. We hope that, among other ideas, varying the temperature, varying the rate of temperature change, and adjusting the duration of baking time will help us achieve this goal. Nevertheless, we have now reached a stage where we can produce and study lithium ions ejected from a chemical target.

VIII. ACKNOWLEDGEMENTS

I would like to acknowledge and thank my mentor Masahiro Okamura for guiding me through my SULI internship experience at BNL and allowing me to use his laser lab and equipment. I would also like to acknowledge his coworkers Takeshi Kanetsue and Shunsuke Ikeda, who taught me a great deal about data analysis for this project and who were instrumental in guiding me through my laboratory experience. Finally, I would like to acknowledge fellow SULI student intern Abigail Zhong, whose work this summer frequently intersected with mine, allowing us to work together at times.

This project was supported in part by the U.S. Department of Energy, Office of Science, Office of Workforce Development for Teachers and Scientists (WDTS) under the Science Undergraduate Laboratory Internships Program (SULI).

IX. REFERENCES

- M. Okamura, *Review of Scientific Instruments* **87** (2016).
American Elements, “Lithium oxide,” (), online; accessed 16-July-2018. <https://www.americanelements.com>.
American Elements, “Lithium hydroxide,” (), online; accessed 17-July-2018. <https://www.americanelements.com>.



FIG. 4: Our first successfully baked Li_2O target pinned against a metal plate, as we prepare to install it into the laser chamber.

Enabling data collection for a cosmic ray shower detector

Junjie Chen

Math, City College of New York, New York, NY 10031

David Jaffe

Physics Department, Brookhaven National Laboratory, Upton, NY 11973

Abstract:

A cosmic ray shower occurs when a cosmic ray interacts in the upper atmosphere. Many of the muons from the resulting shower penetrate the atmosphere and strike the earth's surface. Our detector is designed to create pulse when muons pass through the detector. Some noise will also be caught. A discriminator and an and-gate are used to select the pulse. The discriminator will select the pulse whose voltage is higher than the setting. We put one detector on the top of the other one. So, if a muon passes through, both of the detectors will send a pulse to the and-gate and stimulate a square trigger pulse. Our Arduino board will receive the trigger as a signal that there is a muon coming in. So, all the data including the peak voltage, GPS (Global Positioning System), temperature and pressure is collected for the trigger. However, the GPS time is not accurate enough since it takes time to decode the signal (NMEA sentence) from GPS. So, PPS (Pulse Per Second) which indicates the start of an integer second is used to correct the error with an inner clock Timer 1 of Arduino. We also write two programs to automatically receive and save the data as text file on the Raspberry pi 3 and automatically upload those files into our storage space. By that, we are planning to have more than 20 detectors in different colleges and we are able to read all the data in our lab. From this project, I have gained valuable about the Arduino and processing programing, the GPS UTC time correction method and port communication.

I. Introduction

The aim of this program is to build hundreds of cosmic ray shower (muon) detector. Those detectors will be placed at different places and keep recording data for find cosmic ray shower. My job in our group is write code to collecting data from our detector and do time stamping on those data with the UTC time on Arduino. Those data will saved as text file in Raspberry Pi. I also built an auto-uploading stage which is necessary since we plan to build hundreds of them which means we will have hundreds of Raspberry Pi. Finally, I wrote the code to do the data file analysis to find the coincidence shower.

II. Progress

A. Time stamping

The time stamping is the most important part in the code on data collection since the muon is travelling in light speed and few milliseconds delay will cause huge difference in position. Our accuracy for the time stamping is 500ns. Many things we do to achieve that accuracy.

1. PPS (Pulse per second)

PPS is a high voltage signal coming from the GPS receiver.

It indicates the start of a new second. The reason we use the PPS signal but not directly read the time from GPS is that: the GPS receiver usually send NMEA sentence and decoding for the NMEA sentence takes long time like 0.2 s.

What we do is keeping reading the NMEA sentence (5 Hz) and parsing it, and setting the PPS signal as an interrupt. So, when the PPS signal comes, the interrupt function will be called. In this function, we will read the newest parsed second (NMEA second). And NMEA second +1 will be the actual time of this moment.

The reason is the frequency of NMEA sentence is 5 Hz and the newest NMEA sentence is probably in the form like NMEA senonds.700 (for example 1.700s). Since it takes around 0.2 second to decode that, you actually receive and parse the NMEA sentence at time around NMEA senonds.900 (for example 1.900s). And then at the integer second NMEA seconds +1, the PPS comes.

Now, we have the integer part of our events. Every event comes after that PPS signal will use that number as integer part of the second. We use an internal clock of Arduino mega 2560 board to count the decimal place of the time.

2. Arduino internal clock (Timer 1)

The name of the internal 16 bits clock is TIMER 1. It follows the Arduino frequency to count. So, its frequency is 16 MHz, which means it counts once around every 62.5ns.

The counts between the PPS signal and the events should be recorded. However, since the clock only has 16bit storage space, the counts will return to 0 around every 4ms ($62.5ns * 2^{16} = 4.096ms$). We call this situation overflow. The number of overflows between PPS and events should also be recorded.

So, the overall situation will be like within PPS interrupt function, the TIMER 1 counts and overflow number will be zeroed. And record the counts and the overflows when the events come. Finally, use counts and overflows to calculate the real counts between PPS and events.

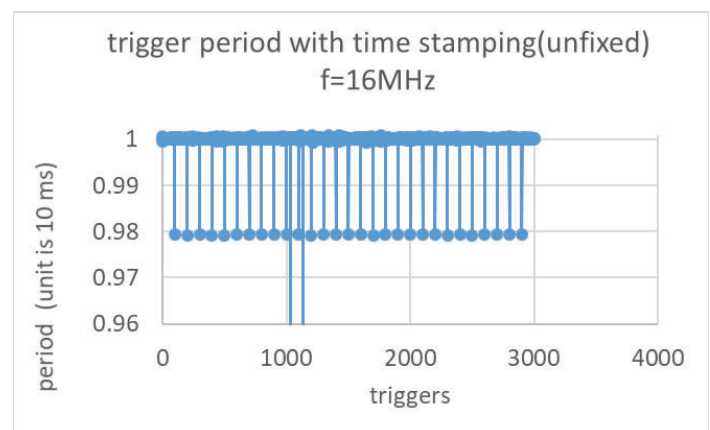


Figure 1.

After we get the real counts, it needs to be converted into time by

$$time = GPS.seconds + 1 + \frac{counts}{f}$$

Where f is the frequency of the Arduino board. However, the frequency is just around 16MHz and it will have thousands counts difference.

Figure one shows what the time stamping will look like when the wrong frequency is used. Each of the drop point represents the time stamping is fixed by the PPS signal.

This is a calculation about how larger the drop will be:

$$\Delta t = \left(sec2 + \frac{count2}{f(not\ fixed)} \right) - \left(sec1 + \frac{count1}{f(not\ fixed)} \right)$$

$$= 1 + \frac{count2 + f(real) - count1}{f(not\ fixed)} - \frac{f(real)}{f(not\ fixed)}$$

$$\Delta(\Delta t)(the\ drop\ at\ the\ end\ of\ the\ second) = 1 - \frac{f(real)}{f(not\ fixed)}$$

(Δt is the period of events. Count1 is the Arduino count of last event before the second PPS and count 1 is the Arduino count of the first event after the second PPS. f(real) is the actual frequency and f(not fixed) is the wrong frequency we used to compute the time. Sec1 is the first PPS time and sec2 is the second PPS time.)

So, we have to measure the actual frequency. Since we already have the PPS signal, we just record the counts between two PPS signal which will become the frequency.

3. Time stamping ability test

We test our Arduino board ability to do time stamping by using two Arduino board with two GPS to measure the same pulse from pulse generator. The results is shown in figure two. Most of the time difference is within 500ns except 2 points. They have like 5us difference.

My hypothesis for the reasons that cause this kind of difference is:

1, The 500ns difference, since one of the Arduino board is always ahead to the other one, might be caused by PPS signal coming at difference time.

2, For the 5us difference, it might be caused by the Arduino board or the Arduino physical property.

This need to be figured out in the future.

B. Auto-uploading to the storage space (Dropbox)

After the data files are saved in the Raspberry Pi, we need to upload those into our Dropbox. Unfortunately, Dropbox does not

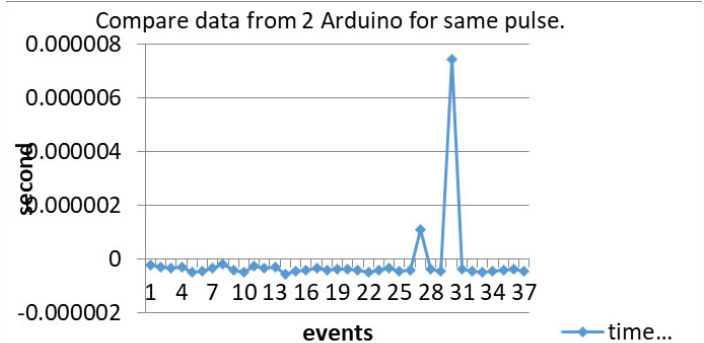


Figure 2.

have a product for Raspbian (Operation System for Raspberry Pi), so it is hard to do auto-uploading.

We find a software called cron_drop that can upload data file every midnight. However, if the date file is being written in by Arduino, it can't be uploaded on Raspbian. So, we use a commend line program to keep copying the data file and upload the copied file.

Moreover, if the data file become too large, the uploading process will be very slow. So, we clear the data file every midnight after the uploading.

C. Data analysis programing

1. The elements controlled by user

There are 4 elements the user can control: number of detectors, gates, length of wires and the minimum number of detectors required to get a shower.

The gate is defined as the largest possible muon arrival time difference between different detectors, which means all the events happened in the gate time range might be caused by a shower. Since the optical path difference is always less than the location difference of detector(Δd), the gate is determined by the formula:

$$gate = \frac{\Delta d}{c}$$

where c is the light speed, and .

There are some background noise on our detector. After the discriminator circuit, it will have frequency like 40 Hz. So, the false coincidence rate (the coincidence caused by the noise which looks like a shower) is calculated by:

$$rate = C * (f)^n * gate^{n-1}$$

Where f is the background noise rate, n is the number of detectors and C is a constant related to n.

This rate should be low enough. That's why we may want the minimum number of detectors required to get a shower.

The length of wire will cause the time delay. Both of the wire of antenna and the wire connect the GPS receiver and the Arduino matter. They will make the measured time is earlier than actually time. So we need to add the delay to our data.

Since the electric signal travels in the light speed. The time delay should calculated by the formula:

$$delay = \frac{\Delta l}{c}$$

Moreover, not every detector will receive muon signal will there is a shower. So, there should be a minimum number of detectors required to get a shower.

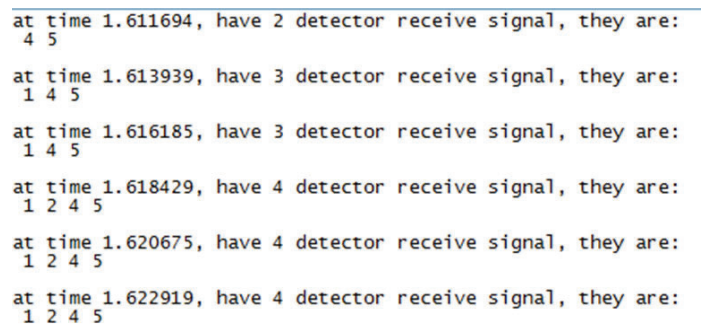


Figure 3.

2. The idea of the programing

We write 3 functions for preparation. First is the function to read data line by line and save them in an array. The second is to find the minimum time data from the array. The last is find the coincidence shower (time difference in the gate) about the minimum data in the array and read the next lane of the coincidence data.

Since the data files are sorted increasingly, we just the first line of all the files and they will be the minimum data of the files they are in.

Then, we use the second function to find the minimum data of the array and it will be the minimum of all the data. Then, we can find the data which is less than the minimum + gate in the array because if those data is not in the gate, other bigger data should not in the gate as well. Then read the next line of the data in the gate (minimum data will always be in the gate) and find the minimum again until the end of the files.

Since the program will reads all the data files once and the time consumed by the minimum function is proportional to the number of files. So, the complexity (c) will be $O(Nn^2)$, where N is the length of data files and n is number of data files.

Figure three shows a sample output of the data file analysis program which shows the time of shower and which detectors got coincidence.

III. Future work

We need to figure out the reason for the error on time stamping (500ns).

Measure the time consumed on each step of the Arduino program.

Reconstruction of the shower:

After we collect the location, time and energy information.

Two methods:

1, Use the time and location of arrival on detectors and the uncertainty of the time stamping to make several inequations to find a possible range of original oscillation point.

2, Use the energy distribution to find the mid point and the angle of the cosmic shower.

IV. Impact on Laboratory or National Missions

The project will find the cosmic ray with different energy level. Some cosmic rays have a kinetic energy greater than 1×10^{18} eV that people never got even with the best accelerators. So, we may have chance to find one a high energy cosmic ray and see what will happen when a high energy cosmic ray comes.

We also want to know where the cosmic ray comes from by the reconstruction. However, due to the earth magnet field affect, we can't the direction of the shower will be the direction of the cosmic ray coming from. More math work needs to be down with the earth magnet field graph.

Automating the development of a Global Nuclear Reaction Data Library

Kayla Clements

Department of Nuclear Engineering, University of Florida, Gainesville, FL, 32611

Gustavo Nobre

Nuclear Science and Technology, Brookhaven National Laboratory, Upton, NY, 11973

Simulation and modeling software used for various nuclear science applications activation, nuclear energy, astrophysics, forensics, etc. require detailed reaction data in order to make accurate predictions and fill availability gaps in experimental data. Reaction evaluation codes such as EMPIRE fill these gaps by combining experimental results with theoretical models. This project, as part of Brookhaven National Laboratory's Department of Nuclear Science and Technology, aims to automate EMPIRE runs and generate reliable, self-consistent evaluated files across the whole nuclide chart, including nuclei off-stability. The program, written as a bash shell script, generates and runs EMPIRE inputs with minimal user input. The final script is capable of employing specific reaction models for different nuclide groups, exemplified by the successful application of an adiabatic model to deformed nuclei, and its infrastructure can be easily modified to employ other models across the entire nuclide chart.

I. INTRODUCTION

ENDF/B and other nuclear data libraries do not have evaluated files for the entire nuclide chart due to the limited availability of experimental data for unstable nuclei. Despite their unavailability, cross sections for nuclei in a wide incident-energy range are crucial for many applications, such as activation, nuclear energy, and astrophysics. In order to predict data such as cross-sections and spectra and fill the aforementioned gaps, nuclear reaction codes are used. These codes use theory-based modeling in order to extrapolate or interpolate data from known nuclides/energy regions to the unknown [1].

EMPIRE, developed in part at Brookhaven National Laboratory (BNL), is one of the most successful and frequently used reaction codes. It combines various models and can calculate differential and angle-integrated cross sections from a few keV up to hundreds of MeV for a variety of projectiles neutrons, protons, light or heavy ions, and photons [1]. The generally accepted format for nuclear data is the Evaluated Nuclear Data Format (ENDF), which is used in most neutron transport codes; EMPIRE outputs can be converted to ENDF using included utility codes such as EMPEND for easier processing and incorporation in various applications.

This project aims to develop a script that automates input generation, any required editing, running of EMPIRE, and output reformatting as an infrastructure for a global model-oriented nuclear data library across the whole nuclide chart. One issue with models that current libraries use is parameter adjustment. When models use fits, or parameter adjustments, based on available experimental data, it creates better predictions for those specific nuclides. However, the more fits are added to a model, the less accurate that model is when extrapolated to nuclides outside of the scope of the original fit. Ideally we could employ predictive mod-

els which could satisfactorily reproduce experimental data with few to no adjustable parameters, so the results can be accurately extrapolated to other nuclides. An automated script streamlines the production and validation of data, and if changes need to be made a user can do so on the general script instead of individual inputs, which can add up when trying to generate data across many nuclides, or for different models. This allows the library to be continuously updated and improved.

II. SCRIPTING METHODS

When handling and coordinating different codes and utilities, an infrastructure consisting of wrapping scripts can be incredibly helpful, increasing efficiency and optimization. Therefore, a substantial amount of time was spent on creating and developing a script, written in bash, that would parse nuclide data from the Wallet Cards [5], create and modify EMPIRE inputs, run calculations and process results. Default EMPIRE input files can be generated using an included graphical user interface Xrun, written using Tcl/Tk, for which all that needs to be added are the targets proton (Z) number, mass (A) number, and incident energies for which calculations should be made [1]. The initial step of the project was to determine what method would be used to identify inputs that the user wanted. We decided to create a comprehensive list of nuclides their A, Z, and neutron (N) numbers, nuclear mass excesses, spin and parity (J^π), half lives, decay modes, branching, etc. using the available information from online wallet cards from the National Nuclear Data Center (NNDC). The user can then input a range of Z and A numbers and a minimum half-life, and the script will parse the comprehensive list and create directories and inputs for only those in the submitted range. The user can also submit a maximum incident energy at which the run will cap. I added options so that the user could choose whether to run EMPIRE on NNDCs cluster using a modified version of qsub, or to run on the mother node [2].

Once the script ran successfully for ground state nuclides, I was able to add utilities for metastable nuclides, which are targets at an excited state with half lives long enough for data to be gathered. Input files for metastable nuclides require an energy level index that can be found in included Reference Input Parameter Library (RIPL) files. The user would normally need to manually edit these files, find the proper energy level index, and set it; the script uses stored energy values from the aforementioned comprehensive list to find and assign the proper index automatically. Although we were not able to successfully run EMPIRE for metastable nuclides due to lack of time to fix a recently-introduced bug in the EMPIRE code, inputs can successfully be written given the user selects the metastable option, leaving them ready to be run and processed once the code is properly fixed by its developers.

The initial goal of the project was to generate data, but after creating a successful infrastructure for this we decided instead

to slightly shift focus and modify the script to run an adiabatic model, the methodology of which is explained in further detail in Section III B. The model explicitly couples channels up to the ground state rotational band for the scripts purposes, we decided to couple up to J^π of 12.0+. The command `qsubEmpire`, used to run on the NNDC computer cluster, also automatically cleans all intermediate files. However, by running a simplified version of the input locally, we are able to see the default-generated collective levels files. When the adiabatic option is set, the script will automatically only write and run inputs for nuclides with even numbers of protons and neutrons, for ease of calculations. It runs at

MeV to generate discrete level and collective level files, then finds the proper energy values for the parities from 0^+ to 12^+ on the discrete level file, and adds the necessary data to the collective level file. It then adds the rest of the incident energies to the input and runs as requested, using the collective level file already in the directory instead of generating another default one.

We were able to submit approximately 10,000 jobs at a time to NNDC's computing cluster, with 200 at a time running in parallel. After the data is generated, a separate utility script recombines output data from each incident energy for total output and cross-section files. These are then formatted and processed to create ENDF files and produce plots that can be viewed using EMPIREs included plotting software ZVView [2]. Cross-section plots for total, elastic, inelastic, capture, etc. channels are generated, as well as angular distributions and differential spectra. The script goes through this process of creating a directory, writing an input, generating/changing necessary default files, and submitting to the cluster, then restarts for the next in-range nuclide.

III. RESULTS

A. General Library

The scripts only restrictions are those of EMPIRE itself; it has the infrastructure to run across the nuclide chart, from light to heavy nuclides, on and off stability. For the purposes of this project we were interested in a neutron as a projectile, but this can be easily changed in the script if other projectiles are needed in the future. In order to simplify things for the initial creation of the script, we decided to run tests excluding meta-stable nuclides, inputs for which require more information than those for ground-state nuclides. After default inputs ran successfully, we changed the ENDF setting to 2, which avoids approximations used when ENDF is set to 1 by printing total emission spectra of neutrons, protons, α particles, and γ instead of individual contributions from each reaction [2]. We also changed from the spherical optical potential model to using coupled channels, which accounts for the direct excitation of the targets rotational states to more accurately reproduce experimental data [3].

We focused on running calculations for the fast region, from 0.002 MeV to 20 MeV, causing the lack of proper matching between resonance and fast regions observed in the plots in Figure 1. Once data from these changed inputs were able to be formatted and processed correctly, we realized that the cross-section plots would have more accurate interpolation with smaller energy bins. Adding approximately five times the number of incident energies produced more accurate plots. Figure 2 demonstrates the range of nuclides for which the script can generate cross section data,

showing how the elastic cross section changes in the fast region across all even ground-state isotopes of Gadolinium in Figure 2a and Tungsten in Figure 2b. Ideally, models run with EMPIRE will eventually have acceptable experimental data with little to no parameter adjustment, so that the results can be accurately extrapolated to other nuclides and fill in gaps in ENDF libraries.

B. Adiabatic Model

Once the script was ready to implement, we had two options: expand the global library by running EMPIRE across the nuclide chart and analyzing this data, or test the infrastructure capabilities of the script by applying a model. We decided to implement an adiabatic model previously developed by Nobre et al. to describe statically-deformed nuclei in the rare-earth region [3]. The model deforms an interpolated Koning-Delaroche (KD) spherical optical potential by explicit channel coupling to the ground state rotational band with only deformation parameters as inputs. According to previous work by Nobre et al., cross sections began to converge after the coupling of 7 channels, so we coupled up to a JPI value of 12.0+. This model is particularly useful because it only requires one small parameterization to conserve the potentials volume integral when deforming. This is done by slightly reducing the radius of the real central part of the potential [3]. This work also showed that the deformed KD potential, without any other parameter adjustment, produced an adequate depiction of experimental data, especially for the real potential. For this implementation of the model, we used deformation parameters obtained from microscopic Hartree-Fock-Bogoliubov (HFB) calculations of nuclear densities, previously done at CEA, France [4]. We applied the model to all even-even isotopes of Gadolinium and Tungsten, dripline to dripline. In order to compare the differences each of the two deformation parameters made, we ran calculations and developed plots for default values, taken from the RIPL files included in EMPIREs package; just the Beta-2 constant from HFB calculations; both Beta-2 and Beta-4 constants are taken from HFB calculations; and, where available, values taken from previous work by Gustavo Nobre et al. [3].

These comparisons were made for Gadolinium and Tungsten from dripline to dripline, and plots comparing the elastic cross sections with different deformation parameters applied for selected isotopes of Gadolinium and Tungsten can be seen in Figure 3. Table 1 compares the applied deformation parameters for selected isotopes, including those in Figure 3.

IV. CONCLUSIONS AND FUTURE

While we tested the script only for ground state nuclides, with and without an adiabatic model, its utility goes beyond that. We have already demonstrated the scripts capabilities in data evaluation for targets off-stability, and can continue to expand the range for which data is available. We were able to generate data for nuclides as low in atomic number as Neon (19) and as high in atomic number as Radon (86), dripline to dripline for 10 elements across the rare-earth nuclides, and apply an adiabatic model for all even-even isotopes of Gadolinium and Tungsten. This project provides an easily expandable base for organizing, generating, and analyzing nuclear data to further along the NNDCs goal of producing accurate, reliable data for use in nuclear applications across the board.

V. ACKNOWLEDGEMENTS

I would like to thank my mentor, Gustavo Nobre, for his support, guidance, and knowledge. This project was supported in part by the U.S. Department of Energy, Office of Science, Office of Workforce Development for Teachers and Scientists (WDTS) under the Science Undergraduate Laboratory Internships Program (SULI).

VI. REFERENCES

- M. Herman. EMPIRE: Nuclear Reaction Model Code System for Data Evaluation.
- M. Herman. EMPIRE-II statistical model code for nuclear reaction calculations. Version 2.18 Mondovi, International Atomic Energy Agency, Vienna, Austria. Sept. 2002.
- G.P.A. Nobre, A. Palumbo, M. Herman, D. Brown, S. Hoblit, F. S. Dietrich. Derivation of an optical potential for statically deformed rare-earth nuclei from a global spherical potential. Physical Review C, Volume 91, Issue 2, APS Physics, Feb. 2015.
- http://www-phynu.cea.fr/science_en_ligne/carte_potentiels_microscopiques/carte_potentiel_nucleaire_eng.html
- <http://www.nndc.bnl.gov/wallet/>

- E. Bauge, J. P. Delaroche, M. Girod, G. Haouat, J. Lachkar, Y. Patin, J. Sigaud, and J. Chardine, Phys. Rev. C 61, 034306 (2000).
- P. T. Guenther, A. B. Smith, and J. F. Whalen, Phys. Rev. C 26, 2433 (1982).
- J. P. Delaroche, G. Haouat, J. Lachkar, Y. Patin, J. Sigaud, and J. Chardine, Phys. Rev. C 23, 136 (1981).
- J. Annand and R. Finlay, Nuclear Physics A 442, 234 (1985).

VII. TABLES

TABLE I. Deformation parameters applied for the deformed KD model. Default values are taken from the RIPL library; HFB calculations from work to be published, G.P.A. Nobre et al.; PRC values are taken from previous work by Gustavo Nobre [3]. (β_2, β_4).

	HFB*	PRC. 3
^{156}Gd	0.3208, 0.1531	0.25, 0.06 [6]
^{158}Gd	0.3203, 0.1410	0.27, 0.04 [6]
^{160}Gd	0.3375, 0.1361	0.29, 0.02 ^a
^{182}W	0.2549, -0.0293	0.223, -0.055 [7-9]
^{184}W	0.2373, -0.0483	0.209 -0.056 [7-9]
^{186}W	0.2297, -0.0609	0.203, -0.057 [7,8]

^a Values obtained by linearly extrapolating the deformation parameters of the lighter Gd isotopes [3].

VIII. FIGURES

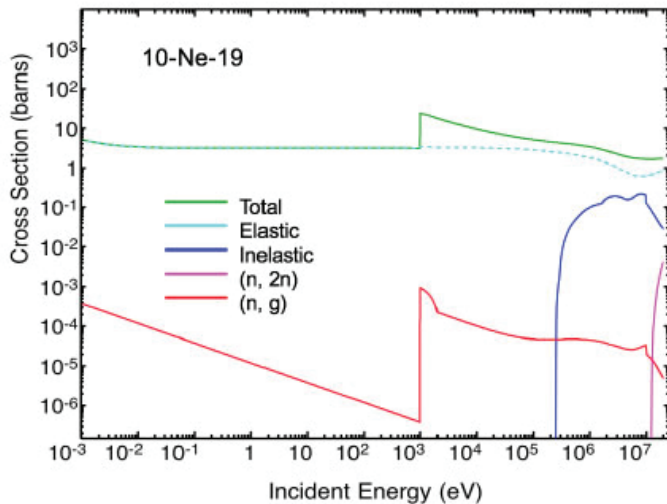


FIG. 1a. Figures 1a and 1b show cross sections for Neon-19 and Radon-216, respectively, for an incident neutron. These plots show just some of the many cross sections that can be generated using EMPIRE. The lack of proper matching between resonance and fast regions is observed in the plots because calculations were only run from $2 \cdot 10^3$ eV to $2 \cdot 10^7$ eV. These plots demonstrate the range of nuclei for which the script can generate cross section data.

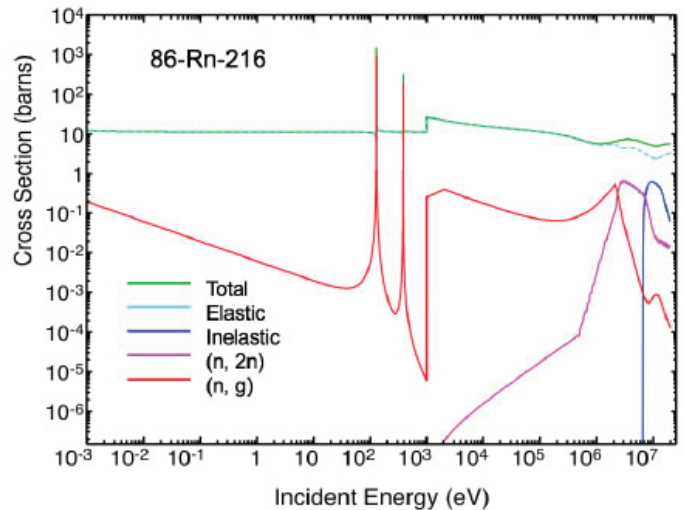


FIG. 1b. Cross sections for Radon-216.

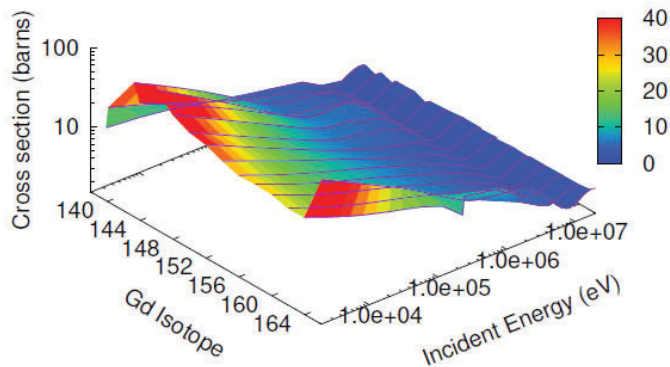


FIG. 2a. Show how the elastic cross section changes from dripline to dripline for Gadolinium in 2a. and Tungsten in 2b. Even isotopes from 138 to 166 are plotted for 2a., with the applied deformation parameters from Table I. These plots demonstrate that data can be generated both for stable and unstable nuclides.

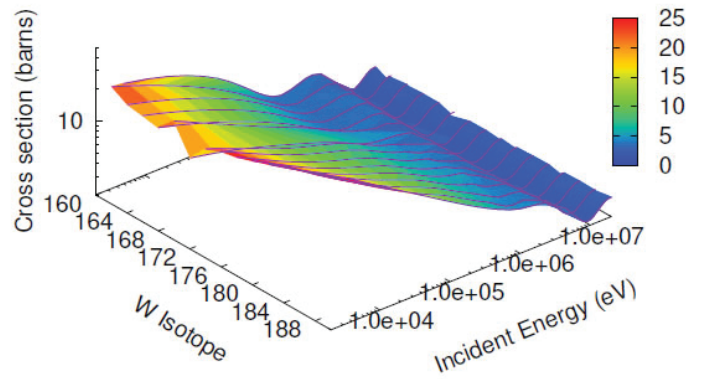


FIG. 2b. Elastic cross section, plotted for even Tungsten isotopes from 160 to 190.

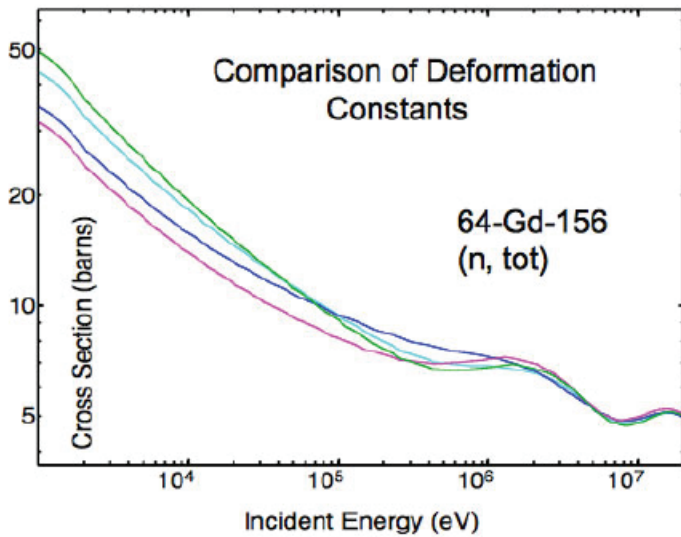


FIG. 3a. Comparison of applied deformation constants for Gadolinium-156 in 3a. and Tungsten-184 in 3b. Default values are taken from the RIPL library; Beta 2 and 4 constants are taken from HFB calculations [G.P.A. Nobre et al., to be published]; Adiabatic values are taken from previous work by Gustavo Nobre [3].

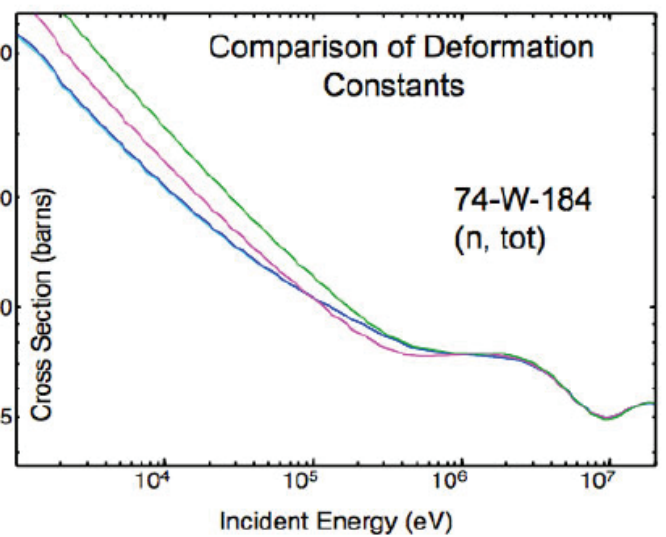


FIG. 3b. Comparison of applied deformation constants for Tungsten-184.

XANES/EXAFS analysis of zirconium-based adhesive thin film

Bryan Conry

Department of Materials Science and Chemical Engineering, Stony Brook University, Stony Brook, NY 11790

Bruce Ravel

Department of Photon Sciences, Brookhaven National Laboratory, Upton, NY 11973

ABSTRACT

In automotive manufacturing, a common practice is the application of an anti-corrosion adhesive thin film to the steel vehicle chassis by submerging in solution. It has been reported, however, that paint on cars having undergone this procedure in H_2ZrF_6 solution is not adhering well. Little is known about the specific chemical composition of the thin film that forms; this study aims to explore the chemical environment and spatial atomic distribution of Zr and Cu (from cupric nitrate in the solution) in the thin film formed under different processing conditions: submerging in the hexafluorozirconic acid solution at 32°C for 30 seconds (32,30), and submerging at 32°C for 240 seconds (32,240). From an extended x-ray absorption fine structure (EXAFS) analysis of Zr in the sample using Artemis XAFS data analysis software, we show that the zirconium composing the film is at a lower degeneracy than a bulk zirconium standard under (32,30) processing conditions, and is distributed amorphously across the steel under the

(32,240) conditions. Further, from an x-ray absorption near-edge structure (XANES) analysis of Cu in the sample using Athena XAS data processing software, we propose an array of Cu compounds by percentage that form on the surface of the film under the (32,30) and (32,240) processing conditions.

I. INTRODUCTION

Chemical pretreatments of metals have been explored for decades to exploit their beneficial properties, including anti-corrosive and adhesive properties. Chromate-based coatings were the first to be widely used, based on their good corrosion protection performance. However, it was shown that these coatings posed a threat of human DNA damage and a heightened risk of lung cancer [1]. As such, chromate-free pretreatments were examined beginning in the late 1990s as a safer alternative, including studies done by Salam & Butt [2] on vanadium-based films and Zhong et al. [3] on cerium-based films. One pretreatment not covered extensively in the literature is a zirconium-based treatment, formed

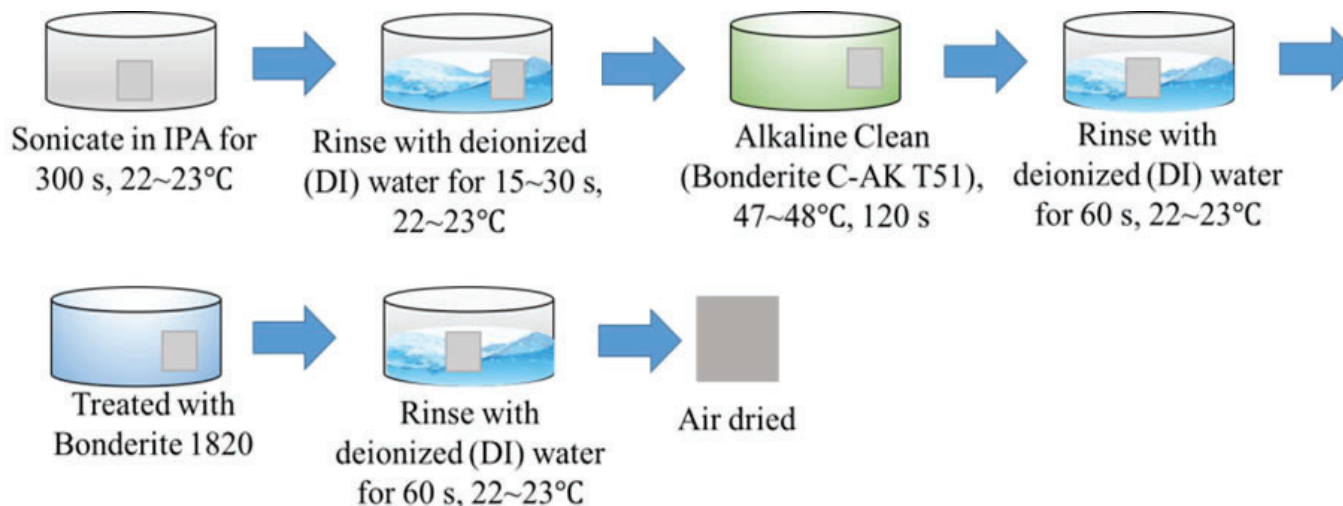


Fig. 1. Thin film sample preparation procedure.

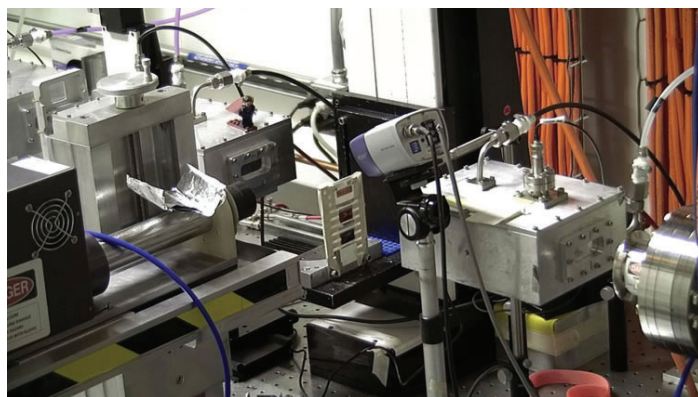
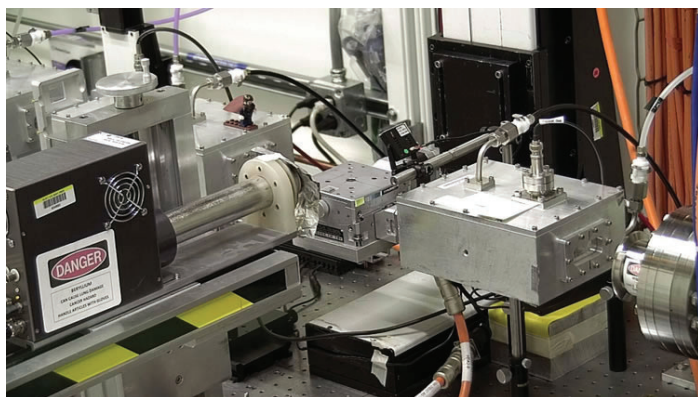


Fig. 2. Setup for measurement of sample (top) and standards (bottom).

by submerging cleaned steel into H_2ZrF_6 (product name Bonderite) solution (Fig. 1).

In addition to considering simply the elemental composition of these thin films, there are processing conditions under which the steel is submerged that must be considered as well. The scope of this project is limited to only a test of changing submerging times, at (32,30) and (32,240) processing conditions.

Through x-ray absorption spectroscopy (XAS) measurements of the two samples, we aim to learn about the chemical environment and spatial atomic distribution of zirconium and copper (from $Cu(NO_3)_2$ in solution) present in the thin film. From measuring the two samples, we will gain a better idea of the chemical properties of the film and how they vary with time submerged in solution. A continuation of this project in the near future will expand this idea across an array of temperatures and submerging times, seeking to find optimal processing condition for promoting adhesion in the application of this thin film.

II. METHODS

The EXAFS equation (Eq. 1) describes the scattering of photoelectrons from an x-ray absorbing atom off adjacent atoms, with some excited photoelectrons returning to the scatterer.

$$\chi^{(k)} = S_0^2 \sum_i N_i \frac{f_i(k)}{kR_i^2} e^{-\frac{2R_i}{\lambda(k)}} e^{-2k^2\sigma_i^2} \sin(2kR_i + \sigma_i(k))$$

Eq. 1. The EXAFS equation.

Variable parameters of Eq. 1, when experimentally determined, aid in understanding many properties of a measured material, including chemical composition and spatial atomic distribution. For a compound of known and published crystal structure data, FEFF [4] calculations of potential scattering paths can be made and used in XAFS analysis software.

Sample measurements were done by fluorescence yield; the sample was hit by x-rays at a glancing angle and fluorescence from the excited state electrons was measured using a fluorescence detector. This technique sought to maximize signal from the thin film and minimize signal from the steel underneath.

Measurements of standard foils (Cu, CuO, Cu_2O , Zr) and powders (ZrO_2) were done by transmission; x-rays are sent straight at the standard, and the attenuation of current between incident photons and those measured by a second ion chamber behind the sample is recorded. A visual of both setups is shown in Figure 2.

SEM images (Fig. 3) were also created for the sample produced under both processing conditions, providing an interesting visual for in both cases. The clusters on the surface were shown previously to be Cu clusters of unknown identity.

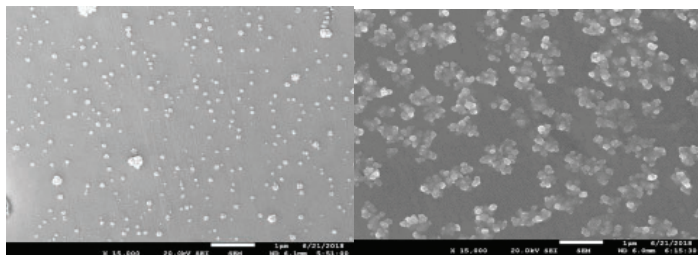


Fig 3. SEM image of the film formed under (32,30) (left) and (32,240) (right) processing conditions.

III. DATA AND RESULTS

A. ZIRCONIUM (32,240)

By the process of passivation, we expect the Zr on the surface of the sample to oxidize; thus, we measured the ZrO_2 standard at the beamline. A crystal data file for this material was imported to Artemis, and scattering paths were calculated. Each scattering path was compared to the Fourier transform of the EXAFS (R-space) of the ZrO_2 spectrum to determine the most significant contributors to the data (Fig. 5).

Once significant scattering paths were identified, they were included in an R-space fit to the data. Parameters S_0^2 , ΔE_0 , ΔR and σ^2 from Eq. 1 were specified and either *guessed* or *defined* in Artemis for each path, a fitting window (green line in Fig. 5) was defined to cover the two significant coordination peaks in the R space plot of the data ($R_{min} = 1.0 \text{ \AA}$, $R_{max} = 3.9 \text{ \AA}$) and a fit was attempted. The evaluated parameters for each scattering path are displayed in Table 1.

O1.1, Zr.2, and Zr.6 were significant enough contributors to support their own σ^2 parameter and maintain a defensible fit. The σ^2 for other paths are defined in terms of those parameters. We observe reasonable values for the defined parameters after evaluation in the fit. The evaluated S_0^2 is a bit higher than we expect, which can be attributed to a number of natural phenomena including sample inhomogeneity and structural disorder.

Reference Zr data was imported into Athena and compared with experimental data (Fig. 8). Both spectra closely resemble the ZrO_2 spectrum.

As discussed earlier, we expect the Zr deposited on the sample to be oxidized; Figure 8 is very strong evidence of this. Thus, a fit (Fig. 9) was attempted for the Zr R-space data from the thin film under $32^\circ C$, 240 s processing conditions using the same *guess* and *def* parameters as the bulk ZrO_2 fit, with the evaluated results in Table 2.

Observing the spectrum from the sample and what appears to be a decent fit, there is a very pronounced peak at $\sim 1.5 \text{ \AA}$, much like the spectrum of the bulk data. This is interpreted to be the Zr-O coordination peak, as can be easily observed from the posi-

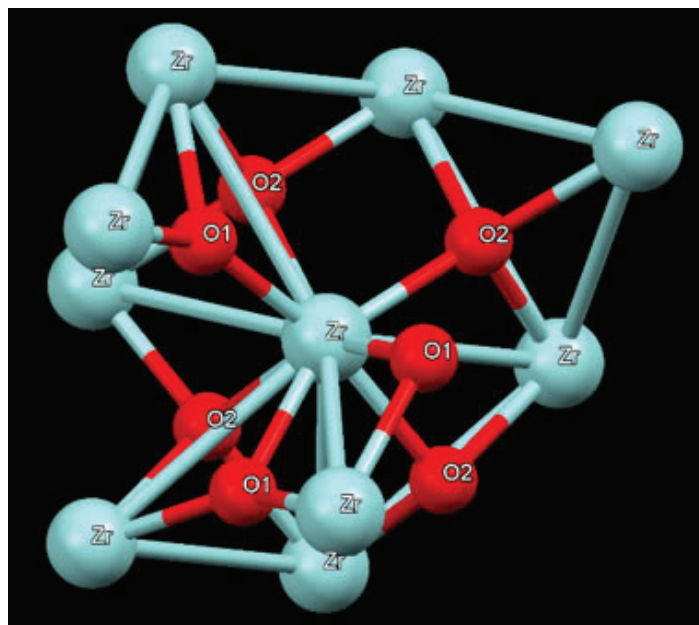


Fig. 4. Ball-and-stick model of ZrO_2 unit cell, consisting of labeled Zr.1, O.1, and O.2 atoms included in scattering paths. Created with Mercury [5] software.

tions of the O contributors in Fig. 5. However, the Zr-Zr coordination peak is significantly reduced in amplitude as compared to the bulk ZrO_2 data, reflected by the large but defensible values of σ^2 evaluated for the Zr scattering paths in Table 2 (σ^2 typically ranges from 0.002 – 0.03 [6]). Two explanations of this phenomena are proposed and tested, with a different fitting model for each case.

One possibility is that the Zr is widely dispersed across the sample and at a low concentration relative to the bulk ZrO_2 . To test this theory, we create a model by introducing a scaling parameter x , multiply the amplitude reduction factor S_0^2 of each scattering path that significantly contributes to the Zr-Zr coordination peak by x , and run another fit. A priori, scaling down the S_0^2 parameter for scattering paths contributing to the attenuated peak in the data should account for the reduction in the signal, if in fact N_i is lower in the data than the bulk. However, the best fit evaluation for x was 1.906 ± 0.854 , not less than 1 as expected; additionally, the σ^2 parameters for the majority of the paths were very large. Evaluated parameters for this fit are displayed in Table 3, with consideration given only to the Zr scattering paths.

S_0^2 yields a decent result; however, almost all scattering paths yield unreasonable values for σ^2 . This model is a test of the degeneracy of each path (N_i in Eq. 1); the proposition of sparsely and widely dispersed Zr atoms on the surface would yield a decreased N , with fewer local atoms for the photoelectrons to scatter off of. Because this model yields indefensible data, we can conclude that

the attenuation of the Zr-Zr peak in the data is not due to a change in concentration of Zr atoms relative to bulk ZrO_2 .

The second possibility is that the sample is amorphously distributed with respect to Zr. A great variation in Zr-Zr bond length would create an interfering radial distribution, and thus is another explanation of a reduced peak. For this model, parameter x is set to equal 1 while σ^2 parameters are allowed to float; here, we are testing σ^2 rather than N . This model is in fact the same fit depicted in Fig. 9. Observing Table 2, the degeneracy of each path is the same as in the ZrO_2 fit. However, the σ^2 values for paths contributing to the Zr-Zr peak, while defensible, are significantly larger than those in Table 1. We can thus infer that the attenuation of the Zr-Zr peak is due an increase in structural disorder among the Zr atoms as compared to the bulk ZrO_2 , and thus an amorphous distribution.

B. ZIRCONIUM (32,30)

The Zr data from the sample produced under $32^\circ C$, 30 s processing conditions was run under the same ZrO_2 fitting model for comparison (Fig. 10).

This fit is noticeably worse than the (32,240) data fit, with an R-factor of more than double. This misfit is due to a difference in the chemical environment of the Zr in the (32,30) sample; one theory explaining this difference is that having been submerged in the solution for a far shorter time, less Zr is deposited on the

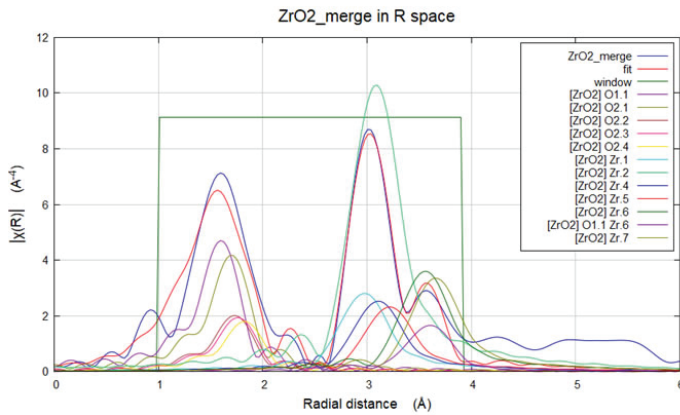


Fig. 5. Contributions of scattering paths to the Fourier transform (R-space) of the ZrO_2 EXAFS data.

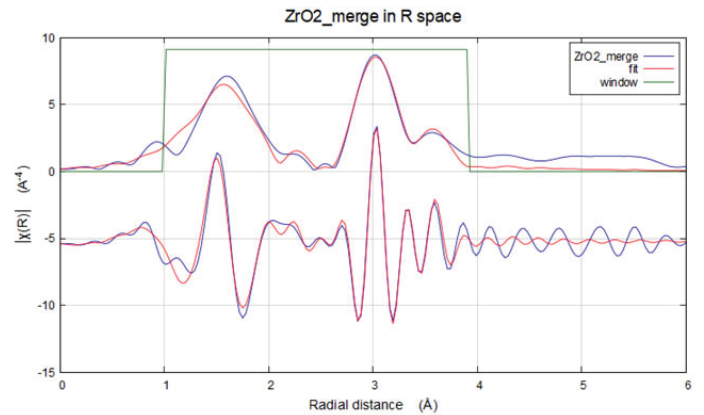


Fig. 6. Fit to ZrO_2 spectrum in R space. Fit made to data within plotting window. The R-factor, or percentage misfit, is 0.0298.

Scattering Paths	Degen	R_{eff}	S_0^2	ΔE_0	ΔR	σ^2
O1.1	2	2.054	1.346 ± 0.210	-6.693 ± 1.467	-0.0197 ± 0.0142	0.00601 ± 0.00284
O2.1	2	2.157	1.346 ± 0.210	-6.693 ± 1.467	-0.0197 ± 0.0142	0.00601 ± 0.00284
O2.2	1	2.189	1.346 ± 0.210	-6.693 ± 1.467	-0.0197 ± 0.0142	0.00601 ± 0.00284
O2.3	1	2.220	1.346 ± 0.210	-6.693 ± 1.467	-0.0197 ± 0.0142	0.00601 ± 0.00284
O2.4	1	2.285	1.346 ± 0.210	-6.693 ± 1.467	-0.0197 ± 0.0142	0.00601 ± 0.00284
Zr.1	1	3.338	1.346 ± 0.210	-6.693 ± 1.467	0.0101 ± 0.0113	0.00776 ± 0.00375
Zr.2	4	3.446	1.346 ± 0.210	-6.693 ± 1.467	0.0101 ± 0.0113	0.00517 ± 0.00113
Zr.4	1	3.469	1.346 ± 0.210	-6.693 ± 1.467	0.0101 ± 0.0113	0.00776 ± 0.00375
Zr.5	1	3.580	1.346 ± 0.210	-6.693 ± 1.467	0.0101 ± 0.0113	0.00776 ± 0.00375
Zr.6	2	3.929	1.346 ± 0.210	-6.693 ± 1.467	0.0120 ± 0.0344	0.00776 ± 0.00375
O1.1 Zr.6	4	4.019	1.346 ± 0.210	-6.693 ± 1.467	0.0120 ± 0.0344	0.00989 ± 0.00472
Zr.7	2	4.030	1.346 ± 0.210	-6.693 ± 1.467	0.0120 ± 0.0344	0.00776 ± 0.00375

Table 1. Data and fitting parameters tabulated for ZrO_2 fit.

metal, and thus less ZrO_2 is formed.

Despite the misfit, the two data spectra appear similar at the two major coordination peaks (Fig. 11). The attenuation of the Zr-Zr coordination peak at $\sim 3 \text{ \AA}$ is nearly the same. To test if the attenuation is due to fewer Zr atoms present, the parameter x is re-introduced, guessed to be 0.1, and multiplied by the S_0^2 parameter for every Zr scattering path.

In the case of the (32,30) data, the floating scaling parameter evaluates to a value below 1, as we expect. Interestingly, the σ^2 parameters are somewhat more reasonable than those in Table 4, using the same parameters – albeit mostly with large error. These factors offer evidence that the attenuation of the (32,30) Zr-Zr coordination peak is due to a lower concentration of Zr atoms in the sample, decreasing N_r .

Additionally, the signal-to-noise ratio (SNR) of the (32,30) spectrum was significantly worse than that of the (32,240) spectrum (Fig. 12). While there is a possibility that the noise in the data collection contributed to error leading to the misfit in Fig. 6,

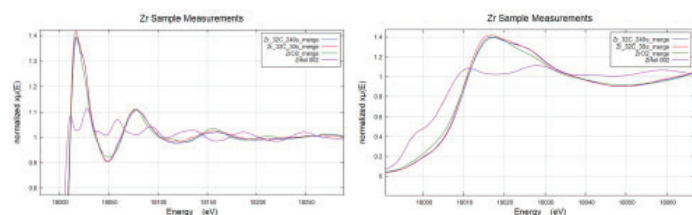


Fig. 8. EXAFS (top) and XANES (bottom) data for Zr samples, ZrO_2 standard, and Zr foil standard.

Scattering Paths	Degen	R_{eff}	S_0^2	ΔE_0	ΔR	σ^2
O1.1	2	2.054	1.052 ± 0.089	-3.231 ± 1.129	-0.001 ± 0.009	0.00113 ± 0.00141
O2.1	2	2.157	1.052 ± 0.089	-3.231 ± 1.129	-0.001 ± 0.009	0.00113 ± 0.00141
O2.2	1	2.189	1.052 ± 0.089	-3.231 ± 1.129	-0.001 ± 0.009	0.00113 ± 0.00141
O2.3	1	2.220	1.052 ± 0.089	-3.231 ± 1.129	-0.001 ± 0.009	0.00113 ± 0.00141
O2.4	1	2.285	1.052 ± 0.089	-3.231 ± 1.129	-0.001 ± 0.009	0.00113 ± 0.00141
Zr.1	1	3.338	1.052 ± 0.089	-3.231 ± 1.129	0.0546 ± 0.0213	0.02690 ± 0.01932
Zr.2	4	3.446	1.052 ± 0.089	-3.231 ± 1.129	0.0546 ± 0.0213	0.01353 ± 0.00265
Zr.4	1	3.469	1.052 ± 0.089	-3.231 ± 1.129	0.0546 ± 0.0213	0.02690 ± 0.01934
Zr.5	1	3.580	1.052 ± 0.089	-3.231 ± 1.129	0.0546 ± 0.0213	0.02690 ± 0.01935
Zr.6	2	3.929	1.052 ± 0.089	-3.231 ± 1.129	0.1600 ± 0.1102	0.02690 ± 0.01936
O1.1 Zr.6	4	4.019	1.052 ± 0.089	-3.231 ± 1.129	0.1600 ± 0.1102	0.01458 ± 0.01107
Zr.7	2	4.030	1.052 ± 0.089	-3.231 ± 1.129	0.1600 ± 0.1102	0.02690 ± 0.01938

Table 2. Data and fitting parameters tabulated for the fit to the sample Zr data (32,240).

Scattering Paths	S_0^2	ΔE_0	ΔR	σ^2
Zr.1	1.048 ± 0.101	-3.243 ± 1.278	0.0573 ± 0.0227	0.354 ± 1463
Zr.2	1.048 ± 0.102	-3.243 ± 1.279	0.0573 ± 0.0227	0.0177 ± 0.0071
Zr.4	1.048 ± 0.103	-3.243 ± 1.280	0.0573 ± 0.0227	0.354 ± 1463
Zr.5	1.048 ± 0.104	-3.243 ± 1.281	0.0573 ± 0.0227	0.354 ± 1463
Zr.6	1.048 ± 0.105	-3.243 ± 1.282	3.673 ± 2187	0.354 ± 1464
O1.1 Zr.6	1.048 ± 0.106	-3.243 ± 1.283	3.673 ± 2188	0.178 ± 732
Zr.7	1.048 ± 0.107	-3.243 ± 1.284	3.673 ± 2189	0.354 ± 1464

Table 3. Data and parameters for fit with $guess\ x = 0.1$, evaluated $x = 1.906 \pm 0.854$.

the noise itself is further evidence of fewer Zr atoms – with fewer atoms to absorb x-rays and produce signal, the SNR is worsened.

C. COPPER

Another element of interest in the film is copper. Cu is present in the hexafluorozirconic acid solution as cupric nitrate, as and as such tends to undergo reactions at the surface of the steel. In particular, large mound-like atomic clusters of copper have been observed on the surface of the thin film under SEM imaging (Fig. 3). Copper oxide is known to be involved in the clusters, as we expect copper to passivate on the surface much like the zirconium.

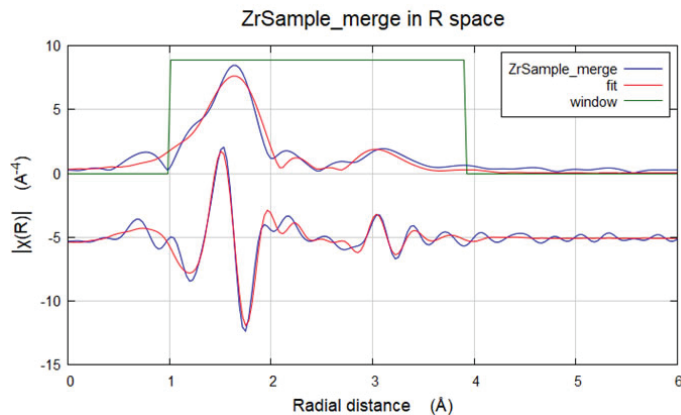


Fig. 9. Fit to Zr data (32,240) from sample in R space. Identical $guess$ and def parameters were used for this fit as for the previous fit. R-factor: 0.0241.

However, Cu has potential to react with many compounds and ions in solution – a number of which are considered here.

The only standards available to measure at the beamline were a Cu foil, Cu(I) oxide, and Cu(II) oxide – their spectra were compared to those measured for Cu in the (32,30) and (32,240) samples (Fig. 13).

Observing Figure 13, the two sample spectra do not follow closely any one other spectrum. It is clear that that Cu in the sample is not one of these compounds exclusively, but it may be a combination of multiple Cu compounds.

An exhaustive literature search was conducted to find stan-

dard spectra of various Cu compounds. Data for three Cu compounds were obtained from the Farrel-Lytle XAFS database, converted to a usable form, and imported into Athena. The linear combination fitting (LCF) tool in Athena can fit a combination of standard spectra to an unknown spectrum and return the best fit – that is, the fit with the lowest R-value.

Data was gathered and collected for XAFS spectra of the above compounds, as well as CuO, CuOHF, and CuF₂ – however, none of these three compounds factored significantly into the LCF of the data.

From these results, it can be interpreted that as steel is sub-

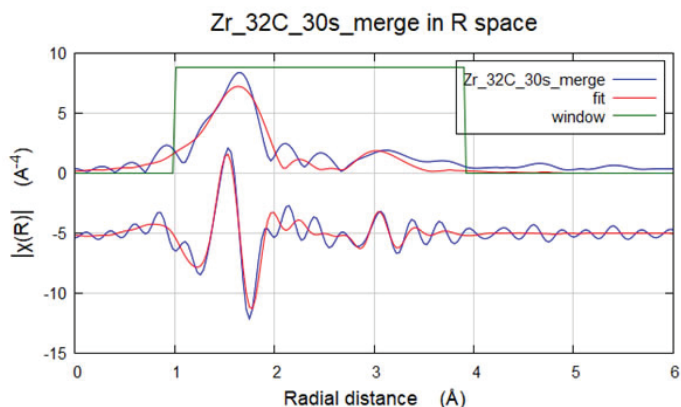


Fig. 10. Fit to Zr data (32,30) from sample in R space. R-factor: 0.0557.

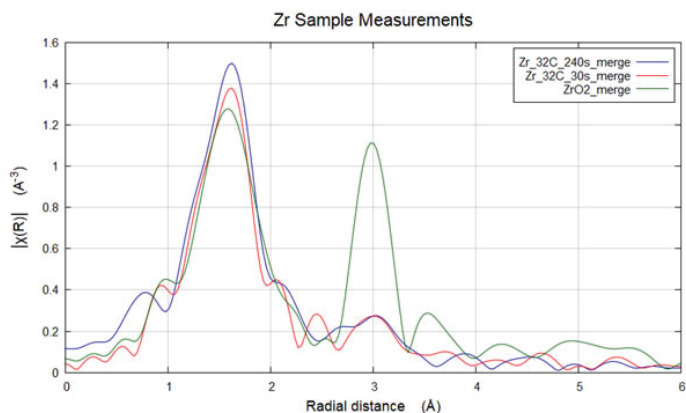


Fig. 11. R-space plot of both sample spectra, with ZrO₂ standard.

Scattering Paths	Degen	R _{eff}	S ₀ ²	ΔE ₀	ΔR	σ ²
O1.1	2	2.054	1.059 ± 0.121	-4.652 ± 1.516	0.0061 ± 0.0130	0.00142 ± 0.00188
O2.1	2	2.157	1.059 ± 0.121	-4.652 ± 1.516	0.0061 ± 0.0130	0.00142 ± 0.00188
O2.2	1	2.189	1.059 ± 0.121	-4.652 ± 1.516	0.0061 ± 0.0130	0.00142 ± 0.00188
O2.3	1	2.220	1.059 ± 0.121	-4.652 ± 1.516	0.0061 ± 0.0130	0.00142 ± 0.00188
O2.4	1	2.285	1.059 ± 0.121	-4.652 ± 1.516	0.0061 ± 0.0130	0.00142 ± 0.00188
Zr.1	1	3.338	1.059 ± 0.121	-4.652 ± 1.516	0.0545 ± 0.0270	0.02690 ± 0.01932
Zr.2	4	3.446	1.059 ± 0.121	-4.652 ± 1.516	0.0545 ± 0.0270	0.01343 ± 0.00337
Zr.4	1	3.469	1.059 ± 0.121	-4.652 ± 1.516	0.0545 ± 0.0270	0.02690 ± 0.01934
Zr.5	1	3.580	1.059 ± 0.121	-4.652 ± 1.516	0.0545 ± 0.0270	0.02690 ± 0.01935
Zr.6	2	3.929	1.059 ± 0.121	-4.652 ± 1.516	0.0983 ± 0.1651	0.03296 ± 0.03075
O1.1 Zr.6	4	4.019	1.059 ± 0.121	-4.652 ± 1.516	0.0983 ± 0.1651	0.01790 ± 0.01725
Zr.7	2	4.030	1.059 ± 0.121	-4.652 ± 1.516	0.0983 ± 0.1651	0.03296 ± 0.03075

Table 4. Data and fitting parameters tabulated for the fit to the sample Zr data (32, 30).

Scattering Paths	S0 ²	ΔE ₀	ΔR	σ ²
Zr.1	1.052 ± 0.124	-4.462 ± 1.612	0.0527 ± 0.0278	0.0161 ± 0.0265
Zr.2	1.052 ± 0.124	-4.462 ± 1.612	0.0527 ± 0.0278	0.0177 ± 0.0071
Zr.4	1.052 ± 0.124	-4.462 ± 1.612	0.0527 ± 0.0278	0.0161 ± 0.0265
Zr.5	1.052 ± 0.124	-4.462 ± 1.612	0.0527 ± 0.0278	0.0161 ± 0.0265
Zr.6	1.052 ± 0.124	-4.462 ± 1.612	0.0834 ± 0.1066	0.0161 ± 0.0265
O1.1 Zr.6	1.052 ± 0.124	-4.462 ± 1.612	0.0834 ± 0.1066	0.0094 ± 0.0152
Zr.7	1.052 ± 0.124	-4.462 ± 1.612	0.0834 ± 0.1066	0.0161 ± 0.0265

Table 5. Data and parameters for fit with *guess* x = 0.1, evaluated x = 0.679 ± 0.555.

merged in solution for longer periods of time, there is an increase in Cu_2O and $\text{Cu}(\text{OH})_2$ present in the film, and a decrease in Cu metal and $\text{Cu}(\text{CO}_3)_2$. If more or less of these compounds are desired, the submerging time can be adjusted accordingly.

IV. CONCLUSIONS AND FURTHER WORK

Under (32,30) processing conditions, the degeneracy of Zr is lower than that of bulk ZrO_2 – that is, submerging steel in the solution under these processing conditions deposits a significantly smaller amount of Zr on the sample than is present in the bulk. Under (32,240) processing conditions, the degeneracy of Zr is like that of the bulk. However, there is more structural disorder in the Zr deposited on the sample than in the bulk, as it is amorphously distributed across the sample.

Admittedly, the Cu data analysis is limited. Without knowing to a reasonable extent the chemical identity of the copper clusters, more quantitative, thorough analysis is very difficult. However, observing the results I did obtain (Table 6), submerging the steel in solution for a longer period of time encourages the formation of Cu_2O and $\text{Cu}(\text{OH})_2$, but decreases the concentration of Cu metal and $\text{Cu}(\text{CO}_3)_2$.

Obtaining $\text{Cu}(\text{OH})_2$ and $\text{Cu}(\text{CO}_3)_2$ standards to measure at the beamline should be the next step in this research, for a more accurate LCF of the Cu data. I would also suggest measuring standards for those compounds that have potential to form on the surface of the film, but did not factor into the LCF, for completeness: CuF_2 and CuOHF . Additionally, a zirconium hydroxide standard ($\text{ZrO}(\text{OH})_2$ or $\text{Zr}(\text{OH})_4$) may be useful in further analyzing the Zr data, as either of these compounds has potential to form in the film.

V. ACKNOWLEDGEMENTS

I would like to give special thanks to my mentor, Bruce Ravel, whose knowledge, teaching, and sense of humor have been

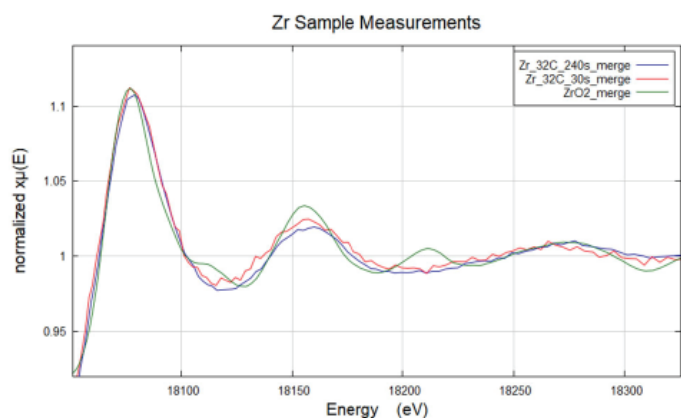


Fig 12. Region of EXAFS for both data sets, with ZrO_2 standard.

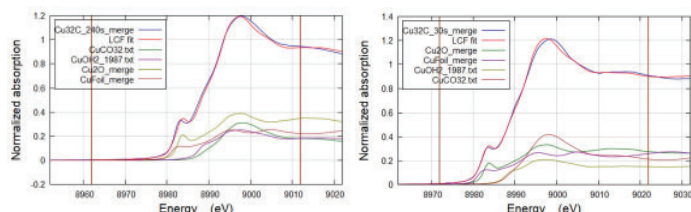


Fig 14. LCF fits for the (32,240) (left) and (32,30) (right) Cu XANES data. Weighted components are plotted below fit.

invaluable to me. I would also like to thank Karen Chen-Wiegart and Xiaoyang Liu for providing the samples. This project was supported in part by the U.S. Department of Energy, Office of Science, and the Office of Workforce Development for Teachers and Scientists (WDTs) under the Science Undergraduate Laboratory Internships Program (SULI).

VI. REFERENCES

- [1] Zaferai, Sadeq Hooshmand. “The Science of Anti-Corrosion Thin Films.” *Corrosionpedia*, 28 Mar. 2016, www.corrosionpedia.com/2/5354/coatings-and-lining/the-science-of-anti-corrosion-thin-films.
- [2] Hamdy, Abdel Salam, and D.p. Butt. “Novel Anti-Corrosion Nano-Sized Vanadia-Based Thin Films Prepared by Sol–Gel Method for Aluminum Alloys.” *Journal of Materials Processing Technology*, vol. 181, no. 1-3, 2007, pp. 76–80., doi:10.1016/j.jmatprotec.2006.03.042
- [3] Zhong, Xiankang, et al. “Characterization and Corrosion Studies of Ceria Thin Film Based on Fluorinated AZ91D Magnesium Alloy.” *Corrosion Science*, vol. 50, no. 8, Aug. 2008, pp. 2304–2309., doi:10.1016/j.corsci.2008.05.016.
- [4] I. Zabinsky, S. I., et al. “Multiple-Scattering Calculations of x-Ray-Absorption Spectra.” *Physical Review B*, vol. 52, no. 4, 1995, pp. 2995–3009., doi:10.1103/physrevb.52.2995.
- [5] “Mercury.” *The Cambridge Crystallographic Data Centre*, www.ccdc.cam.ac.uk/solutions/csd-system/components/mercury/.
- [6] Calvin, Scott. *XAFS For Everyone*. Taylor & Francis Group, 2013.

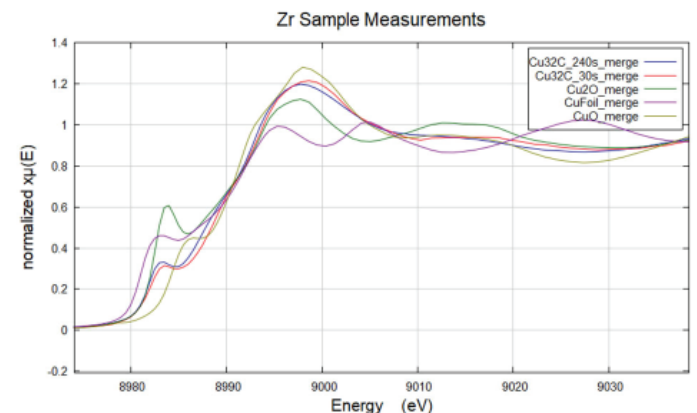


Fig 13. XANES measurement of Cu in both samples, with Cu, CuO , and Cu_2O standards.

	(32,240)	(32,30)
Cu_2O	0.347	0.298
Cu (foil)	0.254	0.270
$\text{Cu}(\text{OH})_2$	0.203	0.170
$\text{Cu}(\text{CO}_3)_2$	0.196	0.263
R-factor	0.00150	0.00123

Table 6. LCF spectral weights by percentage.

Simulated analysis on the properties of ‘tree rings’ in the Large Synoptic Survey Telescope sensors

Matthew S Decaro

Physics Department, University of California, Santa Cruz, CA 95064

Andrei Nomerotski

Physics Department, Brookhaven National Lab, Upton, NY 11973

Abstract

The Large Synoptic Survey Telescope (LSST), a ground-based telescope under construction in the Andes region of Chile, is scheduled to begin observation by 2022 with the intention to explore various aspects of our solar system, the Milky Way, the nature of dark matter and dark energy, and other distant astrophysical phenomena. The Sensor Anomalies Working Group at Brookhaven Laboratory is tasked with studying various systematic effects associated with LSSTs detectors. One systematic, named tree rings after their circularly symmetric geometry, act as lateral electric fields that distort object positions and shapes and must be corrected for to meet the high precision demands of the LSST. PhoSim, a fast monte carlo photon code, is used to simulate interactions with the atmosphere, camera, and silicon that perturb the path of the photoelectrons to their position on an image. In this study we first investigate how the parameters in PhoSim can be adjusted to model the behavior of the tree rings that we observe in Brookhaven sensors. From there we consider various position and shape distortion effects that may arise in the presence of these fields that have not yet been precisely investigated in simulated environments. By fitting distorted objects to a two-gaussian mixture model, we reconstruct various astrometric observables that can be used to analyze distributions of differently distorted objects. We conclude by interpreting differences in these distributions as a unique distortion effect on select objects due to the tree rings.

I. Introduction

A. The Large Synoptic Survey Telescope

The Large Synoptic Survey Telescope (LSST) is a future ground-based telescope located on Cerro Pachón, Chile and is designed to study aspects of dark matter, dark energy, and other distant astrophysical phenomena beginning observations in

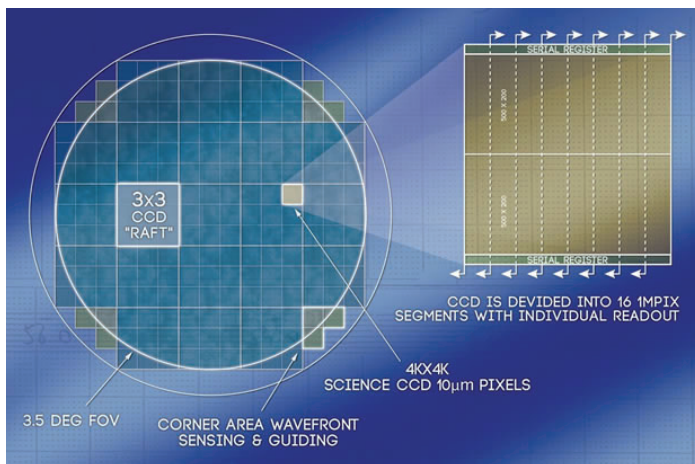


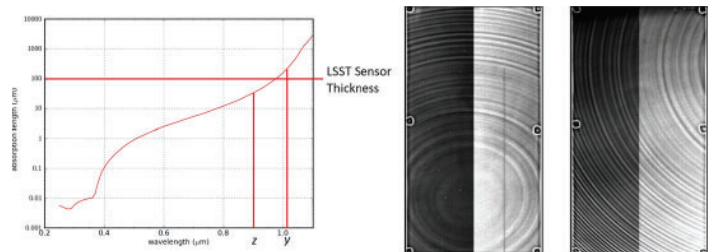
Figure 1: Focal plane and sensor structure of the LSST. [1]

2022. The telescope is equipped with a 3.2 gigapixel camera and will have 20,000 square degree sky coverage with maximum sensitivity in the ultraviolet to near-infrared spectra (u, g, r, i, z, y). Shown in Fig. 1, the focal plane of the telescope comprises 21 science ‘rafts’, each consisting of a 3x3 grid of 4k x 4k pixel CCD sensors and provides a total field-of-view of 9.6 square degrees and an 8.4 meter aperture. Each sensor has a thickness of 100 μm and a 10 μm pixel length.

The Sensor Anomalies Working Group at Brookhaven Lab, a subgroup of LSST, is tasked with investigating various systematic effects associated with the LSST sensors. These range from static effects such as lateral electric fields and anomalous edge behavior to dynamic effects that involve non-linear photometry such as the brighter-fatter effect. Reconciling these systematics will be necessary for the high-precision demands of the LSST data measurements.

B. Tree Rings

Traditionally, thin CCDs have had the disadvantage of a lack of sensitivity in the z and y bands (900 and 1020 nm, respectively). The design philosophy of deep depletion sensors allows for a greater sensitivity to long wavelengths but also has the effect of introducing unique systematics. First observed in the Dark Energy



Figures 2 and 3: Silicon penetration depth versus photon wavelength (left).

Tree ring structure observed in the DECam flats (right). [2, 3]

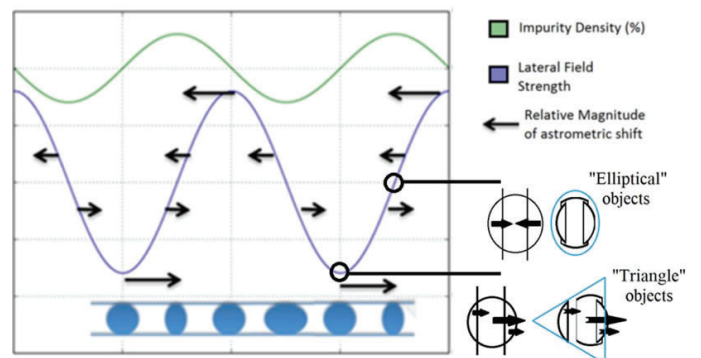


Figure 4: Relationship between dopant variation, lateral field strength, and astrometric distortion. Triangular shape correlated with maximum field strength, while elliptical shapes occur at minimum field strength. [4]

Camera (DECam) CCDs, ‘tree rings’, named after their circularly symmetric geometry as illustrated in Fig. 3, arise as a result of a variation in impurity concentration that manifests during the manufacturing of the silicon wafer. As described by Plazas et al., these rings act as lateral electric fields which displace photoelectrons on a nominal path proportional to the magnitude and direction of the field. [3] These rings have direct implications for the photometry and astrometry of LSST image data; by distorting the pixel size, the number of photons per pixel and the shape of objects deviate from their true representations.

Figure 4 displays the correlated behavior between dopant variation and the corresponding magnitude of the lateral field. At points where the lateral field strength is minimized and changing direction, it is observed that the point-spread function (PSF) is distorted elliptically due to opposite field directions within different portions of the PSF. We suggest that a similar effect occurs at locations where the field strength is maximized; in particular, two contributions of the field combine additively at peaks and troughs of the varying field strength and effectively double the amplitude of the field. For objects in which the field strength changes discontinuously, we suggest that the PSF is distorted into a ‘triangular’ shape, shown above.

C. PhoSim: An LSST Photon Simulator

Simulation tools can be used to better understand properties of the camera and sensor instrumentation and allows for the isolation of various systematics for more detailed investigation. PhoSim, an LSST photon monte carlo generator developed by John Peterson, models the path of individual photons while accounting for properties of the atmosphere, telescope, and camera that can disturb the path of photons to their ideal pixel locations on the sensor, using approximations to simulate these physics in relatively quick time. [5]

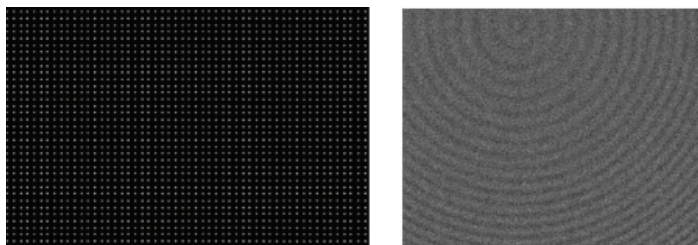
II. Methods

A. Object and Flat Fields

Figures 5 and 6 display object and flat fields. simulated as an evenly spaced grid of noiseless, monochromatic ($\lambda = 400\text{nm}$) point source objects with no overlapping of individual PSFs. Images are simulated with no atmospheric effects and only toggling on/off tree rings in order to measure astrometric shift. Lastly, truth information of first and second moments are obtained using Source Extractor. [6]

B. Object Selection and Parameter Fitting

From Fig. 4, objects with a triangular distortion should be correlated with a maximum astrometric shift. Likewise, elliptical



Figures 5 and 6: Object and flat field images simulated using PhoSim. Lateral field structure due to the tree rings as observed in the flats.

objects should possess a negligible shift. Figure 7 displays the distribution of astrometric shift which can be used to produce a set of first order cuts to select for objects with varied distortion. We then fit these objects to a two-gaussian mixture model using an expectation-maximization likelihood fitter. [7] The six output parameter-estimates of the fitter (flux, first moments, and second moments) are used to construct various observables (separation distance, ellipticity, width) to compare distributions of elliptical and triangular objects.

C. Tree Ring Parameter Selection

Although PhoSim has the functionality to model tree rings in generated images, studies have yet to done to define exact parameters that replicate the ring behavior observed in the sensors tested at BNL. As of PhoSim release v3.7.9, the parameters that control the tree-rings are: period, dopant variation amplitude, ratio, variation, and decay, tabulated in Table 1. For the purposes of this study we would like to produce first-order estimates for the parameters that model the rings seen in ITL production sensors. Flat-field images of various sensors are investigated in H.Y. Park et al (2017), and a sample plot of the photometric variation, shown in Fig. 8, is used to infer estimates of PhoSim parameters.

By inspection of Fig. 8, the period is estimated to be 130 pixels, or 1300 microns. The ratio parameter has negligible impact on tree-ring behavior, so a value of 1.3 is chosen such that the center of the rings appear somewhere on any arbitrarily selected sensor. An estimation for the impurity variation is chosen by first inspecting the peak-to-peak amplitude of variation seen in Fig. 8 ($0.2\% \leq 0.4\%$), and then by following the analysis of B. Beamer et al (2015) correlating photometric variation with the magnitude of impurity variation, shown in Fig. 9. From varying the dopant amplitude between 0.03 and 0.18 in PhoSim, we find that a value of 0.06 best fits the ITL data. It is worth noting that period and impurity concentration vary slightly for different BNL wafers, and that these parameters do not model all LSST rings but serve as qualitative first order estimates.

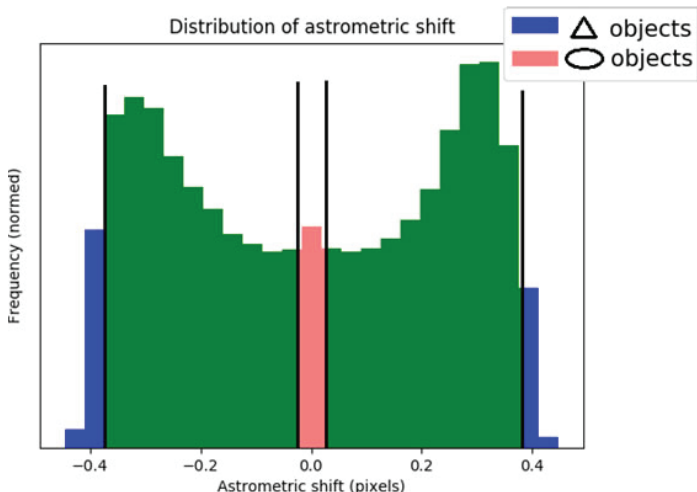


Figure 7: Distribution of astrometric shift. Cuts are made on the center and tail ends of the distribution to separate elliptical and triangular objects, respectively.

PhoSim Parameters	Parameter Definitions	Estimated Values
TreeRingPeriod	Period in microns	1300
TreeRingAmplitude	Percent magnitude of impurity variation	0.06
TreeRingRatio	Area ratio of silicon wafer to chip	1.3
TreeRingVariation	Standard deviation of period in microns	75
TreeRingDecay	Decay distance of variation in microns	15000

Table 1: Definitions and estimates of various PhoSim tree-ring parameters.

Estimates for variation and decay cannot easily be determined by inspection, so these parameters are varied independently from the default PhoSim values in steps sizes of 25 and 5000, respectively. Sample plots similar to Fig. 8 are selected for various combinations of variation and decay, shown in Fig. 10 17. The selected values of 75 and 15000 are chosen as the best first-order estimates. One important note is that the dopant variation observed in BNL sensors appears to have some radial dependence, however this cannot currently be modeled in PhoSim. Variation plots for the BNL sensor and PhoSim images also use slightly different radial ranges, however this difference has no significant effect for this study.

III. Analysis and Results

A. Astrometric distortion due to Tree Rings

Comparisons of triangular and elliptical objects are made by using parameter-estimates of the two gaussian mixture fit. Figure 18 compares distributions of fitted ellipticities for the first fitted gauss. Noticably, objects that are expected to be distorted elliptically have a measurably higher ellipticity, while triangular objects have a lower, but non-zero ellipticity. Likewise, we compare distributions of T in Fig. 19, constructed from second moment parameters $x^2 + y^2$ and is proportional to the size of the object. Observed is a familiar ‘stretching’ and ‘squishing’ of the PSF for elliptical objects, interpreted as a change in the lateral field direction within fractions of the isophotal area. As expected, this effect is not observed for triangular objects which have a constant field direction throughout.

The separation distance between the two gaussians are constructed using first moment parameters (x and y). Observed is a slightly larger width for the distribution of triangular objects. From the quiver plot in Fig. 21, the periodicity in the structure of

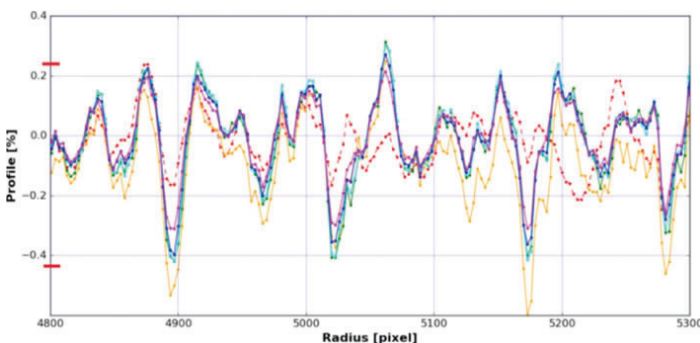


Figure 8: Flux variation observed in sensor ITL-3800C-017. [8]

the separation distance is shown to be correlated with the tree ring amplitude, however there is no significant pattern in the orientation. Similarly, by correlating separation distance with T it is seen that objects which are not stretched or squished tend to also have a larger separation distance.

From the distribution of the fractional flux, triangular objects are seen to have a slightly shifted distribution that is not centered around 0.5. It is observed that the first gaussian will tend to contain roughly two-thirds of the total flux, however it is not clear whether this is simply a characteristic of the fitter or is correlated with the distortion; because this occurs for objects at all phases of the tree ring amplitude we interpret it as the former. Finally, scatter plots of various constructed observables are plotted as functions of the distance to the center of the tree rings in Fig. 25 27. The periodicity of these parameters are correlated with the structure of the lateral fields as portrayed in Fig. 21. It is observed that the separation distance of the two fitted gauss is in phase with the astrometric shift, but is out of phase with T.

IV. Conclusion

The astrometric corrections due to the tree rings pose significant threats to the high-precision demands of the LSST. Using PhoSim, an LSST photon monte carlo simulator, this study investigates a proposed anomalous distortion of objects due to the tree rings. At maximum amplitudes of the lateral field strength, we suggest that object PSF’s are distorted into a triangular shape as opposed to an elliptical distortion at points where the field changes direction. Constraints are set on the structure of the tree rings by adjusting various parameters in PhoSim based on the behavior that is observed in sensors at Brookhaven Laboratory. Objects associated with an elliptical and triangular distortion are selected using astrometric shift as a correlated observable, and are fitted to a two-gaussian mixture model to construct various astrometric observables that can be used to compare distributions of differently distorted objects. By inspecting distributions of ellipticity and T, we observe familiar behavior expected from elliptical objects and significant differences for triangular objects. In particular, the latter have an noticeably lower, but non-zero ellipticity and lack the stretching and squishing effect reminiscent of the change in lateral field direction associated with elliptical objects. We find that these triangular objects are weakly correlated with a larger separation distance between the two gaussians, and that the variation of this separation across the sensor is aligned

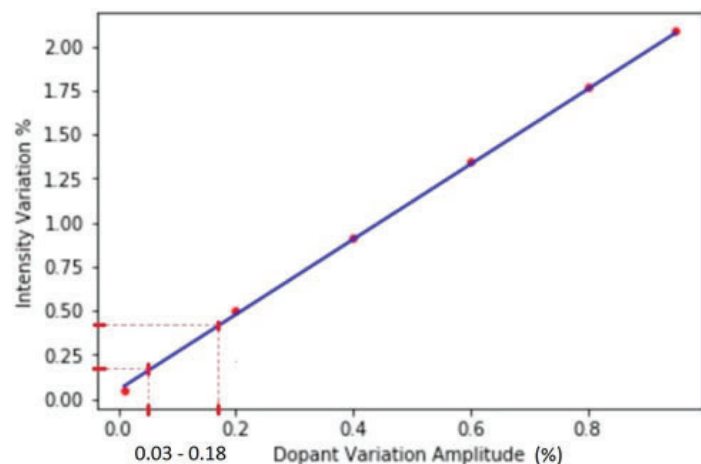
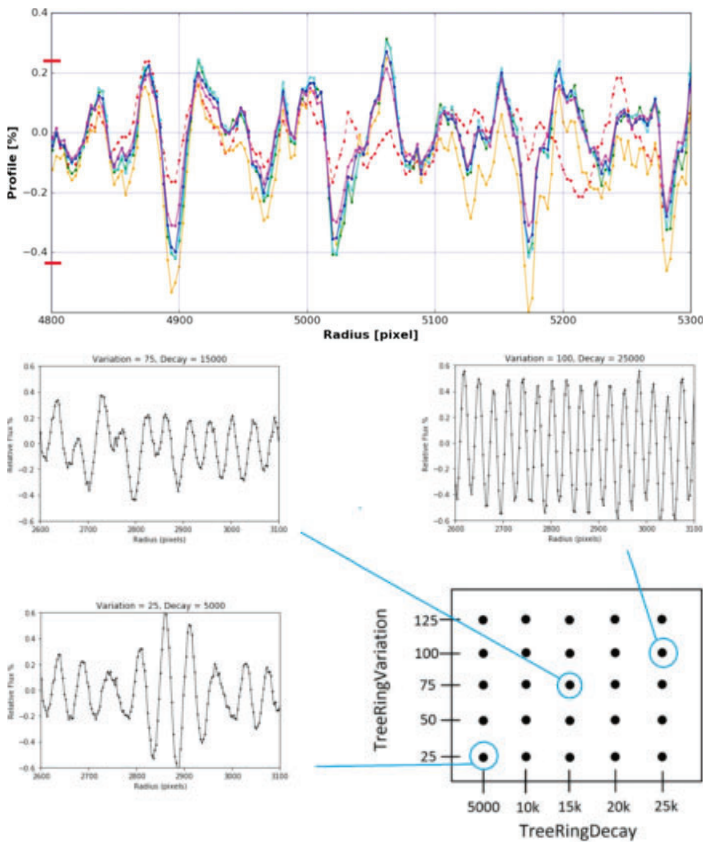
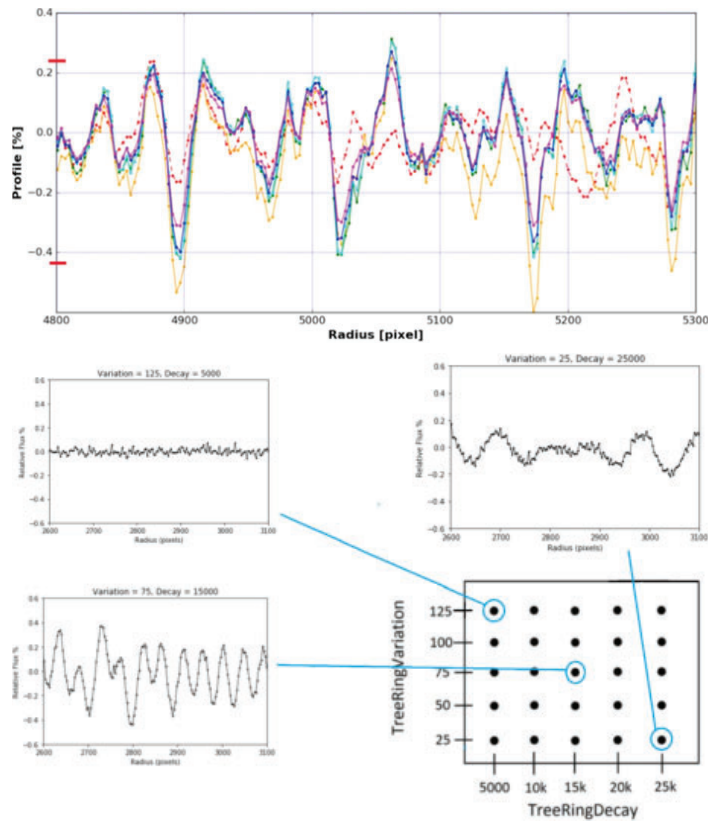


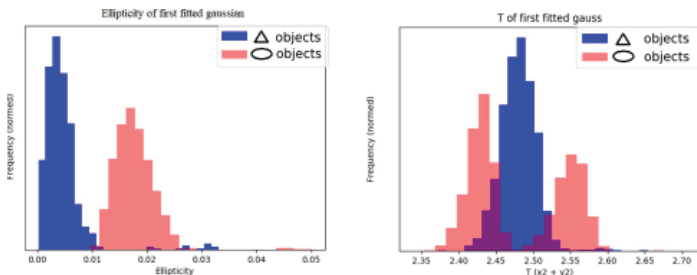
Figure 9: Correlation of flux variation and magnitude of impurity variation. [4]



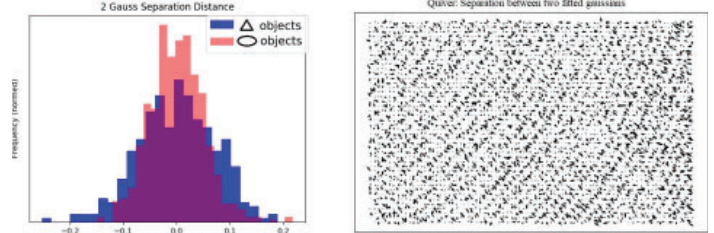
Figures 10 13: Select combinations of variation and decay in the interest of finding a first-order qualitative fit to Fig. 8, framed above.



Figures 14 17: Select combinations of variation and decay in the interest of finding a first-order qualitative fit to Fig. 8, framed above.



Figures 18 and 19: Distributions of ellipticity and T.



Figures 20 and 21: Distribution and quiver of separation distance between two gauss mixture.

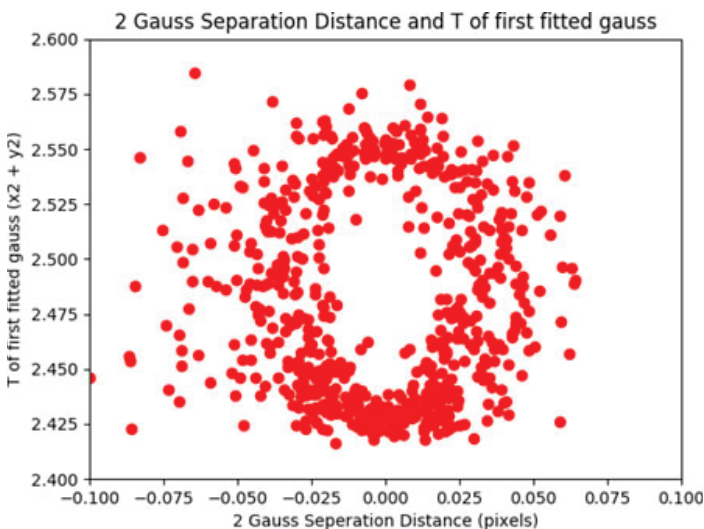
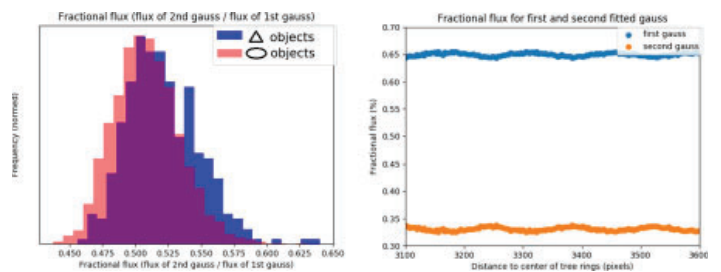


Figure 22: Correlation between fitted gauss separation distance and T.



Figures 23 and 24: Fractional flux between two fitted gaussians. The first gauss is shown to contain roughly twice the flux of the second.

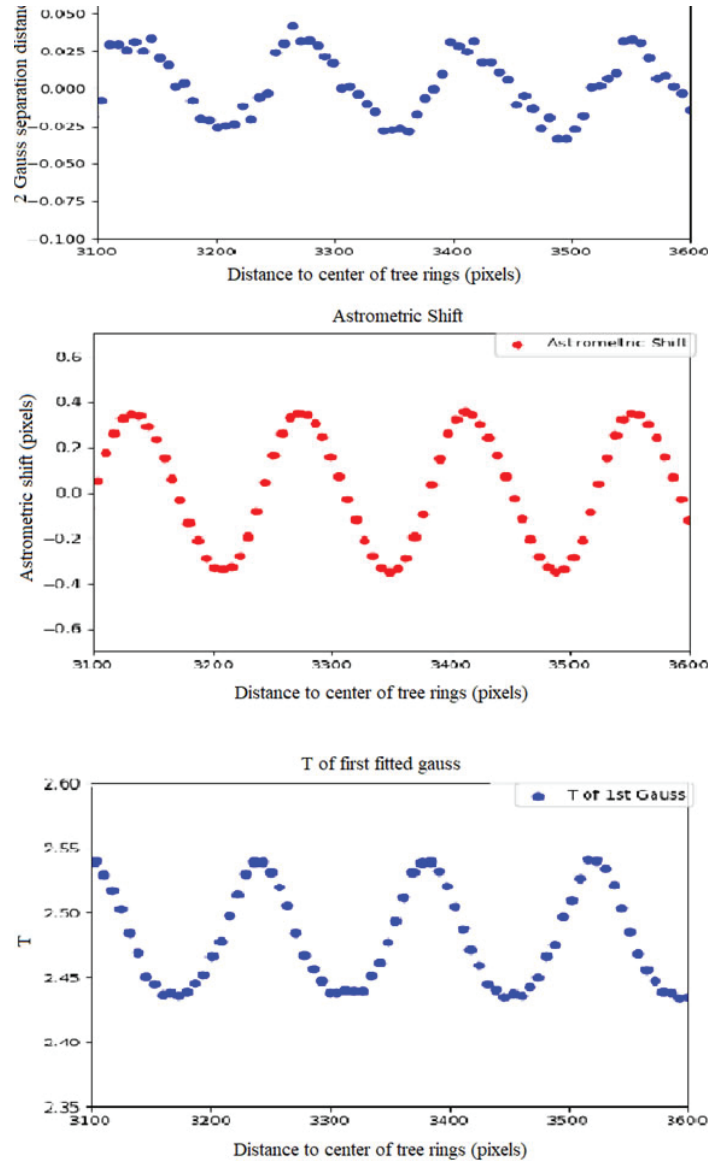
with the structure of the tree rings. Lastly, the distribution of the fractional flux between the two fitted gaussians is weakly shifted for triangular objects. From these significant differences between the distributions of various astrometric observables, we interpret the differences in these distributions as a unique distortion at the maximum lateral field amplitude due to the tree rings.

V. Acknowledgements

This project was supported in part by the U.S. Department of Energy, Office of Science, Office of Workforce Development for Teachers and Scientists (WDTS) under the Science Undergraduate Laboratory Internships Program (SULI).

VI. References

- ¹LSST Focal Plane, LSST Project/NSF/AURA. <https://www.lsst.org/about/camera/focalplane> (2009).
- ²"Penetration depth of different laser wavelength in silicon", <http://www.freiberginstruments.com/upcdmdp/technology/penetration-depth-of-differentlaser-wavelength-in-silicon.html>
- ³A.A. Plazas, G.M. Bernstein and E.S. Sheldon, 2014 On-sky measurements of the transverse electric fields' effects in the Dark Energy Camera CCDs, <https://doi.org/10.1086/677682> *Publ. Astron. Soc. Pac.* **126** 750
- ⁴B. Beamer, A. Nomerotski and D. Tsybychev, 2015 A study of astrometric distortions due to "tree rings" in CCD sensors using LSST Photon Simulator *JINST* **10** C05027
- ⁵J. Peterson, 2014 PhoSim: A code to simulate telescopes one photon at a time *JINST* **9** C04010
- ⁶Bertin, E. Arnouts, S. 1996: SExtractor: Software for source extraction, *Astronomy Astrophysics Supplement* 317, 393
- ⁷Sheldon, E, 2016: Expectation Maximization (2016), GitHub Repository.
- ⁸H.Y. Park, A. Nomerotski and D. Tsybychev, 2017 Properties of tree rings in LSST sensors *JINST* **10** C05015



Figures 25 27: Scatter plots of constructed fit observables as a function of the distance to tree ring center. Two gaussian separation distance is in phase with astrometric shift, and thus aligned with the amplitude of the lateral fields, but is out of phase with T.

Quench behavior estimate and its relation to turn-to-turn stress distribution for a 25 T HTS magnet

John Delaney

Mechanical Engineering, Fairfield University, Fairfield, CT 06824

Ryan Tomastik

Applied Mathematics, University of Connecticut, Storrs, CT 06269

Honghai Song

Superconducting Magnet Division, Brookhaven National Laboratory, Upton, NY 11973

Abstract

Brookhaven National Laboratory (BNL) will shortly receive an IBS 25 T high-temperature superconducting magnet (HTS), made of 14 double pancake coils with mostly copper and also rare-earth barium-copper-oxide (REBCO) tape, with no insulation. The goal of this project is to predict the quench behavior of this magnet to ensure safe operation for this and future magnets. One method to estimate this is the hand calculation known as the MIITS Function. Prior to using the MIITS function an energy dissipation equation, referred to as the CMT equation, gave a rough estimate of the maximum temperature to be about 194 K. The MIITS function uses current decay dependent on the magnet's resistance to calculate the temperature at a given time. Estimating the resistance of the magnet found the temperature to be around 192 K when using the MIITS Function. A second method was then used, a code developed by M. N. Wilson and later modified by Joseph F. Muratore called QUENCH. This code simulates the behavior of a magnet during the quenching process and gives detailed information about its properties. Upon analyzing the data from the program, the maximum temperature during quench is from 271.14 K to 383.59 K depending on where in the magnet is being observed. Thus it appears the IBS magnet that BNL will be receiving will not reach temperatures that will cause damage to the machine. However, information that can only be taken after the magnet is manufactured would help give a more accurate estimation of the final temperature of the magnet.

I. INTRODUCTION

The high temperature superconducting (HTS) technology has a promising future in the world of magnets. These magnets must operate at temperatures that are very low when compared to room temperature, and it is dangerous to the magnet if they were to overheat. The overheating process within a magnet is called quenching, and if left unprotected a quench could destroy a magnet. High temperature superconducting magnets are powerful because, as their name suggests, they can be operated in higher temperatures before this quenching begins.

When a quench begins somewhere in the magnet, that area is called the normal zone because it is at too high of a temperature to be in the superconducting state, and thus it is in the normal state. When the magnet is in the superconducting state it runs at a constant current density. However, once a quench is initiated the once resistant-less superconductor reverts back into a normal state and begins to have resistance. This causes energy to be dissipated in the form of heat into the system and as a result the temperature of the magnet begins to rise in the normal zone.

This normal zone then spreads throughout the magnet and as it spreads it causes other parts of the magnet to also lose its superconductivity. This means that the current can no longer be carried resulting in a quick current decay and an increase in temperature.

In this study the maximum temperature during a quench is desired so that a magnet can be designed to be efficient and safe, and is found using two different methods. The first method uses what is called the MIITS function to directly calculate the temperature during quench. The second method uses a developed code called QUENCH to simulate a magnet going through a quench and outputs information about temperature, current, and other useful properties.

QUENCH is a program in Fortran that was developed in the 1970's by Martin N. Wilson, whose purpose is to simulate the quenching process in a magnet. The complicated process by which this is done is described in his book [1]. Decades later Joseph F. Muratore of Brookhaven National Laboratory modified Wilson's code to be easier to use and to give a more detailed output. Muratore's version of the code is what is used in this study.

QUENCH gives information on propagation velocity, current decay, maximum temperature, resistance, voltage, and more over time. The geometry of the magnet as well as other calculated properties can be inputted into the program so that the maximum temperature can be directly calculated by the program.

The MIITS function calculates an estimation of the final temperature of a magnet during a quench, but it requires more information than QUENCH to use effectively, as it requires a calculation of current decay. However, in order to accurately make this calculation, the time constant needs to be known. The time constant is a value which depends on the inductance and the resistance of the magnet. In most MIITS function applications the resistance value is the value of the dump resistor. However, this magnet is not insulated and therefore there is no dump resistor. For this case the resistance can be taken from the contact resistance. The contact resistance is dependent on the contact resistivity between the windings of the magnet. A MIITS function estimation was calculated under the assumption that the contact resistivity would be constant throughout the magnet. The contact resistivity, however, changes when put under different pressures. ANSYS was used in order to determine that the stress changes at different points of the magnets. This means that the contact resistivity is not actually uniform throughout the magnet.

The MIITS function uses the integral of current density with respect to time and compares it to the integral of the heat capacity divided by electrical resistivity of copper.

$$\int_0^{\infty} J^2(t) dt = \int_{T_0}^{T_{\max}} \frac{C(T)}{\rho(T)} dT \quad (1)$$

This equation uses this information to estimate the final temperature of the magnet after a quench in order to prevent permanent damage to the magnet [2].

II. MAGNET PARAMETERS

The magnet to be studied in this paper is a 14 double pancake coil (DPC) with no insulation operating in 25 T. Each single pancake (SP) coil has 623 turns and has a height of 24.4 mm and a cross-sectional width of 46.7 mm. More information about the magnet is detailed in Table 1.

TABLE 1: Specifications of the DPC HTS Magnet

Parameters	Magnet
Type of coil	Double pancake
Number of double pancakes	14
Number of turns per SP coil	623
Inner/Outer diameter (mm)	105/198.4
Height of magnet (mm)	341.6
Conductor thickness (mm)	0.075
Double pancake axial length (mm)	24.4
Initial current/Critical current (A)	450/900
Inductance (H)	12.6
Magnetic Field (T)	25

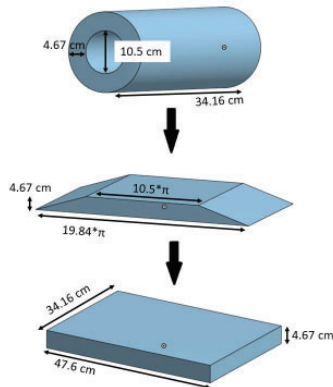


Fig. 1: Diagram of how the magnet is parameterized to be used in the QUENCH code.

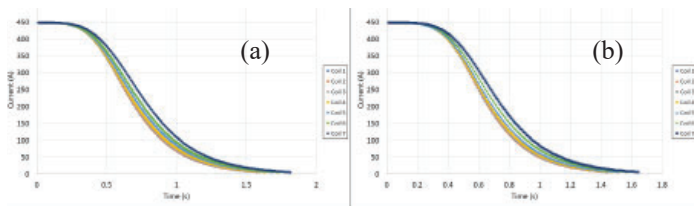


Fig. 3: Graphs of the current decay during a quench at the (a) inner and (b) outer diameter of the magnet. The current decay is calculated for a quench starting at each of the first 7.

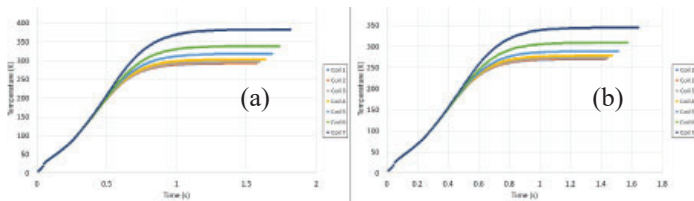


Fig. 4: Graphs of the temperature growth during a quench at the (a) inner and (b) outer diameter of the magnet. The temperature growth is calculated for a quench starting at each of the first 7 coils.

In order for the Wilson QUENCH code to model the magnet, the dimensions of the magnet must be parameterized. The QUENCH program approximates the coil geometry as a rectangular box with coordinates X , Y , and Z , so the magnet must be converted into this form [3]. The X coordinate is the axial length of the coils, which according to Table 1 is 2.44 cm. Since there are 14 double pancake coils, the total width of the magnet is 34.16 cm. The Y coordinate is the radial thickness of the coils, which is 9.92 cm $5.25 \text{ cm} = 4.67 \text{ cm}$. Lastly the Z coordinate is the azimuthal direction, given by the average circumference of the magnet which is equal to 47.6 cm. This transformation is shown in Figure 1.

Since the MIITS function assumes that the magnet is made of

TABLE 2: QUENCH Input Parameters

Parameter	Value
Number of Materials	2
Time step/Number of time steps	0.01/1400
Delay time before dump resistor is inserted	0 sec
Thermal conductivity ratio	0.0184
X/Y/Z dimensions	34.16/4.67/47.6 cm
External dump resistor	0.016
Heating effect on dump resistor	0
Resistance before switch is opened	0.000001
Resistance of external circuit elements	0
Initial propagation velocity	255.4 cm/s
Unit cell area	0.009 cm ²
Operating temperature	4.2 K

Material	Temperature (K)	Resistivity (Ohm*cm)	Volumetric Specific Heat (J/cm ³ *K)
Copper	0	$(2.5 \times 10^{-8}) + 1.67 * T^{2.69}$	$(4.31 \times 10^{-6}) * T^{3.2} + (1.14 \times 10^{-4}) * T$
	30	$(2.5 \times 10^{-8}) + 1.67 * T^{2.69}$	$(8.06 \times 10^{-4}) * T^{1.77}$
	80	$(2.5 \times 10^{-8}) + 1.67 * T^{2.69}$	$-35.74 * T^{-0.55} + 5.1$
	100	$(1.09 \times 10^{-9}) * T^{1.23}$	$-35.74 * T^{-0.55} + 5.1$
ReBCO [1]	0	1.2×10^{-4}	$(2.0 \times 10^{-4}) * T^{2.241}$
	35	1.2×10^{-5}	$(4.1 \times 10^{-3}) * T^{1.4603}$
	80	1.2×10^{-5}	$(4.246 \times 10^{-1}) * T^{0.4092}$

Fig. 2: The equations used by the Wilson QUENCH code to calculate the resistivity and volumetric specific heat of the materials in the magnet at different temperatures.

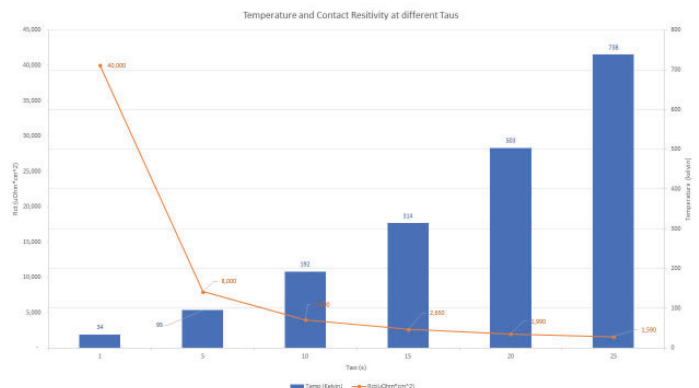


Fig. 5: Graph of experimental Taus used for the MIITS Function and the contact resistivity associated with those Taus

only copper, the same is assumed for the QUENCH code. However it is also assumed for the Wilson QUENCH code that there is superconducting material. The Wilson QUENCH code requires that the resistivity and volumetric specific heat be inputted in the form of different equations depending on the temperature. These equations are listed in Figure 2.

III. RESULTS AND DISCUSSION

A. The Wilson QUENCH Code

The Wilson QUENCH code requires an extensive and detailed list of input parameters in order to run. Some of these had to be calculated while others were already known for the magnet. The propagation velocity and thermal conductivity ratio are two parameters that had to be calculated, which are explained below. All of the other input parameters for the Wilson QUENCH code can be seen in Table 2.

The program gives detailed output data including current decay and temperature growth over time, as well as a maximum temperature. Figure 3 and Figure 4 show current decay and temperature growth in the magnet, respectively, at both the inner and outer radius. It can be seen that the maximum temperature is achieved in the middle of the magnet, coil 7, at the inner radius,

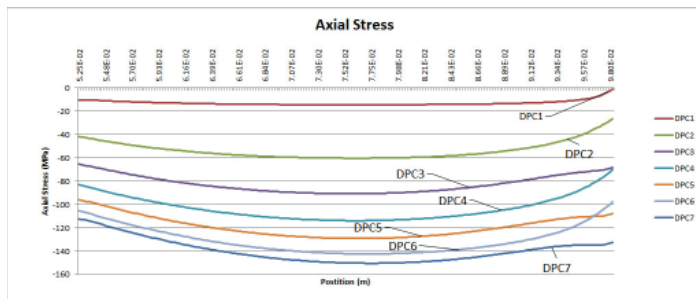
with this temperature being 383.59 K. The lowest temperature is achieved in coil 1 at the outer radius, being 241.14 K. So clearly the inside of the coil becomes hotter than the outside of the coil and the middle of the magnet is where the temperature is the highest. It can also be seen that the current decays faster at the outer diameter. For instance in coil 7 at the outer diameter, it takes 1.64 seconds for the current to completely decay. At the inner diameter in coil 7 it takes 1.81 seconds for total decay.

1. Propagation Velocity

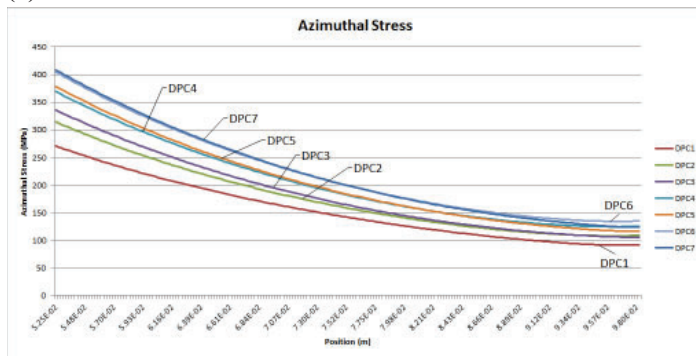
The propagation velocity represents the speed at which the normal zone travels throughout the magnet. It changes as the zone spreads further throughout the magnet, and the QUENCH code calculates and outputs the velocity at each time step.

The initial propagation velocity is required to be input into the program, and it is calculated using the following equation from [3]:

(a) Axial



(b) Azimuthal



(c) Radial

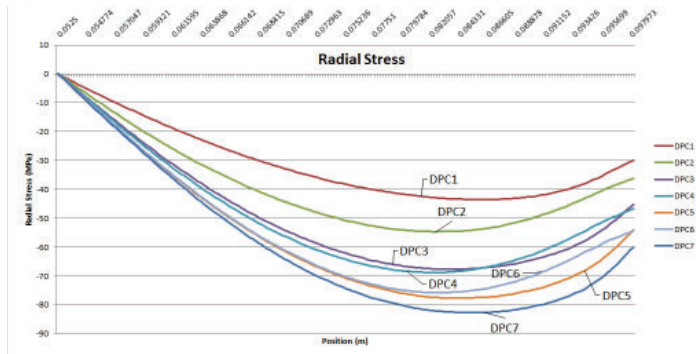
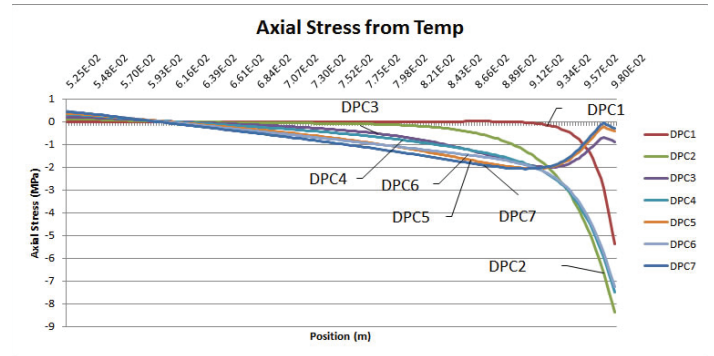
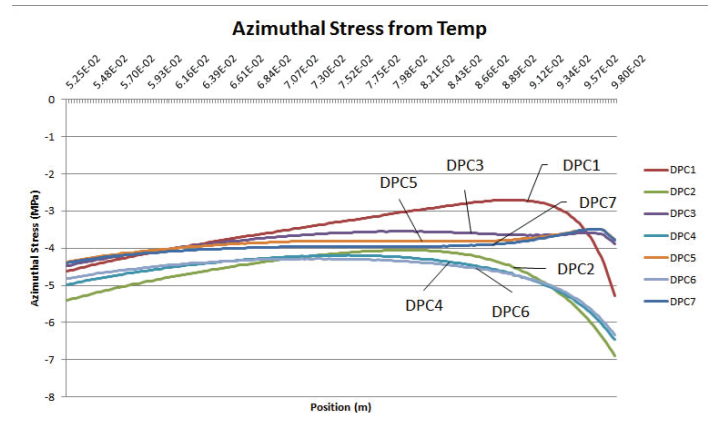


Fig. 6: EM Induced Stress

(a) Axial



(b) Azimuthal



(c) Radial

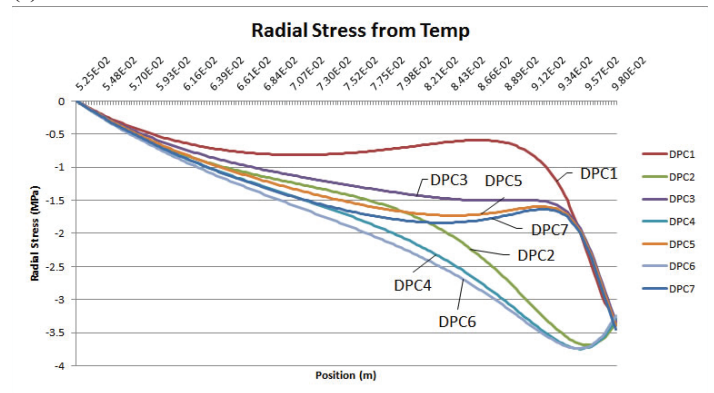


Fig. 7: Thermal Induced Stress

$$V = \frac{I}{A_{metal} * C_{av}} \sqrt{L_0 \frac{T_{share}}{T_{share} - T_{op}}} \quad (2)$$

where A_{metal} is the cross-sectional area of the metal component of the conductor in the unit cell (in m^2), C_{av} is the average specific heat of copper (in $\frac{J}{kgK}$), L_0 is the Lorenz number ($2.45 * 10^{-8} \frac{W\Omega}{K^2}$), T_{op} is the operating temperature (in K), and $T_{share} = (T_{max} + T_o)^{1/2}$ (in K).

Plugging the values of the relevant magnet into Equation 2 gives the value of the propagation velocity to be 255.4 cm/s, which is reasonable when compared to other HTS magnets [6], [7], if perhaps a little high.

2. Thermal Conductivity Ratio

The Wilson QUENCH code requires input of the thermal conductivity ratio in two directions, k_x and k_y . In this case they are both the same, so it is called k_{tot} . The equation given by [3] to find this k_{tot} is

$$\frac{l_{tot}}{k_{tot}} = \frac{l_1}{k_1} + R_{12} + \frac{l_2}{k_2} + R_{23} + \frac{l_3}{k_3} + R_{34} + \frac{l_4}{k_4} + \dots + R_{nl} \quad (3)$$

where l_i is the thickness of each material, l_{tot} is the distance across the unit cell, k_i is the thermal conductivity of each material, and R_{ij} is the resistance between materials. The effects of ReBCO can be ignored in this calculation [3], so the only material under consideration is copper. Additionally, the resistance can be considered to be very small, in this case 0.00001Ω . Then if $l_{Cu} = 70\mu m$, $l_{tot} = 75\mu m$, and $k_{Cu} = 400 W$, Equation 3 gives a k_{tot} of 0.0184.

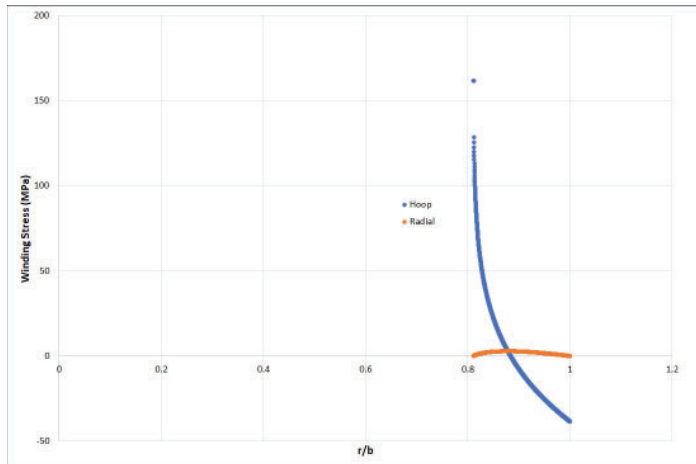


Fig. 8: Graph of the winding stress calculated using MATLAB.

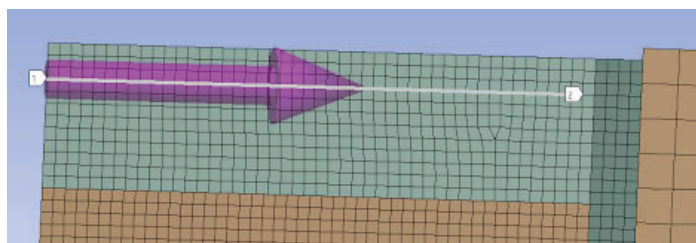


Fig. 10: Stress Path for each DPC

B. The MIITS Function

Prior to performing the MIITS function calculation a rougher estimate calculation was used to find the maximum temperature. An equation that will be referred to as the CMT equation takes the energy stored in the current and the average specific heat and mass of the magnet in order to estimate the maximum temperature.

$$E_{stored} = C_{av} * m * (T_{max} - T_o) \quad (4)$$

Where E_{stored} is the stored energy in the superconducting magnet, C_{av} is the average specific heat of copper (in this case it is taken at 50 Kelvin), m is the mass of the copper in the superconducting magnet, T_{max} is the highest temperature of the magnet and T_o is the original temperature of the magnet before the quench. Rearranging the function we can solve for the final temperature of the magnet after a quench:

$$T_{max} = \frac{E_{stored}}{C_{av} * m} \quad (5)$$

Solving for T_{max} gives a rough estimate of the final temperature to be around 194 Kelvin. This is a rough estimate because the specific heat of copper is taken at an average temperature instead of taking it as a temperature dependent property. In addition, it also does not take into account the resistivity of copper nor the current decay. This was used as a simple equation to give an idea of what the highest temperature in the MIITS Function should be [4].

The MIITS Function was then used to give a more approximate estimate of the maximum temperature. The left hand side of the MIITS function integral evaluates the current density decay of the system. The current decay of the magnet can be represented by the formula:

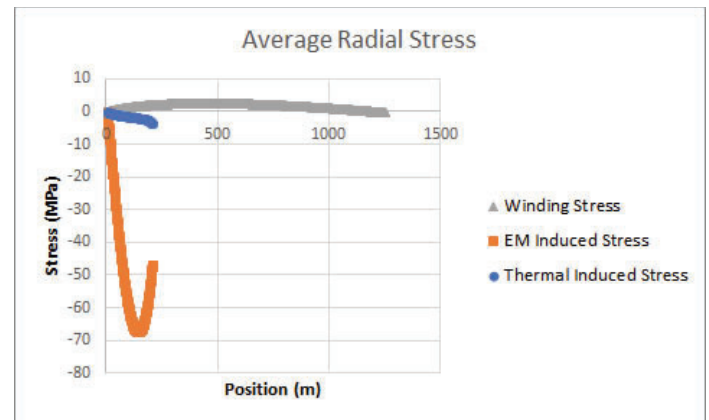


Fig. 9: Comparison of the electromagnetic, thermal, and winding stress in the magnet.

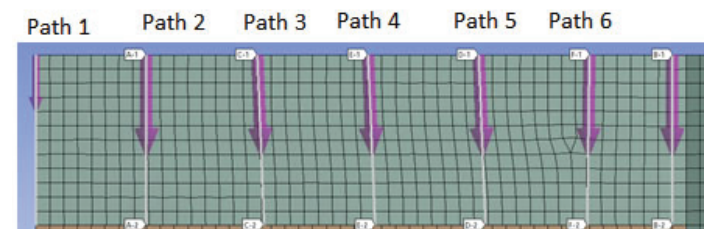


Fig. 11: Stress Path in a Single DPC

$$i = I_o * e^{\frac{t}{\tau}} \quad (6)$$

Where I_o is equal to the operating current, t is equal to the time, and τ is the time constant and is equal to the equation:

$$\tau = \frac{L}{R} \quad (7)$$

The current divided by the area will give the current density decay of the magnet [2].

Since the magnet has not yet been manufactured the resistance value for τ is unknown. For insulating superconducting magnets the dump resistor is typically used for the resistance value of current decay. Since there is no insulation for this magnet there is also no dump resistor. Instead the contact resistance between the turns of the magnet was used for the resistance value. τ was estimated at different values and the final temperature was evaluated at these different τ values. The estimated final temperature for the CMT calculation was used to approximate the τ value of the magnet. The range of τ values that gave a temperature close to the final temperature of the CMT calculation would be the approximate τ value. Once τ was found, the resistance required to achieve this τ was calculated using:

$$R_c = \sum_{i=1}^{N_t} \frac{R_{ct}}{2\pi r_i w_d} \quad (8)$$

C. Contact Stress

In the previous section the contact resistance was considered constant throughout the magnet in order to help estimate the τ and in return the current decay. However, the contact resistance is a property that is dependent on the stress of the magnet. The FEM program, ANSYS, was determined that the stress of the magnet changed depending on the location of the magnet. The Thermal Induced stress and the Electromagnetic Induced stress were found using ANSYS. Radial stress, azimuthal stress, and axial stress were found for both of the induced stresses and can be found in Figure 6 and Figure 7. In order to see how these stresses changed throughout the magnet, stress analysis was performed across each double pancake coil. This path was taken approximately a quarter of the way down from the top of each double pancake coil and can be seen in Figure 10. The stress was data was analyzed from the first seven double pancake coils because the stress was assumed to be symmetric. In order to see how the stress changed in a single double pancake coil, the radial stress

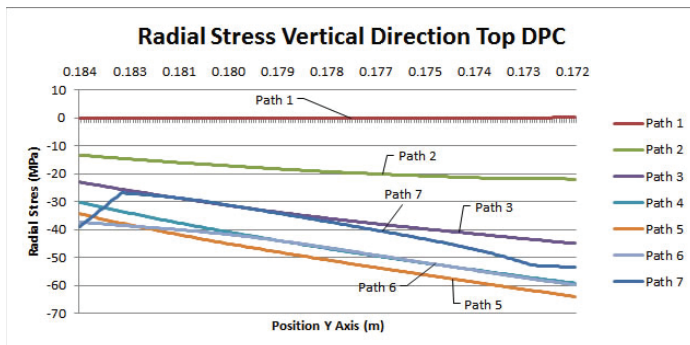


Fig. 12: Radial Stress Top DPC in Height Direction

was taken from seven different paths in the top and middle double pancake coil. This can be seen from Figure 11. The winding stress in the radial direction was found using MATLAB, and can be seen in Figure 8. The electromagnetic, thermal, and winding stress change throughout different parts of the magnet and impact the resistance of the magnet. A comparison of these three stresses can be seen in Figure 9.

IV. CONCLUSION

The quench behavior of a specific magnet was calculated using various methods. The first method was using the MIITS function which gave a reasonable maximum temperature that agreed with an estimated value obtained from the CMT equation. This method required calculating the resistance and in turn the time constant of the magnet using methods that could be beneficial to similar investigation in the future. The second method was using the QUENCH code developed in Fortran by Martin N. Wilson, which is able to give detailed information on the properties of the magnet during a quench.

When a τ of ten seconds was used for the MIITS Function the maximum temperature was found to be 192 Kelvin [5]. This matched closely to the CMT estimate of 194 Kelvin. The different τ values used can be seen in Figure 5.

In conclusion, when the resistance is greater than 2, 650 $\mu\Omega \cdot \text{cm}^2$ and the magnet begins to quench, the final temperature should still remain less than 400 Kelvin in order to operate safely. This data is supported by the program QUENCH in which the highest temperature was found to be 383.59 K. This data implies that the final temperature would result in safe operation even if a quench was to occur. A better estimation could be reached once BNL is in possession of the magnet that way the resistance of the magnet can be found. This would lead to a better approximation of the time constant and current decay. As a result the estimation of the final temperature after a quench would also be better.

V. ACKNOWLEDGMENTS

This project was supported in part by the U.S. Department of Energy, Office of Science, Office of Workforce Development for Teachers and Scientists (WDTS) under the Science Undergraduate Laboratory Internships Program (SULI). We would also like to give our thanks to our mentor Honghai Song, who guided us through our research and helped us along the way when we needed it.

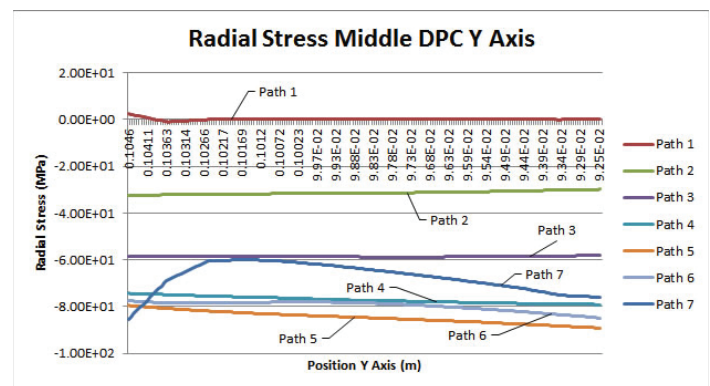


Fig. 13: Radial Stress Middle DPC in Height Direction

VI. REFERENCES

- ¹M. N. Wilson, *Superconducting Magnets*, NY, USA: Clarendon Press, 1983.
- ²K.-H Mess and P. Schmser and S. Wolf, *SUPERCONDUCTING ACCELERATOR MAGNETS*. River Edge, NJ, USA: World Scientific, 1996
- ³*QUENCHS User's Manual*, Brookhaven National Laboratory, Upton, NY.
- ⁴D. Czerwinski, "Modelling the critical parameters of high temperature superconductor devices in transient states," Accessed on July 7, 2018. <http://bc.pollub.pl/Content/3169/modelling.pdf>
- ⁵X. Wang et al., "Turn-to-turn contact characteristics for an equivalent circuit model of no-insulation ReBCO pancake coil," *Supercond. Sci. Technol.*, vol. 26, no. 3, Jan, 2013. Accessed on July 18, 2018. doi:10.1088/0953-2048/26/3/035012, [Online]. Available: <http://iopscience.iop.org/article/10.1088/09532048/26/3/035012/pdf>
- ⁶C. Lacroix *et al.* "High Normal Zone Propagation Velocity in Second Generation High-Temperature Superconductor Coated Conductors with a Current Flow Diverter Architecture." *Supercond. Sci. Technol.*, 20, Mar. 2014. Accessed on July 18, 2018. [Online]. Available: <http://iopscience.iop.org/article/10.1088/0953-2048/27/5/055013>
- ⁷C. Lacroix *et al.* "Normal Zone Propagation Velocity in 2G HTS Coated Conductor With High Interfacial Resistance." *IEEE Trans. Appl. Supercond.*, vol. 23, no. 3, June, 2013. Accessed on July 18, 2018. doi:10.1109/TASC.2013.2239696, [Online]. Available: <https://ieeexplore.ieee.org/document/6409995/>

Making sense of system logs: Implementing centralized system log storing, indexing, querying, and visualizing software on a heterogeneous network

Jonathan Dolde

Department of Physics and Astronomy, University of Iowa, Iowa City, IA 52242

Antonio Wong

Physics, Brookhaven National Laboratory, Upton, NY 11973

Brookhaven National Laboratory is home to the Relativistic Heavy Ion Collider (RHIC) and A Toroidal Large Hadron Collider (LHC) Apparatus (ATLAS) Computing Facility (RACF). The RACF computing clusters are configured with Puppet, an open-source software configuration management tool. Puppet allows for software to be configured centrally across a heterogeneous network of server nodes. Using Puppet, one can centrally manage the four applications that make up the Elastic Stack; Elasticsearch, Logstash, Kibana, and Beats. The Elastic Stack allows for streamlined data processing, searching, and visualization. Installation of the Elastic Stack at the RACF will allow logging data to be easily processed. The ability to organize and visualize logging data is crucial for tracking patterns in system operation, allowing for quicker incident response. This stack was installed on a total of five different nodes; three nodes form an Elasticsearch cluster, one hosts Logstash, and one hosts Kibana. Looking ahead, it may be possible to feed this data into machine learning algorithms to train them to recognize issues faster and more efficiently than staff.

I. INTRODUCTION

A. Background

Brookhaven National Laboratory (BNL) is responsible for much of the high energy physics computational work done in the United States. BNL is home to the only Tier 1 computing facility for the A Toroidal Large Hadron Collider (LHC) Apparatus (ATLAS), and is also responsible for the vast majority of computational power dedicated to the two experiments at the Relativistic Heavy Ion Collider (RHIC) at BNL, the Pioneering High Energy Nuclear Physics eXperiment (PHENIX) and the Solenoidal Tracker At RHIC (STAR). These three experiments require vast amounts of computing power to be able to analyze the millions of particle collisions generated every second. The RHIC ATLAS Computing Facility (RACF) is responsible for these computing capabilities. The hardware infrastructure for the RACF includes approximately 90,000 computing cores, 45 petabytes (PB) of on line disk storage, and over 200 PB of tape storage¹. All of these machines need to be monitored to ensure they are all behaving as expected, which is a decidedly difficult task. Most of the computing resources generate system logs, messages that communicate how software on the system is behaving, including error messages. These system logs can be written in different formats, there are unfortunately many standards that a system's logs can conform to. Most of the machines at the RACF use a format known as the syslog protocol², and example is of which is shown in Figure 1. The syslog protocol enforces strict constraints on how a system logging message is formatted and transmitted, which makes

gathering and analyzing system logs that conform to the the syslog protocol much easier.

B. The Elastic Stack

Each application in the Elastic Stack is an important component of analyzing syslogs at the RACF, but Elasticsearch is what makes up the backbone of the entire stack. According to Elasticsearch's official product page, "Elasticsearch is a distributed, JSON-based search and analytics engine designed for horizontal scalability, maximum reliability, and easy management."⁴ This product description encapsulates the requirements for the need of the RACF. The Elasticsearch cluster is a group of nodes running Elasticsearch that are responsible for storing the desired data. The smallest part of the data stored in Elasticsearch is called a document. A document in our case is a single syslog message. A group of similar documents is called an index, each document must be indexed for it to be searchable. We would only have one index in our implementation, one with all of our syslog messages. The data in an index is broken into shards, where each shard contains some partial amount of index data. These shards allow for us to easily scale our data storage, adding more nodes to our storage cluster without massive amounts of data transfer. These shards also help to speed up searches, allowing for data to be queried across separate nodes. The number of shards can be specified when defining an index. The shards can also be easily replicated, allowing for copies of data to be stored across nodes. Replicate shards allow for redundancy in data storage, preventing its loss in case of node failure.⁵

Elasticsearch is queried through a Representational State Transfer (REST) application programming interface (API). Using commands like GET, PUT, DELETE, Elasticsearch's data can be interacted with through many different clients. However, there is one application that was designed with querying Elasticsearch in mind: Kibana.

```
<100>2 1982-07-10T20:30:40.001Z myservers.com su 201 32001 - BOM 'su root' failed on /dev/pts/7
  → Message: su root ...
  → Encoding: BOM (UTF-8)
  → Structured-Data: -
  → Message ID: 32001
  → Process ID: 201
  → Application: su
  → Hostname: myservers.com
  → 30 mins and 40.0012 seconds after the 20th hour of 10 July 1982 in UTC
  → Version: 2
  → Priority: 100
```

FIG. 1. The standard format for a syslog message. Using a strict protocol for these messages makes parsing them much easier.³

Kibana is a web interface for querying and visualizing data from Elasticsearch. Kibana's 5.6.10 web interface can be seen in Figure 2. Kibana allows for us to query the syslogs we have stored in Elasticsearch through search parameters we pass through Kibana. The real power found in Kibana is the visualization tools. Kibana has a whole suite of data representation options, from basics such as scatter plots and pie charts to more advanced options like coordinate heat maps and real-time timelines. These visuals are created from data pulled from Elasticsearch, then can be exported in various formats. There is also the option to keep these visuals on the Kibana dashboard, which allows you to keep your visualizations running in real time, useful for system monitoring.

So how did we get data into Elasticsearch in the first place? Enter the two other elements of the Elastic Stack, Logstash and Beats. A complete Elastic Stack can use either one or both, allowing for freedom in regards to how you want data to be ingested into Elasticsearch. Beats is a family of lightweight shippers for all types of system data. These include applications like Filebeat, for system logs, Metricbeat, for system metrics, and Packetbeat, for networking data. These programs are installed on whichever node you need information, which is then shipped where it's needed. The Beats framework can send data directly to Elasticsearch for indexing, or to Logstash for more parsing options.

Logstash is a pipeline that parses data and was built to work seamlessly with Beats and Elasticsearch. Logstash can ingest data from many sources, but when working with Beats, data is sent in a lossless and back-pressure sensitive manner⁶. The lossless communication ensure that in the event of a communication failure by either Logstash or Beats, all data will be preserved until the pipeline is restored. Back-pressure sensitive means that Beats will slow down its data transfer if it detects that Logstash is backed up with parsing files. Logstash's main purpose is to parse data fed into the pipeline through pattern matching. There are many different plugins that can be used for reading in types of data, giving Logstash much flexibility in parsing data. Once the data is read in and parsed, Logstash sends the data to Elasticsearch with a guaranteed "at least once" delivery through use of a persistent queue⁷.

II. IMPLEMENTATION

A. How the Elastic Stack will be used at the RACF

How do we take these applications and make them work for the specific needs of the RACF? Let's start at the beginning of our data's journey. Our data can start in two possible locations, syslogs stored on a central syslog server, or on edge servers, where the logging data may not conform to the syslog protocol. I will refer to these two sources as central data and edge data, respectively. Both of these data types start their journey by being discovered by Filebeat, which ensures delivery of their data to Logstash. Logstash then parses these types of data in different ways. For central data, Logstash will have a robust filter that parses syslog data through a plugin called grok, which allows for straightforward pattern matching. The central data is then sent to Elasticsearch for indexing. For edge data, if their system logs conform to syslog protocol, they are sent through the same pattern matching filter. For edge data that doesn't conform to syslog protocol, Logstash would be able to have various filters for the more common log formatting. If there is no patterns found to match to in Logstash filters, then Logstash can try to extract as much information as possible through a skeletal default filter as well as sending a "not parsed" message to Elasticsearch, alerting us to

the a non-standard system log. Once all our data is stored in the Elasticsearch cluster, it can then be queried through Kibana for analysis and visualization.

B. Stack layout at the RACF

The Elastic Stack is installed on five distinct nodes, as well as various nodes having Beats installed on them. In the Elastic Stack cluster, there are three nodes with Elasticsearch installed, all PowerEdge R730xd models. Each of those nodes are be data nodes, responsible for storing Elasticsearch data, as well as being master-eligible nodes. Master nodes are in charge of enforcing the state of the cluster, and can also store data. Another PowerEdge R730xd has a Logstash pipeline running on it, parsing data from Beats and sending it to the Elasticsearch cluster. Kibana is installed on a PowerEdge R610, as Kibana is a much less demanding application than Elasticsearch or Logstash. Finally, Filebeat is installed on our central syslog server as well as various edge servers we're interested in analyzing system log data on.

C. Puppet centralized server management

Rather than installing the Elastic Stack manually on each node that will make up the stack, I used a centralized, open source, management software called Puppet. Puppet is extensively used at the RACF to manage the software of 4400 machines⁸. Puppet operates on the principle of modules, self contained folders with related instruction files, called manifests. A module can have multiple manifests, which can install different software applications, or allow for different configurations of the same software. These modules should be narrow enough in scope to allow for re-usability, so most modules are limited to installing and configuring one software application. Configuration states for the software can be passed to Puppet in many different ways through the use of Hiera (short for hierarchy). Hiera allows for a user to specify the source of configuration parameters. One source is a web interface, Foreman, is used at the RACF to manage the state of the vast majority of the nodes in our system. Configuration parameters files can also be passed through YAML (YAML Ain't Markup Language) files. YAML is a human-friendly data serialization language⁹, which allows for clean formatting of configuration states as well as comments explaining why each parameter is set the way it is.

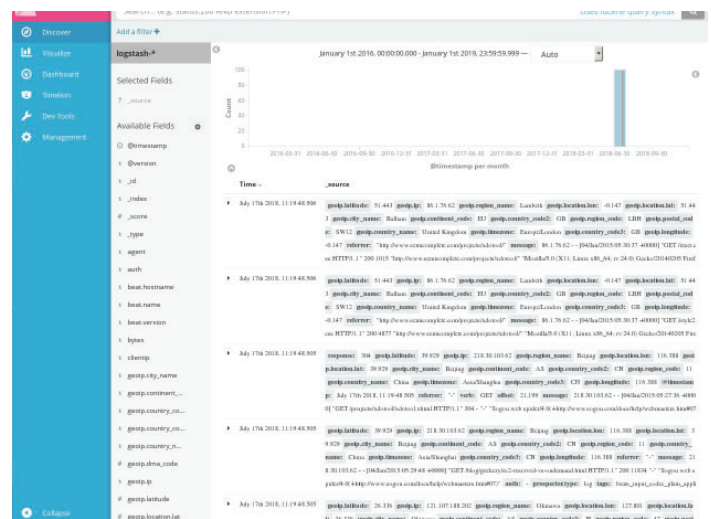


FIG. 2. An example of the Kibana 5.6.10 web interface. The sidebar has many options for data querying.

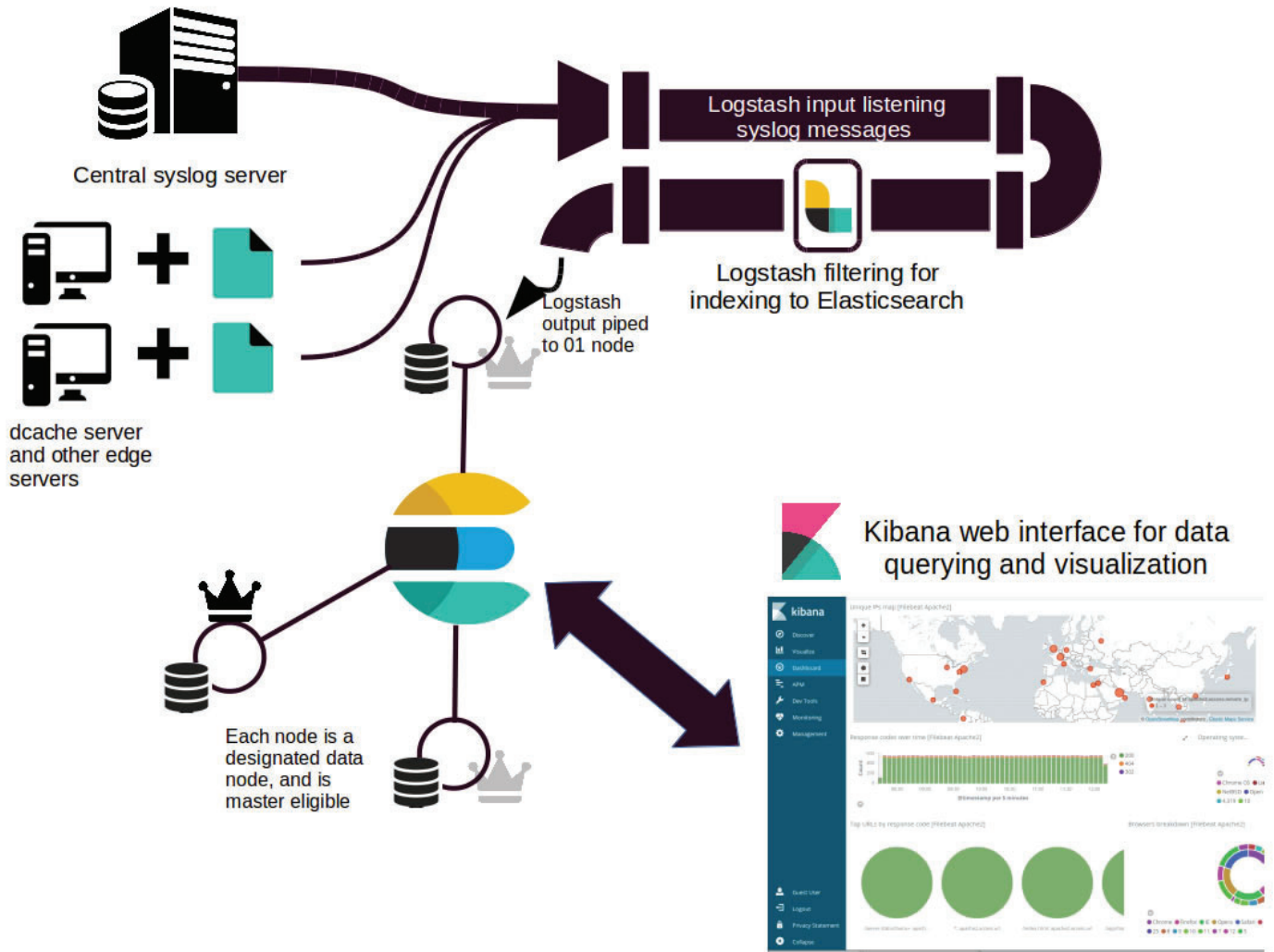


FIG. 3. Diagram of the Elastic Stack pipeline. This figure shows the journey a system log would take at the RACF

In my implementation of the Elastic Stack, I primarily use YAML files to pass configuration parameters to Puppet.

Puppet also maintains an open source repository for many modules, called the Puppet Forge. The Forge is much like github, and allows for easy configuration of software by providing a Puppet module that has been tested by users and oftentimes Puppet developers. The Puppet Forge offers modules for Elasticsearch, Kibana, Logstash, and some Beats. Elastic Co. has released the Elasticsearch, Kibana, and Logstash modules, while the Beats modules come from a variety of developers. In our implementation of the Elastic Stack, we use these Puppet Forge modules to install and configure the stack, as well as modifying the modules to help fit our own specific needs.

The parameters passed to these specific modules govern how each component of the Elastic Stack function and interact with one another. For the Elasticsearch module, an instance of Elasticsearch must be specified, which then sets configuration states such as node name, ports to use for HTTP transfer, and other nodes that instance should be able to discover in order to form a cluster. For the Kibana module, only the network host name and port needed to be specified for our implementation, making it quick to setup. For Logstash, various parameters about how it processes data must be set, as well as passing it a configuration file that specifies how data should be received, parsed, and sent out. For Filebeat, we specified prospectors, units that searched

specific file paths to find data we want to ship to Logstash.

III. DISCUSSION

Having syslogs running through this pipeline is a great way to analyze patterns in error messages and monitoring systems through their logs. I have not been able to collect syslogs for a long enough time to do any analysis myself, but this should prove to be a useful resource in the RACF staff's arsenal for detecting and fixing issues at the SDCC.

Throughout the project, I managed to run into a few issues with the implementation of the Elastic Stack. The way that the RACF usually passes parameters to Puppet is through a web interface called Foreman, which is set up to convert all variables to strings, and so the type validators built into the Forge modules prevented these parameters from being passed, forcing me to use YAML files instead. I also ran into issues with the virtual machines I was working on. These virtual machines were spawned with Red Hat Enterprise Virtualization (RHEV), allowing me to snapshots of the machines, but I encountered a bug within RHEV that prevented me from creating these snapshots. This bug was eventually resolved by Red Hat support. Finally, another setback was caused by authentication issues with Logstash pipelines, which kept me from pushing my code into production for a few days.

IV. CONCLUSION

The capability of searching system logs at the RACF is very important, allowing quick and near-real time analysis of the logs. To implement parsing, storage, searching and visualization of the logs, I installed the Elastic Stack on five nodes at the facility. To implement the Elastic Stack, I first installed the stack on Virtual Machines with Puppet software management. After familiarizing myself with the process, I then moved on to implementation in a production environment, allowing the Elastic Stack to go live on physical hardware. Finally, I ran a few basic queries on the syslogs that I gathered at the end of the project.

V. ACKNOWLEDGMENTS

I would like to thank my mentor, Antonio Wong, for guiding me throughout my experience here. I would also like to thank Jason Smith, my supervisor with whom I worked closely with and received much help from. Furthermore, the entire SDCC staff was extremely welcoming and helpful, allowing my project to go very smoothly. I would like to thank Brookhaven National Laboratory for hosting me, and the Office of Educational Programs for providing fantastic logistical support. This project was supported in part by the U.S. Department of Energy, Office of Science, Office

of Workforce Development for Teachers and Scientists (WDTS) under the Science Undergraduate Laboratory Internships Program (SULI).

VI. REFERENCES

- ¹C. Caramarcu et al., J. Phys.: Conf. Ser. 898 (2017), 082009.
- ²R. Gerhards, “The syslog protocol,” (2009), <https://tools.ietf.org/html/rfc5424>.
- ³M. Wang, “The syslog format,” (2017), <https://blog.rapid7.com/2017/05/24/what-is-syslog/> Image.
- ⁴Elastic, “The elastic stack,” (2018), <https://www.elastic.co/products>.
- ⁵Elastic, “Elasticsearch reference,” (2018), <https://www.elastic.co/guide/en/elasticsearch/reference/current/index.html>.
- ⁶Elastic, “Filebeats,” (2018), <https://www.elastic.co/products/beats/filebeat>.
- ⁷Elastic, “Logstash reference,” (2018), <https://www.elastic.co/guide/en/logstash/current/index.html>.
- ⁸“RACF foreman web interface,” (2018), authentication required to access, not a public website.
- ⁹O. Ben-Kiki, C. Evans, and I. d’ot Net, YAML Ain’t Markup Language (YAML) Version 1.2, YAML, 3rd ed. (2009).

Extracting provenance metadata for the Exascale Computing Project Co-design Center for Online Data Analysis and Reduction

Mohammed Endris, Behiru Shifa, and Mulugeta Dugda

Electrical and Computer Engineering, Morgan State University, Baltimore, MD, 21251

Line Pouchard

Computational Science Initiative, Brookhaven National Laboratory, Upton, NY, 11973

Abstract

Provenance of Big Data is a metadata showing the ancestry and the derivation steps of the given big dataset being converted in data arrangement, combination and calculation by computational workflows during the process of scientific simulations and other computational science analysis. Provenance is becoming an important aspect in high performance and distributed computing to help with reproducibility of scientific results, the replicability of experiments, and the analysis of performance as it can help diagnose potential latencies and crashes in execution, reasons why computations would not complete, and highlight anomalies. From a provenance information, scientists will be able to find the quality of the data based on its historical data and derivations, track back source of errors, allow reproduction of the data and provide attribution of the data sources. In this project we are able to install ADIOS, Pymongo and Parser software which will help to extract and produce provenance metadata. We have worked on sample datasets to store, query and write/read in MongoDB database. Also in this project, we able to write a python code which function to print out on the screen and store the data to the MongoDB database. Additionally, we developed our coding ability with different operating systems, especially with UNIX and Mac operating systems. We have also become familiar with different database management software's including MongoDB, NoSQL, SQL and InfluxDB. The Exascale Computing Project (ECP) has a goal of launching a US Exascale ecosystem by 2021, which will have a tremendous effect on the US and world population by delivering 50 times more computational science and data analytic application power than possible with the DOE High-Performance Computing (HPC) Systems. The extraction of provenance metadata in this project involved both conventional and metrics provenance metadata that can be used in the Co-design center for Online Data Analysis and Reduction (CODAR) for the ECP Project. In High Performance Computing (HPC), the disparity between the computation speeds and the storage capacities and I/O speeds is growing at a much faster rate and CODAR can be implemented to reduce output data volume and alleviate this problem through the study of the metrics or performance provenance metadata, as it is done in this project.

I. Introduction

This paper is about provenance capture and store for big data. Provenance is used for determining the historical lineage of experimental data for scientists in different fields. In the scientific experiment world, big data is studied in distributed and high-performance computing environment and the study of Provenance

of big data will help in the reproducibility of scientific results, the replicability of experiments, the analysis of performance, the detailed trace of how data are processed, and the accuracy of the gained experimental results. Provenance for big Data is defined as the lineage of datasets being transformed in data preparation, integration and calculation by computational workflows during the course of scientific simulations and other computational science analysis. One major purpose of this research is to develop a python script which has the purpose of separating & identifying the provenance data and storing this data to the mongo dB or the database in order to use this provenance data for reproduction and other uses.

II. Method

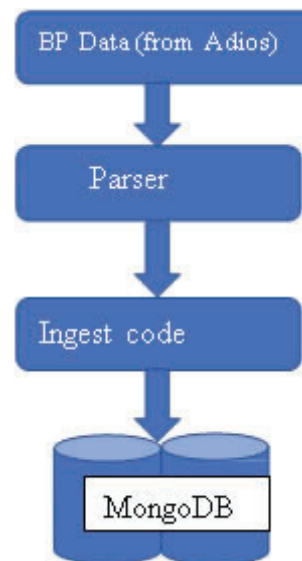


Figure 1. workflow of the whole project

Primary, we have to install different software, mainly ADIOS, Pymongo and Parser in order to make our system ready to be able to access the Parser input BP files and output files

A. Installing ADIOS

We followed the following steps to install ADIOS and ADIOS dependencies.

1. Installing MPICH

- Pip
- ./configure --disable-fortran
- ./configure --enable-shared --prefix=/usr/local/mpich
- mkdir /usr/local/mpich
- sudo mkdir /usr/local/mpich
- ls /usr/local
- sudo chown -R `id -un` /usr/local/mpich
- make
- make install

2. Installing MPI

- Tar -zxf openmpi-filename tar.gz
- Cd openmpi-filename.
- . configure --prefix=/usr/local/openmpi
- Make all
- Make install

3. Installing the ADIOS

By using the following commands

- \$pip3.6 install adios
- \$pip3.6 install adios-MPI
- Installing MongoDB

The reasons why we prefer MongoDB are because MongoDB has flexible schema, it supports associative arrays, designed for big data and aggregation framework.

- Brew update
- Brew install MongoDB
- Mongod
- Mongo

We used the drivers of MongoDB in order to integrate python client application with the data base. This is called PyMongo.



Figure 2- Pymongo

```

>>>506 names and values of attributes =
Key value pairs
Name          Attributes
program_name  0 /home/khuck/src/Example-
Heat_Transfer/stage_write/stage_write'
MetaData:0:0:CPU Cores 4
MetaData:0:0:CPU MHz 2000.000'
MetaData:0:0:CPU Type Intel(R) Xeon(R) CPU X5355 @ 2.66GHz'
MetaData:0:0:CPU Vendor GenuineIntel'
MetaData:0:0:CWD /home/khuck/src/Example-Heat_Transfer/test_sos'
MetaData:0:0:Cache Size 4096 KB'
MetaData:0:0:Command Line ../stage_write/stage_write heat.bp
staged_bp FLEXPATH'
MetaData:0:0:Executable /home/khuck/src/Example-
Heat_Transfer/stage_write/stage_write'
MetaData:0:0:Hostname ktau'
MetaData:0:0:Local Time 2018-06-15T14:13:17-07:00'
MetaData:0:0:Memory Size 8172400 KB'
MetaData:0:0:Node Name ktau'
MetaData:0:0:05 Machine x86_64'
MetaData:0:0:05 Name Linux'
MetaData:0:0:05 Release 4.4.0-127-generic'
MetaData:0:0:05 Version #153-Ubuntu SMP Sat May 19 10:58:46 UTC
2018'
MetaData:0:0:Starting Timestamp 1529097197678517'
MetaData:0:0:TAU Architecture default'
MetaData:0:0:TAU Config -iowrapp
  
```

Figure 3- sample key value pairs meta-data

B. Installing the parser

A parser is a compiler or interpreter component that breaks data into smaller elements for easy conversion into another language. The parser input in the form of bp files from adios and forms a data structure in the form of parse tree.

We used heat transfer data as a sample data for this project. To conduct the project, we have done some software installation that are helpful for analyzing and parsing the provenances of the sample data and we wrote python code that can ingest and store the parsed data. The first tasks of this project are installing software called ADIOS which is I/O System designed for componentization of the input-output (IO)system, enable to address the input-output performance bottleneck in today's high-performance computing application. It is considered to be portable, scalable and efficient. The second step is installing the dependencies of the adios like MPICH4, MPI which are crucial for installing the adios. The third step is installing the parser which is python application package used to parse the provenance information that can be easily stored or manipulated. The fourth step installing the MongoDB data base that used to dump or provenance data. The fourth step is developing python program which will ingest the analyzed data from the parser, and the last and list step is writing a code that store the ingested data to the MongoDB data base into different categories.

III. Result

The result of our project involves extracting a provenance metadata that includes the timer, counter and the trace data of the given heat transfer sample data. Figure 4 below shows the key-value pairs of provenances for the Heat Transfer data and Figure 5 shows the trace data provenance information. The capability of

```

Programme name/communication rank/threads/event_type/function
name/counters/value/event_types_communication
First 20 trace data =
[1 0 1 0 0 nan nan nan nan nan 1529097196654263 0]
[1 0 1 0 1 nan nan nan nan nan 1529097196654371 1]
[1 0 1 0 2 nan nan nan nan nan 1529097196654513 2]
[1 1 1 0 0 nan nan nan nan nan 1529097196656293 3]
[1 1 1 0 1 nan nan nan nan nan 1529097196656433 4]
[1 1 1 0 2 nan nan nan nan nan 1529097196656630 5]
[1 3 1 0 0 nan nan nan nan nan 1529097196660985 6]
[1 3 1 0 1 nan nan nan nan nan 1529097196661109 7]
[1 3 1 0 2 nan nan nan nan nan 1529097196661243 8]
[1 2 1 0 0 nan nan nan nan nan 1529097196663663 9]
[1 2 1 0 1 nan nan nan nan nan 1529097196663759 10]
[1 2 1 0 2 nan nan nan nan nan 1529097196663882 11]
[1 0 1 1 2 nan nan nan nan nan 1529097196694382 12]
  
```

Figure 4- sample trace data

```

timer 38 b'MPI_wait()'
timer 39 b'adios_selection_boundingbox'
timer 40 b'adios_schedule_read_byid'
timer 41 b'adios_perform_reads'
timer 42 b'adios_selection_delete'
timer 43 b'adios_write_byid'
timer 44 b'adios_write'
timer 45 b'MPI_Scatter()'
timer 46 b'MPI_Gatherv()'
timer 47 b'MPI_File_seek()'
timer 48 b'MPI_File_write()'
timer 49 b'MPI_Status_set_elements()'
timer 50 b'MPI_File_close()'
timer 51 b'void cleanup_step() C [(stage_write.c) (188,1)-(200,1)]'
timer 52 b'MPI_Get_count()'
timer 53 b'adios_advance_step'
timer 54 b'MPI_Barrier()'
timer 55 b'Step[1]'
timer 56 b'MPI_File_get_size()'
timer 57 b'Step[2]'
timer 58 b'Step[3]'
  
```

Figure 5- Timer

capturing the metrics and classical provenance together, i.e. the extraction of the two different provenance information, i.e., Figure 4 showing a traditional provenance and figure 5 performance provenance, indicates that we have a system of Provenance Environment (ProvEN). The other output shown in Figure 6 shows the timers. Timers are quantities that the application TAU measures. TAU is a performance analysis tool in ADIOS which provides events of type entry, exit, send and receive in the provenance. Counters are labels that TAU measures, and the trace data includes anomalies indices where the problem occurred when the program is running. Some of the important information obtained from the performance provenance data shown in Figure 5 includes: Event time stamp indices, Counter indices, Communication indices, and Indices of anomalies. These are only four of the thirteen indices shown in figure 5.

IV. Conclusion

Creating an ingesting python script which captures and stores the hybrid provenance metadata to a MongoDB database was successful. Provenance, as described in ProvEN, is currently defined to include two kinds of metadata together and so it shows both the ancestry lineage information as well as the performance information. As a result, Provenance has a considerable value for scientists, businesses, and other data intensive workflows. Our extraction of provenance involved both conventional and metrics provenance metadata that can be used in the Co-design center for Online Data Analysis and Reduction (CODAR) for the Exascale Computing Project (ECP). In High Performance Computing (HPC), the disparity between the computation speeds and the storage capacities and I/O speeds is growing at a much faster rate and so CODAR can be implemented to reduce output data volume and alleviate this disparity bottleneck through the study of the metrics or performance provenance metadata. Our extracted provenance metadata can contribute to this CODAR effort as it involves both conventional and metrics provenance metadata.

V. Acknowledgements

We would like to acknowledge Dr. Line Pouchard and Dr. Mulugeta Dugda for their continuous help and support throughout the research process. We would like to thank BNL's OEP and CSI staff for their continuous support. We extend our thanks to NSF LSAMP program, esp. Dr. Cleo Hughes-Darden for the financial support of the program.

VI. References

- Line Pouchard, Abid Malik, Huub Van Dam, Cong Xie, Wei Xu, and Kerstin Kleese Van Dam (2017), Capturing provenance as a diagnostic tool for workflow performance evaluation and optimization.
- Line Pouchard (2015), Revisiting the Data Lifecycle with Big Data Curation, International Journal of Digital Curation 176, <http://dx.doi.org/10.2218/ijdc.v10i2.342> 2015, Vol. 10, Iss. 2, 176-192 DOI: 10.2218/ijdc.v10i2.342
- Foster et al. (2017), Computing just what you need: Online data analysis and reduction at extreme scales, Euro-Par 2017: European Conference on Parallel Processing, Springer, 2017

VII. Appendix

“””

Dynamic Streaming Parser

Author: Dingwen Tao (ustc.dingwentao@gmail.com) Create: April 2018

Modified: June 2018

Modified by Mohammed Endris and Behiru Shifa for extracting the meta data in the key value pairs and dumping to the mongodb.

“””

```
# prog_names is the indexed set of program names in the
attributes # comm_ranks is the MPI rank
# threads is the thread ID (rank)
# event_types is the indexed set of event types in the
attributes # func_names is the indexed set of timer
names in the attributes # counters is the indexed set
of counter names in the attributes
# event_types_comm is the indexed set of event types
related to communication in the attributes
# tag is the MPI tag
# partner is the other side of a point-to-point
communication # num_bytes is the amount of data sent
```

```
from collections import deque as dq from collections
import Counter as ct import pickle
import itertools import adios as ad import numpy as np
import scipy.io as sio import configparser
import MiLOF
from sklearn.preprocessing import MinMaxScaler from
sklearn.neighbors import LocalOutlierFactor
```

```
def Parser(configFile): method = "BP"
init = "verbose=3;"
```

```
# read parameters from configuration file config =
configparser.ConfigParser() config.read(configFile)
in_bp_file = config['Parser']['InputBPFile'] # input
bp file path
```

```
prov_db_path = config['Parser']['ProvDBPath']
# provenance output database path queue_size =
int(config['Parser']['QueueSize']) # provenance
data size int_func_num = int(config['Parser']
['InterestFuncNum']) # interested function size
```

```
# initialize adios streaming mode ad.read_init(method,
parameters=init)
fin = ad.file(in_bp_file, method, is_stream=True,
timeout_sec=10.0) fout = open(prov_db_path, "wb")
```

```
# read attributes
db = dq(maxlen=queue_size)
name = np.array(['prog_names', 'comm_ranks', 'threads',
'event_types', 'func_names', 'counters', 'counter_
value', 'event_types_comm', 'tag', 'partner', 'num_
bytes', 'timestamp']).reshape(1, 12)
attr = fin.attr nattrs = fin.nattrs
attr_name = list(fin.attr)
attr_value = np.empty(nattrs, dtype=object)
```

```
num_func = 0 func_name = []
for i in range(0, len(attr_name)): attr_value[i] =
attr[attr_name[i]].value # count function number and
names
if attr_name[i].startswith('timer'): num_func = num_
func + 1 func_name.append(attr_value[i])
if attr_name[i].startswith('event_type'): print(attr_
value[i])
attr_name = np.array(attr_name) func_name =
np.array(func_name)
```

```
i = 0
```

```

total_timestep = 0 anomaly_indices = [] while True:
print(">>> step:", i)

vname = "event_timestamps" if vname in fin.vars:
var = fin.var[vname] num_steps = var.nsteps
event = var.read(nsteps=num_steps)

data_event = np.zeros((event.shape[0], 12),
dtype=object) + np.nan data_event[:, 0:5] = event[:,
0:5]
data_event[:, 11] = event[:, 5] data_step = data_event
# count most common functions

int_func = ct(data_event[:, 4]).most_common(int_func_
num) # e.g., [(16, 14002), (15, 14000), (13, 6000),...]

vname = "counter_values" if vname in fin.vars:
var = fin.var[vname] num_steps = var.nsteps
counter = var.read(nsteps=num_steps)

data_counter = np.zeros((counter.shape[0], 12),
dtype=object) + np.nan data_counter[:, 0:3] = counter[:,
0:3]
data_counter[:, 5:7] = counter[:, 3:5]

data_counter[:, 11] = counter[:, 5]

data_step = np.concatenate((data_step, data_counter),
axis=0)

vname = "comm_timestamps" if vname in fin.vars:
var = fin.var[vname] num_steps = var.nsteps
comm = var.read(nsteps=num_steps)

data_comm = np.zeros((comm.shape[0], 12), dtype=object)
+ np.nan data_comm[:, 0:4] = comm[:, 0:4]
data_comm[:, 8:11] = comm[:, 4:7]

data_comm[:, 11] = comm[:, 7]

data_step = np.concatenate((data_step, data_comm),
axis=0)

# sort data in this step by timestamp
data_step = data_step[data_step[:, 11].argsort()]

if i == 0:
data_global = data_step else:
data_global = np.concatenate((data_global, data_step),
axis=0)

# launch anomaly detection anomaly_flag = False
# dynamic interest list if len(int_func) < 3:
print ("Most interested function:\n", func_name[int_
func[0][0]]) else:
print ("Most three interested functions:\n", func_
name[int_func[0][0]], "\n", func_name[int_func[1][0]],
"\n", func_name[int_func[2][0]])

# matching data

global_index = (np.arange(data_step.shape[0]) + total_
timestep).reshape(data_step.shape[0], 1)
data_step = np.append(data_step, global_index, axis=1)

func_data = data_step[data_step[:, 4]==21] # 21 is
adios_close, TODO

```

```

entry_data = func_data[func_data[:, 3]==0] # 0 is entry
in the current data, TODO exit_data = func_data[func_
data[:, 3]==1] # TODO

# generating streaming data in terms of one function
datastream = []
for j in range(0, entry_data.shape[0]): for k in
range(0, exit_data.shape[0]):
if np.array_equal(entry_data[j, 0:3], exit_data[k,
0:3]): entry_time = entry_data[j,11]
exec_time = exit_data[k, 11] - entry_data[j, 11]
datastream += [[entry_time, exec_time]]
break

datastream = np.array(datastream)

# anomaly detection

if (datastream.shape[0]):
scaler = MinMaxScaler() scaler.fit(datastream)
datastream = scaler.transform(datastream)

# Should call MILOF API, but here for simplicity, call
LOF directly clf = LocalOutlierFactor(algorithm="kd_
tree", metric='euclidean') anomalies = entry_data[clf.
fit_predict(datastream)==-1]
if anomalies.shape[0]: anomaly_indices.
extend(anomalies[:, -1].tolist()) anomaly_flag = True

# add or dump queue if anomaly_flag:
# dump queue to file db.appendleft(attr_value)
db.appendleft(attr_name) db.appendleft(nattrs)
print(">>> Identified anomalies and dump data to
binary.") print(">>> Serialization ...")
pickle.dump(db, fout)

# db[0]: the number of attributes # db[1]: the names
of attributes # db[2]: the values of attributes # from
db[3]: the trace data
else:

# add data to queue db.extend(data_step)

print("Size of current timestep =", data_step.shape[0])
total_timestep += data_step.shape[0]
print(">>> Advance to next step ... ") if (fin.advance()
< 0):
break

i += 1

fin.close() fout.close()

print(">>> Complete passing data.") print(">>> Test of
deserialization.") print(">>> Load data ...")
fin = open(prov_db_path, "r") db2 = pickle.load(fin)
print("\n**** Print info ****")
print(">>> Number of attributes =", db2[0]) print(">>>
Passed test of deserialization.") print("Size of total
timestep = ", total_timestep) print (">>>506 names and
values of attributes =") for i in range(0,506):
print((db2[1][i]), (" "), (db2[2][i])) i += 1
print("Trace data = ")

print( np.array(list(itertools.islice(db2, 3, 51))))

print(">>> Indices of anomalies in terms of
entry:", anomaly_indices) print(">>> Passed test of
deserialization.")
fin.close()

```

```

from pymongo import MongoClient import json
client = MongoClient() file_path = "data.json"
with open(file_path, 'w') as outfile: json.dump(data_
global.tolist(), outfile)
db = client.upload3 #creating the database f =
open('data.json')
files3 = db.files3 json = f.read() doc1 = {
"file_name" : "data.txt", "contents" : json}
files3.insert(doc1) outfile.close()

```

```

â#!/usr/bin/env python3 # -*- coding: utf-8 -*- """
This python code extract and separate the timer, counter and
the meta data from the parser output.
Created on Thu Aug 2 15:36:22 2018
@author: Mohammed Endris & Behiru Shifa """"

```

```

with open('output12.txt', 'r') as MetaData: for line
in MetaData:
if 'MetaData' in line: print (line)
MetaData.close()

with open('output12.txt', 'r') as timer: for line in
timer:
if 'timer' in line:
print (line)

with open('output12.txt', 'r') as counter: for line in
counter:
if 'counter' in line: print(line)

```

```

#!/usr/bin/env python3 # -*- coding: utf-8 -*- """
This code code separate the timer and store it to the mongodb.

Created on Thu Aug 2 15:40:24 2018
@author: mohammed Endris and Behiru Shifa """"

```

```

import sys import pymongo
from pymongo import MongoClient client = MongoClient()
db = client.collaction4 files55 = db.files55
with open('output12.txt', 'r') as timer: for line in
timer:
if 'timer' in line: print(*line)

sys.stdout = open("timer1.txt", "a+") f = open('timer1.
txt')
text =f.read() doc = {
"files_name" : "timer1.txt",
"contents" : text} files55.insert_one(doc) timer.
close()

```

An intern's experience as a construction safety engineer at a national laboratory

Trevor Gallagher

Occupational Health and Safety, Keene State College, Keene, NH 03431

Donald Farnam

Facilities & Operations, Brookhaven National Laboratory, Upton NY11973

Abstract

During my time at the Brookhaven National Laboratory (BNL), I was able to expand my knowledge of safety in the workplace. I was able to see the many different sides of safety other than just construction. Here at BNL safety is a core value and everyone is responsible for their own safety. There are many construction projects that go on at BNL throughout the year. As a Construction Safety Engineer (CSE), it is our job to ensure that these jobs get done in a safe and effective manner. We inspect construction areas to identify any noticeable hazards as well as potential hazards. Upon identifying such hazards we need to mitigate them and inform the workers of these hazards and how to properly protect themselves. Even though we go through extensive measures to ensure the safety of the workers, there are times when workers get injured or violate the safety procedure. Some of our everyday activities are performing walkthroughs of the different construction jobs that are going on at BNL. If we find any violations on the job sites, it is our responsibility to report them, notify the worker that is making that violation and to inform them how to do that task in a safe way with no violations. During my time here, I also helped Dari Scuola with composing a list of questions to ask potential inspectors to see if they are capable of inspecting heavy machinery properly. I have also inspected different construction equipment with Don and Dari this summer such as drilling rigs, aerial lifts, cranes, slings, and scissor lifts. I have learned many things while being here at BNL and working with Don and his colleagues. I believe that the field experience of construction is the most important aspect I can learn from. The hands on experience out in the field is where I gained the most knowledge of safety possible and it is where I can practice my skills when dealing with the workers.

I. Introduction

My internship this summer at the Brookhaven National Laboratory was a great opportunity to expand my knowledge of safety in the workplace. Throughout the summer I was able to meet with various Safety Professionals at BNL. I was able to learn a great amount from each one of them whether it was from construction safety to machine guarding. I was exposed to many scenarios in the field of safety that I would not have gotten in the classroom. I was tasked with the responsibility of inspecting construction sites, inspecting machinery, and entering any findings into the construction safety database.

II. Tasks

As a construction safety engineer at BNL you conduct job site inspections to ensure that the work is being completed according to OSHA standards. Throughout completing various job site inspections with Don and Dari, I now know what key violations a safety officer needs to look for. Such violations are trip

hazards, housekeeping, means of egress and regress, and the use of proper personal protective equipment. If any of these hazards are present at the job site then the contractor safety representative for the job must mitigate those hazards immediately. While I became more accustomed with inspecting these job sites with Don I began to familiarize myself in what I need to look for. Over time Don would task me with inspecting these sites by myself to make sure the work was following the Phase Hazard Analysis (PHA) and that there are notable hazards. To have this independence here at BNL has enabled me to gain confidence and great experience that I will be able to learn from for my future in Occupational Health and Safety.

Upon inspecting construction sites we must take note of any findings that we discover. These findings can be hazards or observations made at the time of inspection. For example, during the time of inspection I observe an employee not wearing their safety glasses I take note of that and inform him to put them on. With this finding we take that and submit it onto a safety data checklist for construction at BNL. These checklists are where we record any safe and unsafe activities that go on during the construction process.

Before construction projects begin at BNL, work planning must be completed. The work planning process is a long process, but for good reasons. During this time, many professionals have meetings to discuss the upcoming work that will be conducted. Before work is permitted, multiple forms must be completed and signed. These forms include a 500A form, work permit, and a phase hazard analysis (PHA). I have sat in on numerous work plan meetings where many of these forms were completed with the help of the vast amount of safety, architectural, and electrical engineers. When completing the 500A form various safety professionals discuss what types of hazards are present and may become present during the work process. The different types of hazards that are present or may become present are; Environmental, Facility Issues, Industrial Safety Issues, Radiation Safety, Waste Management, and Industrial Hygiene Issues. With each section of these hazards are also subparts which specify what hazard is present. For example, if there is an Industrial Hygiene Hazard there could be asbestos or mercury that you could possibly come in contact with. If the worker does in fact come in contact with such substances then you must mitigate those hazards with the proper knowledge provided by safety standards and the specialized safety professional you can refer to.

The Work Permit is next form that is required; it analyzes the project to address all concerns involving the work being conducted. These concerns include, radiation concerns, safety and security concerns, environmental concerns facility concerns, surrounding area hazards, work controls, personal protective equipment, required permits, dosimetry/monitoring, and training requirements. Those concerns listed are sections in the form, in each of those sections are more specific hazards. For example, if the job that is

going to be conducted involves handling materials with asbestos, then you would need to check that box in Safety and Security Concerns section of the work permit. When completing this form, you must go through all sections and fill it out according to that job entails. Whatever boxes are checked off, those hazards must have mitigations which would be addressed in the following form.

The Phase Hazard Analysis (PHA) is the last document that needs to be completed and reviewed by a construction safety engineer. This form states the activity/task, what hazards are going to be present when that task is being completed, and the proper way to mitigate those hazards. All construction jobs at Brookhaven National Laboratory must have a PHA. All tasks that are going to be completed during this work project must be stated in the PHA. For every task that is specified there are hazards that need to be listed, followed by the proper mitigations. All contractors that will be working on this job will sign the PHA, agreeing to follow the necessary safety procedures when completing each task listed. The PHA must remain on the job site for contractors to reference. Throughout this process of work planning we illustrate the safest and most efficient way to get the job done. By completing all of these forms we are able to precisely identify all hazards giving the workers a safe working environment.

Other than work planning at BNL, I was tasked with other duties safety professionals encounter. I have inspected heavy machinery and pieces of equipment with the help of Don and Dari instructing me on what to look for. My first inspection at BNL this summer was an aerial boom lift. For the inspection we went through checklist provided by BNL. The checklist is constructed under regulations set by the American National Standards Institute (ANSI) and Scaffold Industry Association (SIA). We went through the checklist and looked for any faults in the boom lift, thankfully there were none. Like the boom lift, I also inspected a scissor lift with Don. The procedure for inspecting a scissor lift is identical with that of a boom lift inspection. Like the boom lift inspection we follow a similar checklist provided by BNL with regulations set by ANSI and SIA. We also take pictures of what we inspect to prove that when we inspected the equipment it met the standards in case a problem were to occur later on. I also had the opportunity to inspect several slings in the machine shop with Dari. These slings ranged from three feet to 20 feet. These slings are used for lifting heavy objects with precision and safety. Since these slings are used for lifting such objects, they need to meet specific regulations set by the Occupational Safety and Health Administration (OSHA). On each sling is a rubber label that specifies the maximum capacity the slings can lift depending on how the sling is positioned. If this label is illegible then the sling can not be used, therefore taken out of service. Upon the inspection there was only one sling that was taken out of service due to the label being illegible. No other slings were frayed or showing any signs of deterioration.

Lifts and slings were not the only thing I had inspected during my time here. I also inspected a lattice crane and a boom truck crane. These inspections are much more time consuming since there is a lot a crane can do. Like the other inspections we follow a checklist provided by the Crane Institute of America. To conduct the inspections we needed a crane operator to follow our instructions to properly assess it. Upon inspection of both cranes, there were no problems. When operating cranes, you need to know how to properly lift objects and do it safely. In order to be able to do that, you need to know how to read a load chart. Lucky

enough, Dari was able to teach me how to properly read a load chart. This chart varies depending on what kind of crane you are using, if it is on outriggers, and if it is lifting from the side. These different factors determine the maximum load capacity the crane can lift. When planning to move loads with a crane, you need to know where the load will be lifted and where it will be rested. Thanks to Dari I am able to properly read a load chart which will help me in the field when cranes are being used.

While working with Mario Cubillo, part of the Safety and Health Services Division, he took me around to various machine shops throughout the Laboratory. While visiting the machine shops he showed me the machine guarding that he had implemented on all machinery. The main attachment that he required all machines to have is an emergency shut off switch. This is a big red button with a yellow wring around to make it stand out visibly. These switches need to be located where the operator of the machine will be using the machine so if there is an emergency while he or she uses that machine, they will be in arm's length to hit that emergency shut off switch. It was a great learning experience to see the extensive machine guarding that is used on tools in a machine shop.

During my time here I was lucky enough to meet with Bob Selvey, an Industrial Hygienist (IH). He showed me all the tools and dosimeters they use to monitor areas such as oxygen, carbon monoxide, and dust from silica. There are many different monitoring tools that an IH uses out in the field to get samples. He showed me a noise monitoring tool that is used to record the amount of noise a worker will be exposed to in the area they will be working in. This monitoring system is simple and can hook up to their waistband so the IH can get an accurate sample for when they use it throughout their work day. To be able to see the Industrial Hygiene of safety I got a better understanding of the different measures us safety professionals can go through to keep workers safe.

Aside from getting out in the field and gaining experience and knowledge that way, I sat down with Dr. Steven Coleman the Deputy Associate Laboratory Director, Employee Safety & Health Directorate, and Radiological Control Division. This meeting was of great importance to me because he is a high level manager which I one day hope to be. To be able to sit down and talk to him about his path to becoming a safety manager was a great opportunity to take notes on what I could do to get there some day. He was able to inform me with what certifications I should get and how soon I should get them.

I believe my time at the Brookhaven National Laboratory has provided me with valuable experiences and knowledge that will be of great value to me in my career. I will be able to implement everything I have learned here both in the classroom and in the work field. The safety culture here at BNL is second to none thanks to people such as Don Farnam and Dari Scuola who help enforce the safety procedures. During my time I was able to meet many Safety Professionals to get a better understanding of their roles at BNL. With meeting various Safety Professionals, I was able to gain knowledge in new areas of safety that I would not be able to in the classroom.

III. Acknowledgments

This project was supported in part by the Brookhaven National Laboratory (BNL), Facilities and Operations under the BNL Supplemental Undergraduate Research Program (SURP).

A novel E3 ligase

Vignesh Gunasekaran

Chemistry, Stony Brook University, Stony Brook, NY 11794

Syed Khalid

Chemistry, Brookhaven National Laboratory, Upton, NY 11973

Abstract

Macromolecular crystallography uses protein crystals to visualize protein structures at the atomic level. At the National Synchrotron Light Source II (NSLS-II), this is accomplished by firing a beam of X-ray waves at the crystals and performing computer analysis on the diffraction patterns of those waves. Once the structure of a protein is determined, its function can be inferred. For my project, I have attempted to crystallize the E3 ubiquitin protein ligase. This protein attaches a molecule called ubiquitin to a target substrate in order to mark it for proteosomal degradation. In order to induce crystallization, the protein was tested with crystal screens, which are various mixtures of precipitants, buffers, and additives. Multiple 96 well plates of crystal screens were automatically prepared for each protein using the Labcyte Echo 550 machine. Once crystal screen plates were prepared, they were then observed every day to check for the presence of crystals or factors that could lead to crystal growth, such as microcrystals. The conditions that led to the crystals/microcrystals were then optimized by repeated testing of those specific conditions with minor changes. After a sufficiently large crystal was produced, it was taken to the beam line for visualization. Diffraction analysis and BLAST search results indicated that a domain of E3 ubiquitin protein ligase is highly similar to HUWE1, a domain which marks a regulator of apoptosis, MCL1, for proteosomal degradation, therefore this domain likely has a similar function to HUWE1. Further studies will be performed to yield a more complete model of the protein. Using the facilities of BNL allowed me to gain experience with a variety of research techniques that will be helpful in my career.

I. Introduction

In the science of macromolecular crystallography, protein crystals are produced in order to gain information about that protein's structure and function. Protein crystals are structures in which microscopic subunits of proteins known as unit cells are tightly packed together to form lattices (orderly periodic arrangements) that repeat in all directions. These crystals are solid materials that typically have clearly defined geometry (cube, diamond, rhombohedral, etc.), although amorphous protein crystals have been produced (McRee, 1999). Protein crystals are usually made in solution, and these solutions must have three components. The first component is the protein that must be crystallized. The second component is a precipitant, or a solution that induces supersaturation of the protein. Supersaturation is a state in which a liquid contains more solute than it would normally be able to accommodate under the present conditions.

Theoretically, it makes sense that supersaturation would produce protein crystals since crystals are essentially arrangements of protein molecules packed tightly together, and supersaturated

solutions have a lot of protein molecules packed tightly together in solution, so there is a high chance that a crystal would precipitate out of this solution (McRee, 1999).

Most eukaryotic tissues contain a regulatory protein called ubiquitin, which can be bound to various substrates in a process known as ubiquitination. This process can affect the target substrate in a variety of ways, such as altering its location, modifying its activity, or most commonly, marking it for degradation via a proteasome. Ubiquitination involves three main steps: activation, performed by E1 ubiquitin activating enzymes, conjugation, performed by E2 ubiquitin conjugating enzymes, and ligation, performed by E3 ubiquitin ligases (our protein of interest, E3 ubiquitin protein ligase, is of this type). E3 ubiquitin ligases recruit E2 ubiquitin conjugating enzymes that have a molecule of conjugated ubiquitin on them and catalyzes the transfer of that molecule from the E2 to the protein substrate. The E3 binds the ubiquitin to a lysine on the target substrate with an isopeptide bond (Pandya et al., 2009). This ubiquitin pathway is illustrated below in Figure 1.

II. Methods and Materials

A. Theory of Sitting Drop Vapor Diffusion:

There are many different techniques that can be used to crystallize a protein. The technique employed in this investigation is known as sitting drop vapor diffusion. In this technique, a large well in a crystallography plate is filled with a reservoir of precipitant, and a droplet containing a protein and precipitant mixture is placed in a smaller well above and to the side of the reservoir. The theory behind sitting drop vapor diffusion is as follows: the reservoir contains a much higher concentration of precipitant than the protein/precipitant droplet. Therefore, as the precipitant in the reservoir evaporates, these vapors will diffuse into the protein/precipitant droplet in a process aptly named vapor diffusion. As vapor diffusion occurs, the protein/precipitant droplet will gradually reach the state of supersaturation necessary for crystal for-

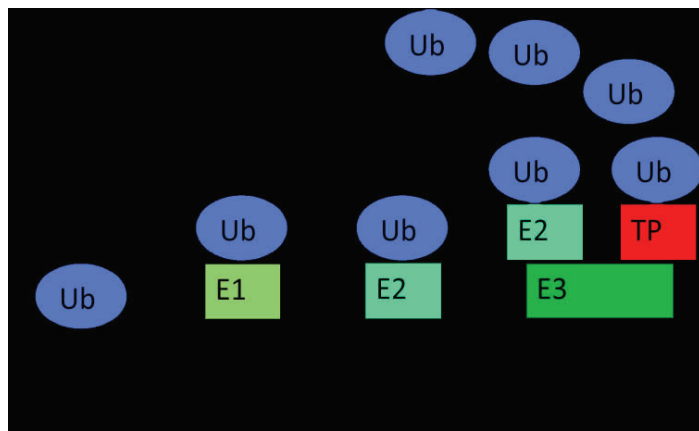


Figure 1 Graphical Representation of the Ubiquitin pathway

mation. It is optimal to induce supersaturation gradually because if it occurs too quickly, then the protein will not precipitate out of solution as a crystal, but as a brown clump-like mass known as a precipitant. This gradual vapor diffusion is the main advantage of the sitting drop vapor diffusion method (Stevens, 2000). The sitting drop method is illustrated below in Figure 2.

Another important reason this method was employed in this investigation was because BNL contains a machine known as the Labcyte Echo 550 (hereafter referred to as the Echo), which completely automates the sitting drop vapor diffusion process. The

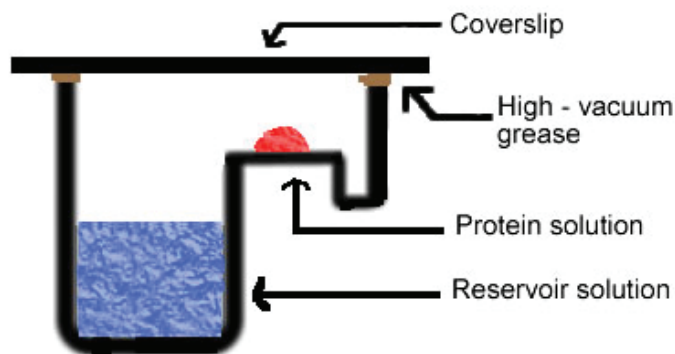


Figure 2 Graphical Representation of the Sitting drop vapor diffusion Method Source: <http://soft-matter.seas.harvard.edu/index.php/File:Drop2.gif>



Figure 3 Protein Crystal obtained from experimentation

machine works in the following manner: a source plate is created by filling one well of the plate with protein, and the other wells with the various precipitants and buffers being tested. This plate is then inserted into the Echo along with a destination plate, where the droplets created by the Echo will be collected. The Echo can then be programmed to fire sound waves underneath specific wells of the source plate, which eject droplets of whatever liquid is inside those wells onto the destination plate.

Therefore, the Echo can be used to automatically eject protein, precipitants, and buffers onto a destination plate. The Echo is also highly efficient; creating a crystallization plate that would take 1-2 hours to create by hand in only 15 minutes.

The gradual vapor diffusion of precipitant and the efficiency of the Echo were the two main reasons sitting drop vapor diffusion was used in this investigation.

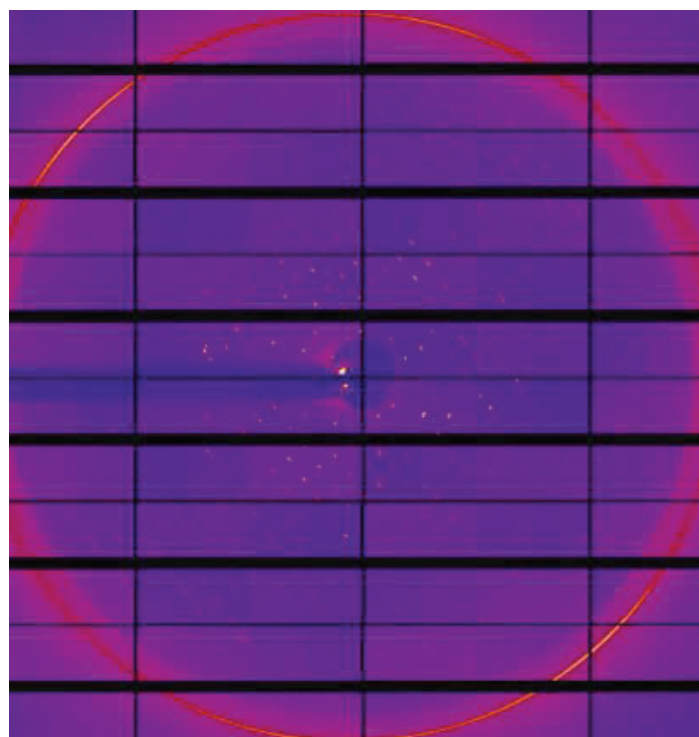


Figure 4 Diffraction taken from 19-ID-D NYX beamline

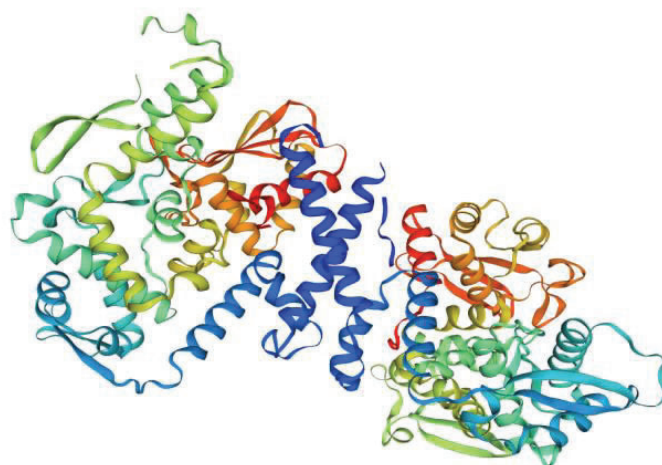


Figure 5 Structural Model of HUWE1 domain Source: <https://swiss-model.expasy.org/>

B. Crystallization and Data Collection:

Crystals of Se-Met-substituted E3 ubiquitin protein ligase were obtained in drops containing a 1:1 mixture of protein solution (7.5 mg/mL) and well precipitant solution. The protein crystallized in orthorhombic space groups (condition: 0.5mM MgCl₂, TRIS-HCL, 30% PEG 8000, Ph 8.0). The crystals were grown at 18°C by sitting drop vapor diffusion method, cryo-protected with 20% glycerol and flash-cooled in liquid nitrogen. Diffraction data sets were collected on a single crystal using the beam line 19-ID NYX with a HF-4M PAD detector at the National Synchrotron Light Source-II (NSLS-II) at Brookhaven National Laboratory. Data were analyzed with HKL2000 package (Otwinowski and Minor, 1997).

III. Discussion and Conclusion

The preliminary data obtained from putting the protein crystal (Figure 3) on the beamline was used to create a diffraction image (Figure 4). The fact that a diffraction image was able to be created is hugely important. This is because even though something may precipitate out of a protein solution that seems to look like a crystal, it may not necessarily be one. It could very well be a salt or some other compound in the precipitant that took on a vaguely crystalline appearance when it precipitated. However, if this were the case, we would not be able to obtain a diffraction image. This is because, unlike protein crystals, salts and other precipitant compounds cannot diffract x-rays. Therefore, the presence of a diffraction image serves to confirm that the crystal we obtained was indeed derived from a protein (Otwinowski and Minor, 1997).

In addition to the diffraction image, many quantitative data were also obtained from the protein crystal (Table 1). Of these, the most important were the unit cell parameters, which are as follows: $a=121.08\text{\AA}$, $b=271.83\text{\AA}$, $c=191.59\text{\AA}$ and $\alpha=\beta=\gamma=90.00^\circ$. As previously stated, protein crystals are made up of unit cells arranged in repeating periodic arrangements known as lattices.

The unit cell parameters are essentially the dimensions of one of these unit cells. The a , b , and c values correspond to length, width, and height respectively, while the α , β , and γ values are the angles between the sides. Normally, the unit cell parameters could be used to derive a protein structure, but since the obtained protein crystal diffracted to a low resolution ($\sim 4.6\text{\AA}$), this cannot be done in this investigation.

Table 1 Quantitative Data obtained from protein crystal

Space group	P2 ₁ 2 ₁ 2 ₁
Molecules per asymmetric unit	2
$V_M (\text{\AA}^3\text{Da}^{-1})$	2.88
Unit Cell	$a=121.08\text{\AA}$, $b=271.83\text{\AA}$ $c=191.59\text{\AA}$ $\alpha=90.00^\circ$ $\beta=90.00^\circ$ $\gamma=90.00^\circ$
Wavelength(\AA)	0.979

Instead, we compared the amino acid sequence of our target protein to those of a database of known proteins using a BLAST

search. After performing this search, it was found that the protein of our interest had a 46% match with a well characterized protein HUWE1 (Figure 5) in the 499-855 amino acid region. HUWE1 is a specific type of E3 ubiquitin protein ligase that marks MCL1, a protein regulating apoptosis, for degradation. Using this information, we can hypothesize that our target protein likely contains a domain that is similar to HUWE1 in both structure and function. This hypothesis is not 100% certain, but it is a promising lead from which to start future investigations into our protein.

In order to improve this investigation, larger, better diffracting crystals must be obtained. There are three main ways to accomplish this. The first is to screen more conditions using the Echo.

Protein crystallography is very much a trial and error science in the sense that you never quite know what conditions will produce good crystals until you try them, so you have to try as many conditions as possible. This is where the automation of the Echo will come in handy. The second way is to optimize the condition that we already found. Inducing slight variations in the concentrations of the compounds or the pH of the solution can have a huge effect on crystal quality (McRee, 1999). The third way is to stabilize the protein. Some proteins have loose structures that prevent them from packing together and forming crystals. However, this can be alleviated by adding some small ligand for the protein to bind to, thus locking it in a specific conformation and making it easier to crystallize (Hassel et al, 2007).

IV. Acknowledgments

I would like to thank my mentor Dr. Syed Khalid and my supervisor Dr. Seetharaman Jayaraman for guiding me through this experiment and enhancing my understanding of protein crystallography. I would also like to thank Dr. Alex Soares for teaching me how to use the Labcyte Echo 550, which greatly enhanced the efficiency of this investigation. Additionally, I would like to thank Brookhaven National Laboratory and the Department of Energy for giving me the opportunity to participate in this internship and the resources to carry out this research.

V. References

- Hassell, Anne M., et al. "Crystallization of protein-ligand complexes." *Acta Crystallographica Section D: Biological Crystallography* 63.1 (2007): 72-79.
- Kantardjiev, Katherine A., and Bernhard Rupp. "Matthews coefficient probabilities: improved estimates for unit cell contents of proteins, DNA, and protein-nucleic acid complex crystals." *Protein Science* 12.9 (2003): 1865-1871.
- McRee, Duncan E. *Practical protein crystallography*. Elsevier, 1999.
- Pandya, Renuka K., et al. "A structural element within the HUWE1 HECT domain modulates self-and substrate ubiquitination activities." *Journal of Biological Chemistry*(2009): jbc-M109.
- Stevens, Raymond C. "High-throughput protein crystallization." *Current opinion in structural biology* 10.5 (2000): 558-563.
- Z. Otwinowski and W. Minor, Processing of X-ray Diffraction Data Collected in Oscillation Mode. *Methods in Enzymology*, 1997; 276:307-326

The updating of radioactive material tags for activated materials

Craig Hamilton

Suffolk Community College, Selden, NY 11784

Andrew Levine and James Williams

Radiological Controls Division, Brookhaven National Laboratory, Upton, NY 11973

Abstract

Since Brookhaven National Laboratory performs many scientific projects and leads the world with its technological advancements it is imperative that we take every safety precaution possible to maintain the health and safety of personnel. During normal operations at the Collider Accelerator Division (CA-D), components and sample items in the beam lines become activated. When the items are removed, they must be surveyed by a Radiological Control Technician (RTC) to determine the amount of potential residual activity. Once surveyed and determined to be radioactive, the item(s) must be tagged and stored in a posted Radioactive Material Area (RMA) as radioactive material. This method has been used for a very long time; however, as procedures have changed the requirements for the Radioactive Material (RAM) tags have also changed. Throughout the summer I have the opportunity to learn about the procedures and techniques that are used by the Radiological Control Technicians and the use of the LUD 19 which is used to perform activation checks on items and materials for potential activation. I have been exposed to many different roles of the HP's here at Brookhaven National Laboratory. The updating of RAM tags is the main project during my time here at the lab. Updating the tags is important since they can become illegible or the materials may decay over time making it necessary to recheck and document any changes that may have occurred. My mentor and I hope to re-tag approximately two hundred items. This will hopefully drastically reduce the number of outdated RAM tags that are in the field. This project just reinforces the importance of safety here at Brookhaven National Laboratory. I have learned how to communicate using the language of the RCT's, use various types of instrumentation and effectively re-tag materials according to procedural requirements.

I. Introduction

While interning here at Brookhaven National Laboratory it became apparent that safety was the pinnacle of all the practices here at Brookhaven National Laboratory. My goal this summer was to gain an understanding of the role that the Radiological Control Technicians (RCT) serve here at the laboratory. They help to ensure safe management of radiological materials onsite. I was able to learn a lot about the procedures and techniques that the RTC's use during their daily routines here at BNL. Throughout the summer, I learned how to properly use the LUD-19, which is an instrument that allows the RCT's to perform activation checks on items used in close proximity of accelerator beam lines. Accuracy of the LUD-19 helps to maintain a safe environment for the radiological workers at BNL. I also had the opportunity to learn about the Tennelec which tests for radioactive contamination. The main focus throughout the summer was to update the Radioactive

Material (RAM) tags due to procedural changes as well as radioactive decay of certain items. It is necessary to update the tags, since overtime the tags become illegible due to water stains or other environmental factors. In order to maintain a safe environment it is important to make sure that all of the tags are clear and legible. Radioactive materials decay over time which decreases the activity, making it necessary to update the tags so that they are current and represent the most accurate radiological information.

II. Method of updating the RAM tags

Updating the RAM tags is important because they create an organized environment and confirms that the radiological information is correct and up to date. RAM tags can become outdated for a number of reasons. The first reason that they need to be updated over time because the writing can become illegible and worn out, so they should be rewritten to make them clear and easy to read. The second reason we update the tags is that over time the procedures set in place may change, making the requirements for the RAM tags different. The ram tags are updated so that they can comply with the rules and regulations set in place by BNL. The third reason we update the tags is that over time the material can decay, so it is important to update them so that they represent the most current and accurate radiation levels. The first step in updating RAM tags is determining if the tag in question is the most current revision and contains all of the necessary information. It is extremely important that the information is accurate because this could lead to a radiological safety incident. If the tag is illegible then it must be updated. The next step is to check for the date, if the RAM tag is old then it is likely that the item could have decayed a significant amount. This would result in an inaccurate radiological information indicated on the tagged item. Once we have established that the RAM tags need to be changed we need to perform an activation check to determine the level of activation that is left on the material. The LUD-19 is very important in the re-tagging process since it allows us to obtain the proper readings required on the RAM tags. Once we have all of the information filled out, we attach the RAM tag to the item.

III. Discussion

Throughout this summer I have had the pleasure of working with the Radiological Control Technicians. I learned many skills that will benefit me in my future such as working with certain types of equipment and working in a group environment. The goal throughout this summer was to see how the RCT's facilitate the management and surveying of radiological materials. They are incorporated in many different aspects here at the lab, and their presence is highly valuable. They are called upon daily to perform activation checks and perform routine maintenance to make sure that the radiological conditions at BNL are safe. The other main aspect throughout this was to learn how to properly use the

LUD-19 and update the RAM tags that are old and out of date. Being up to date on radiological information is very important because overtime the radiation can decay, leaving the radiological readings and the RAM tag to not match up. It is necessary that when someone looks at the RAM tag they get the most current and accurate information on that particular material. There are many facilities that rely on the help of the RCT's, since they help to determine if something has been activated from an experiment that deals with radiation.

IV. Conclusion

Throughout the summer I had the opportunity to learn about the responsibilities of the RCT's. I was able to determine how to properly perform activation checks which is important because you need to calibrate the equipment prior to use . I was also exposed to all of the safety precautions that one must take to avoid the damaging effects of radioactive materials. I have gained valu-

able experience on what it means to be a part of a team and how to communicate with my co-workers to efficiently perform the required tasks. I have been trained on how to use many different types of equipment that are used by the RCT's. Re-tagging the RAM tags was a major component of my experience here at the lab throughout the summer and I am glad I had the opportunity to impact BNL in a positive way.

V. Acknowledgements

I wish to thank my mentor Andrew Levine for his professionalism and generosity during the SURP program. Furthermore I would like to extend my deepest gratitude to all of the RCT's for their patience and support. I would like to thank James Williams for allowing me to learn the necessary skills that will help me in my future. Finally I wish to acknowledge the hospitality and generosity of Brookhaven National Laboratory and the Department Of Energy.

Single photon detection for Bell state coincidences using Timepix3 camera

Andrew Koehler Hardy

Physics and Mathematics, University of Toronto, Toronto, ON, M5S 3H7, Canada

Andrei Nomerotski

Department of Physics, Brookhaven National Laboratory, Upton, NY 11973

Abstract

Bell State Coincidences (BSC) are quantitative indicators of quantum entanglement for Einstein-PR pairs and holds important applications in quantum information science (QIS). The measurement requires high time resolution and good throughput for individual optical photons. The advancements of the Timepix3 application-specific integrated circuit (ASIC) have developed into a camera with nanosecond resolution and high throughput in the order of megaphotons per second. This advancement makes single photon detection a reality. The Timepix3 camera holds a variety of applications in imaging, such as fluorescence lifetime intensity microscopy, or strong field ionization experiments. The success of these previous applications provides a clear path for using Timepix3 camera to conduct BSC. This paper will detail the process and results of BSC for polarized photon coincidences along with discussion about methodology and implications for important QIS research. The camera's nanosecond time resolution observes coincidences of photons entangled through the splitting of one photon from a blue laser to two red photons. These coincidence counts can be converted into a correlation function to quantify entanglement.

I. Introduction

Over the last decade, intense research has been devoted to finding physical systems that can become the backbone of future quantum technologies. The combination of the properties of collective excitations of atoms and quantized fields of light has emerged as one of the most active candidates to achieve quantum communication due to their facility for optical control and ease of interface with one another. One of the most pursued implementations in this area of science is the creation of photonic long-range quantum correlations and its mapping to long-lived atomic arrays. This so-called quantum memory and networking experiments have seen significant recent progress, and many research laboratories in the world are pursuing them intensely. The next technological frontier for the successful development of these applications is the creation of quantum networks of many such quantum devices in which entanglement is shared among multiple network nodes. Harnessing quantum correlations among billions of atoms can be the heart of a new generation of quantum experiments used for enhanced communication of quantum information and quantum-enhanced hyper-sensitive detection of fields and particles. One component of a prototype a long-distance quantum network using a modular approach would require characterization devices for imaging and time-stamping of entangled photons, with nanosecond time resolution, capable of evaluating in real time the quantum network performance. This paper details the data analysis required for the implementation of the Timepix3 camera for this purpose [epr]

II. Experimental Setup

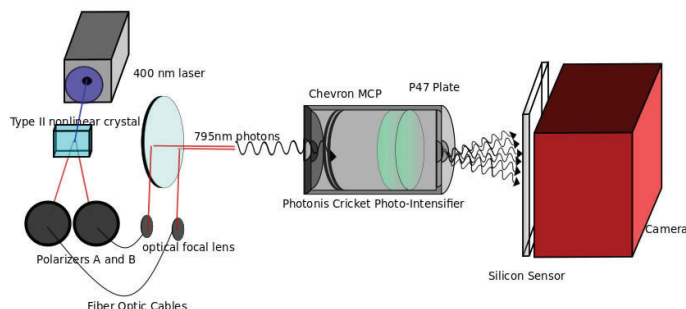
The current joint SBU-BNL QIS collaboration have characterized SPDC-based quantum entanglement by fast 2D imaging performed by the Tpx3Cam mentioned prior. The entangled photons are coupled into two optical fibers and directed to the camera using a set of mirrors (Fig. 1).

A. Intensified Tpx3Cam

Imaging with single photon sensitivity is achieved using a novel intensified camera, Tpx3Cam [tpx3cam], which allows time-stamping of incident photons with 1.5ns time granulation when coupled to an image intensifier. Tpx3Cam consists of a light-sensitive silicon sensor bump-bonded to Timepix3 [timepix3], a time-stamping readout chip. The sensor-chip assembly has 256 256 pixels of 55 55 μm^2 each. The processing electronics in each pixel records the time-of-arrival (TOA) of hits that cross a preset threshold and stores it as a time-code in a memory inside the pixel. The time-over-threshold (TOT) is also recorded serving as an estimate of the light flux seen by the pixel. The readout is data-driven when only pixels with signals above the threshold are recorded. The pixel dead time is only 500ns, which allows multi-hit functionality at the pixel level. The maximum camera throughput is 80 Mpix/sec. The light-sensitive silicon sensor in the camera has a thin entrance window with excellent quantum efficiency and anti-reflective coating. The sensor is optimized for the P47 emission spectrum.

The intensifier in front of the camera is a vacuum device with a photo-cathode followed by a chevron micro-channel plate (MCP) and fast P47 scintillator. Photons are converted to photo-electrons on the photo-cathode and then amplified in the MCP before producing a flash of light in the scintillator. The 18 mm diameter scintillator screen is projected on to the 14x14 mm² sensor with a relay lens with no magnification. The photo-cathode quantum efficiency is 18% for the wavelength of 800nm used for the experiments.

The photon pairs from the single photon source were recorded continuously for extended periods of time. Figure ?? shows the pixel occupancy map and examples of single photons in the camera. The two fibers are clearly visible and correspond to the areas of the highest occupancy. Typical rate in the fiber region was about



30kHz determined by the photon source and intensifier quantum efficiency. The background, uniformly distributed over the photo-cathode surface in the occupancy map, is a spurious dark counts from the photo-cathode. This rate is about 50 times smaller than the useful single photon rate in the fibers and, if desired, can be further reduced by cooling the intensifier. We also note that the background photo-electrons arrive at random time so will be further suppressed by a coincidence requirement between the two fibers.

B. Source of entangled photons

Spontaneous Parametric Down Conversion (SPDC) is a nonlinear process in which a photon of a wavelength λ will, with low probability, be split into two photons of wavelength 2λ . Recent years have seen SPDC emerge as a leading candidate as a reliable source of single photons at atomic wavelengths. The source at hand utilizes a blue pump laser diode tuned to wavelength $\lambda = 405nm$, and a pair of Type I BBO crystals with optical axes perpendicular to one another to generate signal and idler photons at wavelength $\lambda = 810nm$. An additional pair of birefringent crystals ensure maximum spatial overlap of the down-converted photons by pre- and post-compensating for differences in effective optical path lengths.

C. Source of entangled photons

Spontaneous Parametric Down Conversion (SPDC) is a nonlinear process in which a photon of a wavelength λ will, with low probability, be split into two photons of wavelength 2λ .

Recent years have seen SPDC emerge as a leading candidate as a reliable source of single photons at atomic wavelengths. The source at hand utilizes a blue pump laser diode tuned to wavelength $\lambda = 405nm$, and a pair of Type I BBO crystals with optical axes perpendicular to one another to generate signal and idler photons at wavelength $\lambda = 810nm$. An additional pair of birefringent crystals ensure maximum spatial overlap of the down-converted photons by pre- and post-compensating for differences in effective optical path lengths. Polarization entanglement is generated using

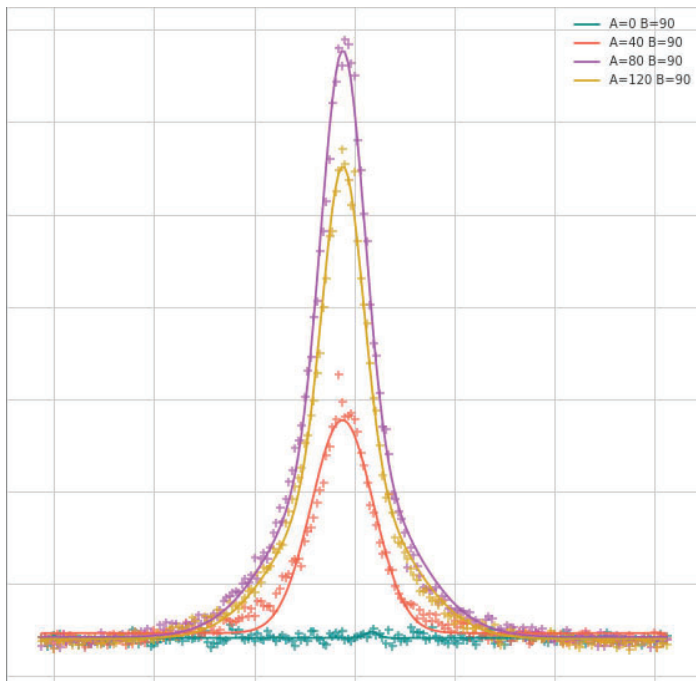


Figure 1: A series of Gaussians that show the difference of coincidence counts depending on polarization.

two BBO crystals (entangled-photon source), and the entangled photons are then fiber coupled and sent to a shaper to create arbitrary spatial modes (phase modulation). The spatially modified photons finally pass through an imaging intensifier before impinging onto the Tpx3Cam CCD.

D. Polarization Entanglement

1. Underlying Theory

Entangled particles satisfy the definition that the complete state of each individual particle must be described with the other as a whole system. This is to say that for two particle states α and β , each with two systems described by the wave functions Φ and Ψ ($\Phi_\alpha + \Phi_\beta$)($\Psi_\alpha + \Psi_\beta$) whereas an entangled state would be $(\Phi_\alpha \Psi_\alpha) + (\Phi_\beta \Psi_\beta)$.

2. Brief History

This phenomenon of entanglement came under the scrutiny of Einstein, Polansky, and Rosen in 1935. They published a paper titled "Can Quantum Mechanical Description of Physical Reality be Considered Complete?". The paper detailed a thought experiment of $\pi \rightarrow e^+ + e^-$ decay. In this decay, ... The resulting famous EPR paradox was not resolved until 1974 by John Bell. His work was later clarified by the CHSH collaboration. It is their resulting inequality used in our measurement of quantum correlation.

E. CHSH Inequality

CHSH defines their inequality as

$$2 \geq |E(a, b) - E(a, b') + E(a', b) + E(a', b')|$$

where $E(a, b) = \int \underline{A}(a, \lambda) \underline{B}(b, \lambda) \rho(\lambda) d\lambda$ represents expected values for outcomes of an experiment, a departure from Bell's probability measurements. In order to calculate the value E for our experiment

III. Results

The important results is the violation of the S value. The current S value calculation results in 2.79 ± 0.01 . This depends upon several factors though and so can change as our project continues. The errors from the covariance matrix of the Gaussian and sinusoidal fits can have a large effect. We are also experimenting with corrections regarding the time resolution of individual pixels. The work remains ongoing.

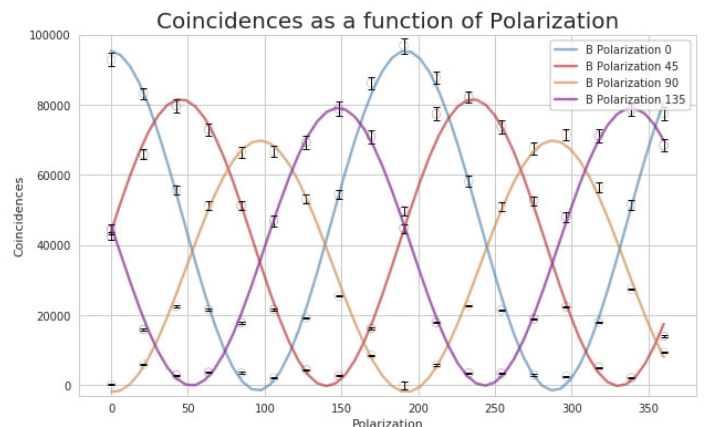


Figure 2: Here all the polarization settings are used to find a sinusoidal relationship between the polarization of the photons and the number of coincidences.

Table 1: The parameters of the sin functions used to fit the polarization function is below

Polarization	Amplitude	Phase	Phase Shift	Offset
0	50890.91	-182.25	-90.01	50942.09
45	42969.15	-179.48	-89.98	44173.08
90	37596.80	181.10	90.00	37122.42
135	41256.24	180.00	89.97	42842.96

IV. Conclusion

With the success of the Tpx3Cam in regards to these quantum information measurements, the data allows for several additional calculations in theory. Long time runs of sixty minutes provide sufficient statistical information to determine the spatial resolution of the S-value. This would allow for quantum information tomography. In addition, the same rate gathered in both experiments allows for the potential to calculate Fock State operators. This quantum operator involved in the second quantization in the FockSpace ($F_v(H) = \bigoplus_{n=0}^{\infty} S_v H^{\otimes n}$) provides a number of double photon creation incidents. The next stage will be installing Tpx3cam in a quantum memory system in order to observe dozens of entangled sources, some stored in Rb cells, which is an early step in the creation of digital programmable quantum computers. (Table 1)

V. Acknowledgements

This project was supported in part by the U.S. Department of Energy, Office of Science, Office of Workforce Development for Teachers and Scientists (WDTS) under the Science Undergraduate Laboratory Internships Program (SULI). The Figueroa Quantum Information Technology Laboratory supplied the space, photon source, and all optical equipment. The Tpx3Cam was supplied by BNL.

Radiation chemistry in molten salts and ionic liquids

Chaudhary Harris

Natural Sciences, Fordham University, 113 W 60th St, New York, NY 10023

James F. Wishart

Chemistry Division, Brookhaven National Laboratory, 98 Rochester St, Upton, NY 11973

ABSTRACT

Molten salts are under serious consideration for use as heat transfer fluids in next-generation nuclear reactors. They can increase reactor performance and safety because they can operate at very high temperatures (500 – 900 °C) and ambient pressure, thus increasing the system’s thermodynamic efficiency while avoiding the hazards of pressurized systems. Molten salt reactors were studied as early as the 1960’s, and in some designs the nuclear fuel is dissolved directly in the salt rather than being contained in fuel rods, as is done in water-cooled reactors. Despite previous work on molten salt reactors, little is known about the chemical effects of the reactor’s high radiation environment on the composition of the molten salt, the fuel components, and the nuclear fission products dissolved in it. Therefore, we are using the Brookhaven National Laboratory Laser Electron Accelerator Facility (LEAF) to study the radiation chemistry of molten salts using pulse radiolysis kinetic spectroscopy techniques with high-energy electrons.¹ As these electrons pass through samples, they cause secondary electrons to be ejected, creating excess positive and negative charges that induce chemical reactions. We used ZnCl₂ (m.p. 290 °C) as the molten salt, and chloride salts of Ru³⁺, Ni²⁺ and Co²⁺ to act as scavengers of the excess charges. The primary transient species formed in pure molten ZnCl₂ are Cl₂⁻ and Cl⁻. Adding metal ions has been more complicated than expected because their chemistries in ZnCl₂ were previously unknown and do not seem to parallel those in concentrated aqueous chloride solutions. In addition to radiation chemistry, I synthesized halide and dimethyl phosphate anion ionic liquids and using Nuclear Magnetic Resonance Spectroscopy to interpret results in order to enhance my laboratory technique for my prospective career in organic chemistry.

I. INTRODUCTION

A. Pulse radiolysis of molten salts

The objective of our project is to submit molten salts and ionic liquids to ionizing radiation in order to assess their fundamental chemistry and their suitability in applications such as nuclear reactors. Ionic liquids and molten salts are dominated by Coulombic interactions between positively and negatively charged species. By custom, the term “ionic liquids” refers to molten salts that are fluid below 100 °C.

At LEAF, electrons accelerated by a microwave frequency photocathode electron gun pass through our samples giving off significant energy. Dr. Wishart has written that, “the incident radiation deposits its energy in increments of tens of thousands of kJ * mol⁻¹ per interaction along its path, creating a track of ionized molecules”.² Understanding what reactions take place in molten salts under radiation is important if they are to be used to replace water as coolants in nuclear reactors.

We hypothesize that metal ions in molten salts (which may come from corrosion processes or from nuclear fuel directly dissolved in the salt) will be impacted by radiation-driven reactions in ways that could interfere with reliable reactor operation. We undertook studies of the radiation chemistry of selected metal ions (Ni²⁺, Co²⁺, and Ru³⁺) in molten zinc chloride to learn about their reactivities in a typical molten salt. We expect CoCl₂ and NiCl₂ to participate in the tetrahedral bonding network of ZnCl₂ in which the cations associate with four chlorides at a time. We predicted that ruthenium will be reduced, and nickel and cobalt can be reduced or oxidized.

B. Synthesis of select ionic liquids

It was my goal to learn to make ionic liquids known for their polarity, thermal stability, conductivity, and significant viscosity that differ in the lengths of the aliphatic chain on the imidazole ring. The methods that this endeavor includes offer valuable experience for the purpose of organic synthesis, purification, and data analysis. The ionic liquids prepared will be used in research being done by Dr. Marie F. Thomas of Fordham University and Dr. Surita Bhatia of Stony Brook University in their study of the dissolution of cellulose by ionic liquid and the rheological properties of the dissolved cellulose solutions. I set out to synthesize 1-dodecyl-3-methylimidazolium bromide ([C₁₂Mim][Br]), 1-decyl-3-methylimidazolium bromide ([C₁₀Mim][Br]), 1-methyl-3-octylimidazolium bromide ([C₈Mim][Br]), 1-hexadecyl-3-methylimidazolium bromide ([C₁₆Mim][Br]), 1-methyl-3-octadecylimidazolium bromide ([C₁₈Mim][Br]), and 1-icosyl-3-methylimidazolium bromide ([C₂₀Mim][Br]). After the bromide salts are achieved, the next objective is to successfully convert them to their dimethylphosphate analogues.

On the conversion of the bromide to dimethylphosphate, Priede, Zicmanis, and Bakis 2014, write that when they perform treatment of alkylimidazolium chloride salts with trimethylphosphate, it results in, “vigorous gas evolution at elevated temperature and formation of the desired compound”³. This means that one of the methyl groups attached to the oxygen atom on the trimethylphosphate evolves from solution as a halomethane gas, bromomethane in our case, when attacked by the lone pair of the nitrogen atom in the imidazolium ring in a SN₂ fashion. The replication and confirmation of Priede et. al.’s work will facilitate ease in the carrying out of such reactions.

II. Methods and Materials

A. Pulse radiolysis of molten salts

We purchased NiCl₂, ZnCl₂, and K₂[RuCl₅H₂O] from Alfa Aesar. We prepared 2 mM and 20 mM solutions of NiCl₂ in the dry glove box since ZnCl₂ rapidly picks up moisture from air to produce HCl and zinc oxide. To limit the amount of material used, we made concentrated stock solutions and then prepared desired

concentrations by serial dilution. The samples were loaded into Suprasil cuvettes, which were evacuated and sealed, after which the samples were heated to liquification.

We performed pulse radiolysis at the LEAF facility in the BNL Chemistry building. This accelerator uses a 3.5 cell, 2856 MHz resonant cavity structure with a 6 mm diameter magnesium photocathode. The power for electron acceleration is provided by an S-band klystron. A chirped-pulse amplified titanium sapphire (Ti:S) laser system is used to generate the photoelectrons for acceleration. Transient absorption signals from a LeCroy oscilloscope were captured by LabVIEW and data analysis was done using Igor Pro.

B. Synthesis of select ionic liquids

For all of the ionic liquids, 1-methylimidazole purchased from Sigma Aldrich was reacted with different alkylbromides from the same supplier. In the formation of the bromide salt, the reaction took place at 70 degrees Centigrade for 24 hours with a magnetic stir bar in reflux after the starting materials were dissolved in acetonitrile. The products were dissolved in dimethyl sulfoxide and deuterium oxide for analysis by NMR Bruker 400 MHz spectroscopy. If deemed to have starting material impurity, solids of ionic liquids having 12 carbons or more were washed in a vacuum tent using ethyl acetate and an ultra-fine frit, and liquids of 12 carbons or less were washed with ethyl acetate and acetonitrile using a separatory funnel.

Bromide salts were converted to the dimethyl phosphate analogues by adding a 10% molar excess of trimethylphosphate and stirring at 110 °C for 2 hours. After the two hours, enough toluene to dissolve the product was added and heated to reflux at 100 °C and then rotovapped off four times.

III. RESULTS

A. Pulse radiolysis of ionic liquids

1. Pure ZnCl₂

The transient absorption spectra of neat ZnCl₂ shows the prompt formation of Cl₂•⁻ radical and its disproportionation to Cl₃⁻ and Cl⁻. As seen in Figure 1, the concentration of Cl₃⁻ decreases with time but it remains significant for many microseconds.

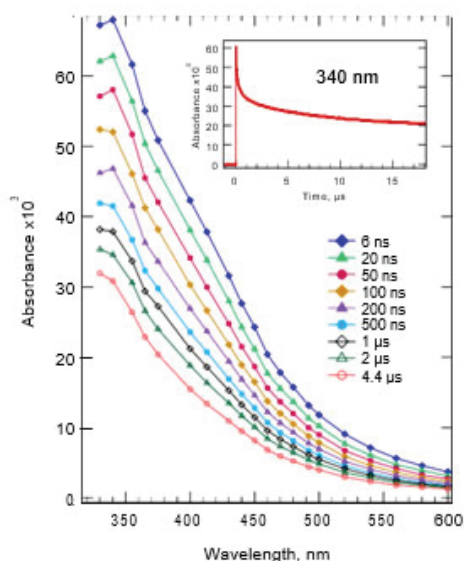


Figure 1. ZnCl₂ transient spectra

A uniformly heated and then rapidly cooled sample of ZnCl₂ forms a glassy structure as illustrated in Figure 2.

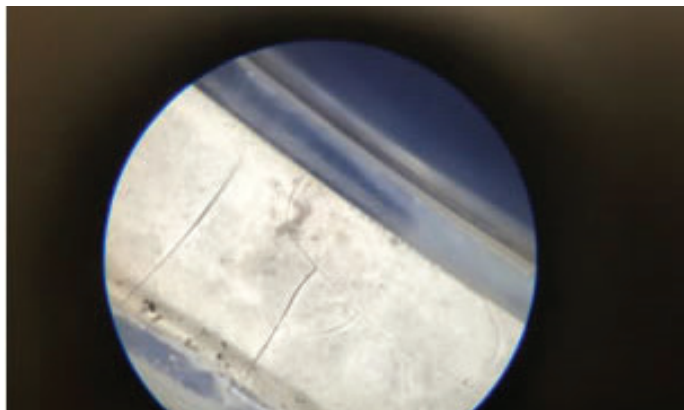


Figure 2. Cooled neat ZnCl₂ forms a transparent glass.

2. CoCl₂ in ZnCl₂

Unexpected results were obtained when CoCl₂ was dissolved in ZnCl₂. As the reaction proceeded, the color of the solution changed from the dark blue color of the CoCl₄²⁻ anion (often seen in stained glass or moisture-indicating silica gel), to the teal color shown in Figure 3. This observation led us to suspend radiolysis work on this compound until we better understand its thermal chemistry. We observed transient species being created by radiolysis, but we cannot understand the reactions until we know the identity of the teal-colored starting species.

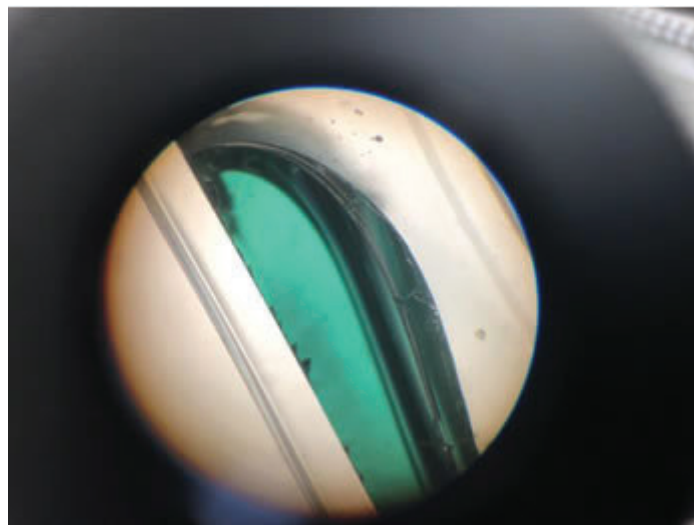


Figure 3. Unidentified Co complex in ZnCl₂

3. K₂[RuCl₅(H₂O)] in ZnCl₂

We expected the [RuCl₅(H₂O)]²⁻ anion to convert to [RuCl₆]³⁻ in molten ZnCl₂,⁴ but it seems that it did not dissolve in the first place. As seen in Figure 4, the transient absorption observed in 2.35 mM Ru resembles that of neat ZnCl₂ and does not point to any new transient species formed from ruthenium. In support of that interpretation, the ZnCl₂ formed many crystals when cooled, suggesting that the undissolved Ru powder was providing many nucleation sites for crystallization.

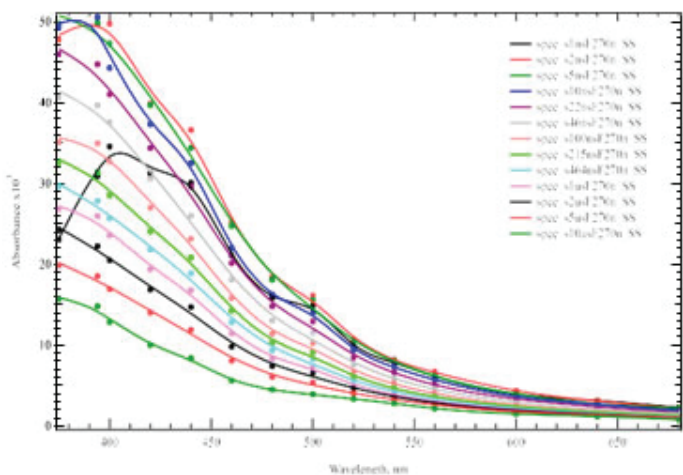


Figure 4. 2.35 mM $K_2[RuCl_5H_2O]$ in $ZnCl_2$ shows kinetics similar to neat $ZnCl_2$.

4. $NiCl_2$ in $ZnCl_2$

Radiolysis of a 2 mM $NiCl_2$ solution produced the transient spectra shown in Figure 5. We observed new absorption bands at 370, 530 and 680 nm, indicating the formation of at least one new species from Ni^{2+} in $ZnCl_2$, which also showed a bleach (absorbance decrease) at 460 nm. When we attempted to make a 20 mM $NiCl_2$ solution we did not see an increase in the formation rate or the product yield when the sample was fully equilibrated, although we did see a slower rate and lower yield just after the sample was originally melted and the $NiCl_2$ and $ZnCl_2$ powders were still mixing (see Figure 6). These observations suggest that the solubility limit of $NiCl_2$ in $ZnCl_2$ is ≤ 2 mM. We are intrigued by the radiolytic behavior of nickel in molten salts because it is a major constituent of the steels used for nuclear reactor coolant systems.

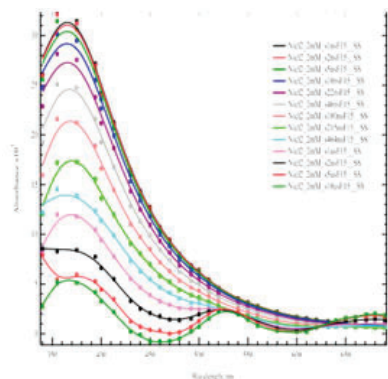


Figure 5. Transient spectra for 2 mM $NiCl_2$ in $ZnCl_2$.

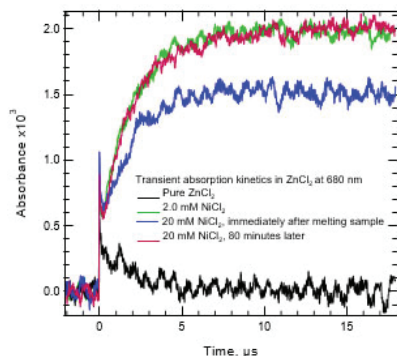


Figure 6. Comparison of reaction kinetics in *nominally* 2 and 20 mM $NiCl_2$.

B. Synthesis of select ionic liquids

1. $[C_{12}Mim][Br]$

Table 1. NMR signals observed for 1-dodecyl-3-methylimidazolium bromide.

Peak	Multiplicity	Integration	Identification
9.18	Singlet	1.00	-N-H
7.69 - 7.76	Doublet	2.09	H-C=C-H
4.14	Triplet	2.08	=N-CH ₂
3.82	Singlet	3.08	-N-CH ₃
3.30	Singlet	4.07	H ₂ O
2.46	Singlet	0.96	DMSO
2.04	Singlet	1.67	Acetonitrile
1.77	Triplet	2.21	-CH ₂
1.19	Multiplet	20.44	-CH ₂
0.83	Triplet	3.00	-CH ₃

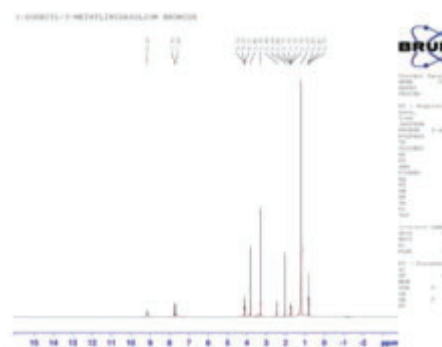


Figure 7. Proton NMR spectrum of 1-dodecyl-3-methylimidazolium bromide

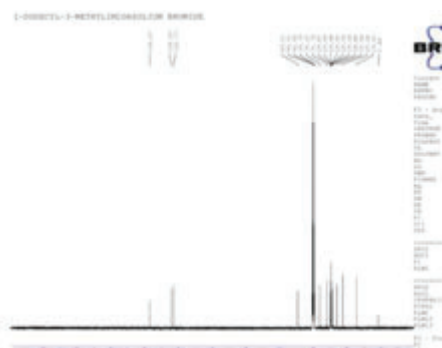


Figure 8. Carbon NMR of 1-dodecyl-3-methylimidazolium bromide

2. $[C_{12}Mim][DMP]$

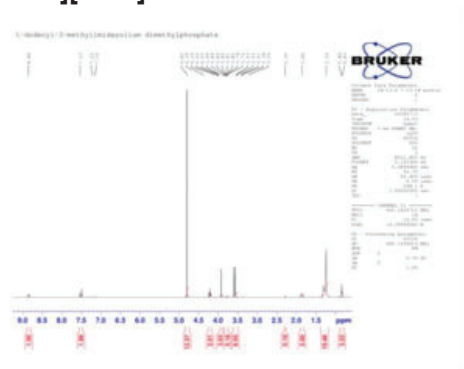


Figure 9. Proton NMR spectrum of 1-dodecyl-3-methylimidazolium dimethylphosphate

Table 2. Signals and their characteristics of 1-dodecyl-3-methylimidazolium dimethylphosphate

Peak	Multiplicity	Integration	Identification
8.86	Singlet	1.00	-N-H
7.53	Doublet	1.99	H-C=C-H
4.80	Singlet	12.37	D ₂ O
4.39	Triplet	2.01	N-CH ₂
3.84	Singlet	3.03	Acetonitrile
3.75	Doublet	6.05	-O-CH ₃
1.86	Triplet	2.00	CH ₂
1.24	Multiplet	19.46	CH ₂
0.86	Triplet	3.22	-CH ₃

Figure 13. Carbon NMR of Trimethylphosphate

Figure 14. Proton NMR of Trimethylphosphate

4. [C₁₀Mim][Br]

Figure 15. Proton NMR Spectrum of 1-decyl-3-methylimidazolium bromide

Table 3. NMR signals of 1-decyl-3-methylimidazolium bromide.

Peaks	Multiplicity	Integration	Identification
9.29	Singlet	1.00	-N-H
7.79	Doublet	2.05	H-C=C-H
4.15	Triplet	2.20	-N-CH ₂
4.13	Singlet	3.13	-N-CH ₃
3.30	Singlet	1.21	H ₂ O
1.73	Triplet	2.43	-CH ₂
1.18	Multiplet	16.40	-CH ₂
0.78	Triplet	3.56	-CH ₃

Figure 10. Phosphorus NMR of 1-dodecyl-3-methylimidazolium bromide

Figure 11. Carbon NMR of 1-dodecyl-3-methylimidazolium dimethylphosphate

3. Trimethylphosphate

Figure 12. Phosphorus NMR of Trimethylphosphate

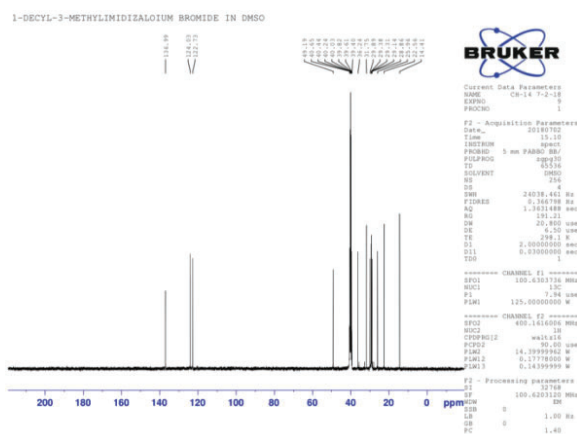
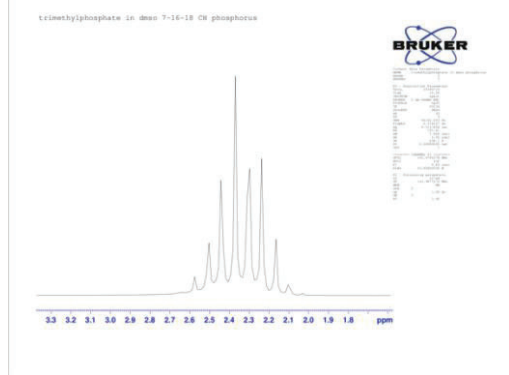
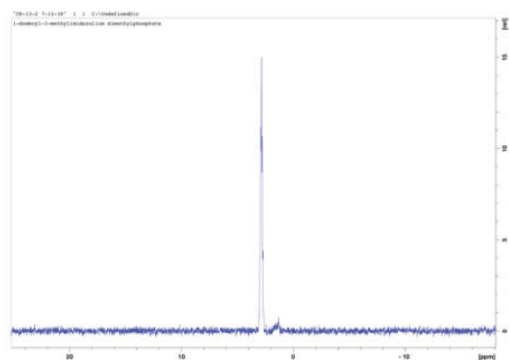


Figure 16. Carbon NMR spectrum of 1-decyl-3-methylimidazolium bromide

5. [C16Mim][Br]

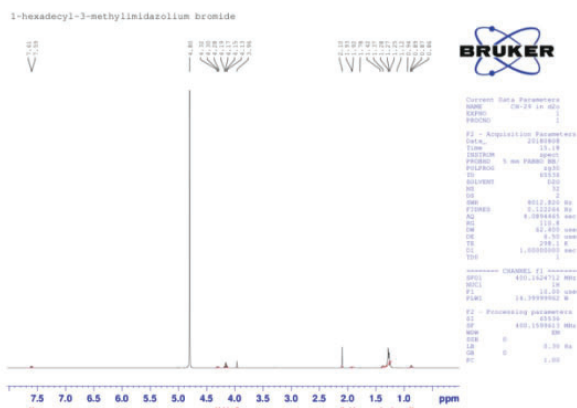


Figure 17. Proton NMR of 1-hexadecyl-3-methylimidazolium bromide

Table 4. Signals and their characteristics of 1-hexadecyl-3-methylimidazolium bromide

Peak	Multiplicity	Integration	Identification
8 – 9 ppm	--	--	Not Observed
7.59 – 7.61	Doublet	2.10	H-C=C-H
4.80	Singlet	2.03	D ₂ O
4.17	Singlet	4.57	-N-CH ₂
3.96	Triplet	2.83	-N-CH ₃
1.93	Singlet	6.45	-CH ₂
1.78	Triplet	2.07	-CH ₂
1.28	Multiplet	36.35	-CH ₂
0.95	Triplet	3.00	-CH ₃

6. [C18Mim][Br]

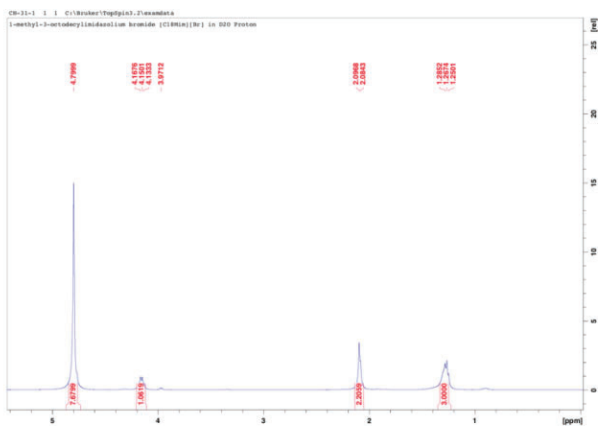


Figure 18. Sufficient peaks were not observed for [C18Mim][Br].

7. [C8Mim][Br]

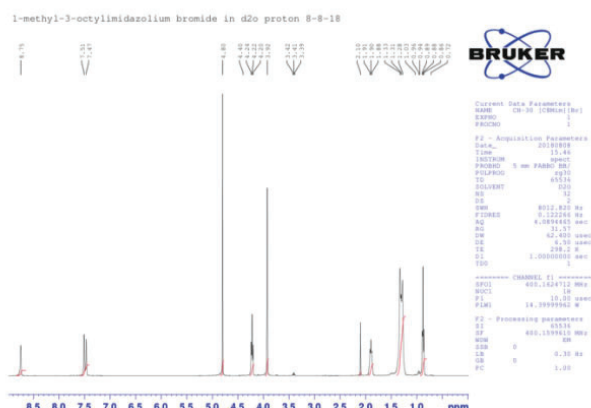


Figure 19. Proton NMR of 1-methyl-3-octylimidazolium bromide

Table 5. Signals and their characteristics of 1-methyl-3-octylimidazolium bromide

Peaks	Multiplicity	Integration	Identification
0.93	Singlet	0.93	-N-H
1.91	Doublet	1.91	H-C=C-H
4.80	Singlet	2.65	D ₂ O
4.24	Triplet	2.00	-N-CH ₂
3.92	Singlet	2.92	-N-CH ₃
1.90	Triplet	2.09	-CH ₂
1.91	Multiplet	10.53	-CH ₂
0.94	Triplet	3.00	-CH ₃

8. [C20Mim][Br]

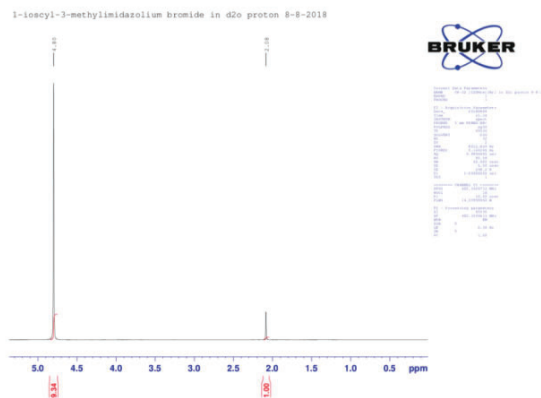


Figure 20. Sufficient peaks were not observed for [C20Mim][Br].

IV. DISCUSSION

A. Pulse radiolysis of molten salts

The key to finding feasible systems for radiolysis studies of transition metals in molten salts begins with ensuring that the metal properly dissolves. In the case of $K_2[RuCl_5H_2O]$, we believe that the metal did not dissolve at all. The transient absorption spectra of $K_2[RuCl_5H_2O]$ in Figure 2 strongly resemble those of pure $ZnCl_2$. In the case of $NiCl_2$ the lack of change in reaction kinetics after sufficient time is allowed for equilibrium leads us to conclude that it is not very soluble in $ZnCl_2$ and the upper limit seems to be ≤ 2 mM. We intend to locate that solubility lim-

it by investigating with even lower concentrations. The case of CoCl_2 is most surprising because it changes color over time. We would expect to see the well-known dark blue color⁵ indicative of CoCl_4^{2-} , but instead a teal color asserts the presence of an entirely different species. We require further studies of cobalt in ZnCl_2 before we can study its radiation chemistry. Our next step is to see if we may be able to dissolve the metals in ionic liquid halides such as 1-butyl-3-methylpyrrolidinium chloride and study their speciation using UV-Vis spectrophotometry.

B. Synthesis of select ionic liquids

We successfully converted $[\text{C}_{12}\text{Mim}][\text{Br}]$ to $[\text{C}_{12}\text{Mim}][\text{DMP}]$. This is illustrated by the change in peak in the phosphorus NMR when we compare trimethylphosphate to $[\text{C}_{12}\text{Mim}][\text{DMP}]$, meaning that the phosphorus atom is now in a different chemical environment, due to the anion's association with the alkylimidazolium cation. In the case of $[\text{C}_6\text{Mim}][\text{Br}]$, the most downfield signal belonging to the proton attached to a sp^2 carbon between two nitrogens on the imidazolium ring was not observed. The reason is that because that is the most acidic proton and is known to proceed in acid base chemistry. We did not retrieve detectable data for $[\text{C}_{20}\text{Mim}][\text{Br}]$ and $[\text{C}_{18}\text{Mim}][\text{Br}]$. We believe that the reason is that they are not appreciably soluble in D_2O . We intend to attempt dissolving these compounds in dimethylsulfoxide and chloroform- D in the future for the purposes of NMR and assess their carbon NMR spectra as well. Once their NMR spectra are interpreted and deemed to contain minimal impurities, their conversion to DMP will be attempted in the same manner as the $[\text{C}_{12}\text{Mim}][\text{Br}]$.

V. ACKNOWLEDGEMENTS

This work was supported by the U.S. Department of Energy, Office of Science, Office of Workforce Development for Teachers and Scientists (WDTS), and the Science Undergraduate Laboratory Internship (SULI) programs and by the Office of Basic Energy Sciences, Division of Chemical Sciences, Geosciences and Biosciences, under contract # DE-SC0012704. We would like to extend our thanks to Bobby Layne, Dr. Lall-Ramnarine, Dr. Marie Thomas, and the BNL Office of Educational Programs for their dedication and support.

VI. REFERENCES

- ¹ Wishart, James F. "Ionic Liquid Radiation Chemistry." *Ionic Liquids Further UnCOILed: Critical Expert Overviews*, edited by Natalia V. Plechkova and Kenneth R. Seddon, John Wiley & Sons, 2014, pp. 259–274.
- ² Wishart, James F., et al. "The LEAF Picosecond Pulse Radiolysis Facility at Brookhaven National Laboratory." *Review of Scientific Instruments*, vol. 75, no. 11, 2004, pp. 4359–4366., doi:10.1063/1.1807004.
- ³ Priede, E., Bakis, E., & Zicmanis, A. (2014, March 8). "When chlorides are the most reactive: A simple route towards diverse mono- and dicationic dimethyl phosphate ionic liquids." Retrieved August 6, 2018.
- ⁴ Seddon, E., & Seddon, K. (n.d.). *The Chemistry of Ruthenium, Volume 19 - 1st Edition*.
- ⁵ "The Equilibrium between Two Coloured Cobalt Species." *LearnChemistry*, Royal Society of Chemistry, Jan. 2018, www.rsc.org/learn-chemistry/resource/res00000001/the-equilibrium-between-two-coloured-cobalt-species?cmpid=CMP00005957.

Developing sPHENIX subsystem outline interface drawings

Michael Harris

Chemical and Molecular Engineering, Stony Brook University, Stony Brook, NY 11794

Donald Lynch

Physics Department, Brookhaven National Laboratory, Upton, NY 11793

Abstract

The super Pioneering High Energy Nuclear Interaction Experiment (sPHENIX) detector, an experiment utilizing the Relativistic Heavy Ion Collider (RHIC), will take measurements during the high-speed collision of ions to give scientists insight into how matter behaved during the first moments after the Big Bang. sPHENIX requires collaboration between scientists and engineers across the globe to design and construct components of the detector which must interface with each other precisely. Standard annotated drawings are of crucial importance when designing and constructing sPHENIX subsystems. Collaborators and subsystem groups need envelope dimensions and information about interface elements. Although Brookhaven National Laboratory has full detail three dimensional models of sPHENIX subsystems, the models contain details that are unnecessary and confusing to include in a simple reference drawing. Outline interface drawings are the solution to this problem because they show clearly outline and interface dimensions only. Omitting extra detail allows a reference drawing to display information in a way that is much easier to understand. The process of creating an outline interface drawing begins with creating an envelope model with the same dimensions and surface features as the existing full detail model of a subsystem. Any internal structure is ignored unless the structure interfaces with another component. This is the case for certain internal threaded holes, for example. Next, the envelope model is projected onto a two-dimensional drawing where all dimensions and surface features of the component are annotated. Sometimes the full detail drawings for particularly important elements are included if any individuals need more information than the outline provides. The completed outline interface drawings are used by subsystem groups for three main purposes: design reference, inspection, and installation. The drawings serve as a standard for these three processes to simply sPHENIX construction.

I. Introduction

sPHENIX is an upgrade to the original PHENIX detector, originally proposed in 2012. It builds upon the findings of PHENIX and works in collaboration with the Large Hadron Collider to further our knowledge of certain properties of quark-gluon plasma. Additionally, the sPHENIX upgrade serves as a precursor to future experiments involving the Electron Ion Collider (EIC) which utilizes much of the same technology, such as the BaBar magnet and some of the calorimeters. sPHENIX is composed of many components and subsystems that must interface with each other precisely. This challenge is only amplified by the fact that these components are constructed and designed in part by scientists and engineers from all over the world. The success of sPHENIX is dependent on collaborator and subsystem groups ability

to share information quickly and with ease. Brookhaven National Laboratory uses Autodesk programs for its data management and computer aided design needs for this project because it excels at

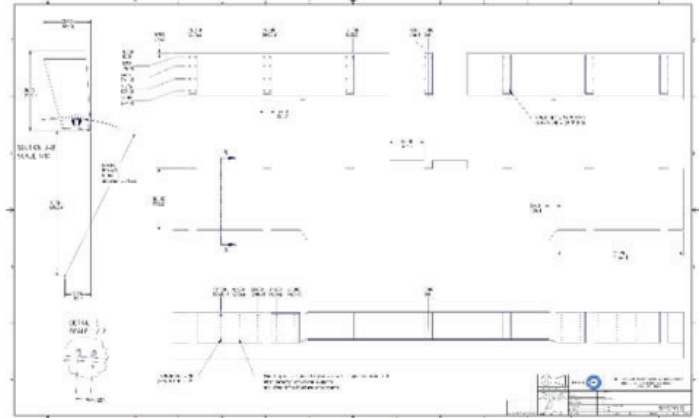


Figure 1. Outline interface drawing of outer HCal chimney sector

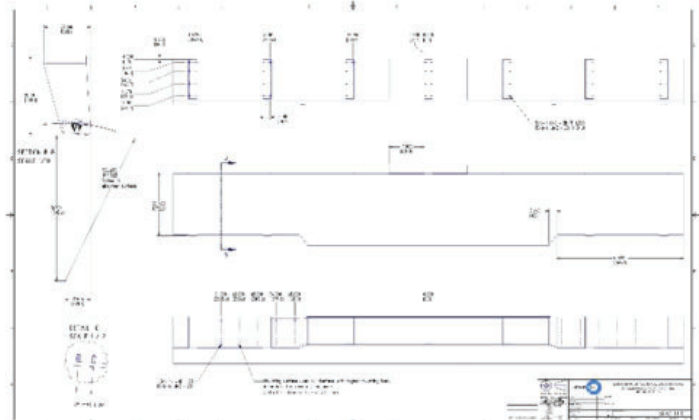


Figure 2. Outer HCal standard sector

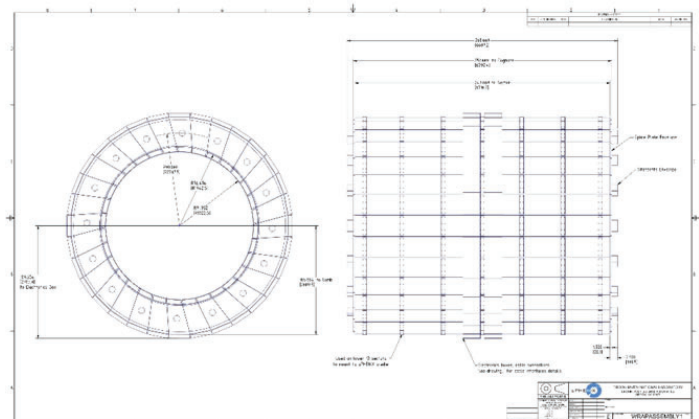


Figure 3. Outer HCal full assembly

information sharing. Preliminary three-dimensional models of sPHENIX subsystems created by laboratory employees are located on the data management program Vault and are only one of the ways that the problems related to delocalized collaboration are solved. The use of these models is not without flaw, however. These full detail models are necessary but not the ideal reference in every situation.

Outline interface drawings are also of crucial importance to the success of sPHENIX. Currently the only way for collaborators to share information regarding the design of subsystems is using the preliminary full detail assembly models made using Inventor. The problem with using these representations is that they contain an excess of detail for many reference purposes. The resulting outline drawings are confusing to look at and make it borderline impossible to discern important interface details from general structural details. The solution is to create outline interface drawings which include outline and interface dimensions but omit internal structures to be used as a more concise reference document. This offers a way to understand each component with more speed and ease, as well as set a standard for the overall dimensions of components that all collaborators can use to work together properly.

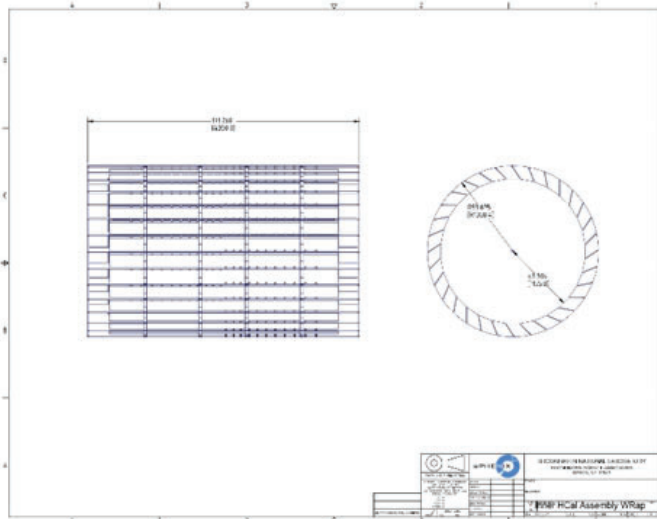


Figure 4. Outline interface drawing of inner HCal full assembly

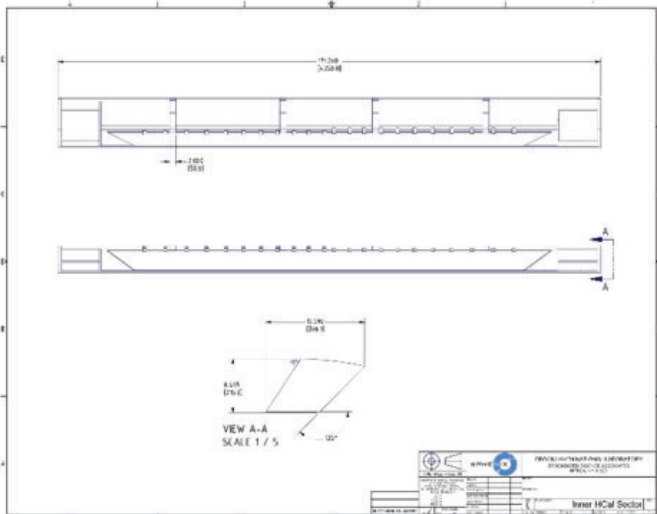


Figure 5. Single inner HCal sector

II. Methods

The development of an outline interface drawing begins with utilizing Autodesk Inventor and the existing full detail three-dimensional models of five components of sPHENIX: the outer Hadronic Calorimeter, inner Hadronic Calorimeter, Electromagnetic Calorimeter, BaBar superconducting magnet, and Time Projection Chamber. The goal of making these drawings is to be able to provide subsystem groups with concise outlines and interface details about the components. A single sheet will display (in a less complex manner) necessary information needed for design, inspection, and assembly of sPHENIX. The same general method was used to make an outline interface drawing for all these components, but each posed different individual challenges.

A. Outer Hadronic Calorimeter

The outer Hadronic Calorimeter (outer HCal) was the first component that required creation of a drawing and was one of the most complex to complete. The general structure of the outer HCal includes 29 standard sectors and 3 slightly altered chimney sectors revolved around a central axis to form a cylindrical shape. The simplest way to create the outline interface drawing was to start with creating a simplified three-dimensional model of a single standard sector from the outer HCal. This involves designing a solid version of the sector with identical outline dimensions and

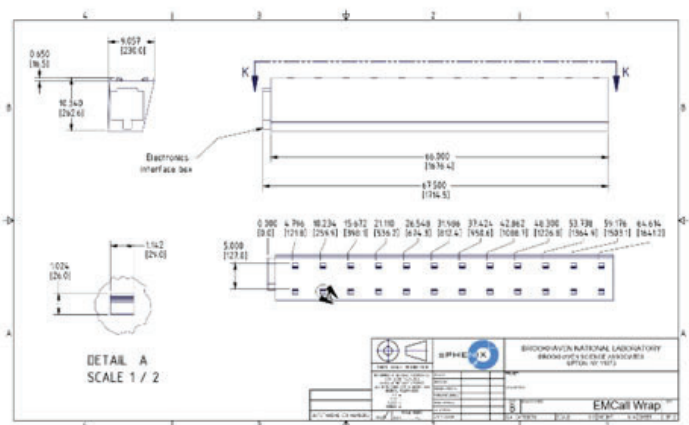


Figure 6. Outline interface drawing of EMCAL north and south sector

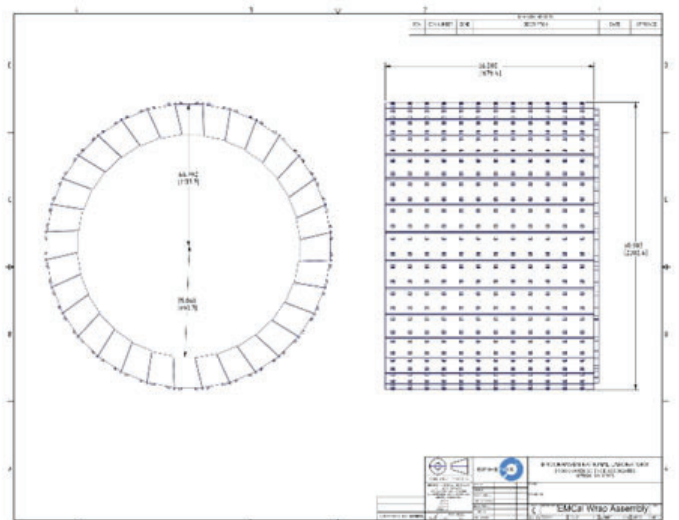


Figure 7. EMCAL full assembly

no internal structures. Interface elements are then added which, in this case, are combs at the top of the sector with threaded holes on top of those combs as well as on the bottom of the sector. Lastly, the outline of two electronics boxes are included on top of the sector. The electronics boxes are general outlines that will contain electronic interface structures like wiring. Once the simplified model is complete, the chimney sector and full outer HCal assembly can be modeled and each of these models is projected onto a two-dimensional Inventor drawing. The final step of the outline interface drawing is to clearly annotate each outline dimension and specifics about interface details, such as threaded hole diameter and depth. For the outer HCal, this involves referencing the electronics box in another drawing so that the reader has access to more detail if desired.

B. Inner Hadronic Calorimeter

The inner Hadronic Calorimeter (inner HCal) is similar in structure to the outer HCal. It is made up of 32 identical sectors revolved around an axis. This cylindrical assembly is shorter in length and diameter than the outer HCal. Additionally, each inner HCal sector is identical, adding simplicity to creating the model. This component does not have any threaded holes necessary to include for reference purposes. The only necessary interface-specific element that is annotated is a series of combs located on the top of each sector.

C. Electromagnetic Calorimeter

The Electromagnetic Calorimeter (EMCal) is composed of 64 sectors, 32 north sectors and 32 south sectors. The simplest way to create a simplified model of the EMCal is to create one unit that is two sectors, the north and south, and to revolve that unit 32 times at 11.25 degree intervals to create a full cylindrical model like the previous models. As the name suggests, the EMCal has many important electrical interface elements both internally and on the surface. For the purposes of this outline interface drawing, many of these elements are left out for the sake of simplicity. This drawing focuses more on the physical outline and mechanical interfaces rather than internal electrical interface elements. The physical interfaces annotated include carriages along the top of each sector as well as the outline of a box that contains electrical structures on the face of each sector.

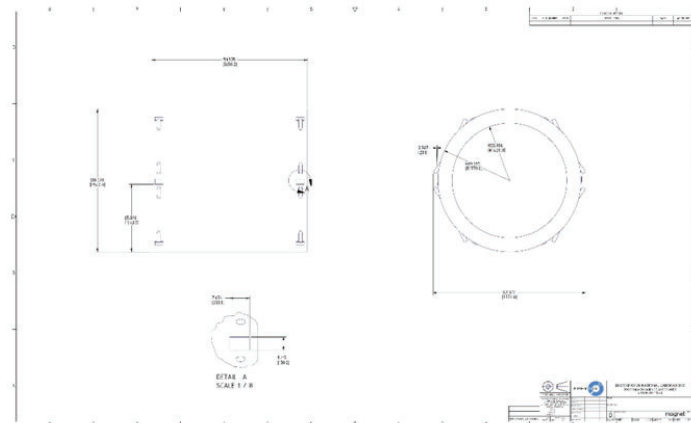


Figure 8. Outline interface drawing of BaBar superconducting magnet

D. BaBar Magnet

The magnet, for the purposes of this drawing, is a solid cylinder with minimal detail on the surface. It was shipped from its home in California for use in the sPHENIX detector. This component is the simplest out of the five because it is solid and contains no complex electrical or internal structures. In terms of surface detail, the only structures added are small details around the out edges of each side of the cylinder, including flat pads.

E. Time Projection Chamber

The Time Projection Chamber (TPC) is also without sectors. The basic construction is two concentric cylinders. The endcaps of these cylinders posed a challenge because of the web-like structure and excess of hardware details. After removing these details and representing the endcaps in a simplified manner, the TPC model was done and an outline interface drawing could be made.

III. Conclusion

Now that the outline interface drawings have been developed for these five subsystems, they will be used for any number of purposes. The main three uses will be as a reference for design, inspection, and assembly. While designing any subsystem in sPHENIX, any given outline interface drawing is crucial because each component must fit together properly with every other component. Each design must consider the details included on these drawings. During the construction and inspection process, it is necessary to have a standard for comparison. The outline interface drawings offer a simple reference that display information in a way that drawings of the full detail models cannot. The assembly process is where all the preliminary steps pay off. Assembling the sPHENIX requires near exact placement of hundreds of subsystems that exist and the outline interface drawings offer an extra source of confirmation for how each component properly interfaces with each other. The drawings prove how valuable they can be in the development and maintenance of sPHENIX.

IV. Acknowledgments

I would like to express my thanks to Donald Lynch and the sPHENIX team for their guidance. This project was supported in part by the U.S. Department of Energy, Office of Science, Office of Workforce Development for Teachers and Scientists (WDTS) under the Science Undergraduate Laboratory Internships Program (SULI).

Building and customizing a data repository with the Invenio/Zenodo platform

John Harrison

Physics Department, Texas A&M University, Corpus Christi, TX 78412

Line Pouchard

Computational Science Initiative, Brookhaven National Laboratory, Upton, NY 11973

Abstract

Zenodo is an open access research repository developed by CERN in order to upload and store particle collision data. The process began by utilizing the installation code as written by CERN found under the Zenodo installation procedure. This particular instance runs on four services: PostgreSQL, Elasticsearch 2.x, Redis and Rabbit MQ. The installation procedure details two methods of installation: Docker and Development. Both of which were installed and run on my personal laptop in order to determine the ease of execution and attempt to fix any bugs that we may encounter before installing it on the machine designated by Brookhaven National Laboratory. The development installation was more suited to our needs as we were able to customize Zenodo to our specifications. The next step was to test the various APIs using a Curl command and Python script. We were then able to write a Python script in order to upload a schema taken in from the National Synchrotron Light Source II and separate it into key-value pairs for ease of search throughout published papers. We will then be able to write Python code that will store and categorize particle data from the National Synchrotron Light Source II (NSLS II). The benefit of this will be the ease of access to particle data which will allow the smooth upload of published research results.

I. Introduction

Scientific results have traditionally been disseminated in publications. With the deluge of data unleashed by modern computational and detector methods, it is crucial to understand and be able to access not only end results but also intermediate datasets and metadata objects that have been used as input and transformed to achieve final results. Data repositories have become a preferred way for storing, searching, sharing, and publishing datasets associated with scientific projects and papers. BNL has designed some of its archives using the open source Invenio software platform developed at CERN (Cowton et al., 2015; Shiers et al., 2016).^[2] Invenio provides the means to develop a state-of-the-art, standards based, archival service based on widely used technologies, the best known is the Zenodo service. BNL has deployed customized instances of Invenio/Zenodo. Invenio is in compliance with the international standard for Open Archival Information Systems (OAI-PMH - CCSDS, 2012) and US Department of Energy data management regulations. The system is backed up by BNL's world-leading extensive disk storage, tape backup, networking and data intensive computing infrastructure. A user interacts with the repository either through the Graphical User Interface for single record upload or through REST APIs for deposit, search, download, and communities. Our effort in this project includes testing and customizing one BNL deployed instance of the Invenio/Zenodo platform, to accommodate new

types of file formats and a metadata schema designed for sample measurements at the NSLSII. The purpose of this project is to create and customize an implementation of Zenodo for use at Brookhaven National Laboratory. Our goal is to have this completely installed and running on our new Linux machine.

II. Installation Procedure

Two procedures were used in order to allow for the smooth execution and ease of publication for this particular instance. The first procedure, employed for the installation and execution for the data repository, can be found under the installation procedure on the main instance of Zenodo.

A. Zenodo Installation

As mentioned previously, the Zenodo installation detailed two methods for proper installation and execution. The first was a simple Docker installation in order to properly build the correct docker images which will then be used to boot up the Zenodo platform. We will use the `docker-compose` tool in order to boot these images up.

In order for us to run Zenodo locally, we used a `docker-compose` configuration which contained the full Zenodo stack. We created a `src` directory in order for us to clone Zenodo from the GitHub repository. Once this was cloned, we were able to use the `docker-compose build` command followed by the `docker-compose up` command. These commands simply built the docker images and then immediately booted them up once the build was complete.

We were then able to run an `init` script, with a `docker-compose run` command, which would create data tables and search indexes as well as some data fixtures. Once finished, we were then able to load some demo records in order to test Zenodo's indexing feature.^[4]

Once all commands have been executed, and all demo records have been loaded we were then able to access our instance via our localhost.

The second installation method as described by Zenodo, is the development installation. This version will prove to be more useful for our project as we are able to customize this installation to our various needs.

Similar to the docker installation, however, the development installation loads only the four services that are needed, PostgreSQL, Elasticsearch 2.x, Redis and Rabbit MQ, in one `docker-compose up` command. We will then create a virtual Python environment using the `virtualenvwrapper` command.

NVM was then installed and immediately sourced in our `.bashrc` directory in order to proceed with installing the npm requirements as we have done previously. Once completed, we were then able to install the fixtures and load demo files in the

same procedure as before, however, with the development installation, we ran a celery worker prior to loading and indexing records. We were then able to test our instance by accessing our localhost.^[4]

Once the Zenodo instance was installed and running on my personal laptop, we were ready to install on the Linux machine. Using a `ssh` command, we were able to access the system remotely in order to begin the installation. Following the same method as before, we attempted the Docker installation first. We received several errors regarding permissions which will have to be reconfigured at a later time. Attempts were made to run the commands as `root`, but to no avail.

Considering the development installation was more suited to our needs, we began that particular installation method. Encountering minor errors that were easily fixed with `sudo` commands, we had the development instance running on the new machine. Due to an error in the firewall of the main system, we were unable to access the instance at this time despite the fact it is running properly.

B. Python Script for Publication

The idea for the Python script came about as a way to alleviate the necessity to manually input all metadata associated with an upload. The Zenodo REST API details a method in which a user can upload and publish a written document, in the form of .pdf, .csv, etc., into the Zenodo database directly from a Python command line.

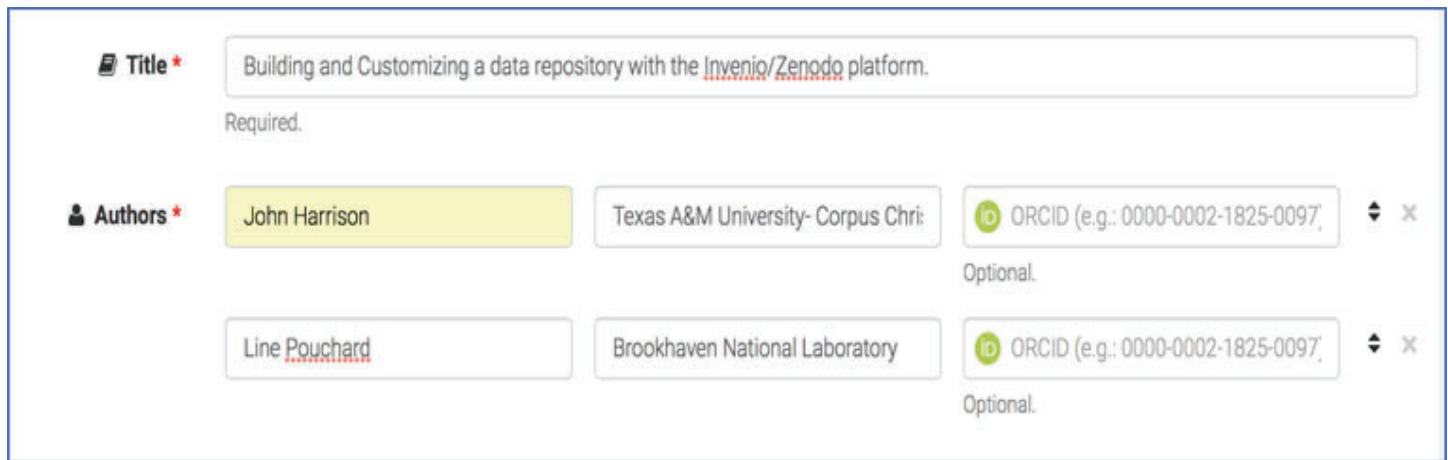
In order for the script to function properly, the `Requests` module must first be installed. This is to help access the particular instance of Zenodo we are publishing through. Later versions of Python, such as the one we used, Python 3, have this module already included in the packaging. If not, it is a simple `pip install Requests` command to have it installed and ready to use. Other important modules required are the `csv` for reading and filing a comma separated value file and the `sys` module.^[5]

The first few lines in the code were written to call the `csv` module in order to build a reader which will interpret a .csv file. The reader will then interpret that file separating the key-value pairs and filing them in a dictionary. This will be utilized later in the code to parse values for the metadata from our schema.

Running the script as written by Zenodo, we encountered a few errors with both Jupyter notebook as well as the terminal itself. Calling upon the `urllib` module, we were able to disable unnecessary warnings that were preventing us from moving forward with our script.

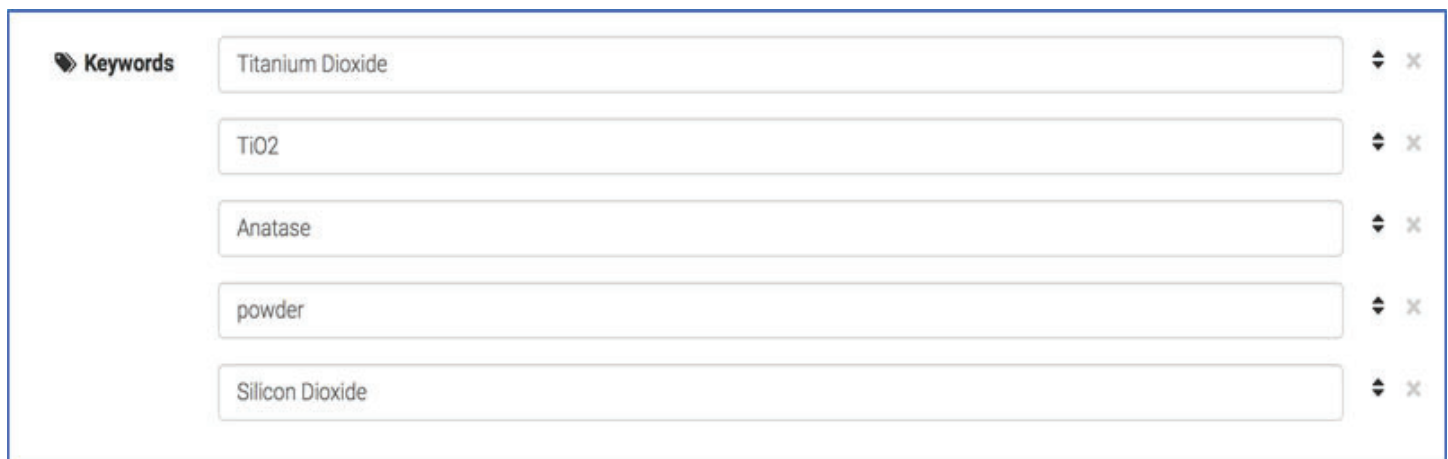
The next lines of code were written to begin the post process. First, we needed to create a token that would allow us to both write and publish material through the database. This token can be created through the applications menu under the account settings in our localhost version of Zenodo. By calling the `requests.get` command we were able to access the localhost's database remotely using our newly created access token.

Again, using our access token to access the database, we can now call the `requests.post` command, to post our data to our



The screenshot shows a web form for Zenodo metadata. The 'Title' field is required and contains the text 'Building and Customizing a data repository with the [Invenio/Zenodo](#) platform.' Below it, the 'Authors' field is also required and contains two entries: 'John Harrison' from 'Texas A&M University- Corpus Chri:' and 'Line Pouchard' from 'Brookhaven National Laboratory'. Each author entry has an optional 'ORCID' field with the value '0000-0002-1825-0097'.

Fig. 1 shows the title and author portion of the metadata from the Python script.



The screenshot shows the 'Keywords' field of the Zenodo metadata form. It contains five entries: 'Titanium Dioxide', 'TiO2', 'Anatase', 'powder', and 'Silicon Dioxide'. Each keyword entry has a dropdown arrow and a close button (X) on the right side.

Fig. 2 shows the remainder of the uploaded metadata as keywords from the schema.

instance of Zenodo. Once, this has been posted, we began the process of filling out the metadata to our post before publishing. This will fill out the title, author and affiliation cells. We can now call upon our csv reader in order to parse the data from our file from the NSLSII and fill it in under the “subjects” category.

Once the metadata has been uploaded, we can begin the process of publication. The last few lines of script, call the same `requests.post` command as before, although this time it is accessing the publish portion of our localhost’s instance of Zenodo.^[5] It will not be officially published until the curator of the particular community we upload to has approved it for publication. It is also important to note, that once this data has been published, it receives a digital object identifier (DOI), and thus can no longer be edited or deleted.

III. Results

This project is not projected to be completed until late fourth quarter 2018 or early first quarter 2019. The results we obtained at this point come in the form of a completed data repository and python script for both the upload as well as the publish procedure. The images are described below.

IV. Conclusion

Zenodo has been widely used by scientists worldwide since its creation at CERN. With the successful installation of the Zenodo GUI, Brookhaven National Laboratory now has their own instance to store and publish data sets. By utilizing the Python script, users can both post and publish a data set as well as upload the metadata needed for that particular upload. The creation of this repository, which will be used throughout BNL, was an essential first step in this project that will continue to be developed in the future.

V. Acknowledgments

Thank you to Line Pouchard with the Computational Science Initiative at Brookhaven National Laboratory for allowing me to work on this project. This project was supported in part by the U.S. Department of Energy, Office of Science, Office of Workforce Development for Teachers and Scientists (WDTS) under the Science Undergraduate Laboratory Internships (SULI).

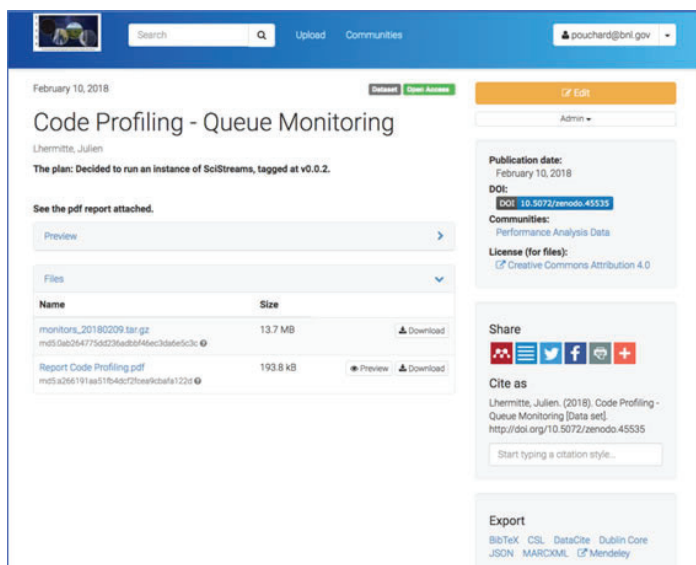


Fig. 3 depicts the created version of Zenodo. This shows the files that have been uploaded featuring both a preview and download option.

VI. References

- [1] Consultative Committee for Space Data Systems (CCSDS). (2012). Reference Model for an Open Archival Information System (OAIS) (Magenta Book CCSDS 650.0-B-1). Retrieved from: <http://public.ccsds.org/publications/archive/650x0m2.pdf>
- [2] Cowton, J., Dallmeier-Tiessen, S., Fokianos, P., Rueda, L., Herterich, P., Kunar, J., Smith, T. (2015). Open data and data analysis preservation services for LHC experiments. Paper presented at the Journal of Physics: Conference Series.
- [3] Shiers, J., Berghaus, F. O., Cancio Melia, G., Blomer, J., Dallmeier-Tiessen, S., Ganis, G., & Simko, T. (2016). CERN Services for Long Term Data Preservation. Paper presented at the iPRES 2016 - 13th International Conference on Digital Preservation, Bern, Switzerland.
- [4] Zenodo: Read the Docs, <https://zenodo.readthedocs.io/en/latest/installation.html#development-installation>
- [5] Zenodo <http://developers.zenodo.org>

Sample metadata acquisition at the National Synchrotron Light Source II

Sabrina Hernandez

Materials Science and Engineering, Massachusetts Institute of Technology, Cambridge, MA 02139

Line Pouchard

Computational Science Initiative, Brookhaven National Laboratory, Upton, NY 11973

While the development of new materials is crucial for the advancement of innovative technologies, these technologies are often limited by the slow, traditional research pathways that lead to material discovery and development. To minimize the time spent discovering new materials, computational models can be developed to predict the conditions needed to produce materials with the desired properties. However, these modeling tools require access to a lot of data and metadata about previously tested materials in order to be accurate and useful. The Computational Science Initiative at Brookhaven National Laboratory (BNL) aims to increase metadata collection of samples brought by users to the beamlines at the National Synchrotron Light Source II (NSLS-II) through the development of a metadata schema. The metadata schema outlines a standard that thoroughly describes samples brought to the NSLS-II beamlines. Prior to arriving, users will submit sample information in accordance with this schema via online forms. Upon submission, a Python script will verify that the information correctly follows the schema format and upload valid submissions to an internal database at NSLS-II. Sample metadata in this database supplements experimental conditions recorded by BlueSky, the NSLS-II data acquisition system, and made accessible to users via a common interface powered by Elastic Search. Users will be able to access this information across different visits to BNL. The metadata schema will be trial tested and modified as needed with samples prepared for the X-ray Powder Diffraction (XPD) and Inner-Shell Spectroscopy (ISS) beamlines. Afterward, the metadata schema will be deployed at these two beamlines for all users, and if successful, adopted at other beamlines as well.

I. Introduction

The development of new materials is crucial for innovation in today's world. However, traditional methods of materials discovery can be very slow, often relying on trial and error to reach the desired properties. In order to reduce the amount of time it takes for new materials to be discovered, machine learning models can be developed. These computational models would be able to predict the conditions needed during synthesis or treatment to reach the desired properties, vastly reducing the time it takes through regular trial and error methods. The caveat for computational models, however, is that the models need access to a lot of data and metadata about currently known and tested materials. Data sharing must be increased across the community for the models to be accurate or useful, thus laboratories must first increase the amount of data collected about samples for this to occur.

The National Synchrotron Light Source II (NSLS-II) at the Brookhaven National Laboratory (BNL) is home to many beamlines wherein users from across the country and around the world

come to test their samples. The synchrotron is a facility that sees enough traffic to give rise to a plenty of data collection. The current issue, however, is that the facility lacks infrastructure and a standard to allow users to provide metadata about their samples. Sample information is often limited to the name of the sample and chemical formula. In order to capture more useful information for machine learning models, more metadata is needed from samples.

The Computational Science Initiative at BNL aims to increase sample metadata collection through the development of a metadata schema. A metadata schema would allow users to give more information that they may know about their sample before arriving to perform experiments. The information can later be linked to the experimental data on a database located within an internal server. The users can then access this information across multiple visits using an Elastic Search interface.

II. Methods

To develop the sample metadata schema, Crystallographic Information File (CIF) format and NeXus format were studied. Both of these formats have standardized naming conventions, and the project was aimed at adopting and modifying terms to be used for the schema at NSLS-II. The schema needed to be simple and easy to use, since the information would be relying on user input. Therefore, only what was considered essential and easy information was included for the initial metadata schema. Modifications could be made as the project continues into its pilot phase, which will be explained in depth later on.

The metadata schema is aimed at only capturing sample metadata, not experimental conditions, which is captured already using the in house BlueSky data acquisition system. Another important factor to consider during the developmental stage is that many users do not know much information about their sample, oftentimes this is the reason they come to the laboratory, so that they may learn more about what their sample is. Therefore, many of the fields must be optional. On the other end, a major concern has been that even with a scientist that knows more information about their sample, they may not be incentivized to complete the entire form. If the form is too long, for example, many would stop reading past the requirements and submit. Therefore, the form must be relatively short.

Once the initial schema was developed, infrastructure for users to input this information was still needed. For familiarity and ease-of-use, Google Forms and Google Sheets were chosen. The form would be sent out to users after their experiment is approved but before the timeslot, and hopefully well in advance before they even arrive. This will give the users plenty of time to respond and allow for the responses to be as accurate as possible, given what the user knows about their sample.

III. Results and Discussion

The metadata schema was developed to have the structure shown in Figure 1. The schema was developed in JavaScript Object Notation (JSON). JSON was chosen due to its validation capabilities and human-readable format. Other formats such as XML were considered due to its compatibility with many programs; however, JSON was ultimately chosen also because there was some infrastructure that NSLS-II had that could take JSON schemas.

The JSON schema was decided to be nested to make different subcategories more clear and human readable. The key name 'sample' was chosen to encompass everything as this is a sample metadata schema, and it is possible that in the future there may be other elements added that are not part of the sample. The key 'name' is simply the sample name, and this may be in any convention the user wishes to use to identify the sample. More specific material identifying names and formulas will be discussed and are located under 'constituents'. The next three key names are 'sample_group_PI', 'sample_maker', and 'collaborators'. The PI is referring to the principle investigator of the group who made the sample, if there is any, the sample maker refers to the individual who made the sample, and collaborators refer to collaborators to the sample maker. These fields were chosen to identify contact people for the origin and knowledge about the sample and how it was made, in case of emergencies. If a sample was purchased, then the company it was purchased from would be written under sample maker. The 'sample_prep_start_date' field refers to the date in which the sample began its preparation. The 'tags' field is meant to allow users to enter in their own tags for future reference, as

```
{
  "sample": {
    "name": "titanium dioxide",
    "sample_group_PI": "Eli Stavitski",
    "sample_maker": "Eli Stavitski",
    "collaborators": "Sabrina Hernandez",
    "sample_prep_start_date": "6/23/2018",
    "constituents": {
      "name": "titanium",
      "chemical_formula": "TiO2",
      "chemical_name_common": "null",
      "chemical_name_mineral": "anatase",
      "phase_state": "powder",
      "cif_url": "http://ruff.geo.arizona.edu/AMS/minerals/Anatase",
      "cif_database_id": "null",
    },
    "tags": "powder",
    "container": {
      "geometry": {
        "holder_type": "capillary",
        "diameter_mm": "1",
        "length_mm": "",
      }
    },
    "in_beam_constituents": {
      "name": "silicon dioxide",
      "description": "null",
      "chemical_formula": "SiO2",
      "chemical_name_common": "null",
      "chemical_name_mineral": "null",
      "sample_dilutant": "boron nitride",
    },
    "out_of_beam_constituents": {
      "name": "",
      "description": "",
      "chemical_formula": "",
      "chemical_name_common": "",
      "chemical_name_mineral": ""
    }
  }
}
```

Fig. 1. Developed JSON schema with example sample information entered.

users will later be able to access their sample information using the Elastic Search interface developed by the Computational Science Initiative.

The next section is under 'constituents', which includes 'name', 'chemical_formula', 'chemical_name_common', 'chemical_name_mineral', 'phase_state', 'cif_url', and 'cif_database_id'. Constituents is meant to refer to the material components. For example, a metal sample of nickel would only be comprised of one constituent, being nickel. However, some samples may be multicomponent systems, thus users must be able to list all the constituents that make up the sample. To denote multiple components are present, users will be asked to list all components in each field in the same order, separated by semicolons. Later, during the validation process, the strings containing semicolons separating components will be split to form lists. This method has a lot of current issues, such as mismatching component information if a user enters in information in different orders. However, the goal of this project is to lay the groundwork for the infrastructure to increase sample metadata acquisition. Therefore, during the early stages the process will be monitored by group members to ensure that information entered is correct. The chosen field names within the constituent section are basic information questions that most scientists would know about their sample. A common name refers to a name that a material might be commonly known as, but is not

Sample Metadata

Please complete this form with information about your sample. Separate tags with a SEMICOLON and NO SPACES.

* Required

sample name *
The name of the sample.
titanium dioxide

sample sample-group-PI
The principle investigator of the group making the sample.
Eli Stavitski

sample sample-maker *
The maker of the sample.
Eli Stavitski

Fig. 2. Google Form that users will complete with their sample information.

	B	C	D	E
1	sample name	sample sample-group-PI	sample sample-maker	sample collaborators
2	Nickel oxide	Eli Stavitski	Eli Stavitski	Sabrina Hernandez
3				
4				

Fig. 3. Corresponding Google spreadsheet from the Google Form the users will complete. The information from this spreadsheet is downloaded by a developed Python script.

the official or proper name. The phase state refers to the state the sample is in, such as powder or solution. The CIF URL and CIF database ID are fields that allow users to enter known crystallographic information, if the sample is crystalline. These fields were meant to replace any section on crystallography, due to the fact that the CIF format exists with predefined field name standards already in use. Thus, if the sample is crystalline and the user knows what the structure is, the user can enter either a link to the detailed information or a database ID.

The next section is all about the sample container. Oftentimes, the samples brought to NSLS-II are contained within or on some type of containers, including capillaries and wafers. It is important to capture the container information, as the beamlines may pick up signals from these containers, and knowing what the container is will help identify these signals during data analysis. The container has a geometry section, which describes the relevant geometric aspects of the container, such as the container type, length, and diameter. The other two sections chosen were in beam and out of beam container constituents. These two sections were chosen since oftentimes some parts of the container are intended to be within the range of the beam where signals are expected, but other parts may not be intended to be within the range of the beam, thus signals may not be expected. In these cases, it is important to still be aware of the existence of these container components, as these parts of the container often still shows up in beamline signals, and for future understanding of the experimental data, it is important to be able to identify where these signals are originating from. The field names within these two sections are identical to the sample constituent sections, aside from the removal of the CIF information and the addition of the sample dilutant. If a sample is in a solution form for the beamline, a sample dilutant is present and must be identified.

After the JSON schema was developed, it was important to

```

_id: Binary('GPI1Z5LpQDax8Y/HCACT+w==')
sample: Object
  container: Object
    out_of_beam_constituents: Object
      chemical_name_mineral: ""
      chemical_name_common: ""
      chemical_formula: ""
      description: ""
      name: ""
    in_beam_constituents: Object
      sample_dilutant: "boron nitride"
      chemical_name_mineral: "null"
      chemical_name_common: "null"
      chemical_formula: "SiO2"
      description: "null"
      name: "silicon dioxide"
    geometry: Object
      length_mm: ""
      diameter_mm: "1"
      holder_type: "capillary"
  constituents: Object
    cif_database_id: "null"
    cif_url: "http://rruff.geo.arizona.edu/AMS/minerals/Anatase"
    phase_state: "powder"
    chemical_name_mineral: "anatase"
    chemical_name_common: "null"
    chemical_formula: "TiO2"
    name: "titanium"
  tags: "powder"
  sample_prep_start_date: "6/23/2018"
  collaborators: "Sabrina Hernandez"
  sample_maker: "Eli Stavitski"
  sample_group_PI: "Eli Stavitski"
  name: "titanium dioxide"

```

Fig. 4. The example sample information as entered in MongoDB.

allow users to enter this information in a simple and easy way. Google Forms and Google Sheets were chosen due to familiarity and their user-friendly interfaces, shown in Figures 2 and 3. Only a few key fields were required, to allow flexibility as not all information would be known by the users about their samples. Upon submission, a Python script would download the information and convert the key value pairs into the nested JSON document format. The script would then validate the document against the developed schema for syntax errors or missing requirements. If the document was valid, it would then be uploaded to MongoDB on an internal server at NSLS-II, shown in Figure 4. The user would then be notified by email that the validation step was successful along with the information they inputted for their own records, shown in Figure 5. If the document was invalid, the user would be notified by email that they made an error, along with the error they made and the information they inputted so that they can make corrections and resubmit. Once the process is complete, the spreadsheet is cleared of all entries to ensure security of the sample information. After this, the only way to access entered information is from the database behind the firewall here at BNL.

The sample schema will be deployed at the ISS and XPD beamlines to test the success of the schema. Changes will be made as seen fit to adapt the schema to have the best possible outcomes. In the future, the project would ideally move away from Google Forms and spreadsheets, as these methods of capturing information are not dynamic. For example, for multi-component systems, users must list each component, separated by semicolons. Since Google Forms data is tabular, there is no method to make the form dynamic and have the capabilities for users to keep adding items. If the schema is moved to a site created for this purpose, the form can be made dynamic, allowing for easier data management.

IV. Conclusion

As a result of the project, a JSON schema was developed that will allow users to thoroughly describe their samples before their arrival to the BNL beamlines. By creating this infrastructure, NSLS-II can increase their sample metadata acquisition and link the metadata to the experimental results for use in future machine learning models. Although there are still issues that need to be faced, the current status of the project lays a foundation that can be built upon in the future.

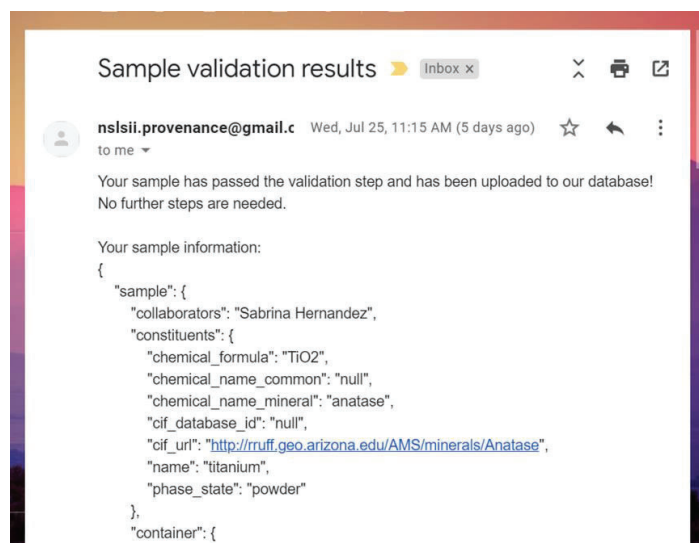


Fig. 5. An example email confirmation after the validation process is complete. This example shows the email for a valid entry.

V. Acknowledgements

I would like to acknowledge my mentor Line Pouchard for her guidance throughout the project, as well as Pavol Juhas, Eli Stavitski, Stuart Campbell, Huub Van Damel, Simon Billinge, and Christopher Wright for their contributions to this project. This project was supported in part by the Computational Science Initiative, the U.S. Department of Energy, Office of Science, Office of Workforce Development for Teachers and Scientists (WDTS) under the Science Undergraduate Laboratory Internships Program (SULI) at Brookhaven National Laboratory.

VI. References

- ¹ JOM (2016). 68, 2053-2064 doi:10.1007/s11837-016-2000-4
- ²International Tables for Crystallography (2006), G, 73-91 doi:10.1107/97809553602060000733
- ³. J. Appl. Cryst. (2015). 48, 301-305 doi:10.1107/S1600576714027575

Spectral and phenological drought assessment in common crops

Gwen Hilles

SUNY ESF Department of Environmental and Forest Biology

Angela Burnett

Brookhaven National Laboratory Department of Environmental and Climate Sciences

Abstract

The economy of growing any type of crop depends largely on the conditions which the harvest is subjected to during its growth period. Factors such as soil quality, water availability, disease incidence, and other environmental stressors determine the viability of biofuel and food crops of interest to the Department of Energy such as poplar, beans, zucchini, and peppers. Monitoring for problems and caring for these species will only become more complicated as the effects of climate change escalate. The remote sensing community seeks to alleviate the burden this creates by developing accurate sensing protocols to monitor changes within plants at the immediate level from afar. My work throughout the duration of my stay here at Brookhaven National Laboratory is devoted to collecting and analyzing spectral, physiological, biochemical, and gas exchange data as it pertains to drought stress in a variety of common crops. By interpreting and comparing the spectral feedback between droughted and sufficiently watered plants at an experimental scale, more accurate predictions can be made from the data gathered in the field. Data gathered using spectrometers, moisture probes, and LI-COR gas exchange machinery illuminates stark deficits in droughted plants when compared with their watered counterparts, in some cases before visible signs of drought are noted. Due to variation between species and the complex nature of drought stress, replicating this research is critically important to determine appropriate ranges for data before progressing to larger scales. Eventually, similar experimentation outside the glasshouse will be conducted and compared to these indices to ascertain the accumulation of error when assessing productivity and stress tolerance remotely. With proper development, this research will improve the way ecosystems and agricultural areas are studied, increase the accuracy and effectiveness of remotely monitoring environmental stress, and help pave the way towards a more sustainable future.

I. Introduction

My stay here at Brookhaven National Laboratory was spent in the company of the plant physiologists in the Terrestrial Ecosystem Science and Technology group. My research was a part of a larger series of experiments regarding spectral and physiological responses to drought in plants with the goal of developing a reliable way of predicting drought stress pre-emptively. The promise of spectroscopy as an indicator of stress and a method of remotely monitoring plants has its origins in early space exploration. The first satellite sent into orbit by NASA equipped with spectral monitoring equipment intended for remote sensing use was the Landsat I, with its MultiSpectral Scanner (NASA). Following this launch, the applications of spectral data as an indicator of plant condition were explored in earnest on the global

scale. With the rise of more accurate and accessible spectrometry technology comes the promise of improved remote monitoring.

The principle behind remote spectral sensing is that all matter releases a certain radiative frequency when exposed to electromagnetic radiation. In this case, this radiation was in the form of light from our probes. These reflectance measurements are unique to the object in question, and act as something of an energetic fingerprint. As shown in the provided figure below, reflectance traces for water, soil, and leaf material all look quite different, and rightfully so.

There are also notable differences between spectra for healthy and dying leaves, which is where my research comes in (GrindGIS). The goal of this experimentation is to develop a reliable way of determining plant stress pre-emptively according to differences between the reflectance of leaf material. However, due to the multitude of variables that factor into the expression of stress in plants, a concrete standard for detecting drought stress is not yet available, as this requires more in-depth measurements of various species and their physiological responses to drought.

II. Gas Exchange

Much of the work that my lab group does is in the Alaskan tundra, monitoring the effects of climate change on unique and

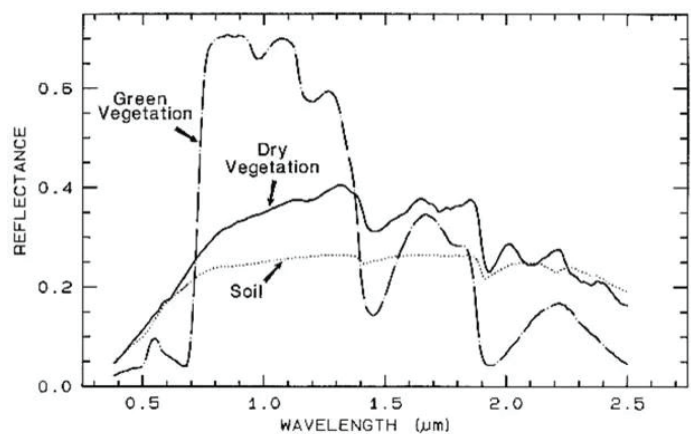


Fig. 1: Comparisons between reflectance of different substrates common to our drought experiment. (Academic Emporia)

vulnerable ecosystems in one of the most extreme environments on the planet. Much of this work is done with the help of LICOR gas exchange machinery, which can monitor a wide range of different measurements including photosynthetic assimilation of carbon, stomatal conductance, and respiratory rate within leaves. Although the constraints of this paper don't allow me to go into detail about the principles behind how the LICORs collect their data, I was able to learn about the inner workings of their machinery and the rationale behind the equations which govern their operation. The backbone of this follows basic assumptions about plant physiology that everyone with any experience in biology at all is aware of, but the detailed ways in which exceptions and complexities are accounted for in the machine's algorithms are impressive, to say the least.

Although these instruments went up to Alaska for most of the duration of my stay, they were available for the first three weeks of my internship, and I got the experience of calibrating these complicated machines, as well as collecting data on the glasshouse plants. Had the LI-CORs been available for the full duration of the experiment, the comparison between the data for the droughted and watered plants at the end of their lives would have been markedly different. The photosynthetic and stomatal conductance data would have been particularly useful to quantify when the leaves we were measuring were truly dead, but even without this data there is still a substantial amount of other data to analyze. As the collection of gas exchange data was effectively impossible for much of the experiment, the LICOR data is omitted here, as it is irrelevant to the discussion of the experiment.

III. Spectra, soil moisture, and supplementary data

Most of the data collected for this experiment was the spectral measurements at both the canopy and leaf levels each morning. This data was obtained through use of the PSR-3500 and related adapters and was accompanied by temperature readings for each measured area, as the ambient temperature of the leaf material also affects the stress levels shown in the spectra. Over the course of the experiment, it appeared that the droughted plants almost always exhibited higher temperature readings than the watered plants, in accordance with their response to stress. Our drought was quantified by daily soil moisture content measurements, collected with the HydroSense II probe from Fisher Scientific at 4pm each weekday. Ideally, the net moisture content of the soil would

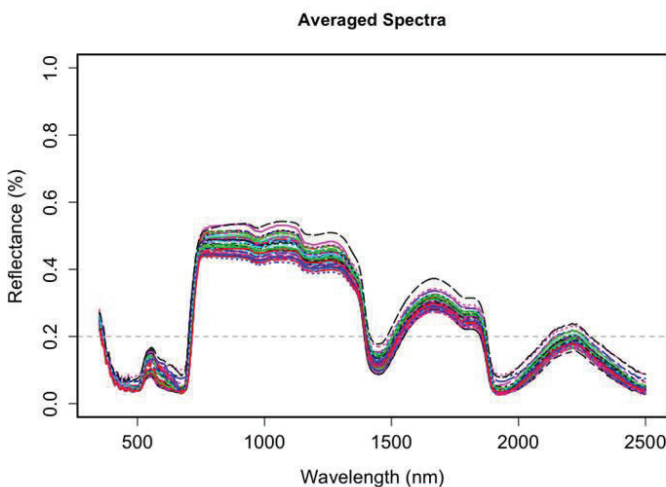


Fig. 2: Experimental averaged spectra.

be measured by measuring the entire weight of each pot and tracking the net loss of water mass over time to avoid error or selectivity in the area in which soil moisture was sampled by the probe. However, for the sake of time and simplicity, the HydroSense was sufficient, and the data produced was in accordance with expected trends for drought.

In addition to the spectral and soil moisture content measurements, other phenological measurements relevant to plant function in response to environmental stress were recorded. These included the tracking of height, branch production, leaf water potential, and biochemical content of the plants as the treatment progressed. The results from each of these categories were compared to the spectral feedback and helped to contextualize the data from our drought. Pictures of the plants were also taken each day to show the visual progression of the drought. In a theoretical application of this research, the goal would be to ascertain the drought status of the plants without the help of additional physiological observations. However, for the purposes of establishing a baseline for detection of drought in a single species, additional markers for what denotes the point at which a plant is considered "dead" are useful. The soil moisture content data showed uniform drops in the droughted treatments for all species, which is to be expected in a hot greenhouse. However, not all plants responded to the drought as quickly as others, which is evident in their spectral readings.

An example spectrum for some of our poplar leaves is shown juxtaposed with an informational graphic in figures 2 & 3.

These particular readings were taken from healthy leaves, as evident in their water peaks, high reflectance, and high green peak in its trace. As the leaves lose their vigor, they uniformly decrease in percent reflectance, and the traces of their visible pigmentation become broader and sloppier. After collecting data for a few weeks it's not difficult to get a sense of what constitutes a "good spec" and a "bad spec," and typically these denotations are directly correlated with the watered and droughted treatments, respectively. However, this was not always the case, and over the course of the experiment it became evident that if a uniform index for drought detection in plants is to be developed, there must be provisions to account for error in the form of poor reflectance values which are not due to plant stress. Readings which are abnormal due to either instrument inaccuracy, extenuous greenhouse conditions, or less-than-optimal collection conditions can easily skew a data set for a watered plant to look like a droughted plant, potentially

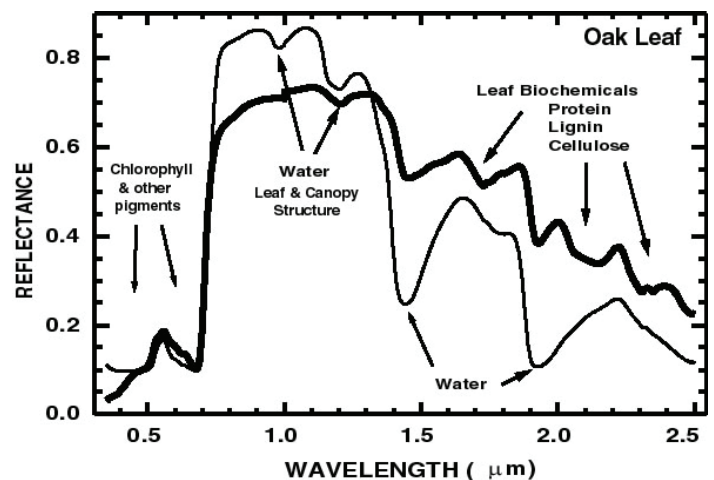


Fig. 3: Spectra with labelled peaks.

invalidating results, and necessitating precautionary measures. In hopes of creating a surveying technique which is both accurate and not too labor intensive, all facets of the data collection must be considered and accounted for.

IV. Future Applications and Summary

Looking forward, I believe that the “real-world” impact of this research will benefit not only the general scientific community but the agricultural industry as well. The capacity to mechanize drought detection at a level with greater predictive accuracy than the average person’s observations is not yet a reality, but with further species-level studies and improved instrumentation is a distinct possibility in the near future. The power of spectral remote sensing has historically always been recognized, but not always been the most accessible or relevant to industry or the general public. With recent advances in spectrometry equipment and research in adjacent fields, reliable remote sensing of stress in plants is just a few steps away. If a few different indices based on the underlying biology of plants within different categories of drought response are developed, this would ameliorate some of the complications with pinpointing stress thresholds based on spectra alone. These indices would depend on similar experimen-

tation with a broad variety of species, but the resulting data would be immensely useful.

My time here at Brookhaven National Lab has been a pleasure, and I’ve expanded my scientific horizons immensely. I’d like to thank everyone who’s helped me along my journey, particularly my mentor and my fellow interns, for their boundless passion and knowledge, as well as their support.

V. Citations

NASA, NASA, landsat.gsfc.nasa.gov/landsat-1/.

“Spectral Signature of Green Vegetation Compared to Dry.”

Academic.emporia.edu, Academic Emporia, academic.emporia.edu.

“Vegetation Spectral Signature Cheat Sheet.” *Grind GIS-GIS and Remote Sensing Blogs, Articles, Tutorials*, 16 May 2017, grindgis.com/remote-sensing/vegetation-spectral-signature-cheat-sheet.

“USGS Spectroscopy Lab - Mapping Biology and Mineralogy in Yellowstone NP.” *USGS Spectroscopy Lab: Spectroscopy of Rocks and Minerals, and Principles of Spectroscopy*, speclab.cr.usgs.gov/national.parks/Yellowstone/ynppaper.html.

Developing a monitoring tool for tracking changes in critical control values at NSLS-II

Jeremy Hirsch

Applied Mathematics & Statistics, Stony Brook University, Stony Brook, NY 11794

Anton Derbenev

Photon Sciences, Brookhaven National Laboratory, Upton, NY 11973

Abstract

The National Synchrotron Light Source II (NSLS-II) at Brookhaven National Laboratory (BNL) has a control system built on the Experimental Physics and Industrial Control System (EPICS) infrastructure.¹ Machine values such as magnet setpoints and motor positions are generally abstracted in software as EPICS Process Variables (PVs). The goal of this project is twofold: first, to create a flexible system monitoring application which tracks and reports changes in PV values in an easily accessible form; and second, to introduce the monitoring application into the control room of the NSLS-II with the potential that it can be utilized in other facilities which also use EPICS. Important functions of the monitoring tool include addition (and deletion) of monitored PVs and their expected values, backing up this configuration in a database, live-tracking of PV values, keeping and plotting a history of changes, showing and alerting on the status of PVs, allowing restoration of live values to expected values, and allowing updating of expected values to live values. The tool is a Python 3.6 application which comes with a clear and simple graphical user interface (GUI) based on the PyQt5 framework. Qt Designer and the pyuic conversion tool were used to design the GUI and import it to the python program. The tool uses Caproto to interface with IOCs in EPICS infrastructure,² SQLite to back up configurations to a database, and Matplotlib to plot the PV history. Git and GitLab service are used for version control. The monitoring tool has been designed to reduce the time required to detect and troubleshoot system issues, and thereby contribute to critical NSLS-II deliverables: reduce machine downtime and increase beam availability for facility users.

I. Introduction

The NSLS-II control system is built on EPICS, and input-output controllers (IOCs) are created within this infrastructure. IOCs are applications which interface with hardware and other IOCs, as a layer between high level user tools and the machine. PVs are facility control values abstracted into software and provided by IOCs. EPICS has grown a moderately sized community of users since its 1994 release, and this collaboration has developed a variety of tools for working with PVs. These tools fill applicable needs for EPICS users, such as value visualization, data collection, processing, archiving, alarm display and announcement. One such tool is the Archiver Appliance, an archiver for PVs that tracks value changes and is used to work with historical data. The Archiver Appliance has features such as clustering appliances, fast storage, a management interface, and various customization abilities.³ MASAR is another tool with a GUI interface that takes snapshots of value sets, recording data such as a value, time stamp, connection status, alarm status, and alarm severity for

a particular time, supporting all scalar and waveform PV types.⁴ The Channel Access Put Log is one more relevant tool, which logs external writings, known as puts, and is used through its web interface.⁵ Simply capturing all this data, however, is not enough for comprehensive and proactive monitoring. Thus there exists a niche for a monitoring tool in which some of the features of existing tools could be combined and new ones added. Important functions of the monitoring tool would include addition (and deletion) of monitored PVs and their expected values, backing up this configuration in a database, live-tracking of PV values, keeping and plotting a history of changes, showing and alerting on the status of PVs, allowing restoration of live values to expected values, and allowing updating of expected values to live values. These functions were all completed and implemented into a user-friendly GUI.

II. Methods

The application was programmed in an object-oriented manner in Python 3.6, with a GUI based on the PyQt5 framework. Consideration was given towards readability of the code and ease of improvement. Qt Designer and the pyuic conversion tool were used to design the visual aspect of the GUI and import it to the python program. The application uses Caproto, a recently created Channel Access protocol library written in pure python, to interface with IOCs in EPICS infrastructure. The application also uses SQLite to automatically save configurations to a local database, and Matplotlib to plot the PV history. Git and GitLab service are used for version control. The application was set up to be run on Debian Linux operating systems in the NSLS-II production environment and can be opened by running a bash script from the terminal.

III. Results

The monitoring tool GUI consists of eight windows: the main window, the add PV dialog, the results dialog, the advanced dialog, the plot history dialog, the database configuration dialog, ubiquitous confirmation dialogs, and an about dialog. All windows have a simplistic and approachable design, which is friendly for new users and supports resizing. These windows are also all properly configured to work with resizing.

All the elements of the main window shown in Figure 1 are fully functional and update in realtime. The 'File' and 'Help' menus allow the user to quit the application or open the about dialog, respectively in their drop-downs. The 'Add PV(s)', 'Advanced', 'DB Configuration', and 'History' buttons open their respective dialogs. The 'Save' button sets the expected value to the current live value of a PV, and updates the database. The 'Restore' button performs a write to a PV and sets it to the expected value (when possible). The 'Delete' button opens up a confirmation dialog in which the user can choose to delete the PV from

the application configuration or cancel the action, and a choice to delete the PV will also remove the PV from the local database. The PV table updates in realtime to reflect the changes in live value and current alarm status. Possible alarm states are magenta, red, yellow, and green alerts. Magenta signifies a disconnected PV, red signifies that the live value and expected value of a PV do not match, yellow signifies that there had been some issue in the past, such as the live value of a PV changing to not equal the expected value, but that it had reverted back, and green signifies no issues with the PV. The status summary bar on the bottom of the window also updates on any change in the status of the PVs and on addition or deletion of PVs. In the case that there are many PVs on the table (as there would be in real use of the tool), the filter box is available to only display PVs with names matching a user-provided regular expression. The table also supports sorting by any column including the alarm level, which allows alarming PVs to appear on the top for a user's attention. The 'Difference' also updates in realtime and will display "N/a" if the live value and expected value cannot be subtracted, i.e. due to ambiguous value types such as string or waveform. Lastly, the expected value can be easily changed by clicking on the expected value item of the specific PV and editing the value within.

The PV adder dialog shown in Figure 2 below, is used to add PVs to the table (and database) by following the instructions

Status	PV Name	Live Val	Expected Val	Difference	Save	Restore	Plot History	Delete
216	SR-C01-TS(EVR-D1A-DiyGen 0)Evt:Trigo-SP	32	32.0	0.0	Save	Restore	History	Delete
217	SR-C01-TS(EVR-D1A-DiyGen 1)Evt:Trigo-SP	46	46.0	0.0	Save	Restore	History	Delete
218	SR-C01-TS(EVR-D1A-DiyGen 2)Evt:Trigo-SP	32	32.0	0.0	Save	Restore	History	Delete
219	SR-C01-TS(EVR-D1A-DiyGen 8)Evt:Trigo-SP	35	35.0	0.0	Save	Restore	History	Delete
220	SR-C01-TS(EVR-D1A-DiyGen 9)Evt:Trigo-SP	31	31.0	0.0	Save	Restore	History	Delete
221	SR-C03-TS(EVR-D1A-DiyGen 0)Evt:Trigo-SP	32	32.0	0.0	Save	Restore	History	Delete
222	SR-C03-TS(EVR-D1A-DiyGen 1)Evt:Trigo-SP	46	46.0	0.0	Save	Restore	History	Delete
223	SR-C03-TS(EVR-D1A-DiyGen 2)Evt:Trigo-SP	32	32.0	0.0	Save	Restore	History	Delete
224	SR-C03-TS(EVR-D1A-DiyGen 9)Evt:Trigo-SP	31	31.0	0.0	Save	Restore	History	Delete
225	SR-C30-TS(EVR-Q2A-DiyGen 0)Evt:Trigo-SP	32	32.0	0.0	Save	Restore	History	Delete
226	SR-C30-TS(EVR-Q2A-DiyGen 1)Evt:Trigo-SP	47	47.0	0.0	Save	Restore	History	Delete
227	SR-C30-TS(EVR-Q2A-DiyGen 2)Evt:Trigo-SP	66	66.0	0.0	Save	Restore	History	Delete
228	SR-C30-TS(EVR-Q2A-DiyGen 3)Evt:Trigo-SP	66	12	54.0	Save	Restore	History	Delete
229	SR-C30-TS(EVR-Q2A-DiyGen 4)Evt:Trigo-SP	35	35.0	0.0	Save	Restore	History	Delete
230	SR-C30-TS(EVR-Q2A-DiyGen 5)Evt:Trigo-SP	35	35	0.0	Save	Restore	History	Delete
231	SR-C30-TS(EVR-Q2A-DiyGen 6)Evt:Trigo-SP	32	32.0	0.0	Save	Restore	History	Delete
232	SR-C30-TS(EVR-Q2A-DiyGen 7)Evt:Trigo-SP	66	66.0	0.0	Save	Restore	History	Delete
233	SR-C30-TS(EVR-Q2A-DiyGen 8)Evt:Trigo-SP	47	47.0	0.0	Save	Restore	History	Delete
234	SR-C30-TS(EVR-Q2A-DiyGen 9)Evt:Trigo-SP	46	46.0	0.0	Save	Restore	History	Delete
235	SR-C30-TS(EVR-666-DiyGen 3)Evt:Trigo-SP	N/a	13	N/a	Save	Restore	History	Delete

Total Pvs: 235, Red Alerts: 1, Yellow Alerts: 1, OK: 232, Disconnected: 1

Figure 1. Main monitor window

Figure 2. PV adder dialog

which are displayed for user reference upon opening the dialog. The results dialog shown in Figure 3 below is an example of the adder operation summary one would see upon adding a small list of PVs. The list of PVs is parsed and any improperly formatted or repeated PVs are skipped over, while the rest of the PVs are added to the table, with the results of the processing clearly displayed for the user to see and acknowledge.

The advanced options dialog shown in Figure 4 performs the more powerful operations. These options operate on all PVs which are not filtered out and use batching techniques to keep time costs of performing operations on possibly hundreds or thousands of PVs low. Due to the potentially dangerous nature of these operations (a database could have thousands of PVs and their expected values deleted in a second), they all come with confirmation dialogs and should be used carefully.

The plot dialog shown in Figure 5 displays a history of up to a hundred PV value changes and disconnects events. The plot updates as new PV values arrive, with disconnect events shown as purple points and normal changes as black points. The tool bar directly below the plot allows the user to manipulate the graph and save a screenshot of the plot if so desired. Additionally the user can choose to clear the history from this dialog with the 'Clear History' button.

Figure 3. Results dialog

Figure 4. Advanced options dialog

The database configuration dialog shown in Figure 6 can be used to switch between existing local databases or to create a new database. Upon opening a database file through this dialog the table is cleared and all connections to PVs from the last database are closed. New connections are then established and the table is populated with PV entries according to the configuration being opened. If a new configuration is created a blank table will be displayed. If the user doesn't have write permissions to the accessed database file, they will be alerted that it is a read-only configuration and that certain capabilities will be disabled, for example adding or deleting PVs. Lastly whenever a database is opened the tool stores the location of the database in a user-specific hidden cache file so that the user can continue their work with the last accessed configuration.

IV. Conclusions and Further Work

The application is fully functional, was tested in the NSLS-II control room, and will become an expert tool for tracking the status of PVs. Additionally, configurations were created to track critical settings of the NSLS-II timing system. There are several major functional design capabilities that could be added to this tool, such as the ability to switch to an archive data mode where

historical values would be retrieved from the Archiver Appliance instead of retrieving live values, waveform and ENUM PV support, logging of tool operations, and the creation of Olog entries on certain actions. Additionally, there are already some user requested improvements such as generating audio alarms in addition to the visual alarms, increasing the visibility of the status sum bar by increasing the size and potentially adding color, and visually disabling buttons when looking at a read-only database rather than just functionally disabling them. While these would all greatly improve the monitoring application, the base project is now complete and fulfills its purpose.

V. References

- ¹Experimental Physics and Industrial Control System. <<https://epics.anl.gov/>>
- ²Daniel, Allan. Caproto. <<https://nsls-ii.github.io/caproto/index.html>>
- ³The EPICS Archiver Appliance. <https://slacmshankar.github.io/epicsarchiver_docs/details.html>
- ⁴Guobao, Shen. MASAR Service. <<https://epics.anl.gov/meetings/2013-10/3%20-%20Other%20Services/4%20-%20MASAR%20Service.pdf>>
- ⁴Ben, Franksen. EPICS CaPutLog Module. <<https://www-csr.bessy.de/control/SoftDist/caPutLog/>>

VI. Acknowledgements

This project was supported in part by the U.S. Department of Energy, Office of Science, Office of Workforce Development for Teachers and Scientists (WDTS) under the Science Undergraduate Laboratory Internships Program (SULI) .

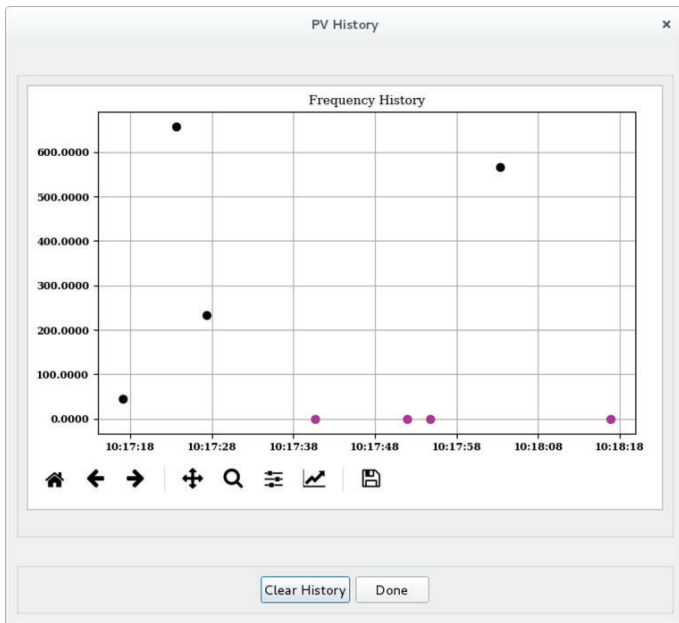


Figure 5. PV History dialog

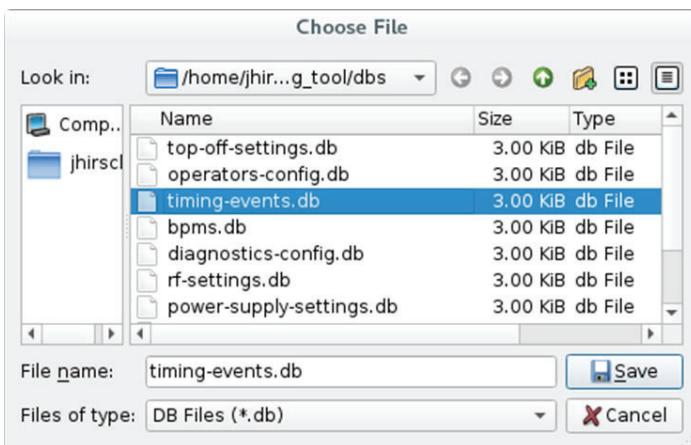


Figure 6. Database configurations dialog

Magnetic field measurements of the production Nb₃Sn quadrupole for the High Luminosity Large Hadron Collider Upgrade Program

B.D Hunt

University of Illinois Urbana-Champaign Urbana, IL 61801

J. Rowe

California State University Sacramento Sacramento, CA 95819

H.C Lo

Stony Brook University Stony Brook, NY 11794

H. Song

Brookhaven National Laboratory Upton, NY 11973

The Large Hadron Collider (LHC) High Luminosity upgrade (Hi LUMI) program requires the development of a new series of Nb₃Sn nal focusing superconducting quadrupole magnets, called MQXF, to increase the peak integrated luminosity of the LHC, a critical step in exploring physics beyond the standard model. The Super-conducting Magnet Division at Brookhaven National Laboratory (BNL) has partnered with Fermi National Accelerator Laboratory (FNAL) and Lawrence Berkeley National Laboratory (LBNL) in the Large Hadron Collider Accelerator Research Program (LARP) currently the Accelerator Upgrade Program supported by US DOE, to develop and test these magnets. Magnetic field characterization of MQXFAP2, the second production prototype constructed at LBNL, will be conducted at BNL using the LHC accelerator Upgrade Program (LARP) PCB harmonic coil developed at FNAL. Accurate field characterization of this magnet is critical for accelerator operation which now requires field accuracy to be within 10⁻⁴. In support of the magnetic measurement systems, we designed and implemented control systems and safety features for the AUP vertical transport motor using LabVIEW. We are also designing a method for transferring control of the magnetic measurement coils from HTBasic into a separate LabVIEW program, and to use this program to perform data analysis on the field harmonics. As a result, we have gained significant experience with National Instruments LabVIEW software. In addition, we have gained considerable knowledge about magnetic field measurements using a variety of instruments and received training in electronic instrumentation, design, and analysis.

I. INTRODUCTION

The Hi-LUMI upgrade, started in 2018, aims to increase the peak energy of the LHC to the 11-14 TeV range and the luminosity to 1 10³⁴cm²s⁻¹ by 2025. To reach this new energy, a series of 11-12 Tesla superconducting magnets are being jointly developed as part of the US LARP program, currently the Accelerator Upgrade Program (AUP) supported by US DOE. In collaboration with FNAL and LBNL, BNL has begun magnetic field harmonic measurement of the Nb₃Sn low-β focusing quadrupole magnet called MQXFAP2 the second full-length prototype magnet. Accurate field shape measurement is critical to modern accelerator applications which now require field shape to be within ≈10⁻⁴

units of accuracy. Achieving a resolution greater than 10⁻⁴ units is a challenge best addressed with the use of a harmonic coil system, which when implemented properly, allows for a resolution of greater than 10⁻⁵ units¹. In collaboration with BNL, FNAL has developed a PCB harmonic coil, the LARP harmonic coil, for the measurement of the prototype MQXF magnets.

II. HARMONIC COIL THEORY OF OPERATION

A rotating coil, when in the presence of a magnetic field, measures the azimuthal variation of the intercepted flux². The induced voltage in the coil, as described by Faraday's Law, is dependent on the coil geometry and the applied magnetic field.

$$V = -\frac{d\Phi_B}{dt} \quad (1)$$

Where

$$\Phi_B = \oint \vec{B} \cdot \vec{da} \quad (2)$$

Harmonic coefficients are related to the azimuthal field variations. With an exact knowledge of coil geometry, harmonic coefficients can be determined through Fourier analysis of the induced voltage signal².

A. Derivation of Harmonic Coefficients

The magnetic induction is given by:

$$\vec{B} = \mu_0(\vec{M} + \vec{H}) \quad (3)$$

Where M is the magnetization, and H is the magnetic field and $\mu_0 = 4\pi \times 10^{-7}$. In the aperture of a magnetic, in other words free space, $M = 0$. Consequently:

$$\vec{B} = \mu_0\vec{H} \quad (4)$$

and

$$\vec{\nabla} \times \vec{H} = 0 \Rightarrow \vec{\nabla} \times \vec{B} = 0 \quad (5)$$

The magnetic induction can now be described as the gradient of a magnetic scalar potential Φ_m . Combining the magnetic scalar potential with $\vec{\nabla} \cdot \vec{B} = 0$ we need Laplace's equation for the magnetic scalar potential:

$$\nabla^2 \Phi_m = 0 \quad (6)$$

Choosing a cylindrical coordinate system where the Z-axis is along the length of the magnet's mechanical axis, the origin located at the center of the magnet, and assuming no Z-dependence in the scalar potential⁵, the radial and azimuthal harmonic coefficients

describing a two dimensional current free region can be written as:

$$B_r(r, \theta) = \sum_{n=1}^{\infty} C(n) \left(\frac{r}{R_{ref}} \right)^{n-1} \sin[n(\theta - \alpha_n)] \quad (7)$$

$$B_\theta(r, \theta) = \sum_{n=1}^{\infty} C(n) \left(\frac{r}{R_{ref}} \right)^{n-1} \cos[n(\theta - \alpha_n)] \quad (8)$$

$C(n)$ and α_n are constants, where R_{ref} is an arbitrary reference radius³. Typically R_{ref} is chosen to be within 50 – 70% of the magnet aperture¹.

B. Induced Voltage in Radial and Tangential Coils

The orientation of a harmonic coil determines its sensitivity to the radial or azimuthal components of the field¹. The radial harmonic coil, termed for a at loop of wire coinciding with the radial plane, is sensitive to the azimuthal component of the magnetic field. Consider the radial coil, shown in Fig 1. The magnetic flux in the radial coil will be:

$$\Phi_r(\theta) = NS \int_{R_1}^{R_2} B_\theta(r, \theta) dr \quad (9)$$

Or from equation 7,

$$\Phi_r(\theta) = NS \int_{R_1}^{R_2} \sum_{n=1}^{\infty} C(n) \left(\frac{r}{R_{ref}} \right)^{n-1} \cos[n(\theta - \alpha_n)] dr \quad (10)$$

Here N is equal to the number of turns of the coil and S is the length of the coil. After evaluating the integral, the equation for the induced flux in a radial harmonic coil simplifies to:

$$\Phi_r(\theta) = \sum_{n=1}^{\infty} \frac{NSR_{ref}}{n} \left[\left(\frac{R_2}{R_{ref}} \right)^n - \left(\frac{R_1}{R_{ref}} \right)^n \right] C(n) \cos(n\theta - n\alpha_n) \quad (11)$$

If the radial coil is rotating at a constant velocity ω and at time $t = 0$ $\theta = \delta$ then $\Phi_r(\theta)$ may be written as $\Phi_r(t)$:

$$\Phi_r(t) = \sum_{n=1}^{\infty} \frac{NSR_{ref}}{n} \left[\left(\frac{R_2}{R_{ref}} \right)^n - \left(\frac{R_1}{R_{ref}} \right)^n \right] C(n) \cos(n\omega t + n\delta - n\alpha_n) \quad (12)$$

From equations 1:

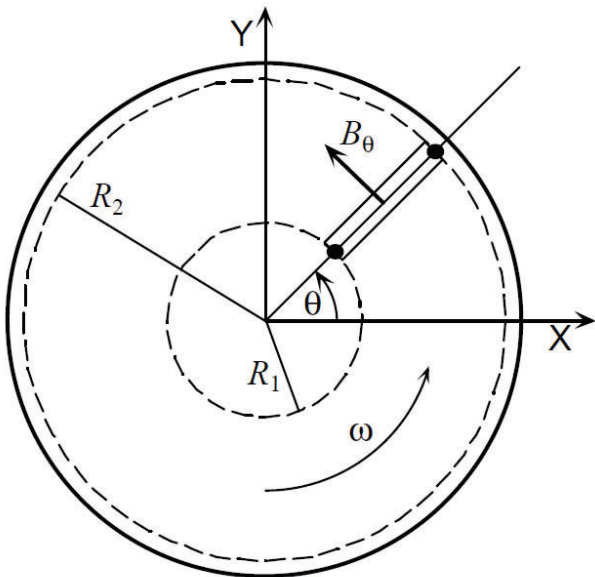


FIG. 1. Cross Section of a Radial Coil²

$$V_{rad}(t) = \sum_{n=1}^{\infty} NSR_{ref} \omega \left[\left(\frac{R_2}{R_{ref}} \right)^n - \left(\frac{R_1}{R_{ref}} \right)^n \right] C(n) \sin(n\omega t + n\delta - n\alpha_n) \quad (13)$$

Providing the geometric parameters of the coils are known, Fourier analysis of this voltage signal will give the amplitude of the harmonics $C(n)$, and the phase α_n ². For pure magnets -- i. e., an ideal dipole, quadrupole, etc. -- the only harmonic term present will be the $2n$ -pole term². All fabricated magnets will have extraneous harmonic terms from construction errors and deformities⁴. For high precision measurements, such as measuring the magnetic field for accelerator magnets, the angular velocity introduces a chance for large measurement error. Slight deviations in the angular velocity can lead to large distortions in the signal and as a result create spurious harmonics. The typical solution to this problem is the use of a voltage integrator². The integrated voltage for a radial coil is:

$$\int V_r(t) dt = - \sum_{n=1}^{\infty} \frac{NSR_{ref}}{n} \left[\left(\frac{R_2}{R_{ref}} \right)^n - \left(\frac{R_1}{R_{ref}} \right)^n \right] C(n) \cos(n\theta - n\alpha_n) \quad (14)$$

The tangential harmonic coil has a loop of wire normal to the radial vector from the rotation axis to the coil's center as seen in Fig 2. The tangential coil is sensitive to the radial component of the magnetic field. The magnetic flux in a tangential coil at radius R_c and angle θ is:

$$\Phi_{tang} = NS \int_{\theta - \frac{\Delta}{2}}^{\theta + \frac{\Delta}{2}} B_r(R_c, \theta) d\theta \quad (15)$$

Or from equation 8:

$$\Phi_{tang}(t) = \sum_{n=1}^{\infty} \frac{2NSR_{ref}}{n} \left(\frac{R_c}{R_{ref}} \right)^n \sin\left(\frac{n\Delta}{2}\right) C(n) \sin(n\omega t + n\delta - n\alpha_n) \quad (16)$$

If the tangential coil is rotating at a constant angular velocity, ω and at time $t = 0$ $\theta = \delta$ then $V_{tang}(t)$ may be written as:

$$V_{tang}(t) = - \sum_{n=1}^{\infty} 2NSR_{ref} \omega \left(\frac{R_c}{R_{ref}} \right)^n \sin\left(\frac{n\Delta}{2}\right) C(n) \cos(n\omega t + n\delta - n\alpha_n) \quad (17)$$

As in the radial case $C(n)$ and n are found through Fourier analysis, and the integrated voltage is used to eliminate the error inducing angular velocity dependence². The integral induced volt-

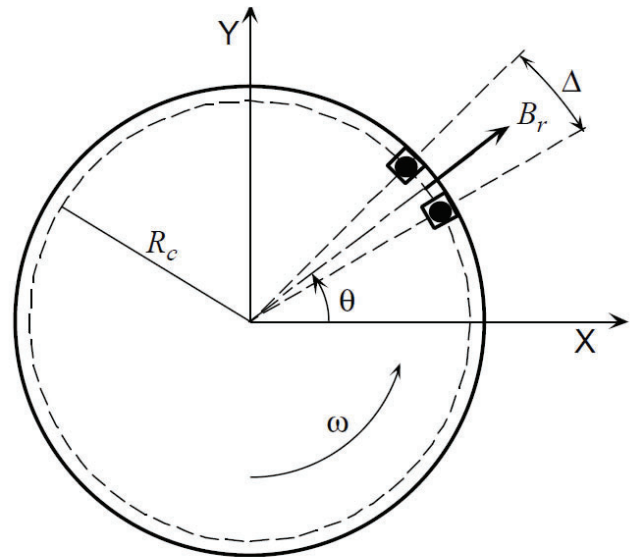


FIG. 2. Cross Section of a Tangential Coil²

age for a tangential coil is:

$$\int V_{tang}(t)dt = -\sum_{n=1}^{\infty} \frac{2NSR_{ref}}{n} \left(\frac{R_t}{R_{ref}}\right)^n \sin\left(\frac{n\Delta}{2}\right) C(n) \sin(n\theta - n\alpha_n) \quad (18)$$

III. METHODS AND MATERIALS

A vertical motor control system was developed to transport the magnetic measurement coils which allows for the use of an existing vertical cryogenic Dewar system. Our contributions to the project consisted of safety features, control systems, and communication between the various magnetic measurement devices. Fig. 3 describes the handshake method developed for communication between the vertical motor control systems and power supply controllers run using LabVIEW and the harmonic coil HTBasic control program which rotates the coil and performs the field measurements using the LARP harmonic coil. The communication features and control systems were designed to facilitate three different measurement plans to categorize the behavior of the magnet. The first is a z-scan measurement that will iterate over the entire length of the magnet from -2396.68 mm to +2396.68 mm in steps of 217.88 mm at the intermediate current of 6.0 kA and at the nominal current of 16.48 kA. Another z-scan will be performed to determine the ability of the magnet to deliver the gradient at peak current, scanning using the 110 mm coil from -853.6 mm to +853.6 mm in steps of 54.37 mm at the ultimate current of 17.89 kA. The second measurement type will perform an I-scan taking measurements from the center of the magnet while ramping up the current in steps of approximately 1kA up to the ultimate current. The third measurement will attempt to perform a dynamic

current scan by comparing the behavior of the field at differing ramp rates of 20 A/sec, 40 A/sec, and 80 A/sec.

The safety features we developed, as shown in Fig. 4, consist of a watchdog timer, AC phase controls, and limit switches to ensure that the system can be controlled safely and reliably from the control room through any of the three measurement plans. In addition to the control and communications features, we were also tasked with producing a LabVIEW program that can control the vertical motor control system using an Aerotech BM 130 motor and Ensemble controller. Fig. 5 shows the front panel of the LabVIEW program with user controls and visible safety features.

IV. RESULTS

As of this writing there have been no magnetic field measurements for the MQXFAP2 production magnet. However, testing of the vertical transport motor has yielded positive results. As seen in Fig 6, there was a high degree of consistency in the vertical transport motor with errors between measurement points <230µm. The relative position error of the Aerotech 3200 motor is $\approx 1.0 \times 10^{-1}\%$ per 217.88mm step -- well within the needed precision. Due to the reproducibility of the position error, it appears that the variations in position are from track deformities, which may be present only in the horizontal testing position. When the track is in the vertical position, it is expected the errors from the track deformity will be negligible.

V. CONCLUSION

The magnetic field measurement of MQXFAP2 is a critical component of the ongoing Hi-LUMI and AUP programs. While there have been no magnetic measurements at this time, initial

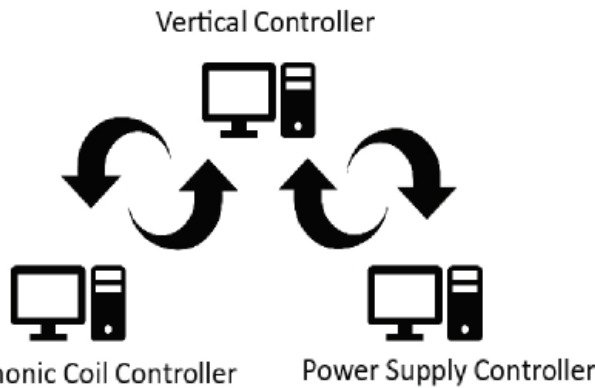


FIG. 3. Diagram of control systems between vertical controller and power supply in LabVIEW, and the harmonic coil controller in HT-Basic.

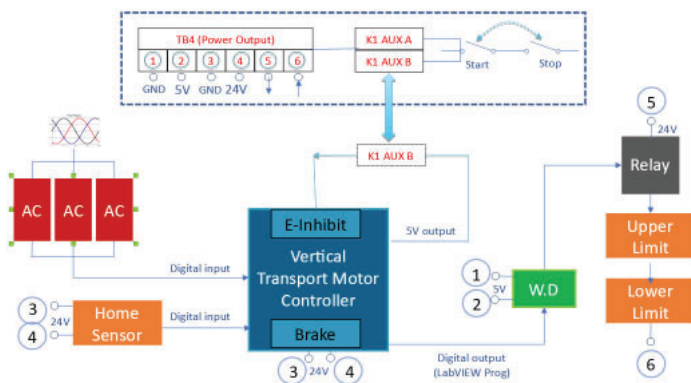


FIG. 4. Safety features implemented in the vertical motor control including a watchdog timer, AC phase controls, and limit switches.

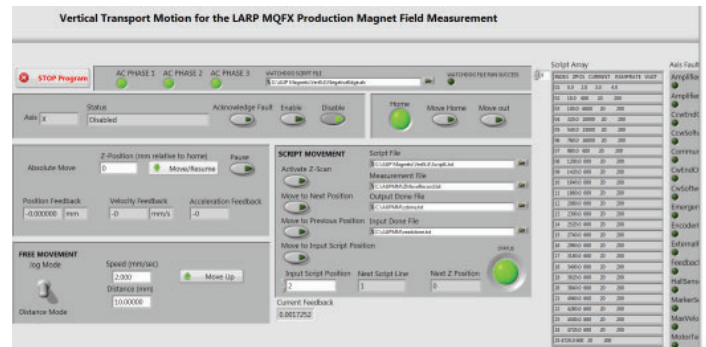


FIG. 5. LabVIEW front panel of vertical motor control system.

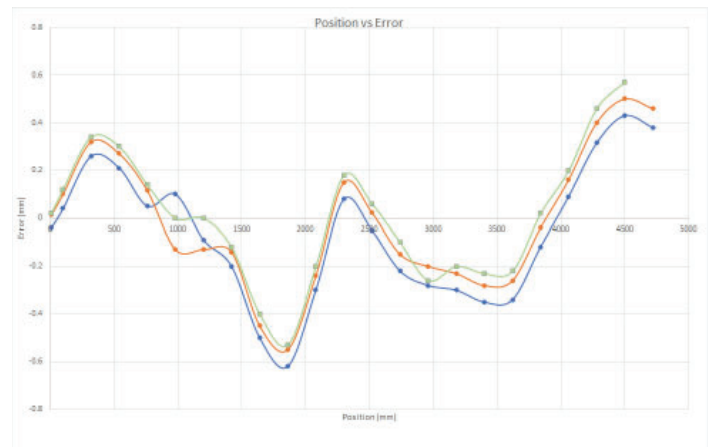


FIG. 6. Horizontal Zscan Data

warm measurements for the magnet are scheduled for late August 2018 and cold measurements likely in October of 2018. We hope that the support systems we have developed will allow for quick and accurate magnetic measurement with the LARP PCB rotating coil in the coming months and that we can continue to provide support for the Superconducting Magnet Division at BNL throughout the next generation upgrade for the LHC.

VI. ACKNOWLEDGMENTS

This project was supported in part by the U.S. Department of Energy, Office of Science, Office of Workforce Development for Teachers and Scientists (WDTS) under the Science Undergraduate Laboratory Internships Program (SULI).

VII. REFERENCES

- ¹K Jain, Animesh Harmonic Coils US Particle Accelerator School on Superconducting Accelerator Magnets June 23-27, 2003, Santa Barbara, California
- ²K Jain, Animesh Harmonic Coils Proc. CERN Accelerator School on Measurement and Alignment of Accelerator and Detector Magnets, April 11-17, 1997, Anacapri, Italy
- ³K Jain, Animesh Basic Theory of Magnets Proc. CERN Accelerator School on Measurement and Alignment of Accelerator and Detector Magnets, April 11-17, 1997, Anacapri, Italy
- ⁴Wackier, L (n.d) The Harmonic-Coil Method Geneva, CH: CERN
- ⁵A valid assumption if the length of the magnet is significantly greater than the aperture

Designing a two-channel data acquisition front-end board for a particle physics cosmic ray muon detector

Ramez Kaupak

Physics Department, Suffolk County Community College, Selden, NY 11784

David Jaffe

Physics Department, Brookhaven National Laboratory, Upton, NY 11973

Abstract

At Brookhaven National Laboratory our group mission is the construction of a cosmic ray muon detector array. Our goal is to construct and place standalone detectors across New York State schools and colleges for gathering information about subatomic particles showers over a vast area. Every detector consists of three main components: a polyvinyl toluene plastic scintillator plate, a photomultiplier tube, and a data acquisition board. My part of the project was to prototype and develop the data acquisition (DAQ) board. The DAQ front-end board is an embedded system which includes amplifiers, discriminators, analog signal shapers, peak detectors, logic gates and multivibrator integrated circuit chips. The circuit board ought to identify the time of arrival of the particle which caused an electric signal, the energy deposited in the detector, filter the noise and hold acquired data for a necessary period of time to communicate with the Arduino board. One possible approach to designing the board is to simulate the circuit in a specialized software, create a printable layout design, obtain a prototype board, test for errors and if the prototype works as expected, submit for automated printing. The major update that was made to the previous design includes a two-fold digital logic component. The new design increases the accuracy and reliability of the recorded data and will be used in a new detector apparatus. As a result of this work, I have added circuit's simulation software (LTSpice) to my repertoire of knowledge.

I. Introduction

The data acquisition front-end board is a circuit board that processes an electrical signal created by the part of the particle detector, a photomultiplier tube (PMT), executes the computing function of the muon detector and sends information for further processing. The proposed technical objectives of this circuit board included computation of the energy deposited by the particle in the detector, the noise filtering of the electrical signal, capability to adjust the threshold for a tested signal and ability to hold the acquired data for a necessary time to communicate with the rest of the data acquisition board unit, Arduino board. All the requirements were met including the additional objective of capability to adjust the duration of the accepting mode of the digital logic unit.

II. Process

The overall design schematic for the data acquisition front-end board is presented in Figure(1). Each OPA691 operational amplifier at the beginning of the system receives signal (sent from designated photomultiplier tube) through the Input_Connector_1_ACX1956-ND and Input_Connector_2_ACX1956-ND

connectors. This part of the data acquisition front-end board amplifies the input pulse using a non-inverting amplifier circuit with a fixed gain and sends it for further computations. After amplification, this signal is split into two branches, digital and analog. An analog branch starts with the Shaper (THS4271 voltage-feedback amplifier), which is a part of the Peak Detector circuit. The shaper subcircuit is used to stretch and invert the signal for the upcoming peak detector unit. The peak detector unit (THS4271 voltage-feedback amplifier) purpose is to measure the peak amplitude that occurs in a waveform and hold this value, using an RC circuit. The next circuit component after the peak detector is the buffer (LTC6268 current feedback amplifier). A buffer provides an electrical impedance transformation from one circuit to another. Because the only summed signal is the subject of interest the role of this buffer is preventing the signal from peak detector to be affected by currents that the following component, the adder, may produce. The adder subcircuit takes in the two signals from their respective buffers and sums their averages, generating one output signal. It has a gain of 1 and does not invert the output signal.

A digital signal branch of the circuit starts with the discriminator (LT1711 rail-to-rail comparator). This sub-circuit is used to set a lower limit on the amplitude of the signal, this is implemented to filter the noise of the photomultiplier tube and increase the reliability of the data. The discriminator unit creates a square wave of an adjustable width and sends it to a coincidence logic unit. The and gate is a simple digital logic unit that computes logical coincidence. The and gate unit, working in conjunction with two discriminator units performs the processing power of the circuit board. This subcircuit computes whether the data should or should not be saved and stored. Only if the output of the digital branch is positive, calculated results of the analog branch will be saved. If none or not all inputs to the and gate are positive, low output results (0V) and no data will be collected by the data acquisition board. The next stage in the circuit is two monostable multivibrators. These integrated circuit components fulfill an objective of creating a time delay between digital and analog branches of the electric circuit. For the data acquisition board to operate correctly a digital signal of the circuit must be delayed due to the fact that an analog branch of the circuit requires approximately 80ns for computations. The first monostable multivibrator delays the incoming digital signal by 155ns and the second monostable multivibrator dictates the moment when the sample and hold unit must start sampling the signal from the adder and provides 250ns to do so. The 155ns time delay is designated to provide enough time for the analog signal to stabilize at the adder output node. In the end, recorded adder output value will be stored on the sample and hold unit until the Arduino board reads it and sends a discharging signal back to the data acquisition board.

III. Discharge mechanism.

Once the Arduino (Arduino mega 2560) board records the analog value on the sample and hold chip, it generates a pulse of 6us and 5V and sends it to the discharge mechanism (BSS138). The short pulse activates the MOSFET (metal-oxide-semiconductor-field-effect transistor) transistor, allowing the peak detector subcircuit to discharge and therefore making the whole system ready for the next signal.

IV. Progress

A design and simulation stages were completed utilizing the LTspice XVII, a freeware computer software implementing a SPICE simulator of electronic circuits, produced by semiconductor manufacturer Linear Technology. Altium, PC-based electronics design software for engineers will be used to create Gerber files (PCB fabrication data files), which later will be sent to a manufacturer for printing.

V. Conclusions

Simulating the circuit board, I used models of the real-world circuit components available on the market. Although the work was theoretical, a big progress in designing the schematics of the board was accomplished. The next step towards the goal of completing the circuit is to transfer the circuit schematics to another software for layout and prototype printing.

VI. References

This project was supported in part by the U.S. Department of Energy, Office of Science, Office of Workforce Development for Teachers and Scientists (WDTS) under the Community College Internships Program (CCI). I would like to especially thank my mentor David Jaffe. Also, a special thanks to my collaborators Raul Luiz Armendariz (QCC) and Aiwu Zhang (BNL), to instructors: Corey Stalerman (QCC), Helio Takai(BNL) and engineers: Steve Boose (BNL), who helped designing the circuit, Emil Zitvogel(BNL) and Marshall Maggipinto(BNL).

VII. Appendix

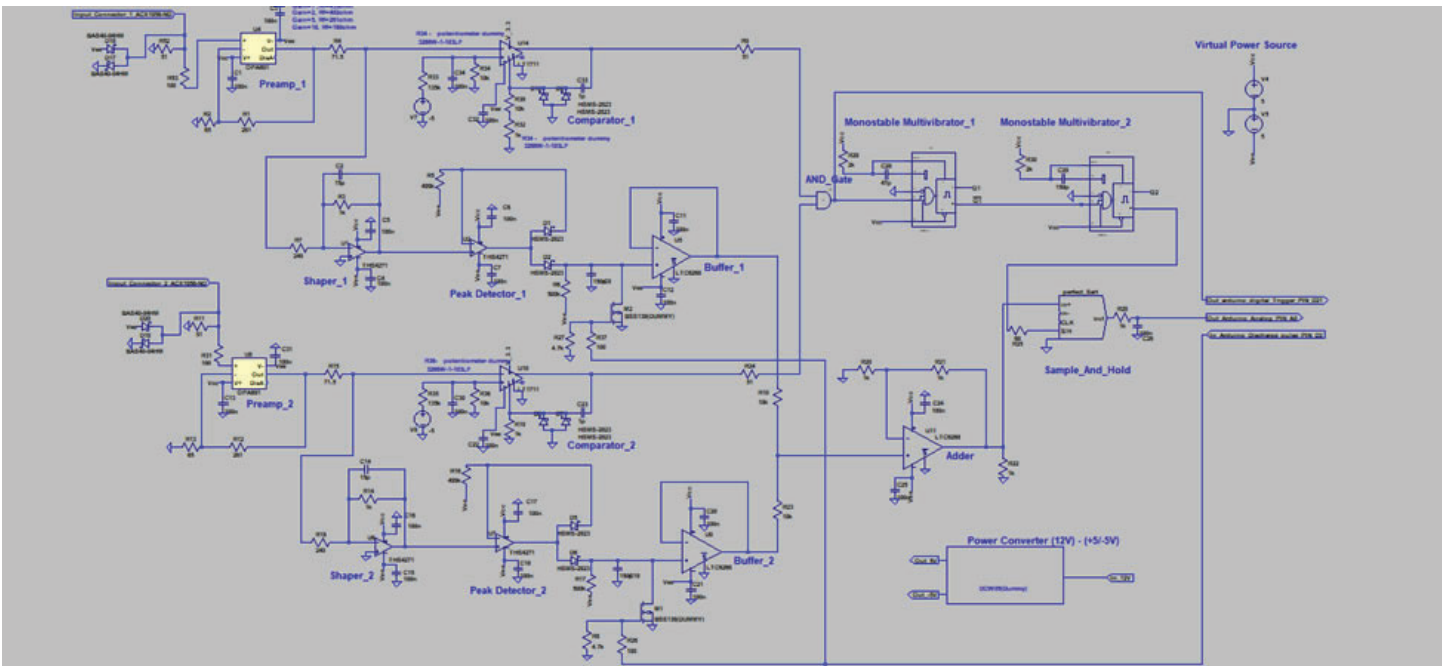


Figure 1: Overall Schematic

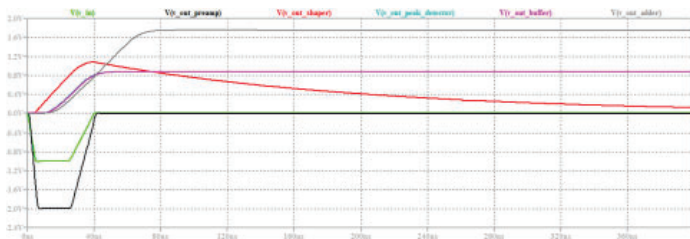


Figure 2: Analog branch simulation results

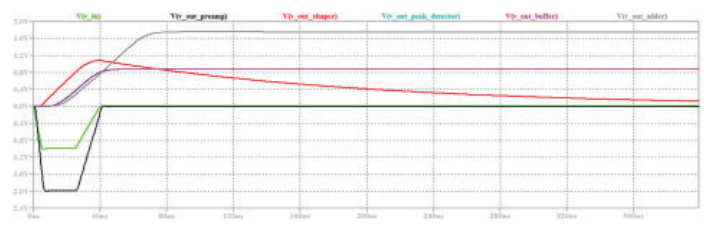


Figure 3: Digital branch simulation results

Value engineering on the infrastructure of the NSLS-II beamlines

John Lavelle

Department of Engineering, The Pennsylvania State University, State College, Pa 16801

Chris Stebbins

Department of Photon Sciences, Brookhaven National Laboratory, Upton, Ny 11973

Abstract

The National Synchrotron Light Source II (NSLS-II) at Brookhaven National Laboratory moves electron particles around a half mile long ring at approximately the speed of light. These particles are then directed into beamlines where research can be conducted at a subatomic level. The beamlines contain an infrastructure that is comprised of Mechanical Utilities, Electrical Utilities, an Equipment Protection System (EPS), and a Personal Protection System (PPS). Research has been conducted which focuses on the infrastructure from a Value Engineering standpoint. One on one interviews occurred with an array of different staff at NSLS-II, including Scientists, Engineers, Technicians, and Project Managers in order to gather their thoughts on what could be improved, from an efficiency, reliability, and safety standpoint. Value Engineering ideas were collected from every part of the beamline process: gathering the requirements, system design, installation, testing, and maintenance of these systems once in operations. From there, “Roundtable” team discussions were held, where each member of their respective group discussed the proposed findings and solutions. Moreover, many of these solutions are going to be implemented at NSLS-II during future Beamline installations. This project has strengthened my ability to think critically when analyzing problems as well as highlight the importance of communication and teamwork.

I. Introduction

The infrastructure of the Beamlines at NSLS-II is comprised of four main categories: Mechanical Utilities, Electrical Utilities, Equipment Protection Systems (EPS), and Personnel Protection Systems (PPS). The Mechanical Utilities group has four main parts of infrastructure which are used. The four main pieces of equipment used are Deionized water(DI water), Process Chilled Water, Gaseous Nitrogen (GN2) and compressed air. The biggest role of the DI water is the ability to keep the vital of the components within the Beamline to certain temperature stability, moreover to not overheat the components. Process Chilled water deals with the cooling of equipment that is not scientific components within the Beamline such as electronic racks. The Gaseous Nitrogen has an intake and outtake valve that deals with the cleansing of the chambers or insides of the piece of equipment. Moreover, the GN2 purifies all the possible impurities within the insides of most components. Lastly, the Compressed air has the role of keeping the insides of the equipment vacuum sealed so that the ability for impurities to become present does not occur. The Electrical Utilities have the role of supplying all power to the Beamlines. The four parts of the Electrical Utilities are the outlets, Wiring, Conduit and Cable tray. The Cable Tray and conduit guide the wiring from point A to Point B. The Equipment Protection system has the duty of monitoring all Equipment within the Beamlines

in order to ensure temperature stability and functionality efficiency. EPS monitors the Beamline components through Input/Output(I/O) module boxes as well as Program Logic Controllers (PLC’s). Finally, PPS has the task of monitoring radiation that is emitted due to the Beamline. Human protection from Radiation is the most important role within the Infrastructure of the Beamlines due to the huge safety factor that is associated with it. My objective was to analyze all four parts of the Infrastructure within the in order to find ways to make the infrastructure more reliable both from a safety standpoint, and operationally cost efficient. These systems all have the role of supporting and facilitating leading edge scientific research at NSLS-II. From a variety of disciplines, through interviews, beamline tours, and team “Roundtable” discussions, opportunities for improvement were identified. These opportunities were wide ranging, from software development, process improvements, to enhancements in team communication and coordination. As a result of this project, several processes and procedures at NSLS-II will be revised to implement these improvements.

II. Methods

The Methods utilized for all four parts of the Infrastructure of the Beamlines were the same when analyzing things from a Value Engineering standpoint. The methods in chronological: from gathering cost and schedule, Beamline tours, One on one interviews, and finally Roundtable discussions. Initially, the focus point was to go and review the cost in order to complete a Beamline. The major reason for going into old cost history was to analyze what part of the Beamline had the majority of the cost and where there could be room for improvement. Secondly, Beamline tours played a huge role in helping understand the four different Infrastructure systems and how they work off each other. To visually view the different infrastructure parts working helped with understanding the concepts and objectives. Thirdly, the one on one interviews were the main way of finding the problems that

Beamline	# of Hutches	Total Actual Cost	Labor Hours Engineer	Labor Hours Tech	Labor Hours Designer	Labor Costs Trades	M&P Costs
NYX	3	332262	141	982	121	41770	91575
XFP	1	180329	58	743	4	34842	50408
CMS	2	199769	82	234	45	73712	75487
TES	1	120085	97	438	52	24627	52022
QAS	3	294900	190	927	186	79799	63745
XFM	3	191400	84	938	175	48133	50639
BMM	2	164677	83	1039	184	17080	41685
FXI	2	27200	179	1915	264	35182	66042
PDF	1	28361	47	178	0	3945	5847

Table 1: Displays the cost and hours for the Mechanical Utilities for several Beamlines

are within the Infrastructure of the Beamlines. The interviews were broken down into the four different groups. A set bank of questions were inquired about in order to hear where things could be improved from a reliability, operational efficiency, and safety standpoint. The bank of questions was broken down into every step of building out a Beamline from the initial design all the way through to the installation and final commission of the Beamline. The value of breaking down the questions into sections was to see where in the process of commissioning a Beamline needs the most improvement from a Value Engineering standpoint. In terms of Interviewees, my Mentor had the ability to set up interviews with Technicians and Engineers within all four Infrastructure groups. After collecting all information from the one on one interviews the next step in the process was to record all information in an organizational format that was formulated into a presentation. Four presentations were created for each of the four infrastructure groups. The presentations were broken down into a slide or two for each part of the process from design to commission. The Proposed solutions to each of the problems were conveyed in the presentations. After Completion of the presentations, Roundtable discussions were then planned in order to display the findings of every individual to the entire group. Each group of the Beamline Infrastructure collectively went through each finding to see what could realistically be integrated into the processes and procedures currently being taken at the National Synchrotron Light Source

II. After the discussion was complete and the proposed solutions were filtered down into the actions that needed to take place, a report was created for each of the groups in order to develop and document all actions that should take place for each specified group.

III. Results

A. Mechanical Utilities

The Mechanical Utilities Roundtable was very effective in finding ways to improve in order to be better from a Value Engineering standpoint. The actions that could potentially take place come from the gathering requirements, design, and Installation parts of the Beamline process. In terms of Gathering Requirements, the way that the utilities group gathers the Beamline requirements needed improvements. An Interface Control drawing that displays different views of the Hutch could be filled out by the Beamline staff. The interface Control Drawing would display all the different features and pieces of equipment in a visual and organized fashion. Secondly, the design for DI water adheres to half inch piping which is relatively small. Due to the Half inch piping there is more risk of buildup and contamination within the pipes. Since altering the size of the DI water piping would be too difficult of an implementation, a Citronox flush monthly would be incredibly influential in minimizing the amount of impurity and contamination build up. Lastly, the Installation of flow meters which reads the flow rate of certain DI water systems does not have a full functioning test. Specifically, EPS flow meters are

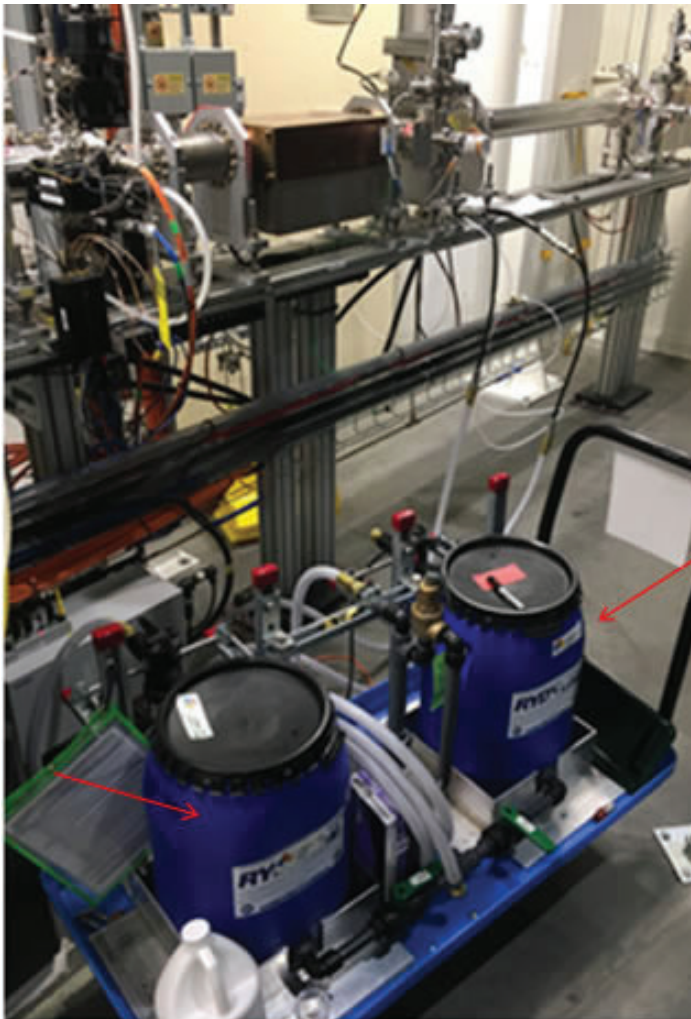


Image 1: Arrow on the left points to the Citronox, arrow on the right points to water.



Image 2: The EPS box should have better ventilation where the arrows are directed.

installed and checked to make sure the flow measurement is accurate. Furthermore, when the Flowmeter sends a signal that carries the value to a control screen the value is occasionally skewed. The control screen is usually monitored by a Mechanical Utilities Engineer therefore causing incorrect value readings. A fully functioning test whenever an EPS flowmeter is installed or altered should occur to ensure that milliamp signal the flowmeter sends out correctly matches the value read on the actual device.

B. Equipment Protection System

EPS also had actions that could take place within the Gathering Requirements, Design, Installation and Testing sections. There was no formal way of gathering requirements for the Beamline staff in order to ensure all requirements were fulfilled for every Beamline. The collective solution was to create Interface Control Drawings with an accompanied spreadsheet in order to ensure what is needed for each beamline as well as where it is needed. This is effective due to the organization and standardization that comes along with it. Secondly, the designs of the EPS boxes are not effectively created for optimal heat ventilation. There has been an occurrence of I/O modules within the EPS boxes to overheat. An analysis of how much heat dissipation in each EPS box should be observed in order to evaluate which ones are more likely to overheat. After analyzing the ones that have a higher heat dissipation, redesign those boxes to create more of a natural ventilation to ensure a more stable temperature. Thirdly, when installing EPS wiring to the Equipment, certain codes are needed for certain sig-

nals in order to ensure the PLC works correctly. New software in Excel was created in order to display certain PLC codes that are needed when wiring and installing the EPS system. This new software expedites the EPS installation for bigger projects. Finally, testing of the EPS/DI water interface needs to become more extensive. As stated in section 'A', there is not a full functioning test of the EPS flowmeter to the Control screens, moreover, causing incorrect milliamp signals to be sent to the Control Screens. A fully functioning test would solve the misreading's that occur within the Control screens.

C. Personal Protection System

The Personal Protection System group had come to the conclusion that four different actions could be taken from a Value Engineering standpoint. Gathering Requirements, Installation, and coordination are the focal points within the buildout process of the Beamlines. In terms of Gathering Requirements, a standardized process needed to be implemented in order to organize the requirements more effectively. An Interface Control drawing (ICD) will be implemented. Multiple views of the beamline and hutches will be present when filling out the ICD in order to capture the requirements needed from each view and angle. Furthermore, it was apparent power provisions needed to be made in order to better test the PPS systems. An outlet will be installed on the outside of the Hutch in order to better ensure more accessible power when having to test the equipment from the outside of the Hutch. Additionally, the amount of space in the Hutch is limited, therefore very valuable and should be used as efficiently as possible. A plausible way to assist this is by installing the PPS aperture hardware earlier in the installation process. Lastly, integrating the PPS system into the EPIC's software is very important. The ability to implement the EPIC's system into the PPS system will better help the coordination between two different groups. An example would be the flow rates on the PPS flowmeters, the flowmeter reading will be able to be viewed on a Control screen if the PPS software is implemented into EPIC's.

IV. Conclusion

After interviewing and holding discussions at "Roundtables", processes and procedures have opportunity for improvement. Specifications within processes and procedures have been and will continue be revised in order to improve deficiencies. When conducting research, it was brought up that the specification document that is sent to vendors for Beamline components have requirements that were outdated. The outdated document created incorrect information due to the duration of time that has passed since creation. An update of every aspect of this document has occurred to the point where the document is completely revised. New and correct values in every section have been implemented, as well as additional information to better explicitly state the requirements needed. Also, coordination between the DI water and EPS interface needed improvement. There was not any communication between EPS and the Mechanical Utilities group when an adjustment of an EPS flowmeter occurred. Since then there have been provisions made where the EPS team has integrated with the Mechanical Utilities when signing documents for correct EPS DI water flow reading checks. Initially, only the EPS team would sign off on a test report for the value of the EPS DI water. Since then the test report has been signed off by a Mechanical Utilities Engineer to ensure the value on their control screen is matched to



Image 3: Arrow is directed to where additional outlet could be installed.

the value that was presented when tested by the EPS team. Overall, processes and procedures at NSLS-II have been and will continue to be revised and improved for future buildout of beamlines.

V. Acknowledgments

I would like to thank my Mentor, Chris Stebbins. Chris has given me great guidance, resources and knowledge throughout the entirety of this project. Secondly, I would like to express my

gratitude to the Office of Educational Programs in their constant attention and assistance towards interns in every program within Brookhaven National Laboratory. Additionally, I extend my appreciation to the Science Undergraduate Laboratory Internships Program (SULI) for giving me the opportunity to gain experience in my field at such a prestigious facility. Lastly, I would like to mention the National Synchrotron Light Source II(NSLS-II), Brookhaven National Laboratory and the Department of Energy for their Hospitality throughout the entirety of this program.

Intercomparison of Particle-Soot Absorption Photometer (PSAP) Sample Filter Media

Pedro A. León Bergodere and Olga L. Mayol Bracero

Department of Environmental Sciences, University of Puerto Rico, Río Piedras Campus, San Juan, PR, 00931

Arthur Sedlacek III, Ernie R. Lewis & Stephen Springston

Department of Environmental and Climate Sciences, Brookhaven National Laboratory, Upton, NY, 11973

Abstract

Changes in Earth's climate (i.e., higher temperatures and severe or prolonged droughts) are occurring because of anthropogenic emissions of both gaseous and particulate matter (aerosols) into the atmosphere. Whereas many gaseous species are known to be warming agents, particles can scatter and/or absorb solar radiation, exerting radiative forcings that may provide a cooling or heating effect on Earth's climate. To better quantify the impacts of aerosols on Earth's radiative balance, many measurement campaigns have deployed the Particle-Soot Absorption Photometer (PSAP), an instrument that measures light extinction by aerosol particles collected on a filter. Although in use for over twenty years, the filter medium (E70) used for this instrument's measurements is no longer produced, necessitating a replacement to maintain continuity with the historical record. To this effect, a laboratory-based measurement study, sponsored by the Department of Energy's Atmospheric Radiation Measurement (ARM) program, is being undertaken at Brookhaven National Laboratory with several PSAP units to evaluate four candidate filter materials (Azumi, WhatmanGF10, Savillex and EMFAB), with the goal of selecting the one that provides the response that most closely mimics the current filter medium. Characterization of the PSAP performance metrics (e.g., the LED wavelengths and flow calibrations), leak testing and software updating were conducted to ensure un-biased data collection indicative solely of the filter media differences. Linear regressions of absorption coefficients using original and candidate filters showed high positive correlations in all cases, but the regression slopes reveal that out of the four candidates, the Savillex filter comes closest in signal response to the E70.

I. Introduction

A. Effects of aerosols on Earth's climate

Aerosols, suspensions of solid and liquid of particulate matter in the air, arise from natural processes (i.e., volcanic emissions or wildfires) in the form of smoke, dust, haze, etc.¹, but their concentrations in the atmosphere have increased since the beginning of the industrial period due to emissions from human combustion activities. Depending on the optical properties of aerosol particles, their radiative forcings (influences on Earth's radiation balance) can be positive (due to light absorption) or negative (due to light scattering)². In relevance to the present work, light-absorbing particles have contributed to climate change and air quality degradation, through atmospheric temperature increases, changes in cloud composition and visibility impairment².

B. Filter-based techniques

To better assess the radiative forcings of aerosols on Earth's climate, many studies have employed filter-based techniques to

infer the light absorption of atmospheric aerosols. These methods typically consist of collecting aerosol particles on a filter through which the attenuation of light is measured. A reference filter is used to ensure that these changes in transmittance aren't due to fluctuations in the instrument's light source.

C. The Particle-Soot Absorption Photometer (PSAP)

One of the most widely deployed filter-based instruments is the PSAP, which measures light extinction by aerosol particles collected onto a filter at three wavelengths³, nominally 470, 522 and 660 nm. The aerosol absorption coefficient, B_{abs} , is a measure of the amount of light absorbed by an aerosol per unit volume of air. The PSAP infers this quantity from Beer's law using the rate of change in transmittance (estimated from a difference between two times) and the flow rate:

$$B_{abs} = -\left(\frac{A}{F * \Delta t}\right) * \ln\left(\frac{Tr_t}{Tr_0}\right) * Fr$$

where A is the area of the filter spot size, F is the volumetric flow rate, Δt is the sampling time period, and Tr_0 & Tr_t are the transmittances before and after the aerosol collection, respectively. The quantity Fr is an experimentally measured transfer function that accounts for the actual transmittance of the column of air drawn through the filter⁴. The PSAP calculates B_{abs} in units of inverse megameters (Mm^{-1}), and higher values are reported during biomass burning events or local contamination activities, such as vehicle emissions⁵.

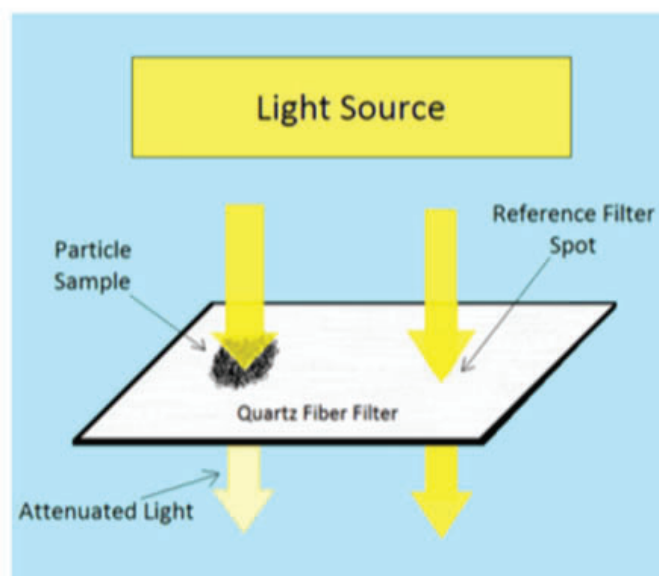


Figure 1. In filter-based techniques, light is shone through a filter on which particles have been deposited and the fraction of light transmitted through the filter is measured.

Image: Courtesy of Julio Rosado

Although the PSAP has been used for over 20 years, its traditional filter medium (glass fiber Pallflex E70) is no longer produced, requiring a replacement to maintain continuity with the historical record. A study to determine the best replacement out of four candidate filter materials (Azumi, WhatmanGF10, Savillex and Pallflex EMFAB), is being undertaken at Brookhaven National Laboratory, with the goal of selecting the one that provides the response that most closely mimics the current filter. Six PSAP units, each with a different filter, are being compared against each other using laboratory-generated and ambient aerosols to determine the best replacement candidate for the E70.

II. Methodology and materials

A. PSAP Calibrations

The six PSAP units were labeled by their serial number and calibrated to ensure their proper operation. The wavelengths of the LEDs of each of the PSAP units were measured using an *Ocean Optics* spectrometer, which also measured the emission lines of a Pen-Ray vacuum mercury lamp for comparison. This lamp produces narrow and intense emission lines in the visible spectrum at precisely known wavelengths. An internal software update to each of the PSAPs was performed as well, consisting of replacing the 1.37 version of the PSAP Erasable Programmable Read-Only Memory (EPROM) chip with the 2.03 version, which allows for a higher data processing resolution: 1 second instead of 4 seconds. In addition, leak tests were conducted by connecting the PSAP vacuum inlet to a pressure pump, and the true flow of the PSAP was compared against its adjusted nominal flow using a *Defender 530-M* and a vacuum pump.

B. Air sampling and data processing

For particle distribution to the PSAPs, a sampling manifold

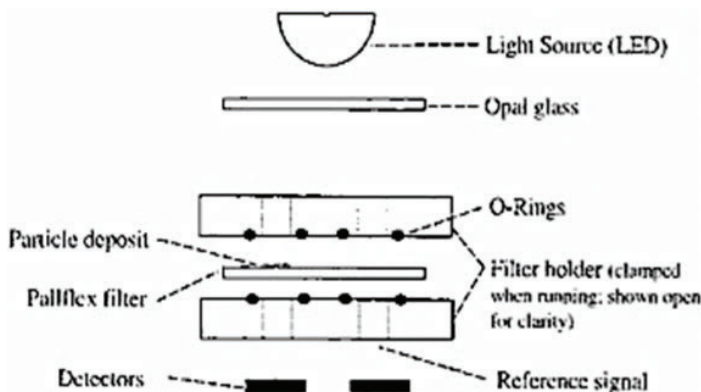


Figure 2. Schematic arrangement of the PSAP features for transmittance measuring.

Image: Bond et al., 1999.



Figure 3. Example of a sample (left) and reference (right) PSAP filter.

was established. The PSAPs were connected via serial ports to separate virtual machines (computer systems) to have their data displayed through ARM's "virtual instrument" (vi), which is a program that processes the B_{abs} as 1-second raw data at each wavelength, from which a 60-second running average is calculated.

C. Filter tests and data replication

Initial tests for B_{abs} measurements sampling air with high-efficiency particulate air (HEPA) filters solely with E70 filters were performed to measure instrument noise. Since the aim of this project is to evaluate the candidate filter response, a sample of an ambient air run was selected to perform a linear regression test between the B_{abs} of the original and candidate filters for all wavelength channels.

III. Results and discussion

Preliminary tests using the E70 filter prior to the candidate evaluations (Fig. 5) provided data with high standard deviations (noise) in some of the instruments. As the units were sampling HEPA (particle-free) air at the time, B_{abs} values were expected to be near 0. Minor modifications were made to the sampling tube configurations, LED signal detector cleaning, etc., to reduce the noise in the PSAP signals. With these changes, the standard deviations of the averaged signals for each wavelength were reduced

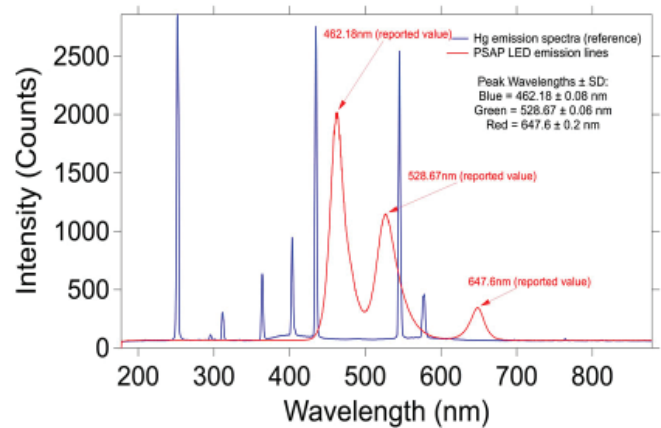


Figure 4. Spectroscopic analysis of the LED wavelength outputs using mercury emission lines as references (PSAP046 values used as example).

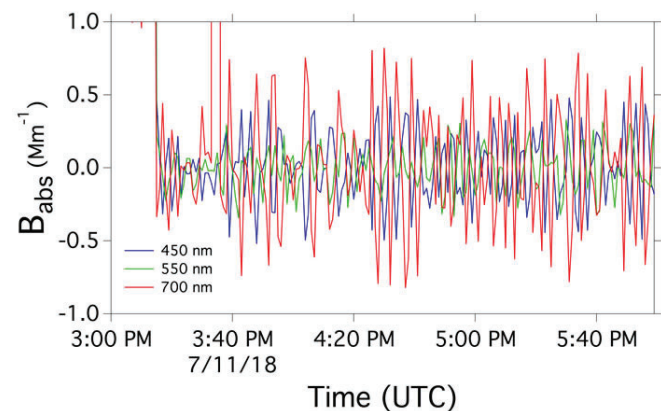


Figure 5. 60-second running average of B_{abs} from first dry HEPA filtered air test with E70 filters, on PSAP unit 046. Standard deviations: Red = 0.43 Mm^{-1} Blue = 0.26 Mm^{-1} Green = 0.16 Mm^{-1}

by factor of nearly 5 (Fig. 6).

No drastic differences among the filter media are evident from measurements of ambient air (Fig. 7). Using one of the E70 B_{abs} data, a linear regression analysis was performed with the filter candidates to further assess their relationship to the E70. The regression analysis for the blue wavelength B_{abs} (Fig. 8) provides correlation coefficients of near unity. However, the regression slopes allow a more solid assessment at which filter responses are closer to the 1:1 line. While the Azumi, Whatman and EMFAB filters give slopes of 1.23, 1.07 and 1.07, respectively, the Savillex filter provides a value of 0.98, meaning that the linear tendency of the B_{abs} values for this particular filter deviates the least from the E70.

The linear regression test for the green and red wavelength B_{abs} (Fig. 9 & Fig. 10, respectively) also gives correlation values of near unity for the Savillex, with all filters exhibiting the same regression as in the blue wavelength B_{abs} ; the Savillex filter now presents a slope value of 0.99 and 1.01, respectively for green and red, whereas the other filters slightly deviate from their values but don't differ drastically.

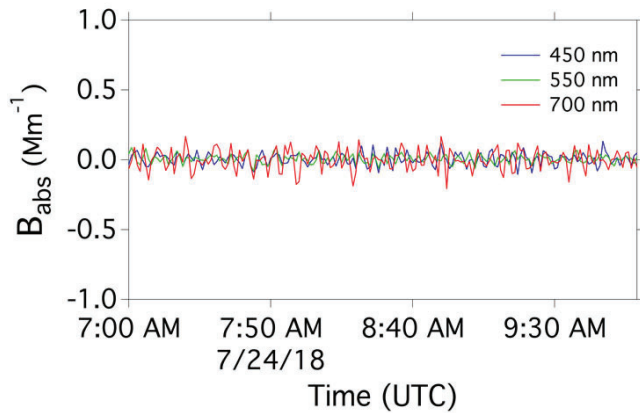


Figure 6. 60-second running average of B_{abs} from dry HEPA filtered air test with E70 filters on PSAP unit 046, after noise assessments and detector cleaning. Standard deviations: Red = 0.07 Mm^{-1} Blue = 0.04 Mm^{-1} Green = 0.03 Mm^{-1}

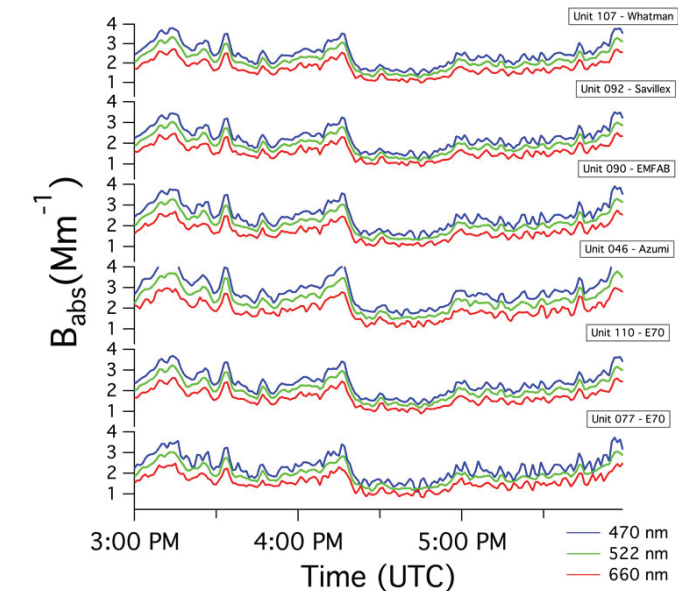


Figure 7. 60-second running average of B_{abs} from all candidate filters sampling ambient air.

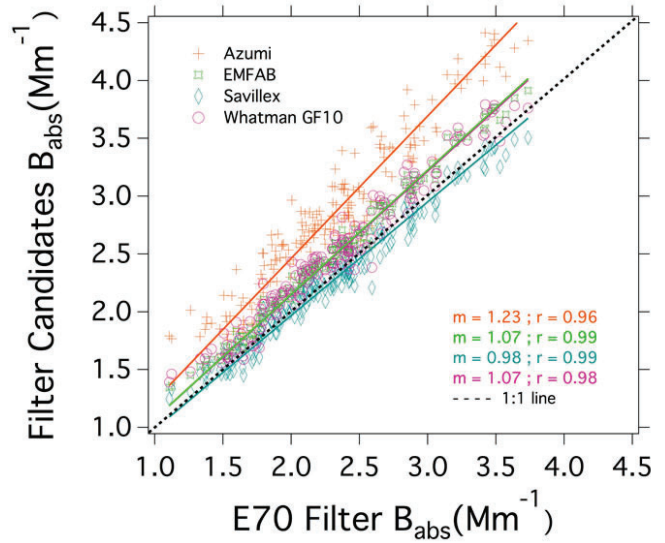


Figure 8. Linear regression test of blue wavelength B_{abs} for candidate and original filters.

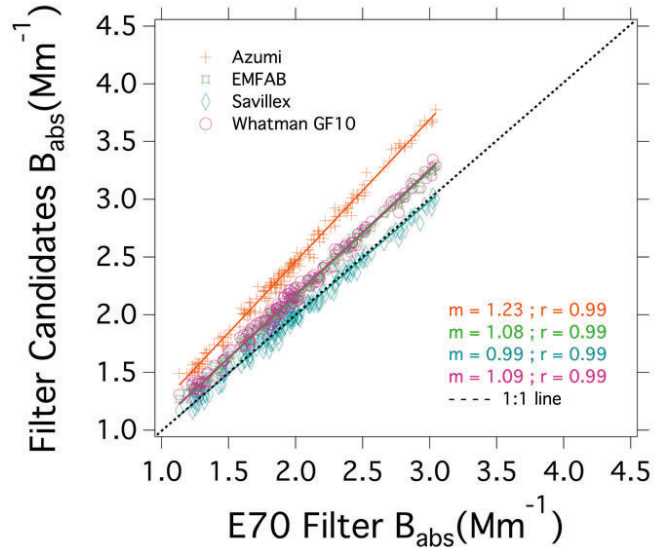


Figure 9. Linear regression test of green wavelength B_{abs} for candidate and original filters.

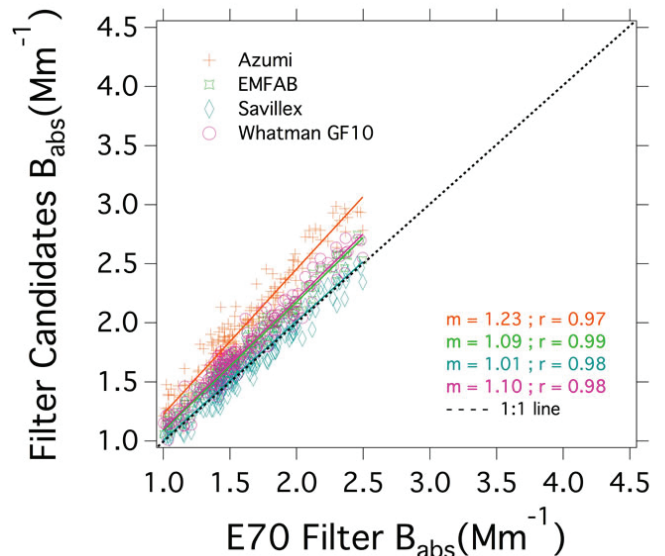


Figure 10. Linear regression test of red wavelength B_{abs} for candidate and original filters.

IV. Conclusions

The results observed in this study offer an initial example of all the candidates' capabilities as replacements for the E70 filter. Although differences in the signal correlations could be distinguished, the slopes from the linear regression tests are all near unity for each wavelength, suggesting that any of them might provide a suitable alternative. Nonetheless, based on these preliminary results, the Savillex filter comes closest to the E70 in signal response.

V. Acknowledgements

This project was supported in part by the National Science Foundation, Louis Stokes Alliance(s) for Minority Participation (LSAMP) at the University of Puerto Rico, Río Piedras Campus under the LSAMP Internship Program at Brookhaven National Laboratory.

VI. References

- ¹Buseck, P. R. and Schwartz, S. E., "Tropospheric Aerosols". *Treatise of Geochemistry*, 1-101 (2003).
- ²Moosmüller, H., Chakrabarty, R.K., and Arnott, W.P., "Aerosol light absorption and its measurement: A review". *Journal of Quantitative Spectroscopy & Radiative Transfer*, 110, 844-878 (2009).
- ³Bond, T. C., Anderson, T. L. and Campbell, D., "Calibration and Intercomparison of filter-Based Measurements of Visible Light Absorption by Aerosols". *Aerosol Science and Technology*, 30, 582-600 (1999).
- ⁴Radiance Research, "Operation Procedures: 3λ PSAP Particle Soot/ Absorption Photometer".
- ⁵Springston, S. R., "Particle Soot Absorption Photometer (PSAP) Instrument Handbook". Department of Energy's Atmospheric Radiation Measurement (2018).

Development of a flexible analysis portal based on Jupyter notebooks for the Brookhaven National Laboratory Scientific Data and Computing Center

Kristy Li

Computer Science and Information Security, John Jay College, New York, NY 10019

Tony Wong and Ofer Rind

Department of Physics, Brookhaven National Laboratory, Upton, NY 11973

Abstract

The Scientific Data and Computing Center (SDCC) at Brookhaven National Laboratory (BNL) provides high performance and high throughput computing (HPC and HTC) services to a worldwide user community. Scientific programs supported by the SDCC include Relativistic Heavy Ion Collider (RHIC) Tier-0, United States A Toroidal LHC Apparatus (US ATLAS) Tier-1 and Tier-3, Belle2 Tier-1, Neutrino, Astro, Lattice Quantum Chromodynamics (LQCD), *Center for Functional Nanomaterials* (CFN), and Condensed Matter Physics and Materials Science (CMPMS).⁴ As a result, the recent focus of research and development has been the usage of the Jupyter Notebook to expand support for data analysis activities. Jupyter is an open-source web platform with support for several productivity-enhancing extensions and tools. It allows documents containing code, equations, and visualizations to be easily shared, results to be communicated effortlessly, and much more. The objectives of this research project are to employ actual code from the ATLAS experiment to demonstrate data analysis using the Jupyter Notebook, to further develop the HTCondor workload management system interface with Jupyter for more direct access to batch farm resources, and to create a viable prototype for further development. By developing such a service, the high-energy physics (HEP) community and many others will be able to perform data analysis in a much more flexible and convenient way.

I. Introduction

Modern experiments rely on a lot of computational power to perform intensive data analysis. This computational power is provided by the SDCCC, a full service computing facility that offers compute capacity and data storage to a worldwide user community. They have around a staggering 1,700 users from over 20 projects such as RHIC Tier-0, ATLAS Tier-1 and Tier-3, Belle 2 Tier-1, Neutrino, Astro, CFN, and others. In order to meet demands that require a lot of computational power, the RHIC-ATLAS Computing Facility (RACF) uses a high throughput computing software called HTCondor to queue computing jobs.² HTCondor is especially useful for performing computational intensive analysis. By design, a single HTCondor collector is able to regulate over 25,000 batch jobs and running jobs, while over 200,000 idle jobs are in the queue.² The workload management tool is able to schedule a lot of jobs to run simultaneously by filling all unoccupied batch slots in a pool rapidly, thus, allowing computing resources to be easily managed and distributed.² Traditionally, interactive analysis at the facility has been run from the command line with the user manually submitting computationally intensive jobs to the HTCondor queue. This can be inconvenient and time consuming as numerous steps are needed to produce results. Es-

entially, since the traditional way to access HTCondor requires relatively a lot of time and effort, it serves as a major barrier to meaningful science being conducted. This is why it is necessary to develop a new method to access HTCondor and make it easier and more effective to perform analysis.

Recently, a new service, however, has been deployed to enable interactive analysis through a web browser in a more flexible manner, while still providing the same functionality, including the ability to access the batch system. This new service is based on the JupyterHub, which is the environment where Jupyter Notebooks are run. The appeal of Jupyter Notebooks is that they provide a flexible platform to perform data analysis through a web browser and support a variety of extensions that add functionality such as Python, Julia, and R, tools like TensorFlow, Keras, and CERN ROOT, and kernels such as JupyROOT. Python, Julia, and R are popular programming languages used for data analysis, while, TensorFlow and Keras are machine learning tools used for deep learning. Both are open-source libraries used to build and train models, however, Keras provides a more simplified interface to TensorFlow, whereas, CERN ROOT is a software tool kit used for data processing, data analysis, data visualization, and data storage. It consists of object-oriented frameworks that allow significant amounts of data to be handled and analyzed, and offers many features such as histogramming, curve fitting, minimization, and etc. On the other hand, the JupyROOT kernel integrates Jupyter Notebooks and CERN ROOT so the functionalities of CERN ROOT could be activated simply by importing the ROOT module. Aside from providing a convenient interactive computing environment and useful features, they can also provide insight into the entire computation process: developing, documenting, executing code, and sharing the results easily as seen in Figure 1 and Figure 2.³

Jupyter Notebooks can be either spawned locally, through Slurm, or through HTCondor with the connection established to the hub and to the browser through the HTTP (hypertext transfer protocol) proxy. As shown in Figure 3, shared storage resources in the cluster are available to the user. After the user opens a secure shell (SSH) tunnel, the server can then be authenticated and spawn a local process that connects back to the user. Subsequently, the SDCC application programming interface (API) can interact with the batch scheduler and submit jobs.

This process occurs through the JupyterHub interface. The JupyterHub is a versatile, interactive analysis tool that serves a broad community and a multi-user hub capable of spawning, organizing, and proxying many instances of the single-user Jupyter notebook.³ The JupyterHub starts a proxy and then by default, sends all the requests to the spawned Jupyter Notebook. The JupyterHub starts a proxy and then by default, it sends all the re-

quests to the Hub. Subsequently, the Hub configures the proxy so the uniform resource locator (URL) can be forwarded to the single-user notebook server. By developing a flexible analysis portal where code can be run interactively and directly through a web browser, with no need to set up a complicated environment, access to computing resources for performing interactive analysis will be improved and simplified by using a Jupyter Notebook to access batch resources through the backend. This will lower the barrier to entry for new users seeking to leverage the vast resources of the SDCC for their analysis.

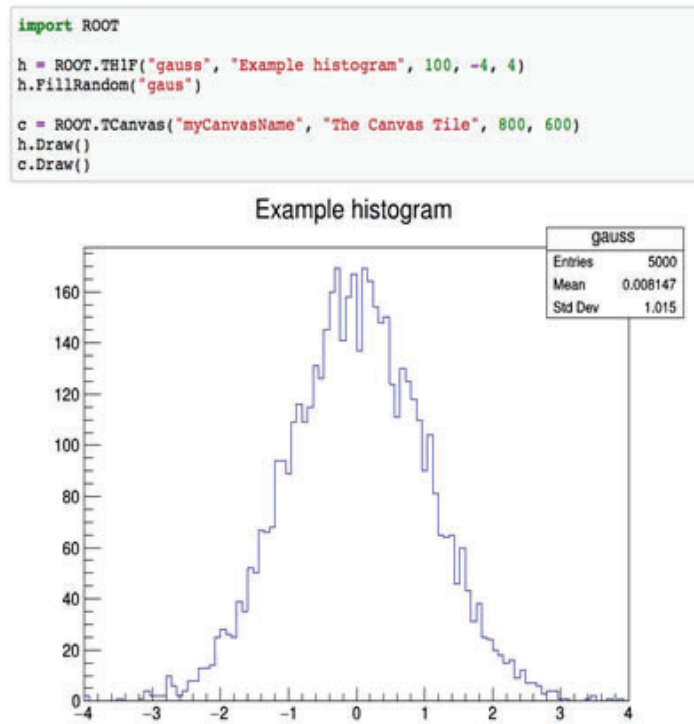


Figure 1. Histogram of the Gaussian Distribution displayed by using ROOT

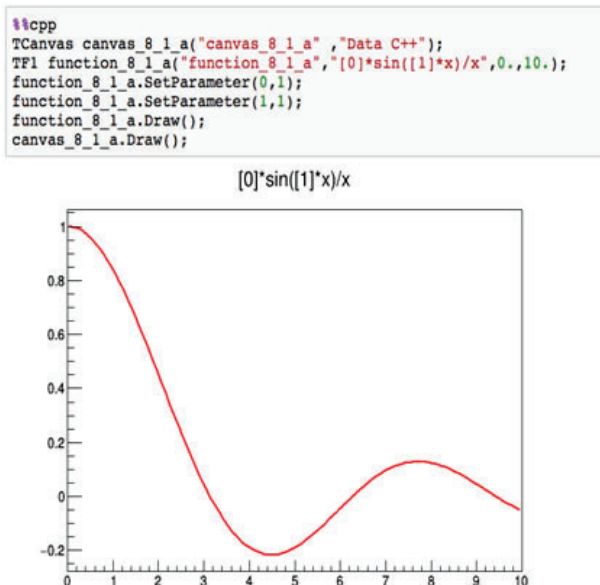


Figure 2. Sinc graph that uses %%cpp magic to write C++ within a Python Notebook using ROOT

II. Methods

In order to develop a tool that can be deployed to simplify the process of data analysis, we first identified the requirements of SDCC stakeholders and familiarized ourselves with commonly used analysis tools such as CERN ROOT, created by the European Organization for Nuclear Research (CERN), TensorFlow, and Keras, and with the HTCondor-based batch software. We also became acquainted with experiment-specific analysis frameworks. As a matter of fact, we built a representative ATLAS analysis software package (Vector Boson Search) as seen in Figure 4 and ran it locally and through HTCondor to understand the analysis being performed.

We then tried to set up the Jupyter notebook kernel for CERN ROOT, taking into account all the ATLAS software dependencies. We tried various methods like implementing environment variables and setup scripts, however, the CERN ROOT ATLAS software was incompatible with Jupyter due to a legacy CERN ROOT software dependency. So, we tried to set up a kernel for the Belle 2 analysis software framework (basf2) instead. We eventually developed a working kernel with the proper environment to support this framework. There are HEP IPYTHON tools built into basf2 to allow interactive physics analysis with Jupyter notebooks. ¹

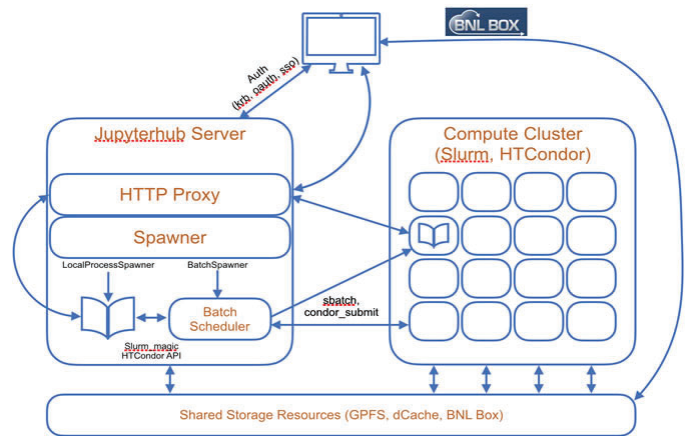


Figure 3. Diagram of JupyterHub server architecture at SDCC

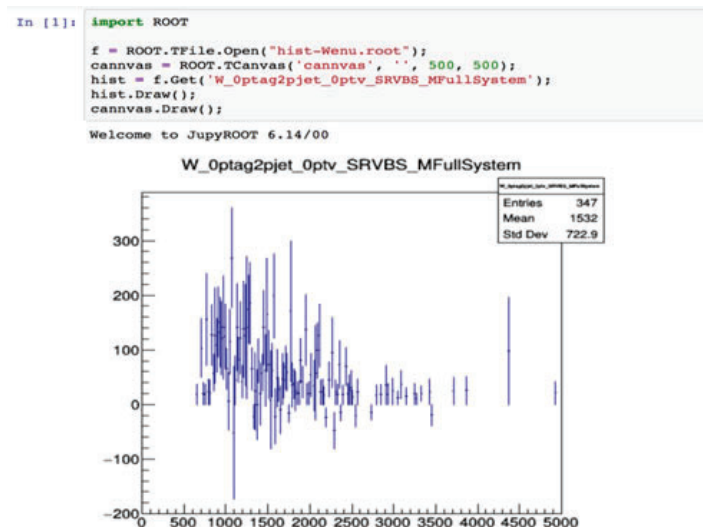


Figure 4. Built and ran a representative ATLAS analysis software package (Vector Boston Search)

Next, I wrote a bash script and ran PyROOT and CERN ROOT code on the HTCondor farm to test the mechanism of code submission. After submitting the job to HTCondor, a histogram was produced as intended. The next step was to adapt my code into the SDCC API and test it out on HTCondor through the terminal. The SDCC API serializes jobs and sends them to the queue through HTCondor by passing in arguments that specify queue commands. Used API to submit test HTCondor batch jobs to the shared pool from within the Jupyter pyROOT kernel and retrieved results for display as shown in Figure 7. Subsequently, I ran it within a Jupyter Notebook with the same commands and the same results were produced. When completed, the Jupyter analysis tool will be provided to the entire SDCC user community. By developing such a tool, it will be easier for the HEP community to perform data analysis as additional steps would be eliminated.

III. Discussion

While trying to develop a flexible analysis portal, I experienced some issues along the way. I had a lot of difficulty trying to set up the ATLAS software environment for CERN ROOT and Belle 2. It proved difficult to set up a working Jupyter Notebook kernel for CERN ROOT using ATLAS analysis software. We needed to take into account many ATLAS software dependencies and go through a great deal of trial and error in implementing the environment variables and setup scripts. In the end, this software turned out to be incompatible with Jupyter due to a legacy CERN ROOT software dependency. This was also the case for one of the ATLAS packages we tried to adapt, which did not work due to limitations in the code. However, a different ATLAS analysis package, basf2 was successfully deployed to the notebook instead.

Similarly, though, I experienced issues with basf2, but this time around, I was able to apply prior knowledge gathered from trying to develop the CERN ROOT kernel for ATLAS notebooks to implement the Belle 2 Analysis Framework in Jupyter. Initially, I experienced problems with setting up the ATLAS software environment for basf2 because the setup script was trying to access and install remote Git repositories, which then caused the kernel to keep crashing and failing to restart. Eventually, it was finally

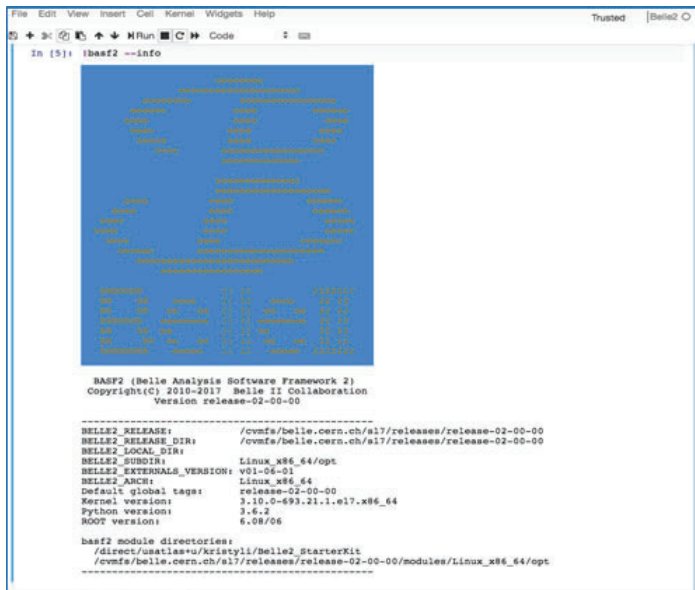


Figure 5. Built and ran a representative ATLAS analysis software package (Vector Boston Search)

setup by exporting certain environment paths and variables that the setup script would normally set up without exporting the Git repositories. As a result, the customized kernel was successfully deployed with the Belle 2 environment.

Throughout this experience, I learned numerous issues may occur when trying to set up complex frameworks and environments for ATLAS software. I came to discover that the software may not always be compatible running in the Jupyter Notebook and can require a lot of additional steps, especially to resolve dependency conflicts.

IV. Conclusion

Currently, the SDCC has multiple JupyterHub portals running and is now able to run within the analysis environment for Belle 2. In addition, there is a new interface to HTCondor through the Jupyter Notebook. Thus, allowing a more flexible and conve-

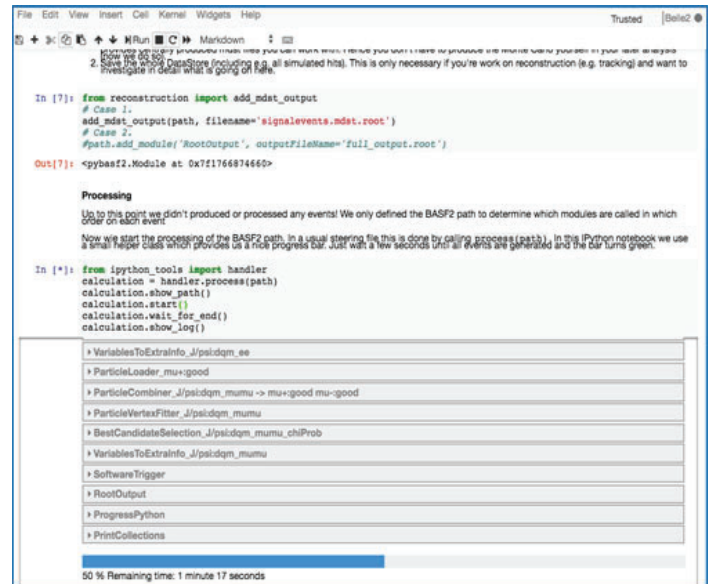


Figure 6. Event Progress bar informing status provided in basf2 through built in HEP IPython Tools

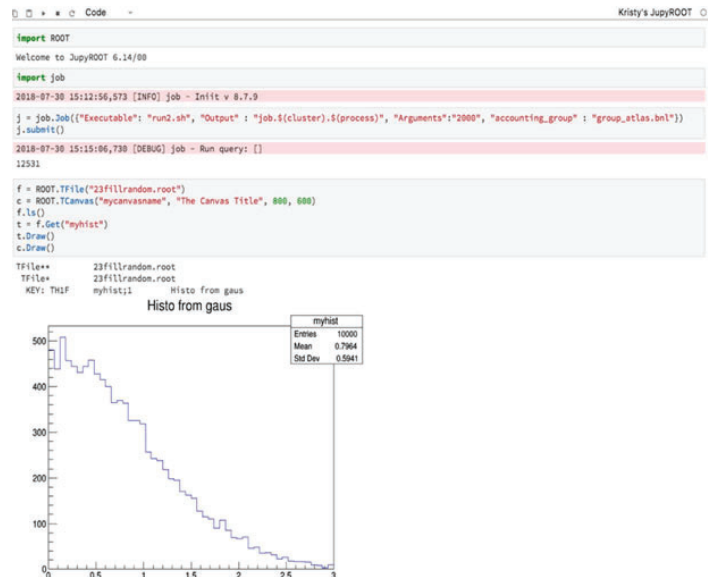


Figure 7: Using SDCC-developed API to submit HTCondor batch jobs to compute farm

nient way to run code on the batch farm compared to the traditional method. We are also in the process of adapting the ATLAS software to the Jupyter environment to run computationally intensive analysis on batch farm resources and making the SDCC API available to the entire user community for performing more high-level computationally intensive analysis. There are still some remaining environment issues for both ATLAS and Belle 2 that need to be resolved. Furthermore, deployment and user testing need to be conducted-extensively as well. In the future, we would like to adapt the ATLAS software in a similar fashion to run on the graphics processing units (GPUs) that make up the SDCC HPC Cluster and expand it for other applications.

V. Acknowledgments

This project was supported in part by the U.S Department of Energy, Office of Science, Office of Workforce Development for teachers and Scientists (WDTS) under the Science Undergraduate Laboratory Internships Program (SULI). I would also like to

thank my mentors Antonio Wong and Ofer Rind for their assistance, patience, and guidance throughout this internship. As well as that I would like to thank Will Strecker-Kellogg for allowing me to use and adapt his API. Finally, I would like to extend my thanks to the rest of the RACF staff for their hospitality, assistance, and encouragement throughout my time here.

VI. References

- [1] T. Hauth, "The Belle II Analysis Framework." PyHEP 2018 Workshop. Sofia, Bulgaria. 7 July 2018. Lecture.
- [2] C. Hollowell, J. Barnett, C. Caramarcu, W. Strecker-Kellogg, A. Wong, and A. Zaytsev, *Journal of Physics: Conference Series* 898, 082014 (2017).
- [3] O. Rind, "Teraflops of Jupyter: A Notebook Based Analysis Portal at BNL." Spring HEPiX. Madison, Wisconsin. 17 May 2018. Lecture.
- [4] D. Yu, "BNL SDCC Site Report." Spring HEPiX. Madison, Wisconsin. 14 May 2018

Design and analysis for the ATF-II CO₂ laser amplifier output window

Paul Li

Department of Mechanical Engineering, Stony Brook University, Stony Brook, NY 11794

Christian Cullen

Collider-Accelerator Department, Brookhaven National Laboratory, Upton, NY 11973

Abstract

The goal of the project was to perform design and analysis for the Accelerator Test Facility upgrade (ATF-II). A larger CO₂ laser amplifier output window and its bracket was designed to withstand pressure from 10 atmospheres of gas, and a valve was chosen to quickly shut off flow in case of a leak. Research was done by evaluating old design documents. ANSYS workbench was used to perform stress analysis. By optimizing the design in ANSYS, it was found that a window with a chamfered edge met safety requirements and had minimal stress concentrations that caused old windows to crack. The window and window mount will be manufactured in the future, and testing will be done according to standards-based management system (SBMS) procedures. The new, larger window will allow researchers to study advanced particle acceleration using a more powerful 10+ TW laser.

I. Introduction

A. Background

The ATF contains a pressure vessel containing 10 ATM of isotopic gas. The CO₂ laser passes through the window into the gas, where it gains energy. The current windows have been prone to cracking near the supports.

B. Scope

Thorough FEA of the window was done to generate viable designs for different viewing areas, providing an upgrade path for stronger lasers. Preliminary design was done for the window

holder assembly, including selection of a valve to shut off any leaks.

C. Structural theory

SBMS includes a guide to pressure vessel window design [1], which uses a set of equations to calculate maximum bending stress. When material is subject to bending forces, it experiences maximum tensile stress in the center of the bottom face, and maximum compressive stress in the center of the top face. This is depicted in Figure 2.1.

According to Roark [2], these equations assume that the thickness of the window is less than a quarter of the diameter – a condition not met in the current window design. This poses two problems that may contribute to cracking in the current windows. Bending stress in the yellow region of Figure 2.2 is higher than equations predict, and there is a stress concentration in the red region.

Two types of failure theories used for brittle materials will be presented in the results: maximum principal stress and Mohr-Coulomb. Max principal stress looks at the single highest stress component. Mohr-Coulomb safety factor [3] [4] is represented by Equation (2.1),

$$SF = \left[\frac{\sigma_{max}}{S_T} + \frac{\sigma_{min}}{S_C} \right]^{-1} \quad (2.1)$$

where σ_{max} is highest tensile stress, σ_{min} is lowest compressive stress, S_T is tensile strength, and S_C is compressive strength. Mohr-Coulomb predicts that material will not fail if it falls within

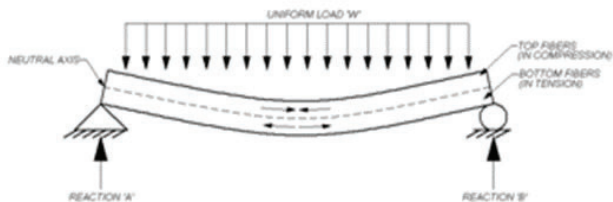


Figure 2.1: Bending stress



Figure 2.2: Free-body diagram

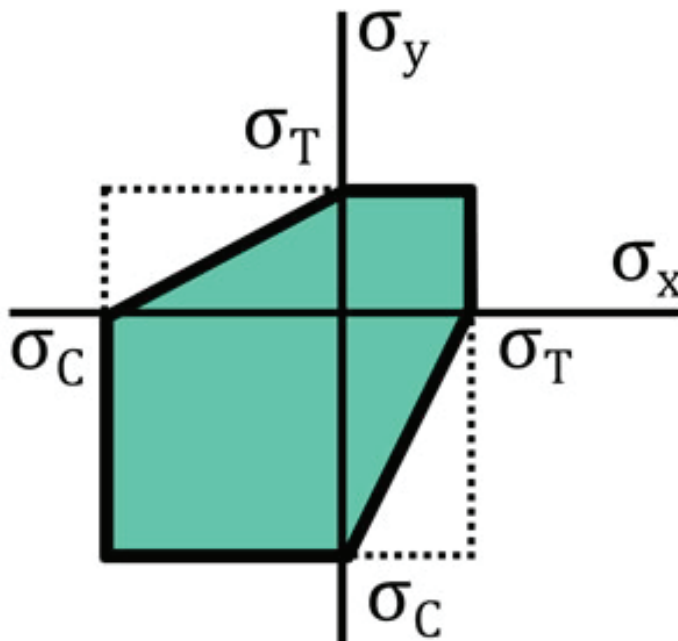


Figure 2.3: Mohr-Coulomb failure theory

the green region of Figure 2.3. When there is pure tension or pure compression, both theories give the same safety factor. When there is a mixture, Mohr-Coulomb gives the more accurate and conservative result.

S_T , S_C , and SF_{min} for the salt window are listed in Table 2.1.

S_T	Tensile Strength [5]	570 psi
S_C	Compressive Strength [6]	3920 psi
SF_{min}	Required safety factor [7]	4

Table 2.1: Mechanical properties and requirements

D. Fluid theory

Fluid flow equations [8] were used to roughly estimate the rate at which gas could escape through a leak from the window. Isentropic and choked flow equations for a converging nozzle were used. An isentropic process involves no heat transfer, so temperature can change. Choked flow is a limiting effect when a further decrease in downstream velocity does not further increase velocity.

Because the gas is mainly helium, an ideal gas, the initial density ρ is found using the ideal gas law, given in Equation (2.2),

$$\rho = \frac{m}{V} = \frac{P}{RT} \quad (2.2)$$

where P is pressure, R is individual gas constant, T is temperature, m is mass, and V is volume. Then, $\rho \times V$ is found using . Next, an iterative process is taken, repeating the following steps at 0.01 s intervals.

Mass flow rate \dot{m} depends on whether choked or non-choked flow occurs. Choked flow occurs when Equation (2.3) is satisfied.

$$\frac{P_{out}}{P} \leq \left[1 + \frac{k-1}{2} \right]^{-\frac{k}{k-1}} \quad (2.3)$$

P_{out} is downstream pressure, P is chamber pressure, and k is specific heat ratio. \dot{m} for choked flow is given by Equation (2.4)

$$\dot{m} = A \sqrt{k \rho P \left(\frac{2}{k+1} \right)^{\frac{k+1}{k-1}}} \quad (2.4)$$

where A is cross section area. For non-choked flow, Equations (2.5) – (2.9) are used:

$$M = \sqrt{\left(\left(\frac{P}{P_{out}} \right)^{\frac{k-1}{k}} - 1 \right) \left(\frac{2}{k-1} \right)} \quad (2.5)$$

$$T_{out} = \frac{T}{1 + \frac{k-1}{2} M^2} \quad (2.6)$$

$$c = \sqrt{kRT_{out}} \quad (2.7)$$

$$\rho_{out} = \frac{P_{out}}{RT_{out}} \quad (2.8)$$

$$\dot{m} = \rho_{out} m c A \quad (2.9)$$

where T_{out} is downstream temperature, T is chamber temperature, c is speed of sound, and ρ_{out} is downstream density.

Finally, Equations (2.10), (2.11), and (2.2) are used to calculate the instantaneous density.

$$m_{new} = m_{old} - \dot{m} * 0.01s \quad (2.10)$$

$$P_{new} = \frac{m_{new}}{m_{old}} * P_{old} \quad (2.11)$$

II. Methods

A. Finite element analysis

To speed up simulation, 2D axisymmetric models were done instead of full 3D models. For each simulation, a geometric model was created in DesignModeler. As depicted in Figure 3.1, the axisymmetric model is revolved around the center line to form a cylindrical 3D model.

Key dimensions were parameterized, so they could be altered. Then, supports and contacts were added, according to Table 3.1.

Contact	Type
Rubber – window	Frictional (coefficient = 0.5)
Rubber – flange	Frictional (coefficient = 0.5)
Window – holder	Frictionless
Holder – flange	Bonded

Table 3.1: Types of contacts

Then, the mesh was generated. In areas of interest, such as the region where the window contacts the rubber gasket, edge size of 0.002 in. was used, whereas in unimportant areas, edge size up to 0.4 in. was used.

Designxploration features were used to investigate the effects of different parameters. Response surfaces were generated, and refinement points were added to improve the curve fit.

B. Valve selection

Excel was used to model fluid flow. Equations (2.2) – (2.11) were used to model each timestep. A custom VBA function was written to determine whether to use choked flow equations. Once

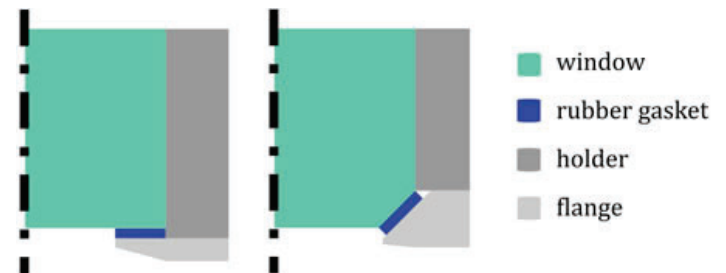


Figure 3.1: 2D axisymmetric model

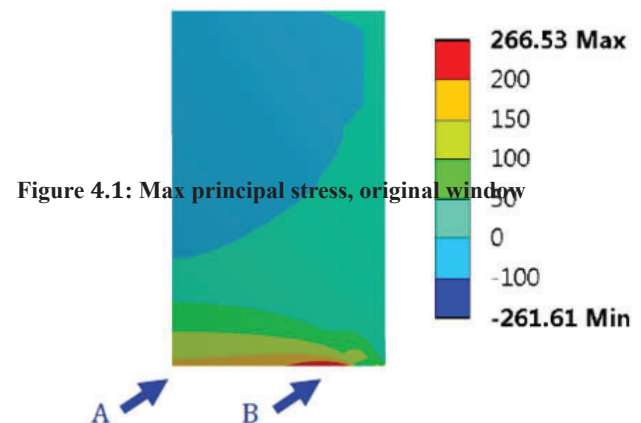


Figure 4.1: Max principal stress, original window

a rough time was found, manufacturer data sheets [9] [10] were used to choose a suitable valve and actuator.

III. Results

A. Current window design

The current window design does not meet the safety factor requirement of 4. Figure 4.1 shows the result for max principal stress.

Table 4.1 lists the discrepancies between SBMS and FEA results.

Location	Stress	FOS
Point A (SBMS)	56 psi	
Point A (FEA)	160 psi	3.5
Point B (FEA)	266 psi	2.1

Table 4.1: SBMS vs. FEA results, original window

As shown in Table 4.2, increasing thickness or support did not sufficiently increase FOS. The first row is the original window.

Diameter	Support	Thickness	FOS
4.72 in.	0.36 in.	3.94 in.	2.1
5 in.	0.5 in.	3.94 in.	2.6
5 in.	0.5 in.	5 in.	2.6
5.5 in.	0.75 in.	3.94 in.	3.4
5.5 in.	0.75 in.	5 in.	3.4

Table 4.2: Effect of diameter and thickness on FOS

B. Proposed window design

Figure 4.2 shows the geometric parameters that were adjusted.

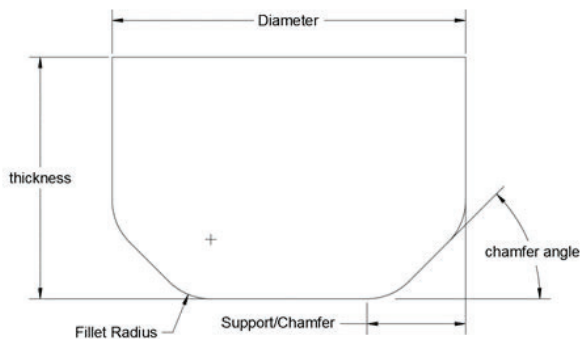


Figure 4.2: Geometric parameters

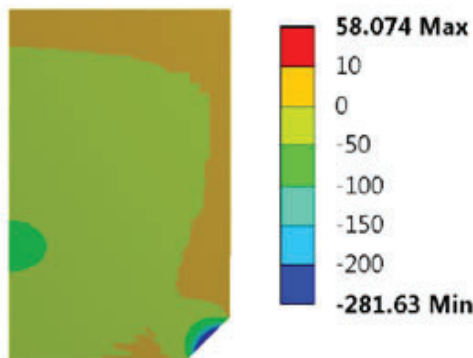


Figure 4.3: Max principal stress, 4 in. chamfered window

It was found that a window with a 45° chamfer, shown in Figure 4.3, reduced stress concentrations. Compared to Figure 4.1, the predominant type of stress is compressive rather than tensile.

Acceptable dimensions for a range of viewing areas are listed in Table 4.3.

	Viewing area	Diameter	Chamfer	Thickness	FOS
1	4 in.	5.0 in.	0.5 in.	2 in.	4.7
2	6 in.	7.5 in.	0.75 in.	2.5 in.	4.9
3	8 in.	10.0 in.	1.0 in.	3 in.	4.9
4	10 in.	12.5 in.	1.25 in.	3.5 in.	4.9

Table 4.3: Proposed dimensions for chamfered window

As shown in Figure 4.4, there is a clear correlation between FOS and thickness. Thickness can be reduced until a certain point, when FOS begins falling.

C. Other parameters

As shown in Figure 4.5, a correlation was found between FOS and chamfer angle.

Plots for FOS vs. thickness were created for 45° and 60° chamfer angles, as shown in Figure 4.6. The proposed dimensions on Table 4.3 use a fillet radius of 0.03 in.

A plot for FOS vs. fillet radius was created for the 4 in. window, as shown in Figure 4.7.

D. Valve selection

Figure 4.8 displays chamber density vs. time for three different nozzle diameters.

If there is a large leak diameter, the valve needs to be shut as quickly as possible. The specifications of the selected valve and actuator are listed in Table 4.4 and Table 4.5.

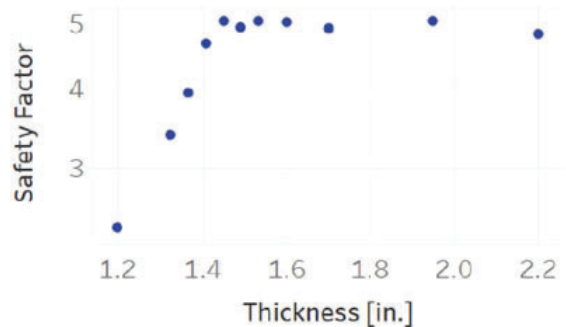


Figure 4.4: FOS vs. thickness, 4 in. chamfered window

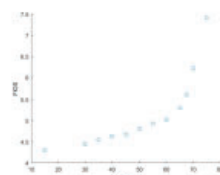


Figure 4.5: FOS vs. chamfer angle, 4 in window

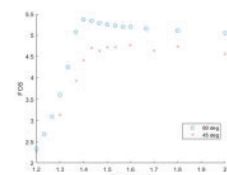


Figure 4.6: FOS vs thickness, 60° chamfer

Valve	Series 9150 ASME Class 150
Bore Size	6 in.
Max pressure	280 psi
Torque required	280 ft-lb

Table 4.4: Jamesbury ball valve

Actuator	VPCL 450 Double Acting
Torque	354 ft-lb (at 80 psi supply)
Closing time	1.5 s

Table 4.5: Jamesbury pneumatic actuator

IV. Discussion

A. Comparison with expected results

The chamfered edge increased the minimum safety factor of the window. There is more compressive stress, but that is okay because salt is much stronger in compression.

A positive correlation was found between chamfer angle and FOS. Intuitively, this makes sense. With a greater angle, the support area is greater, so stress is reduced. Furthermore, the stress concentration is found at the outside corner of the chamfer. With a greater angle, the corner is less abrupt, so the stress concentration is reduced.

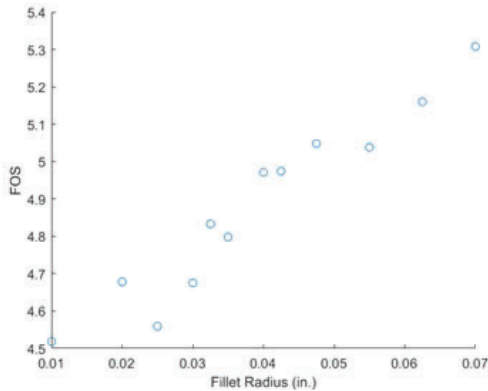


Figure 4.7: FOS vs. fillet radius

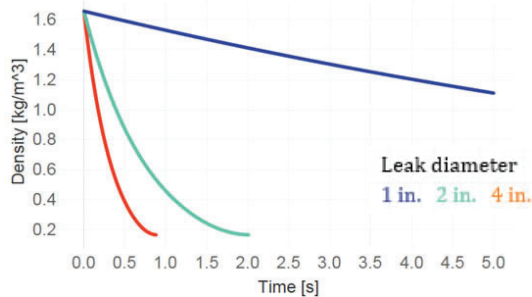


Figure 4.8: Chamber density vs. time

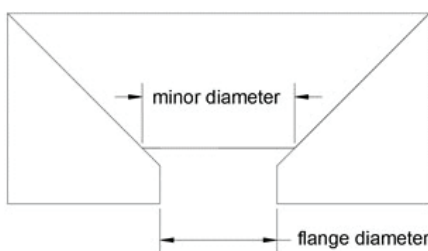


Figure 5.1: Minor and flange diameters

Some comparisons can be made with findings from technical reports produced by the Naval Civil Engineering Laboratory (NCEL) [11]. The reports cover empirical tests on acrylic windows, including conical ones, to find the critical pressure at which they fail. They found that below a certain threshold thickness, critical pressure drops due to bending stress. This is consistent with the results discussed in Section 4.

However, the NCEL project found a 45° chamfer angle had the highest critical pressure. This is inconsistent with the results in Figure 4.5, where a positive correlation was found between angle and FOS. It is unclear what the reason for the inconsistency is. It might be explained in part by difference in the specimens. The Naval laboratory tested smaller (1-2 in. diameter) conical windows made of acrylic, to failure (thousands of psi). The results in Figure 4.5 cover larger (4-10 in. diameter) chamfered cylindrical windows made of salt, to 150 psi.

The NCEL project also found that varying the ratio between minor diameter D and flange diameter D_f had great effect on critical pressure. These parameters are depicted in Figure 5.1. It was found that it is important that flange diameter is smaller than minor diameter, so that the conical surface is always supported even under high pressures.

However, as shown in Table 5.1, reducing flange diameter did not have any effect on FOS. This could be explained by the pres-

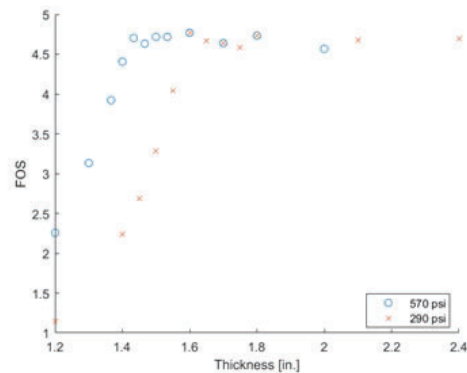


Figure 5.2: FOS vs. thickness, reduced tensile strength



Figure 5.3: Smaller chamfer

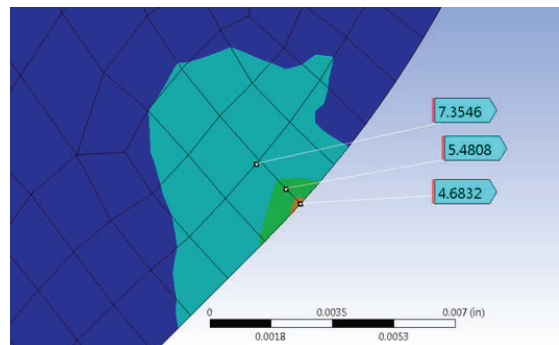


Figure 5.4: Size scale of stress concentration

ence of the rubber gasket and the lower pressure (150 psi) used in the FEA model. The window was not pushed into the opening.

Minor diameter	Flange diameter	FOS
6 in.	6 in.	5.1
6 in.	5.8 in.	5.1
5.8 in.	5.8 in.	5.4

Table 5.1: Modifying minor and flange diameters

B. Mechanical properties

Due to limited availability of mechanical properties of salt, modulus of flexure was used for tensile strength. Later, a paper was found which explained that if the micro-tensile strength of salt is 4 MPa (580 psi), the tensile strength of a sample (5 cm diameter, 5 cm thickness) is 2 MPa (290 psi).

The FEA models were modified to investigate the effect of decreasing the tensile strength. As shown in Table 5.2, it was found that for a thicker window (4 in.), decreasing S_T had no effect on FOS , while decreasing S_C did. This is because the stress concentration is mainly compressive.

Tensile Strength	Compressive strength	FOS
570 psi	3920 psi	4.6
290 psi	3920 psi	4.6
570 psi	3000 psi	3.5

Table 5.2: Reducing compressive vs. tensile strength, for 4 in. thick window

However, it was found that for thinner windows, the area of weakness is the center of the bottom face, due to bending, instead of the outside corner of the chamfer. As shown in Figure 5.2, decreasing S_T caused FOS to decrease.

This is not of great concern because if S_T were used to analyze the current design, FOS would be 1.08. The current window is likely not that weak because it doesn't always crack, and they are tested with 150% pressure. Therefore, $S_T = 570 \text{ psi}$ is likely sufficient. Furthermore, if it is determined that low tensile strength is an issue, the problem can likely be solved by increasing window thickness slightly.

C. Other limitations

One simplification of the FEA model is the omission of the chamfer used to make installing the window easier. This smaller chamfer is depicted on the top face of Figure 5.3.

Another simplification is the design of the window holder and flange. Simple geometric shapes were used to approximate the parts. Detailed design was not done.

Finally, this project only analyzed the single point with the lowest FOS. Figure 5.4 shows a window with a 45° chamfer. The area with $FOS < 4$ is less than 0.001 in. A more thorough analysis would include analysis of the average stress around the stress concentration.

V. Recommendations

Recommendations for the final design of the window and window holder include:

- Use the proposed dimensions listed on Table 2.1.

- Manufacture and test the smallest window first.
- Ensure that the rubber gasket supports the entire chamfer surface
- Ensure that the flange diameter is slightly smaller than the minor diameter
- Check with the manufacturer about their capabilities for rounding out the corners of the chamfer.

It may not be worth further analyzing chamfer angle. A 45° angle provides FOS of 4.7, while a 60° angle provides FOS of 5, which is not a significant increase. A steep angle above 60° may pose certain complications, such as difficulty of manufacturing and the need for better tolerances.

Another recommendation is to implement a camera to monitor the window for cracks. The current design is very thick, so cracks do not propagate through the entire thickness. However, for a thin optimized window, cracks may propagate and cause catastrophic failure if not detected early.

VI. Acknowledgements

I would like to thank my mentor Christian Cullen, as well as the following staff members who provided feedback, advice, and ideas: Marcus Babzien, Mark Palmer, Igor Pogorelsky, Mikhail Polyanskiy, Paul Jacob, and Steven Bellavia. This project was supported in part by the U.S. Department of Energy, Office of Science, Office of Workforce Development for Teachers and Scientists (WDTS) under the Science Undergraduate Laboratory Internships Program (SULI).

VII. References

- ¹Brookhaven National Laboratory, "Guide for Glass and Plastic Window Design for Pressure Vessels," June 2014. [Online]. [Accessed 3 August 2018].
- ²W. C. Young, *Roark's Formulas for Stress and Strain*, New York: McGraw-Hill, 1989.
- ³F. Beer, *Mechanics of Materials*, New York: McGraw-Hill, 2014.
- ⁴ANSYS, "Mohr-Coulomb Stress Safety Tool," [Online]. Available: https://www.sharcnet.ca/Software/Ansys/17.0/en-us/help/wb_sim/ds_MCSST.html. [Accessed 5 August 2018].
- ⁵Crystran, "Sodium chloride data sheet".
- ⁶Matweb, "NaCl material properties," [Online]. Available: <http://www.matweb.com/search/datasheetText.aspx?bassnum=EINOR0761>. [Accessed 5 August 2018].
- ⁷M. Gaffney, Interviewee, *ATF Pressure Recovery System Building 912*. [Interview]. 19 June 2018.
- ⁸P. J. Pritchard, *Fox and McDonald's Introduction to Fluid Mechanics*.
- ⁹Jamesbury, "B107-2EN - Series 9000 Ball Valve".
- ¹⁰Jamesbury, "A11-5EN - VPVL Pneumatic Actuators".
- ¹¹J. D. Stachiw and K. O. Gray, "Conical Acrylic Windows under Short-term Pressure Application," Naval Civil Engineering Laboratory, Port Hueneme, California, 1967.

Developing a Matlab program to test preamplifiers for the sPHENIX detector

Chris Marrs

Electrical Engineering, Villanova University, Villanova, PA 19085

Stephen Boose

Department of Physics, Brookhaven National Laboratory, Upton, NY 11973

Abstract

The Super Pioneering High Energy Nuclear and Ion Experiment (sPHENIX), a proposed experiment utilizing the Relativistic Heavy Ion Collider (RHIC) to replace its predecessor PHENIX, is currently under development at Brookhaven National Laboratory. Its goal is to detect very small particles collisions by implementing a variety of different calorimeters. The two energy measuring portions of this experiment are the Electromagnetic Calorimeter (EMCal), and the Hadronic Calorimeter (HCal). The purpose of these detectors is to collect the incoming data from the particle collisions in order to be later analyzed. These calorimeters contain signal preamplifiers to shape and clean up the incoming pulses caused by the collision, and these boards must be tested. The goal of the project is to create a test procedure using Matlab to collect data from these two different types of preamplifiers and report it. By connecting to the preamp test board, the program initiates the tests and reads the output results, analyzing the incoming data to make sure the preamps meet the detectors design specifications. It then exports all the data into a PDF file, allowing for easy access to the test data, while also identifying the boards that are out of spec. Creating an automatic program to test the preamplifiers is necessary, in order to get accurate and quick results. There are a total of 1,252 EmCal's and 1,536 HCal's, all containing preamplifiers that must be tested. The Matlab program greatly decreases the room for error in the test results, and also creates an efficient way of organizing the large amounts of data/files that are collected.

I. Introduction

The Super Pioneering High Energy Nuclear and Ion Experiment is a proposed upgrade to the PHENIX detector at RHIC. The purpose for this proposed project is to further analyze the quark-gluon plasma (QGP) which was discovered to be a perfect fluid. A perfect fluid is an idealized version of a regular fluid that does not have viscosity or conduct heat. There is much research and experiments that need to be done before the dynamics of this perfect fluid are understood. Once created, the sPHENIX detector, shown in figure 1, will be able to answer the many questions that we have about the QGP and reveal more about the fundamental nature of the universe. It was also provide us with further unknowns about QGP and Quantum Chromo Dynamics that can be address in future scientific experiments at RHIC.

The sPHENIX detector is made up of a variety of different calorimeters and other experiments that all contribute to the output results of each collision. The current design of the experiment requires the implementation of five major components shown in figure 2. These consist of the Magnetic Solenoid, Silicon Tracking, Electromagnetic Calorimeter (EMCal), Inner Hadronic Calorimeter (HCal) and Outer HCal. The Magnetic Solenoid is a large

hollow cylindrical magnet that is 140 cm in radius with a magnet thickness of 33 cm; creating a magnetic field of 1.5 T. The Silicon tracking is a grouping of several layers of silicon that are used to reconstruct the particle paths as well as the momentum of these particles. The next two are energy measuring portions of the experiment. The EMCal and HCal will be able to detect the incoming energy levels of the particles that are created from the collision. All these sections working together will be able to collect the necessary information needed in order to learn more about the fundamental nature of the QGP.

Since the EMCal and HCal sectors are responsible for collecting energy levels of very small particles, there must be a way of amplifying these small incoming signals. In both calorimeters there is a series of collector's preamplifiers and data samplers. The collectors will respond to incoming particles and send a pulse to the preamplifiers which will amplify and shape the wave which is sent to an analog to digital (ADC) converter to digitally store the pulse data.

The EMCal preamplifier board (Figure 3) has sixteen separate channels which can each amplify and shape incoming pulses independent of each other; The HCal preamplifier (Figure 4) on the other hand are single channels boards. In total there will be 1,536 EMCal preamp boards as well as the same number of HCal boards that will be implemented into sPHENIX.

The EMCal and HCal preamps are a necessary part of the detection process and it is essential that they are all working properly in order to get useful data. To make sure all preamps are working properly, each board must go through a series of tests after being assembled before it can be implemented into the experiment. Since there are such a large number of preamplifier boards that will eventually be put into the calorimeters, it would be very beneficial to create an automated test program for these preamps, allowing for quick and easy access to the collected data. It would also make the testing process much more organized for data management and make the process much more simplistic for the user.

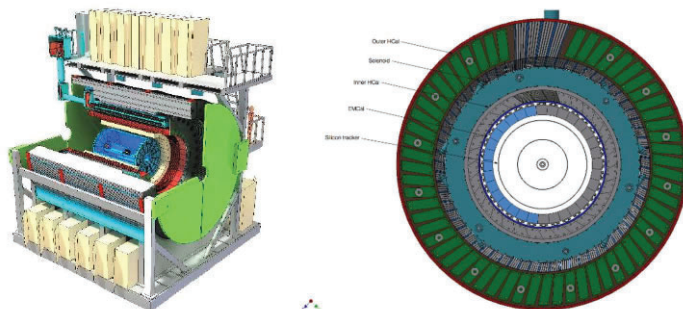


Figure 1 and 2. Engineering model of the proposed sPHENIX detector

II. Methods

A. Choosing a compiler: Matlab

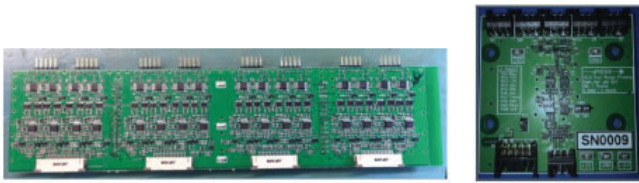
Matlab is computational software that is widely used in the engineering community. It is a very useful tool for matrix manipulation, plotting functions and variables, creation of user interfaces, and interfacing with other programs and devices. As well, Matlab allows a user to download premade functions and programs to allow the user to build more complex applications. All of these attributes contributed to why Matlab is the perfect choice for this program. The project required the ability to create a Graphic User Interface (GUI), manipulate multidimensional array variables, plot graphs, analyze waveforms and generate PDF files, all of which Matlab can provide; this made Matlab the obvious choice of compiler to use for this project.

B. Program overview

The program that was designed creates a graphic user interface that allows a user to input the desired initial conditions for the test, along with the input wave amplitudes that will be processed by the preamps. This allows for the test procedure to be altered at the user's discretion. Upon starting, the GUI will connect to the preamplifier test board and make sure there is a connection. From here, the GUI calls the functions specified by the user to test for Dynamic wave outputs, as well as static voltages and currents for either the HCal or EMCal preamps. After the program is completed, the result is a PDF that gives the output results from the test, and whether the board(s) passed or not.

C. Graphic UserInterface

The GUI for the program is separated into four main sections: The main interface, static conditions, dynamic conditions, and directory settings. Upon starting the program, it will first load the main interface of the GUI shown in figure 5. This contains the inputs for the IP address of the test board, port number, and push buttons to choose between testing an EMCal preamp or an HCal preamp, as well as check boxes to choose whether the user wants to run static tests, dynamic tests or both. Additionally, on the main interface, there is an input box for SN input(s) that changes depending on whether an EMCal or HCal preamp is being tested (Figure 6). When an EMCal preamp is tested, there is an input for only one SN for the one preamp board tested, whereas for the



Figures 3 and 4. The 16 channel EMCal preamp (left) and single channel HCal preamp (right)

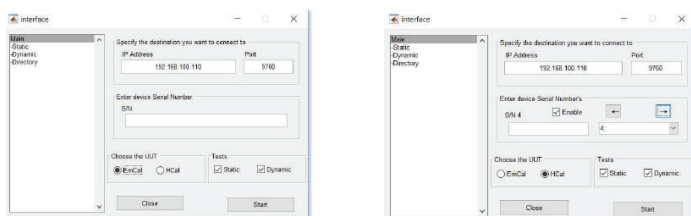


Figure 5. Main interface EmCalselected (left)
Figure 6. Main interface HCalselected (right)

HCal test, the user has the option to test up to sixteen separate preamps at once so there must be an option to input the SN's for all of those boards.

The static conditions section of the GUI allows the user to set the ranges for all the static tests that the preamps will be tested against (Figure 7/8). These include the positive supply current, negative supply current, DAC node voltage ranges, and LED node voltage ranges. For all four of these tests there is an input for the low range value and high range value, and are all included in both the EMCal and HCal tests. There is also an input for the max thermistor temperature which is only included in the EMCal test, and does not have a low range value.

The dynamic conditions section allows the user to set the initial conditions for the dynamic test (Figure 9). It allows inputs for the number of samples, the number of interpolos, and the amplitude of the test pulse with amplifier gain on and off. The test boards ADC collects a total of 24 data points from the preamplifier's output pulse. Most of the significant data is contained in the first half of the data points. By changing the number of samples, a user can choose to use anywhere between 14 to 24 of those samples to be recorded by the program.

Following that, the interpol option of the GUI allows a user to change the number extra data points created by Matlab. The

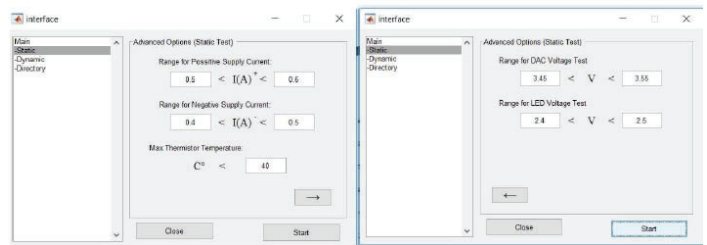


Figure 7 and 8. Static section of the GUI showing all of the input ranges for the static test

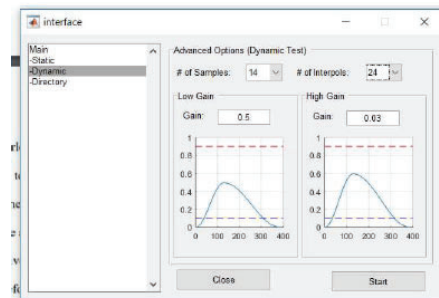


Figure 9. Dynamic section of the GUI

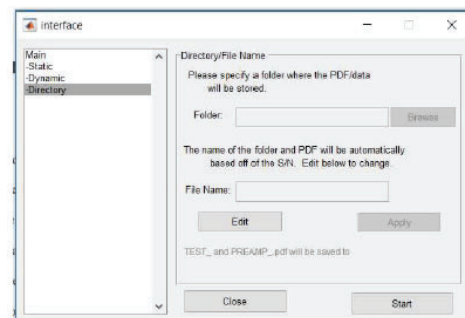


Figure 10. Directory section of the GUI

interpol function provided by Matlab fills in extra data points in-between the collected data allowing for the creation of cleaner looking graphics and more accurate data. The number of interpol shown on the GUI corresponds to the number of extra data points the function creates in-between each of collected data points. This section of this GUI also allows the user to input the amplitude of the test pulse, which then gives an estimated graphic of what the output wave will look like.

The final section of the GUI gives the user the option to select the file location to put all the collected data (Figure 10). Along with this there is also an input to change the folder name which will automatically be set to the last serial number that was inputted.

D. StaticTest

The static test portion of this program is designed to collect and analyze all of the data that is listed in the static section of the GUI. This function connects to the test board and writes to the microprocessor signaling it to collect the data based on the input command. These commands are as follows:

- Command 1: \$I
Collects the current readings for the negative and positive voltagesupply
- Command 2: \$T
Collects the preamp thermistor temperature readings
- Command 3: \$E
Collects the DAC node voltages
- Command 4: \$F
Collects the LED node voltages

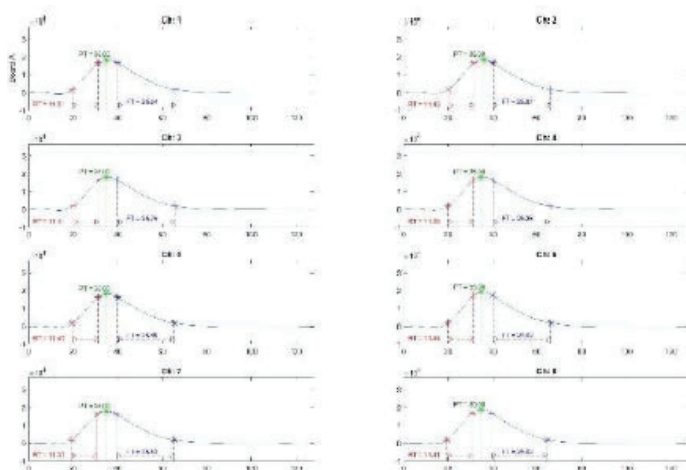


Figure 11. Output graphs of 8 of the 16 EMCAL preamp channels on low gain

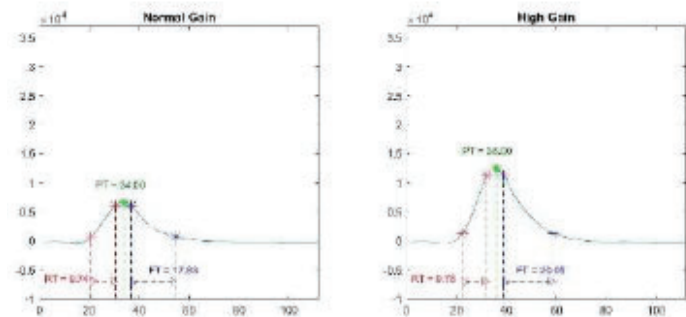


Figure 12. Output of one HCal preamp board with gain normal (left) and high (Right)

After each command is sent, each output is scanned into Matlab variables and tested against the conditions specified in the GUI by the user. If the collected value falls between the specified ranges it will be labeled as “Passed,” and if not, will be labeled as “Failed.” This function will then return two arrays, one for the collected data, and one for the pass/fail data.

E. DynamicTest

The dynamic test function tests the preamps to make sure they are processing input waves the way they are supposed to. Like the static test, this test connects to the test board to allow for interfacing between Matlab and its microprocessor. The commands used are:

Chapter 1. Static Tests

Current:	I (A)	PASS/FAIL
I _(V+)	0.5700	(PASS)
I _(V-)	0.4600	(PASS)
I _(BIAS)	0	(NOT TESTED)

Thermistor:	Temp.	PASS/FAIL	Thermistor:	Temp.	PASS/FAIL
Temp_0	25	(PASS)	Temp_1	31.9000	(PASS)
Temp_2	25	(PASS)	Temp_3	35.5000	(PASS)
Temp_4	25	(PASS)	Temp_5	36.8000	(PASS)
Temp_6	25	(PASS)	Temp_7	37.8000	(PASS)

DAC Voltages:	(V)	PASS/FAIL
DAC_NODE_1	3.5000	(PASS)
DAV_NODE_2	3.5000	(PASS)
DAC_NODE_3	3.5000	(PASS)
DAC_NODE_4	3.5000	(PASS)

LED Voltages:	(V)	PASS/FAIL
LED_NODE_1	2.4700	(PASS)
LED_NODE_2	2.4600	(PASS)
LED_NODE_3	2.4700	(PASS)
LED_NODE_4	2.4900	(PASS)

Total Failed:	0
Total Passed:	15

Figure 13. Static test section of the PDF for an EMCAL preamp

Chapter 2. Dynamic Tests

Board A: Gain Normal, Signal High.

Board A, Channel 1	Data:	PASS/FAIL
Peak Value:	1.9048e+04	(PASS)
Peaking Time:	33 ns	(PASS)
Rise Time:	10.1655 ns	(PASS)
Fall Time:	32.7419 ns	(FAILED)

Board A, Channel 2	Data:	PASS/FAIL
Peak Value:	1.9363e+04	(PASS)
Peaking Time:	34 ns	(PASS)
Rise Time:	10.4224 ns	(PASS)
Fall Time:	26.5771 ns	(PASS)

Board A, Channel 3	Data:	PASS/FAIL
Peak Value:	1.8724e+04	(PASS)
Peaking Time:	33 ns	(PASS)
Rise Time:	10.0945 ns	(PASS)
Fall Time:	28.1807 ns	(PASS)

Board A, Channel 4	Data:	PASS/FAIL
Peak Value:	1.9009e+04	(PASS)
Peaking Time:	33 ns	(PASS)
Rise Time:	10.1636 ns	(PASS)
Fall Time:	27.2791 ns	(PASS)

Board A, Channel 5	Data:	PASS/FAIL
Peak Value:	1.8881e+04	(PASS)

Figure 14. Part of the dynamic test section for an EMCAL preamp

Sets the DAC source voltage. The X's represent inputs for the voltage amplitude so \$D0.8 would set the DAC voltage to 0.8 volts.

Command 2: \$G{H:N}

Sets the gain of the preamp either on or off depending on whether the command is \$GH (Gain High) or \$GN (Gain Normal).

Command 3: \$P0XXXXX

Sets the hexadecimal pulse net mask of the test board. This chooses the channels that the pulse will be sent to. By sending \$PxFFFF the test board will send the pulse through all 16 of the test board channels.

Command 4: \$O{A:B}(0-7)

Chooses the channel that will be read by the ADC. The test board is organized with two boards, A and B, with eight channels each account for all 16 channels that are tested

Command 5: \$AA

Initializes the pulse wave through the selected preamp channel and returns the sampled output wave.

Using these commands the program will set the DAC voltage amplitude based on the GUI input and send a test pulse through the preamp(s). The output wave of each channel is collected separately and stored in arrays. For each channel tested the program will find the rise time, peaking time, and fall time of the output function, and will display all of these values graphically. After this is done, the program takes the statistics for each of these values including mean, standard deviations etc. and tests each channel based on a three sigma deviation from that mean. As the static tests did, this test will also return the pass/fail value of each collected value.

Depending on the preamp being tested, the program will either run the EMCal dynamic test, or the HCal dynamic test. Both collect the same data but handle and display the data in different ways. The EMCal test will graphically display all the channels

output waves together (Figure 11), while the HCal test will display each channels output individually (Figure 12). This is because the EMCal preamps are a single board containing 16 channels, whereas the HCal preamps are single channel boards that need to be documented individually.

F. PDF Generator

The last step for the program is to take all this collected data and display it in a simplistic way. It will generate a PDF file and give a name based on the SN of the board or a specified name given by the user in the GUI and the type of preamp being tested. This PDF allows the end user to easily access and see the tested preamps and if they are running properly. The PDF is separated into two chapters when both static tests are run shown in figures 13 and 14.

III. Conclusion

The finished program is able to collect efficiently all the data necessary to make sure each preamp is working properly. It greatly simplifies and speeds up the tedious process of collecting all of this data which otherwise would have to be done by hand. The program creates an easy to use interface allowing the user to specify a variety of different inputs from testing ranges to input pulse amplitudes. The output PDF creates a centralized document for all of a preamp's data to be stored and easily accessed. With the thousands of preamps that must be tested, it is necessary for this program to exist. This program will ensure that the preamps in the sPHENIX detector will work properly and will continue to help in the advancement of knowledge of the fundamental nature of the universe.

IV. Acknowledgments

This project was supported in part by the U.S. Department of Energy, Office of Science, Office of Workforce Development for Teachers and Scientists (WDTS) under the Science Undergraduate Laboratory Internships Program (SULI).

The design and analysis of the liquid cooling system for the electromagnetic calorimeter of sPHENIX

John Meier

Department of Physics, Stony Brook University, Stony Brook, NY 11794

Rob Pisani

Department of Physics, Brookhaven National Laboratory, Upton, NY 11973

Abstract

Multiple projects utilize the Relativistic Heavy Ion Collider (RHIC) at Brookhaven National Laboratory to collide heavy particles together at high velocities to investigate the components of the particles. sPHENIX, one of the newest projects underway at RHIC, will look to further investigate these particles and their constituents as they collide. The sPHENIX detector is made of multiple concentric layers including the Time Projection Chamber (TPC), the Hadronic Calorimeter (H Cal), and the Electromagnetic Calorimeter (EM Cal). From these layers' electronics, heat is created that needs to be kept from overheating the system. Certain parts, such as the H Cal, need less cooling as they are further to the outside and generate less heat; however, the EM Cal needs greater cooling and will utilize a liquid cooling system. Since the space within the calorimeter is very limited, a solution needs to be found that can both sufficiently pull heat out of the system and fit within the given space. In order to solve this dual problem, we created multiple prototypes that utilized copper tubing and a cool liquid running through the pipes. Then we connected to the circuit boards in the EM Cal using copper braids with copper feet at the end to connect and draw heat out of the boards. Through multiple trials we found a system that sufficiently solved this problem. By creating this design, the sPHENIX project can proceed in the final design of the EM Cal and the construction of the whole detector in the coming years. I have learned about thermal analysis on different systems along with multiple laboratory and construction skills that I can apply to the rest of my time in school and my further career.

I. Introduction

A major facility at Brookhaven National Laboratory is the Relativistic Heavy Ion Collider (RHIC). At this facility, heavy particles are accelerated to high speeds where they are then collided to investigate the internal components of the atom. An upcoming project to utilize the collider is sPHENIX; this project is an upgraded version of its predecessor PHENIX. The detector for sPHENIX will have multiple layers of different detectors that will observe different products of the collision along with multiple characteristics. One of these sections is the electromagnetic calorimeter (EM Cal); this section will observe the electrons and photons that are released during the experiment and their energies. A design aspect that needs to be resolved for this sector is creating a cooling system that will effectively remove heat and cool the circuit boards inside, however, there is a limited space within that complicates the design and requires further inspection. Our goal over the internship was to design and analyze a liquid cooling system for the EM Cal that overcomes the problems presented by the heat load and space. Further complications faced include

designing a flexible, easy to assemble, and easy to open/repair cooling system to make the assembly and maintenance feasible.

II. Methods

A. Absorber Blocks

In the EMCAL there are absorber blocks that serve to absorb electrons and photons from the collision for the circuit boards within to analyze. These blocks are shown in figure 3; they are fabricated from plastic scintillator fibers aligned through brass screens then surrounded by tungsten powder and held together by epoxy. The design for this block is new and untested, so it had unknown thermal characteristics. To determine its thermal conductivity, we used a brass block as a control as it has a well-known thermal conductivity of 109 W/(m K) (2 Thermal). Both blocks were placed in separate insulating foams with a heating pad placed on one end with thermocouples placed at 3 different points: the near, middle, and far end from the heating pad to observe the temperature gradient. By observing each for at least an hour, we were able to obtain these temperature differences and calculate its thermal conductivity relative to the brass.

B. SiPM Board

One significant source of heat within the calorimeter is from the SiPM boards. On the bottom of each SiPM board, there are 16 SiPM which initially produce little to no heat, but as they degrade over the projected 5 year span of the project, this can increase to 1 watt per 16 of these SiPMs—or more simply 1 watt per board. The goal with the SiPM boards is to have them maintain a temperature of 0 degrees Celsius. To achieve this, we designed a model that utilizes copper tubing with cooling liquid flowing through connected to the boards by thermally conductive copper braids that are soldered to both the pipe and the boards. In each sector, there will be 2 loops of the tubing with each going to 48 SiPM boards. The use of copper braids in the design will allow for decent thermal conduction as well as being flexible which will allow for easier construction as each of the boards will be tilted at different angles within the calorimeter.

To test the efficiency of this concept, we created a prototype as shown in figure 4. We attempted to remove conduction and isolate the system by surrounding it with insulation. For testing, we mimicked the heat output using a heating pad at different temperatures of 1, 1.5, and 2 watts to observe the temperature difference at different heats. We flowed cool tap water through the pipes as it gave more stable temperature readings than a chiller and was sufficient for determining the effects on the prototype. Thermocouples were placed at multiple points along our model to measure temperatures; these points were as follows: the bottom of the heating pad, the top of the mock circuit board, at the top of the copper braid, the bridging point of the braid between each pipe, the input and output of the water, and another freestanding

to measure air temperature.

Using the computer program ANSYS, software used to model physical bodies with certain characteristics such as thermal states, we were able to change certain variables with our setups and observe their effects on the system. Notable changes we observed were the effects of the quality of soldering between the tube and the braid in addition to the thickness of the copper braid.

C. Pre-Amplifier Board

The next heat sources within the EMCal are the Pre-Amplifier boards (preAMPs). Every 4 SiPM boards are connected to a preAMP which lays above it. The preAMP will only need to be cooled to 15 degrees celsius instead of the 0 degrees like the SiPM board. The Preamp will lie on top of an aluminum plate of the same dimensions with a thin gap pad material in between. The aluminum plate is then thermally connected by a graphite sheet to an aluminum block that has a copper tube embedded within.

One aspect to investigate was the orientation of this aluminum block with the copper tube. As the copper tube is exposed on one side, we had to outweigh the benefits of each orientation. With the copper tube on top in contact with the aluminum plate it would be closer, but by flipping the orientation, there would be a flat surface for better thermal contact while moving the copper tubing slightly further away.

Next, it's imperative to determine how well the heat is removed from the PreAMP boards, and more specifically, the far edges. Using ANSYS we created a model of the system implementing our custom materials to acquire an accurate representation.

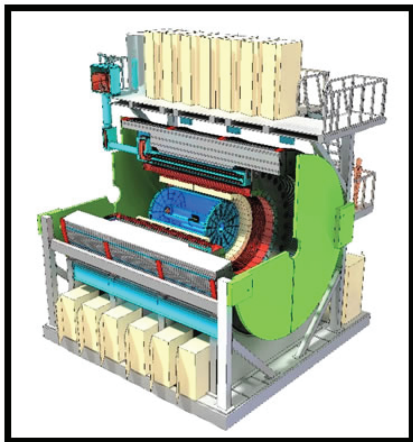


Figure 1. The design for the layout of sPHENIX showing the EMCal as the yellow color towards the center.

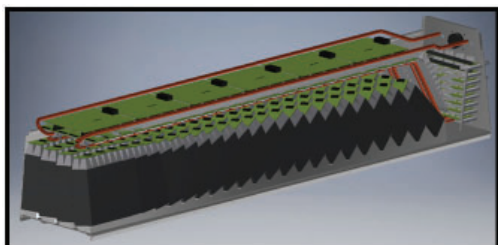


Figure 2. A model of one sector of the EMCal showing the tungsten blocks on the bottom and the circuit boards. From top to bottom, the boards go SiPM board, PreAMP board, and Interface board.

D. Liquid Flow Rate

Within the tubing, a liquid will be flowed that must sufficiently carry the heat out of the system and maintain a liquid form at the low temperatures utilized. When working with liquids to remove heat, there exist ways to optimize heat removal in the system by the way in which the water flows. At low flow rates, liquids will adopt a laminar flow which means that the whole liquid is flowing at the same uniform velocity forward through the pipe, however as flow rates increase, the flow can become turbulent which means that the water will circulate and move throughout the cross-sectional area of the pipe as it flows through. Both flows are shown in figure 9. In our cooling system, a turbulent flow is ideal as the liquid will carry heat away from the edges of the pipe whereas laminar flow can create a layer of insulating warm liquid around the edge that will only conduct heat slowly with a cooler center that doesn't optimize its cooling properties.

The flow rate must be optimized based on other aspects in addition. A higher flow rate will create a more turbulent environment; however, the flow rate must be low enough that the pipes take less impact from the movement of water and minimize any

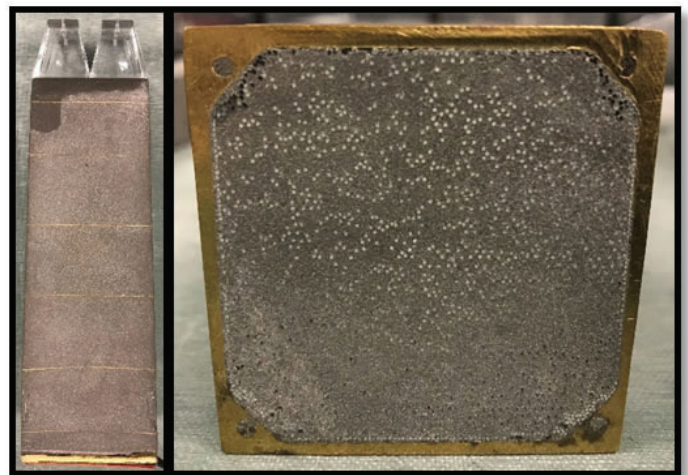


Figure 3. A side and bottom view of the tungsten absorber blocks. With the bottom showing the scintillator fibers imbedded.

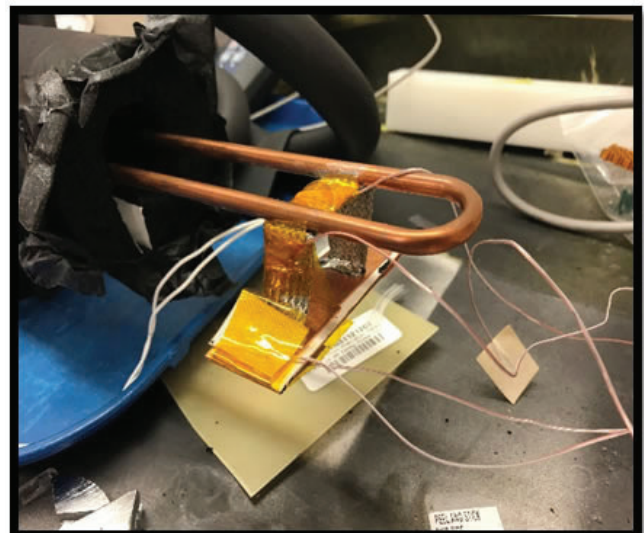


Figure 4. A prototype of our cooling system for the SiPM board with thermocouples attached to measure temperature.

resulting vibration in the pipes that can affect any other internal components decreasing the life expectancy of the system.

Lastly, a liquid needs to be determined that will not freeze at the sub-zero temperatures that are required for cooling while maintaining similar thermal and liquid properties. We decided to utilize a 50/50 water-glycol mixture which will not freeze at 0 degrees Celsius and flow similarly to the water we used while testing.

III. Data and Results

From the design and analysis of the cooling system for sPHE-NIX, we were able to develop a system that can effectively cool the detector within the given space. From tests on the absorber block, we were able to determine that the blocks had a poor thermal conductivity that is 20 to 30 times worse than that of the brass bar used as a control. The temperature graphs are shown in figures 5 and 6. This finding is important to note as it implies that the blocks are decent insulators and will work to prevent the heat from leaking to exterior parts of the system.

The next findings are associated with the SiPM boards. We found that uniformity in solder quality has a small effect on the system which implies that during construction, these points won't be critical and makes the process simpler. In addition, we found the use of copper braids in our current setup to have a 1.7 degree difference between the temperature of the fluid in the pipe and the board below. This indicates that the cooling system is effective and can proceed by implementing this design. Lastly, this experiment is designed for the longevity of the project over about a 5 year span where the heat load is estimated to reach 1 watt per board, but we tested it to be able to function effectively to at least 2 watts per board with only an approximate 6.6 degree difference.

The PreAMP was simulated through the computer program

ANSYS as shown in figure 8. From simulations that proved to be accurate in the case of the SiPM boards, the results with the PreAMP showed a distribution of the cooling out to the edges with only a temperature difference of 0.9 degrees Celsius. This shows an acceptable amount of cooling for what is desired. In addition, from testing the orientation of the blocks that hold the cooling tubes, ANSYS shows only an insignificant 0.03 degree difference from the further distance from the tubing while not taking into account the advantages the surface contacts will offer. This leads us to prefer the orientation where the flat face is up as it should offer a better, more reliable cooling effect.

The last investigated component was the liquid and its flow rate. As a sufficient flow rate needed to be found, we had tested multiple flow rates from slightly above 0 gallons per minute (gpm) up to the max of our gauge at 10 gpm. We found at low flow rates from about 0 to 2 gpm, the temperature of the system would decrease as the flow rate increased but above 2 gpm had no further effect. However, in designing the system, we don't want the water to heat up more than 1 degree from entering to leaving. Assuming it takes all the heat out perfectly, 10 gpm should not raise the temperature of the water past 1 degree when extrapolated tot the full 48 boards it will encounter.

IV. Conclusion

From the experimental designs created and analyzed, progress towards the overall project has been able to proceed. The information on the tungsten-epoxy blocks was quite different from what many people expected, so it gives a new view on how the dynamics of the sector's temperature will work in that regard. In addition, the new design of the SiPM with the knowledge on how certain aspects affect the system provides a functioning model along with more information on how to best construct it. The

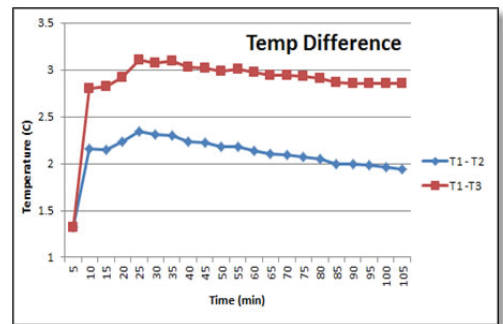
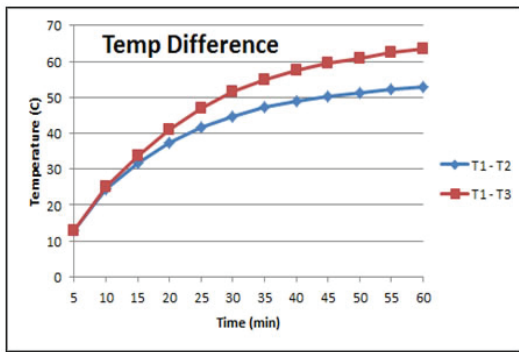


Figure 5 (left) and 6 (right). On the left shows the graph of the tungsten block when a heat pad is applied, and the right shows the brass block. T1 is the closest to the heating pad, T2 is the middle of the bar and T3 at the far end.

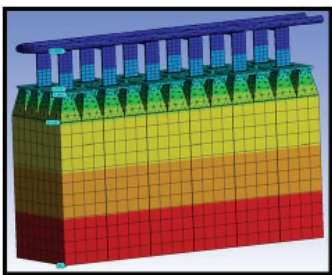


Figure 7. A full thermal analysis of the cooling for the SiPM boards with tungsten blocks and light guides included.

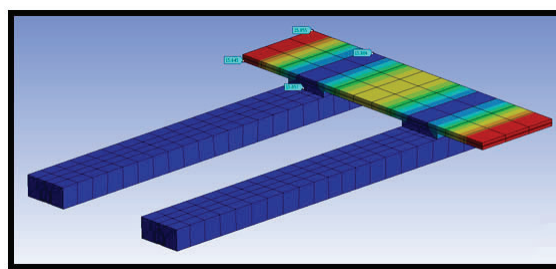


Figure 8. Thermal analysis of the PreAMP board using the current optimal model.

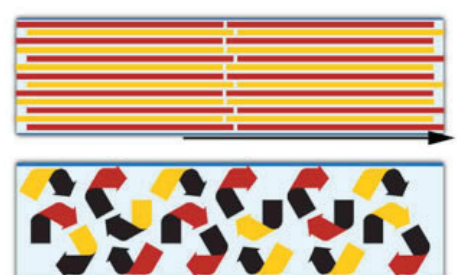


Figure 9. view of laminar (top) and turbulent (bottom) flows within pipes. Shows the movement of water in the tubing (1 Turbulent and Laminar Flow).

preAMP information will contribute to its own effective design on what can be improved and how efficient it is. The flow rate we determined seems to be sufficient on a smaller scale but will require testing on a full model to observe its effects fully.

For future testing on this project more design and testing are required. The full effects of the tungsten blocks will have to be observed with a full setup that is within the casing of the EMCal with heating sources and cooling system applied. In this test, the SiPM board and preAMP board setups will also need to be implemented on a full sector so we can observe effects within the sector along with insulation that can isolate the heat. During this experiment, the effects on the water should be recorded and analyzed to see if it exceeds the 1 degree difference from entrance to exit that is desired. Another part of the EMCal that was not thoroughly investigated over this project are the interface boards; there 6 of these boards per sector and produce about 5 watts each. However, this is a smaller amount of heat compared to the SiPM boards and the preAMP boards so design should be simpler, and implementing the concept of these other parts will prove useful in the interface board's cooling design.

V. References

- “Turbulent and Laminar Flow.” *Water Chiller Remote Air-Cooled Condenser 25 Tons*, 1995, www.advantageengineering.com/fyi/156/advantageFYI156.php.
- “Thermal Conductivity of Common Materials and Gases.” *Densities of Solids*, 2003, www.engineeringtoolbox.com/thermal-conductivity-d_429.html.
- Sawicki, Mikolaj. “Thermal Properties.” *University of Colorado at Boulder*, 2012, www.colorado.edu/physics/phys1110/phys1110_fa12/LectureNotes/Thermal.

VI. Acknowledgments

This project was supported in part by the U.S. Department of Energy, Office of Science, Office of Workforce Development for Teachers and Scientists (WDTS) under the Science Undergraduate Laboratory Internships Program (SULI).

Tests of astronomical image deblenders for gravitational lensing

Lorena Mezini

Astronomy and Physics, Stony Brook University, Stony Brook, NY 11794

Erin Sheldon

Physics, Brookhaven National Laboratory, Upton, NY 11973

Abstract

One of the difficulties of analyzing astronomical images, such as those from the upcoming Large Synoptic Survey Telescope (LSST), is distinguishing between objects. When multiple objects in an image overlap, their light becomes blended and it becomes unclear how much light belongs to each. This limits how well we can measure the effect of weak gravitational lensing on galaxies, an objective of the LSST. The *scarlet* package and the Multi Object Fitter (MOF) have been developed to separate, or deblend, such objects and are both candidate deblenders for the LSST. We ran statistical tests of both by using them to deblend galaxy images that we simulated with the GalSim simulation software package and then, using a method called metacalibration, measured the gravitational shear of the deblended galaxies. We are specifically interested in reducing the fractional shear bias introduced by the deblenders so that we can measure weak lensing effects on the order of 0.1%. Currently, measurements with the MOF deblender have a bias at a fraction of a percent whereas *scarlet* measurements plateau at approximately 1%.

I. Introduction

Weak gravitational lensing is a powerful tool in cosmology. It has provided us with a means of studying the distribution of both luminous and dark matter, as well as dark energy [3]. The effect of gravitational lensing occurs when light traveling through the universe is deflected under the gravitational influence of a massive lens such as a galaxy or a cluster of galaxies. The degree of deflection depends on the mass of the lens. In the weak lensing regime, there is a small degree of deflection that distorts, or shears, the shape of objects such as galaxies and induces ellipticity on the order of 1% [3].

This is a small effect that can only be measured statistically over many galaxies. To that end, survey telescopes image large regions of the sky. The Large Synoptic Survey Telescope (LSST) will begin imaging a 30,000 deg² region of sky visible from Cerro Pachon, Chile in 2022 and produce images that will contain an estimated 20 billion galaxies [4]. In galaxy dense regions of such images, multiple galaxies can overlap and their light blends together, which limits how well the weak lensing effect can be measured. For this reason, “deblender” algorithms, such as *scarlet* [5] and the Multi Object Fitter (MOF) [7], have been developed to separate blended scenes.

A. *scarlet*

Given a set of coordinates, *scarlet* deblends sources, or objects in images such as galaxies, by fitting each with a spectral energy distribution and a non-parametric morphology. It produces a combined model of the entire blended scene, as well as individual models of each source. The *scarlet* user also has the option of setting different constraints on the models and can alter the level at which

they are enforced. Two basic constraints that are applied by default are monotonicity and symmetry. These are based on the assumption that galaxies are for the most part symmetric and that their flux is greatest at the center and falls off as you approach the edges.

One drawback to having images taken at different times is that they will also have different point spread functions (PSFs). This problem is often accounted for by convolving images to a common PSF. It has been demonstrated in the *scarlet* documentation that a partial de-convolution with the PSF produces the best results. To that end, *scarlet* has an option for PSF-matching. The PSF in each band is fit with a target function from which best fit parameters are drawn and used to create a smaller target PSF. The target PSF is used to convolve difference kernels so that they match the input PSF in their band. The PSF convolution can be a lengthy process since the time it takes to complete scales linearly with the number of pixels in the PSF. To make this step more efficient, *scarlet* uses a L0 sparsity penalty that reduces the number of pixels needed in the difference kernel, per band. The difference kernels are then used as the input PSF for each individual source.

B. MOF

Unlike *scarlet*, MOF separates blended scenes by fitting each source with a parametric model. It creates composite models of each galaxy by fitting bulge and disk components separately with Sersic profiles. These profiles are mathematical functions that describe the surface brightness, I , of galaxies. The Sersic profile can be expressed by equation 1 where I_e is the intensity at the radius that encloses half of the light of the galaxy, R_e . n is the Sersic index which describes the shape of the light profile; it can take any value between 0.5 and 4. b is a constant that can be approximated



Figure 1: The image of Stephan’s Quintet, assembled and processed by Robert Gendler and Judy Schmidt, shows the light from the 5 galaxies in the group blending.

as equation 2 for $n > 8$, otherwise it can be expanded as a polynomial and calculated numerically.

$$I(R) = I_e e^{-b \left[\left(\frac{R}{R_c} \right)^{1/n} - 1 \right]} \quad (1)$$

$$b \approx 2n - \frac{1}{3} \quad (2)$$

MOF fits the disk with an exponential profile, which is a Sersic profile with $n = 1$, while the bulge is fit with a De Vaucouleurs' profile, $n = 4$. Each of these components is approximated as a sum of Gaussians and the composite models are determined by taking a linear combination of each component's flux and model. Individual galaxy models are created by subtracting the light from the neighbor's models [7].

Like *scarlet*, MOF also has a form of PSF treatment to deal with different PSFs. It does this by convolving the model with the PSF but does not deconvolve the data.

II. Simulations

Galsim¹ software is used to simulate blended galaxy images. We created simple, two galaxy simulations with one galaxy located near the center of the image and a larger neighbor placed randomly along a circle of radius, r , about the center. A small, random offset between -0.5 and 0.5 was added to each of the galaxies coordinates as well, so the separation between the two galaxies can deviate from r by ± 1.0 pixel.

Galsim gives the option of simulating various types of galaxy models. Many of our simulations used a Sersic profile with index number, n , that is randomly selected between 0.5 and 4.0 . We also created composite models of galaxies in which we modeled the disk as an exponential and the bulge as a De Vaucouleurs' profile. For more complex simulations, we added "knots" of star formation.

Shear, γ , has a γ_1 and γ_2 component. Using the galsim shear option we added $+0.02$ shear in the γ_1 component.

Real observations from ground based telescopes will also have noise and atmospheric and instrumentation effects present in the images. A convolution with a Gaussian PSF is used to mimic the "smearing" effect that the atmosphere has on images. To mimic noise, we create a noise image by drawing randomly from a normal distribution and add it to our simulated image. We adjust the width of this distribution to change the noise level in the image.

A. Metacalibration

The metacalibration [6] method is used to recover the added shear in our simulations. This technique adds some small additional shear to images and measures the response, R , of a shape estimator to it. The responses are used to calibrate the mean two component ellipticity, $\mathbf{e} = (e_1, e_2)$, which is described in metacalibration by equation 3. From this we can also calculate the shear, given in equation 4.

$$e \approx e_{true} + \frac{de}{d\gamma} \gamma + noise = e_{true} + R\gamma \quad (3)$$

$$\gamma = \frac{\langle e \rangle}{\langle R \rangle} \quad (4)$$

The response for each component is calculated using equations 5 and 6 where \mathbf{e}^+ is the measurement made when an image is sheared by some positive value, γ_+ , and \mathbf{e}^- is the measurement

made when an image is sheared by some negative value, γ_- . The magnitude of the additional shear is 0.01 .

$$R = \frac{e^+ - e^-}{\Delta\gamma} \quad (5)$$

$$\Delta\gamma = \gamma_+ - \gamma_- = 2\gamma \quad (6)$$

III. Control tests and results

We are interested in measuring the bias due to deblending. This is calculated using equation 7.

$$bias = \frac{\langle \gamma \rangle - \gamma_{true}}{\gamma_{true}} \quad (7)$$

but, this measurement may also include contributions from other sources of bias. For this reason, it is important to have various control tests that can isolate potential causes of bias. Two of our control tests use simulated images with a single galaxy near the center only to eliminate any bias from blending.

A. No deblender control

We input the original single galaxy image directly to metacalibration and make a shear measurement. Any non-zero bias that we calculate in this test would be inherent to the image or attributed to metacalibration.

Table 1: This table summarizes the measurements from the single object, no model, control tests

Summary of Measurements for Single Object Tests			
Galaxy type	Noise RMS	Number of images	Bias Value
Sersic	10.	3e6	$-0.00162038 \pm 0.00168205$
Sersic w/ knots	10.	1e6	$-0.00479053 \pm 0.00102371$

B. Single object control

We deblend an image of a single galaxy so that we can get a model. The model of the galaxy is then input into metacalibration for shear measurement. The motivation behind this is to see if there is any bias introduced by galaxy models that have no influence from blending with a neighboring galaxy. This test is only done for *scarlet* since MOF returns the original input image when there is only 1 galaxy present which would yield the same result as the no deblender control.

The results are shown in table 2 for *scarlet* run in to different modes – with and without PSF treatment. Including PSF treatment by implementing PSF matching produces a larger bias. This strongly suggests that the PSF is not being handled correctly within *scarlet*.

Table 2: This table summarizes the measurements from the single object model control tests

Summary of Measurements for Single Object			
Type of De-blend	Noise RMS	Number of images	Bias Value
Scarlet w/ PSF Matching	0.1	1e6	$-0.0543007 \pm .00157568$
Scarlet w/ no PSF treatment	0.1	1e6	$-0.00479053 \pm 0.00102371$

C. Additive bias

This control test uses an image with two galaxies, but it differs from our other tests in that we vary the amount of shear added. The purpose of this test is to measure whether or not there is any constant being added to our shear bias measurements regardless of how much the galaxies are sheared. We completed this test for images with a galaxy separation of $r = 9$ that are deblended with *scarlet*. We held one shear component at a constant 0.0, but increased the other from 0.0 to 0.02 in increments of 0.005. We used metacalibration to measure the additive for the changing shear component. These results are plotted in figure 2 in the appendix. The measurements in which both \mathbf{e}_1 and \mathbf{e}_2 equal 0.0 are consistent with 0.0 indicating that there is no additive bias. For points in which either \mathbf{e}_1 or \mathbf{e}_2 are greater than 0.0, there is some deviation from the expected value but it is not by a constant amount which would be the case for an additive bias.

D. Bias as a function of separation between objects analysis and results

In real data, the amount of blending will vary from one set of galaxies to another. For this reason, we measured the fractional bias as a function of separation between the two galaxies. To do this, we created sets of the same two galaxy images and only varied the separation, r , from 7 pixels for highly blended galaxies, to 15 pixels for less blending. The most complex galaxy model we simulate is the bulge+disk+knots of star formation model. In figures 3 and 4, we show the resulting bias from deblending these galaxy types using MOF and *scarlet*, respectively. The results for MOF show a very small, less than 1%, fractional bias at almost all points. This is within the desired range for weak lensing measurements. For *scarlet*, the bias doesn't drop below approximately 1-2%.

E. Position tests

The coordinates of each galaxy refer to the position of the center of the galaxy. We studied the distribution of the differences between the true coordinates of galaxies and the coordinates of the models. Off-centering could cause trouble when we subtract the model of the neighbor from the original image in order to make shear measurements on the center object.

F. Position test results

Ideally, these distributions should be narrow Gaussians, centered around 0.0. We calculate and plot the differences for each galaxy coordinate, labeled p_1 and p_2 , separately. We show the results of the position tests for 7 pixel galaxy separations. The results from MOF are given in figure 5. We only made measurements on the center galaxy for MOF. The *scarlet* results for both galaxies are shown in figures 6 and 7.

G. Position test analysis

The MOF results are as expected, but the *scarlet* results are not. In the low noise case for *scarlet*, the neighbor galaxy distribution exhibits multiple peaks and the center galaxy distribution has a greater width than for MOF. For the *scarlet* noisy results, although there are not visibly multiple peaks, the distributions are wider than for low noise so the peaks may be "covered up" by noise. The multi-peak results in 6 indicates that something may be off in the *scarlet* centering algorithm. In the 7 results, the mean and standard deviation are over $1e3$ orders of magnitude greater than the dimensions of the simulated image. This indicates that *scarlet* is sometimes

shifting galaxies outside of the images.

During the fitting process, *scarlet* uses its current model and one that has been shifted by some specified value, defaulted to 0.2 pixels, to estimate the dipoles that would appear in residuals when models are shifted by some magnitude. This means that the approximated dipoles will only be exact for the 0.2 pixel case and not smaller offsets. We suspect that this is the cause of the strange distributions seen in figures 6 and 7.

The extremely large shifts in galaxy positions introduced in noisy data could be due to *scarlet* not accounting for degeneracy. The linear solver may become unstable when galaxy components become too spatially similar.

H. Noise tests

It is essential that the noise model of the image being input into metacalibration is accurate. We noticed that the *scarlet* models for each galaxy sometimes over fit and absorb some noise. This is not accounted for in the metacalibration noise model and may be a source of bias. To study the extent of the noise effects introduced by modeling with *scarlet*, we measured the mean, and standard deviation on a per pixel basis for the residuals of "original image - model". Ideally, the latter should be equal to the noise RMS value used to generate the noise image and the former should equal 0.0.

I. Noise test results

The results from the noise tests are shown in figures 8 and 9.

J. Noise test analysis

For both noisy and low noise data, we see round structure in the standard deviation and mean residuals. The low noise data mean is greatest at the center, indicating that the model underestimates the flux at the center of the galaxy. The opposite is true for the noisy images. We suspect that this behavior could be a consequence of incorrect center positions.

IV. Conclusion

The gravitational weak lensing effect is very small and we would like to be able to measure it on the order of 0.1%. For this reason, we need the bias versus separation curves to approach 0 bias at large separations. The Multi Object Fitter performs is currently performing well, however, *scarlet* still shows a bias of a few percent even at larger galaxy separations. We were able to identify a couple of issues within *scarlet*, inaccurate center updates and PSF treatment, that when corrected, could reduce this large bias. Beyond the bias levels, *scarlet* offers an advantage over MOF by being non-parametric – it is able to model arbitrary galaxies whereas MOF can only perfectly describe objects that look like its parametric models.

Unlike our simulated images, real sky images will contain multiple galaxies of which more than two can be blended at a time. In the future, we can expand our tests by deblending more realistic simulations of galaxy clusters with N number of galaxies. Rather than using exact coordinates for modeling and shear measurement, we can let Source Extractor [1] detect objects. These more realistic scenarios will give a better estimate of how well the deblenders perform.

V. Acknowledgements

This project was supported in part by the U.S. Department of Energy, Office of Science, Office of Workforce Development for

VI. References

E. Bertin and S. Arnouts. “SExtractor: Software for source extraction.” In: 117 (June 1996), pp. 393–404. doi: 10.1051/aas:1996164.

A. W. Graham and S. P. Driver. “A Concise Reference to (Projected) Sérsic $R^{1/n}$ Quantities, Including Concentration, Profile Slopes, Petrosian Indices, and Kron Magnitudes”. In: 22 (2005), pp. 118–127. doi: 10.1071/AS05001. eprint: astro-ph/0503176.

H. Hoekstra and B. Jain. “Weak Gravitational Lensing and Its Cosmological Applications”. In: *Annual Review of Nuclear and Particle Science* 58 (Nov. 2008), pp.99– 123. doi: 10.1146/annurev.nucl.58.110707.171151. arXiv: 0805.0139.

VII. Appendix

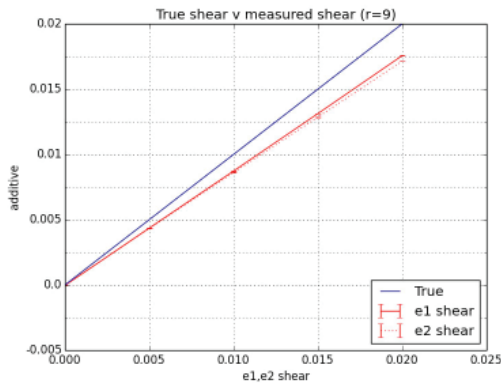


Figure 2: Plot of additive measured as a function of input additive for galaxies with a 9 pixel separation. One shear component was kept at a constant 0.0 while the other was increased from 0.0 to 0.02. Measurements were made on the changing component with meta-calibration. The blue line corresponds to the expected results and the red solid and dashed lines correspond to measurements on the changing component. When input e_1 and e_2 are 0.0, the measured additive are consistent with 0.0 which indicates there is no additive bias.

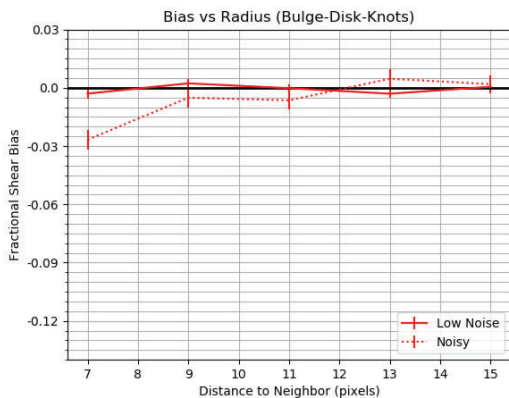


Figure 3: Two blended galaxies are simulated using the bulge+disk+knots of star formation model. For various separations, they are debled with MOF. Metacalibration is used to recover the shear. The fractional shear bias is plotted as a function of galaxy separation. The dotted line corresponds to debled noisy images, and the solid corresponds to debled images with little noise.

Ž Ivezić et al. “LSST: from Science Drivers to Reference Design and Anticipated Data Products”. In: *ArXiv e-prints* (May 2008). arXiv: 0805.2366.

F. Moolekamp and P. Melchior. “Block-Simultaneous Direction Method of Multipliers: A proximal primal-dual splitting algorithm for nonconvex problems with multiple constraints”. In: *ArXiv e-prints* (Aug. 2017). arXiv: 1708.09066 [math.OC].

E. S. Sheldon and E. M. Huff. “Practical Weak-lensing Shear Measurement with Metacalibration”. In: 841, 24 (May 2017), p. 24. doi: 10.3847/1538-4357/aa704b. arXiv: 1702.02601.

A. Drlica-Wagner et al. “Dark Energy Survey Year 1 Results: The Photometric Data Set for Cosmology”. In: 235, 33 (Apr. 2018), p. 33. doi: 10.3847/1538-4365/aab4f5. arXiv: 1708.01531.

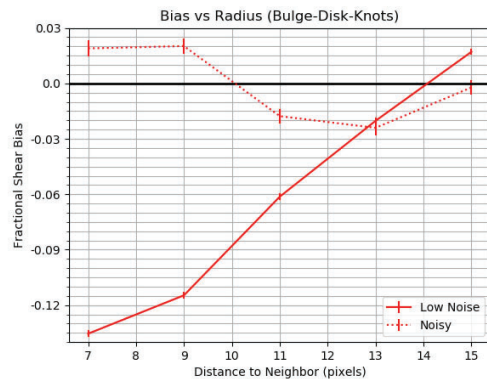


Figure 4: Two blended galaxies are simulated using the bulge+disk+knots of star formation model. For various separations, they are debled with scarlet. Metacalibration is used to recover the shear. The fractional shear bias is plotted as a function of galaxy separation. The dotted line corresponds to debled noisy images, and the solid corresponds to debled images with little noise.

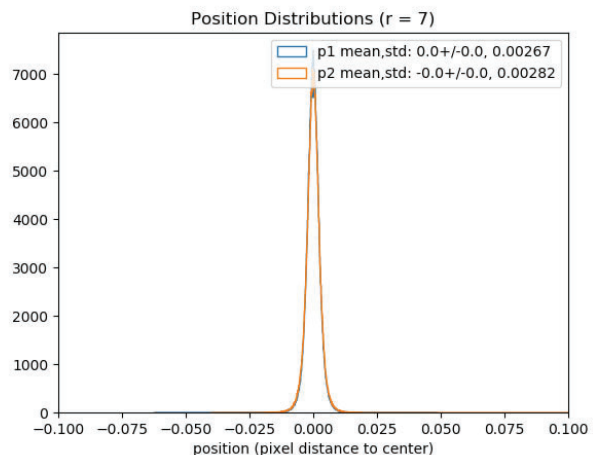


Figure 5: The histogram shows the differences between the true coordinates and modeled coordinates for the center galaxy in a low noise image debled with MOF. The separation between the center galaxy and neighbor in this set of images is 7 pixels.

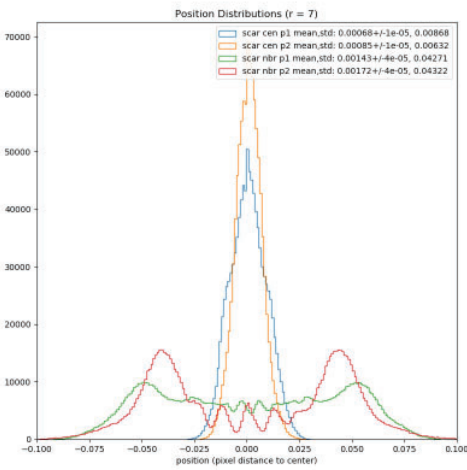


Figure 6: The histogram shows the differences between the true coordinates and modeled coordinates for the center, labeled “cen”, and neighbor, labeled “nbr”, galaxy in a low noise image deblended with *scarlet*. The separation between the center galaxy and neighbor in this set of images is 7 pixels. Multiple peaks in the distribution indicate a problem with the centering algorithm.

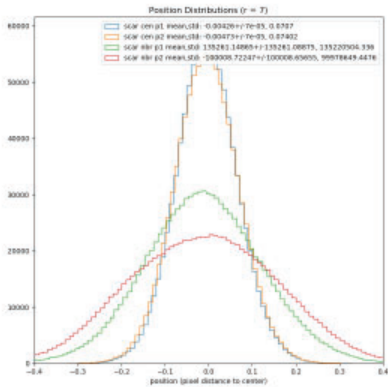


Figure 7: The histogram shows the differences between the true coordinates and modeled coordinates for the center, labeled “cen”, and neighbor, labeled “nbr”, galaxy in a noisy image deblended with *scarlet*. The separation between the center galaxy and neighbor in this set of images is 7 pixels. The wide distribution and large means indicate there is a problem with the centering algorithm.

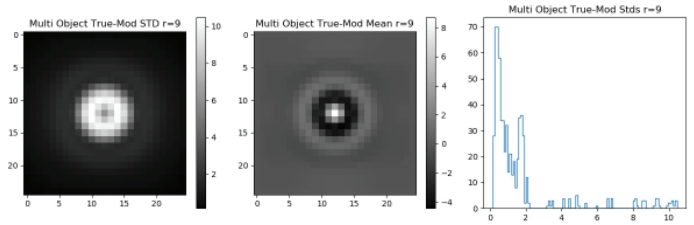


Figure 8: We measured the mean, and standard deviation on a per pixel basis for the residuals of “original image - model”. The galaxies in these images had a 9 pixel separation and a 0.1 noise RMS value. The first frame shows the standard deviation, second the mean, and the third is a histogram of the standard deviations per pixel.

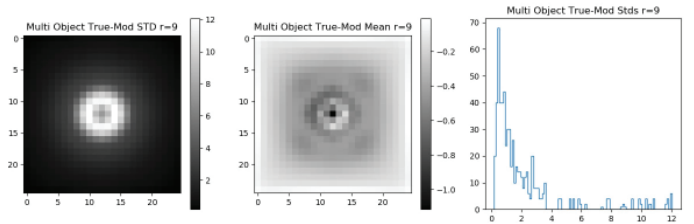


Figure 9: We measured the mean, and standard deviation on a per pixel basis for the residuals of “original image - model”. The galaxies in these images had a 9 pixel separation and a 10 noise RMS value. The first frame shows the standard deviation, second the mean, and the third is a histogram of the standard deviations per pixel.

Black carbon and carbon monoxide source assessment in the Amazon during the Green Ocean Amazon (GOAmazon) 2014/5 Campaign

Maité Morales Medina and Olga L. Mayol-Bracero

Natural Sciences Faculty, Department of Environmental Sciences, University of Puerto Rico, Rio Piedras Campus, San Juan, PR. 00925-2534

Arthur Sedlacek III and Ernie R. Lewis

Department of Environmental and Climate Sciences, Brookhaven National Laboratory, Upton, NY 11973

ABSTRACT

Human activities, such as the combustion of fossil fuels and biomass burning (BB), contribute to global climate change and affect Earth's radiative budget. To provide a better understanding of these effects, the Atmospheric Radiation Measurement (ARM) Climate Research Facility of the US Department of Energy undertook the Green Ocean Amazon (GOAmazon) campaign. In this study, combustion products such as black carbon (BC) and carbon monoxide (CO) were measured in 2014-2015 in the Amazon rainforest at Manacapuru, Brazil. However, some of these measurements were influenced by emissions from a local diesel generator that was used to support the sampling site. As the ratio of BC to CO concentrations differs for different BC sources (such as biomass burning, urban environments, and diesel generators), this ratio was used to determine time periods when the measurements were affected by local diesel generator emissions. Using a regression line between concentrations of BC and CO, the ambient background CO concentration was determined to be 85 ppbv for the Amazon rainforest. An unbiased BC/CO ratio was obtained by subtracting the CO ambient background concentration before taking the ratio. This procedure enabled us to distinguish between biogenic emissions and local diesel generator emissions, which were assumed to have a BC/CO ratio greater than 10 ng/ppbv-m³. Future plans are to analyze the data for which generator emissions have been removed to identify and study the influences of BB and urban air masses on climate.

I. INTRODUCTION

Aerosols, particles in liquid or solid form suspended in the atmosphere, play an important role in Earth's radiative balance¹ and climate through both direct and indirect effects (Fig. 1). Direct effects consist of changes in the surface radiative forcing due to scattering or absorption of light by aerosol particles. Scattering reflects the light out of atmosphere and exerts a cooling influence on climate, whereas absorption of solar radiation by atmospheric particles exerts a warming effect². Indirect effects are changes in Earth's radiative budget as a consequence of changes in the numbers and size distributions of cloud droplets (Fig. 1, right). Every cloud droplet forms on an aerosol particle that has acted as its nucleation core, and an increase in aerosol particle number concentration is generally associated with an increase in number of smaller cloud droplets, resulting in more light being scattered upward and out of the atmosphere, providing a cooling effect².

Black carbon (BC) is the major light-absorbing aerosol spe-

cies in the atmosphere and thus is an important contributor to direct radiative forcing². BC is generated from internal combustion engines, biomass burning, and biofuel burning. Previous studies have shown large differences among estimates of the effect of black carbon on climate. This topic has been examined extensively, yet it is not well understood³.

To provide a better understanding about the effects of BC on Earth's radiative forcing, the Atmospheric Radiation Measurement (ARM) Climate Research Facility of the US Department of Energy undertook the Green Ocean Amazon (GOAmazon) campaign. As part of the field campaign, the ARM Mobile Aerosol Observing System (MAOS) was deployed outside the city of Manacapuru (Brazil) and operated starting late January 2014 until December 2015. During this period, species such as BC and carbon monoxide (CO) were sampled as tracers of incomplete combustion (resulting from biomass burning, urban environments, and diesel generators). However, the measurements of these substances can be influenced by contamination from local sources, in which emissions do not represent typical atmospheric contributions, either natural or anthropogenic. As the ratio of BC to CO concentrations differs for different combustion sources, this ratio is used in this study to determine time periods when the measurements were affected by local diesel generator emissions. Before taking this ratio, the CO ambient background concentration must be subtracted from the measured CO concentration. The CO ambient background, mainly product of oxidation of biogenic, with longer atmospheric lifetime than BC, can influence the analysis of the BC/CO ratio. These other factors could increase the ambient CO concentration by approximately 30%, especially in rural regions⁴.

II. METHODS

A. Sampling Site

The MAOS was deployed 8 km north of the city of Manacapuru, Brazil, in the heart of the Amazon rainforest (Fig 2). A diesel generator, used to support the sampling site when the electric

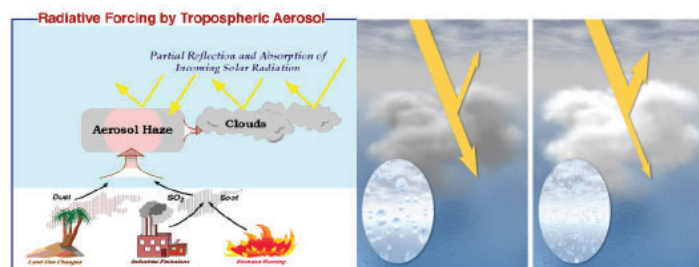


Figure 1: Direct (left) and indirect (right) effect induced by the concentration of aerosol particles in the atmosphere.

service was interrupted, was located between 220 – 245 degrees and 10 m from the container.

B. Measurements

Combustion products such as BC and CO were measured. The CO concentration was measured with a carbon monoxide/water vapor/nitrous oxide (CO/H₂O/N₂O) analyzer (CO-ANALYZER)⁵. This instrument, manufactured by Los Gatos Research, uses a fourth-generation cavity enhanced absorption technique. The instrument provides less than 1 ppbv precision in 1 second with accuracy from 5-10% and 5-second time resolution. The concentration of BC was measured using a Single-Particle Soot Photometer (SP2) (Droplet Measurement Technologies company) which detects the mass of individual BC or BC-containing particles using laser-induced incandescence. As the BC in the particle is heated through absorption of the laser light, it incandesces, and the emitted light is detected by the SP2⁶. The measurement of BC refractory (rBC) mass concentration is proportional to the magnitude of the incandescence signal⁷.

C. Analysis

The data from January to October 2014 were analyzed in this study. To determine the CO ambient background concentration, a linear regression was made with 5-min averages of BC and CO concentrations for April 4 to April 6, 2014. The intercept is the CO ambient background concentration, which was assumed to be valid for the entire year. This was subtracted from the measured CO concentration and the difference was used to calculate the BC/CO ratio for the entire time period considered.

Based on previous analysis, the BC/CO ratio for biomass burning events was estimated as 9 ng/ppbv m³⁴. Generator emissions on our previous analysis were identified by examining emissions when the wind was 220°-245° relative to the container where the SP2 is located, and the resulting statistical histogram of the BC/CO ratio for these conditions resulted in a BC/CO ratio of 10 ng/m³; thus, ratios of this magnitude or greater were considered to have resulted from the diesel generator (Fig 3).

III. RESULTS AND DISCUSSION

CO ambient background concentrations vary between wet and dry season in the Amazon, mainly due to greater deforestation and biomass burning during dry seasons⁸. However, since the deforestation around the sampling site is not drastic, it is assumed that the ambient CO background will remain constant throughout the year. Based in the linear regression shown in Figure 3, this value was determined to be 85 ppbv. The difference in BC/CO ratio determined with and without subtraction of the ambient CO background value is shown in Fig. 4.

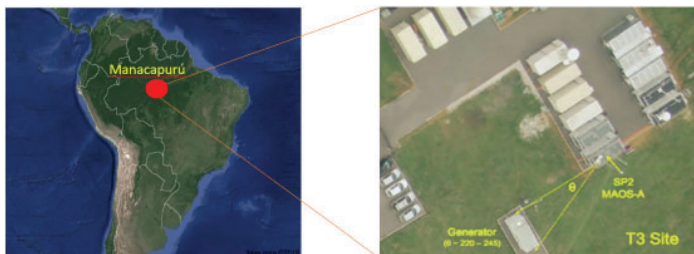


Figure 2: GOAmazon sampling site location in Manacapuru, Brazil (left) and the location of the diesel generator relative to the MAOS container with the SP2 (right).

Since the generator was so close to the sampling site, emissions from this source were not diluted in the atmosphere, drastically increasing the concentrations measured for both CO and BC during short period of time. However, since diesel combustion is the major global source of BC⁸, the BC/CO ratios increases altering the identification of other sources of combustion. As a result, values were identified to distinguish between generator and generator-free emissions, as show in Figure 5.

IV. Conclusion

Carbonaceous aerosols play an important role in climate forcing. Therefore, it is crucial to understand their atmospheric concentrations. While former investigations have applied the BC-CO correlations^{9,10}, this study utilizes the BC/CO ratio as a tracer to identify local diesel generator emissions. The CO ambient background concentration was determined to be 85 ppbv for the Amazon rain forest for a time period in April 2014. Local diesel generator emissions were identified using the BC/CO ratio method as a tracer of this event. Future plans are to analyze the filtered data to identify and study the influences of BB and urban air masses on climate.

V. Acknowledgement

This project was supported in part by the National Science Foundation, Louis Stokes Alliance(s) for Minority Participation (LSAMP) at (Name of School) under the LSAMP Internship Program at Brookhaven National Laboratory.

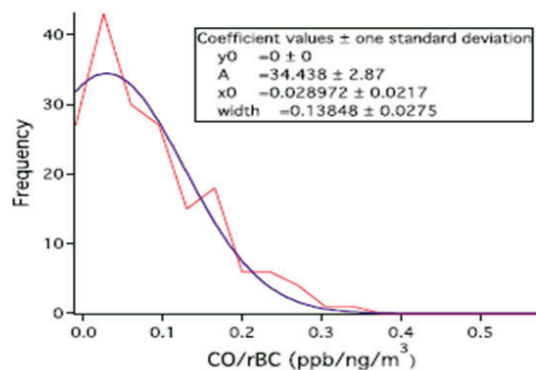


Figure 3: Statistical histogram of the BC/CO ratio, based on our previous analysis.

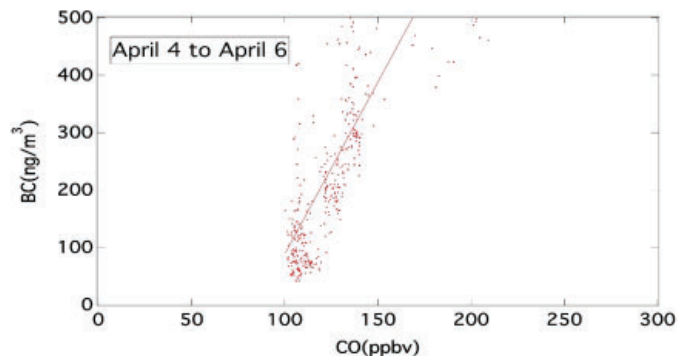


Figure 3: Linear regression used to obtain the CO ambient background concentration with the linear equation.

VI. References

- Mark Z. Jacobson (2001) Strong radiative heating due to the mixing state of black carbon in atmospheric aerosols, *Nature*, Vol 409
- Peter R. Buseck and Stephen E. Schwartz (2003) *Tropospheric Aerosols Treatise of Geochemistry*, Vol 4
- T. C. Bond (2013) Bounding the role of black carbon in the climate system: A scientific assessment, *Journal of Geophysical Research: Atmosphere*, Vol 118, 5380–5552.
- Spackman, J. R (2008), Empirical correlations between black carbon aerosol and carbon monoxide in the lower and middle troposphere, *Geophysical Research Letters*, Vol. 35.
- Springston, S. (2015) *Carbon Monoxide Analyzer (CO-ANALYZER) Instrument Handbook*
- Schwarz, J. P., et al. (2006), Single-particle measurements of midlatitude black carbon and light-scattering aerosols from the boundary layer to the lower stratosphere, *Journal of Geophysical Research: Atmosphere*, Vol 111.
- Scott J Goetz, Matthew Hansen, Richard A Houghton, Wayne Walker, Nadine Laporte and Jonah Busch (2015) Measurement and monitoring needs, capabilities and potential for addressing reduced emissions from deforestation and forest degradation under REDD, *Environmental Research Letters*, Vol 10, Number 12.
- Nazar Kholod, Meredydd Evans, and Teresa Kuklinski (2016) Russia's black carbon emissions: focus on diesel sources, *Atmospheric Chemistry. Physics*, Vol 16, 11267–11281.
- Darrel Baumgardner, G. Raga, O. Peralta, I. Rosas, and T. Castro (2002) Diagnosing black carbon trends in large urban areas using carbon monoxide measurements, *Journal of Geophysical Research*, Vol 107.
- R. Subramanian, G. L. Kok and D. Baumgardner (2010) Carbon over Mexico: the effect of atmospheric transport on mixing state, mass absorption cross-section, and BC/CO ratios, *Atmospheric Chemistry Physics*, Vol 10, 219–237.

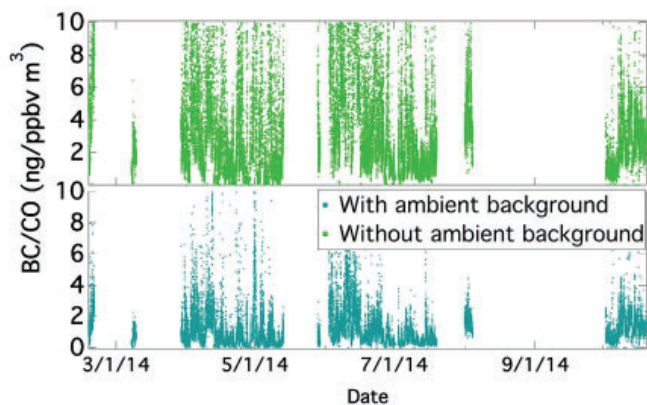


Figure 4: BC/CO ratio with and without the CO ambient background concentration.

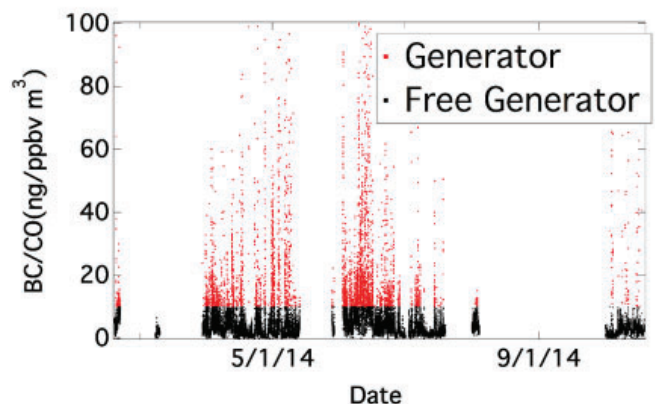


Figure 5: Time periods when the BC/CO ratio was greater than 10 ng/ppbv m³, which were considered to be local diesel generator influence, are shown in red.

Spectra of identified particles in gold on gold fixed target collision at 4.5 GeV with STAR detector

Jesus D. Negrete

Department of Physics and Astronomy, University of California Riverside, Riverside, California 92521

Jason Bryslawskyj

Department of Physics and Astronomy, University of California Riverside, Riverside, California 92521

Aihong Tang

Physics Department, Brookhaven National Laboratory, Upton, NY 11973

Abstract

The Relativistic Heavy Ion Collider (RHIC) at the Brookhaven National Laboratory (BNL) can be used for gold on gold nuclei fixed target collisions at a center of mass energy ($\sqrt{s_{NN}}$) of 4.5 GeV. Measuring spectra of identified particles with the Solenoidal Tracker at RHIC (STAR) detector is done to understand the collision and to help determine whether a Quark Gluon Plasma (QGP) state was created from the collision. In addition to protons, π^\pm and K^\pm being identified, Δ^{++} , Δ^0 and Λ are identified by searching for their decay products known as daughter particles. Δ^{++} , Δ^0 and Λ are identified by analyzing the momentum and mass of their daughter particles that are identified by the reconstructed mass of the detected particles.

I. Introduction

A heavy ion collision transpires when two nuclei traveling near the speed of light collide and this also creates many particles. These particles can be detected with the Solenoidal Tracker at RHIC (STAR) detector, specifically using two of its subdetectors, the Time Projection Chamber (TPC) and Time of Flight (TOF) detector that accurately measures particles' momentum and mass. Evaluation of the properties of particles that are created after the collision is fundamental in understanding the system of the collision.

The Relativistic Heavy Ion Collider (RHIC) at the Brookhaven National Laboratory (BNL) is used to accelerate nuclei to 99.9995% the speed of light and collide them create a Quark Gluon Plasma state (QGP). The STAR experiment operates to understand the QGP by detecting collision products at varying collision energies $\sqrt{s_{NN}}$. The TPC is a large cylindrical volume filled with P10 (90% Argon, 10% Methane) gas that helps in analyzing the particles detected from the energy that the particles lose to the gas as they travel through the cylinder.¹ As charged particles pass through the gas, they ionize it, allowing their trajectories to be measured. The TOF detector is located at the exterior of the TPC and can accurately measure the time taken for a particle to travel from the collision vertex to the detector.² The charge of a particle is determined by having the two subdetectors be placed inside a large solenoidal magnet. The charge of a particle is determined by the way the particle bends in the magnetic field. Positively charged particles would bend counter-clockwise while negatively charged particles would bend clockwise. The momentum of these particles will also be proportional to the strength of the magnetic field. A fixed target collision is a type of collision that has a gold foil target stationary inside of the detector. Groups of billions of gold ions called bunches are accelerated by RHIC until reaching the desired energy for the collision. Collisions occur by having the beam graze the foil target.

II. Analysis

A. Particles identified directly

The identification of particles created from a collision is done by using the accurate measurements of the momentum and mass by the TPC and TOF detector. The identities of the detected particles are verified by comparing the reconstructed mass to the known mass of particles that are expected to be created from this collision. Many particles are expected to be created from a heavy ion collision and three of them are p (protons), π^\pm (pions) and K^\pm (kaons). The raw spectra for these particles are plotted as a function of the transverse mass (m_T) vs the rapidity (y) of the particles as shown in Figure 1. The transverse mass (m_T) is given by:

$$m_T = \sqrt{m^2 + p_T^2} \quad (1)$$

where m is the rest mass of the particle and p_T is the transverse momentum. Rapidity (y) is a measurement of the direction that the particle is moving with respect to the beam axis and is described by:

$$y = \frac{1}{2} \ln \left(\frac{E + p_z}{E - p_z} \right) \quad (2)$$

where E is the energy of a particle and p_z is the momentum in the z direction.

B. Particles identified indirectly

Other particles expected to be created after the collision but were not detected directly by the detectors because of their decay time, can be searched by analyzing their decay products known as daughter particles. Decaying particles that are investigated involve the Δ^{++} that decays into a p and π^+ , Δ^0 that decays into a p and π^- and Λ which can decay to either a p and π^- or a \bar{p} and π^+ . To establish if the decay products of a particle were detected, the invariant mass (M) of an investigated particle is calculated using:

$$M = \sqrt{m_0^2 + m_1^2 - 2(E_0 E_1 - p_0 p_1)} \quad (3)$$

where m is the rest mass of a particle, E is the energy of a particle, and p is the momentum of a particle. The subscripts on the mass, energy and momentum are used to differentiate one daughter particle to the other one. A particle is identified by comparing the invariant mass to the known rest mass of the particle.

To determine if Δ^{++} was initially created, all p's and π^+ 's in the same event are paired together. Using the properties of the paired particles, the invariant mass is calculated and plotted. To improve the signal, the background is estimated by intentionally matching p's and π^+ 's from different events (see Figure 2). The events are only allowed to be mixed if the difference in the z vertex is less than 0.5 cm. The estimated background is scaled by a normalization constant that will allow for the unmixed events

histogram to be subtracted by the mixed events histogram (see Figure 3). The normalization constant is calculated using:

$$Norm = \frac{\int_a^b \text{Unmixed event histogram}}{\int_a^b \text{Mixed event histogram}} \quad (4)$$

where the values a and b indicate an area outside of the peak where the background is dominant. The region used in the normalization of p and π^+ histograms is between 1.5 and 1.75 GeV/c². This area is used to normalize the mixed events by having the mixed event histogram be scaled by the value from equation (4).

In searching for Δ^0 the process described above is followed but instead the particles paired together are all the p's and π^- 's. The region used to normalize the p and π^- histograms is between 2.4 and 2.8 GeV/c².

Λ also follows the same process described above but Λ is searched for by pairing all p's and π^- 's and all \bar{p} 's and π^+ 's. Furthermore Λ has additional parameters that must be considered because it has a longer decay time than other particles being investigated in this paper. One condition for a pair to be used in calculating the invariant mass for Λ is that the distance between the pair must be less than 1 cm. This condition is applied to pair particles that are near each other. Another condition used is for the distance of closest approach (DCA) to be less than 1.5 cm. The DCA cut is applied to select particles whose centers are close to each other and follows up on the previous condition. The last condition considered is that the estimated decay length for the pair must be greater than 3 cm. This condition takes the half-life of Λ into consideration by excluding the particles with a shorter decay length. When mixing events for Λ these conditions are used with the previously stated condition that the difference in z vertices be less than 0.5 cm.

The spectra of protons, pions and kaons shown in Figure 1

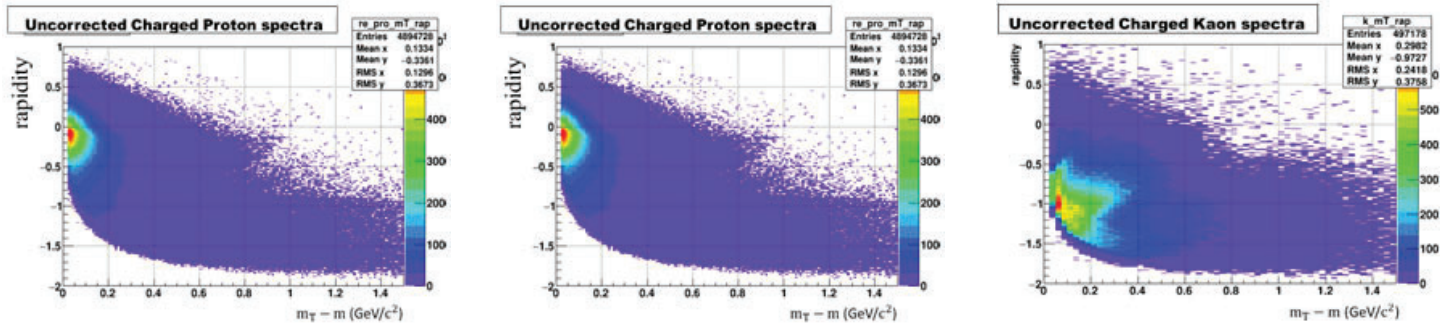


Figure 1: Left plot is the uncorrected charged spectra of protons as a function of ($m_T - m$) vs rapidity. Center figure is the uncorrected charged spectra of pions as a function of ($m_T - m$) vs rapidity. Right plot is the uncorrected charged spectra of kaons as a function of ($m_T - m$) vs rapidity.

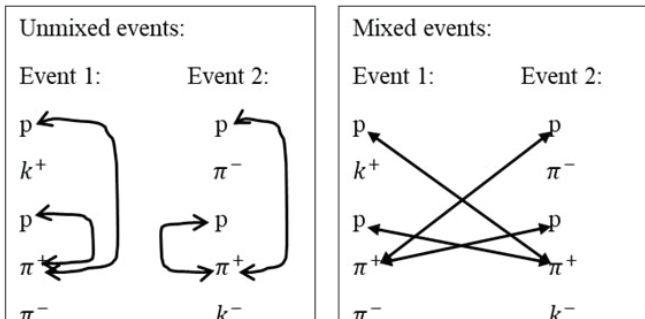


Figure 2: Example of how pairing for p and π^- is performed. Left box demonstrates how pairing works in the same event. Right box shows pairing for mixing events.

are uncorrected and will be corrected by accounting for the acceptance and efficiency of these particles. Figure 2 demonstrates how the background is estimated by intentionally matching particles together that are from different events. The background is estimated by this mixing technique that only allows for mixing to occur if the previously mentioned conditions are satisfied. Mixing could be done with more events but the background estimation with only one event provides sufficient statistics. The histogram for the p and π^+ pairs after the background subtraction in Figure 3 was fit with a gaussian where the peak is at 1.241 GeV/c². Comparing this fitted mass to the rest mass of Δ^{++} of 1.232 GeV/c², the fitted mass has a relative error of 0.731 percent. The rest mass of Δ^{++} also lies within one sigma of the fit and the signal indicates that Δ^{++} was created in this collision. The histogram for the p and π^- pairs in Figure 4 after having the background subtracted, was fit with a gaussian where the peak is at 1.237 GeV/c². The fitted mass has a relative error of 0.406 percent with the rest mass of Δ^0 being 1.232 GeV/c². The rest mass of Δ^0 is also within one sigma of the fit and indicates that Δ^0 was created in this collision. Although the histogram in Figure 5 of the daughter particles of Λ did not have the estimated background subtraction, the histogram still shows a strong signal near the rest mass of Λ . Estimating the background for Λ will be done to create a stronger signal and will be fitted to a gaussian to further support that Λ was created in this collision.

III. Conclusion

The mass of detected particles was used in determining whether they were either a kaon, pion or proton. Δ^{++} , Δ^0 and Λ were searched for by pairing all particles in the same event that are known to be created from their decay. In determining if these decaying particles were initially created from this collision, the invariant mass is calculated from the pairs' given momenta and mass. By calculating the invariant mass from the pairing and by

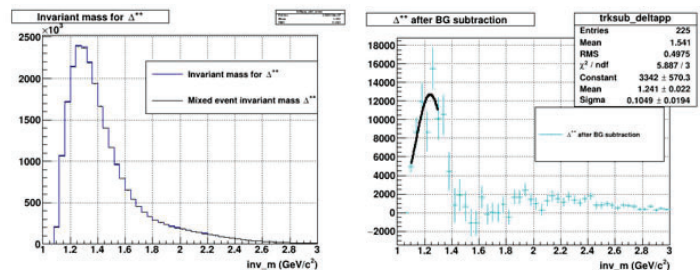


Figure 3: Invariant mass from the p and π^+ pairs. Left plot shows the unmixed events (blue) and mixed events (black) histogram that is normalized. Right plot shows the unmixed events subtracted by mixed events. Fitted mass is 1.241, rest mass is 1.232 GeV/c².

subtracting the estimated background from mixed event pairing, the signal shows that Δ^{++} and Δ^0 were identified to exist in this collision. The histogram for Λ did not have the estimated background subtracted but still exhibited a signal for Λ and was identified to have existed in this collision. Having found these decayed particles to exist, other particles may be identified by using this method. Future work will involve correcting the spectra of protons, pions and kaons and to further improve the signal for the particles detected. The anisotropic flow of the system will also be calculated in the future for the particles that were identified to better understand the collision and to help in verifying whether a QGP was created at this energy level.

IV. Acknowledgement

This project was supported in part by the Brookhaven National Laboratory (BNL), Physics under the BNL Supplemental Undergraduate Research Program (SURP). I would like to thank the MARC U STAR program for supporting me throughout the summer and Jason Bryslawskyj for allowing me to work with him this summer.

V. References

- ¹M. Anderson et al, Nucl.Instrum.Meth. A499 (2003) 659-678 nucl-ex/0301015
- ²M. Shao et al, Nucl.Instrum.Meth. A558 (2006) 419-429 nucl-ex/0505026

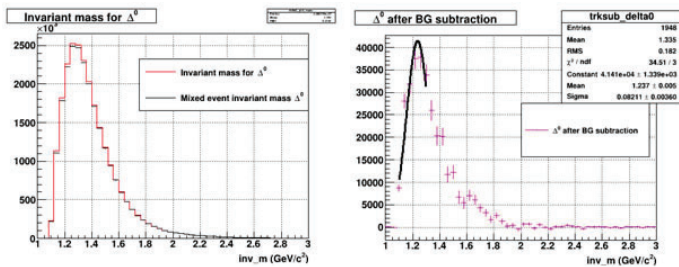


Figure 4: Invariant mass from the p and π^- pairs. Left plot shows the unmixed events (red) and mixed events (black) histogram that is normalized. Right plot shows the unmixed events subtracted by mixed events. Fitted mass is 1.237, rest mass is 1.232 GeV/c^2 .

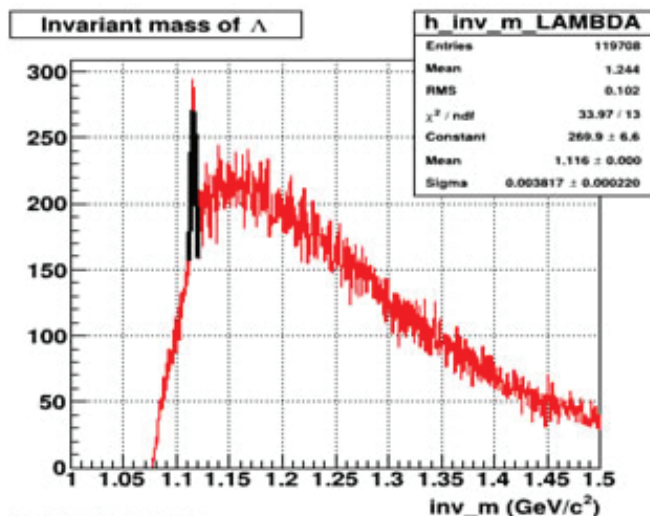


Figure 5: Invariant mass of p and π^- pairs and \bar{p} and π^- pairs. Fitted mass is 1.116, rest mass of Λ is 1.115 GeV/c^2 .

Development of the hardware for the puck visualization system for determining the presence of samples under liquid nitrogen

Rachael Ng

Mechanical Engineering, Stony Brook University, Stony Brook, NY 11794

Justin Wei

Mount Sinai High School, Mount Sinai, NY 11766

Edwin Lazo and Herbert J. Bernstein

Photon Sciences, Brookhaven National Laboratory, Upton, NY 11973

ABSTRACT

The National Synchrotron Light Source-II (NSLS-II) accelerates electrons to nearly the speed of light, resulting in x-rays that are emitted at beamlines. The highly Automated Macromolecular Crystallography (AMX) and Frontier Macromolecular Crystallography (FMX) beamlines, use a six-axis robotic arm sample changer coupled to a high-capacity dewar to increase throughput, offer remote access, and fully automate data collection. Samples are “fished” onto caps at room temperature and are flash frozen in liquid nitrogen (LN_2) right into the pucks, which are then loaded into the dewar. The puck visualization system must be able to detect caps, distinguish cap types (ALS vs. SPINE), and determine if the caps are tilted, all while being submerged in LN_2 . This system is comprised of three core components: the hardware (cameras, bracket, and liquid nitrogen window), the image analysis software, and the inventorying of the data collected. This project focuses on designing the hardware that will capture the best possible images under LN_2 for processing. The bracket will hold three cameras and be mounted onto the dewar. Through much testing, a final design emerged in which the camera bracket will be cylindrical with an opaque top and have translucent sides to achieve uniform illumination with ambient lighting. The cameras will look through the LN_2 window, which resembles a transparent bucket and will be partly submerged in LN_2 . This drastically reduces blurriness due to bubbling of LN_2 and allows the cameras to capture sharp images. With the final CAD design completed, the next stage is to fabricate a prototype. The image analysis software being developed in parallel by another student will generate contour plots onto the averaged image with a contrast filter to detect caps, distinguish cap types, and determine cap orientation (tilted caps). The inventorying of the samples mounted will be integrated with this software and will store the information in the database. The puck visualization system is important because it can prevent collisions of the robotic arm and the dewar and increase throughput by inventorying samples, which enable advancements in medicine, pharmaceuticals, and life sciences.

I. INTRODUCTION

A. AMX/FMX Beamlines

The AMX and FMX beamlines are currently the only two beamlines in the National Synchrotron Light Source-II that routinely use robotic arms to automate the sample changing process. The entire process of loading the caps that contain the protein

samples from the dewar to the goniometer is highly automated and is constantly being improved. This automation has allowed for remote access to the beamline, which allows users to send their protein samples to NSLS-II and their samples will be loaded into the dewar by the beamline staff. Meanwhile, they are able to use the beam to test their protein crystals wherever they are located in the world, as long as they have computer access. As seen in Figure 1, the robotic arm takes samples out of the high-capacity dewar and mounts them in a specific location to be able to run tests on the sample.

B. Protein Crystallography

Protein crystallography is a technique used to determine the position of molecules in protein crystals that ultimately give the structure of the protein. It involves protein purification, crystallization, irradiation to x-rays, phase determination, followed by model building, and refinement.¹ The protein crystals are exposed to high energy X-rays (typically 5 to 20 keV) at the beamlines.

C. Importance of the Puck Visualization System

The puck visualization system will be crucial in preventing collisions between the robotic arm and the dewar. All of the technology and equipment in the hutch is extremely expensive, so it is crucial to avoid collisions to save time and money that would have to be spent to repair damages. Additionally, collisions lead to a loss of productivity, since people are then not able to use the beamline to its fullest extent. This system will reduce collisions by determining the type of cap and identifying tilted caps (Figure 2). Having the ability to tell where there are no caps helps circumvent time lost and maintain high productivity by avoiding confusion about where caps are located. Being able to detect the difference

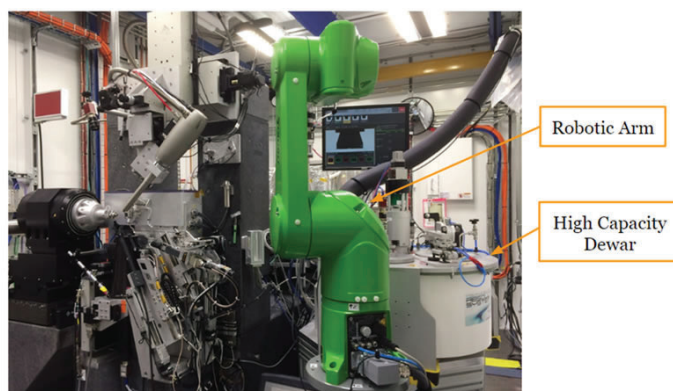


Figure 1. Overview of the inside of the AMX beamline hutch

between SPINE caps and ALS caps prevents collisions because the system is only compatible with SPINE caps; ALS caps can potentially cause a collision at the goniometer. Being able to detect tilted caps also prevents collisions because tilted caps are not able to fit properly in the gripper. The puck visualization system will also allow the inventorying of samples, which will show the number of samples loaded in the dewar and the number of samples actually mounted. If these two values are not equal, this prompts the questions of why there is a discrepancy and how to eliminate this discrepancy, which will aid in increasing throughput.

II. METHODS AND MATERIALS

A. Laboratory and Beamline Testing

1. Testing to Determine the Optimal Dimensions and Illumination

Designing the camera bracket required conducting a series of tests to define the optimal dimensions and illumination needed to achieve the sharpest image. The sharper the image, the higher the accuracy with which the image analysis software is able to detect all of the necessary characteristics. These tests required beamline and laboratory access to determine the camera height and which combinations of material and finishes would let in enough light without reflections. The height of the camera lens from the puck was chosen to maximize the field of view of the camera, allow enough ambient light to enter the lens, and to keep the focusing range of lens from reaching its limits. Another boundary condition that had to be taken into consideration was cap perspective; the pins of the outer caps start to angle outwards due to perspec-

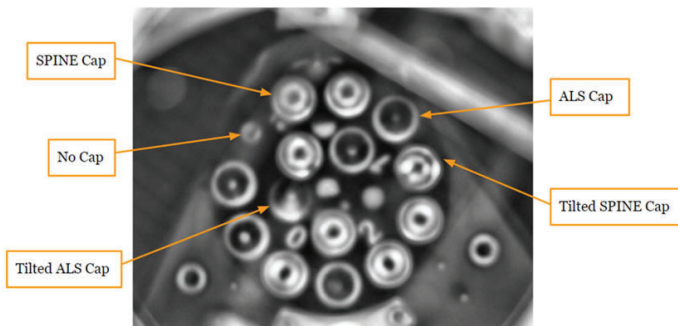


Figure 2. Puck with SPINE and ALS caps, no caps, and tilted caps (image without LN₂ window, contrast filter, averaged 50 times)

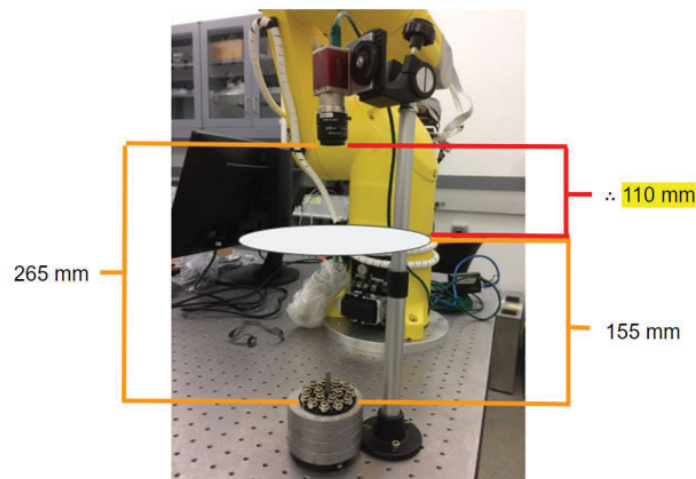


Figure 3. Determining height of camera lens to puck

tive. If the camera was farther away, the puck became smaller in the field of view, which made it a bit harder to see the cap. Therefore, a balance had to be struck so that the camera was not too close or too far from the puck and then the focus was optimized for that specific height (Figure 3).

An ideal image was one that was sharp, but also had diffuse uniform lighting that illuminated each cap equally. To keep the puck visualization system as simple as possible, using ambient light already in the beamline hutch was ideal, rather than having to develop a completely separate lighting system. Thus, testing was done with a few plexiglass parts, including a cylindrical part and a flat rectangular top, to mimic the setup of a potential prototype. These illumination tests required changing these parts to either opaque, translucent, or transparent to see if using only ambient lighting was sufficient and what opacity these parts had to be to achieve the most diffuse and uniform lighting possible. As seen in Figure 4, a translucent piece of plexiglass that was glass beaded produced the most uniform lighting.

2. Testing Throughout the Filling/Emptying Cycle of the Dewar

Since liquid nitrogen constantly boils off because its boiling point is extremely low at $-195.8\text{ }^{\circ}\text{C}$,² the dewar was set so that once the LN₂ level went below 94%, it would start filling until

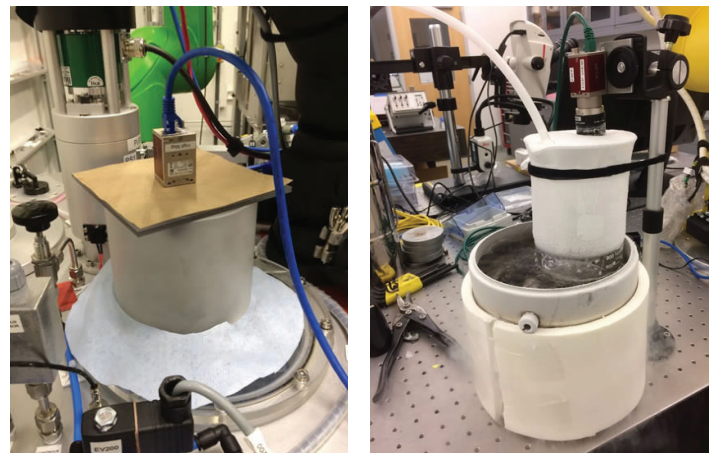


Figure 4 (left). Mock setup of camera bracket

Figure 5 (right). Setup to test cryostream effectiveness

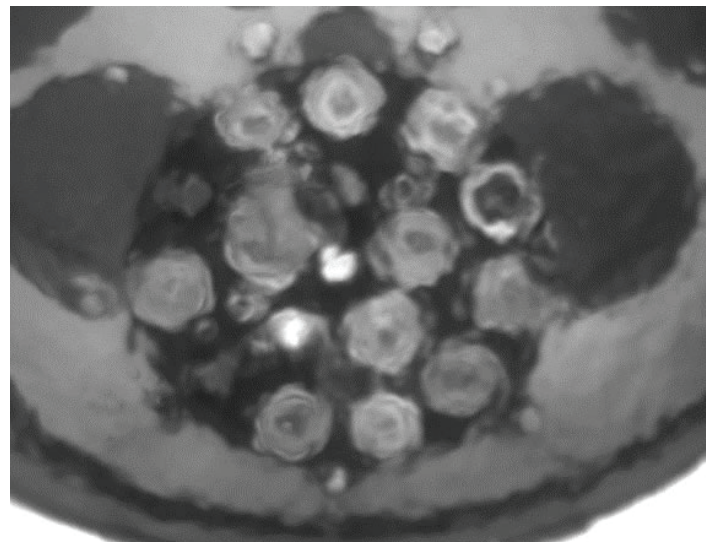


Figure 6. Image with no averaging or filters

the level reached 97% and then it would stop filling and allow the dewar to empty until it reached 94% again, completing the cycle. Additionally, when the filling process first started (LN₂ valve first opens), the LN₂ level actually dropped first until it reached 90% and then it finally started to raise. The images were collected using the setup in Figure 4 and the camera was able to view directly through the clear window plate and into the dewar. Images were collected at approximately every other whole number (97%, 95.5%, 94%, 92%, 90%) throughout the filling and emptying cycle of the dewar. All of this previous testing was done with a puck placed at plate position A. Further testing was done at plate B and C and the images were not as clear. Additionally, clear images were not able to be attained at all of the different LN₂ levels. Thus, a liquid nitrogen window was deemed necessary to reduce bubbling at the surface of the LN₂ and allow for the collection of sharp images.

3. Testing the Liquid Nitrogen Window Concept

The liquid nitrogen window will resemble a clear bucket, in which the bottom portion will be submerged in LN₂. To prove that the LN₂ window would produce sharper images, a borosilicate PYREX beaker was used to simulate the window and a camera was positioned over it to capture the images. Another test that was done was to determine whether or not using a cryostream, or a stream of gaseous nitrogen, would prevent condensation and frost from forming on the bottom of the LN₂ window. As seen in Figure 5, the borosilicate beaker was secured over the puck, which was in a dewar filled with LN₂ and the bottom of the beaker was submerged in LN₂. The top of the beaker was covered with a parafilm

that would stop air and moisture from entering. Only two holes were cut into the plastic film; one for the camera and one for the cryostream. The cryostream continuously forced out any air or moisture that may have been able to enter the beaker.

III. RESULTS

A. Results from Testing Throughout the Filling/Emptying Cycle of the Dewar (No LN₂ Window)

All the images had to be averaged at least ten times and have a contrast filter on them since the images without averaging and filtering were too blurry to be used (Figure 6). The sharpest images without the LN₂ window were taken during the liquid nitrogen filling process when the LN₂ level of the dewar was around 90% and increasing, which is shown in Figure 7. In contrast, the blurriest images were also taken during the filling process, but when the LN₂ level dropped from around 94% to 90%. However, when testing different plate positions (plate B and C), all of the images were too blurry to use. These positions produced worse images because the heater strips on the clear window plate were not completely flat, which reduced the quality of the images. Additionally, clear images where the pin of each cap was able to be reliably seen were not able to be collected at every different LN₂ level. Thus, we determined that there must be a liquid nitrogen window to be able to counteract the effect of bubbling on the images.

B. Results from Testing the Liquid Nitrogen Window

The images using the LN₂ window (Figure 9) were drastically sharper than the images without the LN₂ window (Figure 8). Without the LN₂ window, only in the best conditions (filling 92%- LN₂ level rising) were caps present, cap type, and caps tilted able to be detected. In the worst conditions (filling 92%- LN₂ level dropping), only caps present and cap type were able to be detected. Using the LN₂ window, caps present, cap type, and caps tilted are able to be reliably detected under all conditions (any LN₂ level and any plate position). Thus, based on the quality of the images with and without the LN₂ window, the LN₂ window is imperative to achieving clear images.

Additionally, the N₂ gas allowed the bottom of the beaker to be free of condensation and frost even after fifty minutes (Figure 10). This cryostream will constantly push out any air or moisture so that condensation and frost cannot form.

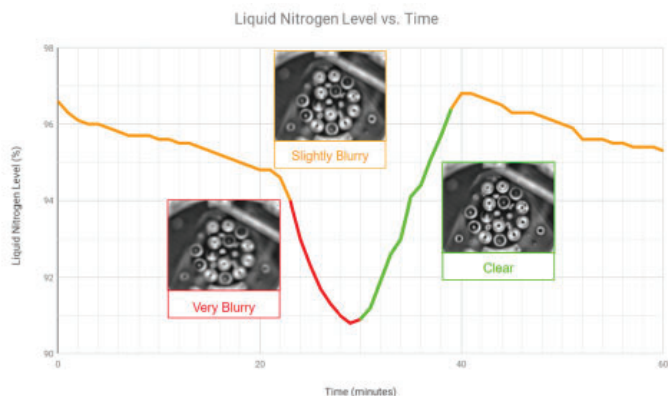


Figure 7. Graph of liquid nitrogen filling/emptying cycle at plate A

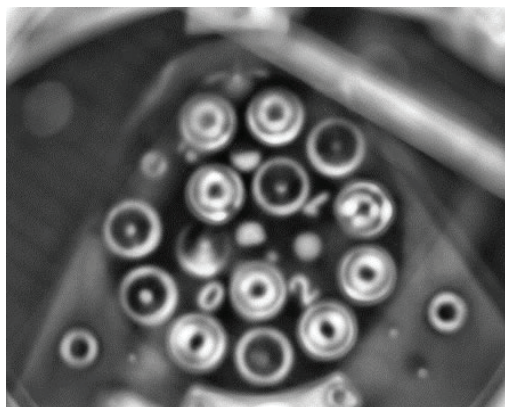


Figure 8. Image without LN₂ window

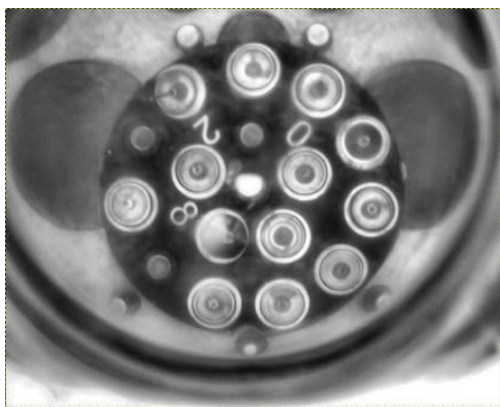


Figure 9. Image with LN₂ window

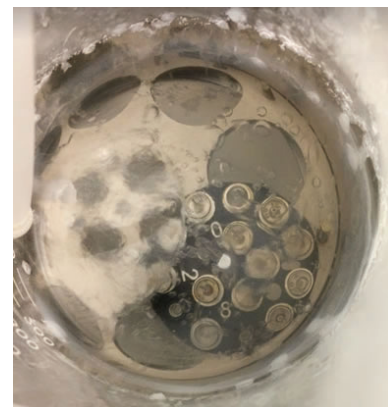


Figure 10. Image of bottom after 50 minutes

C. Image Analysis Software and Sample Inventorizing

The image analysis software being developed in parallel by another student will generate contour plots onto the averaged image with a contrast filter to be able to tell all key characteristics of the cap.³ The clearest images were captured using the LN₂ window. Throughout testing, the images collected were given to this other student for feedback on the clarity of the different characteristics, which was used to improve the images. Figure 12 shows the contour plot of Figure 11, which is the original image that is averaged from ten images and has enhanced contrast. The lack of a cap simply looks like a single bright dot. ALS caps appear as a bright thin outer ring with a bright dot in the center while SPINE caps have a bright thick outer ring and a dark center. Additionally, tilted caps are distinguished by the elliptical nature of the cap and a line that may appear as a result of the pin extending outwards. The inventorizing of the samples mounted will be integrated with this software and will save the information collected in a database.

IV. CONCLUSION

A. Final Design of Camera Bracket and Liquid

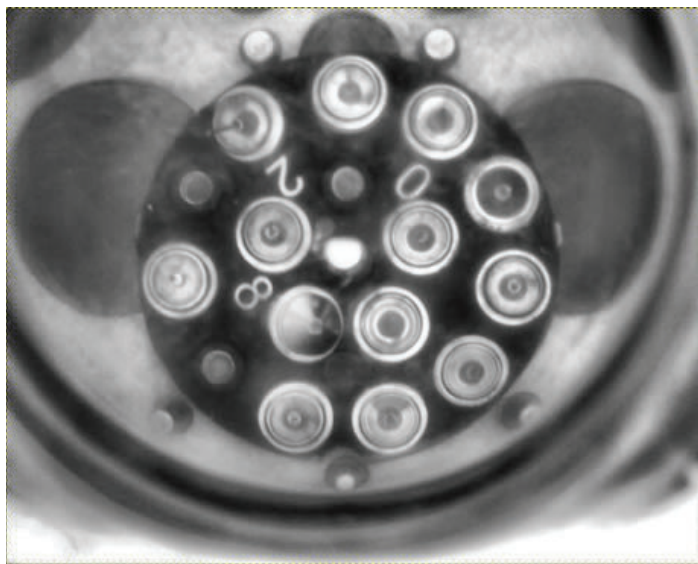


Figure 11. Original image with filters

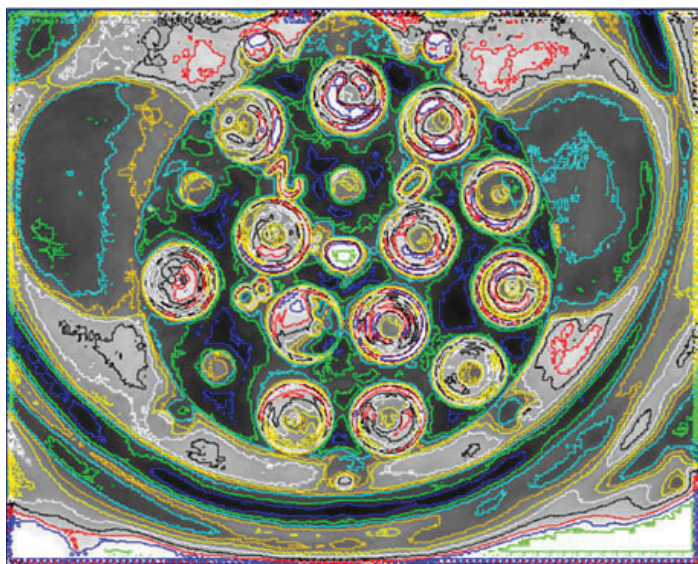


Figure 12. Contoured image

Nitrogen Window

In conclusion, the best images taken were with the LN₂ window. The final design will include a bracket that will hold three cameras and be mounted onto the dewar. As seen in Figure 13, the final design of the camera bracket will be cylindrical and have an opaque top and translucent sides to achieve uniform illumination with ambient light. The cameras will view through the LN₂ window, which will look like a transparent bucket and will be partly submerged in the LN₂ (Figure 14). It will also have a continuous flow of N₂(g) to prevent condensation and frost. This window will drastically reduce bubbling and allow the cameras to collect sharp images.

B. Ongoing and Future Work

Currently, the best-suited materials and manufacturing processes are being determined for each part of the prototype. The top plate of the camera bracket will be made of anodized steel to give it a matte black finish and to allow conduction of heat if heaters were to be placed on top to prevent frost if needed. The cylindrical base of the camera bracket will be made of acrylic and will be frosted on the outside. The liquid nitrogen window is more complex because it must be able to withstand cryogenic temperatures and also be able to be brought up to room temperature occasionally. Additionally, at least the bottom must be optically clear and transparent. Ideally, the entire window will be made of a monolithic piece of borosilicate glass, which is able to be exposed to LN₂, rather than a plastic material, since plastics tend to become brittle in cold temperatures.⁴ The LN₂ window will consist of two separate parts: an outer flange that screws into the dewar and an inner glass bucket with a lip that sits right inside the outer flange. The inner part will be somewhat sandwiched in place so pressure will be applied evenly, reducing the chance of the glass piece cracking. Future plans involve fabricating a prototype, based on the CAD model, that is able to be integrated with the image analysis software.

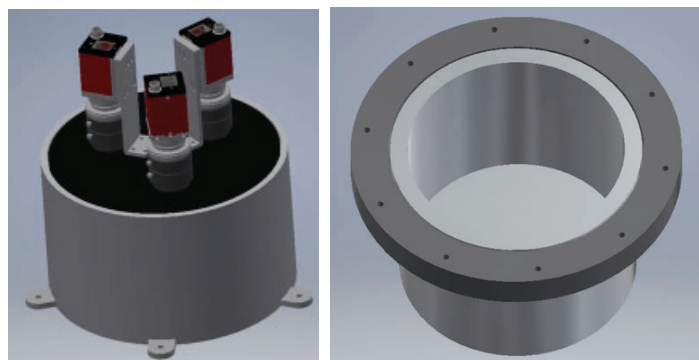


Figure 13 (left). CAD model of camera bracket

Figure 14 (right). CAD model of LN₂ window

V. REFERENCES

- ¹Wlodawer, A., Minor, W., Dauter, Z., Jaskolski, M. "Protein Crystallography for Non-Crystallographers, or How to Get the Best (But Not More) From Published Macromolecular Structures." November 2007.
- ²Young, J.A. "Nitrogen, Liquid." Journal of Chemical Education. October 2003.
- ³Wei, J. "Development of the Software for the Puck Visualization System for Determining the Presence of Samples Under Liquid Nitrogen." National Synchrotron Light Source- II, Brookhaven National Laboratory. August 2018.
- ⁴Hechtel, K. "Design Considerations for the Use of Plastic Materials In Cryogenic Environments." Curbell Plastics Inc. October 2014.

VI. ACKNOWLEDGEMENTS

I would like to thank my mentor, Edwin Lazo, for all of his guidance throughout this project, as well as the rest of the AMX/FMX beamline staff. I would also like to thank the hospitality and kindness of Brookhaven National Laboratory, especially that of the National Synchrotron Light Source-II. This project was supported in part by the U.S. Department of Energy, Office of Science, Office of Workforce Development for Teachers and Scientists (WDTS) under the Science Undergraduate Laboratory Internships Program (SULI).

Using Monte Carlo methods to estimate occupational dosage during ^{225}Ac production

Drake Niedzielski

Physics Department, Rensselaer Polytechnic Institute, Troy, NY 12180

Kin Yip

Collider-Accelerator Department, Brookhaven National Laboratory, Upton, NY 11973

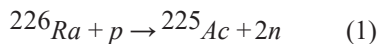
Abstract

Since alpha emitting isotopes such as ^{225}Ac , ideal for radiation treatment, are in short supply, the Medical Isotope Research and Production program at Brookhaven National Laboratory (BNL) is developing new pathways for ^{225}Ac production. One proposed pathway is to resurrect the EBCO cyclotron at BNL to irradiate a ^{226}Ra target for 40 hours in a 16 MeV proton beam. Using MCNPX and CINDER software to simulate this process, we found that 1.26 Ci of ^{225}Ac could be produced from 300 mg of ^{226}Ra . To ensure workplace safety, we modeled the detailed geometry of lab 2-66C in Bldg. 801 and performed Monte Carlo simulations to estimate the radiation outside the lab as the irradiated sample is processed in a hot cell. We found the maximum dose outside the lab to be about 9×10^{-5} rem/h. To reduce occupational dose, we recommend 2" thick steel shielding covering the sample insertion passage. These ^{225}Ac production runs could help cover the EBCO cyclotrons operational costs.

I. Introduction

Alpha sources like ^{225}Ac are ideal for targeted radiation therapy. Possessing a high linear energy transfer, they can damage the DNA of nearby cancer cells while their short range mitigates damage to surrounding tissue.[1] ^{225}Ac is especially suited for radiation therapy due to its 10 day half-life, short enough to pass through the patient while allowing enough time for processing and distribution.[2] According to the DOE Isotope Program's customer feedback, the estimated demand for ^{225}Ac is roughly 50-100 Ci/year, however domestic supply is only about 1.5-1.7 Ci/year.[3] Additionally, the most popular method of production milks ^{225}Ac from a ^{229}Th cow,[4] meaning that the supply of ^{225}Ac is limited by that of ^{229}Th . This is, obviously, not an ideal situation.

The Medical Isotope Research and Production (MIRP) program at Brookhaven National Laboratory (BNL) seeks to improve this situation and is currently developing new pathways for ^{225}Ac production. One proposed pathway of interest is the low-energy cyclotron route, a (p, 2n) reaction shown in equation 1.



Previous studies indicate that this reaction has a cross section peak around 16 MeV.[5] The decommissioned EBCO TR-19 cyclotron at BNL would be resurrected for production runs, irradiating a ^{226}Ra target in a 16 MeV proton beam, exciting the reaction in equation 1. After 40 hours of total exposure over a period of 4 days, the irradiated sample would be transported to lab 2-66C in Bldg. 801 for further processing. It is this proposed project for which the authors hope to estimate the production yield and radiation hazard.

Using the Monte Carlo N-Particle eXtended (MCNPX) 2.7.0 and CINDER 1.05 software packages, we calculate the activity of

each of the isotopes produced, including of course ^{225}Ac , and use those to compute the dosages at key locations inside and outside of lab 2-66C. We primarily focus on the dosages outside of the lab as they pose a less obvious hazard than those inside the lab. Performing the same dosage computations with additional shielding, we hope to bring the dosages outside the lab to consistently safe levels.

II. Methods

A. ^{225}Ac Production

300 mg of ^{226}Ra is deposited on an Al substrate. This sample is then put in either a 10° or 20° target head, which is then inserted into a target chamber. The target chamber is then placed in the EBCO cyclotron which will be operated at 16 MeV. The cyclotron's proton beam has a 1 cm diameter and a current of $200 \mu\text{A}$. The beam will be run for 10 hours each day, allowing a 14 hour resting period, for a total of 4 days. The sample, now containing many new isotopes, is then taken to lab 2-66C in Bldg. 801 for further processing, where it will sit in a lead-shielded hot-cell.

B. Target, Hot-cell, and Simulation Setup

As shown in figure 1, the target apparatus that holds the ^{226}Ra sample consists of two separable parts: a target chamber and a choice of either a 10° or a 20° target head. An Al substrate, on which the ^{226}Ra is deposited, is inserted into a slot in the target head, at its respective angle. It is held down by a fastener plate with a rectangular hole in the middle to allow direct beam exposure. The target head is then inserted into the target chamber, possessing a bore hole for the proton beam to reach the ^{226}Ra sample. Both the 10° and 20° target apparatus were modeled as MCNPX input files based on scale-accurate schematics for the 20° target head sitting inside the target chamber. The 20° target head was modeled exactly according to the schematics, but it was found that the angle was closer to 18° in the schematics. Since there were no specific schematics for the 10° target head, an exact 10° angle was used and the rest of the dimensions were chosen so that the effective area of the ^{226}Ra as seen by the proton beam matched the listed value in the schematics. The validity of the geometry was checked using the MCNPX geometry plotter.

For both targets, a 16 MeV proton source with a 1 cm diameter was used for regular simulation runs, but runs using 14 MeV and 19 MeV were done on the 10° target to explore the effects of beam energy on ^{225}Ac yield. MCNPX computations of neutron fluxes through the radium were performed on the input files using 1 node (32 cores) on the CORI supercomputer in NERSC.1 A maximum of 35 million events were used to run the 10° target simulations and 50 million to run the 20° target simulations.²

The MCNPX output and history files were then used by CINDER to compute the abundances and activities of the isotopes produced from the radium. The production process history, 10

hours of beam exposure then 14 hours of decay, repeated for 4 days, was specified in CINDERs activation history and the $200\mu\text{A}$ of the beam was accounted for with the flux normalization factor, $snorm$, obtained by dividing by the charge of a proton, see equation 2. One of the input files that we used for CINDER activation, which contains the activation history and flux normalization, can be found in Appendix A.

$$snorm = \frac{200\mu\text{A}}{1.602 \times 10^{-19} \text{C}} = 1.248 \times 10^{15} \text{s}^{-1}$$

Finally, a gamma source script was run on the MCNPX and CINDER outputs to create gamma source cards (SDEF) of the irradiated target that are directly used as sources in MCNPX input files modeling lab 2-66C. In short, SDEF cards exist for 10° at 14, 16, and 19 MeV and for 20° at 16 MeV.

The detailed geometry of lab 2-66C in Bldg. 801, shown in figures 2 and 3, was modeled according to several blueprints and measurements made during a visit by the authors. The irradiated target was placed in the middle of the hot-cell adjacent to the fume-hood and aligned to the center of the insertion passage. Both hot cells have 6" thick lead walls with thin steel coating, neglected in our model, and a lead-glass window for viewing. The source positioning represents a worst case scenario where there are paths for the radiation to escape the lab without passing through lead or concrete. Moving the sample away from the axis of the insertion passage would likely improve the outside dosages. At the time of writing, lab 2-66C does not have any door, thus it is absent in the model. Some of the blueprints used to construct the model were in contradiction with each other, reporting lengths

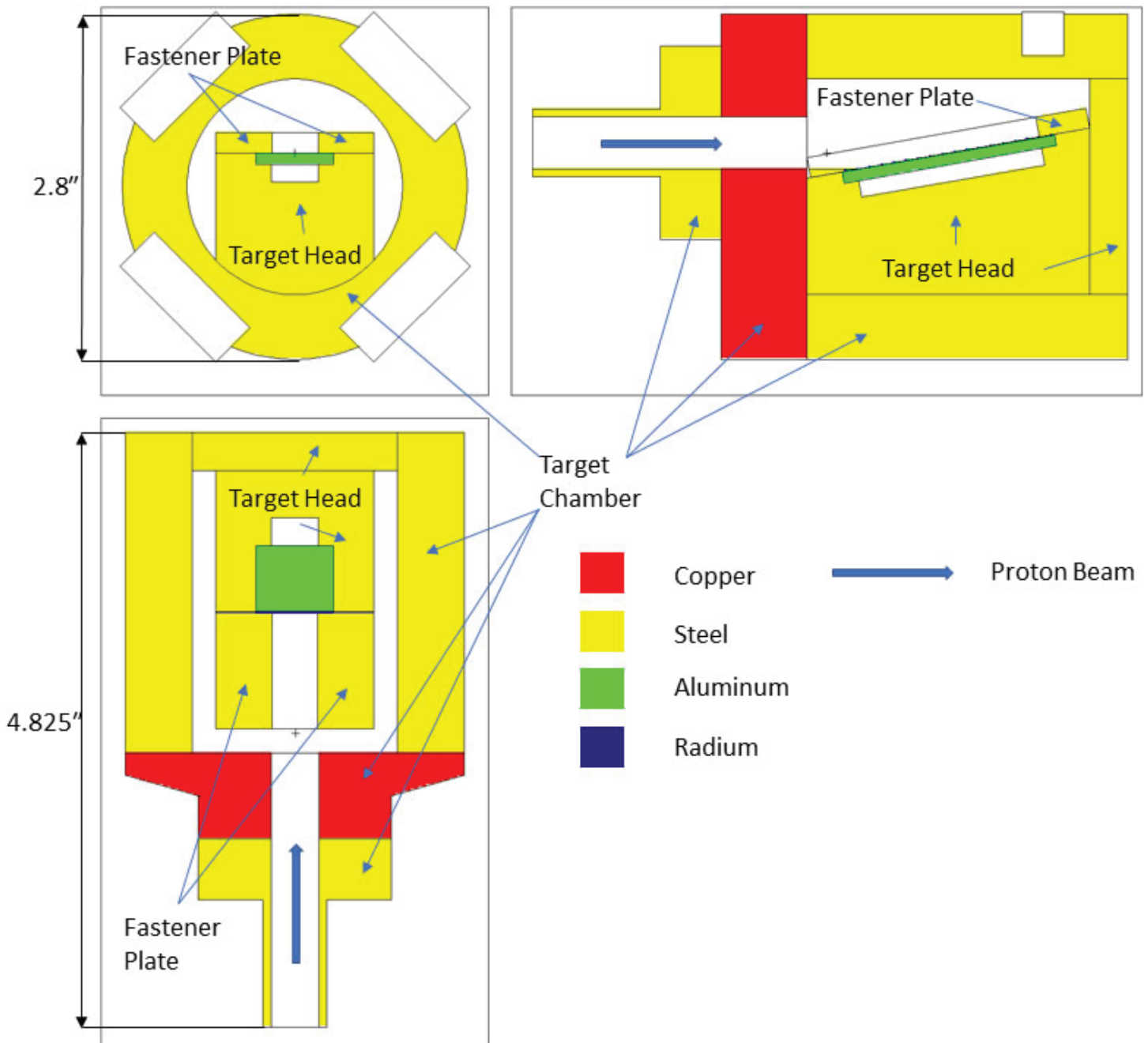


Figure 1: The 10° target apparatus is depicted above. MCNPX's geometry plotter was used to generate the 3 slices of the model in the XY, YZ and ZX planes. The white spaces represent vacuum in the model. The ^{226}Ra is very thinly deposited on the upper surface of the aluminum substrate and is barely visible even in color print.

of hot-cells that would not fit in the room. Measurement confirmed the authors suspicion that the reported hot-cell dimensions were a factor of two off. Additionally, a thin piece of steel covering the wall recess and insertion passage is ignored in our original model and left as a variable shielding parameter.

MCNPX was used to estimate radiation dosages due to the irradiated sample at the locations shown in figures 2 and 3 with varying source type and shielding parameters. Estimations were done for the 10° and 20° sources in the absence of any additional shielding. For academic curiosity, a simulation run using the 10°

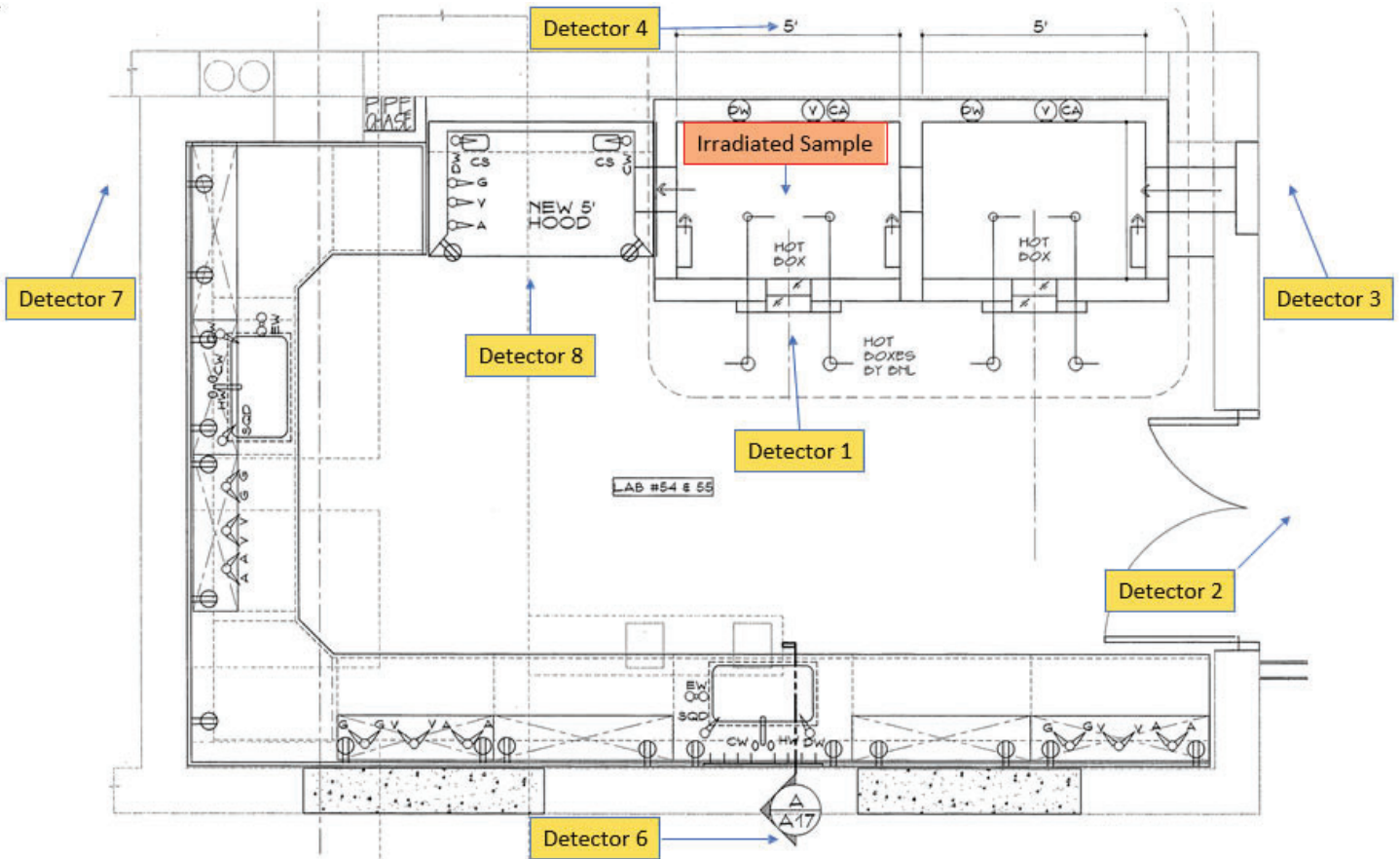


Figure 2: Shows the top view of lab 2-66C. Each of the detectors are placed 10 cm in front of the closest surface to help the tally error decrease faster. All detectors shown lie in the same plane as the irradiated sample. Detectors 1, 3, 4, 6, 7 are orthogonally in line with the sample, sharing either the same x or z coordinate. Detector 5, not shown, lies directly above the sample and is shown in figure 3.

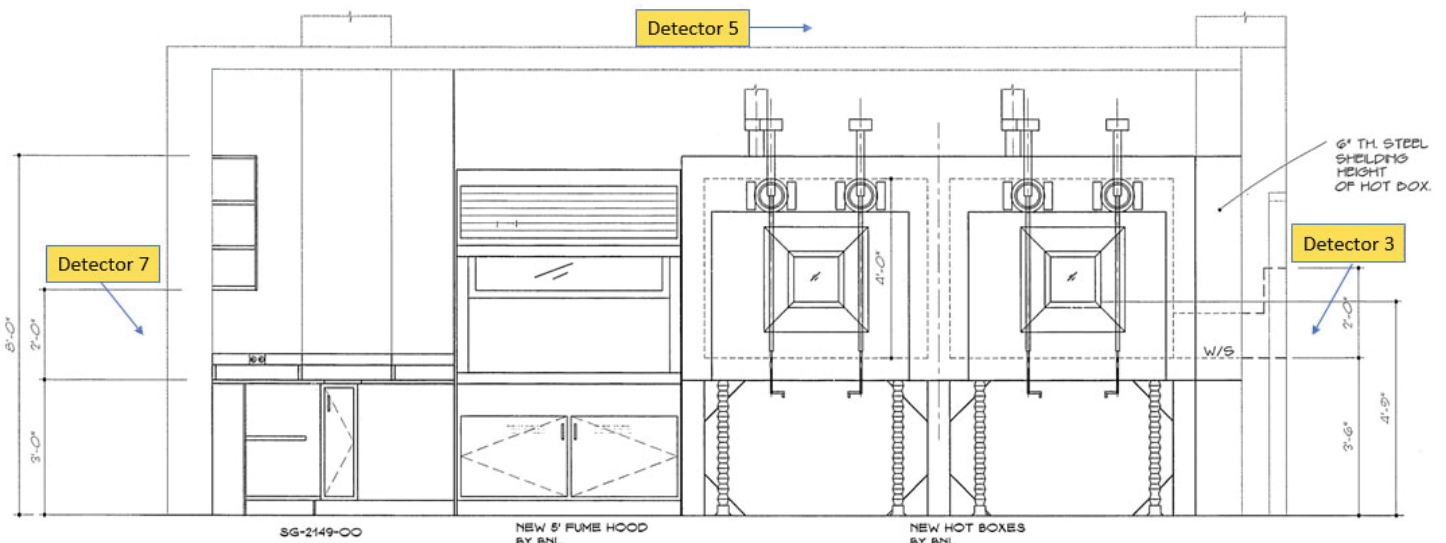


Figure 3: Shows the side view of lab 2-66C. Each of the detectors are placed 10 cm in front of the closest surface to help the tally error decrease faster. All detectors shown lie in the same plane as the irradiated sample.

source was done without the self-shielding effects of the radium. In an effort to reduce dosage, runs were done using the 10° source with a steel shield covering the sample insertion passage, thickness varying from 0.5" to 2" in increments of 0.5". A mesh tally, shown in figure 4, was performed using the regular 10° source to produce a dosage map of lab 2-66C at the height level of the source. Finally, runs were done using the 10° source created with 14 and 19 MeV to explore the effect of beam energy on 225Ac production.

III. Results and Discussion

Since the Al substrate that holds the radium is also subjected to the same beam exposure, we attempted to calculate its gamma spectrum using CINDER. However, the activity of the Al cell was 0 within the limitation of MCNPX. Thus, it suffices only to consider the effects of the radium when computing dosages in the model of lab 2-66C.

Table 1: Dosages at detectors in figures 2 and 3, where the naked run had no 226Ra layer but only the gamma source

Detector #	10° target [rem/h]	20° target [rem/h]	Naked 10° target [rem/h]
2	$4.33 \times 10^{-6} \pm 0.9\%$	$5.43 \times 10^{-6} \pm 0.8\%$	$4.43 \times 10^{-6} \pm 0.8\%$
3	$8.81 \times 10^{-5} \pm 0.8\%$	$1.13 \times 10^{-4} \pm 0.8\%$	$1.10 \times 10^{-4} \pm 0.6\%$
4	$1.10 \times 10^{-5} \pm 9.9\%$	$1.61 \times 10^{-5} \pm 9.4\%$	$1.04 \times 10^{-5} \pm 6.2\%$
5	$3.10 \times 10^{-5} \pm 4.1\%$	$4.03 \times 10^{-5} \pm 4.4\%$	$3.52 \times 10^{-5} \pm 5.9\%$
6	$2.38 \times 10^{-6} \pm 16.4\%$	$3.01 \times 10^{-6} \pm 14.2\%$	$2.45 \times 10^{-6} \pm 19.7\%$
7	$2.11 \times 10^{-5} \pm 5.7\%$	$2.99 \times 10^{-5} \pm 6.7\%$	$2.48 \times 10^{-5} \pm 5.6\%$
8	$5.79 \times 10^{-4} \pm 0.5\%$	$6.95 \times 10^{-4} \pm 0.5\%$	$6.00 \times 10^{-4} \pm 0.5\%$

Table 2: Effect of Steel Shield Thickness on Detector 3

Dosages Thickness [inches]	Dosage [rem/h]
0.0	$8.81 \times 10^{-5} \pm 0.8\%$
0.5	$7.03 \times 10^{-5} \pm 3.8\%$
1.0	$5.74 \times 10^{-5} \pm 5.6\%$
1.5	$4.56 \times 10^{-5} \pm 8.5\%$
2.0	$3.41 \times 10^{-5} \pm 8.9\%$

After 40 hours of 16 MeV beam exposure, the 10° target had a total activity of 9.51 Ci while the 20° target had an activity of

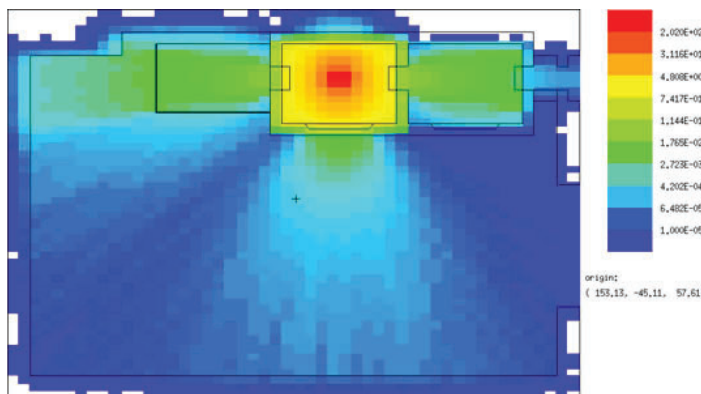


Figure 4: Shows the dosages across lab 2-66C from a top down view comparable to figure 2. A 10 degree target irradiated in a 16 MeV beam was used as the radiation source. The upper and lower cabinets are not visible in the model at the height level of the irradiated sample.

8.52 Ci. 3 Of the total activities, 225Ac accounted for 1.26 Ci and 0.87 Ci respectively, see figure 5. Thus the the 10° target is preferable from the standpoint of efficiency. Despite having a lower activity, the dosages around lab 2-66C are consistently higher with the 20° target see table 1. This is not contradictory, however, since the dose is due only to gamma radiation and dosage does not necessarily correlate linearly with activity, but depend on the energy distribution of the gamma radiation. So, from the standpoint of safety, the 10° target is also the preferable choice. Since the 10° target is the most preferable, unless otherwise specified, all other computations were done using the 10°/16 MeV sample as a source.

The location in the lab with the highest radiation dosage, excluding the inside of the hot-cell, is unsurprisingly just outside of the hot-cell looking into the lead-glass. With nothing else changed, the dosage is roughly 2×10^{-3} rem/h (detector 1). More importantly the highest dosage outside of the model lab 2-66C is right in front of the sample insertion passage. With no additional shielding the dosage is about 9×10^{-5} rem/h (detector 3).

With the addition of a 2" steel door covering the sample insertion passage the dosage can be brought down to about 3.5×10^{-5} rem/h, which is comparable to the dosage elsewhere outside the lab. See table 2 for more details. Despite the fact that lab 2-66C has no door at the time of writing, the dosage by the doorway is about 4.3×10^{-6} rem/h, which is low enough not to warrant additional shielding. In fact, the absence of a door could prove beneficial for the airflow to the fumehood in the lab.

Table 3: Dosages at detectors in figures 2 and 3 for 10° targets

Detector #	14 MeV target [rem/h]	16 MeV target [rem/h]	19 MeV target [rem/h]
2	$7.59 \times 10^{-7} \pm 1.1\%$	$4.33 \times 10^{-6} \pm 0.9\%$	$2.00 \times 10^{-5} \pm 0.6\%$
3	$1.15 \times 10^{-5} \pm 1.5\%$	$8.81 \times 10^{-5} \pm 0.8\%$	$4.40 \times 10^{-4} \pm 0.6\%$
4	$1.23 \times 10^{-6} \pm 26.8\%$	$1.10 \times 10^{-5} \pm 9.9\%$	$5.91 \times 10^{-5} \pm 8.3\%$
5	$4.37 \times 10^{-6} \pm 12.0\%$	$3.10 \times 10^{-5} \pm 4.1\%$	$1.68 \times 10^{-4} \pm 3.5\%$
6	$3.35 \times 10^{-7} \pm 55.5\%$	$2.38 \times 10^{-6} \pm 16.4\%$	$1.11 \times 10^{-5} \pm 10.5\%$
7	$2.67 \times 10^{-6} \pm 15.6\%$	$2.11 \times 10^{-5} \pm 5.9\%$	$1.11 \times 10^{-4} \pm 5.0\%$
8	$1.49 \times 10^{-4} \pm 0.7\%$	$5.79 \times 10^{-4} \pm 0.5\%$	$2.47 \times 10^{-3} \pm 0.4\%$

For academic curiosity, we examined the self-shielding effects of the radium by removing the material cell from the simulation while leaving a naked source. We found that almost all locations had consistently higher dosages without self-shielding accounted for, but only slightly. At the location of interest, outside the insertion passage, the dosage without self-shielding was roughly 1.1×10^{-4} rem/h as opposed to 8.8×10^{-5} rem/h with self-shielding. See table 1 for more details. The non-self-shielding effect is small likely because the 226Ra is very thin, 77.3 μm.

Studies conducted indicate that there should be a cross section peak for the 225Ac producing reaction, equation 1, around 16 MeV.[5] In our MCNPX simulations, we only used neutron interaction data for 226Ra while proton interaction was computed with a model. Thus we were curious if MCNPX was able to reproduce results consistent with reference [5]. Performing the MCNPX simulation runs with 14 and 19 MeV proton beams, we found that they had total activities of 5.23 Ci and 20.57 Ci,4 and respective 225Ac yields of 0.99 Ci and 0.61 Ci. Both yields being less than the 1.26 Ci produced using the 16 MeV proton beam indicates a cross section peak somewhere between 14 and 19 MeV, consistent with reference [5]. A breakdown of the produced isotope activities can be found in Appendix B. Performing MCNPX dosage tallies

at the detector locations, shown in figures 2 and 3, and using the irradiated targets created using 14 and 19 MeV beams, we found that higher energy beams produced consistently higher dosages. Those dosages are shown in table 3. To check the reasonability of CINDERS isotope decay calculations, an activation run was done using the 10¹⁶ MeV MCNPX output and an extra 24 hours of decay after the 40 hour beam exposure over 4 days. Based on the Bateman equation for isotope activity decay, one expects the activity of the parent isotope to decay exponentially and the daughter isotope activities to approach that of the parent times the probabil-

ity the parent decays into that daughter. We observed this behavior in the alpha decays of the 2 most prominent decay chains, ²²⁵Ac and ²²⁴Ra. However, the activities of the isotopes produced by beta decay in these 2 chains were occasionally very off from expected. The authors do not have a good explanation for this at the time of writing. Though this issue does not affect the activity of ²²⁵Ac that we have found, it does put some doubt on the total activities from all isotopes stated in this report. This issue, however, does not affect the radiation dosages outside the hot-cell room as the dosage is due to the gamma radiation only.

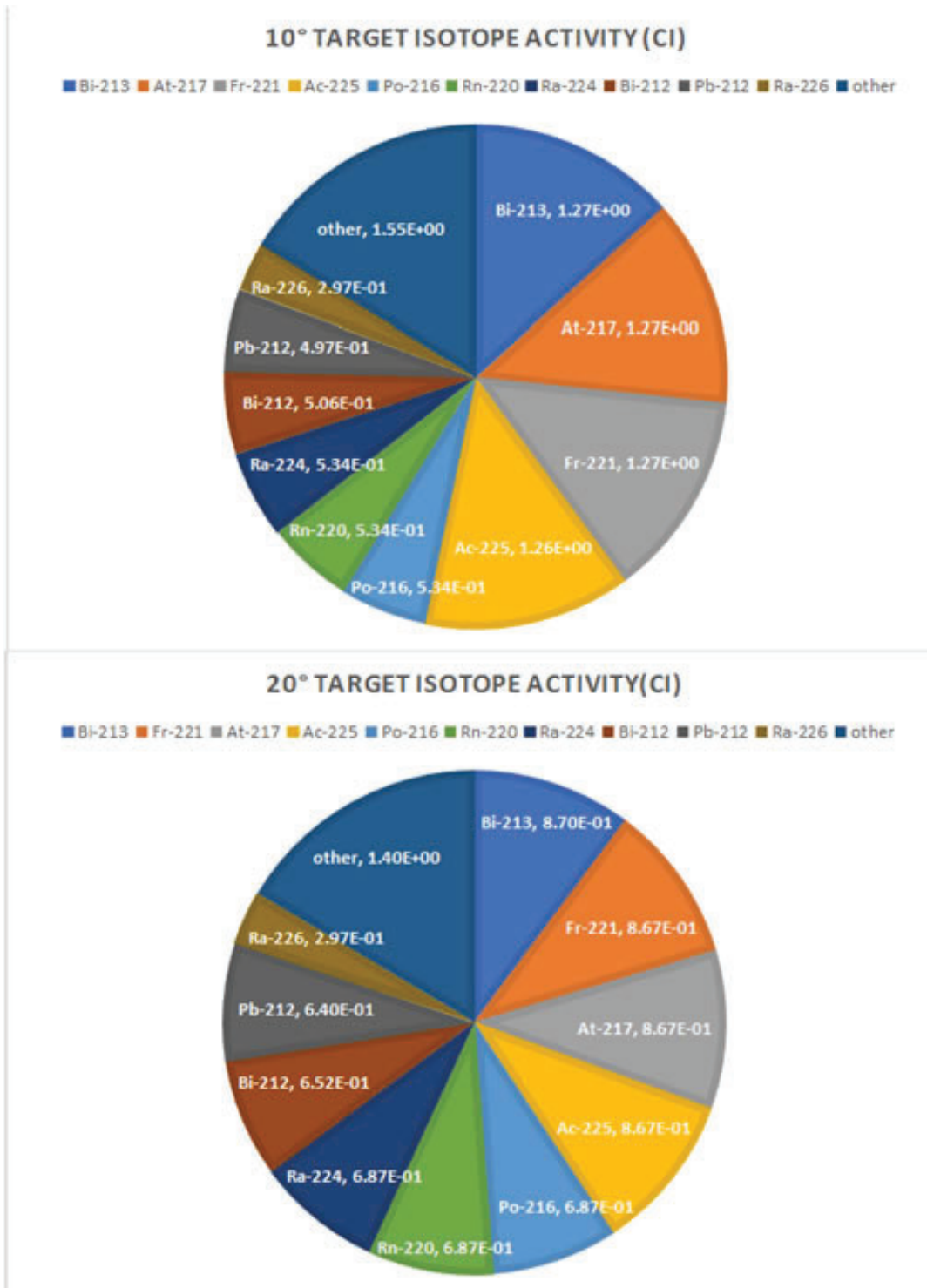


Figure 5: Shows the activity of each of the isotopes produced in the 10° and 20° irradiated samples using a 16 MeV proton beam. Total activities are 9.51 Ci and 8.52 Ci respectively.

IV. Conclusion

Among all configurations that we attempted, the 10° target irradiated at 16 MeV gives the best ²²⁵Ac yield. At 16 MeV, the 10° target head yields 1.26 Ci per 300 mg ²²⁶Ra while the 20° head yields only 0.87 Ci per 300 mg ²²⁶Ra. Additionally, the 10° target provides less of a radiation hazard inside and outside lab 2-66C as the irradiated sample is processed. Our estimated yields of ²²⁵Ac using different beam energies are consistent with predictions of a previous study that a cross section peak for the reaction shown in equation 1 occurs around 16 MeV.[5]

The aluminum substrate on which the ²²⁶Ra is deposited does not seem to contribute to the activity of the sample, validating our practice of examining only the irradiated sample activity. Due to the thinness of the ²²⁶Ra layer, the self-shielding effect on the dosages is indeed very small.

The most significant source of error likely comes from the inability to take measurements of details inside the hot-cells and behind the sample insertion passage, e.g. the shape and thickness of the steel doors in the hot-cells. Exact dimensions were not given in the prints for lab 2-66C and had to be inferred from the scale of the drawings. Since these details are so close to the radiation source they may have some effect on the dosages at detectors in the same solid angle as viewed from the source.

V. Acknowledgements

I would like to thank my mentor, Kin Yip, for providing guidance, sharing his knowledge, and telling many stories throughout this summer. This project was supported in part by the U.S. Department of Energy, Office of Science, Office of Workforce Development for Teachers and Scientists (WDTS) under the Science Undergraduate Laboratory Internships Program (SULI).

VI. End Notes

¹The National Energy Research Scientific Computing Center (NERSC) in Berkeley, CA has several high performance computing systems of which CORI is one, <http://www.nersc.gov/systems/cori>.

²Number of events was chosen to keep simulation runs under a 4 hour time limit. The 20° target ran faster for some non-obvious reason.

³The accuracy of these figures are discussed in the final paragraph of this section.

⁴Again, the accuracy of these figures is discussed in the final paragraph of this section.

VII. References

- S. Kojima, J. Cuttler, N. Shimura, H. Koga, A. Murata, and A. Kawashima, "Present and future prospects of radiation therapy using α -emitting nuclides," *Dose Response*, vol. 16, p. 18, 2018.
- B. Allen, "Systemic targeted alpha radiotherapy for cancer," *J. Biomed. Phys. Eng.*, vol. 3, p. 6780, 2013.
- C. Cutler, "Ebc cyclotron for ac-225 production startup and operating cost," Dec. 2017. Project proposal by the Medical Isotope Research and Production Program.
- D. Scheinberg and M. M. Devit, "Actinium-225 in targeted alpha-particle therapeutic applications," *Curr Radiopharm*, vol. 4, pp. 306–320, 2011.
- C. Apostolidis, R. Molinet, J. McGinley, K. Abbas, J. Mollenbeck, and A. Morgenstern, "Cyclotron production of ac-225 for targeted alpha therapy," *Applied Radiation and Isotopes*, vol. 62, pp. 383–387, 2005.

VIII. Appendix A

```
title lines
DECAY 10deg 14MeV
files
bigza file /project/projectdirs/m1840 ec/cinder
1.05/data/bigza mcnpx outp Ra Target9 .o
mcnpx histp histpe
run options
dname DECAY 10deg 14MeV dcounter 1
splprods 1 tabular 1 verbose 1

cinder options tst 1.0e 5
signif 1.0e 16 kchn 0
klib 0
nfe 3 nosame 0 russ 1
library/project/projectdirs/m1840 ec/cinder
-1.05/data/c90lib0742
normalization
snorm 1.248e+15

#run 10 hours , rest 14 hours history
1 1
10.0 h
10.0
14.0 h
1 1
10.0 h
10.0
14.0 h
1 1
10.0 h
10.0
14.0 h
1 1
10.0 h
10.0
14.0 h

celllist radium
1
```

IX. Appendix B

10 ⁰ , 14 MeV		10 ⁰ , 16 MeV		10 ⁰ , 19 MeV		20 ⁰ , 16 MeV	
Isotope	Activity [Ci]	Isotope	Activity [Ci]	Isotope	Activity [Ci]	Isotope	Activity [Ci]
Bi-213	9.95E-01	Bi-213	1.27E+00	Po-216	2.92E+00	Bi-213	8.70E-01
At-217	9.92E-01	At-217	1.27E+00	Rn-220	2.92E+00	Fr-221	8.67E-01
Fr-221	9.92E-01	Fr-221	1.27E+00	Ra-224	2.91E+00	At-217	8.67E-01
Ac-225	9.92E-01	Ac-225	1.26E+00	Bi-212	2.77E+00	Ac-225	8.67E-01
Ra-226	2.97E-01	Po-216	5.34E-01	Pb-212	2.72E+00	Po-216	6.87E-01
Po-218	1.53E-01	Rn-220	5.34E-01	Tl-208	9.94E-01	Rn-220	6.87E-01
Rn-222	1.53E-01	Ra-224	5.34E-01	Po-212	6.62E-01	Ra-224	6.87E-01
Pb-214	1.52E-01	Bi-212	5.06E-01	Bi-213	6.07E-01	Bi-212	6.52E-01
Bi-214	1.52E-01	Pb-212	4.97E-01	Fr-221	6.06E-01	Pb-212	6.40E-01
Ac-226	5.35E-02	Ra-226	2.97E-01	Ac-225	6.06E-01	Ra-226	2.97E-01
Rn-218	4.51E-02	Tl-208	1.82E-01	At-217	6.05E-01	Tl-208	2.34E-01
Ra-222	4.51E-02	Po-218	1.53E-01	Ac-224	4.83E-01	Po-218	1.53E-01
Th-226	4.51E-02	Rn-222	1.53E-01	Ra-226	2.97E-01	Rn-222	1.53E-01
Pb-209	3.76E-02	Pb-214	1.52E-01	Po-218	1.53E-01	Pb-214	1.52E-01
Tl-209	2.09E-02	Bi-214	1.52E-01	Rn-222	1.53E-01	Bi-214	1.52E-01
Xe-135	5.24E-03	Po-212	1.21E-01	Pb-214	1.52E-01	Ac-224	1.14E-01
I-133	4.78E-03	Ac-224	8.84E-02	Bi-214	1.52E-01	Ac-226	6.04E-02
In-115*	4.30E-03	Ac-226	7.58E-02	Ac-226	1.06E-01	Rn-218	5.09E-02
Cd-115	4.06E-03	Rn-218	6.39E-02	Rn-218	8.97E-02	Ra-222	5.09E-02
Ag-109*	4.00E-03	Ra-222	6.39E-02	Ra-222	8.97E-02	Th-226	5.09E-02
Pd-109	3.99E-03	Th-226	6.39E-02	Th-226	8.96E-02	Pb-209	3.29E-02
Ce-143	3.95E-03	Pb-209	4.79E-02	At-216	4.84E-02	Tl-209	1.83E-02
I-132	3.58E-03	Tl-209	2.66E-02	Fr-220	4.84E-02	At-216	1.14E-02
Te-132	3.41E-03	At-216	8.86E-03	Ra-225	2.70E-02	Fr-220	1.14E-02
Sn-121	3.31E-03	Fr-220	8.86E-03	Pb-209	2.29E-02	Ag-112	6.46E-03
Ag-112	3.17E-03	In-115*	8.05E-03	Xe-135	1.83E-02	I-133	5.94E-03
Rh-105	3.13E-03	I-133	7.98E-03	Ce-143	1.80E-02	Ra-225	5.92E-03
Y-93	2.78E-03	Cd-115	7.51E-03	I-133	1.46E-02	Ag-109*	5.73E-03
Pd-112	2.75E-03	Rh-105	6.83E-03	Tl-209	1.28E-02	Pd-109	5.73E-03
Pm-149	2.35E-03	Xe-135	6.48E-03	Ag-112	1.10E-02	Pd-112	5.47E-03
Xe-133	2.34E-03	Ag-112	6.14E-03	I-132	1.09E-02	Rh-105	5.16E-03
Sr-91	2.18E-03	Ag-109*	5.56E-03	As-77	1.04E-02	Ce-143	4.79E-03
Ag-113	2.13E-03	Pd-109	5.56E-03	Te-132	1.04E-02	In-115*	4.71E-03
Mo-99	2.08E-03	I-132	5.37E-03	Pd-112	9.38E-03	I-132	4.46E-03
Tc-99*	1.91E-03	Ce-143	5.18E-03	Sr-91	9.35E-03	Cd-115	4.36E-03
I-135	1.74E-03	Pd-112	5.17E-03	Y-93	8.03E-03	Te-132	4.21E-03
As-77	1.49E-03	Te-132	5.06E-03	Pr-145	7.63E-03	As-77	3.93E-03
La-140	1.46E-03	Ra-225	4.84E-03	Xe-133	7.57E-03	Xe-135	3.92E-03
Nb-97	1.39E-03	As-77	4.24E-03	Ag-109*	7.20E-03	Sn-121	3.80E-03
Y-91*	1.38E-03	Sn-121	4.09E-03	Pd-109	7.20E-03	Pm-149	3.48E-03
Sb-127	1.36E-03	Xe-133	3.57E-03	Mo-99	6.99E-03	Kr-85*	3.00E-03
Y-92	1.34E-03	Y-93	3.53E-03	Tc-99*	6.68E-03	Y-92	2.90E-03
Ag-111	1.33E-03	Pm-149	3.44E-03	I-131	6.37E-03	Pm-151	2.82E-03
Kr-85*	1.33E-03	Kr-85*	3.42E-03	Sb-127	6.35E-03	Xe-133	2.76E-03
Zr-97	1.29E-03	Y-92	3.20E-03	Rh-105	6.33E-03	Sr-91	2.47E-03

Nb-97*	1.23E-03	Nb-97	3.19E-03	I-135	6.17E-03	Y-93	2.38E-03
La-141	1.16E-03	Ag-111	3.12E-03	In-115*	6.15E-03	La-140	2.31E-03
Te-127	1.13E-03	Zr-97	2.96E-03	Y-91*	5.93E-03	Nb-97	2.17E-03
Ba-140	1.01E-03	Nb-97*	2.81E-03	La-140	5.93E-03	Zr-97	2.01E-03
Te-129	9.35E-04	Mo-99	2.60E-03	Sn-121	5.84E-03	Ba-140	1.98E-03
I-131	7.97E-04	Ba-140	2.60E-03	Te-127	5.84E-03	I-131	1.96E-03
Sb-129	7.93E-04	La-140	2.54E-03	Y-92	5.74E-03	Nb-97*	1.91E-03
Ru-105	7.89E-04	Tc-99*	2.38E-03	Ba-140	5.68E-03	Ag-111	1.88E-03
Nd-147	7.13E-04	Sr-91	2.35E-03	Cd-115	5.64E-03	Pr-145	1.81E-03
Pr-143	6.27E-04	Pm-151	2.23E-03	La-141	5.29E-03	Mo-99	1.76E-03
Ra-225	6.19E-04	I-135	2.20E-03	Kr-85*	5.11E-03	Ag-113	1.75E-03
Pr-145	6.01E-04	Te-129	2.02E-03	Pm-149	4.89E-03	Kr-83*	1.70E-03
Br-82	5.77E-04	Ag-113	1.98E-03	Kr-83*	4.53E-03	Tc-99*	1.61E-03
Kr-83*	5.17E-04	Ru-105	1.89E-03	Nb-97	3.65E-03	Nd-147	1.60E-03
Ce-141	5.14E-04	Nd-147	1.88E-03	Ag-111	3.51E-03	Y-91*	1.57E-03
I-130	5.08E-04	I-131	1.86E-03	Zr-97	3.39E-03	Sm-153	1.52E-03
Y-90	4.91E-04	Sb-127	1.83E-03	Nb-97*	3.22E-03	Te-127	1.39E-03
Rb-88	4.91E-04	Sb-129	1.75E-03	Br-82	3.19E-03	Ru-105	1.35E-03
Kr-88	4.40E-04	Te-127	1.74E-03	Pr-143	3.15E-03	Te-129	1.33E-03
Y-87	4.13E-04	Kr-83*	1.72E-03	Pm-151	3.00E-03	La-141	1.32E-03
In-117*	4.03E-04	Pr-145	1.67E-03	Te-129	2.59E-03	Sb-127	1.18E-03
Pm-151	3.92E-04	La-141	1.60E-03	Nd-147	2.51E-03	I-135	1.16E-03
Sr-89	3.89E-04	Y-91*	1.49E-03	Ag-113	2.49E-03	Sb-129	1.12E-03
Po-216	3.78E-04	Sb-128	1.33E-03	Ce-141	2.49E-03	As-76	9.09E-04
Rn-220	3.78E-04	Sm-153	1.28E-03	Sb-129	2.21E-03	Pr-143	9.06E-04
Ra-224	3.78E-04	I-130	1.14E-03	Ge-77	2.12E-03	Ge-77	8.62E-04
Bi-212	3.59E-04	As-76	1.06E-03	Y-90	1.93E-03	Y-90	7.32E-04
Pb-212	3.53E-04	Br-82	1.02E-03	Rb-88	1.72E-03	I-130	7.24E-04
In-117	3.32E-04	Ge-77	1.01E-03	Ru-105	1.68E-03	In-117	7.12E-04
Ru-103	3.22E-04	Pr-143	9.06E-04	Kr-88	1.54E-03	Sm-156	6.38E-04
Rh-103*	3.22E-04	Rb-88	7.95E-04	I-130	1.49E-03	Rb-88	6.32E-04
Ba-135*	3.02E-04	Ce-141	7.51E-04	Te-131*	1.47E-03	Zr-89	6.07E-04
Nb-96	3.02E-04	Sm-156	7.44E-04	Sb-128	1.43E-03	Y-89*	6.06E-04
Pr-142	2.94E-04	Kr-88	7.12E-04	Br-83	1.39E-03	Nb-96	6.04E-04
Ga-72	2.90E-04	Nb-95*	7.12E-04	Ga-72	1.38E-03	In-117*	5.99E-04
Sb-119	2.90E-04	Zr-89	7.08E-04	Sr-89	1.36E-03	Ce-141	5.88E-04
Zn-72	2.88E-04	Y-89*	7.07E-04	Sb-122	1.19E-03	Br-82	5.83E-04
Xe-135*	2.84E-04	Nb-96	7.05E-04	Zn-72	1.10E-03	Ga-72	5.66E-04
Sm-153	2.76E-04	In-117	6.87E-04	Cs-136	1.05E-03	Kr-88	5.66E-04
I-123	2.62E-04	Ga-72	6.45E-04	Xe-135*	1.01E-03	Zn-72	5.61E-04
Y-87*	2.59E-04	Zn-72	6.40E-04	Y-91	9.67E-04	Y-86	5.47E-04
Sb-128	2.41E-04	Y-86	6.39E-04	In-117*	9.47E-04	Br-83	5.23E-04
Sb-122	2.39E-04	Sr-89	6.33E-04	Ga-73	9.31E-04	Te-131*	5.21E-04
Cs-136	2.25E-04	In-117*	5.81E-04	Ge-73*	9.19E-04	Sr-89	4.86E-04
Y-91	2.25E-04	Y-90	5.61E-04	Sm-153	8.41E-04	Sb-122	4.77E-04
Rh-105*	2.25E-04	Rh-105*	5.39E-04	Sr-92	8.19E-04	Sr-92	4.35E-04
Zr-89	2.16E-04	Br-83	5.26E-04	In-117	7.95E-04	Nb-95*	4.07E-04

Y-89*	2.15E-04	Sr-92	4.89E-04	Br-77	7.60E-04	Cs-132	4.07E-04
Nb-95*	2.04E-04	Pd-111*	4.35E-04	Ru-103	7.03E-04	Ru-103	4.00E-04
Ga-73	2.01E-04	Ag-111*	4.26E-04	Rh-103*	7.02E-04	Rh-103*	3.99E-04
Ge-73*	1.98E-04	Ru-103	4.18E-04	Y-87	6.38E-04	Xe-133*	3.96E-04
Sr-92	1.87E-04	Rh-103*	4.17E-04	Rb-82*	6.13E-04	Rh-105*	3.84E-04
Ge-77	1.58E-04	Xe-135*	3.59E-04	As-76	6.06E-04	Ga-73	3.10E-04
Br-83	1.58E-04	Ba-135*	3.53E-04	Xe-133*	5.94E-04	Ge-73*	3.06E-04
Cd-117	1.33E-04	Sr-83	3.48E-04	Pr-142	5.92E-04	Y-91	3.03E-04
Tl-208	1.29E-04	Pr-142	3.43E-04	Br-76	5.65E-04	Sr-83	2.99E-04
Pd-111*	1.24E-04	Pd-111	3.42E-04	Y-86	5.61E-04	La-135	2.95E-04
Ag-111*	1.22E-04	Eu-157	3.26E-04	Eu-157	5.34E-04	Rh-100	2.94E-04
Rn-217	1.19E-04	Sb-122	2.78E-04	Cs-131	4.89E-04	Pr-142	2.94E-04
Rb-86	1.10E-04	Y-91	2.69E-04	Cu-67	4.88E-04	Eu-157	2.79E-04
Xe-133*	1.08E-04	Cd-117*	2.36E-04	Rh-105*	4.77E-04	Sb-128	2.70E-04
Sn-125	1.06E-04	I-124	2.16E-04	Zr-95	4.66E-04	Cd-117*	2.47E-04
Te-131*	1.05E-04	Eu-156	2.14E-04	Sm-156	4.51E-04	Cd-117	1.91E-04
Cs-131	9.78E-05	Rh-101*	2.11E-04	Zr-89	4.21E-04	Xe-135*	1.90E-04
Pd-111	9.77E-05	Te-131*	1.96E-04	Y-89*	4.21E-04	Eu-156	1.84E-04
Po-212	8.61E-05	Cd-117	1.87E-04	Nb-95*	4.08E-04	Rh-101*	1.81E-04
Te-129*	8.30E-05	Pm-148	1.82E-04	As-78	3.95E-04	Rb-86	1.65E-04
Zr-95	8.11E-05	Xe-133*	1.81E-04	Rb-86	3.84E-04	Rb-84	1.61E-04
Ac-224	6.19E-05	Cs-136	1.75E-04	Xe-131*	3.37E-04	Zr-95	1.55E-04
Cd-115*	5.75E-05	Cs-132	1.58E-04	Te-131	3.30E-04	Te-129*	1.36E-04
As-74	5.73E-05	Rn-217	1.52E-04	Cd-117	3.12E-04	Pd-111*	1.24E-04
As-78	5.06E-05	Rb-84	1.51E-04	Nb-96	3.02E-04	Ag-111*	1.22E-04
Cd-117*	4.88E-05	Rb-86	1.28E-04	Tc-95	2.97E-04	Te-131	1.17E-04
Y-90*	4.10E-05	Xe-129*	1.23E-04	La-135	2.95E-04	As-74	1.15E-04
Te-125*	3.74E-05	Ga-73	1.21E-04	Kr-79	2.95E-04	As-78	1.11E-04
I-125	3.61E-05	Ge-73*	1.20E-04	Rh-100	2.94E-04	Xe-129*	1.05E-04
Tl-210	3.18E-05	Zr-95	1.14E-04	Sb-119	2.90E-04	Rn-217	1.04E-04
Nd-149	3.06E-05	Cs-131	1.14E-04	Nb-90	2.73E-04	Rb-81	1.02E-04
At-218	3.06E-05	Te-129*	1.14E-04	Cs-132	2.71E-04	Cs-131	9.78E-05
Ce-144	2.98E-05	Br-80	1.09E-04	Ru-97	2.30E-04	Pd-111	9.77E-05
Pr-144	2.98E-05	Br-80*	1.01E-04	Ce-144	2.12E-04	Br-80	9.31E-05
Xe-127	2.93E-05	As-78	9.87E-05	Pr-144	2.12E-04	Br-80*	8.69E-05
Sr-85	2.93E-05	Ce-144	8.65E-05	Ce-137	2.09E-04	Ce-144	8.54E-05
La-142	2.80E-05	Pr-144	8.65E-05	Te-129*	2.07E-04	Pr-144	8.54E-05
Ba-136*	2.52E-05	Xe-127	6.83E-05	Sn-125	1.98E-04	Xe-131*	8.48E-05
Te-127*	2.41E-05	As-74	6.69E-05	Eu-156	1.96E-04	Ru-106	6.83E-05
Te-131	2.36E-05	Ru-106	6.16E-05	Sb-126	1.92E-04	Rh-106	6.83E-05
Ru-106	2.23E-05	Rh-106	6.16E-05	Rb-81	1.85E-04	Sn-125	6.64E-05
Rh-106	2.23E-05	Sn-125	4.71E-05	Tc-96	1.80E-04	Nb-95	5.71E-05
Tc-95*	1.78E-05	La-142	4.48E-05	As-74	1.72E-04	Nd-149	4.21E-05
Nb-91*	1.75E-05	Te-131	4.41E-05	Rb-84	1.61E-04	Y-90*	4.10E-05
Nb-95	1.35E-05	Nd-149	4.09E-05	Pm-148	1.56E-04	La-142	3.78E-05
Sb-124	1.35E-05	Nb-95	3.98E-05	Nb-95	1.32E-04	Po-212	3.61E-05
Rb-83	1.27E-05	Cs-134*	3.65E-05	Cd-117*	1.26E-04	Tl-210	3.18E-05

A * next to an isotope indicates a meta-stable nuclear isomer.

ENDF/B-VIII.0 library application to nuclear astrophysics

Lauren Osojnak

Physics, Vassar College, Poughkeepsie, NY 12604

David Brown

National Nuclear Data Center, Brookhaven National Laboratory, Upton, NY 11973

Abstract

The Cross Section Evaluation Working Group (CSWEG) is a collaborative effort across national labs, industry, and universities to produce ENDF/B.¹ This group recently released the ENDF/B-VIII.0 nuclear reaction data library. ENDF/B-VIII.0 is the product of many years of effort to improve the quality and accuracy of nuclear data for the public. It possesses potential impacts for nuclear astrophysics such as modeling internal stellar processes and accounting for elemental abundances in the universe. This project will assess potential astrophysical impacts of ENDF/B-VIII.0 using FUDGE, a program that performs nuclear data testing and processes nuclear data such as ENDF/B-VIII.0, to translate the ENDF library into a reaction rate library in REACLIB format. Once FUDGE is able to complete this translation, the impact of new nuclear data on astrophysical processes can be determined through a series of tests of nuclear astrophysical processes including X-Ray bursts, r-process, s-process, and hydrostatic carbon-oxygen burning. This project aims to aid the nuclear data community's ability to run nucleosynthesis calculations and the nuclear astrophysics community's ability to gain access to new nuclear data. Additionally, this project aims to increase the influence of ENDF/B-VIII.0 by broadening its usage in the nuclear astrophysics community.

I. Introduction

Nuclear reactions power certain crucial astrophysical events and are responsible for the origin and evolution of the elements through the process of nucleosynthesis. Nucleosynthesis simulation codes require a nuclear reaction rate library to perform any simulations. The more accurate the library, the more accurate the simulations will be. ENDF/B-VIII.0 is the most current release of the ENDF/B evaluated nuclear reaction data library and is used in the modeling of nuclear reactors, weapons, and detector systems as well as a variety of other applications. FUDGE is one of several codes that can process the ENDF library. Using FUDGE, we can compute the Astrophysical Reaction Rate (ARR) from cross section data in the ENDF/B-VIII.0 library, allowing us to provide these rates to nucleosynthesis simulations. The astrophysical community does not have a standardized reaction rate library and we feel that the overall high quality of the ENDF/B-VIII.0 library could form the basis for a new standard library, aiding both the nuclear physics and astrophysics communities.²

A. Nucleosynthesis

Nucleosynthesis is a process that creates new nuclei from lighter nuclei. This process is responsible for the Big Bang's production of light elements, via Big Bang nucleosynthesis. Heavy nuclei were created from these original light elements, such as Hydrogen and Helium, by stellar nucleosynthesis. Stellar nucleo-

synthesis reactions proceed by fusing light elements and giving off energy and includes the following processes, the slow neutron capture process (s-process), CNO cycle, proton-proton chain, proton capture (p-process), and triple alpha process. Although still uncertain, it is hypothesized that heavier nuclei, with atomic numbers greater than Iron (the iron peak), are created from supernova nucleosynthesis. If the hypothesis is correct, supernova nucleosynthesis would include the rapid neutron capture process (r-process) and rapid proton capture process (rp-process).³ In 2018, the LIGO experiment presented the momentous discovery of gravitational waves by observing a neutron star merger and thus began the dawn of "multi-messenger" astrophysics. Multi-messenger refers to the observation of astrophysical events through emissions across the electromagnetic spectrum in addition to observations heard via gravitational wave rippling. This emergence of multi-messenger astrophysics corresponds with nucleosynthesis studies and therefore increases the current importance of nuclear astrophysics. LIGO observed Iron, along with heavier elements such as Gold and silver, in the emission spectrum of this collision from what is thought to be rapid neutron capture nucleosynthesis. It was inferred that neutron star collisions are the main source of the production of elements heavier than Iron in the universe.⁴ The ARR, used in nucleosynthesis calculations, can be calculated directly from the governing equation, Eq. 1.⁵

$$ARR = N_A \langle \sigma v \rangle \quad (1)$$

Eq. 1 requires the nuclear reaction cross section σ and the relative velocity v averaged over a thermal ensemble of neutron and target nuclei at temperature, T .

$$\langle \sigma v \rangle = \left(\frac{8}{\pi\mu}\right)^{1/2} \frac{1}{kT^2} \int_0^\infty \exp\left(\frac{-E}{kT}\right) \sigma E dE \quad (2)$$

The nuclear abundance, Y , can be calculated with the ARR. N_A is Avogadro's number, ρ is the density of the target material, and j, k , and l are the reactants. The N 's specify how many particles of species i are created or destroyed in a reaction. This equation is one of the many reaction rate equations that require the ARR in calculations.⁶

$$\dot{Y} = \sum_j N_j^i \lambda_j Y_j + \sum_{j,k} N_{j,k}^i \rho \lambda Y_j Y_k + \sum_{j,k,l} N_{j,k,l}^i \rho^2 N_A \lambda Y_j Y_k Y_l \quad (3)$$

B. ARR and REACLIB

The most widely used astrophysical reaction rate library format is the REACLIB format.⁷ The nuclear reaction rate libraries in the REACLIB format store seven parameter fits for ARR's, as well as the Q-value for the reaction in MeV, citation of the reaction, and whether the reaction is a weak, resonant, nonresonant or a reverse rate. REACLIB is not accurate for computing the ARR out of the range of $0.1 \text{ GK} < T < 10 \text{ GK}$. Thielemann et al. showed

that the ARR's that are stored in REACLIB can be parameterized by the following equation.⁸

$$\lambda = \exp \left[a_0 + \sum_{i=1}^5 a_i T_9^{\frac{2i-5}{3}} + a_6 \ln T_9 \right] \quad (4)$$

In Eq. 2, each a_n is a parametrization constant and T_9 is the temperature in GigaKelvin. There are two versions of the REACLIB format. REACLIB 2, the most current version of the format, includes chapter headings prior to each reaction. Conversely, the format REACLIB 1 has chapter headings before the first reaction in a chapter only. The SkyNet reaction rate library, used in this project, is in the REACLIB 2 format.

II. Methods

The Python code to convert ENDF files into the REACLIB 2 file format is outlined in a UML diagram in Figure 1. The code recreates an exact REACLIB file format and assigned each component to a stored variable. A second python code imports an ENDF file and extracts necessary parameters to match the REACLIB format. REACLIB format possesses the constants for the parameterized Eq. 4. In order to use this parametrization with ENDF, a least squares fitting algorithm was used to solve a matrix equation for these constants as a vector. The algorithm used was `numpy.linalg.lstsq` which looks at all values of x that minimize the following expression.

$$\|\vec{A} - \vec{x}B\|^2 \quad (5)$$

The ARR was computed from a Python routine in FUDGE implementing Eq. 2. Another matrix was created with at least 24 temperatures, as recommended by Theilemann et al. to ensure the fit's accuracy.⁹ These were the matrices used to solve for the parametrization constants using Eq. 4. The A vector, Eq. 7, is the the log of the ARR. The B matrix, Eq. 9, is a manipulation of Eq. 4 to create a matrix of the various temperatures. The x vector, Eq. 8, is the vector of seven parameters according to Eq. 4.

$$\vec{A} = \vec{x}B \quad (6)$$

$$\vec{A} = \begin{bmatrix} \ln(\lambda(T_0)) \\ \ln(\lambda(T_1)) \\ \dots \\ \dots \\ \ln(\lambda(T_n)) \end{bmatrix} \quad (7)$$

$$\vec{x} = \begin{bmatrix} a_0 \\ a_1 \\ a_2 \\ a_3 \\ a_4 \\ a_5 \\ a_6 \end{bmatrix} \quad (8)$$

$$B = \begin{bmatrix} 1 & T_0^{-1} & T_0^{-1/3} & T_0^{1/3} & T_0 & T_0^{5/3} & \ln(T_0) \\ 1 & T_1^{-1} & T_1^{-1/3} & T_1^{1/3} & T_1 & T_1^{5/3} & \ln(T_1) \\ & & & \dots & & & \\ & & & \dots & & & \\ 1 & T_n^{-1} & T_n^{-1/3} & T_n^{1/3} & T_n & T_n^{5/3} & \ln(T_n) \end{bmatrix} \quad (9)$$

With these constants, the ENDF values are fitted using the same parametrization as REACLIB. This fitted plot is compared to the non-fitted plot of the same data from FUDGE. The fitted and non-fitted ENDF data are plotted with the REACLIB database included in the SkyNet nucleosynthesis code.¹⁰ Temperatures are kept within the range of $0.1GK < T < 10GK$ as required. Combining aspects of the code shown in Figure 1 with FUDGE allowed ENDF/B-VIII.0 files to be translated and analyzed into REACLIB format. Using least squares fitting, a vector of the parametrization constants is computed that could then be included in the plot to test out the fitting algorithm's accuracy against the original ARR computer from FUDGE.¹¹

III. Results

The plots in Figures 2, 3, and 4 are example neutron capture reactions ARR's calculated from the ENDF/B-VIII.0 library, in orange, and the SkyNet REACLIB library, in blue.¹² The reasoning behind choosing these three specific neutron capture reactions to analyze is explained in the respective figure captions. The scatter-plot, in red, shows the ARR's computed directly from Eq. 3 with ENDF/B-VIII.0. The accuracy of the REACLIB parametrization is verified by the similarity of the parameterized and non-parameterized ARR calculations, shown in orange and red respectively. The difference in ARR between KADoNiS and ENDF/B appears to exponentially increase as temperature increases. The differences in the nuclear data library, KADoNiS from the REACLIB file, and ENDF/B-VIII.0 is noteworthy for further investigation because these rates should be standards across the scientific community, as they are not arbitrary values.¹³ The large difference in plots for the fitted and parameterized ENDF/B-VIII.0 of Iron neutron capture reveals that the fitting method used in this project may not be ideal and that further investigation is needed.

IV. Discussion

This project provides a code that translates ENDF/B-VIII.0 files into REACLIB format and analyzes the ARR's of different nuclear data libraries. The next step in this larger scale project is to compute ARR's for the entire ENDF/B-VIII.0 library and analyze these fits. These results, once checked for accuracy, can serve as input data for stellar nucleosynthesis programs such as SkyNet¹⁴ and MESA.¹⁵ These nucleosynthesis simulators can further the applications of the library on the future of astrophysics. Especially of interest, the rapid neutron capture process nucleosynthesis code of SkyNet incorporated with ENDF/B-

VIII.0 reaction rates may provide insight into the origin of elements heavier than Iron. In the future, this project's code will hopefully be able to compute inverse and weak reaction rates along with different isomers to encompass entire nuclear libraries. A major application that this research can have on the wider scientific community is through the National Ignition Facility (NIF). NIF is the largest laser facility ever built, and can create temperatures and pressures comparable to the cores of gas giants and eventually stellar interiors. This report will eventually be able to provide more reliable ARR data that can support projects such as NIF.¹⁶ This project uncovers major disagreements between ARR's according to different nuclear data libraries.

V. Acknowledgments

I would like to give a special thanks to David Brown for welcoming me as a student intern and patiently guiding me through

this entire project and invaluable summer experience. This project was supported in part by the U.S. Department of Energy under the Science Undergraduate Laboratory Internships Program (SULI).

VI. End Notes

- ¹The name ENDF is an anachronism as it means “Evaluated Nuclear Data File” but the ENDF library is currently composed of 15 sublibraries including the neutron cross section, thermal neutron scattering, charged particle, atomic, and decay sublibrary. The “B” in ENDF/B indicates the “release” library. ENDF/A was the “development” area of ENDF/B. Roman numerals denote the version of the ENDF/B library. This project will focus on the most current version, ENDF/B-VIII.0.
- ²Brown, D.: ENDF/B-VIII.0: The 8th Major Release of the Nuclear Reaction Data Library with CIELO-project Cross Sections, New Standards and Thermal Scattering Data, in: Nuclear Data Sheets (2018), 1–142.
- ³Gorielya, S. / Martínez Pinedo, G.: The production of transuranium elements by the r-process nucleosynthesis, in: Nuclear Physics A (2015), 158–176.
- ⁴Abbott, B.P.: Observation of Gravitational Waves from a Binary Neutron Star Inspiral, in: Physical Review Letters (2017), 1–18.
- ⁵Rolf, C. / Rodney, W.: Cauldrons in the Cosmos, in: University of Chicago Press (1988).
- ⁶Thielmann, F. K.: Astrophysical reaction rates from statistical model calculations, in: Atomic Data and Nuclear Data Tables (2000), 1–351.
- ⁷Cyburt, R. H.: The JINA REACLIB database: its recent updates and impact on type-I x-ray bursts, in: The Astrophysical Journal Supplement Series (2010), 240–252.
- ⁸Thielmann, F. K.: Astrophysical reaction rates from statistical model calculations (2000).
- ⁹Thielmann, F. K.: Astrophysical reaction rates from statistical model calculations (2000).
- ¹⁰J. Lippuner, L. F. Roberts: SkyNet: A Modular Nuclear Reaction Network Library, in: The Astrophysical Journal Supplement Series (2017), 1–31.
- ¹¹Mattoon, C. M.: Generalized Nuclear Data: A New Structure (with Supporting Infrastructure) for Handling Nuclear Data, in: Nuclear Data Sheets (2012), 3145–3171.
- ¹²Brown, D.: ENDF/B-VIII.0: The 8th Major Release of the Nuclear Reaction Data Library with CIELO-project Cross Sections, New Standards and Thermal Scattering Data (2018); J. Lippuner, L. F. R.: SkyNet: A Modular Nuclear Reaction Network Library (2017).
- ¹³Dillmann, I.: The Karlsruhe Astrophysical Database of Nucleosynthesis in Stars Project Status and Prospects, in: Nuclear Data Sheets (2014), 171–174.
- ¹⁴J. Lippuner, L. F. R.: SkyNet: A Modular Nuclear Reaction Network Library (2017).
- ¹⁵Paxton, B.: The Karlsruhe Astrophysical Database of Nucleosynthesis in Stars Project Status and Prospects, in: The Astrophysical Journal Supplement Series (2010), 1–35.
- ¹⁶Moses, E. I.: The National Ignition Facility: ushering in a new age for high energy density science, in: Physics of Plasmas (2009).

VII. References

- Abbott, B.P.: Observation of Gravitational Waves from a Binary Neutron Star Inspiral, in: Physical Review Letters (2017), 1–18.
- Brown, D.: ENDF/B-VIII.0: The 8th Major Release of the Nuclear Reaction Data Library with CIELO-project Cross Sections, New Standards and Thermal Scattering Data, in: Nuclear Data Sheets (2018), 1–142.
- Cyburt, R. H.: The JINA REACLIB database: its recent updates and impact on type-I x-ray bursts, in: The Astrophysical Journal Supplement Series (2010), 240–252.
- Dillmann, I.: The Karlsruhe Astrophysical Database of Nucleosynthesis in Stars Project – Status and Prospects, in: Nuclear Data Sheets (2014), 171–174.
- Gorielya, S. / Martínez Pinedo, G.: The production of transuranium elements by the r-process nucleosynthesis, in: Nuclear Physics A (2015), 158–176.
- J. Lippuner, L. F. Roberts: SkyNet: A Modular Nuclear Reaction Network Library, in: The Astrophysical Journal Supplement Series (2017), 1–31.
- Mattoon, C. M.: Generalized Nuclear Data: A New Structure (with Supporting Infrastructure) for Handling Nuclear Data, in: Nuclear Data Sheets (2012), 3145–3171.
- Moses, E. I.: The National Ignition Facility: ushering in a new age for high energy density science, in: Physics of Plasmas (2009).
- Paxton, B.: The Karlsruhe Astrophysical Database of Nucleosynthesis in Stars Project – Status and Prospects, in: The Astrophysical Journal Supplement Series (2010), 1–35.
- Rolf, C. / Rodney, W.: Cauldrons in the Cosmos, in: University of Chicago Press (1988).
- Thielmann, F. K.: Astrophysical reaction rates from statistical model calculations, in: Atomic Data and Nuclear Data Tables (2000), 1–351.

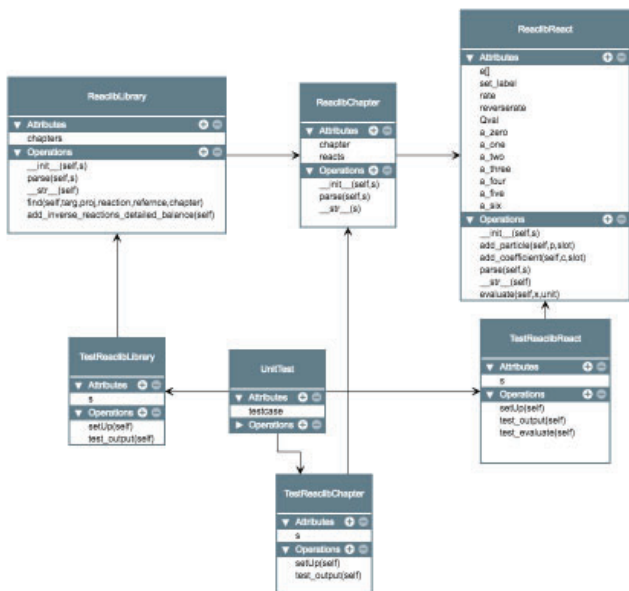


Figure 1: This is a Unified Modeling Language (UML) diagram for the Python code written to output REACLIB 2 format. The headings in blue are the classes that format the REACLIB file. ReaclibLibrary splits the library into individual reactions and inputs this into the other two classes ReaclibChapter and ReaclibReact to be further evaluated. ReaclibChapter delegates which lines of reactions are chapter headings and which lines are the actual numbers contributing to the calculation of the ARR. It will evaluate the different chapter headings and then output the reaction block to be passed onto the ReaclibReact class. This class will store each element of the reaction section as the number and position of projectiles, targets or ejectiles represents by e[], a set label for citations, which type of rate the reaction is, the Q value of the reaction, and the seven parameterization constants. Unit tests are used to test each class of this code. The functions gnds crossSection to Reaclib ARR coefficients and gnds reactionSuite to ReaclibLibrary, retrieve the cross section data from ENDF/B-VIII.0, after converting the data to the GNDS format using FUDGE GNDS file conversion. The numpy.linalg.lstsq function is used within the gnds crossSection to Reaclib ARR coefficients function to implement Eq. 5 from the cross section data. These individual functions do not belong to a class and are not explicitly shown on the UML diagram

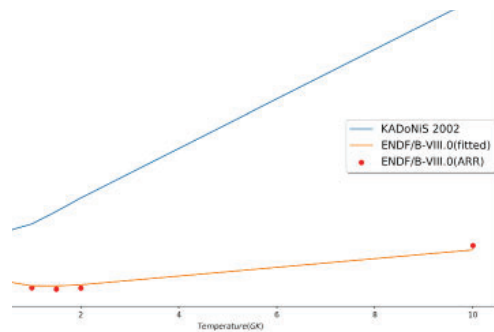


Figure 2: This figure shows the proton neutron capture reaction. This is an important reaction because it is the dominant mechanism for the production of Deuterium that occurs in the universe. This specific neutron capture reaction was a part of Big Bang nucleosynthesis, the foundation for all other nuclear reactions to occur. The figure shows that the KADoNiS rates, from SkyNet REACLIB, and ENDF/B-VIII.0 reaction rates are similar curves near the lower temperature range and diverge as temperature increases. The ENDF/B-VIII.0 reaction computed using the FUDGE ARR calculation has a strong overlap with the fitted ENDF/B-VIII.0 data from the REACLIB parametrization.

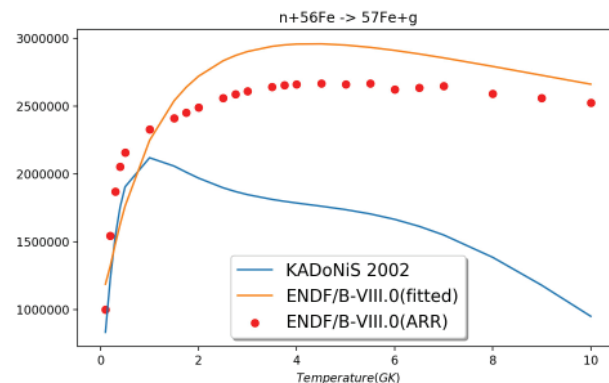


Figure 3: This figure shows the neutron capture reaction of ^{56}Fe . This reaction is vital to understanding stellar nucleosynthesis because Iron is the first of the heavy nuclei. This is noteworthy because the heavy nuclei are hypothesized to require the r-process from supernovae nucleosynthesis for formation formed rather than stellar nucleosynthesis which forms the lighter nuclei. This graph requires particular attention because it raises questions to the suitability of the fitting parameterization. The fitted ENDF/B-VIII.0 ARR and the FUDGE ARR from GNDS file of ENDF/B-VIII.0 have different curves. It is clear that there is a difference between the KADoNiS and ENDF/B-VIII.0 libraries that diverges as the temperature gets larger, but this trend is consistent with other reactions in the libraries, Fig. 2 and 4. But this graph is distinctive because the fitted ARR does not seem to be accurate. Further investigation into this discrepancy is needed. The general shape of the graph of FUDGE ARR and fitted ARR of ENDF/B-VIII.0 are similar but their comparative scale is not nearly as close as in figure 2 and 4.

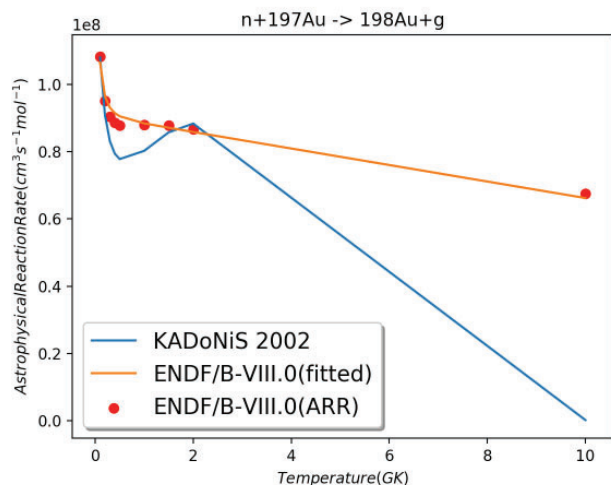


Figure 4: This figure shows the neutron capture reaction for ^{197}Au . This is an important reaction because it is a neutron standard reaction that was recently re-evaluated. Yet, some astrophysical data libraries still use in-correct values, for example, KADoNiS. This figure exemplifies these incorrect values from KADoNiS. KADoNiS has an unclear peak in its data that does not match with ENDF/B-VIII.0, either fitted or unfitted.¹⁸ This difference in the two libraries still diverges as the temperature increases as observed in Figure 2 and 3. The fitted ARR relatively matches the FUDGE computation of the ENDF/B-VIII.0 ARR, as it does in Figure 2. This graph supports the accuracy of the fitting procedure.

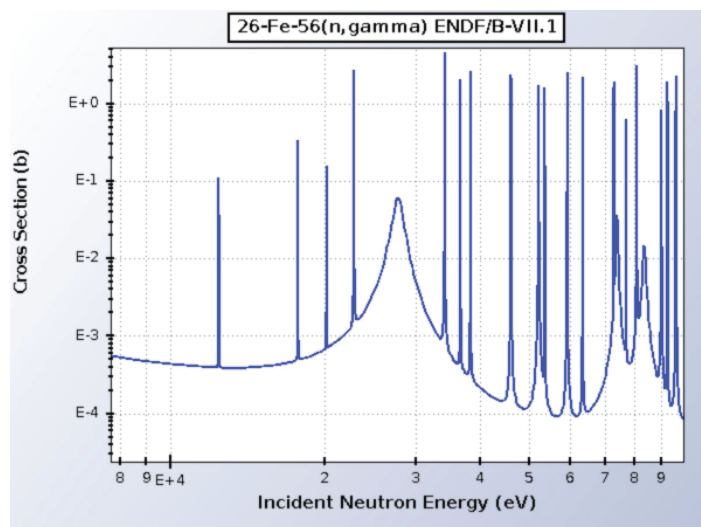


Figure 5: This figure shows the neutron capture reaction for ^{56}Fe from the National Nuclear Data Center at Brookhaven National Laboratory. This figure is zoomed in on the energy range relevant for the calculation of the ARR's needed for REACLIB format. The vertical axis plots cross sections and the horizontal axis plots energy in eV in the range of $0.1 \text{ GK} < T < 10 \text{ GK}$. The gaps in the cross section at 30 keV make Iron very useful in experimentation, as it can be used to filter the energy of incident neutrons. This dip may have lead to the odd behavior of Figure 3.

Investigating the structure of laccases for biofuels

Shahla Partowmah

School of Business, State University of New York College at Old Westbury, Old Westbury, NY 11568

Robert Collins

Department of Physical Sciences, Quinnipiac University, Hamden, CT 06518

Alexei Soares

Photon Science Directorate, Brookhaven National Laboratory, Upton, NY 11973

Abstract

The purpose of this paper is to discover the structure of various bacterial and archaea laccases for alteration and use in biofuel technology. This project is currently pending results which are being reached through protein crystallography and x-ray diffraction analysis. The whole of this experiment aims to solve the structure of a specific bacterial laccase using protein crystallography and x-ray diffraction to understand laccase function and characteristics. The Echo™ (labcyte) is used to eject nano-liter sized samples from crystallization kits and protein samples using sound waves travelling through water on to a plate which is routinely analyzed for crystals. Currently, the best crystals have been diffracted at approximately 1.8 Å; and the data is being analyzed by expert crystallographers and beamline scientist to evaluate the structure of the molecule. Laccase proteins, copper-containing enzymes which catalyze oxidation reactions, greatly benefit bioremediation as their only byproduct is water. After results, research will advance into the manipulation of the laccase to function in different environments. This research allows BNL to benefit the environment. By means of crystallization techniques developed at BNL, this project can promote other DOE initiatives like biofuels and bioremediation efforts in the nation. I learned the value of consistent observation and note taking for the replication of positive results. My internship at BNL has offered the opportunity of pursuing a wide array of careers including crystallographer, beamline specialist, laboratory technician and more. It refined my lab skills and taught me the biochemistry of laccases. Because of my participation in SULI, I will discover the type of projects that interest me while displaying quality experience when pursuing a PHD in medicine.

I. Introduction

Laccases are found in plants, fungi and insects and they are one of the few enzymes with the capability of degrading lignin. Lignin exists in plant cell walls as a tough fibrous material blocking access to cellulose and hemicellulose. Degrading lignin is essential to unlocking the potential energy stored in all of plants. The sole by-product of a laccase reaction is water. In present day, the most effective laccases are produced by fungi in very small amounts. The cost of producing laccases is extremely high due to the time and resourced needed.

In 2015 fossil fuels saw the lowest percentage of energy consumption at 81.5%, and the greatest rate of growth for renewable energy at only 10% of total U.S. energy consumption.¹ There are

environmental, economic and energetic benefits of increasing biofuel consumption to replace fossil fuels. Ever diminishing fossil fuels excrete a large amount of air pollution when consumed. The most current common form of biofuel used is ethanol made from corn, sugar cane and other mass-produced crops.

Using the sugar present in corn, corn ethanol is manufactured. Biofuels produced with the sugars present in corn, sugar cane and others result in a vast amount of waste due to lignin which blocks cellulose and hemicellulose. This development is not only inefficient but energy extensive, requiring a surplus of fertilizer and water. A great alternative to expending useful and diminishing crops is to use crops that are easy to grow, useless for other purposes and are common such as grasses or even corn stover. Shifting to a cellulosic biomass allows the use of a higher percentage of the crop for biofuel production. This way, the carbon dioxide resulting from the use of fuels could be used in the same crops grown for biofuel production.

(Fossil fuels still dominate U.S. energy consumption despite recent market share decline, n.d.)

Most laccase enzymes known today are produced from fungi. They have limited thermal stability, are prone to inhibition and activation, and have an acidic optimal pH level. The laccases in fungi are highly reactive but also very expensive to produce as the fungi only contain this enzyme in small amounts. Fungi is also costly to grow. An alternative to fungal laccases is bacterial and archaea laccases which are easier to produce using recombinant protein expression. To solve the molecular structure of a diverse set of laccases from bacteria and archaea, this experiment uses protein crystallography. The structure will then inform future searches for laccases and allow design and engineering of better performing enzymes.

To reach the structure of this molecule, this experiment will crystallize various laccase proteins in a laboratory using crystallization kits, echo™ (labcyte), and x-ray diffraction at Brookhaven National Lab's beamline. The echo is a robot capable of pipetting dissolved and suspended solutions in droplets as little as 2.5 nL.

II. Methods

Proteins require a precipitant, buffer and sometimes an additive to crystallize. Plates of hundreds of combinations of chemicals and proteins are made along with a 'reservoir' to slowly dehydrate the protein. The Echo™ (labcyte) uses sound waves to eject nano-liter size mixtures of crystallization kits onto the plate along with the laccase protein. It quickly and efficiently generates thousands of crystallization trials without consuming much material.

With the echo, there are multiple plates that are used includ-

ing mitogen plates which have a mylar surface, greiner plates with a plastic surface and atlas plates which are 3D printed at Brookhaven National Lab. Atlas plates allow for different surfaces because the material is adhered to it. The crystallization plates available were Hampton crystal Screen 110/112, Hampton crystal Screen cryo, nextal cryo, JCSG, JCSG 2-3-4-lite, nextal peg suite, hampton HR144, and JB basic. Unlike other scientific experiments, this is experiment involves exploratory research thus there is no need to alter only one variable. Various plates can be created with different proteins, precipitants, additives, and buffers. The amount of nL ejected is also varied when making extrapolation plates.

The following is a summary of all the crystallization efforts conducted in the lab:

- Different types of plates were created with separate mixtures for the different proteins with protein and precipitant at 30 nL, 30 nL and 30 nL, 40 nL respectively.
- Plates were observed and analyzed over a period of time with paid attention to crystal formation.
- Crystals formed were documented, harvested and frozen for x-ray diffraction.
- Frozen crystals were shot at the beamline to assess diffraction. A trained crystallographer used the diffraction patterns to conclude a structure.
- Optimal conditions were extrapolated for improved results.

III. Results and Discussion.

The first success was seen with the indistinct protein 2A crystal which was grown with condition 96 from nextal cryo's screen crystallization kit. The buffer in this condition was 0.085 M MES pH 6.5, the precipitant 10.2% (w/v) PEG 20000, and the cryoprotectant 15% (v) Glycerol. The diffraction for this crystal was around 13 Å which was extremely high and to far to receive a slight reading for the structure of the molecule. A picture of this crystal can be seen below. Note: the shape of the crystal is cuboidal.

Next are pictures of crystals from protein 2B which diffracted to 3.8 Å. This result was achieved by using a follow up plate with precipitants and buffers that had a potential in creating crystals. This prospective was evaluated by the amount of noise or fuzz seen in previous plates. The crystal below involved the use of solution 46 from cryo kit 2 which included 0.6 M sodium phosphate as the first salt, 0.6 M potassium phosphate as the second salt, 0.075 M HEPES sodium salt pH 7.5 as the buffer and 25% (v/v) Glycerol as the cryoprotectant. In addition to the kit, 0.170 M NaCl was used as an additive.

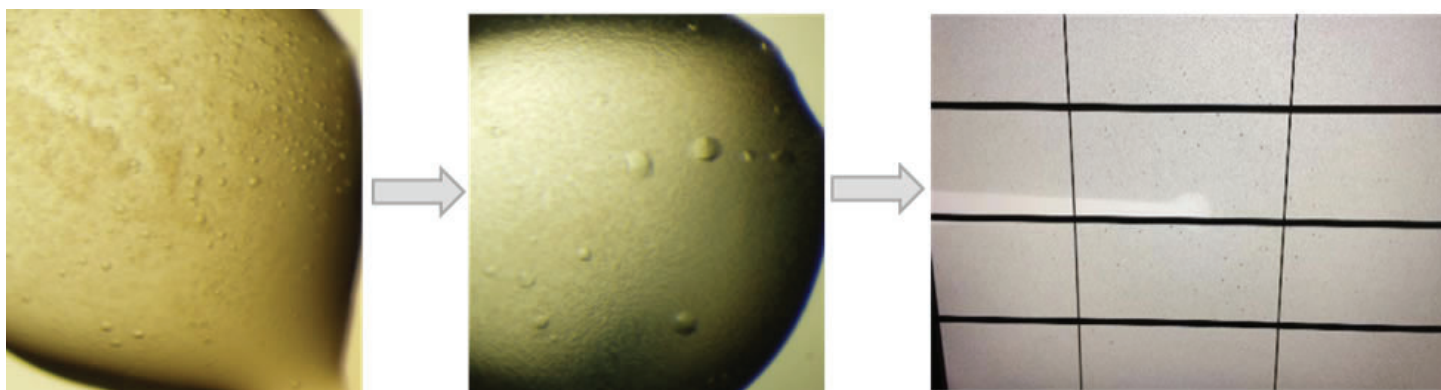
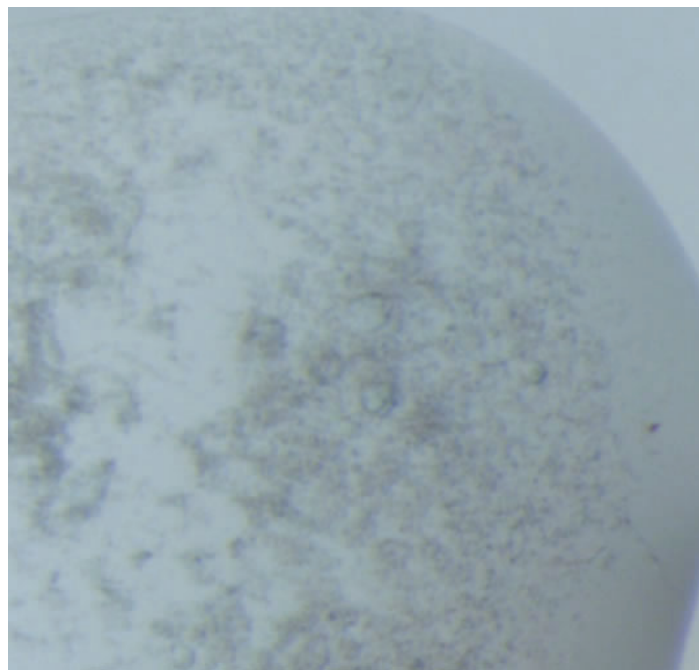
Although 3.8 Å is a fairly good result, it is inadequate to

solve the structure of the molecule. The first and second image show the growth of crystals and the third image depicts the diffraction patterns used to assess the structure. Notice, the crystals are much more visible compared to previous results, but they are still cube shaped.

Finally, after various trials of using changing proteins amounts and also consuming additives in supplement to precipitants, a different shape of crystal was formed. Protein 2E formed needle like crystals with the mixture of 30 nL of protein 2E, 20 nL of precipitant 15% PEG 8000 + 15% PEG 400, 5 nL of the buffer bis-tris pH 6.0 and 5 nL total of the additives sucrose, trehalose, glucose and galactose. A picture of these crystals can be seen below:

The diffraction data gained from this crystal is currently being evaluated by Alexae Soares at Brookhaven National Lab for structure assessment and amino acid pattern.

Due to the high yield of crystals in the last experiment, and the availability of remaining protein, an extrapolation plate was made with protein 2E for observation and analysis of better diffracting crystals and different shapes of crystals. On the parent atlas plate, plate 1 was made exactly the same as before with ratios of 30nL :5nL: 5nL: 20nL; protein, additive, buffer, and precipitant respectively. In tray 2, the amount of precipitant was varied at 10 nL in row 3 and 30 nL in row 6. In tray 3, the amount of



additive varied at 2.5 nL in row and 7.5 nL in row 6. In tray 4, the amount of buffer varied at 2.5 nL in row and 7.5 nL in row 6. In tray 5, the amount of protein varied at 40 nL in row and 50 nL in row 6. Tray 6 also involved a varying of protein amount at 60 nL in row 3 and 70 nL in row 6. In tray 7, the amount of precipitant varied at 40 nL in row and 50 nL in row 6. Lastly, in tray 8 the amount of additive and buffer were both varied at 7.5 nL additive and 2.5 nL buffer in row 3 and 2.5 nL additive and 7.5 nL buffer in row 6. Besides the varied measurements, everything remained the same as the initial 1.8 Å diffracting crystals conditions. Only rows 3 and 6 were used to conserve the use of protein and the remaining protein will be used for hanging drop experiments.

IV. Conclusion

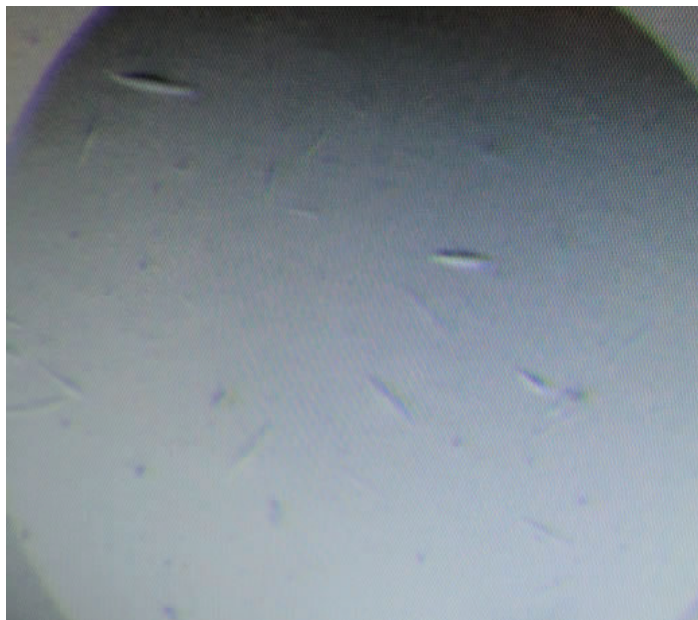
This is an ongoing project which will require more and better diffracting crystals to assess the structure of the various bacterial and archaea laccases. Currently, protein 4 and 5 have crystallized and the diffraction resolution is to be determined with next beam time. Protein 2E was diffracted at the last beamtime to 1.8 Å and efforts are being focused on targeting the structure of that molecule. A crystal's diffraction can be refined by changing the concentrations of precipitants and additives as well as the ratio off protein and precipitant. This experiment will require more crystallization conditions and extrapolations to achieve a better diffracting crystal.

V. Acknowledgements

With thanks to: Department of Energy (DOE), Alexei Soares from Brookhaven National Laboratory (BNL), Robert Collins from Quinnipiac University, Noel Blackburn from Office of Educational Programs (OEP), Student Undergraduate Laboratory Internships (SULI), Maria Zulema Cabail from SUNY College at Old Westbury, and everyone who has guided me at BNL. This project was supported in part by the U.S. Department of Energy, Office of Science, Office of Workforce Development for Teachers and Scientists (WDTS) under the Science Undergraduate Laboratory Internships Program (SULI).

VI. Bibliography

Fossil fuels still dominate U.S. energy consumption despite recent market share decline. (n.d.). Retrieved from eia: <https://www.eia.gov/todayinenergy/detail.php?id=26912>



Electronic structure characterization of metal organic frameworks using ambient pressure photoelectron spectroscopy

Brianna Perris

Chemistry, Binghamton University, Binghamton, NY 13902

Ashley Head

Center for Functional Nanomaterials, Brookhaven National Laboratory, Upton, NY 11973

Abstract

Photoelectron spectroscopy (PES) is a widely used technique to study the electronic structure of the surface molecular structures. A high-energy photon beam ionizes the sample, resulting in ejected electrons with specific kinetic energies that carry chemical information. Conductive materials easily replenish the positive charge left behind on the surface by the removal of the negatively charged electrons. However, in insulators, electrons are not free to flow to replenish the positive charge, so PES is not an advantageous technique. This charge can alter the measured binding energy and yield inaccurate data. In this study, ambient pressure PES is used to study this previously unattainable electronic structure of insulating metal organic frameworks (MOFs) by dosing the chamber with an inert gas to replenish the charge. MOFs are microporous materials with high surface area that can adsorb gases into their crystalline structures. Several sample preparation methods and gas environments were prepared to determine the optimal conditions to measure accurate ionization energies of insulating MOF. Loose and dropcast MOF powders continued to accumulate positive charge during PES measurements, despite 10 mbar of Ar. Forming a thin film by pressing the powders between two copper plates yielded the ideal thickness of MOF sample and ionization energies close to previously measured values.

I. INTRODUCTION

A. UiO-66 MOF

Metal organic frameworks (MOFs) are of high interest to scientists all over the world due to their incredible gas capturing abilities. MOFs contain series of repeating units made of metal-containing units linked with organic ligands to create a structure with pores. These pores have been shown to be effective at adsorbing gases or trapping different molecules. Depending on the metal or ligands used, the properties of the MOF such as thermal stability, surface area, pore size, and electronic reactivity can vary. Thus, there are thousands of different MOFs that have been discovered, each with their unique properties and different abilities to trap different molecules. Omar Yaghi, a pioneer of MOFs, discovered a MOF that has the ability to convert humidity into drinking water, a revolutionary new tool that can help people in drought-stricken areas.¹ Another study was able to use MOFs to destroy chemical warfare agents.²

In this study, the MOF UiO-66 was studied. UiO-66 is made up of $Zr_6O_4(OH)_4$ units linked by 1,4-benzodicarboxylic acid (BDC) ligands, as seen in figure 1.

In previous studies, this MOF has shown stability at relatively high temperatures, in addition to having high porosity. There have been numerous studies that show the reactivity for adsorbing gases increases when there a defect, such as a missing BDC linker.⁴ This absent linker allows for a larger opening to the pore center of the MOF. The positively charged zirconium in the center is the main source for reactivity and is how gases are trapped inside. One property of this MOF that has not been thoroughly

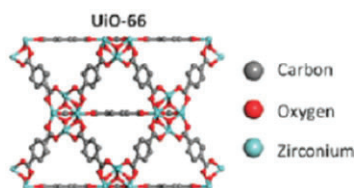


Figure 1. Structure of UiO-66³

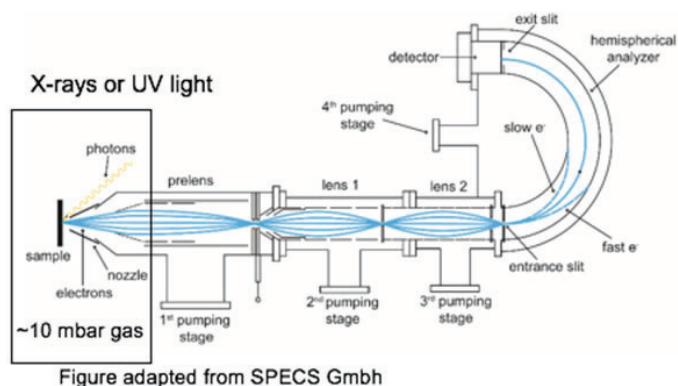


Figure adapted from SPECS GmbH

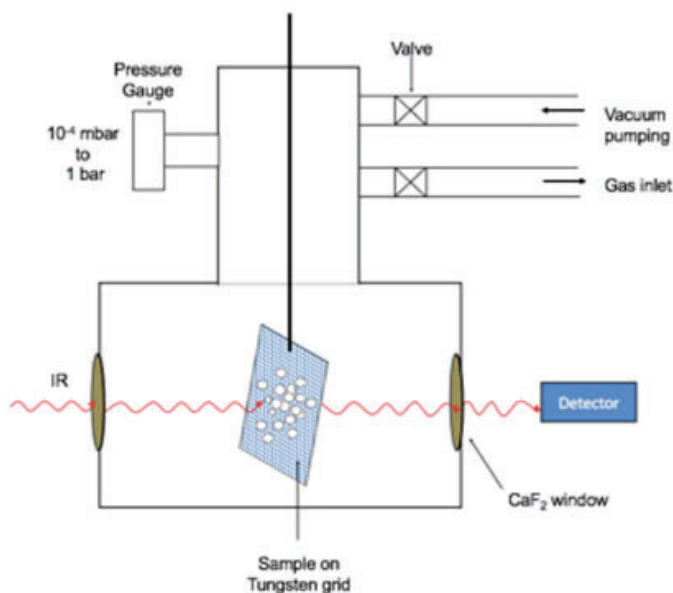


Figure 3. Schematic of transmission IR spectroscopy

studied, however, is its electronic structure, especially under gas adsorption conditions. Due to its framework structure, UiO-66 is an insulator. This property makes it very difficult to measure the binding energies, which probes electronic structure, with current spectroscopic methods, since there is significant charge buildup if the sample is ionized. Ambient pressure x-ray photoelectron spectroscopy (AP-XPS) can be used to reduce this charge and measure the binding energy of insulators.

In order to do AP-XPS, we prepared several samples with various techniques and thickness. The electronic structure of each sample was measured under various pressures and temperatures. The results of study paves the way for future *in situ* studies of gas adsorption and reactivity of MOFs.

B. Ambient pressure X-ray photoelectron spectroscopy

Photoelectron spectroscopy (PES) is a technique used to measure the electronic structure of a molecule. It contains differential pumping and electrostatic lenses to create an ultra high vacuum (UHV) and allows for PES data collection of solid samples, as seen in figure 2.

By illuminating a sample with a high energy photon, electrons are ejected with specific kinetic energies dependent on the atomic energy level from which it was ejected. The kinetic energy of these electrons is measured, and the binding energy of the atom can be determined, using equation 1.

$$BE = E_{\text{photon}} - KE - \phi \quad (1)$$

where BE is the binding energy of the electron, E_{photon} is the energy of the incident radiation, KE is the kinetic energy of the ejected electron, and ϕ is the work function, which is a correction factor based on the instrument. The two main types of PES are ultraviolet photoelectron spectroscopy (UPS) and X-ray photoelectron spectroscopy (XPS). UPS uses ultraviolet light to eject the valence electrons of an atom. Valence electrons are not bound as tightly to the nucleus due to shielding by the core electrons. XPS has a higher frequency, allowing core electrons to be photoionized. Since gases scatter electrons, the technique is typically done in UHV. However, with ambient pressure PES, gases can be introduced without effecting the energy measurements. This is due to a series of electrostatic lenses and differential pumping, that refocuses the electrons and minimizes gas interference.

Since the exact binding is critical in identifying the elements and subshells involved, all sources of error should be minimized. One source of error that can cause inaccurate results is charging

in insulators. The technique inherently generates a positive charge in a sample by removing a negative electron. The charge is replenished for insulators but not for conductors. It will take progressively greater amounts of energy to eject these electrons, and thus result in a measured binding energy higher than its true value. One way to solve this issue is to replace the electrons that are being ejected by electron bombardment. However, electron sources require UHV and are not compatible with *in situ* gas adsorption studies of solid. In ambient pressure XPS, due to the differential pumping and electrostatic lenses, UHV is not needed and inert gases can be dosed around the sample to replenish the electrons.

C. Infrared Spectroscopy

Infrared (IR) radiation falls between visible light and microwave radiation on the electromagnetic spectrum, with a wavelength of 700-1000 nm. In IR spectroscopy, the amount of energy is not high enough to excite electrons, but it can probe the vibrational modes of bonds in molecules. In order to measure these vibrations, there must be a change in dipole moment of the molecule. In powder transmission, an IR beam is transmitted through the sample, and the absorbance or the transmittance of the light is measured, as seen in figure 3. By mounting the sample in a UHV environment, this method allows for controlled environments and is good for powders pressed onto a mesh, such as UiO-66 on tungsten mesh.

II. Methods

A. Instrumentation

The photoelectron spectrometer used to take measurements of the electronic structure was the analyzer SPECS Phoibas 150-NAP electron energy analyzer with a 1D delay line detector. The X-rays were from a monochromated Al anode (1486 eV), with a spot size of $\sim 300 \mu\text{m}$ and pass energy of 50 eV for all. The valence spectra were measured with a He I lamp (21.2 eV). The infrared spectrometer used was a Bruker Vertex 80V.

B. Preparation of samples

1. UiO-66 on dropcast Au coated Si wafer

A minimal amount of UiO-66 powder was suspended in ~ 0.5 mL methonal. A drop of the suspension was placed onto a clean gold coated silicon wafer. This sample was mounted on the XPS sample holder by spot welding the corners with tungsten foil.



Figure 4. UiO-66 dropcast on Au coated Si wafer



Figure 5. UiO-66 pressed into indium foil



Figure 6. UiO-66 pressed between copper plates

2. UiO-66 pressed into In foil

A piece of indium foil was spot welded with tantalum strips to the sample holder. The top of the indium foil was scraped. UiO-66 powder was pressed into the foil with a gradient of thickness.

3. UiO-66 pressed between Cu plates

A small amount of UiO-66 powder was placed in between two copper plates, which were then pressed at 1 ton for around 10 seconds in a hydraulic press. The plates were separated and the plate with the most UiO-66 was used.

C. Measurements of samples

The UiO-66 on dropcast Au coated Si wafer sample was moved around inside the analysis chamber until the cone was above a spot on the sample that yielded the highest electron counts. XPS data was taken in UHV, 1.0 mbar N_2 and 2.0 mbar N_2 . The nitrogen was pumped out and UPS data was taken under UHV for a valence spectrum. In UHV, the sample was heated from 350 K to 700 K at 50 K increments, and XPS was measured at each temperature.

The UiO-66 pressed into indium foil sample was positioned on a thick spot so no indium could be seen underneath. XPS was measured at pressures of UHV, 0.5 mbar, 1.0 mbar, 2.0 mbar, 3.5 mbar, 4.5 mbar, 6.0 mbar, 8.0 mbar, and 10.0 mbar nitrogen.

XPS data was taken of UiO-66 pressed into copper plates at 5 mbar, 8 mbar, and 10 mbar argon at room temperature. At 10 mbar argon, XPS was measured at temperatures from 323 K to 573 K in 50 K increments.

UiO-66 pressed into tungsten mesh was analyzed using transmission IR spectroscopy. A tungsten background scan was taken and subtracted from the sample scans. An IR spectrum was collected at temperatures of 296 K, 423 K, 523 K, and 573 K.

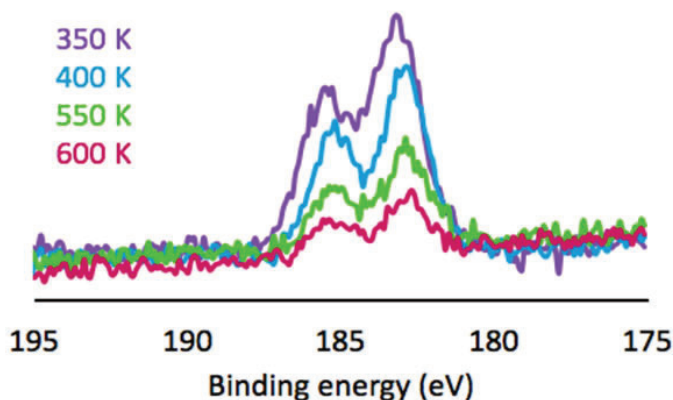


Figure 7. XPS of UiO-66 on Au coated Si wafer of Zr 3d in UHV at varying temperatures

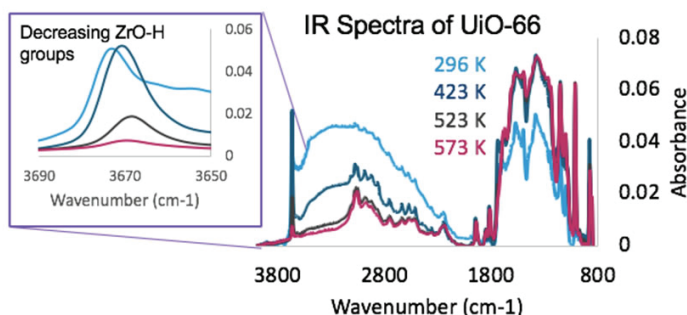


Figure 8. IR spectrum of UiO-66 on tungsten mesh at varying temperatures

III. Results and Discussion

A. UiO-66 on Au-coated Si wafer

The UiO-66 sample dropcast on the gold coated silicon wafer was analyzed using the XPS. A fixed energy scan was initially taken to optimize the sample location that would result in the highest electron counts. A scan was taken of the energy region of zirconium 3d to determine the binding energy. Since UiO-66 is an insulating material, the measured binding energy was higher than the actual value. This is due to progressively stronger pull the electrons feel from the nucleus as the shielding from other electrons decreases. One way to replenish the ejected electrons is to dose with an inert gas that can donate electrons to the MOF. Nitrogen gas was dosed into the chamber at varying pressures to observe its effect. It was seen that as the pressure increases, the binding energy slightly lowers.

Another parameter that was measured was the effect of temperature on electronic structure. As seen in Figure 7, as the temperature increases, the binding energy of Zr 3d shifts slightly lower.

The lowest binding energy measured was 182.77 eV at 600 K, which is close to the literature value of 182.54 eV.⁵ However, the intensity of the Zr 3d peaks dramatically decreases as the temperature increases. It was thought to be the result of the MOF decomposing at temperatures around 600 K. A paper published by Carlo Lamberti shows that crystallinity of UiO-66 is stable up to 648 K, and then pore collapse.⁶ To determine the decomposition temperature of the MOF, a transmission IR spectrum was taken of the UiO-66 on tungsten mesh. The resulting spectrum can be seen in figure 8.

As the temperature increases, the MOF is activated around 523 K, meaning all of the solvent from synthesis is removed. This can be seen by the decreased OH peak around 300 cm^{-1} as the temperature increased until it stabilized at 523 K. Another notable peak change is around 3670 cm^{-1} , where the ZrO-H bond decreases when the temperature is increased. At 573 K, the peak is practically flat, which validates the XPS data that the MOF is decomposing around 573 K.

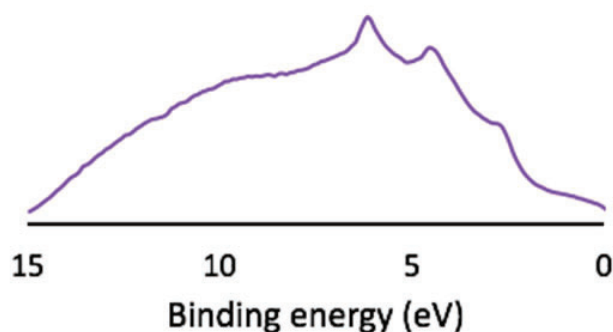


Figure 9. UPS of UiO-66 on Au-coated Si wafer in UHV

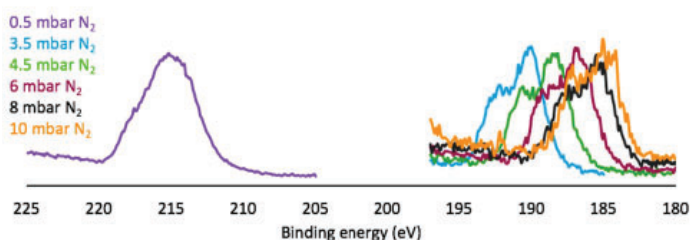


Figure 10. XPS of Zr 3d UiO-66 pressed into indium foil at varying pressures of nitrogen

Another important aspect of the electronic structure is the valence shell. To see the binding energy of electrons in these shells, UPS was used, and the resulting spectrum can be seen in figure 9. In addition to too much signal from the substrate, the particles would become charged and hop to the cone, sticking to the entrance of the electron analyzer and blocking the signal.

This spectrum only reveals that there is gold, which means the sample is too thin to measure with UPS. Other preparation methods are needed to prepare a sample with optimal thickness.

B. UiO-66 on indium foil

To create a thicker layer, UiO-66 powder was pressed into indium foil. Indium foil was chosen for its softness and allows for easy compaction of the powder. This sample was significantly thicker than the dropcast sample, so when XPS was measured in UHV, the binding energy shifted dramatically, around 42 eV higher than the expected value. This was due to the positive charging of the sample, since the electrons were not being replenished. In the dropcast sample, the layer was so thin that it was able to recharge from the gold substrate; however, on the indium foil, the sample was too thick and caused significant charge buildup. To dissipate this charge, nitrogen, an inert gas, was dosed into the chamber. Figure 10. shows the effects of varying pressures of nitrogen on the binding energy of Zr 3d.

As the pressure of nitrogen increased, the binding energy of Zr 3d significantly lowers. The lowest binding energy measured was 184.29 eV in 10 mbar N₂. However, since a lower binding energy was measured previously in the dropcast sample, it was assumed that this binding energy is not accurate, due to the significant charging. It was hypothesized that this was due to the sample being too thick. Another sample preparation method was needed so that it is not too thin, yet not too thick.

C. UiO-66 on copper plates

The sample was measured with XPS at pressures of 5 mbar, 8 mbar, and 10 mbar of argon. It was observed that just like before, increased pressure of inert gas dissipates the charge for all elements and lowers the binding energy. The spectra can be seen in figure 11.

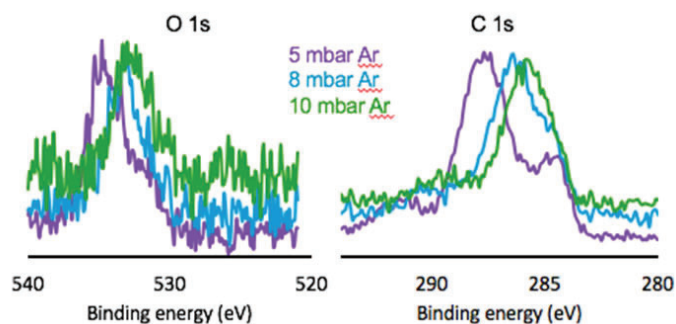


Figure 11. XPS of UiO-66 on Cu at varying pressures argon

Table 1. Binding energies of Zr 3d 5/2

Sample	Literature ⁵	UiO-66 on Au/Si wafer in UHV at 550 K	UiO-66 on In foil in 10 mbar N ₂	UiO-66 on Cu in 10 mbar Ar at 573 K
Binding energy (eV)	182.54	182.77	184.29	183.24

Both the O 1s and C 1s binding energies lowered as the pressure was increased. One issue of this dosing of gas method is that at higher pressures, it is hard to differentiate between the sample carbon and adventitious carbon on the surface. At 5 mbar argon, it can be seen that there are three peaks. The peak around 292 eV corresponds to carboxylate, 288 eV is the carbon in the UiO-66, and 284 eV is extra adventitious carbon on the surface. As the pressure increases, the MOF peak lowers, and overlaps with the adventitious carbon peak. Extra calculations would be needed to subtract out the peak if used for quantitative measurements.

Seeing that 10 mbar argon yielded the lowest binding energy, the effect of temperature at this pressure was studied in hopes for the most accurate binding energy of zirconium. Figure 12. shows the spectra of Zr 3d at 298 K, 523 K, and 573 K in 10 mbar argon.

As the temperature increases, the peaks shift slightly lower; however, this can be due to the effects of the heater and not the actual binding energy of the MOF. When the MOF reached 573 K, the peaks became much sharper and distinct. This is due to the loss of DMF solvents and physisorbed water at 573 K.⁶ Once 573 K is reached, the measurements should be just of the MOF with no solvent or other impurities.

The binding energies of all three samples can be compared, as seen in table 1. To our knowledge, there is very few reported binding energy values for Zr 3d 5/2, and they are around 182.54 eV. The closest binding energy obtained was 182.77 eV, which was from the UiO-66 Au/Si wafer in UHV at 550 K. However, this sample was too thin to perform UPS, so it is not the optimal sample. The UiO-66 prepared on the copper plates had a binding energy of 183.24 eV, which is also close to the expected value.

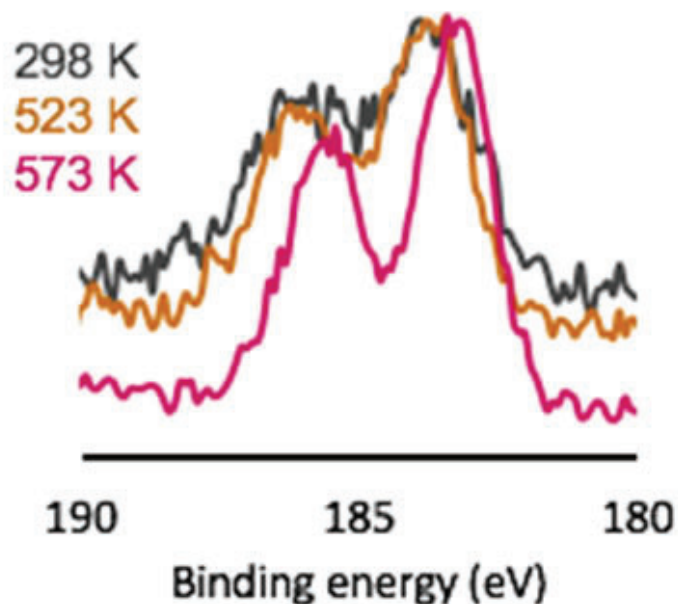


Figure 12. XPS of Zr 3d UiO-66 on Cu in 10 mbar Ar at varying temperatures

While this sample deviated from the expected value, the sample was unable to hop to the analyzer entrance and block the signal. Due to instrument problems, the UPS data was not collected.

IV. Conclusion

Ambient pressure photoelectron spectroscopy proved to be a valuable technique to study the electronic structure of insulating metal organic frameworks. By dosing the sample with an inert gas, the charge caused from removing electrons was mostly replenished, allowing for an accurate measurement of the binding energies. The best sample preparation method was pressing between two copper plates, so that the optimal thickness for measurements was developed. This data will be beneficial in future experiments to compare electronic structure of loose MOF to a oriented thin film MOF.

V. References

¹H. Kim, S. Yang, S. R. Rao, S. Narayanan, E. A. Kapustin, H. Furukawa, A. S. Umans, O. M. Yaghi, E. N. Wang. (2017). Water Harvesting from Air with Metal-Organic Frameworks Powered by Natural Sunlight. *Science*, 356, 430-434.

- ²J.E. Mondloch, M.J. Katz, W.C. Isley, P. Ghosh, P. Liao, W. Bury, G.W. Wagner, M.G. Hall, J.B. DeCoste, G.W. Peterson, R.Q. Snurr, C.J. Cramer, J.T. Hupp, O.K. Farha. (2015). Destruction of chemical warfare agents using metal-organic frameworks. *Nat Mater.* 14(5), 512-6
- ³J.B. DeCoste, T.J. Demasky, M.J. Katz, O.K. Farha, J.T. Hupp. (2015). A UiO-66 analogue with uncoordinated carboxylic acids for the broad-spectrum removal of toxic chemicals. *New J. Chem.* 39, 2396-2399
- ⁴D.M. Driscoll, D. Troyga, P.M. Usov, A.J. Maynes, A.J. Morris, J.R. Morris. (2018). Characterization of undercoordinated Zr defect sites in UiO-66 with vibrational spectroscopy of adsorbed CO. *J. Phys. Chem. C*, 122(26), 14582-14589
- ⁵L. Shen, R. Liang, M. Luo, F. Jing, L. Wu. (2015). Electronic effects of ligand substitution on metal-organic framework photocatalysts: the case study of UiO-66. *Phys. Chem. Chem. Phys.* 17, 117-121
- ⁶L. Valenzano, B. Civalieri, S. Chavan, S. Bordiga, M. Nilsen, S. Jakobsen, K.P. Lillerud, C. Lamberti. (2011). Disclosing the complex structure of UiO-66 metal organic framework: a synergic combination of experiment and theory. *Chem. Matter.* 23, 1700-1718

VI. Acknowledgements

This project was supported in part by the U.S. Department of Energy, Office of Science, Office of Workforce Development for Teachers and Scientists (WDTS) under the Science Undergraduate Laboratory Internships Program (SULI).

Lithographic calibration patterns for Low Energy Electron Microscopy

Brady Robertson

Cabrillo College, Aptos, CA95003

Jerzy (Jurek) Sadowski

Center for Functional Nanomaterials, Brookhaven National Laboratory, Upton, NY 11973

Abstract

This project makes use of Brookhaven National Laboratory's Center for Functional Nanomaterials' (CFN) clean room. Within the clean room I produce microscope calibration chips, which are gold patterned on single-crystal silicon chips using various techniques such as spin coating, ultraviolet lithography, and physical vapor deposition. Once complete, the patterns are confirmed for precision and coherency with both optical and atomic force microscopes (AFM). The calibration patterns are used in CFN's two Low Energy Electron Microscopes (LEEM) to align the electron 'optics' so that they may produce better, more crisp images. LEEM is especially useful for viewing surfaces in real time and can be used to investigate surface catalysis, topography, and reactions such as those that take place at the electrodes of new battery technologies. As the CFN is a user facility, this project works directly to help produce successful research endeavors for a multitude of research institutions.

I. Introduction

This project completes work in both National Synchrotron Light Source II (NSLS II) and Center for Functional Nanomaterials (CFN), both are user facilities, meaning anyone doing nonprofit work may apply to use time with the instruments at no cost. These are world class facilities and instruments, NSLS II is currently the world's brightest light source for soft X-rays, which the X-ray Photoemission Electron Microscope (XPEEM)/LEEM Spectro-Microscopy Endstation makes use of to do "Spectroscopic surface microscopy, band mapping, elemental mapping, [and] micro-diffraction" [1]. The electron lenses in electron microscopes will undergo a level of drift over time through the metals they are made of slowly acquiring magnetic charge. This slowly warps the optics, which can be refocused, but lose calibration. The solution to this inevitable issue is to calibrate the optics with a sample that has known feature sizes. The main scope of this project was to create these calibration samples with UV lithography.

The calibration itself is an iterative process, we run down the line of magnetic lenses [2], calibrating each one, and by the time we have calibrated the last lens the first lens is now out of alignment, though less so than before, by iterating this process a few times the field of view achieves correct calibration. The calibration process is repeated for each pre set field of view. From 100 μm down to 2 μm .

II. Progress

The creation of a calibration sample is a multi step process lasting over a day. The process is as follows: cover the base substrate of single crystal silicon with photosensitive resist; expose

the resist to ultraviolet light through a mask of the final pattern desired; heat the sample to harden the polymer not exposed to UV light. Submerge the substrate into a mild base called developer, which will wash away the resist exposed to uv light leaving canyons in the shape of the pattern on the mask. Heat the sample again to make the remaining resist no longer photosensitive, load the sample into a physical vapor deposition chamber, where a thin layer of titanium is deposited which helps the next much thicker layer of gold adhere to the surface of silicon in the canyons left in resist. And lastly liftoff involves soaking the sample in organic solvent overnight so that all remaining resist is dissolved, taking all unwanted gold with it. What is left is the gold and titanium that made direct contact with silicon in the canyons left after development, this will be in the exact pattern of the mask that blocked uv light. After quick sonication to remove any straggling gold foil, and quantification of height and scale in AFM the sample is ready to be used in the calibrations of LEEM/PEEM electron-optics. [3]

First spin coating is used to create a uniform and thin layer of what is called "resist", a light sensitive polymer that will eventually form the physical shape, or lack thereof, of the desired pattern. In spin coating the sample is attached to a rotating table and a layer of resist, held on by surface tension, is dripped onto the surface. The sample is then spun at thousands of rotations per minute to create a uniform and atomically thin layer, with the depth of that layer determined by the rate of spin. Two layers of resist were used, the bottom layer dissolves at a faster rate in the development solution, leading to an overhang of the top layer (see figure 1), this is useful in that it prevents the deposited gold from sticking to the sides of the canyon and remaining after liftoff. Exposure and development times are inversely proportional as to how well the resist might take on the pattern; with less exposure, the resist is not decomposed enough by the UV light, requiring longer development, but often leading to under etching; and the reverse is true for over exposure, which leads to quick development times and over etching.

After development, a process of soaking and agitating samples in the base MF-312, a final bake of the samples is done to make the resists lose their photosensitivity, they may then be brought out of the UV protective environment of the lithography room. Optical microscopy is performed on samples to confirm effective exposure and development, and based on what is seen adjustments are made in exposure/development times to reach optimal conditions. Successful samples undergo electron beam physical vapor deposition of a 5-10 nm adhesion layer layer of titanium followed by a 60 nm layer of gold. Gold is used because with its low work function of ~ 3.5 eV it is visible as contrast in PEEM, which has a limited energy range, and the usage of PEEM in the calibration process allows the electron gun calibration to

be avoided until later in the calibration, simplifying the process. The samples coated with gold are then soaked overnight in remover-1165, an organic solvent, at 80° C. This lifts off the remaining resist, leaving only gold in the desired pattern. Samples were then surveyed with atomic force microscopy (AFM) which is able to provide quantitative scaling data as well as the height characteristics of the calibration pattern. The tops of the gold patterning should be flat, but in early samples spikes were seen on the tops of the features forming rings around the outside often taller than the features themselves (see figure 2a). The presence of the spikes makes focusing in LEEM/PEEM less precise, where one can vary the depth of focus and the apparent size of the feature changes, an undesired effect when utilizing the sizes of features as a ruler. The presence of these spikes was due to the gold deposited on side-walls connecting with the gold deposited on the tops of the features, which in itself is a product of not enough undercutting [5]. This problem was eliminated in future generations (see figure 2b).

The fine details of the smallest patterns were investigated with AFM, which allowed for quantitative scale investigation in both the X Y plane and Z heights. Statistical analysis into the periodic regularity of arrayed calibration patterns proved to be within an acceptable error of about 3% (see figures 5 and 6). In calibration we found that the LEEM/PEEM optics were radically out of calibration field of view by upwards of 50%, this was further out calibration than ever before, in distrust of such a high level of mis-calibration we recalibrated the AFM, which is where we got our scale measurements; it was only off by 3%, not nearly enough to account for the 50% difference seen in PEEM.

III. Future work

Ultimately the calibration patterns were not able to reach the lithographic limits in feature size of 5 μm. The calibration patterns' 10 μm squares had rounded corners, and the 5 μm appeared only as circles (see figure 3). Had the smallest features been squares then the calibration of LEEM/PEEM at the smallest fields of view would have been more precise. So there is still room for improvement in the production of calibration samples with honing in the lithographic exposure and development process, which is where the fidelity of mask to sample is. Additionally the process could be run run at a higher production scale. Currently one sample is produced at a time. But as the mask has 25 instances of the calibration pattern on it, a larger silicon wafer can be exposed all at once, then cut apart into single samples after, thus greatly streamlining the production of calibration samples. With finer lithographic features resolved the project may move on to the creation of lithographically produced electrodes for use in the study of room temperature ionic liquids.

IV. Impact on Laboratory Mission

As the CFN and the NSLS II are user facilities, this project works directly to help produce successful research endeavors for a multitude of research institutions. With access to functional tools, the users can have confidence in their results. The skills gained in this internship can be brought to a variety of fields and are quite tradable. AFM and LEEM/PEEM in particular are useful for a wide range of materials and surface science projects. The UV lithography process can be implemented in the making of substrates used in the study of room temperature ionic liquids, which have attractive uses as electrolytes in batteries [4]. Batteries are struggling to find growth in performance at amatching rate with

efficiencies of technologies like solar power or computer chip performance and are acting as a bottleneck in the adoption of various energy technologies' adoption. So fundamental research into potential paths towards improved battery technologies is crucial. Funding for the project comes from the United States Department of Energy through its Science Undergraduate Laboratory Internship (SULI) program.

V. Conclusions

The project goal was to create LEEM/PEEM calibration samples using UV lithography techniques. The lithographic process proved challenging and multiple iterations were required before acceptable samples were created. Quantitative analysis of inter dot distances and surface morphology was completed with AFM. Though not optimum, with rounded instead of sharp corners in pattern features, the samples proved viable in LEEM/PEEM calibration. The samples were utilized in calibration of a LEEM/PEEM system and proved useful by showing that the field of view for the microscope was 50% larger than it needed to be. This issue was fixed in calibration of the microscope's many electronic lenses.

VI. Acknowledgements

This work was supported in part by the U.S. Department of Energy, Office of Science, Office of Workforce Development for Teachers and Scientists (WDTS) under the Science Undergraduate Laboratory Internship (SULI) program. Jerzy (Jurek) Sadowski for Mentorship. Ming Lu and Gwen Wright for training and guidance.

VII. References

- Proximal Probes Facility. *Center for Functional Nanomaterials* Available at: <https://www.bnl.gov/cfn/facilities/proximalProbes.php>. (Accessed: 3rd August 2018)
- ELMITEC Elektronenmikroskopie GmbH. Manual Low Energy Electron Microscope, model LEEM III.
- Mack, C. Semiconductor Lithography (Photolithography) - The Basic Process. *The Basics of Microlithography* Available at: <http://www.lithoguru.com/scientist/lithobasics.html>. (Accessed: 3rd August 2018)
- MicroChemicals. *Lithography Trouble Shooter* (2012).
- Sitaputra, W., Stacchiola, D., Wishart, J. F., Wang, F. & Sadowski, J. T. In Situ Probing of Ion Ordering at an Electrified Ionic Liquid/Au Interface. *Advanced Materials* **29**,1606357 (2017).
- Subtractive vs. Additive Lithography Process. *Positive vs. Negative Tone Photoresists* Available at: <http://www.microchem.com/Prod-LithographyOverviewSubAdd.htm>. (Accessed: 3rd August 2018)

VIII. Appendix

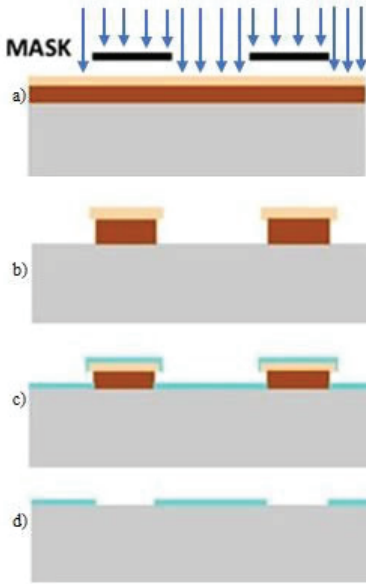


Figure 1:

a) The blue arrows represent the UV light, blocked by the mask, that cures the two layers of resist (light and dark brown)

b) The exposed areas of resist are washed away in a development bath. The bottom resist dissolves faster than the top, leaving an undercut.

c) Au is deposited onto the entire surface. The undercut prevents sidewall adhesion of Au to reach the bottom Au.

d) The sample is soaked in heated solvent overnight to lift off the remaining resist, leaving only the bottom patterned Au.

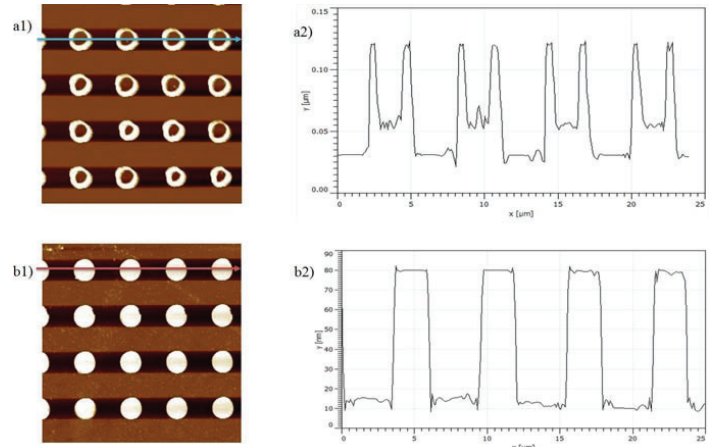


Figure 2: a1) and b1) are Atomic Force Microscopy image (25 μm across) of the smallest lithographic features. Brightness corresponds to height. a1) and b1) represent early and recent attempts respectively. a2) and b2) are cross sectional height graphs corresponding to the blue and red arrows in a1) and b1) respectively. In a2) the two peaks of the repeating “M” shape are artifacts left by gold sticking to the walls of resist, a symptom of not enough undercutting, an issue resolved by b2).

1st smallest squares:		2nd smallest squares:	
avg of avgs:	1.55 %	avg of avgs:	1.24 %
(of stdev/avg)		(of stdev/avg)	
largest stdev/avg:	3.3 %	largest stdev/avg:	2.2 %
smallest stdev/avg:	0.72 %	smallest stdev/avg:	0.78 %
average distance:	5.984 μm	average distance:	9.887 μm

Figure 4: Statistical analysis of inter-dot distances.

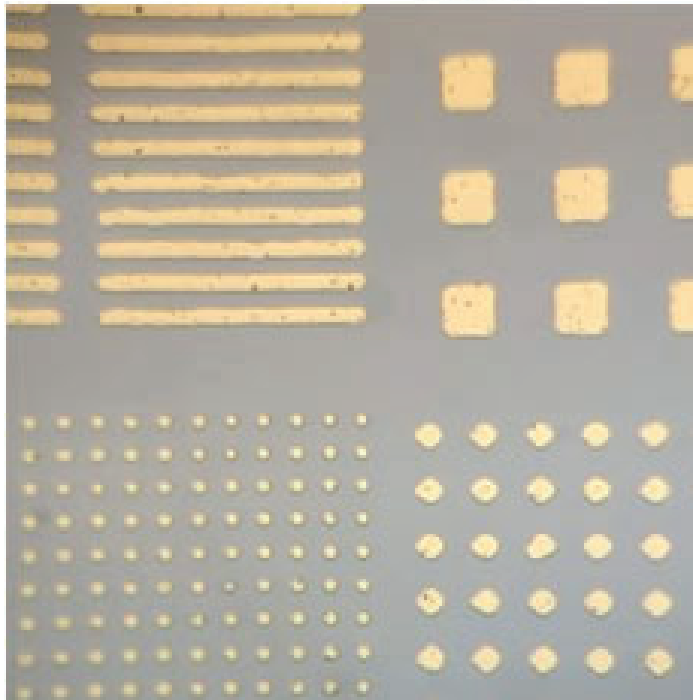


Figure 3: Optical microscope image: Smallest features in lithographic calibration pattern. The smallest circles are 3 μm .

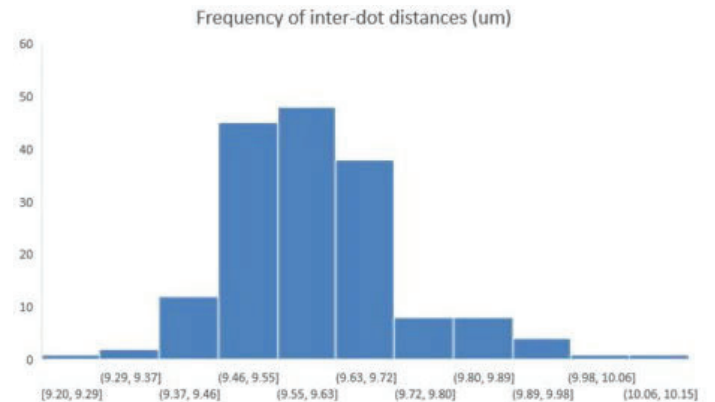


Figure 5: Comparison of inter-dot distances (μm) for the second smallest squares, sampled with AFM across 112 dots from 7 samples.

Name	Institution	Role
------	-------------	------

Jerzy (Jurek) Sadowski	CFN BNL	Project lead
------------------------	---------	--------------

Scientific facilities: Clean Room, Center for Functional Nanomaterials, and National Synchrotron Light Source II, Brookhaven National Laboratory

Purification and Crystallization of sucrose transporters (SUC2) from *Arabidopsis thaliana*

Zahir Safie

University of New Haven, West Haven, CT 06516

Desigan Kumaran

Brookhaven National Laboratory, Upton, NY 11973

Abstract

Photosynthesis in leaves produces sugars, primarily a source of carbons skeleton and energy carrying molecule sucrose, distributed from source leaves to support growth of and carbon storage by heterotrophic sink organs. In this process, sucrose has to pass through a number of membranes. The membrane proteins that transport sucrose across the membrane are sucrose transporters (SUCs). Sucrose transporters play a key role not only in the phloem loading and unloading processes, but also in the exchange of sucrose between beneficial symbionts as well as pathogens such as nematodes and parasitic fungi. Plant sucrose transporters belong to the major facilitator superfamily (MFS), characterized as energy-dependent sucrose/H⁺ symporters and are distantly related to hexose transporters in bacteria, fungi, plants and animals. Despite having abundant literatures about the biochemical and cellular information of these sucrose transporters at cellular level, the exact transport mechanism at molecular level is not clear. The first step in understanding the mechanism of sucrose transporter is to determine the three dimensional structure of this membrane transporter. To determine the structure, we must express our transporter protein in culture, purify it to homogeneity, and crystallize the sample for X-ray diffraction studies. In this study, the SUC of choice is SUC2 from *Arabidopsis Thaliana* which have been previously cloned. We were able to express SUC2 in auto induction medium, lysed the cells, isolated the membrane fraction and solubilized with 1% DDM. The solubilized protein was purified by size exclusion chromatography and successfully crystallized. Hopes for the future, after crystallization is to determine the structure by using X-ray crystallography to get the three-dimensional structure of the macromolecule.

I. Introduction

Sucrose plays a critical role for transport in all species of plants. It is the transport of photo assimilated carbon and it acts as an aid for plants that cannot perform photosynthesis, by providing carbon skeletons and energy for the plant's organs. Sucrose has recently been discovered to travel from the sites of synthesis to the sites of utilization or storage in sink organs. Sucrose transporters play a fundamental role for the plant, as they regulate sucrose distribution in the plant, intracellularly and at the whole plant level. The expression of sucrose transporters are closely monitored at every level; transcriptional, post-transcriptional and post-translational. In addition to the sucrose molecule functioning as a signal, light quality and phytohormones also play essential regulatory roles.

Membrane proteins are fundamental in order to facilitate the transport of sucrose within plants. Sucrose is transported from the source leaves to provide stable growth and carbon storage of

heterotrophic sink organs. In heterotrophic tissues such as roots, developing leaves, and seeds, sucrose is the main photosynthetic product that is transported by the phloem. The major facilitator superfamily, MFS, contain plant sucrose transporters and are vaguely related to the hexose transporters in bacteria, fungi, plants and animals. The plasma membrane of companion cells expresses SUT, or Sucrose Transporters. SUT sieve elements within the phloem and catalyzes the H⁺-coupled uptake of sucrose. AtSUC2, along with eight other SUT homologs are encoded by the genome, *Arabidopsis*. AtSUC2 is expressed within the companion cells of source leaves; it functions as the main phloem-loading transporter; and, as evidenced by the severe phenotype of insertion mutants, it is crucial for the transport of sucrose.

Arabidopsis sucrose transporter, AtSUC2, is highly expressed in leaves. A plasma-membrane sucrose-H⁺ symporter is encoded by the SUC2 gene. By the usage of a translational fusion of the SUC2 promoter to the N-terminus of β -glucuronidase (GUS) and the GUS histochemical assay, the SUC2 promoter DNA sequence transformed. This signified that it had a high specificity to the phloem of all green tissues of *Arabidopsis*.

The purpose of this experiment is to identify the location of SUC2 within the cell. Once SUC2 has been located, purification (Coli and Studier) and identification techniques are used to crystallize the protein. Then, an x-ray will form a three-dimensional structure of the protein. Due to genetic modification, the possibilities become infinite which assist in the creation of biofuel.

To begin crystallization using a protein crystallographic project, a protein of choice must be concentrated and purified. The purified protein must be in a homogenous form and have a low polydispersity state (Smith). The solubility of the protein depends on many factors, temperature, the pH of the buffer, the type of salt present in the buffer and other co-factors. The type of crystallization method used to bring the solution into supersaturation is dependent upon the protein ("Introduction to Protein Crystallization: Basics Ideas"). It is typically done by decreasing the solubility of the protein, gradually. The most common way to reduce protein solubility by crystallization is by adding a precipitant, such as polyethylene glycol and ammonium sulfate, which will bind to the water molecules. Vapor diffusion causes the precipitant concentration to increase and the amount of solvent available for the protein is decreased, resulting in protein precipitation and crystals, under correct conditions.

Vapor diffusion is the idea of movement from a mixture containing a sample and reagent when placed in vapor equilibration with a liquid reservoir of the reagent, forms a drop. This drop will contain a lower reagent concentration than the reservoir. Ultimately, the water vapor in the drop will leave and end up in the reservoir, achieving equilibrium. As this happens, the sample will increase in relative supersaturation. This means that both, the sample and reagent have increased in concentrations as the water

is leaving the drop for the reservoir. Equilibration is then reached when the reagent concentration in the drop is approximately the same as that in the reservoir. This method of vapor diffusion can be completed in two formats: a hanging-drop or a sitting-drop (which was our choice for this experiment). After crystal formation, have been identified, the crystal is extracted from the sample. The sample undergoes what X-ray crystallography, which is a technique used to help determine the molecular and atomic structure with a beam of incident x-rays. This method is effective because the beam is diffracted in many different directions, and, the measurements of beam intensity and angles allows for a three-dimensional picture of atom positions to be created, along with their bonds and other information (Chayen and Saridakis). This information are then matched with a protein structure database of similar proteins and with a use of computer software's like MODELLER or Phyre, a homologous model is formed. Homology modeling is the idea of constructing a target protein, based on using the three-dimensional structure, a similar or related homologous protein and its amino acid sequences to generate a digital image of the protein (Vyas et al.).

II. Materials/Method

Glycerol stock of *Arabidopsis thaliana* SUC1 was provided to start the initial mini culture to identify whether cells will grow or now. MDAG media is the primary used for the experiment, but through previous attempt, LB media is also tested to see how well the cells would grow (All mini culture steps were same as MDAG). 5 ml MDAG solution were added into a tube, followed by 5 μ L of Kanamycin which was prepared fresh. A scratch sample of the glycerol stock of SUC1, was inoculated into the tube. The tube was place in a rotational incubator set for 200 rpm at 37°C overnight. Large scale ZYM -5052 culture media was prepared at 500 ml in 2800 ml flask. After overnight incubation at tubes were removed from the incubator, all showing signs of cell growth with a cloudy liquid. Glycerol stock of each tubes were made and stored in -80°C. 2 ml of Kanamycin was added to the ZYM- 5052 media, followed by 1 ml of mini culture stock from MDAG tube. The large flask were placed incubator for 4 hour at 200 rpm and 37°C. After 4 hours the incubator was changed to 18°C for 45 hours.

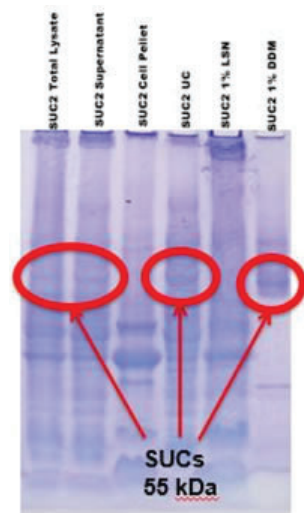


Figure 1. SDS-PAGE gel after Cell Lysis, showing band for protein (SUC) solubilized by DDM

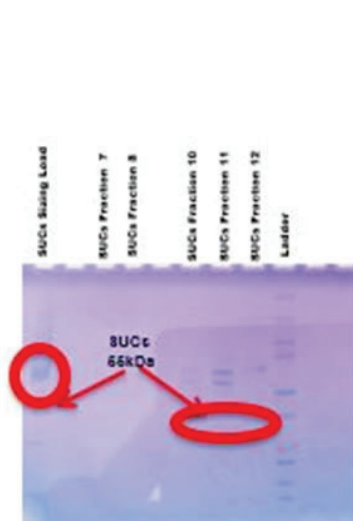


Figure 2. SDS-PAGE gel Size Exclusion Chromatogram

After 45 hours, the cell cultures were harvested in large centrifuge bottle. The bottle is centrifuged for 20 minutes at rpm. The supernatant is removed and the cells were stored in 4°C.

Lysis buffer with Bug Buster stock was made to lyse the cell. 50 ml of lysis buffer were added to the pellet. With the use of a sterile glass stir rod, the cell pellet was stirred up ready to be homogenized. A homogenizer was used to really break of the cell and get rid of any clumps. A base buffer solution was prepared, label Buffer A. The homogenized slurry was then taken to a microfluidizer and passed through 4 times to really lysis the cells and separate all the components. 20 μ L of the collected sample was transferred into a 1.5 ml microcentrifuge tube for SDS Page gel. The slurry mix was then transferred into three centrifuge tubes and was centrifuged at 14,000 rpm for 30 minutes below 10°C. 20 μ L of supernatant sample was collected for gel. The supernatant were then transferred into two ultracentrifuge tubes, then spun for 1.5 hours at 36,000 rpm at 4°C. In a 1.5 ml microcentrifuge tube, 20 μ L of Buffer A was added, along with a scratch of the cell pellet left after supernatant was transferred. After ultracentrifuge, the supernatant was collected and stored in fridge. The remaining cell pellet was resuspended with, 5 ml each, of a prepared mixture of Buffer A and 1% Sodium N-Lauroylsarcosinate (LSN). Then all collections were transferred into in 15 ml tube and left overnight in rotation to bring out inner membrane fraction. The dissolved solubilized materials were transferred into a centrifuge tube and spun at 11,000 rpm for 15 minutes. 20 μ L supernatant was collected for gel, and the remaining was collected into a flask and stored, leaving a insoluble pellet. 1% DDM was dissolved in 30 ml Buffer A. That mixture was then transferred to tube to resuspend the cell pellet and dissolving it. Contents were transferred into a cleaner tuber and set to rotate for 45 minutes in 4°C. After rotation the solubilized pellets were transferred into a centrifuge tube and spun at high speed of 12,000 rpm for 10 minutes. 20 μ L of sample was collected and supernatant was transferred into 30 kD column tube to increase concentration. All 20 μ L samples collected, received 10 μ L of Laemmli 2x loading buffer. A SDS Page Gel electrophoresis was done with for all sample collected.

The 30 kD column tubes were spun a few times at 5000 rpm to give, so 1 ml of sample remained to be used in a chromatogram. The fractions which correlated the appropriate peaks on the chromatogram were collected. A SDS page gel was done again to

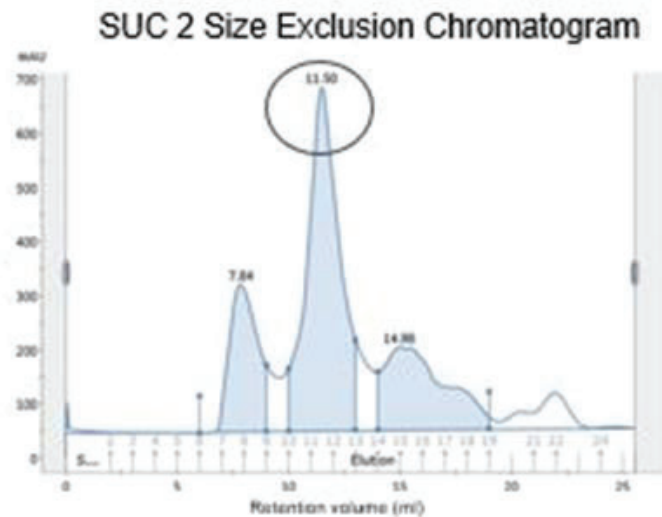


Figure 3. Size Exclusion Chromatogram purified SUC2

test the samples from the chromatogram. Once the protein have been identified, the total amount of protein in the samples were calculated in milligrams and concentrated to 1 ml. That sample was then used to set crystallization. Using “the robot” which was thoroughly cleaned with deionized water, two screening kits were used, Index Ht and MembFac Ht, to setup two 96 well sitting vapor diffusion plate. 8.2 μ L of sample and reagent was used to create a droplet in the well, which was seal air tight with a clear film and store in a cold room. The plates were examined daily the first week for precipitation and crystal growths, then every three days onwards.

III. Results/ Discussion

The target membrane protein SUC2 have been identified on many different trials at the expected molecular mass of 55 kDa. The protein was identified in the outer membrane fraction which is solubilized with 1% n-dodecyl- β -D-maltoside (DDM) as seen by the band on the SDS Page Gel (Figure 1). The solubilized membrane fraction of SUC2 have been purified with Size Exclusion Chromatogram and that was verified by SDS Page gel for the fractions that are represented by the peak, fraction 11 and 12 (Figure 2). Based on the retention volume (11.5ml) of the sizing chromatogram we predicted the oligomeric state of the SUC2 is dimer (Figure 3). The protein was concentrated, and crystallization trials were set up using commercial and our own screen. One commercial screen (Hampton Research) solution (0.1M sodium malonate, 30% PEG 1000 and 0.1M Tris pH 8.0), gave tiny crystals after a few days (Figure 4). Based on that, in-house screens were made using the same ingredients with different pH and PEG percentage settings. This screen gave some formation of tiny crystals and clusters of crystals.

The gene product of Arabidopsis sucrose transporter 2 (SUC2) is expressed in the E. Coli at 20°C. SUC2 localized at the outer membrane was solubilized after cell lysis with different detergents. The inner membrane fraction is removed by adding 1% n-lauryl sarcosine. Through screening method 1% DDM detergent, was effective in solubilizing the SUC2 outer membrane fraction as seen on the SDS Page Gel. At this point the protein is about 80% pure. Even though the SUC2 has histidine tag at the C-terminal end of the protein, it failed to bind to the Ni-NTA resin that might be due to the non-availability of the His-tag to the resin. The size exclusion chromatography gave a predominant peak at the retention volume of 11.5 ml on the Superdex 200 increase 10/300 GL column. The commercially available (Hampton Research solutions) high-throughput screen solutions gave micro crystals that are protein. Further optimization of crystallization

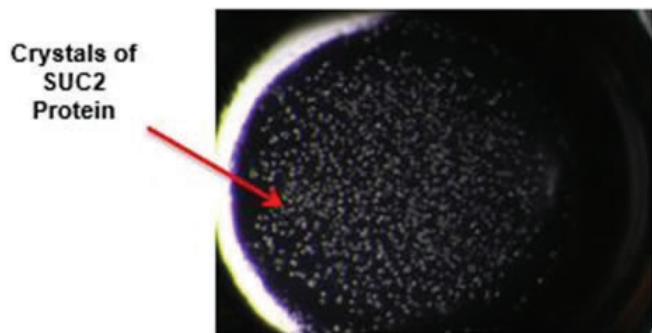


Figure 4. Micro crystal formation for SUC2 protein

condition is in progress. Due to timing, X-ray crystallography of the protein was not done but with the use of homology modelling and similar protein information, SUC2 monomeric and dimeric structure were modelled (Figure 5).

IV. Conclusion

In the present study, it can be concluded that the purification techniques and crystallization screening trials were successful, because all objectives were met throughout the process. SUC2, sucrose transporter protein was found in the outer membrane of the cell which was confirmed by the western-blot (data not shown) and SDS Page Gel. For the first time, SUC2 is purified to homogeneity and crystallized. The constructed homology model, gives a look into the how the protein is folded, oligomeric state and how it can be orientated within the membrane of the cell. But the template structure used to model SUC2, Xylose transporter, belongs to MFS superfamily with very low sequence identity (only 15%). Therefore, the real crystal structure might be different from the model and so it is necessary to determine the structure. Since we already got crystallization condition, it may not be very difficult to optimize the condition further to produce diffraction quality crystals. Certainly, this study is a great start in the process of deriving the molecular mechanism of this transporter and for genetic manipulation to enhance the biomass production in plants.

V. Appendix

- MDAG media (100ml)
 - 93.70 ml H₂O, 200 μ l .1M MgSO₄, 20 μ l 1000x Metal Mix, 875 μ l 40% Glucose, 800 μ l 25 % aspartate, 2 ml 50 x M, 2.8 ml Amino Acid
- ZY Media (1 Liter)
 - 1 L H₂O, 10 g Tryptone, 5 g yeast
- ZY-M 5052 (500 ml)
 - 460 ml ZY Mix, 1 ml MgSO₄, 100 μ l 1000x Metal Mix, 10 ml 50 x 5052, 10 ml 50 x M, 500 μ l Kanamycin, 500 μ l Culture
- Lysis Buffer (120 ml)
 - 6 ml 10x Bug Buster Stock, 12 ml NaCl, 4.8 ml Tris pH 8.0, 60 mg Lysozyme, .6 ml PMSF, 1 Protease Inhibitor Tablet, 7.5 ml 5% Glycerol, 5 μ l DNase, H₂O remainder
- Buffer A (500ml)
 - 20 ml 40 mM Tris pH 8.0, 40 ml 400 mM NaCl, 31.25 5% Glycerol, 2.5 ml 10 mM Imidazole, 500 μ l DTT, Remainder H₂O
- 1% DDM/Buffer A (30 ml)
 - 300 mg DDM, 30 ml Buffer A

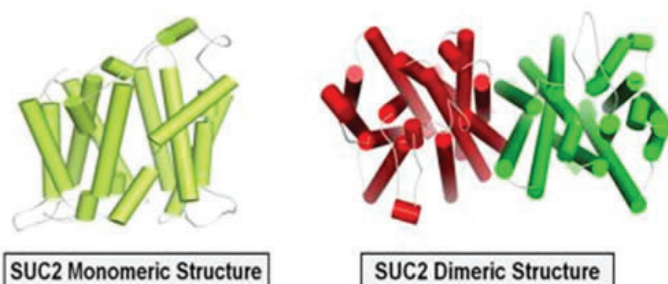


Figure 5. Homology of SUC2 protein in monomeric and dimeric form.

7. 1% LSN/Buffer A (30 ml)
 - 300 mg Sodium N-Lauroylsarcosinate, 30 ml Buffer A
8. .01% DDM/Buffer A (250 ml)
 - 25mg of DDM, 250 ml Buffer A

VI. References

Chayen, Naomi E, and Emmanuel Saridakis. "Protein Crystallization: From Purified Protein to Diffraction-Quality Crystal." *Nature Methods* 5.2 (2008): 147–153. Web. 27 July 2018.

- Coli, E, and F William Studier. T7 Expression Systems for Inducible Production of Proteins from Cloned Genes In. N.p. Web. 31 July 2018.
- "Introduction to Protein Crystallization: Basics Ideas." N.p., n.d. Web. 27 July 2018.
- Smith, Sinead Marian. "Strategies for the Purification of Membrane Proteins." Humana Press, 2011. 485–496. Web. 27 July 2018.
- Vyas, V K et al. "Homology Modeling a Fast Tool for Drug Discovery: Current Perspectives." *Indian journal of pharmaceutical sciences* 74.1 (2012): 1–17. Web. 27 July 2018.

Process controls using LabVIEW software

Maxwell Santiago

Suffolk Community College, Selden, 11784

Piyush Joshi

Brookhaven National Laboratory, Upton, NY 11973

ABSTRACT

When we receive a testing magnet we must attach the top hat in order to suspend it into a cryostat. The top hat contains two high power vapor cooled leads that make the electrical connection with the magnet within the Dewar. The flow of the helium vapor needs to be properly maintained so pressure doesn't exceed a certain limit and so liquid helium can be used more efficiently. This was accomplished by creating a LabVIEW PID (proportional, integral, derivative) program that opens a valve to a certain position as a result of increasing or decreasing pressure. Each lead is fitted with a flow controller and a bypass valve which is there for insurance if the program malfunctioned. Since the leads are cooled by boiled off liquid helium they can form ice around them causing some electrical issues. We can prevent the formation of ice by supplying warm nitrogen to the leads by using a device I created called FLO (frosted, leads, operation). This device is completely mechanical and has no connection with any computer software.

I. Introduction

A. Procedure

Here at the superconducting magnet division or SMD we do research and development of superconducting magnets for labs across the globe as well as for our own use at the realistic heavy ion collider or RHIC. To test a magnet we need to mechanically connect it to the top hat and lower the magnet and the attached top hat into a Dewar. The top hat is how power is transferred to the magnet as well as what actually suspends the magnet in the Dewar. The top hat contains two copper leads that have holes through them so it can vent boiled off liquid helium which is used to cool down the leads as well as maintaining internal pressure. Once in the Dewar, the magnet can be put under vacuum and brought down to 1.9 kelvin using liquid helium to be prepared for testing. 1.9k liquid helium sits on the upper part of the top hat while 4k liquid helium stays below the lambda plate and fills up the Dewar. Once the magnet and top hat get around 1.5k and around 24Ka is sent through the top hat the electromagnetic coils start to become superconducting. Once superconducting, the coil losses all electrical resistance meaning any amount of power can flow through the coil freely without addition of heat or power loss. When a coil is in a superconducting state it becomes extremely sensitive and if the coil is moved or if there quick temperature change it can cause a quench. A quench is when a superconducting magnet loses its superconductivity and suddenly gains electrical resistance making the coil gain heat energy. The coil sits in a liquid helium bath and when heat is added to the coil, the supercool liquid helium boils off of the now warm magnet. When liquid helium evaporates it can expand up to approximately 760 times its original size causing pressurized vapor to violently exit out of relief valves making a very loud noise and creating a colossal sized cloud of helium vapor which can be dangerous.

II. Project

A. Problem

The top hats leads have holes at the bottom which allow for helium vapor to vent through the bottom and get exhausted at the top. The vapor is exceptionally cold and can condense the air around the leads creating ice which can cause electrical issues and also pressure issues. The ice can act as a chemical conductor at very high amps and causes the magnet to short when power is added making it difficult to experiment. The other issue is that ice can sometimes block relief valves and the venting holes for the helium vapor which can cause a buildup of pressure in the Dewar which can damage the equipment.

B. Solution

To prevent ice formation, heated nitrogen gas is sent to the surface of the leads through a plastic enclosure using a flow controller that has been given the name FLO or the frosted leads operation. FLO is designed to regulate the flow of ambient temperature nitrogen using three Dwyer flow meters, two at 200square cubic feet per hour and one at 400SCFH. Nitrogen will then pass through one of three inline heaters, each controlled by its very own variable voltage transformer or variac. After heating the gas, three silicon tubes will then travel out of the device, two going to the top hats leads while the other will go to a mole transporter. We use nitrogen gas to accomplish this because nitrogen is very good at displacing moisture; that's why it is used for pumping and purging. The flow of the helium vapor is also an important aspect to operations and needs to be controlled to maintain proper use of liquid helium. Helium is not cheap and costs roughly 30 cents per cubic foot and its takes a great deal of effort to liquefy so usage of liquid helium needs to be appropriate. Controlling the flow of the exhaust vapor is done by using two alicat flow controllers (one for each lead) and a LabVIEW PID program. A PID or proportional, integral, derivative is type of feedback loop controller and works by the user setting a setpoint and the computer program tries to match the setpoint as fast and as precise as it can. The vapor cooled leads PID works by pressure transducers sending the live feed pressure to the computer which becomes the setpoint. The computer then sends out a 4-20 mA signal that tells the flow controller to open to a certain position which respect to the pressure in the leads.

III. Materials

Materials and funds are very important when it comes to design and fabrication but the materials used can also play major roles in how a device works. With any device a frame needs to be constructed to house all of the components that will actually do the process. For the nitrogen warming device, FLO, we used aluminum uni-strut, which was found in the basement, to build a 4x1 foot frame. From there we began assembly of the device using inline heaters and variacs or variable voltage transformers which

were actually used in the Isabel experiment many years ago. The last components used were three Dwyer flowmeter so pressure and flow rate (SCFH) could be read easily to anyone. The only part that was actually purchased were stainless steel pipe fittings, everything else was salvaged from older, out of commission experiments.

The vapor cooled leads PID program was never implicated due to lack of resources and time. The original design called for two Alicat flow controllers, two bypass valves, one data acquisition device (DAQ) and the PID program. The only thing that would need to be purchased is the Alicat flow controllers and the DAQ, but these three items would have costed roughly over a three thousand dollars. Funds are extremely important because unfortunately if there is no money there is no equipment meaning there is no research. The PID program was designed as a simulation program which means it shows how the program would have acted in a real live situation but without buying any expensive hardware.

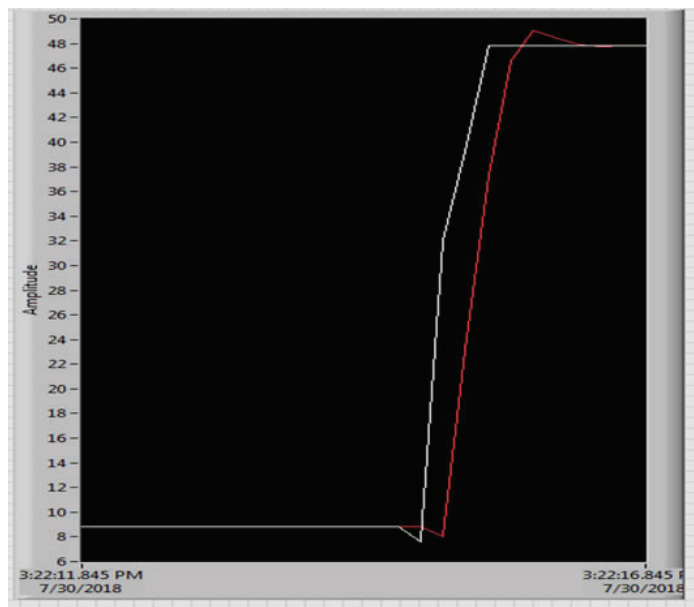
IV. Results

A. Simulation

The LabVIEW PID program did exactly what it was supposed to do and dynamically moved valve position due to pressure increase/decrease. Whenever the setpoint, pressure, would rise the computer simulation would tell the flow controller valve to open more to allow for more flow of helium vapor. With correct steady state error the program had minimal overshoot and a fast reaction time to the increasing pressure as seen below.

B. Hardware

The flow controlling device is 100% mechanical and fully operation with successful tests. The device, FLO, did a very good job at removing moisture from the leads surfaces and keeps them nice and warm during the high pot testing. Large amounts of ice would form above the enclosure and a lot of condensation would form below it meaning that the area that was treated by the warm gas stayed comfortably warm and dry to the touch. While two tubes go directly to the top hats leads one tube would go to the coil of a mole transporter to keep it as dry as possible because the coil is very fragile.



V. Acknowledgments

I would like to acknowledge and give thanks to everyone who has helped me learn and develop along the span of these ten weeks. I would like to thank my mentors Piyush Joshi and William McKeon for everything they have done to help me learn as much as I can as well as becoming my friends in the process. I would also like to thank everyone in the superconducting magnet division for not only making my time here educational but for making it fun. Lastly I would like to acknowledge the office of education OEP staff for all the work they do trying to make every intern as successful and professional as they can.

This project was supported in part by the Brookhaven National Laboratory (BNL), Superconducting Magnet Division under the BNL Supplemental Undergraduate Research Program (SURP).

Figure 1.
White line represents pressure (setpoint)
Red line is flow controller position (program)

Investigating the effects of drought on crop species using biochemical analysis

Kelly Scanlon

Biology Department, Sacred Heart University, Fairfield, CT 06825

Angela Burnett

Environmental and Climate Sciences Department, Brookhaven National Laboratory, Upton, NY, 11973

Abstract

As the world's population increases and the effects of climate change alter our agricultural system, it will become necessary to change the way we currently grow crops in order to meet a rising demand for food. To achieve this change we must look at the limiting factors of growth in plants and how plants will respond to differing environmental conditions, such as drought. Using biochemical assays I looked at the impact of drought on plants at the chemical level. Samples for assays were harvested from either drought or watered plants, and using extraction protocols, I was able to separate ethanol-soluble metabolites (glucose, sucrose, fructose, and low degree polymerization (LDP) fructan) from ethanol-insoluble metabolites (starch, high degree polymerization (HDP) fructan) for each sample. Using a pipetting robot and a plate reader, the levels of each metabolite in the extracted samples could be determined. The increased levels of average nitrate and protein and decreased level of starch found in the drought samples shows a significant relationship between drought and metabolite levels. This gives insight into which biochemical characteristics are more greatly affected by drought stress and can allow signs of drought stress in plants to be more easily detected, which can then help us to develop a method for increasing future crop yields. As a result of this summer, I have added biochemical analysis to my repertoire of laboratory techniques. Additionally, I am now familiar with the basics of both a plate reader and a robotic liquid handling system.

I. Introduction

To meet a rising demand for food that is being hindered by the effects of climate change, we must look at the how crops will respond to differing environmental conditions, such as drought. Drought conditions are becoming more prevalent and it will become necessary to recognize what is happening at a chemical level in plants in order to determine how we might be able to save crops suffering from drought stress in the future¹. Due to their sessile nature, plants are perceived as helpless when it comes to changing their ambient environments, but in reality, plants possess various internal processes that allow them to react beneficially in stressful situations². These mechanisms have evolved in plants of all different species and vary depending on the environment specific species are found in. For example, some plants will react to drought stress by increasing their protein production. This happens because drought acts as a threat and some plants will respond to such a threat by maximizing structural protection in the hopes that the threat will not be able to damage it³. Many of these processes have to do with internal mechanisms involving metabolite regulation and production, which vary depending on the species of crop.

Molecular control mechanisms for stress tolerance are based specific genes whose job is to respond to stress through signaling, transcriptional control, and protection of membranes and protein. This shows possibilities that can apply gene control to agriculturally and ecologically important plants that are in danger of being lost to drought in the future⁴. Biochemical analysis can be performed to see how metabolite levels differ among different species and to get a better understanding of what kind of effects drought can have on crops. It is predicted that different crop species will react differently to drought stress and that drought stress will have a significant effect on metabolite levels within each crop species.

II. Methods

A. Plant samples

Ground tissue samples of *Sorghum bicolor* (Sorghum), *Raphanus sativus* (Radish), and *Helianthus annuus* (Sunflower) which were taken from the Brookhaven National Laboratory Greenhouse were from crops that received either drought or watered treatment. Samples collected were freeze-dried in liquid nitrogen and were stored in a -75 freezer until they were grinded. Grinded samples were then cryo-weighed to approximately 26 mg each.

B. Metabolites

Metabolite analysis was carried out at Brookhaven National Laboratory starting with ethanol extractions of the freeze-dried ground tissue samples. Ethanol-soluble carbohydrates (glucose, fructose, sucrose and low degree of polymerization (LDP) fructan) were separated from ethanol-insoluble metabolites (starch, high degree polymerization (HDP) fructan) which created a supernatant containing the former and a pellet containing the latter.

Ethanol-soluble carbohydrates were measured following protocol by Harrison, Pollock and Gallagher (1997), which calls for using a continuous enzymatic substrate assays where the amount of hexose is proportional to the production of NADPH (measured at A_{340}). Glucose was determined first by calculating the difference between the absorbance associated with right before and after Hexokinase is added. Fructose was measured by the difference between Hexokinase and PGI. Sucrose was measured by the difference between PGI and Sucrose phosphorylase. Fructan with low degree of polymerization was then determined by calculating the difference between Sucrose phosphorylase and Exo-inulinase/Endo-inulinase cocktail.

Starch is solubilized by heating and then digested to glucose with amyloglucosidase and α -amylase. Fructan with high degree of polymerization is solubilized by heating and then digested to glucose and fructose with exo-inulinase and endo-inulinase. Exo-inulinase and endo-inulinase have also been found to degrade starch at a low rate therefore fructan is determined by subtracting

the hexose content resulting from the starch degradation from the hexose content from simultaneous fructan and starch digestion. Glucose released from starch degradation and glucose and fructose released from then starch plus fructan degradation are determined using a continuous enzymatic substrate assay where the amount of hexose is proportional to the amount of NADPH produced (measured at A340). A standard curve is used to calculate the amount of starch or fructan in glucose equivalents⁵.

C. Protein Assay

The bicinchoninic acid (BCA) assay is a one-step version of the Lowry assay. Under alkali conditions divalent copper ions form a complex with peptide bonds in which Cu^{2+} is reduced to the monovalent ion. The production of Cu^+ is a function of protein concentration and incubation time. The Cu^+ is detected by reaction with BCA that results in the development of an intense purple color (measured at A_{562}). The protein content of unknown samples is determined spectrophotometrically by comparison with known protein standards.

D. Nitrate assay

Nitrate is converted to nitrite by nitrate reductase in the presence of NADPH. PMS is added to convert NADP^+ back to NADPH because NADP^+ interferes with the subsequent Griess reaction. Sulfanilamide and NNEDA react with nitrite in the Griess reaction to produce a diazo product detectable at 540nm.

III. Results

Levels of starch, nitrate, and protein were compared for all three crop species by plotting the measurements of watered plants verse drought plants over time. Higher levels of starch measured in all 3 crop species shows a significance of species and treatment type and shows significant variations of starch composition between the three species. Measurements showed that Radish contained the least amount of starch overall compared to Sunflower and Sorghum (Figure 1).

Protein levels fluctuated for all three species and remained somewhat constant throughout the duration of the experiment for both watered and drought plants, yet overall showed higher levels in drought compared to the watered. Once again Radish contained the least amount of this metabolite overall while Sorghum showed the highest levels of protein (Figure 2). In terms of nitrate levels, Radish showed much larger measurements compared to the other two species while Sorghum results were the lowest. Overall, ni-

trate levels were higher in all three species for drought treatment throughout the entirety of the experiment (Figure 3).

IV. Discussion

Protein levels were found to be higher in droughted plants for the three crop species. A possible explanation for this is that plants act in defense during times of drought stress. Previous studies have shown that proteins related to defense, stress, transcription and translation play an important role in drought response and that there is a correlation between protein and transcript levels. Research has said shown that in order to deal with water-deficit stress, plants have developed mechanisms to regulate their cells and optimize their physiology and metabolism to survive drought stress at both the cellular and organ level⁶. It could have been expected that drought plants would have lower levels of protein due to the assumption that a plant loses its structure when it is deprived of water. A possible explanation for the higher levels of protein and nitrate found in the drought plants could be that they were putting all of their efforts into the lasting leaves that were being collected, causing results to show higher levels in remaining leaves than if it were compared to the content of the entire plant. Higher levels of nitrate in drought samples can also be explained by higher levels of waste in drought plant. There is also the concept that nitrate is taken up through the roots and, under normal circumstances, is supposed to be converted into amino acids, but due to the stress the plant is under is no longer performing regular photosynthetic activities so the nitrate pools inside in leaves.

The lower levels of starch found among drought samples for all three crop species can be explained by the idea that during drought stress, a plant will close its stomata in order to reduce water loss through transpiration. If stomata are closed, photosynthesis can no longer take place, and therefore carbohydrate production is limited, resulting in lower levels of starch and sugars⁷.

V. Conclusion

The increased levels of average nitrate and protein and decreased level of starch found in the drought samples shows a significant relationship between drought and metabolite levels. This gives insight into which biochemical characteristics are more greatly affected by drought stress and can allow signs of drought stress in plants to be more easily detected, which can then help us to develop a method for increasing future crop yields. In the future, more crop species should be tested for a wider range of metabolites, over a longer period of time in order to increase

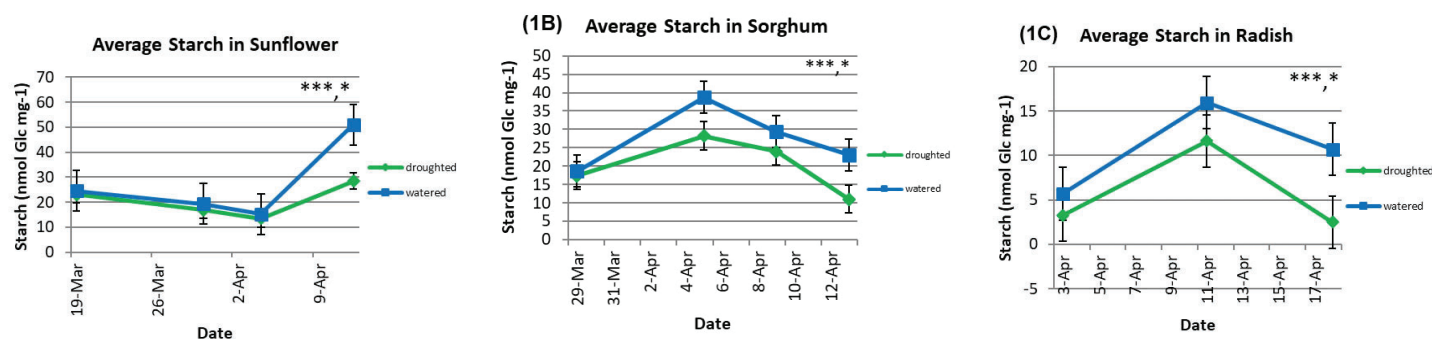


Figure 1. Average levels of Starch (nmol Glc mg-1) in Sunflower (A), Sorghum (B), and Radish (C).

*** denotes a significant effect of species ($p < 0.001$) and * denotes significant effect of treatment ($p < 0.05$). Error bars represent standard error.

resulting data that can be compiled into larger scaled results. I also think further research into the specific proteins used during defense in plants should be considered, rather than only overall protein levels in general.

VI. References

¹McDowell N, Pockman WT, Allen CD, Breshears DD, Cobb N, Kolb T, Plaut J, Sperry J, West A, Williams DG, Yepez EA. 2008. Mechanisms of plant survival and mortality during drought: why do some plants survive while others succumb to drought?. *New phytologist*.178(4):719-39.

²Angela C. White, Alistair Rogers, Mark Rees, Colin P. Osborne. 2015. How can we make plants grow faster? A source–sink perspective on growth rate. *Journal of Experimental Botany*.67(1):31–45.

³Burnett AC, Rogers A, Rees M, Osborne CP. 2016. Carbon source–sink limitations differ between two species with contrasting growth strategies. *Plant, cell & environment*. 39(11):2460-72.

⁴Wang W, Vinocur B, Altman A. 2003. Plant responses to drought, salinity and extreme temperatures: towards genetic engineering for stress tolerance. *Planta*. 218(1):1-4.

⁵Harrison J, Gallagher JA, Pollock CJ. 1997. A simple and rapid method for the analysis of water-soluble carbohydrates from small segments of cereal leaf tissue. *Journal of Plant Physiology*.151(6):654-9.

⁶Cao Y, Luo Q, Tian Y, Meng F. 2017. Physiological and proteomic analyses of the drought stress response in *Amygdalus Mira* (Koehne) Yü et Lu roots. *BMC plant biology*.17(1):53.

⁷Cornic G. 2000. Drought stress inhibits photosynthesis by decreasing stomatal aperture—not by affecting ATP synthesis. *Trends in plant science*. 5(5):187-8.

VII. Acknowledgements

This project was supported in part by the U.S. Department of Energy, Office of Science, Office of Workforce Development for Teachers and Scientists (WDTS) under the Science Undergraduate Laboratory Internships Program (SULI) and thank you to my mentor Angela Burnett for her support and wisdom.

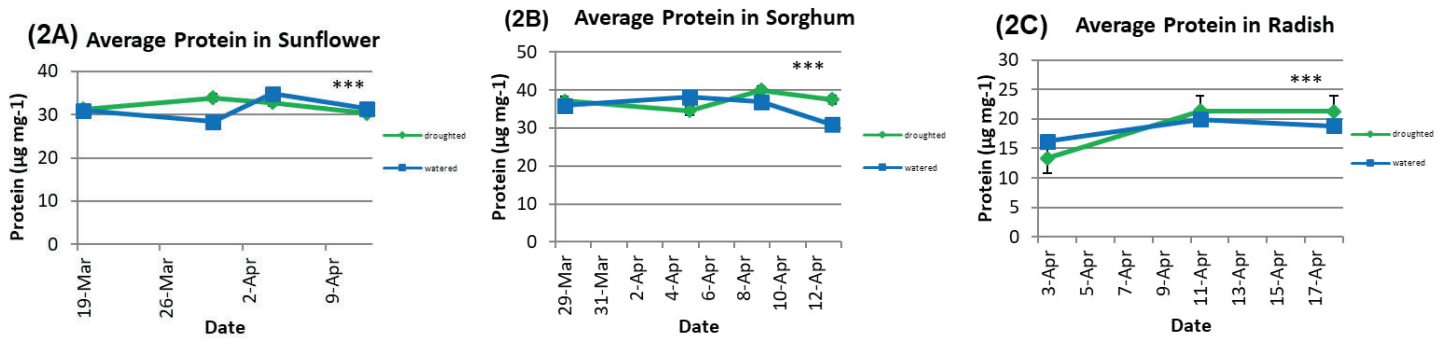


Figure 2. Average levels of Protein (µg mg⁻¹) in Sunflower (A), Sorghum (B), and Radish (C). *** denotes a significant interaction between species and time (p<0.001). Error bars represent standard error.

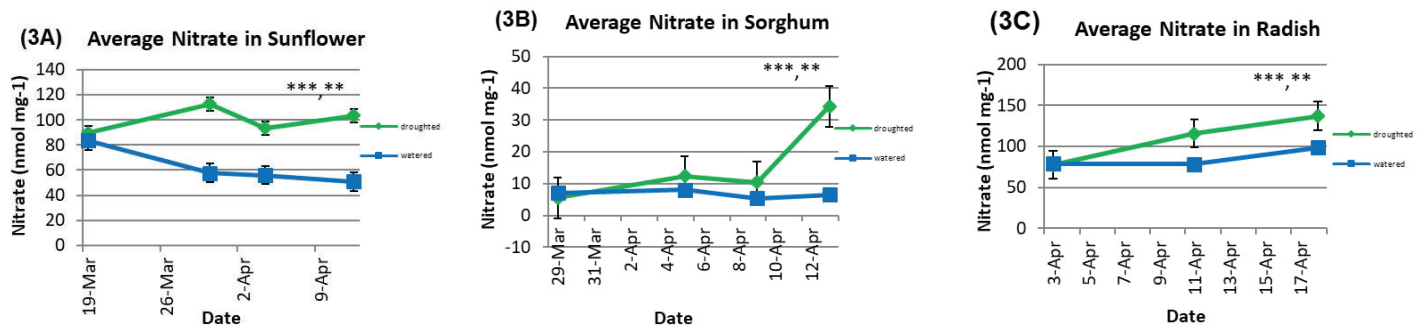


Figure 3 Average levels of Nitrate (nmol mg⁻¹) in Sunflower (A), Sorghum (B), and Radish (C). *** denotes a significant interaction between species and time (p<0.001) and ** denotes a significant interaction between treatment and time (p<0.01). Error bars represent standard error.

CCD sensor calibration using ^{55}Fe spectra

Jackson Schall

Department of Natural Science and Mathematics, University of Toledo, Toledo, OH 43606

Ivan Kotov

Brookhaven National Laboratory, Upton, NY 11973, USA

Abstract

In our applications a charge-coupled device (CCD) is used to register photons. The CCD in this experiment has 16 channels, each with independent amplifiers resulting in a distinct gain in each channel. Calibrating the channels becomes essential to ensure a uniform signal output. The goal of this experiment is to employ a spectroscopic calibration approach using the $\text{Mn } K_{\alpha}$ line. The robustness of this method is tested using well-known line energies in ^{55}Mn X-ray spectrum. The study is performed over the sensor temperature range. Measurements were taken using X-rays from an Iron-55, ^{55}Fe , source and a silicon E2V-CCD250 sensor. ^{55}Fe is an unstable isotope which has two well-known emission peaks. These spectral lines, $\text{Mn } K_{\alpha}$ and K_{β} , have energies 5.89 keV and 6.49 keV respectively. The sensor calibration procedure uses K_{α} X-rays to determine a conversion factor for sensor output from analog-to-digital (ADU) units to electron volts (eV). The sensor is exposed to the radioactive source for 4s. Data sets were obtained in the temperature range of 158 - 242 K. This calibration method is accurate within $\sim 0.6\%$ of documented line energies.

I. Introduction

A. X-rays

Iron-55 ($^{55}_{26}\text{Fe}$) is an unstable isotope of Iron, containing 26 protons and 29 neutrons. This isotope decays via electron capture to Manganese-55 ($^{55}_{25}\text{Mn}$), see fig. 1. This creates a vacancy in the "K" shell of the ($^{55}_{25}\text{Mn}$) atom [1].

The atom readjusts quickly, a higher energy electron transitions to the hole creating either an Auger electron with an energy of 5.19 keV 60% of the time [3], or an X-ray of varying energies, represented by Siegbahn notation. K_{α} X-rays denote the transition of an electron from the 2p orbital to the 1s orbital, there are two energies created by spin orbit interactions with the nucleus, $K_{\alpha 1}$ and $K_{\alpha 2}$; with energies 5.8987 and 5.8876 keV and probabilities of 16.2% and 8.2% respectively [4, 5]. The difference in energy is small enough that we cannot resolve the separation using this sensor. The weighted average of $K_{\alpha 1,2}$ is 5.8950 keV which we use to calibrate the sensor. K_{β} X-rays represent electron transitions from the 3p shell to the 1s shell; with an energy of 6.4904 keV and probability of 2.85% [4, 5]. Errors in the measurement arise from uncertainties in the input energy, as well as possible energy loss in inactive sensor material. The X-rays created from the K_{α} emission mode in Manganese are known to high precision, $\pm 0.01 \text{ eV}$. An ^{55}Fe source provides high X-ray statistics. Statistical uncertainties of $\sim 0.01\%$ [6] can be achieved. The K_{α} peak can be modeled using Gaussian distribution.

B. Data

Data were collected using CCD250-152 at the following temperatures; 158 K, 176 K, 195 K, 214 K, 223 K, and 242 K. Sets of X-ray exposures, bias exposures, and flat field images were collected for each temperature. The image files were organized in the directory tree with temperature folder being the root of each branch. The X-ray data set contains 200 ^{55}Fe 4s exposures. These six sets are analyzed and this enables us to look at individual segments of the sensor.

The number of detected X-ray clusters for the K_{α} line varies from $\sim 70,000$ - 1,000,000 events per segment as can be seen in fig 2. This can be explained by the experimental setup geometry. The sensor segment layout is depicted in fig 3. The ^{55}Fe is a point source and the radiation over the sensor is not uniform. The correlation between events and distance to the radiation source can be clearly explained. In fig. 2 we can see the detected X-rays can be seen to fall off as the distance to the source increase.

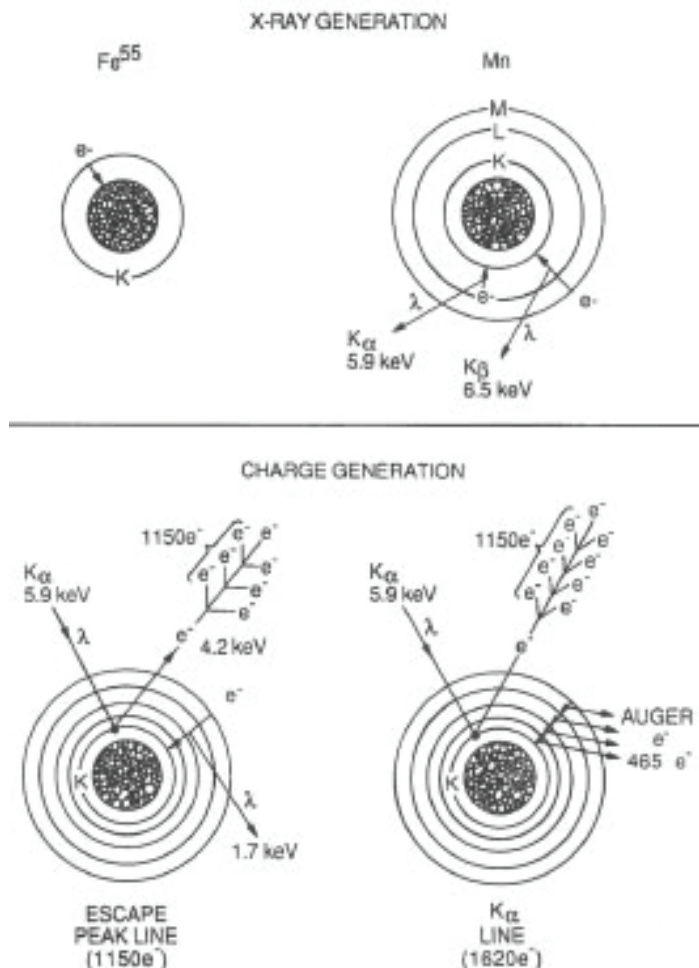


Figure 1: Illustration of Electron absorption (above) and Escape peak mechanism and K_{α} line emission (below)

II. Fit function and calibration

A. Fit

The following equation was used to fit the temperature data and calibrate the sensor to the weighted average of the $Mn K_{\alpha 1,2}$ line energy.

This user defined fit function is a sum of two Gaussians and a polynomial of the 4th degree. The Gaussian functions each fit the $Mn K_{\alpha}$ and K_{β} lines respectively, and the polynomial accounts for the background. The fit parameters are defined as followed; A is the amplitude of the distribution, μ is the mean, σ is the width of the peak, and a_i are the coefficients of the polynomial. Figure 4 show the fit function applied to a single channel at the lowest temperature.

B. Calibration procedure

Calibration of the sensor is done by acquiring the gain for each channel. The gain is calculated using the weighted average of the $Mn K_{\alpha 1,2}$ energies, 5.8950 keV, divided by the fitted peak position. The peak position varies from channel to channel in ~ 500 -545 ADU, $\sim 10\%$ variation. After applying the gain to each channel, the $Mn K_{\alpha}$ peaks lie within 0.02% of the $K_{\alpha,\beta}$ weighted average energy.

The calibration procedure is illustrated in Fig 5 and 6. The Fig 5 shows the raw spectrum of channel 2 at 195 K, and figure 6 shows the same spectrum after calibration is applied. The resultant units of the calibrated spectra are keV.

III. Results and Discussion

Analysis of individual channels revealed that channel 4 has a lower resolution than other segments. This assessment held true at all temperatures below the highest temperature, 242 K, and was clearly seen in the spectral widths of the $Mn K_{\alpha}$ line, seen in figure 7. Throughout the rest of this analysis, all channels will be combined excluding channel 4.

A. Manganese-55 X-rays

The full domain of the calibrated spectra collected by the CCD can be seen in figure fig. 6. In this section we focus on the two dominant peaks $Mn K_{\alpha}$ and K_{β} .

The K_{α} peak width for each channel is presented in fig. 7. The best resolution is produced at 195 K in the lower half of the CCD. Excluding the first 9 channels in analysis does not greatly effect the line width of the combined spectra, however, it does provide far less statistics. In conclusion we have avoided excluding more than one channel to benefit our analysis with more statistics.

Further, the low resolution of channel 4, visible in fig. 7, can be explained by a charge transfer efficiency (CTE) problem in this channel. The fig. 8 shows X-ray image in channel 4 and an other channel. One can see tails formed around the X-ray hits in channel 4. They are caused by a poor CTE and this causes the resolution degradation [2].

Hits in channel 4 have tails in horizontal direction, to the right of central pixels.

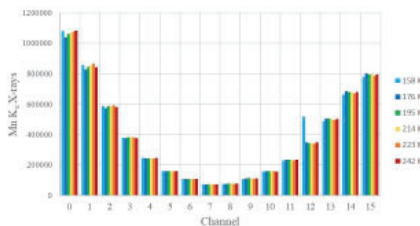


Figure 2: Integrated $Mn K_{\alpha}$ distribution. Colors represent each temperature dataset.

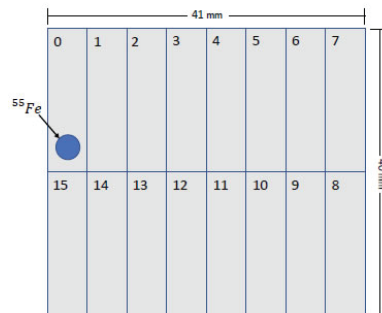


Figure 3: CCD250 channel layout. Blue circle denotes approximate location of X-ray source [7]

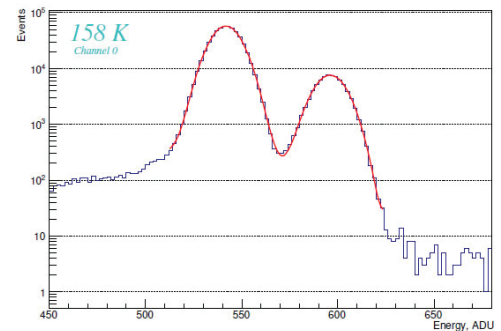


Figure 4: $K_{\alpha,\beta}$ peaks fit with equation (1). With a range from 512 - 624 ADU and $\frac{\chi^2}{NDF} = 2.93$

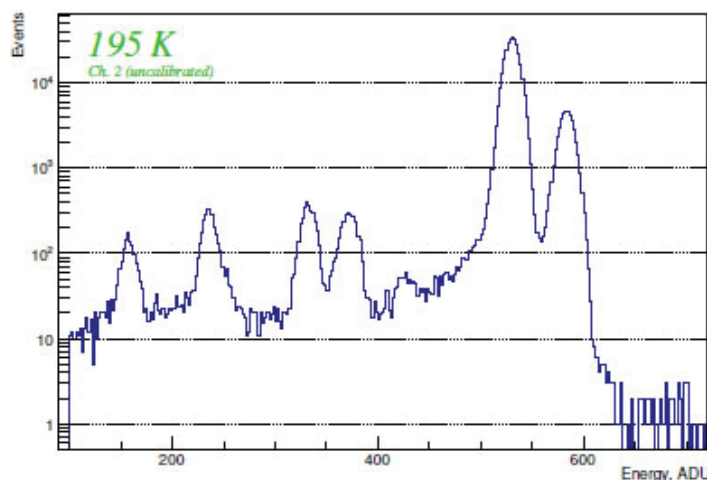


Figure 5: X-ray spectrum in units of ADU

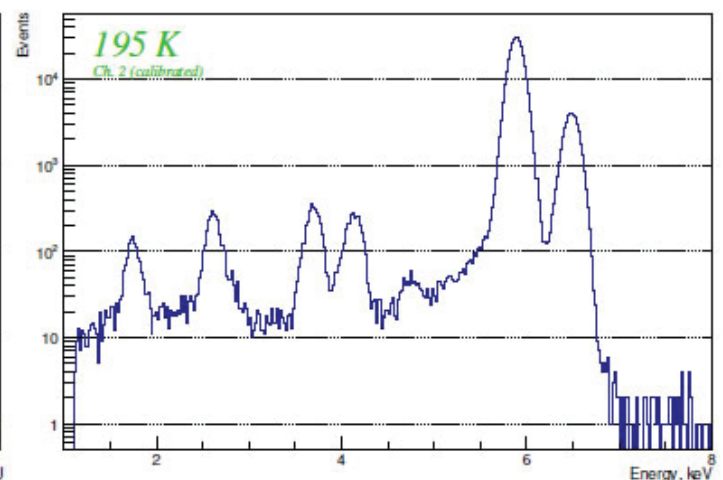


Figure 6: X-ray spectrum in units of keV

B. Lower energy peaks

$Mn K_{\alpha,\beta}$ X-rays dominate the spectrum, but there exist a few lower energy peaks which are interesting for analysis.

Figure 9 shows the lower energy part of the X-ray spectrum. The following lines are visible; $^{14}Si K_{\alpha}$, $^{17}Cl K_{\alpha,\beta}$, $^{20}Ca K_{\alpha}$, and $^{25}Mn K_{\alpha}$ escape [6]. The $Si K_{\alpha}$ peak is fit with one Gaussian and a 2nd degree polynomial to account for back-ground. $Cl K_{\alpha,\beta}$ lines are fit with two Gaussians and a 4th degree polynomial. $Ca K_{\alpha}$ and $Mn K_{\alpha}$ escape peaks are fit with two Gaussians and a 4th degree polynomial. The full fit functions can be seen in figs. 10 to 15. Full results and parameters for each temperature can be seen in tables tables 2 to 4.

Using the fit functions displayed in figs. 10 to 15, we compare the mean value of each spectral peak to the known energy to obtain the relative error. The mean value, or line energy, is displayed in table 1.

The largest difference in mean energies from documented

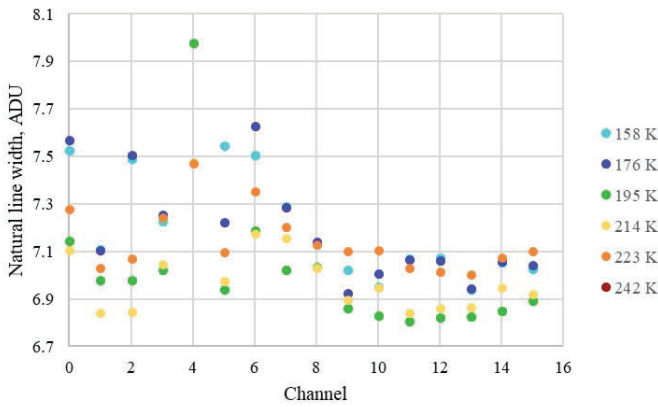


Figure 7: Spectral widths as a function of channel

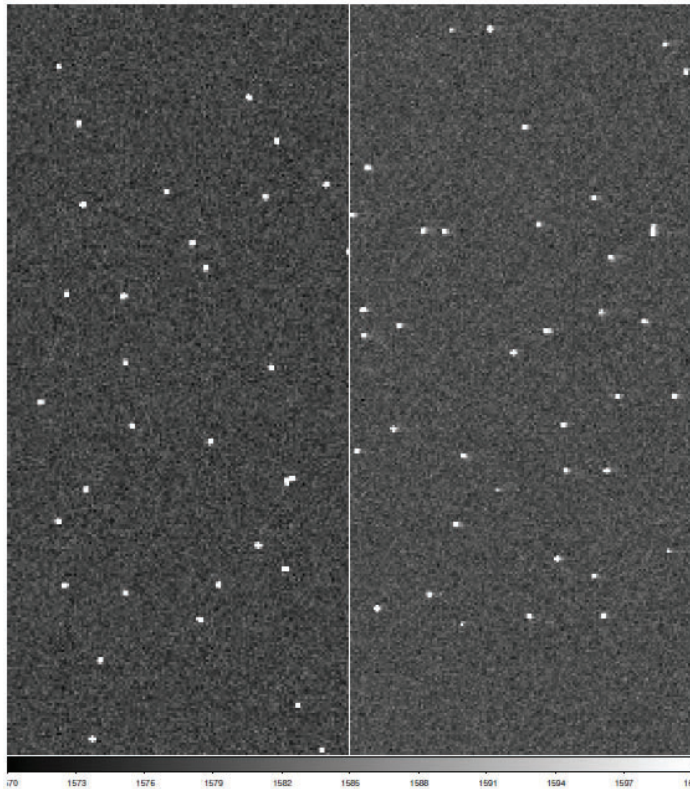


Figure 8: Channel 11 (left) Channel 4 (right)

values from [4], is at 242 K, we discuss this further in section 4. The relative error shows us how well the CCD is calibrated after using our method. Over the full temperature range it was found, Silicon K_{α} ranged from 0.01 – 0.37% deviation from documented line energies. Chlorine K_{α} from 0.04 – 0.12%, $Cl K_{\beta}$ from 0.1 – 0.4%, and Calcium K_{α} from 0.01 – 0.14%. There is no temperature dependence in the fitted values and this concludes that our calibration method is successful. The error in the fitted peak position increases with temperature and this is because of the resolution degradation.

At 1.73998 keV Silicon has a K_{α} emission line, this is the lowest energy peak visible to the sensor also having the least statistics. Using the peak positions and widths from the fitted and calibrated spectra, we find that this is the most accurate calibrated peak.

The $Mn K_{\alpha}$ escape line is a complex structure which is also contaminated by the $Ca K_{\beta}$ peak [4]. The $Mn K_{\alpha}$ is composed of 4 individual energy lines;

$Mn K_{\alpha 1} - Si K_{\alpha 1}$, $Mn K_{\alpha 2} - Si K_{\alpha 1}$, $Mn K_{\alpha 1} - Si K_{\alpha 2}$, and $Mn K_{\alpha 2} - Si K_{\alpha 2}$ [6]. We choose not to use this combination of energies to check our calibration method. However, in table 4 the $Mn K_{\alpha} esc.$ was used in the fitting routine, but was not suitable as an evaluation for sensor calibration.

IV. Further Discussion

Here we would like to discuss the large difference in resolution at the highest temperature (242 K) versus the lower temperature range. From figure 16, there is a very visible difference in line width of ~ 2.5 ADU. As is clearly seen in figs. 17 and 18 more dark current observed in the 242 K. dataset than at lower temperatures, The dark current shot noise is causing the line width increase [2].

Temp, K	$Si K_{\alpha}$	$Cl K_{\alpha}$	$Cl K_{\beta}$	$Ca K_{\alpha}$
158	1741.4 ± 0.9	2619.5 ± 0.8	2812.3 ± 0.7	3686.7 ± 0.5
176	1738.7 ± 1.0	2620.6 ± 0.8	2819.3 ± 0.8	3688.1 ± 0.5
195	1746.5 ± 0.8	2623.4 ± 0.8	2819.1 ± 0.7	3691.2 ± 0.5
214	1740.2 ± 0.9	2620.7 ± 0.7	2819.4 ± 0.5	3686.7 ± 0.5
223	1745.0 ± 0.9	2625.7 ± 1.1	2818.3 ± 1.1	3693.3 ± 0.5
242	1745.9 ± 1.9	2619.8 ± 1.8	2827.0 ± 5.8	3694.9 ± 0.9
ref. ⁴	1739.98 ± 0.01	2622.39 ± 0.01	2815.6 ± 0.1	3691.68 ± 0.01

Table 1: Calibration table in electron volts calculated using values from [4]

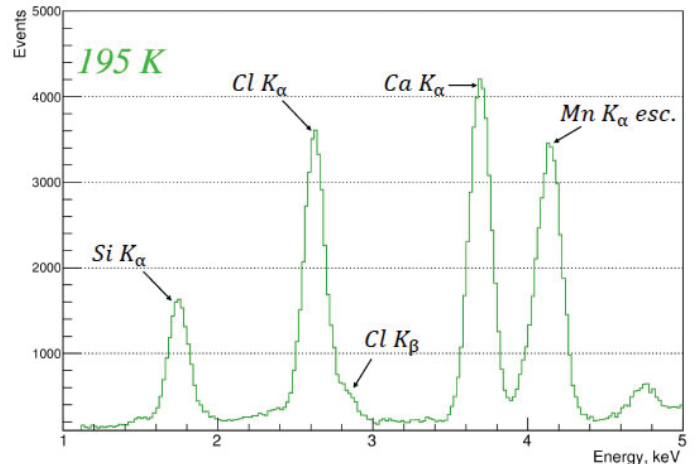


Figure 9: labeled energy peaks and such

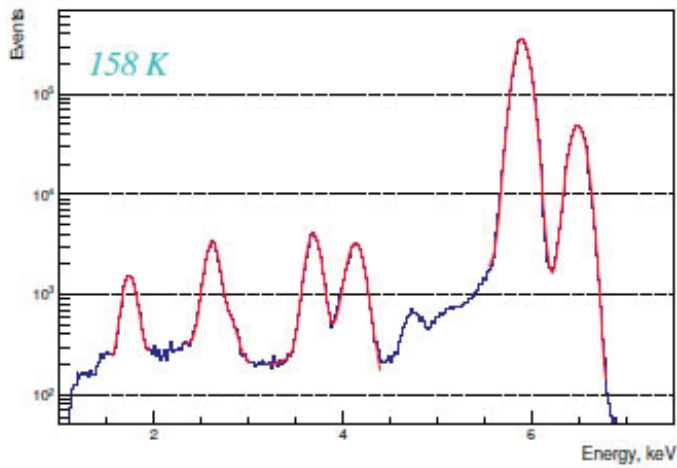


Figure 10: 158 K fitted X-ray spectra

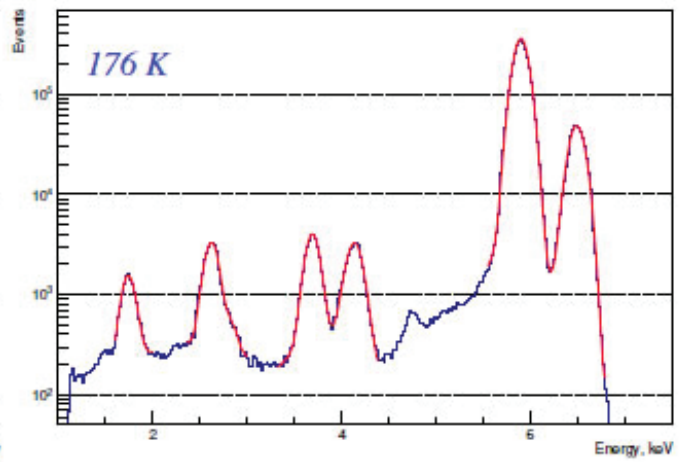


Figure 11: 176 K fitted X-ray spectra

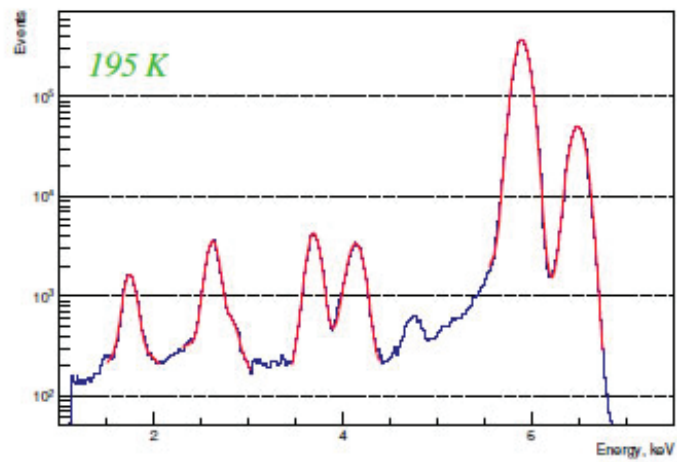


Figure 12: 195 K fitted X-ray spectra

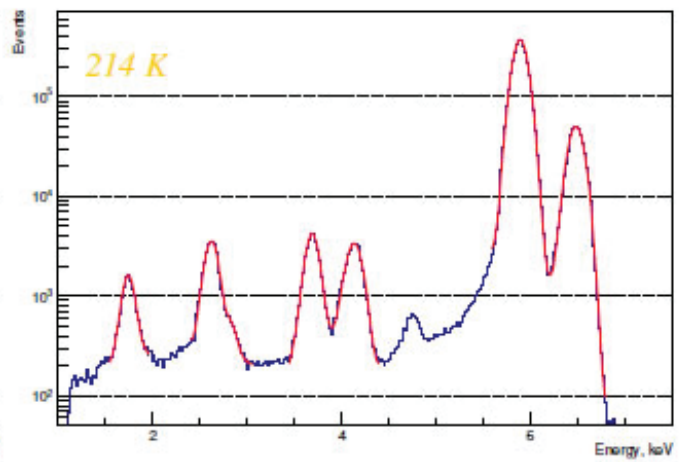


Figure 13: 214 K fitted X-ray spectra

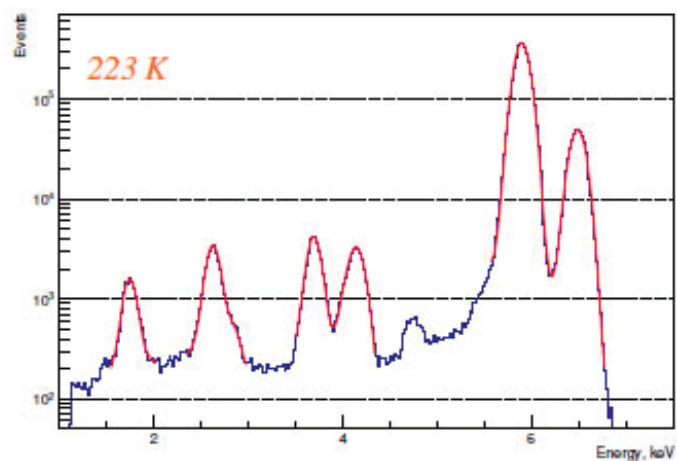


Figure 14: 223 K fitted X-ray spectra

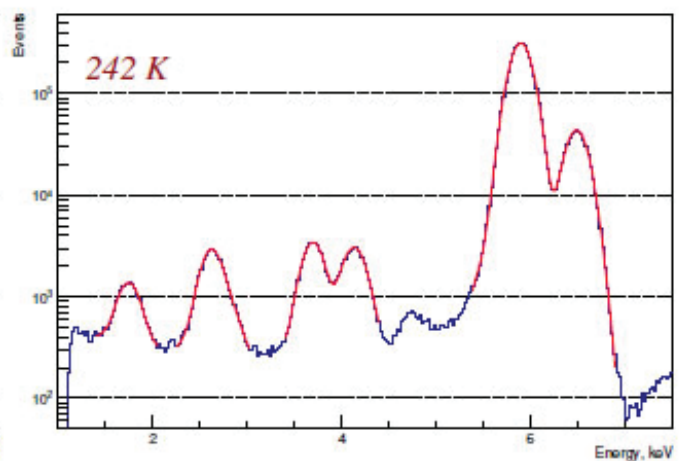


Figure 15: 242 K fitted X-ray spectra

V. Conclusion

Calibration of the sensor utilizing the documented line energy of $Mn K\alpha$ proved to be an accurate technique. After calibration the mean line energies in the lower energy spectra lay within 0.6% from the documented values.

VI. Acknowledgments

I would like to thank my mentor, Ivan Kotov, for his patience and professionalism throughout the duration of this internship. This project was supported in part by the U.S. Department of Energy, Office of Science, Office of Workforce Development for Teachers and Scientists (WDTS) under the Science Undergraduate Laboratory Internships Program (SULI).

VII. References

- ¹W.N. Cottingham and D. A. Greenwood. *An Introduction to Nuclear Physics*. Cambridge University Press, 2 edition, 2001.
- ²James R. Janesick. *Scientific Charge-Coupled Devices*. SPIE Press, 2001.
- ³M.-M. Bé, V.Chisté, C. Dulieu, E. Browne, C. Baglin, V. Chechev, N. Kuzmenko, R. Helmer, F. Kondev, D. MacMahon, and K.B. Lee. *Table of Radionuclides*, volume 3 of *Monographie BIPM-5*. Bureau International des Poids et Mesures, Pavillon de Breteuil, F-92310 Sèvres, France, 2006.
- ⁴A. Thompson et al. X-ray data booklet, 2009. <http://xdb.lbl.gov/xdb-new.pdf>.
- ⁵R.B. Firestone S.Y.F. Chu, L.P. Ekström. The lund/lbnl nuclear data search, 1999. <http://nucldata.nuclear.lu.se/toi/nuclide.asp?iza=260055>.
- ⁶P.O'Connor I. V.Kotov, H. Neal. Pair creation energy and fano factor of silicon measured at 185 k using 55fe x-rays. 7 2018.
- ⁷Ccd250-82 back illuminated hi-rho high performance ccd sensor, 2018.

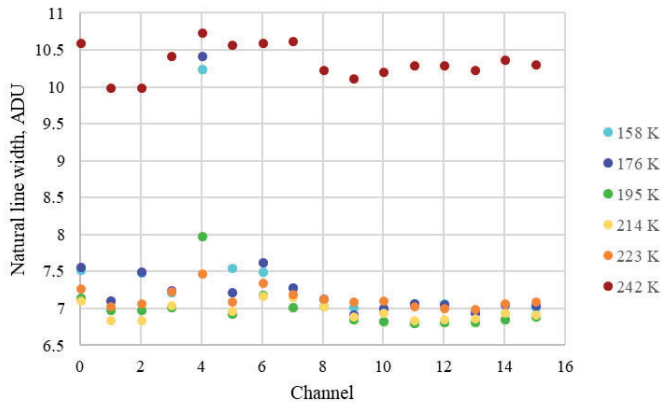


Figure 16: Spectral widths, σ , of $Mn K\alpha$ lines. Colors represent the temperature range

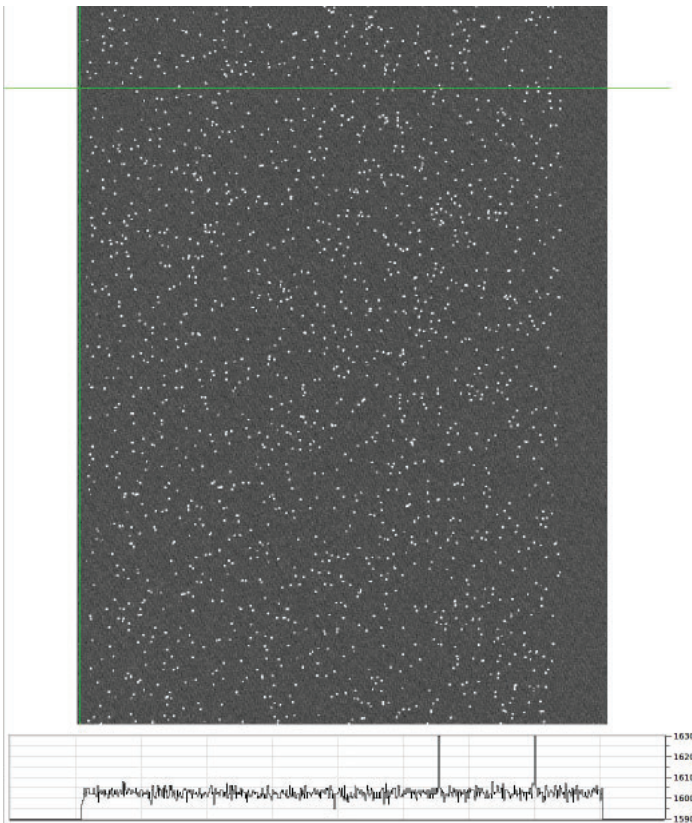


Figure 17: 158 K image area vs overscan area

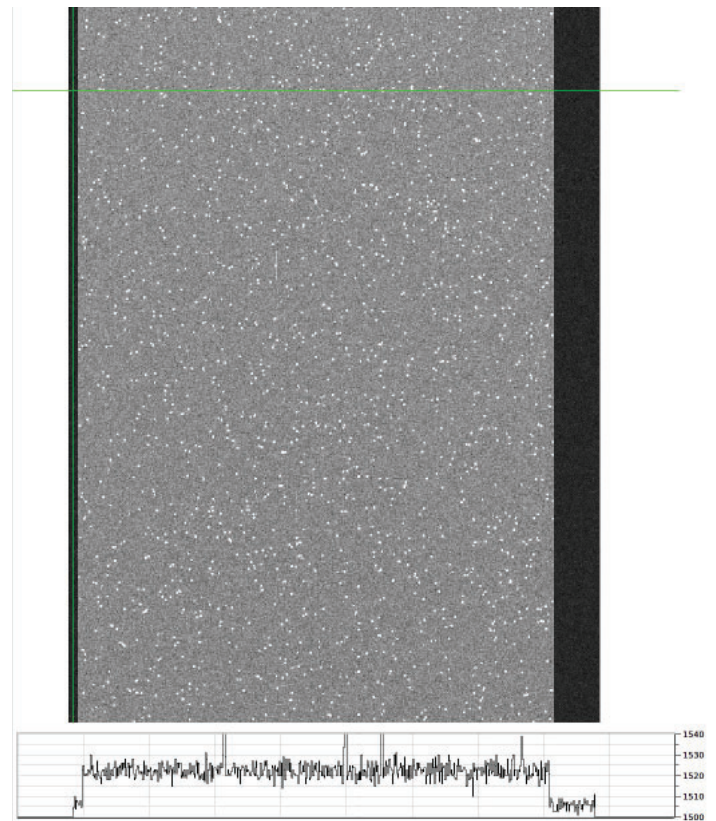


Figure 18: 242 K image area vs overscan area

Comprehensive stray radiation measurements inside the first optical enclosure of the 07-ID-A beamline at NSLS-II

Aaron R. Taylor

Department of Chemistry, Texas Southern University, Houston, TX 77004

Erika I. Martinez

Department of Mathematics, Texas Southern University, Houston, TX 77004

Jessica E. Schweitzer

Department of Health Science, Stony Brook University, Stony Brook, NY 11790

Mark Harvey

Department of Physics, Texas Southern University, Houston, TX 77004

Steve Coleman

Radiological Control Safety, Brookhaven National Laboratory, Upton, NY 11973

Abstract

The National Synchrotron Light Source II (NSLS-II) is a next generation research facility for scientist and engineers. NSLS-II currently produces the brightest synchrotron light in the world, which can be focused and used to perform high energy x-ray experiments. The purpose of this study was to comprehensively measure stray radiation within the first optical enclosure (FOE) of beamline 07-ID-A for dedicated undulator and mirror conditions produced at NSLS-II. Of note, the magnitude of scatter radiation in FOE hutches is unclear as Monte Carlo simulations have only been used to predict the dose rates. Measurements were performed with multiple gamma and neutron detectors including the Fluke 451P, Canberra InSpector 1000 gamma spectroscopy unit, WENDI-2 & FG 40 survey meter, REM Ball and thermoluminescent dosimeters (TLDs). These detectors were used to measure the amount of stray radiation that is scattered within each FOE. The FLUKA Monte Carlo radiation transport code was used to determined detector placement longitudinal and lateral to the beamline within the FOE. Measurements of the average gamma dose rate in 07-ID-A was approximately 3.36 ± 2.1 mrem/h. Furthermore, the neutron dose rates were down an order of magnitude to about 0.000871 ± 0.00035 mrem/h.

I. Introduction

The National Synchrotron Light Source II (NSLS-II) at the Brookhaven National Laboratory (BNL) came online in 2015. NSLS-II consists of a linac, where electrons are injected into the booster ring and accelerated to relativistic speeds before entering the storage ring where they emit synchrotron light into a given FOE for x-ray diffraction experiments [1]. The NSLS-II provides synchrotron radiation of ultra-high brightness and exceptional spatial and energy resolution. It will also incorporate advanced insertion devices, optics, detectors and robotics, along with a suite of various instruments designed to maximize the scientific output of the facility [2]. This facility will eventually house up to 60 different beamlines to serve various aspects of a ubiquitous scientific scope including canted insertion devices and multiple hutches [3]. NSLS-II can operate in 2 different modes: top off and decay. The two modes refer to the shutter configurations within

the storage ring. Top off mode allows the photon shutters to remain in an open position allowing an uninterrupted flow of synchrotron light to the various beamlines, while constantly injecting electrons every minute or so. The decay mode has the shutters in a closed position, so that no synchrotron light can be released into the beamlines and electrons injection is less frequent (~ 1 injection/day). FLUKA simulation have been used extensively at NSLS-II to predict the magnitude of scatter dose rates to ensure the safest work conditions. Stray radiation measurements were performed for the first time in the FOE of 7-ID-A beamline to compare with the simulated results. There are two main types of primary radiation considered at NSLS-II: synchrotron radiation and gas bremsstrahlung(GB). The synchrotron radiation is used to conduct diffraction experiments, while the GB is excess stray radiation produced inside the storage ring due to beam gas interactions. Detectors were placed within the FOE to measure the scatter gamma and neutron dose rates under controlled conditions. This 7-ID-A beamline is unique consisting of two separate branches to split the synchrotron light within the FOE. Our results suggest that the maximum gamma (neutron) dose rates of 41.06 ± 3.69 mrem/h (0.00138 ± 0.002 mrem/h) was produced on axis at near the soft branch mirror tank (M1), while the maximum off-axis gamma (neutron) dose rates of 1.30 ± 0.027 mrem/h (0.00267 ± 0.01 mrem/h) occurred near M1. Furthermore, the Monte Carlo results from FLUKA seemed to over predict the stray dose rates by a factor of ~1. These measurements could also help in lowering the cost to build the additional beam line stations at NSLS-II in the future.

II. Methods

A dedicated series of measurements was performed to assess the magnitude of both secondary gamma and neutron radiation dose rates produced within the 7-ID-A beamline for the first time.

Several detectors were used to acquire the measured data of the secondary scatter radiation and included the following: FLUKE 451P survey meters for gammas; Canberra InSpectorTM 1000 hand-held Multichannel Analyzer with a LaBr probe (1.5 in x 1.5 in; energy resolution ~3%) for gamma spectroscopy; WENDI-2 for neutrons and accompanying FH 40 G survey meter for gammas; NRD neutron ball from Thermo Fischer Scientific. The

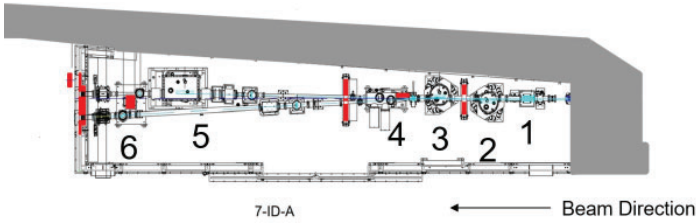


Figure 1. Horizontal view of the FOE 7ID-SST at NSLS-II using the FLUKA Monte Carlo toolkit. The main beamline components are illustrated by the numbers.

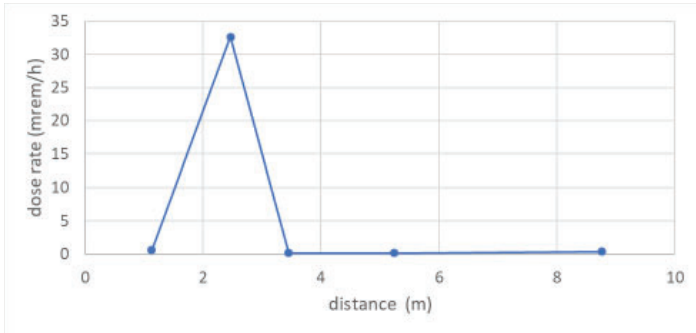


Figure 3. The mean gamma dose rate produced along the beam components of FOE 7ID-SST is shown as a function of the distance away from the upstream wall. These measurements were performed approximately 1.4 m above the floor at fixed positions along the central beamline axis. The line is introduced to direct the eyes.

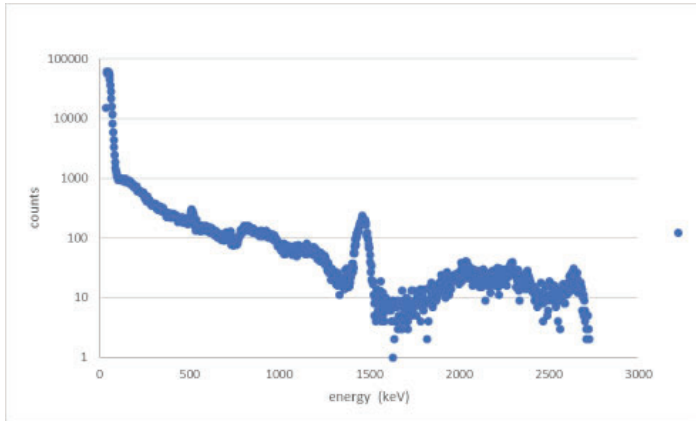


Figure 5. Preliminary bremsstrahlung spectrum measured with the LaBr probe of the Canberra InSpector 1000. Background measurements have not been removed. This measurement was performed approximately 1.4 m above the floor at the first mirror tank (L1) of the L branch.

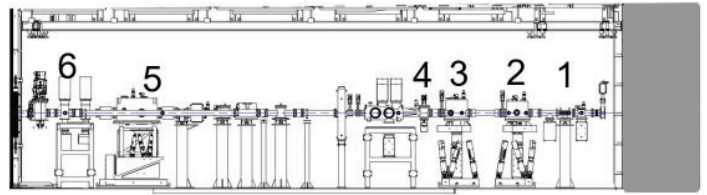


Figure 2. Vertical view of the FOE 7ID-SST at NSLS-II using the FLUKA Monte Carlo toolkit. The main beamline components are illustrated by the numbers.

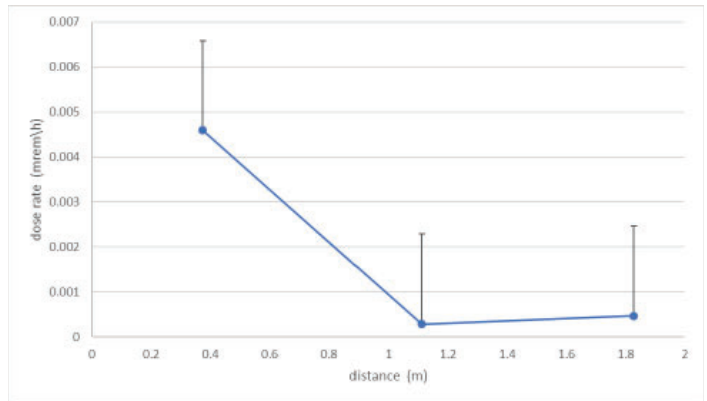


Figure 4. The mean gamma dose rate produced along the beam components of FOE 7ID-SST is shown as a function of the distance away from the ratchet wall to the outboard wall. Using run 1. These measurements were performed approximately 1.4 m above the floor at the FM across the central beamline axis. The line is introduced to direct the eyes.

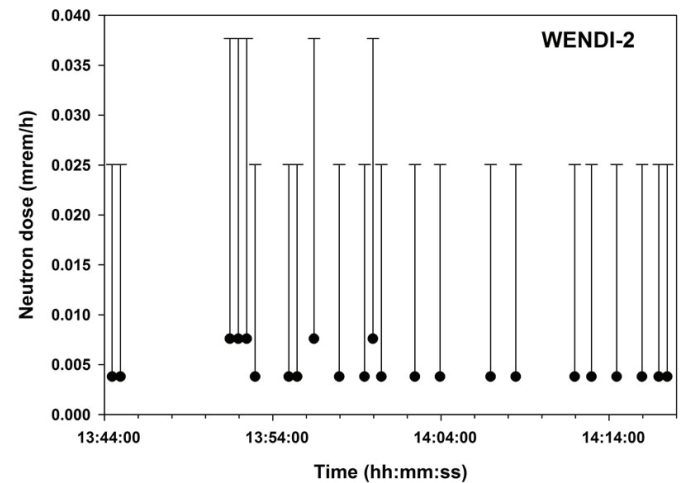


Figure 6. The neutron dose rate recorded within the FOE 7ID-SST is shown as a function of the dose rate vs time. These measurements were performed approximately 1.4 m above the floor at fixed positions on the central beamline axis at the first mirror tank of the tender branch (L1).

Figure 7 (left). The FOE 7ID-SST is shown with the gamma detectors positioned at the first mirror of the soft branch (M1). The neutron detectors are positioned at the white beam stop(WBS). Measurements are taken along and across the beam axis

FLUKE 451P survey meter is a 230 cm³ air ionization chamber with dimensions of 4.0 in x 8.0 in x 6.0 in pressurized to 125 psi for gamma detection in the energy range of 25 keV to 2 MeV. The WENDI-2 detector is comprised of a polyethylene cylindrical shell (9.0 in diameter x 12.6 in length) with an inner ³He proportional tube (dimensions 0.6 in x 1.0 in) that is encased by tungsten powder. It is coupled to a FH 40 G survey meter for measurements of the neutron ambient dose equivalent rate from thermal energies up to 5 GeV. The FH 40 G survey meter detector has a Geiger Muller tube (7.7 in x 2.9 in x 1.7 in) for gamma detection in the energy range from 36 keV to 1.3 MeV. Secondary neutron dose rate measurements were also carried out from thermal energies up to 10 MeV with the NRD neutron ball. This detector uses an ASP2e Eberline survey meter with a 9.0 in diameter outer spherical shell of cadmium loaded polyethylene housing a BF₃ tube (0.6 in X 1.0 in). Finally, 6 electronic personal dosimeters (EPDs) were deployed to measure secondary gamma dose rates at targeted locations in the FOE. The detectors were placed at specific locations throughout the FOE to measure the produced gamma and neutron dose rates both longitudinally and laterally to the beamline consistent with FLUKA Monte Carlo predictions of scatter dose in the 7-ID-A beamline. Of note, these simulations predicted a wide scatter dose rate range from 1.0 X 10⁻⁴ mrem/h to 100 mrem/h. Detectors were positioned longitudinally and laterally at the following locations in the FOE 7-ID-A beamline: first fixed mask, L branch mirror 1 (L1), M branch mirror 1 (M1), white beam stop (WBS), L branch mirror 2 (L2), and the photon shutter. The FH 40 G survey meter and the Canberra Inspector 1000 LaBr Probe were primarily positioned along the beamline axis, while the Fluke 451Ps, WENDI-2 and NRD detectors were positioned off-axis along the outboard side.

III. Results

Figure 1 shows the experimental setup of the detectors relative to the beam line axis in the FOE of 7-ID-A and illustrates a location where data were measured throughout the experiment. Figure 2 shows the mean gamma dose rate as a function of the longitudinal distance away from the upstream wall to the downstream wall. Of note, the dose rates were measured near L1 and M1 with the mean dose rate peaking at 36.2 ± 0.01 mrem/h at about 3.0 m away from the upstream wall. In Figure 3, a lateral plot is shown of the gamma dose rate as a function of distance away from the ratchet wall to the outboard wall within 7-ID-A. The gamma dose rate falls off uniformly away from the beam central axis. Figure 4 shows a plot of the gas bremsstrahlung spectrum measured with the LaBr probe of the Canberra InSpectorTM 1000 at L1 under the following conditions: closed EPU; closed U42; L1 in and M1 in. An annihilation peak appears at 511 keV peak, while the spectral peaks around 1250 keV is currently be analyzed and 1460.8 keV peak is K-40. Figure 5 is the mean neutron dose rate measured at L1. The neutron measurements were indistinguishable from background in all case. Figure 6 shows the position of the WENDI-2, NRD balls, LaBr probe, FH 40 G survey meter and 451-P detectors used to measure lateral and longitudinal dose rates. Table 1 shows the experimental conditions considered in this study with the mean gamma and neutron dose rates at each measurement location The highest dose rates of 38.3 ± 3.69 mrem/h were measured at M1 by the FH 40 G survey meter along the central beam pipe. The dose rates measured with the EPDs are shown and indicate that largest dose rates occur at the

first mirror tank of the tender branch (L1).

IV. Discussion

In conclusion, the first scatter radiation data were measured within the FOE of 7-ID-A. Secondary scatter radiation produced within 7-ID-A was mainly present at L1 and M1 near the upstream wall, with both undulators in the closed position and mirrors L1 and M1 in. Dose rates fell off considerably approaching the downstream wall and thus, were more consistent with the background. The highest gamma dose rate of 38.3 ± 3.69 mrem/h was measured at M1. The gamma dose rates measured lateral to the central beamline axis were a maximum at the central axis and decreased by a factor of 10 out near the outboard wall. The neutron dose rates for all conditions within the FOE were indistinguishable from background due to the low incident beam energies used by 7-ID-A beamline. Any excess neutrons present may result from quantum tunneling effects. Our preliminary results of the spectrum indicate an annihilation peak around 511 keV, while the K-40 peak appears in all the uncorrected spectra. It is interesting to note that EPD data were consistent with FLUKA prediction values. The current FOE shielding requirements at NSLS-II are less than 0.05 mrem/h. Due to the accuracy of the simulations, a new procedure for building the FOE could change resulting in a decreased cost to construct the hutches leading to more availability of funds.

Run	EPD 1	EPD 2	EPD 3	EPD4	EPD 5	EPD 6
1	0.4	0.2	0	0.4	0	0
2	0.4	0.2	0	0.4	0	0.2
3	0.4	0.2	0.2	0.4	0	0.2
4	0.6	0.2	0.2	0.4	32.6	0.2
5	0.6	0.2	0.2	0.4	32.6	0
6	36.4	0.6	0.2	0.4	64.8	0
7	6.2	0.2	0	0	30.4	0
8	24.8	0.2	0	0	41	0
9	24.8	0.2	0	0	32.6	41
10	0	0.2	0	0	0	0
11	0	0	0	0	0	0
12	0	0	0	0	0	0
13	18.6	0.6	0.2	0.2	32.4	0.2
14	19.6	0	0	0	32.4	0
15	0	0	0	0	0	0
16	0	0	0	0	0	0
17	0.2	0	0	0	0	0
18	2.4	0.2	0	0	35.2	0
19	0	0	0	0	0	0
20	11.6	0	0	0	0	0
21	17.6	0	0	0	2.6	0
22	0	0	0	0	0	0.4
23	9.2	0.4	0.2	0	32.4	0.4
24	0	0.2	0	0	30.8	0

Table 1. The FOE 7ID-SST is shown with the gamma detectors positioned at the first mirror of the soft branch. The neutron detectors are positioned at the white beam stop. Measurements are take a long and across the beam axis

V. References

1. Hu, Y, Dalesio, L, 2015, Diagnosing and Controls of NSLS-II: A Bright New Light for Science, Proceedings of ICAP2015, 84-86
2. Job P.K., Casey W.R., 2011, Radiological considerations for bulk shielding calculations of national synchrotron light source-II, Nucl. Instr. and Meth. in Phys. Res. A 660 1 – 6
3. Tanabe, Toshi, Charles Kitegi, Ping He, Marco Musardo, Oleg Chubar James Rank, Peter Cappadoro, Huston Fernandes, David Harder, and Todd Corwin. "The Latest Status of NSLS-II Insertion Devices." *Journal of Physics: Conference Series* 493 (2014)
4. Job, P.K., & Moe, H.J.(1995). Dose rate estimates in the first optical enclosure due to particle beam loss in the insertion device transition region during injection. United States. doi:10.2172/88519.
5. Ren, Dan; Du, Ping-An; He, Yin; Chen, Ke; Luo, Jing-Wen; Michelson, David G. (2016). A Fast Calculation Approach for the shielding effectiveness of an enclosure with numerous small apertures. *Transactions on Electromagnetic Compatibility*. Part 1, Vol. 58 Issue 4 DOI: 10.1109/TEMC.2016.2547739
6. Ibrahim B; Caglar, Me, F. (2016). Investigation of Magnetic Shielding Parameters of rectangular enclosures with apertures at 0 to 3 GHz. *Electromagnetics*. Vol. 36 Issue 7, p 434-446. DOI: 10.1080/02726343.2016.1220907
7. Karami, H. , Moini, R., Seyed H. H.; Maftooli, H. , Mattes, M., Mosig, J. R. (2014). Efficient Analysis of Shielding Effectiveness of Metallic Rectangular Enclosures Using Unconditionally Stable Time-Domain Integral Equations. *Transactions on Electromagnetic Compatibility*. Vol. 56 Issue 6, p 1412-1419. DOI: 10.1109/TEMC.2014.2315719
8. W. Yun, B. Lai, S. Davey, D. R. Haeffner, D. Shu. (1995). The Pennsylvania State University CiteSeerX Archives ANL/APS/TB-21 Radiation Shielding of Insertion Device Beamlines Using a Mirror as the First Optical Element. <http://citeseerx.ist.psu.edu/viewdoc/summary?doi=10.1.1.646.8149>
9. Hu, Y, Dalesio, L, 2015, Diagnosing and Controls of NSLS-II: A Bright New Light for Science, Proceedings of ICAP2015, 84-86
10. Job P.K., Casey W.R., 2011, Radiological considerations for bulk shielding calculations of national synchrotron light source-II, Nucl. Instr. and Meth. in Phys. Res. A 660 1 – 6
11. Tanabe, Toshi, Charles Kitegi, Ping He, Marco Musardo, Oleg Chubar James Rank, Peter Cappadoro, Huston Fernandes, David Harder, and Todd Corwin. "The Latest Status of NSLS-II Insertion Devices." *Journal of Physics: Conference Series* 493 (2014)
12. Battistoni, G. et al. "Applications of FLUKA Monte Carlo Code for Nuclear and Accelerator Physics." *Nuclear Instruments and Methods in Physics Research Section B: Beam Interactions with Materials and Atoms* 269.24 (2011): 2850-856.
13. Agostinelle, S. et al. 2003, Geant4- a simulation toolkit, Nucl. Instr. And Meth. In Phys. Res, A506 250-30
14. Benmerrouche, M, 2017, 06BM BMM Beamline Radiation Shielding Analysis
15. Devienne A., Aymerich N., Garcia-Fuste M.J., Queralt, X., 2015, A comparative radiation study at ALBA synchrotron facility between Monte Carlo Modeling and radiation monitors dosimetry measurements, *Radiat Phys and Chem* 116 365-367
16. Job P.K., Casey W.R., 2011, Radiological implications of top-off operation at national synchrotron light source-II, Nucl. Instr. and Meth. in Phys. Res. A 648 15 - 21
17. Ahmed, A.S., Benmerrouche, M. Cubbon, G., 2015, Monte Carlo simulation study to calculate radiation dose under beamloss scenarios in Top-up operation mode for HXMA beamline at Canadian Light Source, *Radiat Meas* 74 31-38
18. Asai, J., and H. Hirayama. "Shielding Design Study against Gas Bremsstrahlung for the CLS first Optics Enclosures." N.p., 2007
19. Canberra, Mirion Technologies, 2014, Gamma and X-Ray Detection
20. Canberra, Mirion Technologies, 2014, Neutron Detection and Counting
21. Job P.K., Casey W.R., 2007, Preliminary Material Requirement for the Supplementary Shielding at NSLSII, NSLS II Project at Brookhaven National Laboratory
22. Owens A., "Synchrotron light source and radiation detector metrology." *Nuclear Instruments and Methods in Physics Research Section A: Beam Interactions with Materials and Atoms* 695 (2012): 1-12.
23. Asai J., Coulthard I., "Radiation shielding considerations against gas bremsstrahlung for the BioXAS beamlines at the Canadian Light Source." *Nuclear Instruments and Methods in Physics Research Section A: Beam Interactions with Materials and Atoms* 622 (2010):492-501.

Wire-Cell tomographic imaging evaluation

Deepsana Shahi

Physics, Adelphi University, Garden City, NY 11530

Hanyu Wei, XiangPan Ji, Mary Bishai

Physics, Brookhaven National Laboratory, Upton, NY 11973

Abstract

Event reconstruction of real data from LArTPC provides some major challenges in signal processing inefficiency and dead channels. These challenges are currently being investigated by quantitatively analyzing data and simulation processed using the Wire-Cell imaging algorithms. Wire-Cell is a tomographic event reconstruction tool that is used in analyzing MicroBooNE data. Reconstructed and truth tracks are generated by tuning an analysis chain of simulation followed by signal processing and imaging algorithms with dead channels in the normal region. The performance of Wire-Cell imaging is then evaluated by analyzing ghosts, broken reconstructed tracks, absent reconstructed tracks, and well reconstructed tracks. This evaluation also consists of clustering which aims to bridge the gaps caused by broken tracks and de-ghosting. Understanding inefficiencies in the overall performance of tracks will improve the current imaging algorithm development.

I. Introduction

Micro Booster Neutrino Experiment (MicroBooNE) consists of cryostat filled with 170 tons of liquid argon, which has 85-ton within TPC. LArTPCs observe neutrino events located on the Booster Neutrino Beamline (BNB) at Fermi lab. It produces high resolution images of tracks created by charged particles inside the detector. The cathode plane in MicroBooNE LArTPC is -70 kV which has a drift electric field of 0.273 kV/cm. The anode plane consists of 3 wire planes (U, V and Y), where the induction planes (U and V) are inclined +60 and -60 with respect to the collection plane (Y) where three planes of wire is at 3mm pitch. Also, there are 32 8-inch photomultiplier tubes (PMTs) behind the anode wire planes. In order to study particles efficiently, events need to be reconstructed. To do so, improvements in signal processing allows various approaches to display events. [1]

A. How does LArTPC work?

LArTPC detector observes neutrino interactions and measures energy and track angle for particles. It also collects both light and charge information so that events can be reconstructed which provides additional information about the particles. As charged particles enter the detector and collide with argon atoms, it ionizes argon atoms. [2] As ionization electrons drift through liquid argon in the form of scintillation photons, it loses energy and light travels to the edge of the detector. At the edge, each photon is absorbed by the face of a photomultiplier tube (PMT). Ionization electrons drift in 273 V/cm field towards three wire planes as shown in Figure 1. As the electrons drift, they create signals on the induction wire planes (U and V) and collect on the collection plane (Y). Signals are produced on wires and those signals produce complex waveform and give electronic noise. Using

multiple wire planes with different angles helps create 3D event reconstruction. [3]

II. Event Reconstruction

A. Wire-Cell Reconstruction Method

In wire-cell, the word wire refers to the region centered around the wires and cell refers to where the three wire (U, V, Y) planes overlap and charges are measured. Wire-cell technique is as follows: [8]

- Preparing data: Filter noise and deconvolve wire response to obtain the integrated charge on the fired wires. Form time slice by slicing the deconvolved charge spectrum.
- Data imaging: main concept of wire-cell imaging is the tomographic nature of LArTPC. All three wire planes above threshold in a time slice with associated cells carry some drifted charge that needs to be identified. Each wire plane is a 1D projective view of the 2D image of charge hits given a time slice.
- Patterns: look at particle clustering in space and time slices and arrange the patterns- tracks, showers, blob, etc.
- Identify particles and kinematics behind tracks.

In other words, local charge matches across the three wire planes in a time slice creates an image. The image time slices are then joined together to create a 3D image. From pattern recognition, 3D image can be recognized. In LArTPCs, event reconstruction mostly looks at neutrino interactions which starts from a single vertex and has multiple final states.

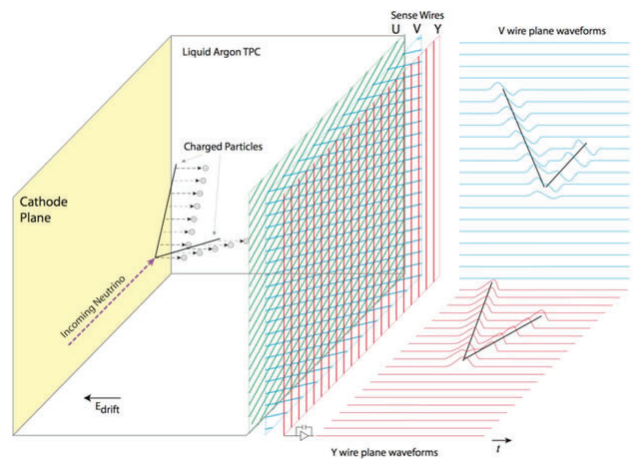


Figure 1: Illustration of the signal formation in a time projection chamber (TPC) with representation of three wire (U, V, Y) planes. Two wire planes (U, V) sense induced charge which is collected by third wire plane (Y). [3]

B. Wire-Cell Software

The “Wire-Cell” algorithm used in this process initially identifies a group of wires in each of the three projections which has time bins. The reconstruction process is very dependent in the continuity of the particles being tracks or showers. Each particle needs to be reconstructed according to the position of the particle hits in three projections and is built such that individual 2D projection matches with the 3D. However, there are chances that ghost particles are created during the process. [8]

The software used to do the evaluation are as follows:

1. Wire-Cell Prototype

The prototype is integrated with reconstruction algorithms for LArTPC detectors. It removes excess noise and achieves: [9]

▫ Signal Processing

When electrons drift, it produces field responses on all three wires which produces electronic responses by giving a shaping and amplifying electronics. When those signals are digitized and de-convoluted, it extracts charge from signal. This whole process in LArTPC is known as charge signal formation. First, signal deconvolution is carried out in frequency domain. This technique converts wire signals to a standard form so that the charge hits are reconstructed. Second, the excess noise in the electronics chain and coherent noise are removed. Lastly, the estimated signal gives the number of ionization electrons.

The electrons produce a field response on the closest wire along with neighboring wires. The LAr Soft software implements the deconvolution process in signal processing procedure. [6] A Fast Fourier Transform (FFT) is applied to convert time domain into frequency domain,

$$M(\omega) = R(\omega)S(\omega) \quad (1)$$

Using anti-FFT, the time domain is recovered $S(t)$, but this doesn't give an average response function. So, a 2D deconvolution is applied. It involves both time and wire domain while recovering the original ionization electron distribution.

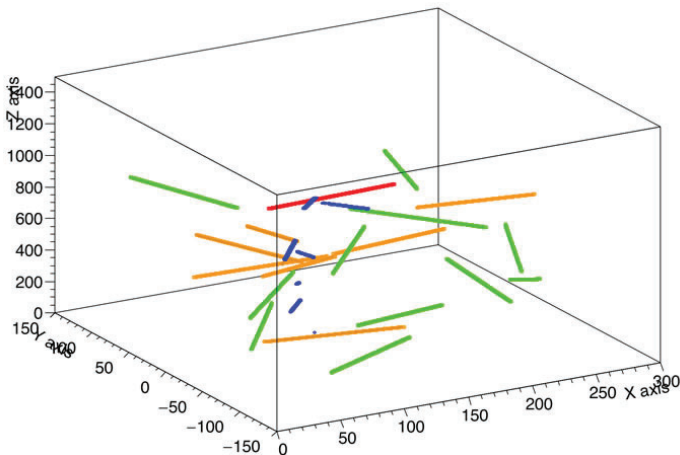


Figure 2: Track classification display for simulated track with dead region and signal processing. Green represents true tracks surface and good, yellow represents true tracks surface and broken, blue represents ghost tracks, and red represents true track surface and absent.

$$M_{t_0} = \int [R_0(t-t_0)S_i(t)dt + R_1(t-t_0)S_{i+1}(t)...]dt \quad (2)$$

$$M_i(\omega) = R_0(\omega)S_i(\omega) + R_1(\omega)S_{i+1}(\omega) + .. \quad (3)$$

where, M_i is measured signal, $R(t)$ is detector response function, and $S(t)$ is real signal. This measured signal is the combination of signals from both induction and collection planes. It also extracts ionization charge from induction wire planes. [6]

▫ Tomographic Imaging

Tomographic imaging technique is applied for a single-phase LArTPC wire readout since the drifting of ionization electrons in wire planes (U, V, Y) corresponds to the moving detector in tomography. The fundamental and detector information needs to be integrate to fully understand the principles of tomographic event reconstruction: [7]

- Time: *time* when ionization electrons arrive at the anode wire planes.
- Charge: number of ionization electrons measured on each wire.
- Geometry: 1D position of each fired wire.
- Sparsity: given a time slice, the charge hits are sparse.
- Positivity: Only ionization electrons drift to the wire plane, with the same sign of charge.
- Connectivity: fully active LArTPC detector, the charge hits are connected if they come from the same track.

These implementations give many information to reconstruct original charged particle information. The basic idea behind using this algorithm is it uses charge information for 3D reconstruction. It describes signal values that belongs to a single time bin in wire planes as having sets of polygon pixels in 3D; each wire has it's set of pixels. The algorithm determines charge values based on

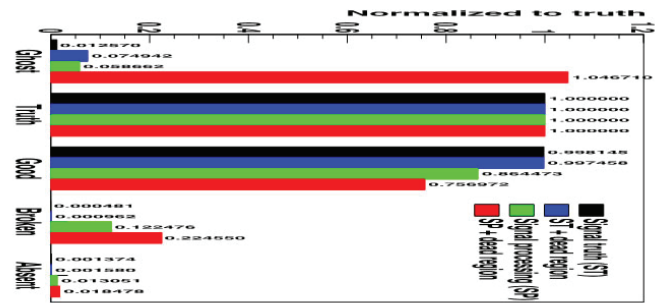


Figure 3: Representation of overall performance of 800 tracks (~15000 tracks) without clustering classified with simulation scenarios. Without clustering, the broken track is problem.

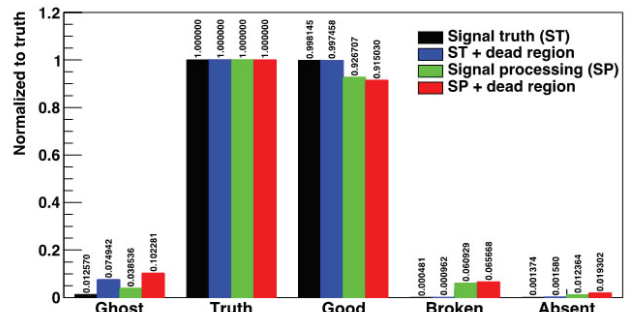


Figure 4: Representation of overall performance of 800 events (~15000 tracks) with clustering classified with simulation scenarios. With clustering, broken track is fixed somehow, but the ghost length is then a problem and needs to be understood.

the three sets of wires to perform 2D imaging and obtains event information to get the ionization pattern in liquid Argon. [9]

2. Wire-Cell Toolkit

WCT implements the full simulation of TPC signals, including diffusion, 2D (longitudinal and transverse) field responses, electronics, and pre-amplifier noise. [10] In order to reproduce interactions between particles, following details need to be understood about detector responses, [4]

- Deposition: Use of Monte Carlo simulations for liquid argon ionization electrons from charged particles.
- Drifting: Provides statistics in understanding ionization electrons, diffusion, recombination, and charge quenching fluctuations.
- Ducting: Induction and collector charge on anode wires.
- Digitization: Converting analog to digital signals using electronics.
- Dissonance: Noise modeling using real data.
- Electric field: Ionized electrons drifting from tracks to anode wires which has to do with *deposition* and *drifting*. Modeling electric field using Garfield simulation which has to do with *ducting*.
- Electronic Responses: Matching cold ASIC responses to liquid argon drift speed (1.1 mm/ and simulations of electronic response *digitization*.
- Wire Responses: Convolution of electric field and electronics response. Verifying simulated and measured wire response in wire signals.

3. BEE

Bee is a web-based application used to visualize and display the reconstructed events for LArTPC.

Evaluation of tracks are performed by first using the Wire-

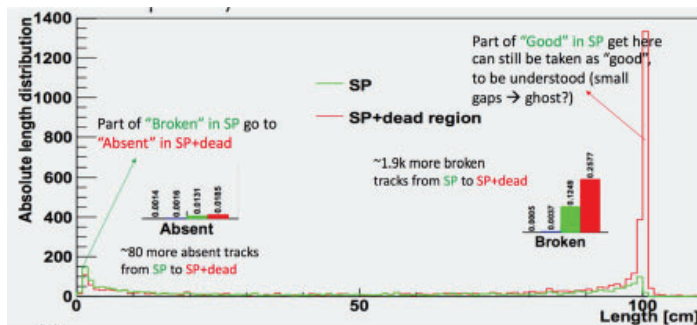


Figure 5: Preliminary representation of broken track length where each piece represents summation of length

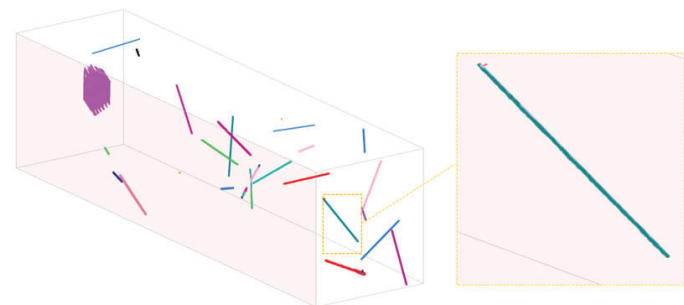


Figure 6: An example of a good track that is considered to be broken from implemented imaging code. [11]

Cell Toolkit to get simulated data followed by Wire-Cell Prototype. BEE is then used to debug and display tracks and understand the outcome if necessary.

III. Evaluation

The basic performance of Wire-Cell Imaging is evaluated by simulating ideal tracks which consists of integrating the following in 20 1-m tracks within TPC volume:

- Uniform 4pi angular distribution and center position distribution: track direction and position.
- Minimum Ionization Particle (MIP): construct ionization signals that have similar neighboring wires magnitude.
- Diffusion, electronics calibration, field and wire response.

A. Track classification

Tracks can be evaluated by first classifying them into different categories:

- Ghosts: no true tracks for reconstructed tracks.
- Broken reconstructed tracks: true track overlaps with multiple reconstructed tracks or single track with length < 95 cm.
- Absent reconstructed tracks: true track overlaps nothing.
- Well reconstructed tracks: true track overlaps with a single reconstructed track and length > 95 cm.

B. Simulation scenarios

- Signal Truth represents the “perfect” signal processing without any inefficiencies and signal represents full TPC simulation. After simulating 800 tracks, there are four different imaging algorithm evaluation:
- Signal Truth + Imaging: perfect with negligible issues.
- Signal Truth + Dead region + Imaging: perfect track reconstruction with couple of ghost tracks.
- Signal + Signal Processing + Imaging: couple of ghost tracks, broken and absent tracks.
- Signal + Dead region + Signal Processing + Imaging: many ghosts and broken tracks.

C. Understand broken track length

In imaging phase, the cause of broken tracks in wire plane viewpoint is expected to be due to inefficient signal processing

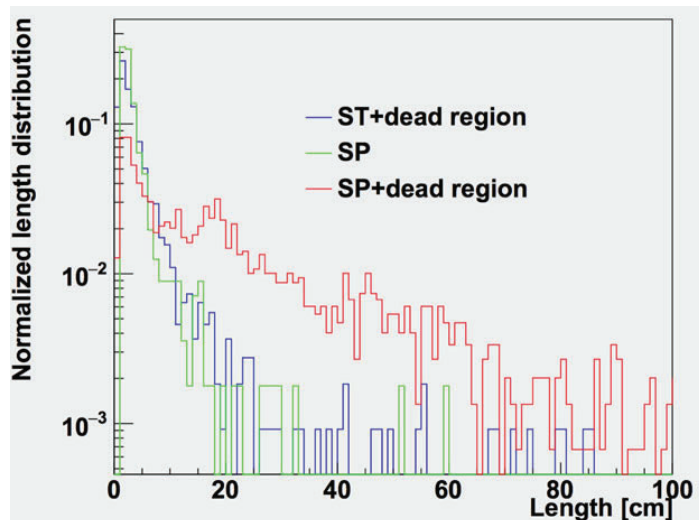


Figure 7: Preliminary representation of the amount of ghosts with length distribution: large amount of ghosts with signal processing and dead region.

for induction planes. As shown in Figure 3, there are approximately 1,900 broken tracks for 800 events. The events are then eye scanned using BEE application to further investigate inconsistencies and make observations on how many different cases of broken tracks exists.

1. First input:

There were a lot of tracks that were being considered broken when it has a good track and a small dot from different tracks as shown in Figure 4. After classifying these tracks as good, there are still about ~1400 tracks that are considered broken.

2. Second input:

Other broken tracks can be classified as being broken when they either have other tracks or cluster-like tracks crossing it or close it.

D. Understand ghosts after clustering

After the above preliminary analysis, imaging and clustering is evaluated. Clustering algorithm identifies the spatial positioning of two dimensional reconstructed hits by using wire and time information to incorporate how charges are clustered together. Ghosts are basically fake charge hits of small clusters that are disconnected from TPC activities.

Most ghosts appear in dead region when dead region is included in the algorithm. Approximately ~60% of ghosts seem to be smaller than 2 cm and large ghost tracks needs to be understood. Ghosts in events seem to be “true” ghosts; ghosts seem to be caused by unresponsive wires instead of bugs in signal processing and imaging code.

IV. Conclusion

From the preliminary results, broken tracks are understood without further clustering. There are imperfect charge matching among wire planes due to noise dominated fluctuation of deconvolved charge. The issue seems to be fixed when clustering is involved. However, there are “long” ghosts which needs further understanding and fixing in the future.

V. Acknowledgments

This project was supported in part by the Brookhaven National Laboratory (BNL), Physics Department under the BNL Supplemental Undergraduate Research Program (SURP). I would also like to thank Mary Bishai, Hanyu Wei, XiangPan Ji, and Xin Qian for teaching, guiding, and supporting me.

VI. REFERENCES

- [1] T. Katori [MicroBooNE Collaboration], arXiv:1107.5112
- [2] C. Rubbia, “The Liquid Argon Time Projection Chamber: A New Concept for Neutrino Detectors,” CERN-EP-INT-77-08.
- [3] V. Meddage [MicroBooNE Collaboration], arXiv:1710.00396 [physics.ins-det].
- [4] M. Mooney, arXiv:1511.01563 [physics.ins-det].
- [5] B. Baller, JINST 12, no. 07, P07010 (2017) doi:10.1088/1748-0221/12/07/P07010 [arXiv:1703.04024 [physics.ins-det]].
- [6] J. Joshi et al. [MicroBooNE Collaboration], arXiv:1511.00317 [physics.ins-det].
- [7] X. Qian, C. Zhang, B. Viren, and M. Diwan ,

arXiv:1803.04850v2 [physics.ins-det].

- [8] E. D. Church, “LArSoft: A Software Package for Liquid Argon Time Projection Drift Chambers,” arXiv:1311.6774 [physics.ins-det].
- [9] Wire-Cell Reconstruction Package, [http://www.phy.bnl.gov/wire-cell/].
- [10] Wire-Cell toolkit, [https://wirecell.github.io].
- [11] <https://www.phy.bnl.gov/twister/bee/set/c284b7db-35f9-4d6b-8345-4e6c3ad18003/event/0/>
- [12] C. Adams et al 2018 JINST 13 P07006.

Integrating X-ray simulation with data acquisition software

Kaleb Swartz

College of Engineering and Computing, Miami University, Oxford, OH 45140

Maksim Rakitin

NSLS-II, Brookhaven National Laboratory, Upton, NY 11973

Abstract

Acquisition software is used at the National Synchrotron Light Source II (NSLS-II) facility specifically so that beamline scientists can conduct their research in a more effective and accurate manner. Bluesky and Ophyd are Python libraries created for data acquisition at NSLS-II, allowing scientists to represent real or virtual motors, detectors, and optics, which can be moved and controlled by the user while also performing scanning procedures. The Synchrotron Radiation Workshop (SRW) is another software module that allows for the simulation of beamline source and optics through its web interface Sirepo, which is viewed as a graphical user interface. The motive for this project was to integrate Bluesky, which was already used at the beamlines, with Sirepo, in such a way as for feedback to result between the configuration of the virtual motors and optics with the visual representation and data provided by Sirepo. This integration was done by creating a Sirepo virtual environment with a local server that communicates with Python programs in such a way as for the simulated data to be accessed and modified over the course of a Bluesky “scan” (experimental procedure). The user is given full control over the tunable optics and parameters for any simulated beamline that is imported into the local Sirepo server. This project will allow for scientists to easily switch between real experimental data acquisition and “virtual” data acquisition

based totally on software (in typical experimental approaches). While the project works for any Sirepo beamline’s optical components, further integration for other aspects of the simulation schema will occur in the future. As an intern, I have gained valuable experience in the realms of: efficient Python programming, understanding version control software, implementing Python data libraries, and critical thinking skills.

I. Background

Sirepo [1] is a browser-based graphical user interface that uses a software module called SRW (Synchrotron Radiation Workshop) to simulate beamlines, with existing simulations coming from a variety of locations including NSLS-II, APS, and LCLS. One has the ability to modify optic parameters while even adding or removing optics from the selected beamline. Whenever a change is made to the simulation, the resulting intensity plots are changed and a new result is shown.

Figure 1 shows how a user can interact with Sirepo, altering the parameter values of the *Aperture* optical element. Any optical elements you see at the top of the image could be added to the beamline definition area which would then alter the resulting intensity reports.

Figure 2 shows the resulting intensity sample report “After Propagation” plot for the NSLS-II CHX beamline. An “after” and “before” propagation plot are shown for any selected beamline.

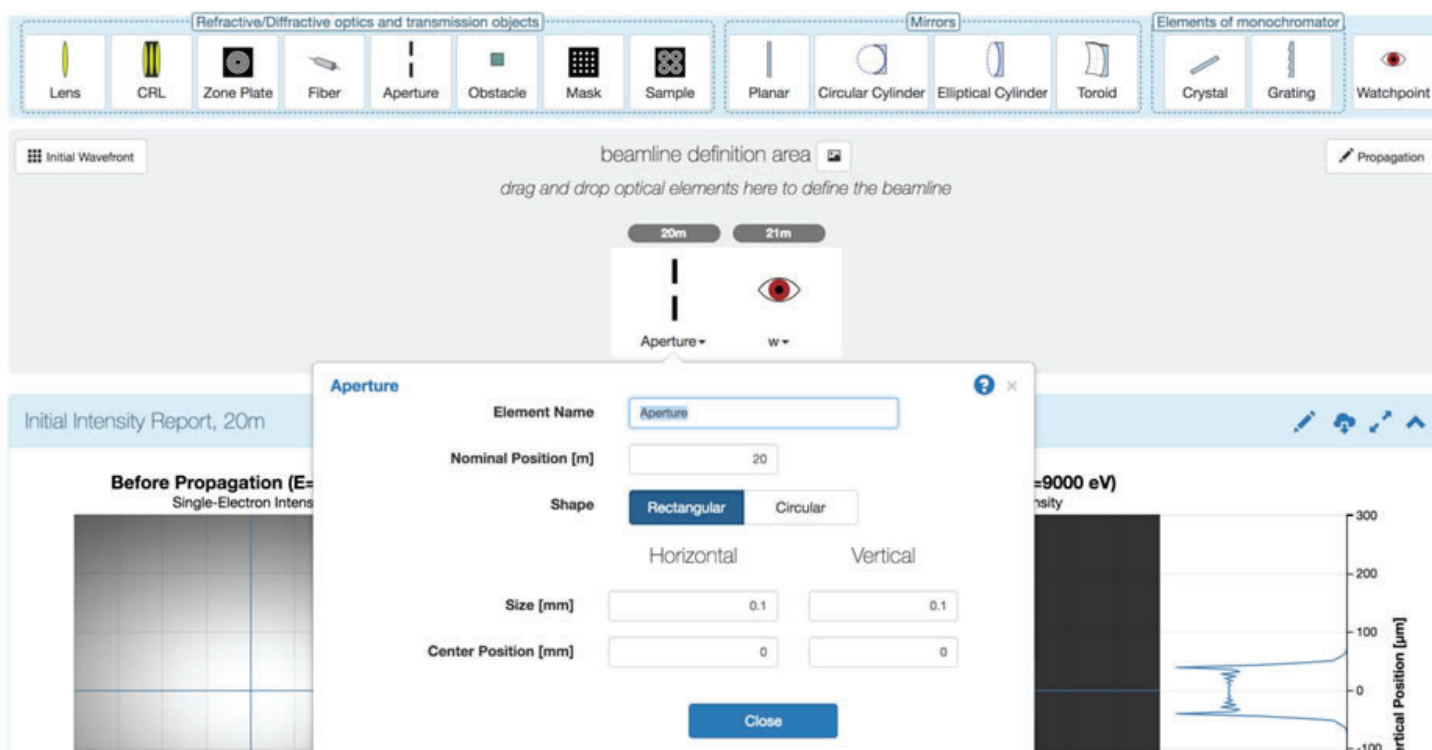


Figure 1: Sirepo browser-based interface [1]

These plots change based on optic parameter values.

Ophyd [2] is a python library that is used for hardware abstraction, enabling a convenient and unified interface with real or virtual motors, detectors, and optics, which can be moved and measured by a user.

Bluesky [3] is a library for experiment control and collection of scientific data and metadata. During the course of a “scan” (experimental procedure), data is collected and saved for the user.

The Databroker [4] Python package provides a simple, user-friendly interface for retrieving stored data and metadata from multiple sources.

II. Introduction

The design and commission of a beamline often require undergoing many simulations to achieve optimal performance. Sirepo addresses this challenge by means of an interactive browser-based graphical user interface, leveraging the existing software solutions for X-ray source and optics simulations. For example, SRW allows one to calculate parameters of the undulator radiation and wavefront propagation with high accuracy based on the Fourier optics approach. On the other hand, beamline staff and users may need to perform a “virtual” experiment before their scheduled experiments at the light source facilities using the data acquisition software already in use. During operations it may also be advantageous to be able to test new scanning and/or alignment procedures virtually to ensure they can be quickly integrated without using valuable “beamtime”. At NSLS-II, APS, and LCLS, a Python based software stack (Ophyd, Bluesky, and Databroker) is used to acquire experimental data. It was considered to be beneficial if the software components could be integrated to allow for Bluesky interaction with Sirepo simulated devices, enabling beamline staff and users to easily switch between real experimental data acquisition (with real X-rays) and “virtual” data acquisition based totally on software. This integration would create a new tool for scientists to prepare for an experiment by running a simulated version of the experiment first or test new features prior to their use.

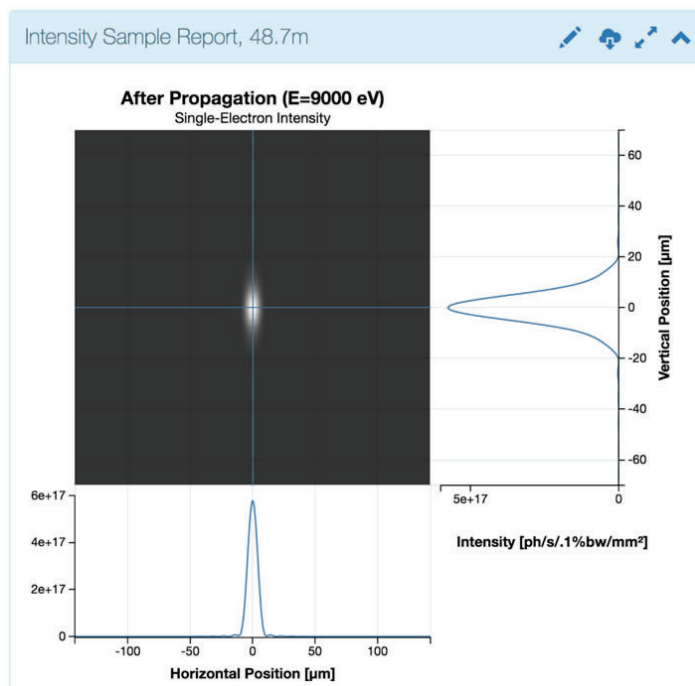


Figure 2: Sirepo resulting intensity sample report

III. Objectives

There were several objectives for this project:

- Implement a convenient interface to Sirepo, allowing an external caller to trigger a simulation;
- Connect the existing virtual Ophyd components to Sirepo, creating feedback between the configuration of the virtual motors and optics and the resultant simulated data fed through the virtual detectors;
- Allow the interface to be used to perform a (multi-dimensional) search of optical parameters of the source and beamline optics by means of custom Bluesky plans, where arbitrary parameters can be used to perform scans with Sirepo/SRW as a “virtual” (or simulated) detector.
- Address exponential growth of experimental datasets and the need for real-time processing as the experimental parameters can be fed to Sirepo simulations, producing results that can adjust the Bluesky adaptive experimental scans by means of on-the-fly feedback, similar to what was done with the on-the-fly tomography data reconstruction [5].

IV. Methods and Materials

Before starting the project, some Python data libraries had to be learned including Matplotlib, NumPy, SciPy, and domain specific library xray-vision. Using xray-vision’s plotting tool, a library called SRW-parser was created allowing for horizontal and vertical 2D cuts to be customized [6].

Figure 3 shows a plot created by SRW-parser using xray-vision. The user has control over location of the horizontal / vertical

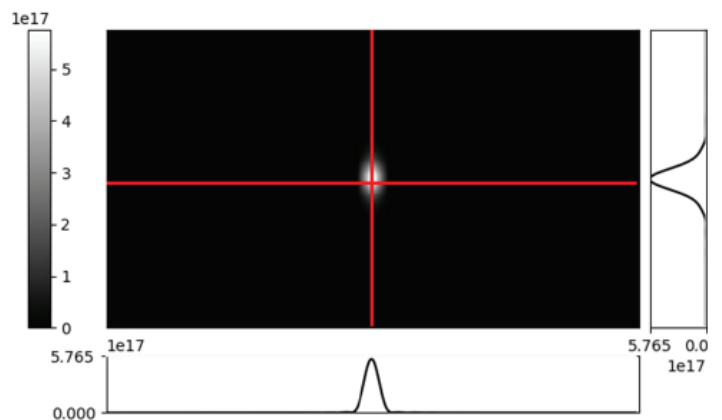


Figure 3: x-ray vision visualizing SRW data

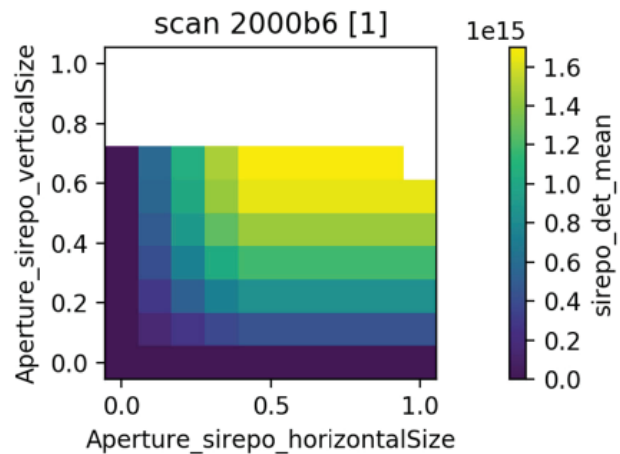


Figure 4: Bluesky scan with virtual Sirepo detector

cuts and can even add labels, an extent, and title to the graph. The .dat file being displayed is directly downloaded from Sirepo.

In order to connect Bluesky and Sirepo, many steps were required. First, an http connection had to be established between the client/server. Once this connection was established, a JSON dictionary of a Sirepo data model could be parsed and read by the client programs. Sirepo components were then created representing the entire list of optics while Ophyd device objects, which are used to represent virtual motors and detectors, were created to represent the optic parameters. The user is then given the option to select specific Sirepo components with their corresponding parameter types. Once selected, any kind of Bluesky scan could be performed using the Ophyd devices.

V. Results

The results of this project are as follows: a user has full control over any Sirepo beamline simulation, allowing them to tune optic parameter values throughout the course of a Bluesky scan. This integration allows for real beamline experiments to be directly compared to a virtual counterpart, while also allowing quick and easy long virtual experimentation.

Figure 4 shows the result of a Bluesky grid scan in which the Sirepo aperture horizontal and vertical positions are changed over a course of 100 scans, which results in this detector mean distribution. The project resides on GitHub [7], and is evolving. This scan shows just a very small amount of the capability of this integration, as this is just an example of one type of Bluesky scan with one optic's parameters being changed. As some beamlines have 10 or so optics with many parameters each, the different kinds of use cases and plots resulting from this integration is extremely large.

Figure 5 shows the current options for a user when performing a Bluesky scan using a Sirepo simulation. Once connected to a Sirepo server, a simulation ID can be found at the end of the URL. After putting this into the program, the selectable optics and parameters are shown which the user can then select. Once selected, these become Ophyd objects and can then be used in a real Bluesky scan.

VI. Discussion and Conclusion

Developing software has always been something that I have wanted to do professionally, and this first real-world experience has been a journey that I will never forget. Learning a new programming language, Python, as well as a variety of data libraries has made me better prepared for learning new things in the future, as well as implementing what I have learned here into my own life.

```
Please enter sim ID: qyQ4yILz
Tunable parameters for Bluesky scan:
OPTICAL ELEMENT:  Aperture
PARAMETERS:      ['verticalOffset', 'horizontalSize', 'title', 'verticalSize', 'horizontalOffset', 'shape', 'position', 'type', 'id']

OPTICAL ELEMENT:  w
PARAMETERS:      ['position', 'type', 'id', 'title']

WATCHPOINTS:     {'w': '21.5'}
Please select optical element: Aperture
Please select watchpoint: w
Please select parameter: horizontalSize
Please select another parameter or press ENTER to only use one: verticalSize
```

Figure 5: User options for scan

This project is not yet complete, but the work done so far is a great foundation for the ultimate end goal. The tool in its current state works with any kind of beamline simulation provided by Sirepo, but is only configured for the beamline optics with corresponding before and after propagation plots. The next step of this project includes making the tool able to handle much more data from the Sirepo schema including all of the plots on the source page of the Sirepo interface. Even in its current state, the project would offer a lot of utility in simulating a beamline experiment. Before an official release however, the user will have more options in tuning the simulation options in the exact way that they want.

VII. References

- [1] Radasoft, *Synchrotron Radiation Workshop*, <https://sirepo.com/srw>
- [2] Brookhaven National Lab, *Ophyd*, <https://nsls-ii.github.io/ophyd>
- [3] Brookhaven National Lab, *Bluesky Data Collection Framework*, <https://nsls-ii.github.io/bluesky>
- [4] Brookhaven National Lab, *Data Broker*, <https://nsls-ii.github.io/databroker>
- [5] Brookhaven National Lab, *Epics*, <https://epics.anl.gov/meetings/2018-06/talks/06-11/BlueSky/Bluesky-at-APS.pdf>
- [6] Brookhaven National Lab, *SRW-parser*, <https://pypi.org/project/SRW-parser>
- [7] Brookhaven National Lab, *Sirepo-bluesky*, <https://github.com/NSLS-II/sirepo-bluesky>

VIII. Acknowledgements

I would first like to thank my mentor, Maksim Rakitin, for all of the time and effort he put in to help me this summer. He took time out of his own work day to teach me new things and ensure that I was always making progress. I would also like to thank Brookhaven National Laboratory and the U.S. Department of Energy for creating such a welcoming and inspiring learning environment. This project was supported in part by the U.S. Department of Energy, Office of Science, Office of Workforce Development for Teachers and Scientists (WDTS) under the Science Undergraduate Laboratory Internships Program (SULI). Special thanks to the DAMA group at NSLS-II and Radasoft LLC for the continued support throughout the project.

Creation of the App Conversion Tool and App Discovery Tool for the centralized deployment mechanism of the NSLS-II control system using Bash and Ansible

Ian Talla

Computer Science, Stony Brook University, Stony Brook, NY 11794

Anton Derbenev

Photon Science, Brookhaven National Laboratory, Upton NY 11793

Abstract

The National Synchrotron Light Source II (NSLS-II) at Brookhaven National Laboratory produces X-ray radiation used for looking at materials at the atomic and molecular levels.¹ The NSLS-II Control System is based on the EPICS infrastructure and much coordination is needed amongst the machinery that makes the accelerator and beamlines function. The goal of this project is to create a set of two applications which will be an important part of the controls software delivery mechanism, SiNgular Application Configuration Kit (SNACK). The App Discovery Tool and the App Conversion Tool will provide a mechanism to increase the automated deployment coverage of the system. The App Discovery Tool will find input-output controller applications (IOCs)² that have not been converted to the SNACK format. Ansible³ scripting language is used for this task because it can automate the searching of IOCs without manual access to any IOC server. Then, the App Conversion Tool will take those IOCs and structure them according to SNACK format (into the directories Configuration, Generated, Source). Bash scripting is used for this task as Bash is good for reading files and moving directories, actions necessary to restructure any IOC. These tools will help developers to make a transition to SNACK as seamless as possible. Widespread usage of SNACK as a software deployment solution will increase the maintainability of the accelerator and beamline machinery. In return, the NSLS-II facility will have more machine uptime and more time for users to operate the beamlines. Because of this project, I am now familiar with Bash scripting, Ansible, modern version control and workflow organizational tools, software requirements management, and have practiced creating programs that standardize the deployment and running of controls applications. In addition, this project has helped me to practice generic coding and machine automation.

I. Introduction

A. The NSLS-II and its functions

The NSLS-II stands for the National Synchrotron Light Source II. Created since 2009 and commissioned since 2013, the NSLS-II was designed to produce the brightest intensity of X-rays to be used as a microscope for scanning materials at the atomic and molecular levels. This level of accuracy means that the NSLS-II is used for many different scientific applications, ranging from block copolymers to organic biochemistry and even nanomaterials. NSLS-II will help find different sources of energy and improve energy usage and energy storage by scanning the bound-

aries of where energy is being transferred and moving energy to improve the efficiency of batteries, turbines and other similar machinery. Improving all of those will help move the world into a new energy age. Besides that, the NSLS-II is open to other people who will need such fine-scale scanning of materials. It is therefore necessary to make the NSLS-II facility run with as minimal disruptions as possible to facilitate all these science experiments.

B. The SNACK kit

NSLS-II is a facility that needs to run machinery for a long time. The software and hardware requires a lot of coordination and the ability to remain online for weeks, if not months, at a time. Having a consistent software delivery and version control strategy is necessary to prevent disasters like losing the data to run hardware because of a power outage or memory failure. The SiNgular Application Configuration Kit (SNACK) aims to establish a centralized deployment solution. It provides a uniform mechanism to deploy any input-output controller (IOC) and shut it down, amongst many other features. Furthermore, SNACK holds information on every input-output controller, providing a centralized configuration reference that is not tied to NSLS-II databases alone. SNACK capitalizes on the fact that any input-output controller will have files that relate to how it will be started up (Configuration), the functions it will perform when running (Source), and files made while running the application (Generated). SNACK runs on Ansible, an automation tool known for reliability. Finally, SNACK works with input-output controllers. Input-output controllers (IOCs) are applications that take instructions from a remote computer and apply them to some hardware and are necessary because they directly connect to the machinery, making them efficient. Many input-output controllers are necessary to make the accelerator and beamlines function.

C. The problems that maintainers of input-output controllers face

While there were no major operating issues associated with deployment practices, there are plenty of potentially problems which can make the facility controls unnecessarily hard to manage, upgrade, and recover. The problem is the haphazard deployment of these IOCs. Structures of IOCs vary because an IOC's functions does not depend on good IOC structure. Because an IOC is not required to have a uniform structure, one will not know where the files that run the IOC go or the information the IOC stores or the autosaved files' location without inspecting the IOC configuration directly. IOCs are kept in a repository, but there is not much ease of redeployment because deployment varies

from IOC to IOC and relies on the individual repository upkeep. Overall, maximum runtime at NSLS-II depends on a lack of accidents and a single person maintaining an IOC for a lifetime. SNACK-deployed IOCs do not have this problem because there is only one deployment path and an IOC is made easier to understand, so anyone can deploy an IOC and know which parts of it do what functions. However, expert developer knowledge is still required for in-depth maintenance and troubleshooting.

A facility-wide conversion to SNACK is a substantial effort as an IOC must be found and then sorted into the Configuration/Source/Generated directories, deciding whether a file is meant to be for startup or for operations while running. The Application Discovery and Conversion Tools take care of finding and then restructuring an IOC to prepare it for SNACK integration.

II. Methods

A. The App Discovery Tool

Because there are close to 900 input-output controllers on the accelerator controls side alone, for SNACK to be useful there must be a way to know at a glance which IOCs have been deployed manually and with SNACK. The App Discovery Tool will inspect a directory that is expected to contain only IOCs and then output a list of IOCs that have been delivered with SNACK and those that have been deployed by other means. The App Discovery Tool will look for a recipe.yml file because SNACK-deployed applications will have a recipe.yml file which have vital deployment modules. This tool will ultimately help the rest of SNACK serve its purpose by making it clear which apps have not been deployed by SNACK. The App Discovery Tool will identify targets for the App Conversion Tool which will make a conversion to SNACK much easier.

The discovery tool is implemented using Ansible, an automation solution well known for consistency and accessing a remote computer without needing Ansible on the remote computer, meaning this tool is really geared towards a quick glance in remote IOC hosts. The tool has a convenient command line interface provided by a bash script.

The App Discovery Tool, despite its name, can be made to function more as a general-purpose reporting utility in practice. This tool can easily be expanded to provide much more information about IOCs. Even considering that this program is supposed to have basic functionality, the discovery tool picks up on unrecognized directories left in an IOC directory. This could be easily extended to report the location of the IOC, its function, the time it has been up, the IOC structure and various other information.

B. The App Conversion Tool

The App Conversion Tool is the tool that aids with restructuring of a given IOC to fit the format of SNACK. SNACK format implies separation of an IOC into Configuration, Source, and Generated files. Configuration files are typically unique to one IOC because they usually set hardware specific parameters, while Source files are used for IOCs of the same type because one driver is usually shared by the same hardware. An example is if there are two IOCs that both control quadrupoles (magnets that focus the line in a perpendicular line to the path traveled), quadrupole IOC 1 would have its own Configuration files and quadrupole IOC 2 would have its own Configuration files, but both quadrupole IOCs would need the same power supply controller driver to interface with the hardware. Meanwhile, both IOCs would have unique

Generated files containing IOC values data. SNACK considers any application to be a combination of configuration, source, and generated files with the cast majority of IOCs following this assumption; it sets up this categorization so that one can easily deploy the application if something disastrous were to happen to the software. In this way is the maintainability of IOCs increases. The App Conversion Tool automates the main part of the IOC structure conversion. Instead of spending significant time on manual file sorting, users can apply the tool to organize the structure of their IOCs according to the format expected by SNACK.

This tool is implemented as a Bash script because Bash is good at reading files and moving directories. The program is also local to an IOC host as opposed to the Ansible-based App Discovery Tool which is meant to reach out to many IOC hosts.

In the future, this tool can be made to send the Configuration and Source directories to the correct repositories, with the Source code part being formatted to fit GitLab repository standards. This step would automate a good amount of the preparation part of deployment, requiring a maintainer/engineer only to set the correct links between files to ensure that the IOC would run.

C. The real convenience of these tools, and how they function within the SNACK workflow

These tools are meant for convenience and automation of a lengthy process of converting IOCs in the controls system to the SNACK format. The convenience of both tools relies on two major assumptions. The App Discovery Tool relies on the fact that any SNACK-deployed IOC has a recipe.yml file which contains vital deployment information. The App Conversion Tool relies on the fact that all IOCs have parts of them that specify how they should be started up, how they should be run after being started up, and files that are generated when the IOC is made and operated. Furthermore, most IOCs do not have different directory structure. These two essential assumptions make the App Discovery Tool and App Conversion Tool simple for both tools to function. It is because of those facts that SNACK can have a recognizable format and therefore automate the separation of files into the Configuration, Source, and Generated files. The App Discovery Tool and App Conversion Tool are not central parts of SNACK; even in terms of deployment, they only cover the first two steps in deploying an IOC with SNACK. It is still the users' job to upload the

The Structure of an Input-Output Controller (IOC)

A normal IOC and an SNACK IOC

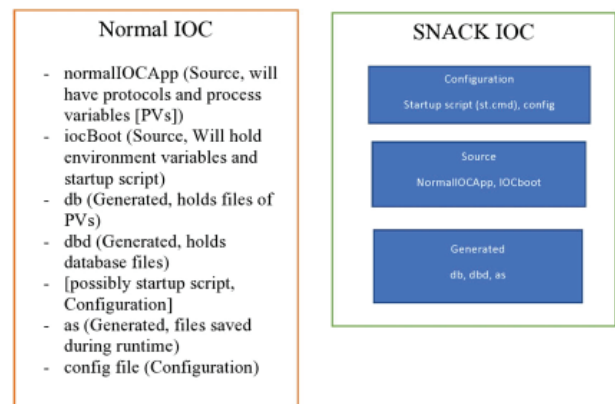


Figure 1: Comparison between a normal IOC and a SNACK IOC

Configuration and Source file to their respective repositories and to set up everything that makes a SNACK deployment possible. However, they do take out the tedium of finding IOCs and sorting directories. My tools are not only convenient but will expand the userbase of SNACK users because my two tools will automate looking for IOCs and facilitate a conversion to the SNACK format.

III. Results

The App Conversion Tool has been tested on production IOCs and has successfully converted those IOCs into a SNACK structure. That tool is estimated to work for all IOCs; most IOC conversions do not have to provide a separate conversion rules file as most IOCs have similar structures.

The App Discovery Tool has been tested on all beamline IOC hosts. It discovered 1244 beamline IOCs, none of which have converted to be deployed with SNACK. It also discovered 77 directories that were not IOCs.

IV. Conclusion

Overall, the App Discovery Tool and the App Conversion Tool provide a necessary convenience upon further usage of SNACK. The App Discovery Tool will check for unconverted IOCs and the App Conversion Tool will convert the normal IOC structure into a SNACK structure; the real importance is that both processes are automated. With such a tedious task cleared, the NSLS-II will benefit from an increased system maintainability after a uniform deployment practice is established because any

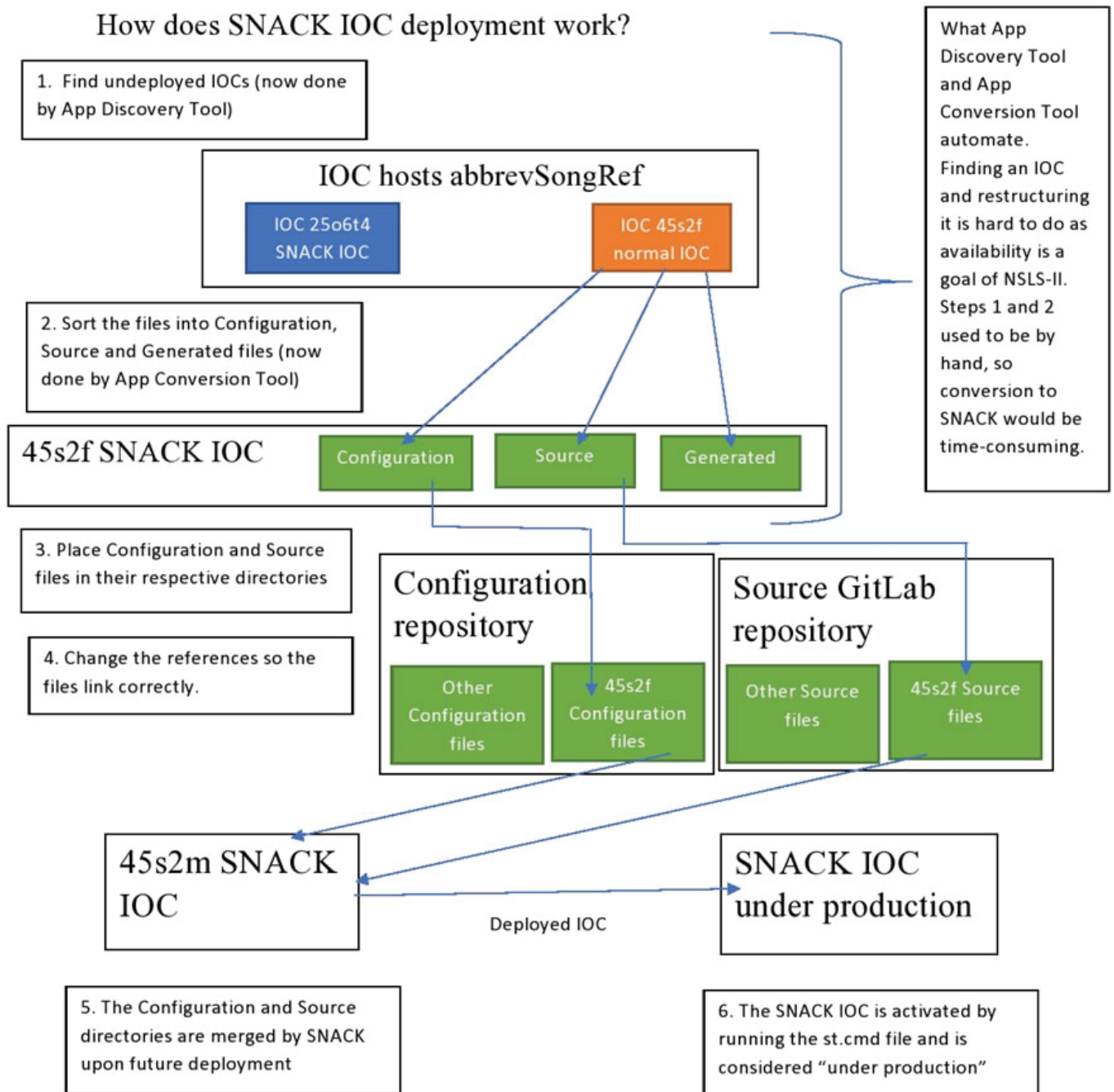


Figure 2: SNACK deployment process.

failures can be recovered from much more quickly. Future beamlines will be able to have that convenience of quick deployment and will have a mechanism to bounce back from software issues with not much struggle. Overall, this project helps the longevity of NSLS-II by making the controls more maintainable.

V. Acknowledgements

This project was supported in part by the U.S. Department of Energy, Office of Science, Office of Workforce Development for Teachers and Scientists (WDTS) under the Science Undergraduate Laboratory Internships Program (SULI).

VI. References

- ¹US Dept. of Energy, Brookhaven National Laboratory. <https://www.bnl.gov/ps/nsls2/about-NSLS-II.php>
- ²M. Kraimer. <https://epics.anl.gov/EpicsDocumentation/AppDevManuals/AppDevGuide/3.12BookFiles/chapter1.html>
- ³Ansible. <https://www.ansible.com/overview/it-automation>

Expression, purification, and characterization of sucrose transporter SUC1 from *Arabidopsis thaliana*

Gianna Trillo

State University of New York College at Oneonta, Oneonta, NY 13820

Desigan Kumaran

Brookhaven National Laboratory, Upton, NY 11973

ABSTRACT

Sucrose transporters (SUCs) transport sucrose, the major carbon source molecule in plants, across plant membranes. Sucrose is produced at photosynthetic source organs (i.e., leaves) and are transported to sink organs like roots and stems. In order to advance carbon storage within plants, sucrose transporters can be targeted and manipulated to increase biomass production. Plant sucrose transporters belong to the major facilitator superfamily (MFS) and are distantly related to hexose transporters in bacteria, fungi, plants and animals. Knowledge about the structural and transport mechanisms at the molecular level is very limited, even though a significant amount of biochemical information is known about these transporters. Determining the structure of the protein requires the expression, purification and crystallization of it. The plant being used within this experiment is *Arabidopsis thaliana*, which has nine different sucrose transporters. The specific gene being analyzed within this experiment is the SUC1 gene. Using autoinduction, SUC1 in *E. coli* was expressed. The cells were then lysed and the membrane fraction was isolated by an ultracentrifuge. The inner membrane fraction was removed by being dissolved in lauryl sarcosine (LSN). The outer membrane fraction was solubilized with 1% dodecyl maltoside (DDM), and then purified by gel filtration followed by hydrophobic interactions chromatography. The purified SUC1 gene was concentrated and crystallization trials were carried out. High-throughput commercial and our homemade crystallization screens were used and applied using the sitting drop vapor diffusion technique. The outcome of this experiment resulted in microcrystals. The next step is to optimize the microcrystal conditions in order to get bigger crystals. Once bigger crystals are obtained, x-ray diffraction at NSLS II can be performed.

I. INTRODUCTION

Sucrose, photo-assimilated carbon, is a source of energy and carbon skeleton for sink organs¹. Sucrose must pass through multiple membranes within a plant, and is considered to be a major determinant of plant productivity and carbon accumulation. The primary structure of sucrose transporters is highly conserved and belong to the Major Facilitator Family (MFS). It is predicted to have 9 transmembrane α -helices. SUCs are necessary to improve plant biomass productivity and sustainability. The objective of this project is to purify the sucrose transporter (SUC1) from *Arabidopsis thaliana* and determine its three-dimensional structure. I have chosen to work with *Arabidopsis thaliana* because it is a model plant system. The structure is needed in order to manipulate the biomass production of the plant through its structural information. To determine the three-dimensional structure, we need to purify and crystallize the transporters.

II. MATERIALS AND METHODS

SUC1 was cloned in pAL vector and was expressed using the autoinduction procedure developed at Brookhaven National Laboratory by Dr. Bill Studier and a glycerol stock of *Arabidopsis Thaliana* SUC1 was provided to start the mini culture. The purpose of the mini culture was to determine if cell growth was a possibility or not. The media that was primarily used within the experiment was MDAG, however, LB media was also tested to see how well the cells would grow within them. 5mL of MDAG solution was added into a tube with 5 μ L of Kanamycin. Next, we began to inoculate the cells and a sample was scratched off of the glycerol stock of SUC1. The sample was then grown overnight in a rotational incubator at 37°C and 200 rpm. 500mL of ZYM 5052 media was then prepared within a flask, and after incubation the following day, it was apparent that cell growth had occurred. The tube was removed from the rotating incubator and within it contained a cloudy liquid. Glycerol stock of the tube was made and stored in -80°C. 2mL of Kanamycin was added into the ZYM 5052 media, as well as 1mL of mini culture stock. The flask containing the ZYM 5052 media was placed in the rotating incubator for 4 hours at 200 rpm and 37°C. After the 4 hours, the incubator temperature was changed to 18°C and remained this way for 45 hours. After 45 hours, the cell cultures were then harvested in a large centrifuge bottle. The bottle was centrifuged for 30 minutes at 14,000 rpm. The supernatant was removed and the cells were stored at 4°C. Lysis buffer was then made to lyse the cell. The reagent used to perform chemical lysis consisted of Bugbuster, in the presence of sodium chloride, lysozyme and DNAase at pH=8.0. 50mL of lysis buffer was added to the pellet, and then stirred with a glass stir rod that was cleaned and prepared for the sample. The purpose of using the glass rod to break up the pellet with the lysis buffer was to get it ready to be homogenized. A homogenizer was then cleaned, and then used to break the cell further, to get rid of any large parts of the pellet. Once the cell was homogenized, it was brought to a microfluidizer to lyse the cells more. It went through the microfluidizer 4 times in order to ensure that all parts of the cell were separated. 20 μ L of the sample was transferred to a 1.5mL microcentrifuge tube for SDS Page gel. Afterwards, the previously homogenized mix was transferred into three centrifuge tubes to be centrifuged at 10°C, going 14,000 rpm for 30 minutes. 20 μ L of the supernatant was then collected for the gel. The remaining supernatant was then transferred into two ultracentrifuge tubes and was spun at 4°C, going 26,000 rpm for an hour and a half. Buffer A was then created to be used as a base buffer. 20 μ L of Buffer A was then added into a 1.5mL microcentrifuge tube with a scratch of the cell pellet that was left over after the supernatant was transferred. After using the ultracentrifuge, the remaining supernatant was collected and stored in a refrigerator. The cell pellet was then resuspended with 5mL of Buffer A and 1% Sodium N-Lauroylsarcosinate (LSN). The remaining

	PEG vs pH - 8/1/18											
	1. PEG 4000	2. PEG 4000	3. PEG 4000	4. PEG 4000	5. PEG 4000	6. PEG 4000	7. PEG 8000	8. PEG 8000	9. PEG 8000	10. PEG 8000	11. PEG 8000	12. PEG 8000
A. Sodium Citrate pH 5	10%	15%	20%	25%	30%	35%	10%	15%	20%	25%	30%	35%
B. Bis-Tris pH 5.5	10%	15%	20%	25%	30%	35%	10%	15%	20%	25%	30%	35%
C. MES pH 6.8	10%	15%	20%	25%	30%	35%	10%	15%	20%	25%	30%	35%
D. Bis-Tris Propane pH 6.5	10%	15%	20%	25%	30%	35%	10%	15%	20%	25%	30%	35%
E. HEPES pH 7.8	10%	15%	20%	25%	30%	35%	10%	15%	20%	25%	30%	35%
F. HEPES pH 7.4	10%	15%	20%	25%	30%	35%	10%	15%	20%	25%	30%	35%
G. Tris pH 8.0	10%	15%	20%	25%	30%	35%	10%	15%	20%	25%	30%	35%
H. Tris pH 8.5	10%	15%	20%	25%	30%	35%	10%	15%	20%	25%	30%	35%

collection was transferred into a 15mL tube and left to rotate overnight. The purpose of the overnight rotation was to dissolve and take out the inner membrane fraction. The inner membrane fraction is the soluble supernatant, while the outer membrane is the insoluble pellet. Afterwards, we dissolved 1% DDM in Buffer A. We also dissolved 0.01% DDM in 250mL of Buffer A to create a sizing buffer to wash the column within the chromatogram. Affinity chromatography was performed to purify the protein. Size exclusion chromatography was then done on SUC1 to analyze the peaks. The protein had contamination so hydrophobic interaction chromatography was completed. The salting out method was used so that any contaminants with a high salt concentration would bind to the column, and only the purified protein would come out. After the chromatograms, the fractions that were involved with the peaks were taken and analyzed through SDS-Page Gel. The sample was later concentrated and set up for crystallization trials.

Crystallization trials were set up using commercial screens from Hampton Research, as well as “homemade” screens. The sitting drop vapor technique was used to carry out the crystallization trials. A list of the screens we used consist of Index-HT, Memb-Fac-HT, PEG RX-HT, PEG vs pH and crystallization screens. The PEG vs pH screen was a homemade 96-well screen, that contained the following:

III. RESULTS AND DISCUSSION

The protein present within the outer membrane and solubilized in 1% DDM fraction was identified and confirmed by using SDS Page gel (figure 1). Different detergents were screened for solubilization and the one that was most efficient was DDM. The SUC1 protein was purified by performing size exclusion chromatography (figure 2). The highest peak present had a retention volume of 14.9 mL, and the peak fractions were analyzed by SDS Page gel (figure 3).

Hydrophobic interaction chromatography was carried out to ensure the purity of the protein (figure 4). The salting out method was used here so that a higher salt concentration would allow SUC1 bind to the column. Microcrystals have begun forming after 5 days from the D5 and D6 conditions of the Hampton Research

PEG 6,000 Grid screen (figure 5). The crystallization conditions are 30% PEG 6000 and Tris pH=8.0, and 30% PEG 6000 and Bicine pH=9.0. We are still in the process of optimization of the crystals, however, when optimization does occur, we will be able to use diffraction quality crystals at NSLS II to determine the true three-dimensional structure of the proteins.

A. Homology Modeling

Homology modeling is the creation of a theoretical three-dimensional protein structure based on the proteins amino acid sequence. The xylose transporter was used as the template to model the SUC1 structure because it was the only structure available in the MFS family. Based on the reference chromatogram, it was concluded that oligomeric state of the protein is a dimer.

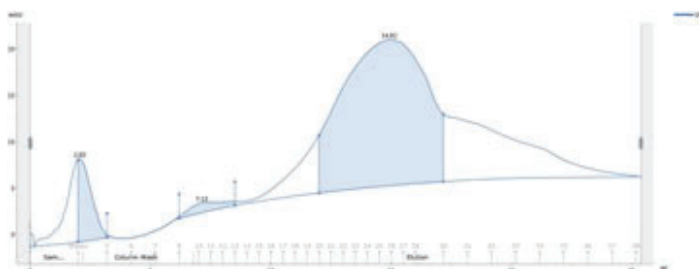


Figure 2. Size exclusion chromatogram

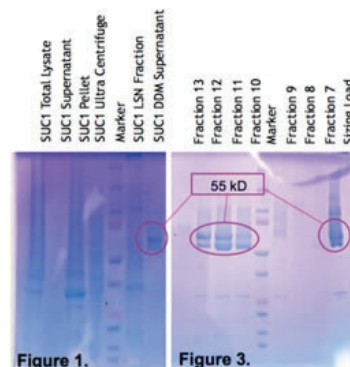


Figure 1. SDS Page Gel to indicate protein is located in outer membrane fraction
Figure 3. SDS Page Gel after size exclusion chromatography

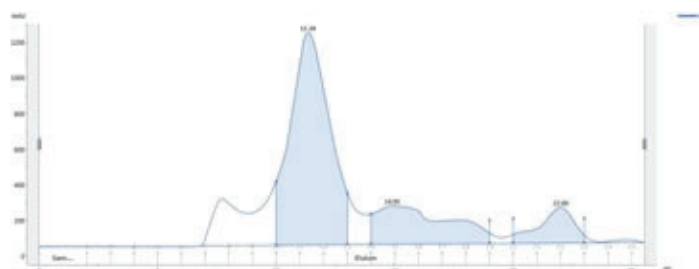
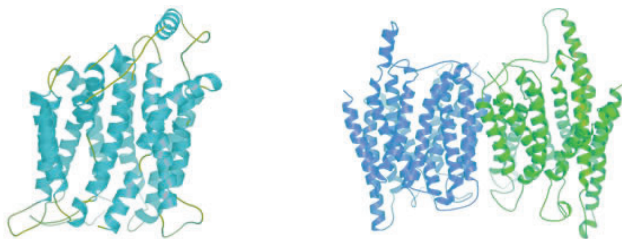


Figure 4. Hydrophobic interaction chromatogram



SUC1 Monomeric Structure SUC1 Dimeric Structure

IV. ACKNOWLEDGEMENTS

I would like to thank my mentor, Desigan Kumaran, for taking me as an intern this summer and allowing me to take part in this amazing project. I would also like to thank Dr. Crysten Blaby, Dr. Ian Blaby and Dr. Miriam Pasquini for allowing me to use their labs and for all of the help while working on this project. This project was supported in part by the U.S. Department of Energy, Office of Science, Office of Workforce Development for Teachers and Scientists (WDTS) under the Science Undergraduate Laboratory Internships Program (SULI).

V. LITERATURE CITED

Studier, F. W. (2018). T7 expression systems for inducible production of proteins from cloned genes in *E. coli*. *Current protocols in Molecular Biology*, e63.
 “Sucrose Transporters in Plants: Update on Function and Structure.” *Egyptian Journal of Medical Human Genetics*, Elsevier, 30 Mar. 2000, www.sciencedirect.com/science/article/pii/S0005273600001425.

VI. APPENDICES

- MDAG Media (100mL)
 - a. 93.70mL H₂O, 200μL .1M MgSO₄, 20 μL 1000x metal mix, 875μL 40% glucose, 800μL 25% aspartate, 2mL 50 X M, 2.8mL amino acid
- ZY Media
 - 1L H₂O, 10g tryptone, 5g yeast
- ZYM 5052 Media
 - 460mL ZY mix, 1mL 1M MgSO₄, 100μL 1000x metal mix, 10mL 50 X 5052, 10mL 50 X M, 500μL 1000x concentrated antibiotic, 500μL culture shock
- Lysis Buffer (120mL)
 - 6mL of 10x bugbuster, 4.8 mL of 1M Tris pH=8, 10mL OF 400mM NaCl, 0.5mg/mL of lysozyme, 1 tablet of protease inhibitor, 600μL of 0.5mM PMSF, 5μL of DNAase, 7.5mL 5% glycerol, and the remainder as H₂O
- Buffer A (1L)
 - 40mL of 40mM Tris pH=8, 80mL of 400mM NaCl, 62.5mL of 5% glycerol, 5mL of 10mM imidazole, 500μL DTT, remainder as H₂O
- Kanamycin
 - 5μL of 5000x kanamycin
- 1% LSN with Buffer A (30mL)
 - 300mg Sodium-N-Lauroylsarcosinate, 40mL Buffer A
- 1% DDM with Buffer A (30mL)
 - 300mg DDM, 30mL Buffer A
- 0.1% DDM with Buffer A (250mL)
 - 25mg of DDM, 250mL Buffer A



Figure 5. Microcrystals of SUC1 obtained from Hampton Research PEG 6,000 Grid Screen. Crystals were obtained even though different high-throughput crystallization screens like MembFac, PEGRx, Index and Crystal screens were set up. The crystals are still growing but are too tiny to mount and check with X-ray diffraction at NSLS II. The structure of SUC1 can be determined if better diffraction quality crystals are obtained.

Evaluation of the ACQ1001-FMC Digitizer

Abby Tse

Department of Computer Science, Fordham University, Bronx, NY 10458

Yong Hu

Department of Photon Science, Brookhaven National Laboratory, Upton, NY 11973

Abstract

The currently installed digitizer, ICS-710, used for measuring beam intensity at the National Synchrotron Light Source (NSLS-II), has reached its end of life. As a result, we have purchased a new digitizer, ACQ1001-FMC (24-bit), and evaluated its performance in this study. Unlike the ICS-710, the ACQ1001-FMC comes with embedded EPICS (Experimental Physics and Industrial Control System) IOCs (Input/Output Controllers) providing all the process variables (PVs). We manipulate those PVs through Control System Studio (CSS), which enables us to assess the digitizer's resolution, accuracy, and precision. Noise and distortion adversely affect the digitizer's performance so we investigate it by measuring the effective number of bits (ENOB). We have accomplished this by connecting a terminator to one of the channels and used Python/NumPy to compute the ENOB. In order to evaluate the digitizer's accuracy and precision, we have also examined the voltage linearity. A precise DC calibrator provides voltages ranging from -10 to 10 volts into one of the channels. We collect the readbacks and plot them with Python's polyfit function. Throughout the study, four trials have been conducted to determine the ENOB and the linearity. The measured ENOB and linearity coefficient are consistently 19.73 bits (~ 20-bit) and 0.9995 (very close to 1.0), respectively. The results of this study show that the ACQ1001-FMC digitizer is a good fit for replacing the ICS-710 because, despite the noise and distortion, it is precise, accurate, and has high resolution.

I. Background

The NSLS-II is a third-generation synchrotron facility that provides ultra-bright light with exceptional beam stability and a broad energy range (from infrared to hard x-ray). The creation of this bright light originates from the linear accelerator (linac) where the electron gun generates electrons and accelerates them to 200 MeV. The transport system then carries these electrons

to the booster ring where they expedite to 3 GeV. Subsequently, the transport system sends these electrons to the storage ring where 500mA of current (at 3 GeV) circulate. Eventually, they pass through superconducting bending magnets known as undulators to produce synchrotron radiation. Ultimately, the beamlines capture this radiation and use it to image samples across different disciplines [Ablett et. al. 2006]. A schematic of the major components of the NSLS-II is shown in figure 1.

At each of the accelerators (linac, booster ring, and storage ring), sensors are emplaced to measure the charge and current of the electrons. The data that the sensors gather is in the form of analog signals. For the central processing unit (CPU) to interpret these signals, we need to convert them to digital data. Digitizers perform this conversion through a process called pulse code modulation (PCM), as illustrated in figure 3. In this process, the signals are first sampled (based off of Nyquist's theorem), then quantized (to reduce data size), and finally encoded to binary. This conversion ultimately enables software programs such as EPICS and CSS Studio to monitor and display the conditions of the accelerators.

II. Hardware Specifications

In this study, we examine the ACQ1001-FMC digitizer, manufactured by D-TACQ solutions. This digitizer is made up of two parts: the ACQ1001 carrier and the ACQ430FMC analog input module. The ACQ1001 carrier is a shortbread design which compacts the digitizer circuitry into a simple rectangular box. It encompasses a single slot field programmable gate array (FPGA), Xilinx ZYNQ Soc Z-7020, which runs on Linux [Milne, 2014]. The carrier also connects to the console, ethernet, and a 12V DC supply through the front panel. The rear panel consists of eight

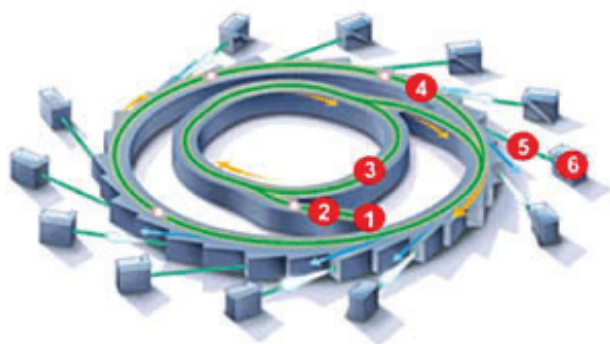


Figure 1- Major components of the NSLS-II: (1) electron gun, (2) linear accelerator, (3) booster ring, (4) storage ring (5) beamlines (6) workstation. Source: <https://www.bnl.gov/nsls2/images/synchrotron.gif>

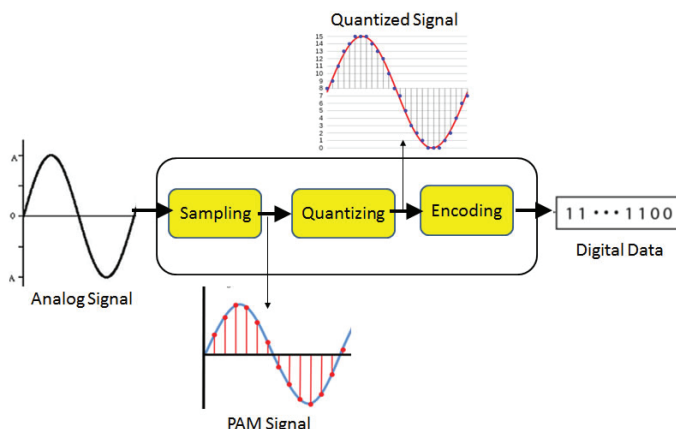


Figure 2- Pulse code modulation Source: <https://blogs.synopsys.com/vip-central/files/2015/04/PCM.png>

ACQ430FMC analog input channels that sample at a high speed of 128k bits per second (bps) [Milne, 2015]. The specification of the ACQ430FMC is shown in figure 3.

Additionally, the rear panel has three LEDs to indicate functionality: CLK, TRG, and ACT.

- CLK lights green to indicate the usage of a valid clock signal
- TRG lights green to indicate usage of a valid trigger signal
- ACT flashes green to indicate detection of Linux activity.

The images of the front and rear panels are shown in figure 4.

III. Connectivity

We first establish communication to the digitizer through the console. Subsequently, the terminal emulator program, Minicom, facilitates the login to root, enabling the setup of a static IP address. This IP address establishes a transmission control protocol (TCP) allowing the exchange of data through channel access. D-TACQ solutions provide an easy method to control the digitizer. They have a repository on GitHub containing operator interfaces (OPIs) that are compatible with CSS. These OPIs connect to and graphically display all the PV values embedded in the FPGA. After running the simulation, we abstract the values of the PVs through EPICS using the “caget” command. A schematic of this

#	Parameter	Value
1	Number of Channels	8
2	Sample Rate	Per channel simultaneous
	High Speed Mode	128 kHz
	High Resolution Mode	52 kHz
3	Resolution	24 bits
4	Coupling	DC, Differential Input
5	Input Impedance	1MΩ
6	Input Voltage Range	±10 V
7	Input Voltage Withstand	±30V
8	Offset Error	0.01% FS with numerical calibration
9	Gain Error	0.01% FS with numerical calibration
10	INL	±0.002% FS
11	CMRR	>60dB FS @ 1 kHz
12	THD	-106 dB*
13	SFDR	107 dBc*
14	SNR	
	High Speed Mode	104 dB*
	High Resolution Mode	108 dB*
15	Analog Input BW	80kHz
16	Crosstalk	<90dB @ 1kHz FS Input
17	Digital Filter:Pass Band	0.453 Fsample
	Digital Filter:3dB	0.490 Fsample
	Digital Filter:Stop Band	0.547 Fsample
	Digital Filter:Attenuate	95 dB

* Typical values measured at full scale with a 9.76kHz input

Figure 3- Performance specification of the ACQ430FMC [Milne, 2015]



Figure 4- View of the front panel (left) and rear panel (right) of the ACQ1001-FMC digitizer

process is shown in figure 5. We use this platform to perform the resolution and voltage linearity tests.

A. Resolution Test

The effective number of bits (ENOB) examined in the resolution test, evaluates how the internal and external noise affects the digitizer’s performance. We study internal noise by connecting a terminator (figure 6) to one of the channels, thereby eliminating external noise.

This test is run on the CSS Studio Volts Live Plot OPI and we collect the values with EPICS. Once the configuration is set up, the simulation is run for about ten minutes before the data condenses into a text file. We perform the tests and analyze the results across four days. Using Python, we take the values from the text file and find the standard deviation (figure 7) of it.

We plug the standard deviation as “rms noise” into the formula, $ENOB = N - \log_2(\text{rms noise}/\text{LSB})$, and compute the ENOB. To further our studies, we plot a fast Fourier transform (fft) graph with NumPy.

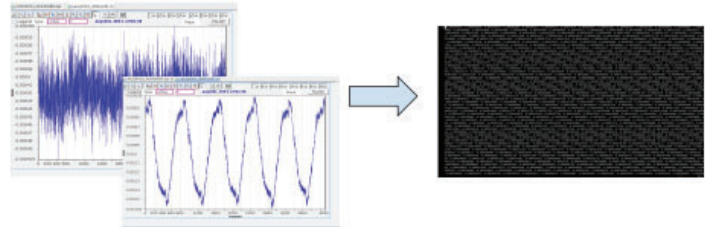


Figure 5- Schematic of how EPICS retrieves 4,096 voltage samples through the “caget” command and puts it into a text file.

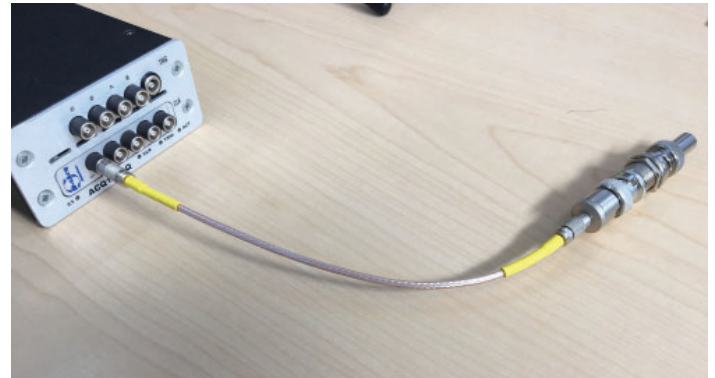


Figure 6- Terminator connected to channel one of the ACQ1001-FMC

$$\sigma = \sqrt{\frac{\sum (X - \bar{X})^2}{n - 1}}$$

Figure 7- Standard deviation formula

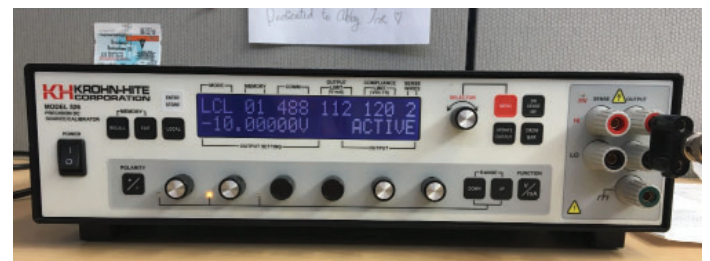


Figure 8- DC Calibrator

B. Accuracy and Precision Test

In the accuracy and precision test, we examine voltage linearity. A precise DC calibrator (figure 8) connects to one of the channels and feeds in voltages ranging from -10 to 10 Vs. Similar to the previous test, the simulations are run on the CSS Studio Volt Live Plot OPI. We collect the readbacks every 1 V and use EPICS to compress the data into a text file. We gather the data for four days and compute the average of each data set with Python. These averages are then put into a comma separated value (csv) file. Using the polyfit function in NumPy, we graph the line of best fit and incorporate error bars. Finally, we abstract the linearity coefficients from the graph.

IV. Results

A. Effective Number of Bits

Date	June 29	July 5	July 6	July 10
With terminator	19.72671775	19.7348454	19.69047274	19.73076437
Without terminator	14.47750989	15.95844621	16.87532671	15.70751698

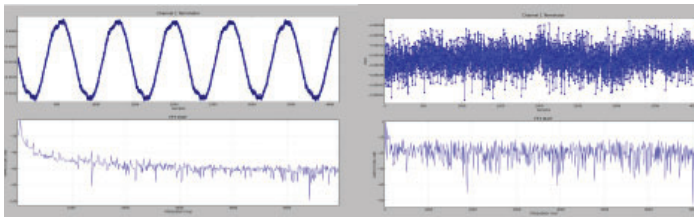


Figure 9- Table of the computed ENOB with and without a terminator, across four days.

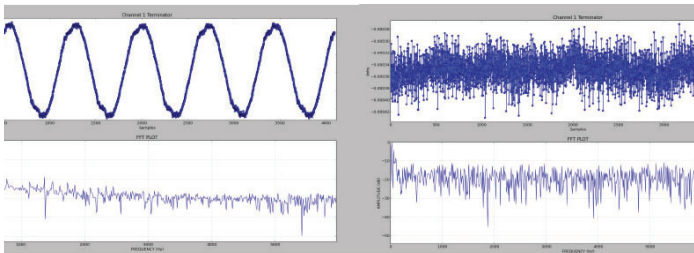


Figure 10- June 29th's fft plots without a terminator (right) and with a terminator (left)

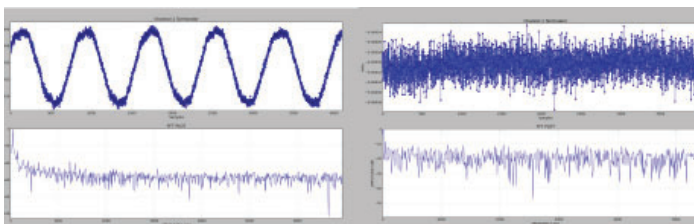


Figure 11- July 5th's fft plots without a terminator (right) and with a terminator (left)

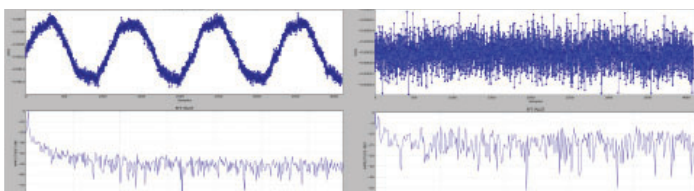


Figure 12- July 6th's fft plots without a terminator (right) and with a terminator (left)

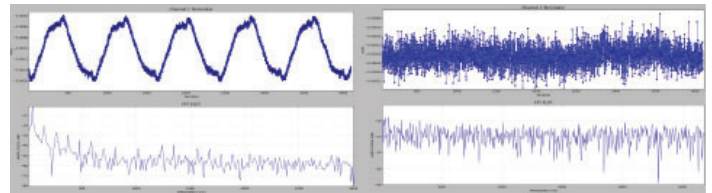


Figure 13- July 10th's fft plots without a terminator (right) and with a terminator (left)

B. Voltage Linearity

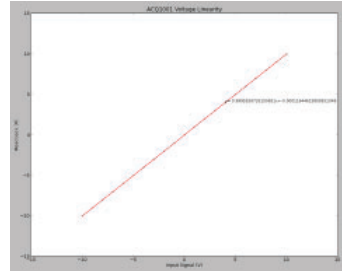


Figure 14- July 3rd's voltage linearity data

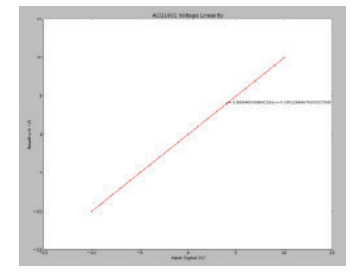


Figure 15- July 5th's voltage linearity data

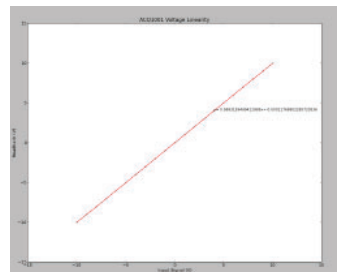


Figure 16- July 6th's voltage linearity data

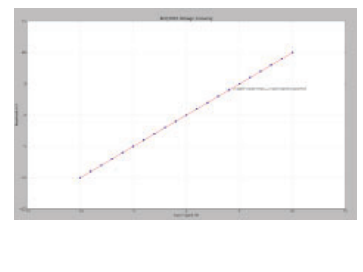


Figure 17- July 10th's voltage linearity data

V. Discussion

Across the four days of testing, the terminator ENOB consistently reports 19.73 bits (~ 20-bit). We hypothesize that the noise and distortion come from the differences in grounding. The digitizer grounds with its 12V DC supply whereas the CPU grounds with a power outlet. These two grounds conflict because they are

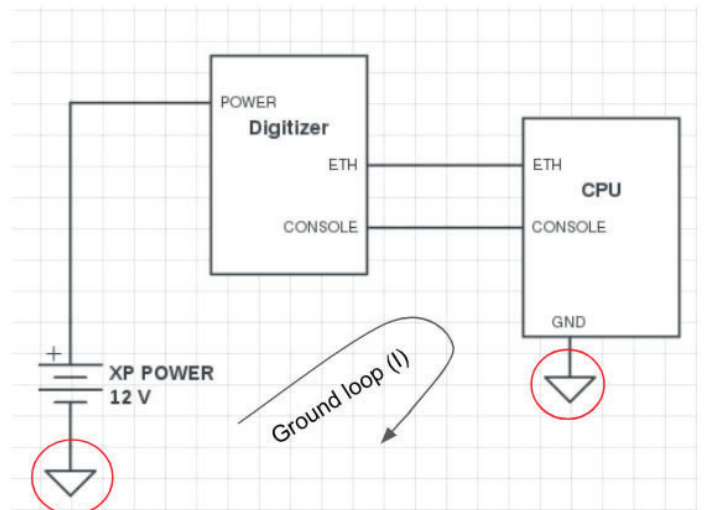


Figure 18- Ground loop between the CPU and the digitizer

at different potentials, thus creating a ground loop (galvanic path). This ground loop is the probable cause of the voltage fluctuations we call noise. A schematic of this ground loop is shown in figure 18.

On the other hand, the ENOB without a terminator varies across the four days. It is difficult to determine why we observe this variation because we did not record how loud the external background noise was. However, interestingly, on July 6th, the ENOB without a terminator is the highest and the ENOB with a terminator is the lowest. On that day, we note that it was raining and the humid air could contribute to the lower terminator ENOB.

The fft plots show that the noise averages around 50-60 dB without the terminator and 10-20 dB with the terminator. Subtracting the 50-60 dB of overall noise with the 10-20 dB of internal noise, we presume that 40-50 dB of noise is external noise. Furthermore, this suggests that 10-20 dB of internal noise is the cause of the net loss of approximately 4 bits of resolution, resulting in a 20 bit ENOB.

The voltage linearity coefficients are consistently 0.9995, with one value being 0.9993 on July 6th. The reason for this could be the same reason that on the same day we report the terminator ENOB to be lower than the rest of the days (due to humidity). However, overall the coefficients across the four days show that the ACQ1001-FMC is a precise and accurate digitizer because the linearity coefficients are very close to 1.

VI. Conclusion

The ENOB is very close to 20 bits, with only a loss of 4 bits due to internal noise and distortion. Additionally, we can describe the voltage linearity curve with a first-degree polynomial. These results support that the ACQ1001-FMC is a precise, accurate, and high-resolution digitizer because it exceeds the performance of the currently installed digitizer (ENOB= 17 bits). Therefore, we believe that the ACQ1001-FMC is a good fit for replacing the ICS-710.

X. Appendix

```
1 import numpy as np
2 from math import sqrt
3
4 def mean(lst):
5     """calculates mean"""
6     sum = 0
7     for i in range(len(lst)):
8         sum += lst[i]
9     return (sum / len(lst))
10
11 def stddev(lst):
12     """calculates standard deviation"""
13     sum = 0
14     mn = mean(lst)
15     for i in range(len(lst)):
16         sum += pow((lst[i]-mn),2)
17     return sqrt(float(sum) / (len(lst) - 1))
18
19 data = np.loadtxt('noisy.txt')
20
21 print stddev(data)
```

Figure 19- Python code to calculate the standard deviation

VII. Further Work

We could perform supplementary tests to enhance our understanding of the digitizer. One test that would be essential to understanding the July 6th deviation would be the thermal drift test. This test would enable us to assess whether we could use the digitizer for thermal-sensitive applications or whether we need to implement temperature compensation means. Moreover, since the digitizer's function at NSLS-II is to measure beam intensity, it would be crucial to perform the beam loss monitor (BLM) stimulator test in further studies. This stimulation would allow us to assess whether the digitizer meets the resolution requirements.

Other enhancements to this study would be to continue to perform the tests for longer, allowing us to see if its performance is stable. Additionally, we could perform a comparison study to see how this digitizer's performance contrasts with others on the market.

VIII. Acknowledgements

This project was supported in part by the U.S. Department of Energy, Office of Science, Office of Workforce Development for Teachers and Scientists (WDTS) under the Science Undergraduate Laboratory Internships Program (SULI). I would like to give special thanks to my mentor, Yong Hu and Brookhaven National Laboratory for their hospitality.

IX. References

- Ablett, J, et. al. *Conceptual Design Report National Synchrotron Light Source II*. Brookhaven National Laboratory , Dec. 2006, www.bnl.gov/nsls2/project/CDR/NSLS-II_Conceptual_Design_Report.pdf.
- Milne, Peter. *ACQ1001, ACQ1002 Hardware Installation Guide*. D-Tacq Solutions Ltd., Apr. 2014, www.d-tacq.com/resources/InstallationGuides/ACQ1001_Installation_Guide_Rev_3.pdf.
- Milne, Peter. *ACQ430FMC Product Specification*. D-Tacq Solutions Ltd., 14 Jan. 2015, www.d-tacq.com/acq400ds/acq430fmc-product-specification.pdf.

```
1 import numpy as np
2
3 data = np.loadtxt('neg10V.txt')
4
5 mean =np.mean(data)
6
7 print mean
```

Figure 20- Python code to compute average

```

1 import numpy as np
2 import matplotlib.pyplot as plt
3 import csv
4
5 #open the comma-separated values (CSV)
6 with open("Dc.csv", "r") as f:
7     data = [row for row in csv.reader(f)]
8     xd = [float(row[0]) for row in data]
9     yd = [float(row[1]) for row in data]
10
11 # sort the data
12 reorder = sorted(range(len(xd)), key = lambda ii: xd[ii])
13 xd = [xd[ii] for ii in reorder]
14 yd = [yd[ii] for ii in reorder]
15
16 # make the scatter plot
17 plt.grid (color='b', linestyle='-', linewidth=0.1)
18 plt.scatter(xd, yd, s=30, alpha=.9, marker='x', color="g")
19
20 # determine best fit line
21 par = np.polyfit(xd, yd, 1, full=True)
22
23 slope=par[0][0]
24 intercept=par[0][1]
25 xl = [min(xd), max(xd)]
26 yl = [slope*xx + intercept for xx in xl]
27
28 # coefficient of determination, plot text
29 variance = np.var(yd)
30 residuals = np.var([(slope*xx + intercept - yy) for xx,yy in zip(xd,yd)])
31 Rsqr = np.round(1-residuals/variance, decimals=4)
32 plt.text(.9*max(xd)+.5*min(xd), .9*max(yd)+.5*min(yd), 'y= ' +str(slope) + 'x+' +str(intercept), fontsize=10)
33
34 print "variance =", float(variance)
35 print "residuals =", float(residuals)
36 print (slope,intercept)
37
38 #label the graph
39 plt.xlabel("Input Signal (V)")
40 plt.ylabel("Readback (V)")
41 plt.title('ACQ1001 Voltage Linearity')
42
43 # error bounds
44 yerr = [abs(slope*xx + intercept - yy) for xx,yy in zip(xd,yd)]
45 par = np.polyfit(xd, yerr, 2, full=True)
46
47 #yerrUpper = [(xx*slope+intercept)+(par[0][0]*xx**2 + par[0][1]*xx + par[0][2]) for xx,yy in zip(xd,yd)]
48 #yerrLower = [(xx*slope+intercept)-(par[0][0]*xx**2 + par[0][1]*xx + par[0][2]) for xx,yy in zip(xd,yd)]
49
50 plt.plot(xl, yl, 'r')
51 plt.errorbar(xd, yd, yerr, fmt='o')
52 plt.show()

```

Figure 21- Python code to plot the voltage linearity graph

```

1 import numpy as np
2 from numpy.fft import fft
3 from numpy import log10
4 from pylab import subplot, plot, show, grid, xlabel, ylabel, title
5 import matplotlib.pyplot as plt
6
7 numpt = 4096
8 fclk= 43407.5
9 Doutw = np.loadtxt("noiseless.txt")
10
11 subplot(211)
12 plot(Doutw[:4096], '-o')
13 xlabel('Samples')
14 ylabel('Volts')
15 title('Channel 1 Terminator')
16
17 Dout_spect=fft(Doutw)
18 Dout_dB=20*log10(abs(Dout_spect))
19 maxdB=max(Dout_dB[1:numpt/2])
20 subplot(212)
21 plot(np.arange(0, numpt/2-1)*fclk/numpt, Dout_dB[1:numpt/2]-maxdB)
22
23 title('FFT PLOT')
24 xlabel('FREQUENCY (Hz)')
25 ylabel('AMPLITUDE (dB)')
26 grid ('on')
27
28 show()

```

Figure 22- Python code for the fft plot.

Analysis of the Data Challenge 2 catalogs generated for the Large Synoptic Survey Telescope by the Dark Energy Science Collaboration using the Friends-of-Friends catalog matching algorithm.

Bhairav Valera

Department of Physics, College of Engineering, University of Illinois at Urbana-Champaign, Urbana, Illinois, 61801
Anže Slosar

Department of Physics, Brookhaven National Laboratory, Upton, New York, 11973

Abstract

Commissioned by the Dark Energy Science Collaboration (DESC) for the Large Synoptic Space Telescope (LSST), Data Challenge 2 (DC2) is the second generation of the LSST Data Management System (DMS) that contains catalogs that archive information about Deep-sky objects such as star clusters, nebulae, and galaxies. Information about an object includes, but is not limited to, right ascension, declination, parallax, radial velocity, and apparent magnitude. The purpose of DC2 and indeed, other data challenges, is to combine scientific algorithms into a general DMS that meets the data processing goals of the LSST. My research deals with testing the functionality of one such algorithm: Friends-of-Friends (FoF) catalog matching, which takes objects in the input catalog and the output catalog and matches them by grouping them based on linking length. The main method of testing was writing Python code that produced plots and graphs of the results from the FoF algorithm. Research is still ongoing, but these plots have given us a promising picture about the viability and correctness of the FoF algorithm and demonstrated its use in a broader DMS.

I. Introduction

The LSST is an extremely large and complex project undertaken by the DESC. After first light in 2019, the telescope will conduct a wide, fast, deep survey of the sky covering 18,000 square degrees. 40 billion objects will be documented corresponding to approximately 50 petabytes of data. A Data Management system or general processing framework is thus required to analyze the vast amount of data. Additionally, testing the viability of a variety of processing algorithms must also be done in order to ensure bug-free results. In order to test the processing algorithms, mock data was generated using N-body simulations that included the effects of Dark Matter Halos on galaxy clustering, weak lensing, gravitational effects, etc. This mock data represented an input catalog with each data point representing an astronomical object and its identifying information such as right ascension, declination, magnitude (brightness), and red shift. After performing other simulations that account for atmospheric turbulence, expansion, and other factors on the input catalog, an output catalog was produced with the same objects, but different data point values. The FoF Catalog Matching algorithm was then written in order to match the input and output catalogs.

II. Methods

The main methods used in testing the FoF algorithm was the

Python programming language interpreted on the Jupyter Development platform. Due to the size of the data, we used the Cori Supercomputer at the National Energy Research Scientific Computing Center (NERSC) in order run Python notebooks quickly and efficiently. Several Python libraries were used to improve the functionality of our notebooks. They include NumPy, which adds support for matrices, arrays, and higher level mathematical functions, SciPy, which adds plotting, fitting, and image processing, AstroPy, which allows for data tabulation and celestial coordinate transformations, and finally, GCR, or Generic Catalog Reader, which accesses table-like catalogs, allows flexibility with modifying the data, and returns results in an efficient manner.

III. Results

The results as found from the preliminary testing showed promise regarding the FoF algorithm's use in LSST's data management system. Beginning with figure 1, this plot is a 2D histogram showing the frequency of which pairs were matched correctly. The scale was logarithmic, the horizontal axis represents the number of input catalog objects and the vertical axis, the number of output catalog objects. It is evident that most of the objects have a one-to-one match. This is what is desired using a linking length of 1 arc second, that is, the input object was, at the most,

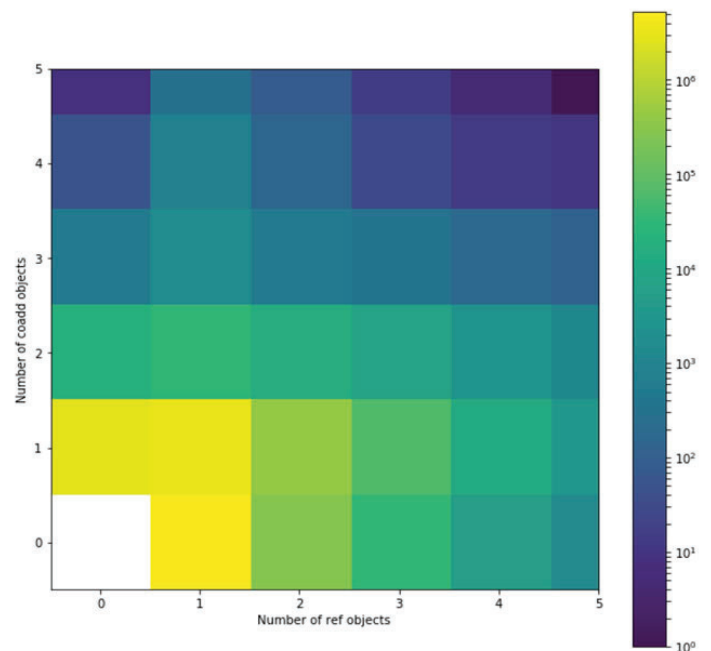


Figure 1.

separated from any member of the output catalog by a sweep of 1 arc second. There are however, some input catalog objects that did not get matched with any objects in the output catalog. The one-zero bin represents objects that existed in the input catalog, but remained undetected in the output catalog. This is because the simulated output catalog does not cover the full range of the input catalog. Additionally, detection efficiency of the FoF algorithm is not 100%, which leads to some objects in the output catalog that otherwise would have been matched, to remain lost. Finally, some sources are very faint and thus, aren't picked up at all when reading through the catalog, but they still remain included because they have an impact on other measurements involving weak gravitational lensing.

The same goes for the objects in the zero-one bin. They represent fake detections, that is members of the output catalog that don't have a corresponding input catalog match. This occurs because of two reasons: 1) the data contains many points, and thus, a lot of noise along with it. This noise creates fluctuations in the brightness of the objects in the output catalog. The brightness of an object directly correlates with its detection ability, so the smaller its brightness due to fluctuations, the more likely it is to not be detected. 2) Extra artifacts such as scattered light due to atmospheric effects, bleed-off from bright stars, and cosmic rays such as those ejected from gamma ray bursts and quasars, also appear to act like extragalactic objects, thus "creating" objects that are not really there. To deal with these fake objects, one must manually remove them from the zero-one histogram bin.

Furthermore, objects in the two-one and two-two bins (actually any bins that have more than one object) represent undetected blends. Blending is the phenomenon in which two or more astronomical objects overlap due to their position in the sky being less than 1 arc second apart. These objects get grouped together regardless of the number of objects present or their true location. Additionally, lensing effects also are involved. Gravitational lensing occurs when light passes through a gravitational field, and thus, spread out across a wide area of space. This has the effect of

"creating" more objects within each group than there actually are. In order to counteract the effects of blending and to properly sort the objects into their respective input and output bins, a photometric deblending algorithm must be implemented.

Moving onto figure 2, further evidence of the FoF algorithm's viability is seen when plotting the change in the right ascension and declination of the coordinates for the one-one bin, that is, the coordinates for all objects that have matched perfectly. It is seen that most of the points center around a zero delta for the right ascension and zero delta for the declination, that is, the points that have input and output matches have nearly identical right ascension and declination coordinates. This is the expected result, and additionally, implies that the objects in the input and output catalog are indeed the same.

Figure 3 histograms the angular coordinate separation between all of the input and output objects in the one-one bin. Most of the points show very small separation with very few showing separation close to 1 arc second. This is an important statistic because it demonstrates that FoF algorithm indeed only matches points that are only linked below the 1 arc second threshold. The 1 arc second threshold is important because if the linking length becomes too large, the algorithm will start to merge all points in the input and output catalog regardless of whether or not they are supposed to be matched, that is, blend objects together.

Moving onto figure 4, $y = axe^{-bx^{0.88}}$ this is a semilog plot of the histogram in figure 3 fitted with an exponential function in the form: where A and B are the constants, 162014.200 and 14.904 both having units of inverse arc seconds. This exponential function creates a good model for predicting the number of points given an angular separation variable. Notably, many of the points will be separated by very small angular sweeps and that the number of points that are separated by longer distances will die off like a negative exponential function, that is, it is less likely to find more points at higher angular distances.

Moving on, LSST is an optical telescope that has 6 different bands of operation: U, G, R, I, Z, and Y, ranging from short to

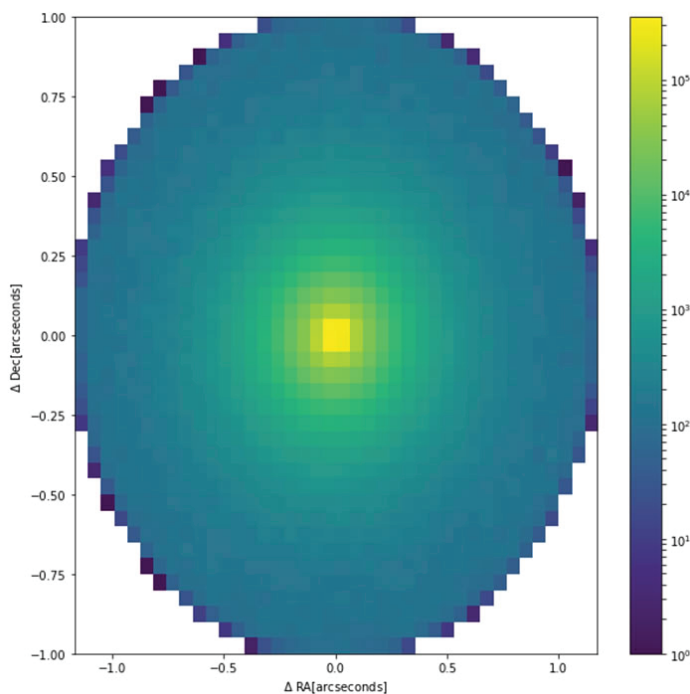


Figure 2 Delta Right Ascension v. Delta Declination

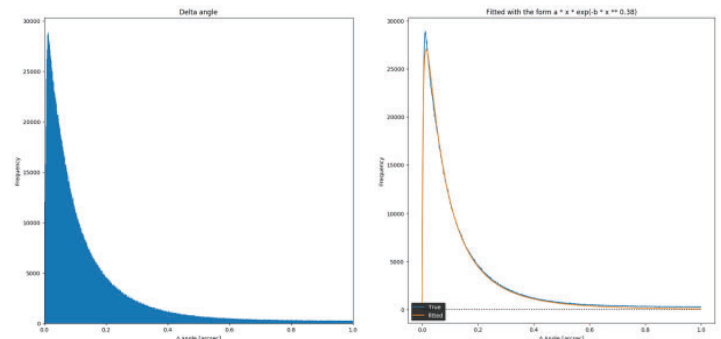


Figure 3 Angular Separation

Figure 4 Fitted Histogram Values

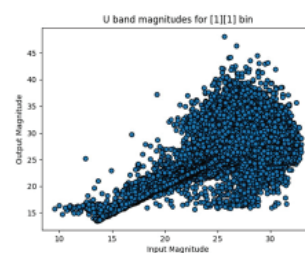


Figure 5 U-Band

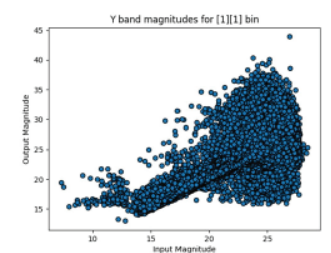


Figure 6 Y-Band

long wavelengths (320nm to 1050nm). This is done to observe as much of the sky as possible because that wavelength range corresponds to everything between near-infrared to near-ultraviolet, including visible light.

Figures 5 and 6 show the magnitudes of the U and Y bands of LSST. As seen, there is a good correlation at brighter magnitudes, that is, from about 24 to 15, the magnitudes lie on a line, implying that there is good matching. On the lower end, that is, higher magnitude numbers, the flaring exists primarily because of noise in the data. This noise can be reduced using lensing filters to diminish the size of the data points as follows.

Figure 7 shows the effects of the HSC Lensing Filters on the output data. Each lensing filter accounts for the effects of lensing including a reduction in resolution, magnitude, blending, and the flux of light from a lensed object. Furthermore, filters on the magnitudes are also applied in order to remove any fake objects that may have been the result of high magnitude bleed off. The result of adding more filters reduces the count of the objects in each bin as expected. The significance of this result is that one can assess the efficiency of the flags, that is, do they cut out members only in the output catalog, or do they cut members in the input as well. The latter is an erroneous result and therefore, the filters still require fine-tuning for accuracy.

Figure 8 shows the comparison between the filtered data's magnitude (brightness) and input data's magnitude. There is strong correlation between both as the data points go up in a straight line, further implying that the FoF algorithm is successful in determining which data points from the input and output catalogs should be grouped together. However, there is a rather

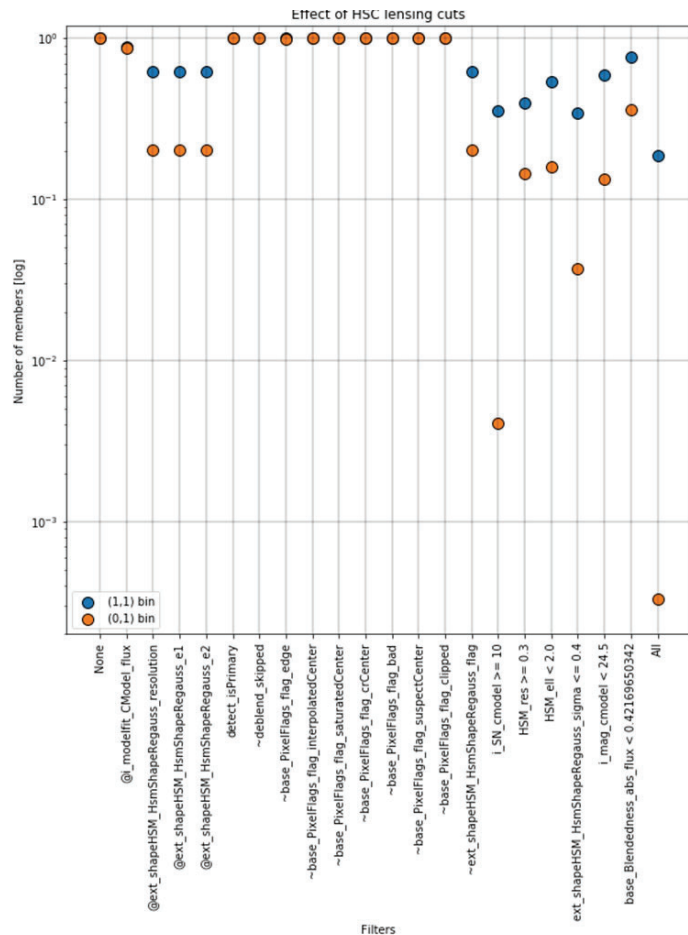


Figure 7 HSC Lensing Cuts

large group of points centered approximately around the [24][20] magnitude. While these objects are not very bright, (higher the magnitude number corresponds to a lower magnitude), they are prominent and show significant deviation from the linear correlation. The best way to analyze this discrepancy is to create “postage stamps” of the objects in question. These “postage stamps” are images of the objects, or better, the patch of the sky that these objects reside in. The image will then show what is causing the objects in the output to “cluster” whether it be gravitational lensing or even a faulty detection of the output catalog. The research into this matter still remains ongoing.

IV. Conclusions

Overall, testing of the FoF Catalog Matching algorithm proved to be successful in many ways. Over the coming months, more testing will continue on the entire data management pipeline as more results from Data Challenge 2 and subsequent data challenges are made available. Additionally, deblending algorithms will be run in tandem with FoF Catalog Matching in order to achieve better data resolution. The Data Management System should be operational by first light in 2019.

V. Acknowledgements

I would like to thank my mentor Anže Slosar for his continued guidance and support during this project. Additionally, I would like to thank the members of the U.S. Department of Energy Office of Educational Programs for their sponsorship through the Science Undergraduate Laboratory Internships (SULI) program.

VI. References

- Abate, Alexandra. “LSST Project.” LSST Project | Dark Energy Science Collaboration, LSST Corporation, 2018, [lsstdesc.org/LSST](https://www.lsst.org/LSST).
- Juric, Mario, et al. “The LSST Data Management System.” Arxiv.org, University of Washington, Seattle, 24 Dec. 2015, arxiv.org/pdf/1512.07914.pdf.
- Sanchez, Javier. “Introduction to the DESC Data Challenge 2 (DC2).” Linea.gov.br, Dark Energy Science Collaboration, 2017. PDF File.

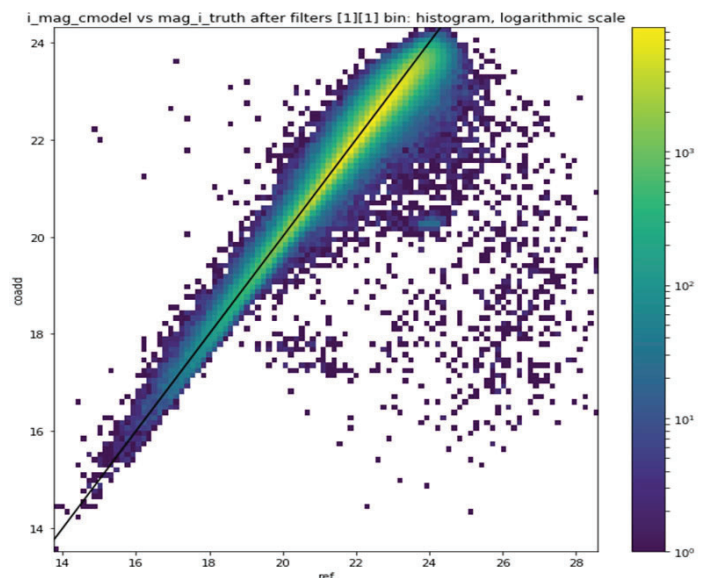


Figure 8 Filtered and True Magnitudes

Observational analysis of pollinators and their resources: Long Island Central Pine Barrens Forest

Dulaine Vining

Natural Sciences, Southern University at New Orleans, New Orleans, LA. 70122

Timothy Green

Environmental Science Division, Brookhaven National Laboratory, Upton, NY. 11973

Abstract

Long Island Central Pine Barrens forest provide an array of varied ecosystems for pollinators, vegetation, and other species. Pollinators *Bombus* species (bumblebees) and their resources e.g., *Securigera varia* (purple crown vetch) and other vegetative species were observed on solar farm and forest interior sampling sites used for this baseline observational study during early June through July of 2018. The Long Island Solar Farm (LISF) at Brookhaven National Laboratory (BNL) encompasses flat- opened terrains and meadowlands leading into forest's edges, compared to forest interiors which are usually comprised of scattered patches of sunlight, shrubs, and dense canopy. This baseline study will focus on bumblebee sightings/visitations between solar arrays #1 and #2 of the LISF. Analyzing and comparing sightings/visitations during observation periods was used to determine the preferred vegetative resource selected by bumblebees at random geographical locations. In contrast, I was only able to collect data in the solar farm for 3 weeks and the remainder of observations were completed in the forest interior. Inconclusively, lack of full flight season of bumblebees creates a need for continuation and funding of this baseline research. Possible findings could include frequency points of bumblebees increases/decreases on solar farms and forest interior based on the available resources. Furthermore, continuing this project may include: understanding phenological periods of the northeastern region, whether reduction of vegetative species is based on climate, selectivity or other unknown factors that possibly play a role in increase/decrease frequency of sightings/visitation to the solar farm versus interior forestry points by bumblebees of Long Island Central Pine Barrens forest.

I. Introduction

Long Island Central Pine Barrens forest sits on approximately 42,500 hectares of land¹ which Brookhaven National Lab comprises approximately 5%². The solar farm is a renewable energy project that services power to several thousands of residents in the surrounding communities. In addition, the solar farm provides unrestricted access allowing plants and pollinator diversity to increase. Current data during the same observational period highlights solar farm areas confirming multiple sightings of bumblebees with purple crown vetch as the dominant flowering plant species. An observational analysis between the solar farm and interior terrains of the Pine Barrens forest will seek to understand available resources necessary to sustain bumblebees during flight seasons. In addition, there are multiple other factors; whether its environmental or normal phenological periods,³ in which the months of June and July sightings of bumblebees are zero. Long Island Central Pine Barrens forest interiors yields dense populations of trees e.g., Pine trees, Oak trees, and patchy

colonies of shrubs e.g., blueberry and huckleberry are evidence of bumblebee visitations. Much can be hypothesized about Long Island Central Pine Barrens forests lack of natural water resources, which is a necessary element to promote increase pollination within the forest interior. However, it remains unclear if resources of bumblebees are based on selectivity of specific plant species, phenological periods, and/or unknown visitation traits of *Bombus* spp. During data collecting periods, observations show the solar farm, meadowlands, and forest edges are preferred resources for bumblebees where populations of purple crown vetch were abundant. At some point during one full flight season (provide full flight season for bumblebees as a point of reference) other than the months June and July, bumblebees migrate to terrains where flowering plants are in abundance within the Long Island Central Pine Barrens forest preserve.

II. Material & Methods

To ensure a clear comparative analysis between both sampling sites, the solar farm and the forest interior certain points were randomly selected to compare pollinators, plant's locations, and resources of bumblebees. Solar farms were the primary sampling sites for observations and data collection for this baseline research study. Hand-held devices (Kestrel Model 3000) were used during data collection period of early June through early July. Most, if not all the species collected were members of the *Bombus*. A total of five quadrants (1 m²) were used to identify specific vegetative species on each 50m line transect to ensure accuracy of collecting and identifying pollinators and plants. In the forest's interior, radio- transmitters outfitted for eastern box turtles were used primarily as comparative sampling sites to gain geographical locations. At each random location, a 7 m radius was used as guidance observing pollinators and identifying vegetation within that point. Observational analysis and data collecting were required to capture or omit sightings of pollinators within forest's interiors. Data was analyzed by comparing forest interior to solar farms, meadowlands, and forest edges observational sighting of *Bombus* within these terrains.

III. Results

Data proves between the months of June and July no sightings of bumblebees were observed (figure #1). Data were also inconclusive due to inability to capture data during an entire full flight season. Outside of the data collection period it remains unknown at what part of the phenological period of bumblebee's sightings increases/decreases within the forest's interior. Solar farms, meadowlands, and the forest's interior were optimal resources for bumblebees, rather than the forest's interior. Although blueberry shrubs were the dominant plant species (figure #2), it is unclear why bumblebees gravitate to solar farms; a sharp contrast from forest interior areas during the same flight season.

IV. Discussion/Conclusion

Much can be hypothesized about pollinators; however, the facts prove *Bombus* spp are not the prevalent pollinators during the observational periods between June and July. With randomly selected geographical coordinates, it is unknown the visitational timeframes of bumblebees within the forest's interior currently. Sightings of multiple scattered patches of shrubs with blueberry as the dominant plant species observed at these randomly selected locations indicates at some point during one flight season bumblebees are possibly partly responsible for cross pollinating and pollinating plants within the forest's interior. Noticeably, upon observing various arrays containing different terrains within Long Island Central Pine Barrens forest, natural water resources sightings were infrequent. Precipitation was not considered as a possible variable; possibly, it should be noted as a factor in resources for pollinators. Water is essential to flowering plants and is necessary for promoting growth. Without previous data, environmental factors cannot be ruled out e.g., drought conditions, selectivity of terrains or plant species by bumblebees, or global declinations of *Bombus* spp. It is worth to mention, the gypsy moth was observed in all arrays of the forest interior, meadowlands, forest edges, and solar farms. The gypsy moth is not a main pollinator; however, it could be one or multiple factors affecting bumblebee's frequency/visitations to forest interior areas, mainly upon visits from moths and other insects that destroys a variety of plant resources where bumblebees may visit ⁴. Naturally, without an abundance of plant species within the forest's interior at certain times of the flight season sightings will be limited of pollinators. Furthermore, future research and funding of this baseline project will assist other study researchers with necessary data and tools to better understand pollinators are their resources on Long Island Central Pine Barrens forest.

V. Works Cited

(n.d.).
Brookhaven National Lab. (n.d.). Retrieved from [bnl.gov](https://www.bnl.gov/stakeholder/naturalResources.php):
<https://www.bnl.gov/stakeholder/naturalResources.php>
 Campana, R. J. (1999). *Arboriculture: History and development in North America*. East Lansing: East Lansing University Press.
Central Pine Barrens Joint Planning Commission. (2018).
 Retrieved from <https://pb.state.ny.us/central-pine-barrens/overview/>

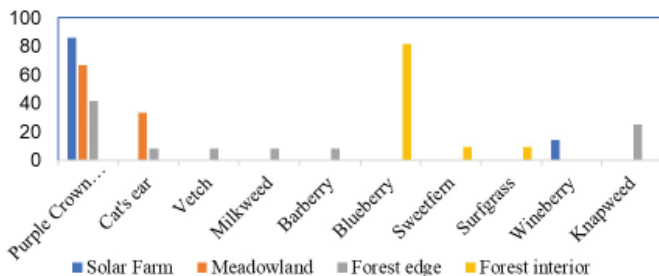


Figure 1. Percentage of plant diversity in sampling sites at BNL: Purple Crown Vetch was the dominant flowering plant located on solar farms, meadowlands, and forest edges. Data during observational period also shows the forest's interior main plant species were blueberry at each random site.

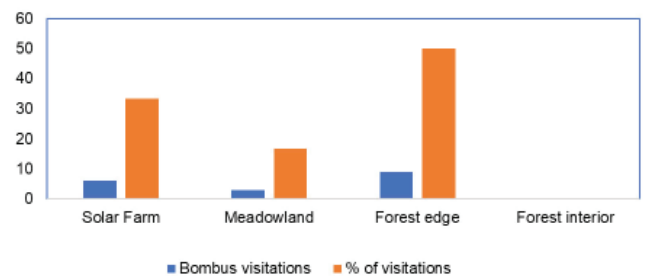


Figure 2. Percentage of *Bombus* visitations: Forest edges were the dominant selective locations chosen by bumblebees. Next, the solar farm where other variety of plant species were located. Notice the forest interior with zero sightings, compared to other sampling sites.

Implementation of a digital repository catalog prototype using the Invenio framework at the Scientific Data and Computing Center

Jaelin Williams

Mathematics, Computer and Information Science, SUNY at Old Westbury, Old Westbury, NY, 11568

Antonio Wong and Carlos Gamboa

Physics, Brookhaven National Laboratory, Upton, NY 11973

Abstract

The Scientific Data and Computing Center (SDCC) at Brookhaven National Laboratory (BNL) plays an integral role in addressing the scientific challenges presented by data-driven and computational activities within the Relativistic Heavy Ion Collider and A Toroidal LHC Apparatus Computing Facility (RACF). One of the core areas of research and development at the SDCC is the protection and preservation of scientific information and knowledge acquired at the various research facilities at BNL. A rising necessity of the scientific community is the need for a software framework to develop applications to implement a digital library system for archiving and publishing information, scientific data, and publications. By adopting the Invenio open-source software framework developed by the European Organization for Nuclear Research (CERN) at the SDCC, we can efficiently facilitate a large-scale digital repository at BNL. This framework provides the software basis for the laboratory to manage publicly accessible digital resources in the repository instantiated by the Invenio framework. There are two main phases in the Invenio prototype that I worked on. The initial phase is deploying and testing the development instance Integrated Library System on a local and virtual machine; the final phase is rolling out the code to a production environment. This procedure involved replicating the component installation of an instance multiple times and then transferring to an automated instance. Upon deploying a demo instance, Invenio allows for records with pre-defined schema to be uploaded to the site and retrieved. Multiple successful Invenio instance prototypes have been generated towards a polished and production-ready digital repository for the SDCC.

I. Introduction & Hypothesis

For additional background on Invenio and its applied purposes, it is necessary to understand the facilities that require the utility of the framework, as well as analyze the structure of it and its components. The RACF at BNL allocates computing services for the experiments conducted at the Relativistic Heavy Ion Collider (RHIC) at BNL, the US-based collaborators in the ATLAS experiment at the Large Hadron Collider at CERN, the collaborators in the Large Synoptic Survey Telescope project, in addition to other experiments throughout the world¹. As a core contributor of the RACF, the SDCC provides high performance and data intensive computing, management and preservation². Data accessibility and distribution are vital to the discourse of discovery for both the scientific community and the public, which is evidently why CERN developed Invenio.

Invenio is an open-source software framework written in Py-

thon that provides the necessary tools to manage digital resources in data management systems and institutions. It is comprised of Flask (a microframework written Python), Jinja2 (a template engine for Python), and Celery (an open-source asynchronous job queue written in Python). In terms of the application architecture, Invenio is built on-top of the Flask web development framework, and it adds an application factory on top of Flask. The Invenio application factory is implemented by the base module and assembles the app in five phases: application creation, configuration loading, URL converter loading, flask extensions loading and blueprints loading. The Invenio application module implements the default Flask applications for Web Server Gateway Interface (WSGI), CLI (command-line interface), and Celery (job queue). For the scientific community, the adoption of Invenio allows for the development of applications that would allow for scientific data, information and publications to be archived and published to a digital library system for later access. It can also be made publicly accessible if desired. CERN used their Invenio framework to create some repositories of their own, including Zenodo, CDS Videos, and CERN Open Data.

Providing a repository powered by the Invenio framework to BNL can prove to be substantially useful, thus, I conducted guided research and testing at the SDCC at BNL to establish an Invenio prototype.

II. Materials, Methods & Implementation

The first step to begin the initialization and implementation of an Invenio digital repository prototype was to conduct research on the core components of Invenio. CERN's official Invenio website³ and attached Invenio documentation⁴ included detailed instructions on how to initiate an Invenio framework demo instance through the compilation of the necessary operational components, which are also referenced on their site. To better understand how Invenio works, the individual working parts of the framework had to be dissected to obtain a comprehension of their use cases, implementation and possible troubleshooting methods.

Docker, the first component, is a computer program that conducts containerization (OS-level virtualization). Accompanying Docker is Docker Compose, which is a tool for defining and running multi-container Docker applications. Next is Node.js; an asynchronous JavaScript runtime used to build scalable network applications, and along with it, NPM; a JavaScript package manager (pm) that is the default pm for Node.js. The successive components are Cookiecutter, a tool for creating projects from project templates, and virtualenv, a utility used to create isolated Python environments. Last, is Bootstrap, which is an opensource front-end framework used to design websites and web applications. In addition to the installation components, there are also services and

dependencies that accompany a deployed instance. These include a database (either PostgreSQL or MySQL), Elasticsearch, which is a search engine that uses the representational state transfer protocol, Redis, an open source in-memory data structure store that is used as a database, cache and message broker/organizer, and RabbitMQ, a message-broker software that manages and transfers queues.

Through the installation and configuration of all the necessary Invenio segments, the demo instance was able to run on my local workstation. At this timeframe, a user could create an account on the site, login to the system, search for a record using keywords, and obtain a requested record. Furthermore, the demo instance that was deployed allowed me to create and POST a record (using curl) to the development server through my virtual environment in the terminal, and after it was uploaded to the demo site, it could be retrieved by a simple search query based on the schema of the record.

The next task was to deploy Invenio through a virtual machine to move closer towards a production model. Previously, the Invenio test instance was only accessible on my physical desktop, so its utility was somewhat impaired in scope. By deploying the instance on a virtual machine owned by BNL, the repository became accessible to the entire RACF at the lab. This process was more efficient and seamless than it was on the local machine because of the greater familiarity acquired from the installation processes and troubleshooting methods that were encountered initially. The following course of action was to daemonize (automate) the application to make it better integrated. This process entailed initializing configuration files that contain instructions for process execution.

Up until this point, the demo instance that had been deployed was only reachable via the local machine and the virtual machine that I had been testing on. To transition to an integrated application setup, the instance needed to be hosted on a server that was available to the target userbase (in this case, the RACF). To get this to work, the services of three utilities were required; supervisor, nginx and uWSGI. Supervisor is a client/server system that allows users to control processes within UNIX based systems. With this tool, the necessary configurations were ran in the background and their statuses could be monitored. Nginx is a reverse proxy server, of which, was used to host the instance through https redirection. uWSGI is a software application used for building host services; it works very closely with nginx. After these components were configured, I deployed the production server that is

accessible to the whole facility. Now, if anyone in the RACF uses my virtual machine's URL, they can access the site.

At this moment, the Invenio instance that I deployed was configured and themed with the preassigned defaults that were set by the Invenio developers at CERN. It is a prototype so reconfiguration is expected; to customize it, I adjusted the theme, text and logos to suit my preferences. The Invenio demo theme color is a light blue, which is consistent with their logo. I decided to alter the main theme color to one that I'd describe as "Brookhaven red" (a darker shade of the color of the dot in the letter 'a' of the BNL logo). This was done by changing the default value of the main color profile. Additionally, I replaced the blue Invenio logo with the official white BNL logo provided by the laboratory site. Now, my instance has a more BNL-like design language. The subsequent and final phase was to experiment with pyresttest, which is a Python-based RESTful API testing and micro-benchmarking tool. This utility allows users to pass a JSON and URL to the server more conveniently than curl, since preconfigurable parameters could be set instead of defining the schema manually each time.

III. Discussion & Conclusion

The Invenio software framework provides a plethora of tools and resources that make it a tremendously versatile and robust baseline for creating large-scale digital repositories. It has the potential to become an important piece in data preservation and access for experiments conducted at RHIC and under the ATLAS experiment here at BNL, as it has already for the LHC and ATLAS at CERN. My experimentation and testing were a microcosm of the possibilities that Invenio offers to developers that use it. Working with a web-based framework was a new endeavor for me, and there were many obstacles and challenges that I was presented with. Despite these difficulties, I succeeded in deploying a customized, functional production instance to the RACF.

IV. Acknowledgements

This project was supported in part by the U.S. Department of Energy, Office of Science, Office of Workforce Development for Teachers and Scientists (WDTS) under the Science Undergraduate Laboratory Internships Program (SULI). I would like to extend a special thanks to my mentor Antonio Wong, as well as to my supervisor Carlos Gamboa for their guidance, assistance and hospitality throughout the duration of this program. Also, I want to thank each of the other administrators, staff and scientists who helped make my experience under the SULI program at Brookhaven National Laboratory a fruitful one.

V. References

- ¹De Stefano, J. S. "The RHIC and ATLAS Computing Facility." RACF Computing Facility, 5 Jan. 2017, www.racf.bnl.gov/.
- ²"BNL Scientific Data and Computing Center." BNL Scientific Data and Computing Center, www.bnl.gov/compsci/SDCC/.
- ³"Welcome - Inveniosoftware.org." Welcome - Inveniosoftware.org, invenio-software.org/.
- ⁴"Invenio v3." Invenio v3 - Invenio 3.0.0 Documentation, CERN, invenio.readthedocs.io/en/latest/.



Figure 1. These are some repositories built using Invenio which include Zenodo, CDS Videos and CERN Open Data. Image courtesy of CERN via invenio-software.org



Figure 2. Invenio documentation homepage
Image courtesy of CERN via invenio.readthedocs.io 4

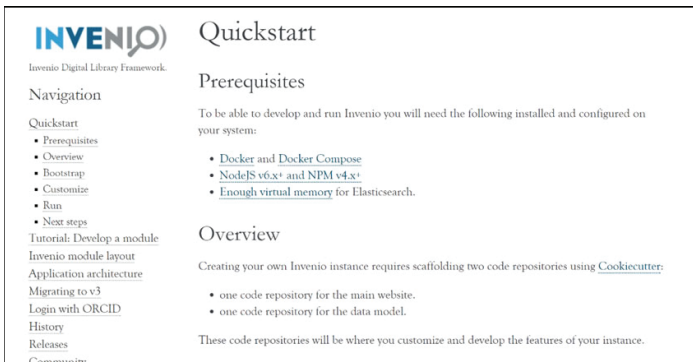


Figure 3. Invenio Quickstart page with installation components
Image courtesy of CERN via invenio.readthedocs.io 4

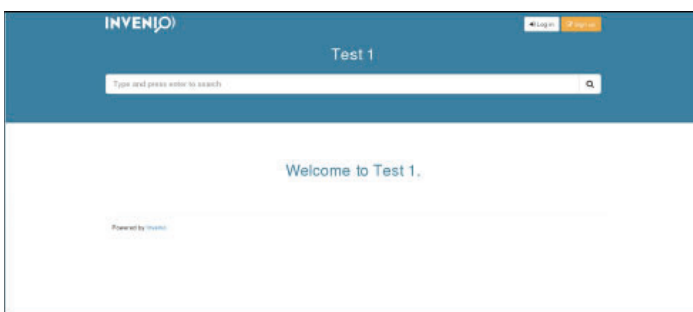


Figure 5. Initial Invenio test instance homepage

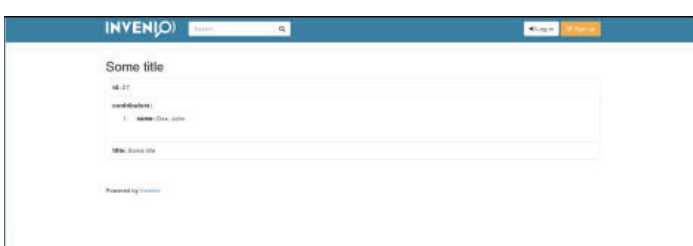


Figure 7. Initial Invenio test instance record page

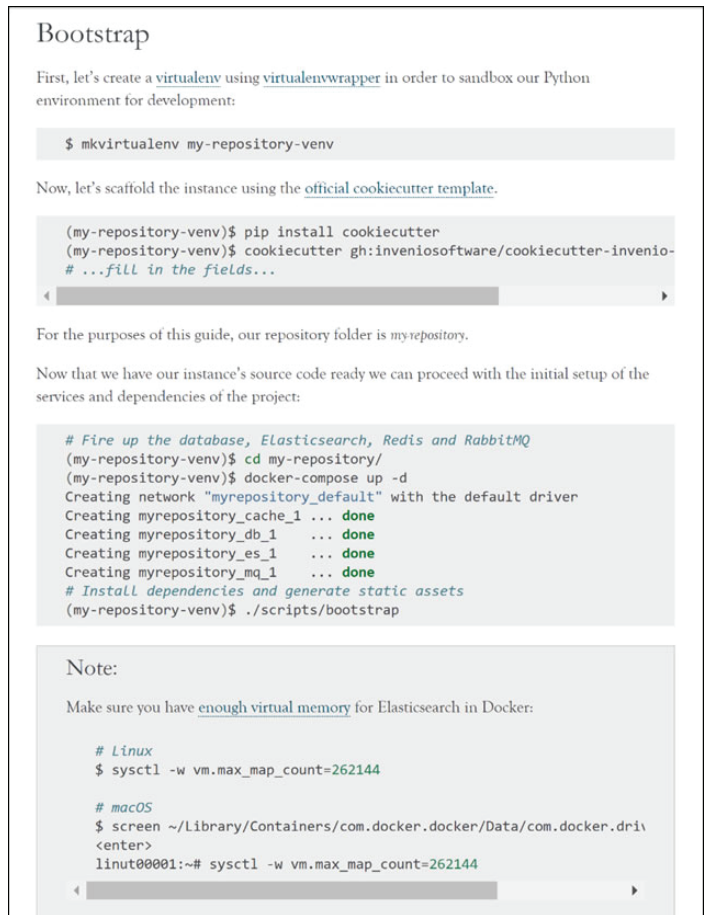


Figure 4. Invenio Quickstart page with service and dependency components
Image courtesy of CERN via invenio.readthedocs.io 4

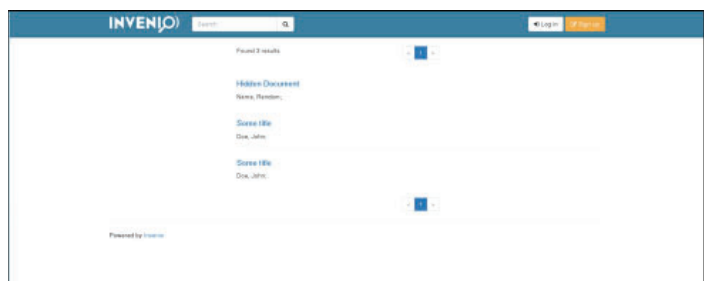


Figure 6. Initial Invenio test instance search query page

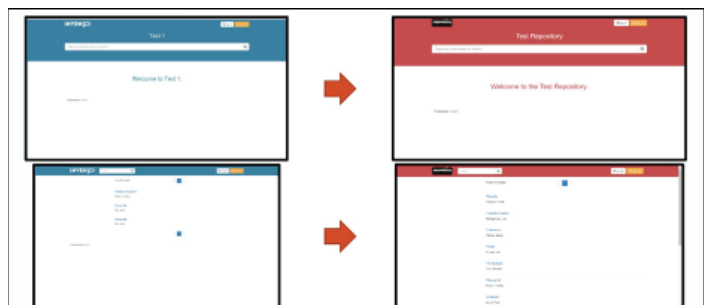


Figure 8. A comparison of the default instance and the modified test instance